

AD-A148 132

U  
Bulletin 54  
(Part 2 of 3 Parts)

20000804037

# THE SHOCK AND VIBRATION BULLETIN

Part 2  
Ship Shock, Shock and  
Blast and Ground Shock

JUNE 1984

A Publication of  
THE SHOCK AND VIBRATION  
INFORMATION CENTER  
Naval Research Laboratory, Washington, D.C.

Reproduced From  
Best Available Copy



DTIC  
ELECTE  
AUG 15 1984  
S A D

Office of  
The Under Secretary of Defense  
for Research and Engineering

Approved for public release; distribution unlimited.

84 08 09 047

**SYMPOSIUM MANAGEMENT**

**THE SHOCK AND VIBRATION INFORMATION CENTER**

**J. Gordan Showalter, Acting Director**

**Rudolph H. Volin**

**Jessica Hileman**

**Elizabeth A. McLaughlin**

**Mary K. Gobbett**

**Bulletin Production**

**Publications Branch, Technical Information Division,  
Naval Research Laboratory**

**Bulletin 54**  
**(Part 2 of 3 Parts)**

# **THE SHOCK AND VIBRATION BULLETIN**

**JUNE 1984**

**A Publication of  
THE SHOCK AND VIBRATION  
INFORMATION CENTER  
Naval Research Laboratory, Washington, D.C.**

**The 4th Symposium on Shock and Vibration was held in Pasadena, California, October 18-20, 1983. The Jet Propulsion Laboratory in Pasadena was the host.**

**Office of  
The Under Secretary of Defense  
for Research and Engineering**



Blast and Ground Shock

ASSESSMENT OF SEISMIC SURVIVABILITY R. E. McClellan, The Aerospace Corporation, El Segundo, CA	193
GROUND SHOCK EFFECT ON SOIL FIELD INCLUSIONS R. E. McClellan, The Aerospace Corporation, El Segundo, CA	203
PENETRATION OF SHORT DURATION AIRBLAST INTO PROTECTIVE STRUCTURES J. R. Britt and J. L. Drake, Applied Research Associates, Southern Division, Vicksburg, MS	209
A COMPUTATIONAL PROCEDURE FOR PEAK INSTRUCTURE MOTIONS AND SHOCK SPECTRA FOR CONVENTIONAL WEAPONS S. A. Kiger, J. P. Balsara, and J. T. Baylot, USAE Waterways Experiment Station, Vicksburg, MS	223
PRELIMINARY DESIGN CRITERIA AND CERTIFICATION TEST SPECIFICATIONS FOR BLAST RESISTANT WINDOWS G. E. Meyers, W. A. Keenan, and N. F. Shoemaker, Naval Civil Engineering Laboratory, Port Hueneme, CA	227

PAPERS APPEARING IN PART 1

Welcome

WELCOME

Robert J. Parks, Associate Director, Space Science and Exploration, Jet Propulsion Laboratory, Pasadena, CA

Keynote Address

KEYNOTE ADDRESS

Robert S. Ryan, George C. Marshall Space Flight Center, Huntsville, AL

Invited Papers

DNA ICBM TECHNICAL R&D PROGRAM

Colonel Maxim I. Kovel, Director, Shock Physics Directorate, Defense Nuclear Agency, Washington, DC

SOME DYNAMICAL ASPECTS OF ARMY MISSILE SYSTEMS

Dr. James J. Richardson, Chief, Structures and Mechanics, U.S. Army Missile Command, Redstone Arsenal, AL

AIR FORCE SPACE TECHNOLOGY CENTER SPACE TECHNOLOGY — EMPHASIS 84

Colonel Frank J. Redd, Vice Commander, Air Force Space Technology Center, Kirtland AFB, NM

REFLECTIONS ON TRENDS IN DYNAMICS — THE NAVY'S PERSPECTIVE

Henry C. Pusey, Consultant, NKF Engineering Associates, Inc., Vienna, VA

ELIAS KLEIN MEMORIAL LECTURE — MODAL TESTING — A CRITICAL REVIEW

Strether Smith, Lockheed Palo Alto Research Laboratory, Palo Alto, CA

SOLUTIONS TO STRUCTURAL DYNAMICS PROBLEMS

Dr. George Morosow, Martin Marietta Corporation, Denver, CO

WHERE IS THE REAL LITERATURE ON AIRBLAST AND GROUND SHOCK?

Dr. Wilfred E. Baker, Southwest Research Institute, San Antonio, TX

MIL-STD-810D

TAILORING INITIATIVES FOR MIL-STD-810D ENVIRONMENTAL TEST METHODS AND ENGINEERING GUIDELINES

David L. Earls, Air Force Wright Aeronautical Laboratories, Wright-Patterson AFB, OH

ACCELERATION RESPONSES OF TYPICAL LRU'S SUBJECTED TO BENCH HANDLING AND INSTALLATION SHOCK

H. Caruso and E. Szymkowiak, Westinghouse Electric Corporation, Baltimore, MD

IMPACT OF 810D ON DYNAMIC TEST LABORATORIES

Dr. Allen J. Curtis, Hughes Aircraft Company, El Segundo, CA

**THE CHANGING VIBRATION SIMULATION FOR MILITARY GROUND VEHICLES**  
Jack Robinson, Materials Testing Directorate, Aberdeen Proving Ground, MD

PANEL DISCUSSION — MIL-STD-810D

PAPERS APPEARING IN PART 3

Structural Dynamics

**STRUCTURAL MODIFICATIONS BY VISCOELASTIC ELEMENTS**  
P. J. Riehle, Anotrol Corporation, Cincinnati, OH

**STOCHASTIC DYNAMIC ANALYSIS OF A STRUCTURE WITH FRICTIONAL JOINTS**  
Q. L. Tian and Y. B. Liu, Institute of Mechanics, Chinese Academy of Sciences and D. K. Liu,  
Space Science & Technology Centre, Chinese Academy of Sciences, Beijing, China

**MODAL ANALYSIS OF STRUCTURAL SYSTEMS INVOLVING NONLINEAR COUPLING**  
R. A. Ibrahim, T. D. Woodall, and H. Heo, Department of Mechanical Engineering, Texas Tech University,  
Lubbock, TX

**DISCRETE MODIFICATIONS TO CONTINUOUS DYNAMIC STRUCTURAL SYSTEMS**  
Y. Okada, Ibaraki University, Hitachi, Japan, B. P. Wang, University of Texas at Arlington, Arlington, TX,  
and W. D. Pilkey, University of Virginia, Charlottesville, VA

**REANALYSIS OF CONTINUOUS DYNAMIC SYSTEMS WITH CONTINUOUS MODIFICATIONS**  
B. P. Wang, University of Texas at Arlington, Arlington, TX, Y. Okada, Ibaraki University, Hitachi, Japan,  
and W. D. Pilkey, University of Virginia, Charlottesville, VA

**A POLE-FREE REDUCED-ORDER CHARACTERISTIC DETERMINANT METHOD FOR LINEAR VIBRATION  
ANALYSIS BASED ON SUB-STRUCTURING**  
B. Dawson, Polytechnic of Central London, London, England, and M. Davies, University of Surrey,  
Guildford, Surrey, England

**DETERMINATION OF SHEAR COEFFICIENT OF A GENERAL BEAM CROSS SECTION BY  
FINITE ELEMENT METHOD**  
C. M. Friedrich and S. C. Lin, Westinghouse Electric Corporation, Bettis Atomic Power Laboratory,  
West Mifflin, PA

Machinery Dynamics

**GEAR CASE VIBRATION ISOLATION IN A GEARED TURBINE GENERATOR**  
R. P. Andrews, Westinghouse Electric Corporation, Marine Division, Sunnyvale, CA

**EFFECT OF COUPLED TORSIONAL-FLEXURAL VIBRATION OF A GEARED SHAFT SYSTEM  
ON THE DYNAMIC TOOTH LOAD**  
S. V. Neriya, R. B. Bhat, and T. S. Sankar, Concordia University, Montreal, Quebec, Canada

**PRECISION MEASUREMENT OF TORSIONAL OSCILLATIONS INDUCED BY GEAR ERRORS**  
S. L. Shmuter, Ford Motor Company, Manufacturing Processes Laboratory, Dearborn, MI

**THE ANALYSIS BY THE LUMPED PARAMETER METHOD OF BLADE PLATFORM FRICTION  
DAMPERS USED IN THE HIGH PRESSURE FUEL TURBOPUMP OF THE SPACE  
SHUTTLE MAIN ENGINE**  
R. J. Dominic, University of Dayton Research Institute, Dayton, OH

Vibration Problems

**TRANSIENT VIBRATION TEST CRITERIA FOR SPACECRAFT HARDWARE**  
D. L. Kern and C. D. Hayes, Jet Propulsion Laboratory, California Institute of Technology, Pasadena, CA

**VIBRATIONAL LOADING MECHANISM OF UNITIZED CORRUGATED CONTAINERS WITH  
CUSHIONS AND NON-LOAD-BEARING CONTENTS**  
T. J. Urbanik, Forest Products Laboratory, USDA Forest Service, Madison, WI

**LEAKAGE-FLOW INDUCED VIBRATIONS OF A CHIMNEY STRUCTURE SUSPENDED IN A LIQUID FLOW**  
H. Chung, Components Technology Division, Argonne National Laboratory, Argonne, IL

**THE EXPERIMENTAL PERFORMANCE OF AN OFF-ROAD VEHICLE UTILIZING  
A SEMI-ACTIVE SUSPENSION**

E. J. Krasnicki, Lord Corporation, Erie, PA

**EFFECT OF AIR CAVITY ON THE VIBRATION ANALYSIS OF LOADED DRUMS**  
S. De, National Research Institute, W. Bengal, India

SESSION CHAIRMEN AND COCHAIRMEN

<u>Date</u>	<u>Session Title</u>	<u>Chairmen</u>	<u>Cochairmen</u>
Tuesday, 18 Oct. A.M.	Opening Session	Dr. Ben Wada, The Jet Propulsion Laboratory, Pasadena, CA	Dr. J. Gordan Showalter, The Shock & Vibration Information Center, Naval Research Laboratory, Washington, DC
Tuesday, 18 Oct. P.M.	Elias Klein Memorial Lecture. Plenary A	Dr. J. Gordan Showalter, Shock and Vibration Information Center, Naval Research Laboratory Washington, DC	
Tuesday, 18 Oct. P.M.	Ship Shock	Mr. Gene Remmers, David Taylor Naval Ship Research and Development Center, Bethesda, MD	Dr. Michael Paksyts, NKF Engineering Associates, Vienna, VA
Tuesday, 18 Oct. P.M.	Space Vibration	Mr. Jerome Pearson, Air Force Wright Aeronautics Laboratories, Wright-Patterson AFB, OH	Mr. John Garba, Jet Propulsion Laboratory, Pasadena, CA
Wednesday, 19 Oct. A.M.	Plenary B	Mr. William J. Walker, Boeing Aerospace Company, Seattle, WA	Dr. George Morosow, Martin Marietta Corporation, Denver, CO
Wednesday, 19 Oct. A.M.	Structural Dynamics	Mr. Edward Fleming, The Aerospace Corporation, Los Angeles, CA	Dr. John Gubser, McDonnell Douglas Astronautics Company, St. Louis, MO
Wednesday, 19 Oct. A.M.	MIL-STD-810D Session I, Rationale	Mr. John Wafford, Aeronautical Systems Division, Wright Patterson AFB, OH	Mr. Robert Hancock, Vought Corporation, Dallas, TX
Wednesday, 19 Oct. P.M.	Shock	Mr. Ami Frydman, Harry Diamond Laboratories, Adelphi, MD	Mr. Martin Walchak, Harry Diamond Laboratories, Adelphi, MD
Wednesday, 19 Oct. P.M.	MIL-STD-810D Session II, Implementation and Use	Mr. Rudolph H. Volin, Shock and Vibration Information Center, Washington, DC	Mr. W. W. Parmenter, Naval Weapons Center, China Lake, CA
Thursday, 20 Oct. A.M.	Blast/Ground Shock	Mr. William Flathau, U.S. Army Engineer Waterways Experiment Station, Vicksburg, MS	Mr. George Coulter, U.S. Army Ballistic Research Laboratory, Aberdeen Proving Ground, MD
Thursday, 20 Oct. A.M.	Machinery Dynamics	Dr. David Fleming, NASA Lewis Research Center, Cleveland, OH	Dr. Hanson Huang, Naval Surface Weapons Center, Silver Spring, MD
Thursday, 20 Oct. P.M.	Vibration Problems	Dr. Robert S. Reed, Jr., Naval Surface Weapons Center, Silver Spring, MD	Dr. Larry Pinson, NASA Langley Research Center, Hampton, VA
Thursday, 20 Oct. P.M.	Short Discussion Topics	Mr. Howard Camp, Jr., U.S. Army Electron Research and Development Command, Ft. Monmouth, NJ	Mr. E. Kenneth Stewart, U.S. Army Armament Research and Development Command, Picatinny Arsenal Dover, NJ

## SHIP SHOCK

### TWO-DIMENSIONAL SHOCK RESPONSE OF A MASS

#### ON ENERGY-ABSORBING SHOCK MOUNTS

R. E. Fortuna, Research Assistant, The Pennsylvania State University  
University Park, PA 16802

and

V. H. Neubert, Professor, The Pennsylvania State University  
University Park, PA 16802

The paper presents results of experimental and analytical studies of side-loaded, annealed, low carbon steel rings used as shock mounts. In a previous paper, reference [1], experimental static load-deflection curves were presented for side-loaded tubes loaded in three directions, called the compression, shear and roll directions. The two-inch diameter rings were driven deep into the plastic range, with deformation in each direction up to 70-80 per cent. of the ring diameter. Theoretical solutions in the plastic range exist only for the rings in compression, in references [4] and [3]. The load-deflection curves for side-loaded rings or tubes were compared with those for axially-loaded tubes, aluminum honeycomb, and a double-reverse corrugated metal in [1]. An advantage of the side-loaded tubes is that the load-deflection curves are almost flat after yielding occurs. Axially-loaded tubes and honeycomb show an initial high peak and a subsequent sharp drop-off in load, associated with buckling. Dynamic test results for the side-loaded rings under one-dimensional loading in compression were also presented in reference [1], obtained in a drop-table shock machine. Attenuation of transmitted acceleration similar to that achieved with Aeroflex mounts was achieved with only about half the rattle space required because of the permanent deformation of the side-loaded rings. The purpose of the present work was to obtain experimental data and carry out an associated analysis for the rings under combined loading, in compression (or tension) and roll. The study was supported by the Office of Naval Research under Contract No. N0014-79-c-0149.

#### INTRODUCTION

In a previous paper, Neubert [1], discussed the behavior of some metal configurations which could be used as nonlinear, energy-absorbing shock mounts. The configurations were aluminum honeycomb and low carbon steel end-loaded tubes, side-loaded tubes and a double-reverse-corrugated metal. The side-loaded tubes appeared to have two advantages: (1) they could be used as three-dimensional mounts deforming in compression, shear and roll and (2) in these three directions, the load-deflection curves were smooth with always positive slope and could be represented approximately as bilinear curves, with elastic stiffness  $k_e$  and plastic stiffness  $k_p$ .

In [1], analytical and experimental results were given for the dynamic response of a single-degree-of-freedom system on parallel and series arrangements of nonlinear mounts.

The present paper represents an extension of ref. [1]. Additional data is included for rings and U-shaped mounts in compression, to show how variations in  $k_e$  and  $k_p$  may be achieved in practice. The major portion of this paper deals with the two-dimensional experimental and theoretical response of a mass on side-loaded rings excited in a drop-table shock machine. It is demonstrated that the dynamic behavior can be predicted well during the loading phase of the response. This material is summarized from reference [2].

#### EXPERIMENTAL STATIC BEHAVIOR OF SIDE-LOADED RINGS

Experimental static load-deflection curves for three directions for side-loaded tubing were given in Fig. 21 of Ref. [1]. The rings were 2" dia. x 1/2" long x 0.065" thick. Four tubes were arranged in mounting clamps and tested in the clamps, as they might

be used in a practical application. The directions of loading are depicted in Fig. 1.

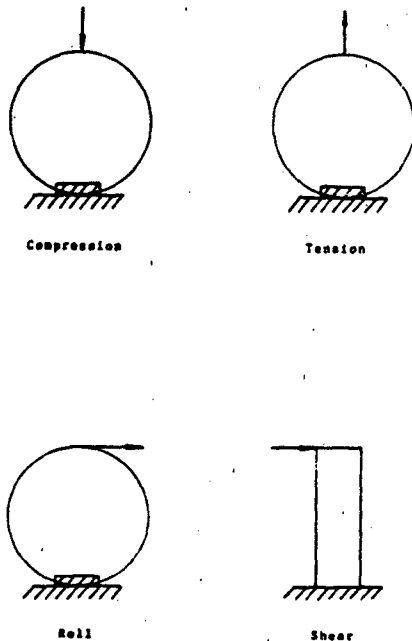


Fig. 1 - Response directions for side-loaded rings

A theoretical solution for the behavior of a ring in compression was presented by Kwang [3] and DeHunts and Hodge [4]. The ring is loaded between two platens as in Fig. 2a. Initially there are two point loads as shown, but as the ring deforms into the characteristic peanut shape, there are four point loads which move out from the center line of the ring, as shown in Fig. 2b. A point loading may be maintained by applying the load through small steel cylindrical bearings as in Fig. 2c and 2d. This affects the plastic stiffness  $k_p$ . To demonstrate this effect, a test was begun with a ring between two platens as shown in Fig. 3 and deformed about  $1/2$ " when the loading was terminated and the ring unloaded. Then the cylindrical bearings were inserted and the same ring re-loaded. Of primary interest is the fact that after yielding the slope of the load deflection curve using the bearings is much less than when the ring was simply between the two platens without the bearings. When mounting clamps are used, the load stays at the center-line and the situation approaches that of Fig. 2c. The ring used for Fig. 3 (note inset) had radius  $R=1$ ", length  $L=2$ ", thickness  $t=1/8$ " and  $W=2$ ". For  $W=2$ ", the configuration cross-section is circular. For  $W=2$ ", and  $R=1$ ", the cross-section is oval or a "double-U" shape. Load-deflection curves are

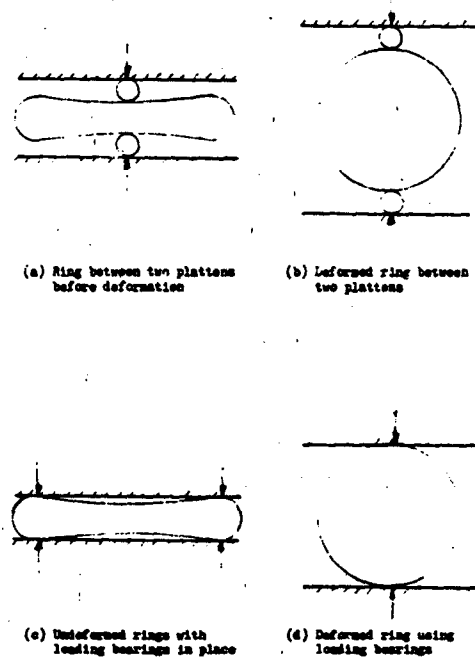


Fig. 2 - Deformed Ring

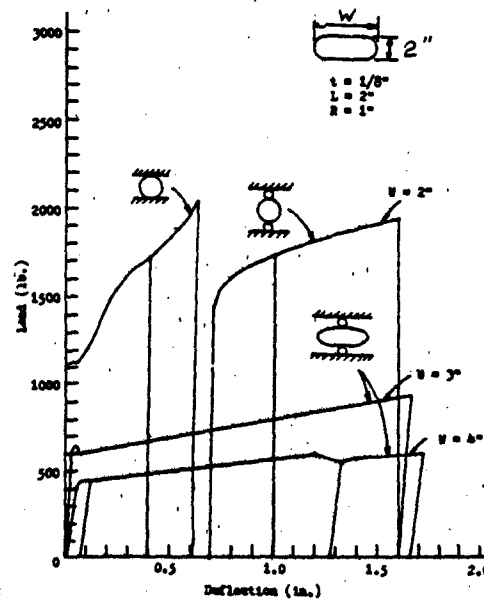


Fig. 3 - Load-deflection curves for rings and Double-U mounts in compression

also shown for two double-U shaped mounts, made of low carbon steel. The elastic stiffness and the plastic stiffness are both decreased by increasing  $W$ . Equations for predicting

the elastic stiffness and yield load of U-shaped metal mounts were given by Burns [5].

For the present two-dimensional tests on the shock machine the rings were tilted at a 30° angle, so two coordinate systems were used, as in Fig. 4.

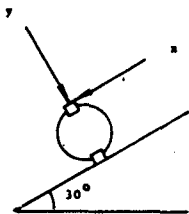


Fig. 4a - x and y loading directions

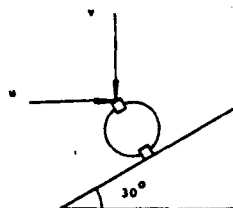


Fig. 4b - u and v loading directions

Fig. 4 - Loading directions for stiffness transformations

The x and y directions (Fig. 4a) correspond to the roll and compression directions, respectively, while the u and v directions, Fig. 4b, are the horizontal and vertical directions. In Fig. 5, load-deflection curves are shown for the roll (x direction) and tension and compression (y direction). As expected, the slopes in the elastic range for tension or compression are approximately the same. The x-y axes are principle directions of loading for the ring, such that in the elastic range, the forces and deflections would be related by a diagonal flexibility matrix.

$$\begin{Bmatrix} F_x \\ F_y \end{Bmatrix} = \begin{bmatrix} S_{xx} & 0 \\ 0 & S_{yy} \end{bmatrix} \begin{Bmatrix} x \\ y \end{Bmatrix} \quad (1)$$

On the other hand, the u-v axes are not principle, and a load in the u direction produces deflections in both the u and v directions, so the flexibility matrix is full:

$$\begin{Bmatrix} F_u \\ F_v \end{Bmatrix} = \begin{bmatrix} S_{uu} & S_{uv} \\ S_{vu} & S_{vv} \end{bmatrix} \begin{Bmatrix} D_u \\ D_v \end{Bmatrix} \quad (2)$$

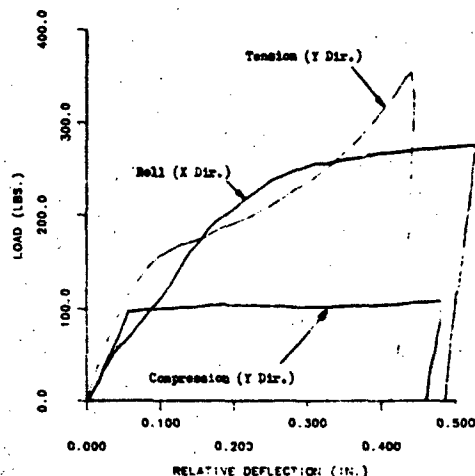


Fig. 5 - Plot of relative deformation versus load for one ring in three directions

The load-deflection curves for the u and v directions are shown in Fig. 6. In matrix

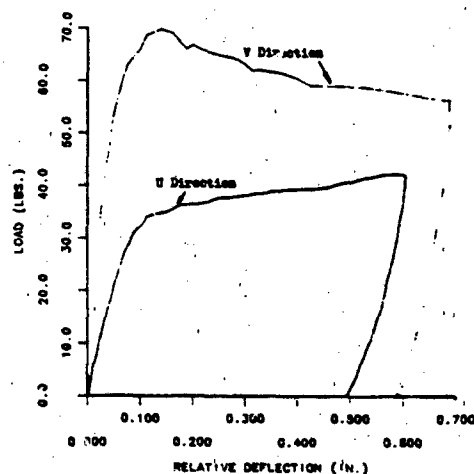


Fig. 6 - Plot of relative deformation versus load in the u and v direction for one ring

terminology, the flexibilities were measured in the u and v directions rather than stiffnesses, since measurement of true stiffnesses requires applying constraints against motion. For the x-y axes, the elastic flexibility matrix is diagonal, so  $S_{xx}^{-1} = k_{xx}$  and  $S_{yy}^{-1} = k_{yy}$ , where the k's are stiffnesses.

The theoretical representation of the load-deflection curves, as shown in Fig. 7, was

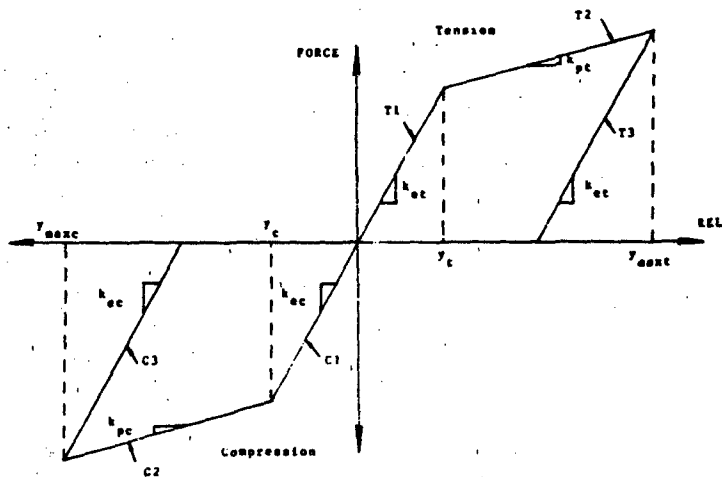


Fig. 7 - Generalized force-relative deflection plot

taken as bilinear. There are three branches of the curve in tension and three in compression, designated T1, T2, T3, C1, C2 and C3 respectively. The stiffnesses are

$K_{et}$  = elastic stiffness of branches T1 and T3, during loading and unloading

$K_{pt}$  = plastic stiffness in branch T2 during loading

$K_{ec}$  = elastic stiffness in branches C1 and C3

$K_{pc}$  = plastic stiffness in branch C2

The yield deformations are  $y_t$  and  $y_c$  and the maximum deformations are  $y_{maxt}$  and  $y_{maxc}$  at which point unloading begins.

The values of  $k_e$  and  $k_p$  used in the theoretical analysis are given in Table 1. The unloading stiffness in branches T3 and C3 varies with the  $y_{max}$  achieved before unloading begins, because the shape of the deformed specimen varies considerably with  $y_{max}$ . The analytical unloading stiffness was taken as  $k_e$ .

#### THEORETICAL APPROACH

The theoretical analysis was done using the coordinates of Fig. 8. The location G is the center of mass of the rigid body mounted on the rings, which in turn are attached to a rigid support. The surface of the rigid support is inclined at an angle with the horizontal. The support experiences a prescribed motion  $v_0$  in the vertical direction. The absolute coordinates for the point G are designated as  $x_1y_1$  and the motions of the attachment points between the rings and the mass are  $x_2y_2$  and  $x_3y_3$ . The relative displacements

TABLE 1  
Stiffness values for a single ring  
( $l=1/2"$ ,  $R=1"$ ,  $t=.065"$ )

Tension;	
Elastic stiffness	= 1967.0 lb/in
Plastic stiffness	= 357.0 lb/in
Unloading stiffness	= 17000.0 lb/in
Yield deformation	= 0.075 in
Compression;	
Elastic stiffness	= 2076.0 lb/in
Plastic stiffness	= 14.0 lb/in
Unloading stiffness	= 28082 lb/in
Yield deformation	= 0.0602 in
Roll;	
Elastic stiffness	= 270.67 lb/in
Plastic stiffness	= 61.51 lb/in
Unloading stiffness	= 14588.0 lb/in
Yield deformation	= 0.2 in

across the rings are then,

$$\begin{aligned}
 x_{1r} &= x_1 - v_0 \sin \alpha \\
 y_{2r} &= y_2 - v_0 \cos \alpha \\
 x_{3r} &= x_3 - v_0 \sin \alpha \\
 y_{4r} &= y_4 - v_0 \cos \alpha
 \end{aligned} \tag{3}$$

Since the body of mass  $m$  is assumed rigid, and using the distances as marked on the free body diagrams, the displacements are related as follows using a small angle approximation

$$\begin{aligned}
 x_1 &= x - b \sin \theta \\
 y_2 &= y + a \sin \theta
 \end{aligned}$$

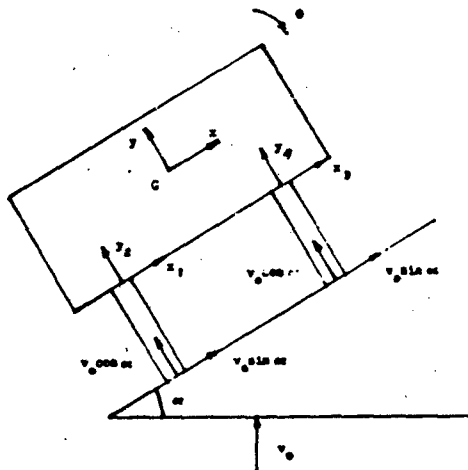


Fig 8 - Displacement Parameters

$$x_3 = x - d \sin \theta \quad (4)$$

$$y_4 = y - c \sin \theta$$

Equations (4) may now be substituted into equations (3) to express the relative displacements across the rings in terms of  $x$ ,  $y$ ,  $\theta$  and  $\dot{v}_0$ .

$$x_{1r} = x - b \sin \theta - v_0 \sin \alpha$$

$$y_{2r} = y + a \sin \theta - v_0 \cos \alpha \quad (5)$$

$$x_{3r} = x - d \sin \theta - v_0 \sin \alpha$$

$$y_{4r} = y - c \sin \theta - v_0 \cos \alpha$$

The inertia forces assumed at the center of mass at C are shown in Fig. 9 as  $\ddot{m}x, \ddot{m}y$ , and  $J\ddot{\theta}$ , where  $J$  is the rotational inertia of the mass. For the experiment, the values were  $m = 20 \text{ lb/g}$  and  $J = 0.280 \text{ in.}^2 \cdot \text{sec}$ . The free-body diagram shows the forces  $F_i$  transmitted to the mass from the rings and the weight  $W$  of the mass. The three dynamic equations are

$$\begin{aligned} \ddot{m}x &= F_1 + F_3 - W \sin \alpha \\ \ddot{m}y &= F_2 + F_4 - W \cos \alpha \end{aligned} \quad (6)$$

$$J\ddot{\theta} = -F_1 b + F_2 a - F_3 d - F_4 c$$

The forces are then related to the relative displacements according to the branch of the load-deformation curve as designated in Fig. 7. A typical set of equations for the compressive loading are:

$$\begin{aligned} F_2 &= k_{ec} y_{rel} && \text{on C1} \\ F_2 &= k_{pc} y_{rel} + (k_{ec} - k_{pc}) y_0 && \text{on C2 (7)} \end{aligned}$$

$$F_2 = (k_{ec} - k_{pc})(y_c - y_{max}) + k_{ec} y_{rel} \quad \text{on C3}$$

Here,  $y_{rel} = y_2 - v_0 \cos \alpha$ . There are similar equations for  $F_1, F_3$ , and  $F_4$ .

The equations were solved using the Fourth Order Runge-Kutta numerical integration method.

#### EXPERIMENTAL APPROACH

The experimental arrangement is shown in Fig. 10. The mass  $m$  consisted of the two steel plates, each  $1/2 \times 8 \times 8.75$ ". Four rings, each having  $1 \times 1$ ",  $R=1$ " and  $t=0.065$ ", were used and mounted symmetrically with respect to C, so the dimensions were

$$\begin{aligned} a &= c = 2" \\ b &= d = 1.6" \end{aligned} \quad (8)$$

The values of  $\alpha$  used were  $\alpha=0^\circ$  and  $\alpha=30^\circ$ , with the support for  $\alpha=30^\circ$  shown in Fig. 10. The supporting plates and angles were rigidly welded together and the  $1/2 \times 12 \times 8$ " steel plate was bolted to the top of an IMPAC Drop Table Shock Machine, manufactured by Monterey Research Labs.

The positions of five accelerometers, at locations A thru E, are shown on Fig. 10. The accelerometer E measured the base input  $\ddot{v}_0$ . The  $\ddot{x}$  was obtained from accelerometer A,  $\ddot{y}$  from accelerometer C, and  $\ddot{\theta}$  from accelerometers B and D.

The base acceleration  $\ddot{v}_0$  achieved is shown in Fig. 11. The duration of the main pulse is about 0.0150 seconds with a maximum value of about 52g. The machine is equipped with air brakes to assure that a second drop does not occur.

#### EXPERIMENTAL AND THEORETICAL RESULTS

Tests were made first for  $\alpha=0$ , without the rigid support system of Fig. 10. Related theoretical and experimental results are shown in Figs. 11 thru 13. The experimental and theoretical results for  $\ddot{y}$  are presented in Fig. 11. The maximum transmitted acceleration is about 25g, but this value could be increased or decreased simply by increasing or decreasing the yield load of the rings. The yield load may be changed by using longer or shorter rings, or more or less rings. The results for relative displacement versus time are shown in Fig. 12. The apparent frequency of motion after yielding indicates that actual plastic stiffness was less than the value used for the theoretical analysis. The associated theoretical load-displacement curve is given in Fig. 13. The loading is entirely compressive, tension is never achieved, which is one of the primary advantages of yielding mounts. Only about half the rattle space is required compared to that which would be needed for elastic mounts.

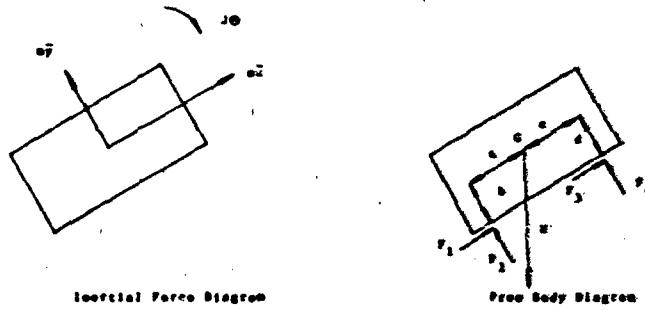


Fig. 9 - Free body and inertial force diagrams for two-dimensional shock case

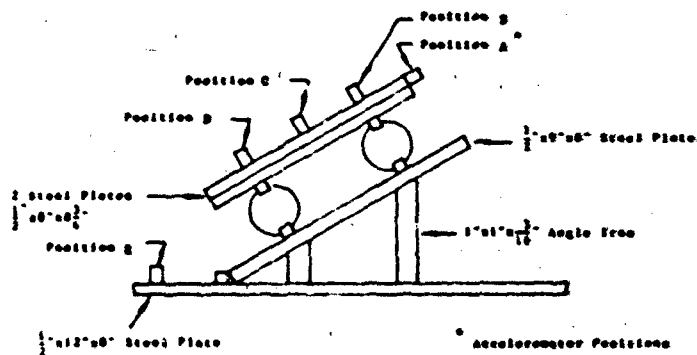


Fig. 10 - Experimental support structure

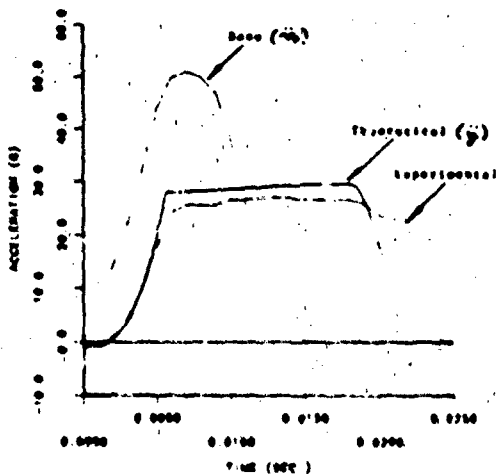


Fig. 11 - Plot of acceleration versus time in the y direction for  $\alpha=0.0^\circ$

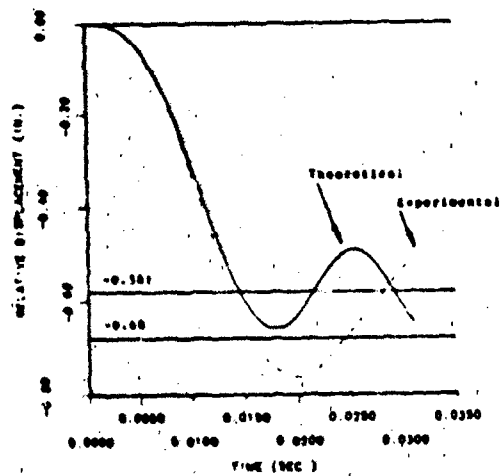


Fig. 12 - Plot of relative displacement versus time for  $\alpha=0.0^\circ$

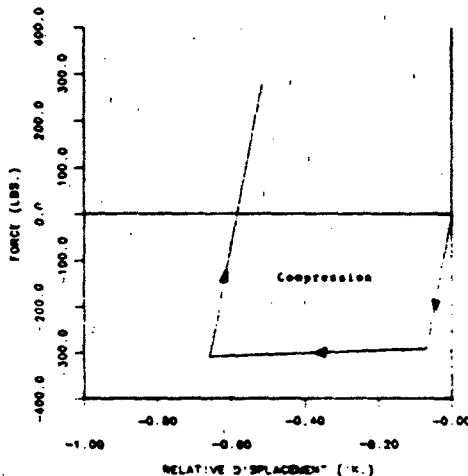


Fig. 13 - Plot of Force versus relative displacement for  $\alpha=0.0^\circ$

Results for drop-table tests for  $\alpha=30^\circ$  are shown in Figs. 14 thru 21. The input acceleration is now in the  $v$ -direction (Fig. 4), so there are resulting accelerations  $\ddot{x}$  and  $\ddot{y}$ . The  $\ddot{y}$  is shown in Fig. 14. The result is predicted reasonably well up to and including the maximum of about  $24g$ , but then there is considerable disagreement. The  $\ddot{x}$  are graphed in Fig. 15. The base acceleration maxima is about  $28g$  input and the measured maxima is about  $16g$ . The timewise agreement between predicted and measured values is reasonably good, but the spread at  $0.0100$  seconds indicates some weakness in the roll directions not predicted by the theoretical model. The angular acceleration is predicted surprisingly well, as given in Fig. 16, up to  $0.0300$  seconds. The angular displacement versus time is given in Fig. 17. The maximum angle achieved is  $0.07$  radians =  $4.0$  degrees, which is relatively small compared to the tilt angle  $\alpha=30^\circ$ . The relative displacements for each ring are given in Figs. 18 thru 21. The experimental curves for displacement were obtained by integrating twice the acceleration-time curves, so they are subject to error, most usually due to error in locating the zero acceleration on the record.

#### SUMMARY AND CONCLUSION

The dynamic response was predicted using load-deflection properties obtained from one-dimensional tests in compression-tension and roll. For the one-dimensional dynamic response, when  $\alpha=0.0^\circ$ , the agreement between predicted and measured acceleration is excellent (see Figure 11), indicating very little material rate effect on yield loads. The theoretical relative displacement agree well with the experimental relative displacement for the first loading (see Figure 12), but the maximum

experimental relative displacement is 15% higher than the maximum theoretical value. The theoretical plastic stiffness appears to be too high. In any case, the results from the one-dimensional dynamic test show that the theoretical analysis is reasonably accurate for this simple case.

The two-dimensional dynamic test was performed with the angle of tilt  $\alpha$  set at  $30^\circ$ . The theoretical accelerations obtained for this test were fairly accurate. The acceleration in the  $x$  direction and the angular acceleration predicted the experimental results very well (see Figures 15, and 16). In the  $y$  direction, the theoretical response is very accurate during the initial loading. After this maximum point, the accuracy of the theoretical results begin to deteriorate. The theoretical relative displacements in both the  $x$  and  $y$  directions are accurate up to the maximum acceleration. These results show that the combined compression-tension and roll actions have a distinct effect on the load-deflection properties beyond the yield deformation. The stiffnesses in the combined directions of motion are very difficult to predict but are very important after yielding of the ring.

The theoretical computer approach is very versatile, and is limited in accuracy primarily by the input parameters. Once the reliable stiffness terms are obtained, the computer program is an extremely effective analysis tool. Furthermore, the computer program does provide a general representation of a shock mount's absorbing characteristics even using the simple in-dimensional stiffness terms.

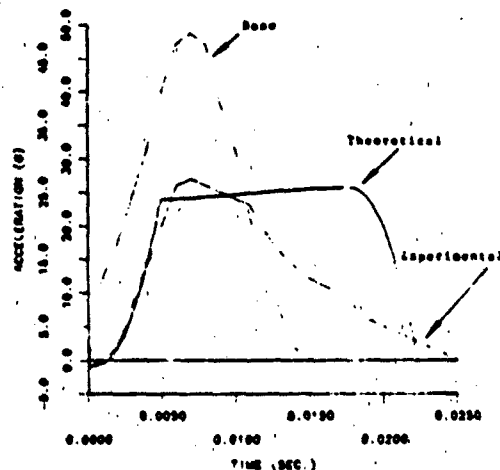


Fig. 14 - Plot of acceleration versus time in the  $y$  direction for  $\alpha=30.0^\circ$

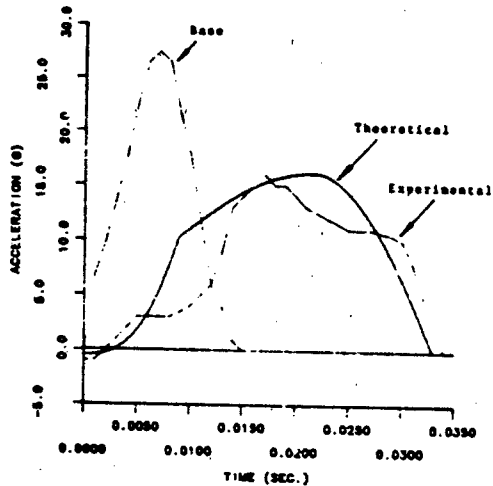


Fig. 15 - Plot of acceleration versus time in the x direction for  $\alpha=30.0^\circ$

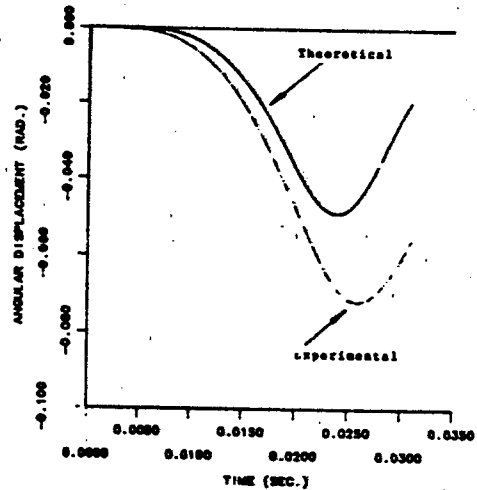


Fig. 17 - Plot of angular displacement versus time for  $\alpha=30.0^\circ$

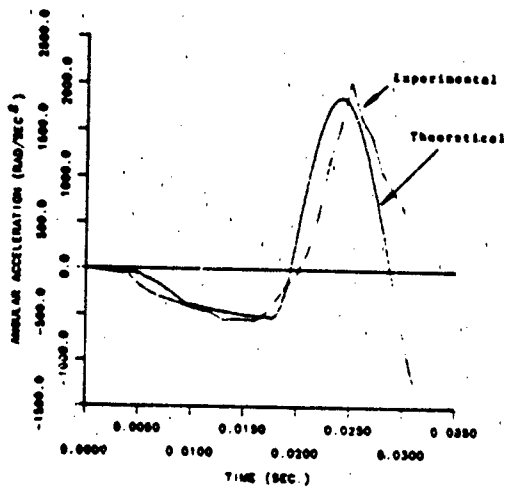


Fig. 16 - Plot of angular acceleration versus time for  $\alpha=30.0^\circ$

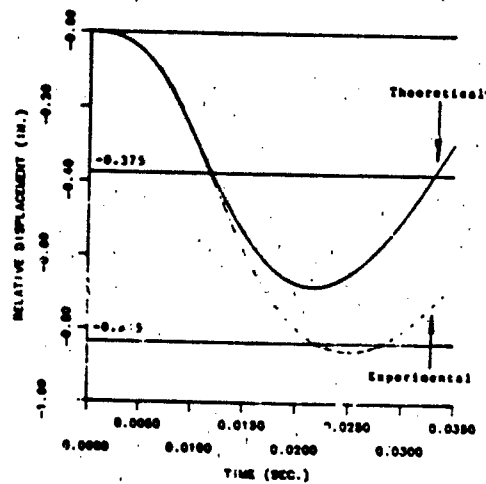


Fig. 18 - Plot of relative displacement versus time in the x direction for ring #1 ( $\alpha=30.0^\circ$ )

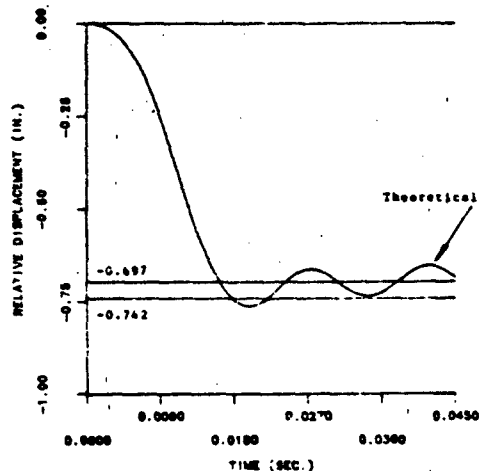


Fig. 19 - Plot of relative displacement versus time in the y direction for ring #1 ( $\alpha=30.0$ )

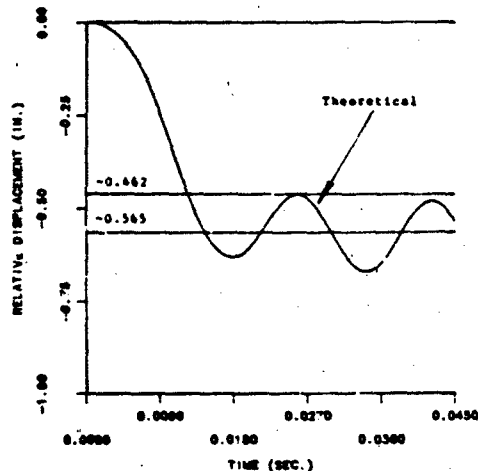


Fig. 21 - Plot of relative displacement versus time in the x direction for ring #2 ( $\alpha=30.0$ )

The two-dimensional absorbing characteristics of the side-loaded ring are summarized in tabular form for various values of maximum acceleration for each test where the angle of tilt was  $30^\circ$ .

In both the x and y directions, Table 2 shows that the side-loaded tube is a very effective energy absorber. This tube could be used in many applications where protection from shock loading is important. The transmitted acceleration could be further reduced by using rings with a lower yield point, but the relative displacement would increase. The yield load  $P$  in compression is related to the tube thickness  $t$ , the yield stress  $\sigma_y$ , the tube radius  $r$ , and the tube length  $L$  by (Ref. [1])

$$P_0 = \frac{\sigma_y t^2 L}{r} \quad (9)$$

The tube acts like a mechanical fuse and the maximum transmitted acceleration is directly proportional to the maximum yield load, if the plastic stiffness  $k_p$  is small. The plastic stiffness is lower for point loading than for spread loading, as achievable between platens (see Fig. 3).

Except for references [2] and [3], there has been little analysis of side-loaded rings deformed into the plastic range in the three directions. More theoretical research is needed.

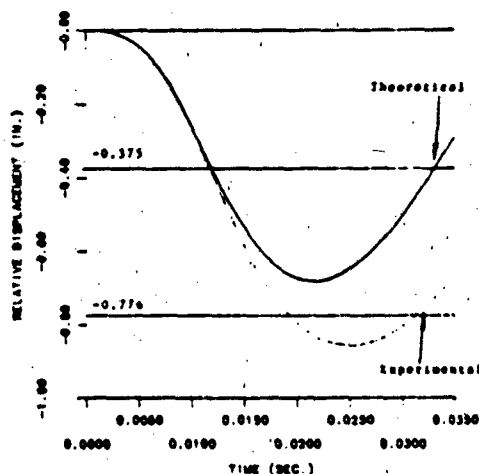


Fig. 20 - Plot of relative displacement versus time in the y direction for ring #2 ( $\alpha=30.0$ )

TABLE 2  
Experimental and theoretical acceleration results

Maximum acceleration in the x direction			
	Input Base	Transmitted Theoretical	Transmitted Experimental
Case #1	28 g	16 g	-
Case #2	27 g	17 g	17 g

Maximum acceleration in the y direction			
	Input Base	Transmitted Theoretical	Transmitted Experimental
Case #1	46.5 g	26 g	26 g
Case #2	48.5 g	26 g	27 g

REFERENCES

1. Neubert, V. H., "Analysis of Energy-Absorbing Shock Mounts," Shock and Vibration Bulletin No. 51, part 2, pp 149-167, May 1981.
2. Fortuna, R. E., "Two-Dimensional Shock Response of a Mass on Energy-Absorbing Shock Mounts," Master of Science Thesis, The Pennsylvania State University, August 1983.
3. Hwang, Chintsun, "Plastic Collapse of Thin Rings," Journal of Aerospace Science, pp. 819-826, December 1953.
4. DeRuntz, J. A., Jr. and Hodge, P. G., Jr., "Crushing of a Tube Between Rigid Plates," Journal of Applied Mechanics, pp. 391-395, September 1963.
5. Burns, A. B., Guide for the selection & Application of Shock Mounts for Shipboard Equipment, Contract No. Nobe-78963, Bu Ships Code 423, Sept. 1, 1961.

DISCUSSION

Mr. Whang (David Taylor Naval Ship R&D Center): Your forcing function was an acceleration with some rise time, and then it was flat. Then it decayed to zero.

Mr. Fortuna: Yes.

Mr. Whang: Your resistance function bothers me. First, you have a linear portion, then you have an elasto-plastic portion, and then it decays to zero. Could it have gone below zero?

Mr. Fortuna: Yes. It would have gone below zero, and it would have circled back plastically. You questioned whether the resistance function stops at zero. The analysis lets it go down below zero, and it would also let it go back elastically. However, when we ran it, it would never do anything other than oscillate elastically at its unloading point.

Mr. Whang: So if you had a velocity rise, then a linear decay and then rise again, it is possible that you could have your maximum displacement in three different ways; the initial phase then on its way back and possibly a third phase.

Mr. Fortuna: Yes, it would allow it to do that.

Mr. Whang: We did something similar.

## OPTIMUM DESIGN FOR NONLINEAR SHOCK MOUNTS FOR TRANSIENT INPUTS

K. Kasraie, Research Scientist  
Firestone Tire & Rubber Company  
Central Research Laboratories  
Akron, Ohio 44317

and

V. H. Neubert, Professor  
The Pennsylvania State University  
University Park, PA 16802

The State Space Method for Optimal Design of Vibration Isolators given by Hsiao, Haug and Arora [1] is used and advanced to include a more general class of problems encountered in the optimal design of shock absorbers. In contrast to the State Space Optimization of [1], in which forcing functions, cost function and performance constraints are explicitly independent of the state variable vector at some floating boundaries, in the new formulation of the problem, forcing functions, cost function and performance constraints can be a function of the state variable vector at some moving boundaries. An example of this type of problem is the design of the elastic-plastic shock absorbers for optimum performance during loading and unloading.

Sixteen different shock absorbers with viscous damping and a bi-linear spring are designed for optimum response to a shock of finite duration imposed by the supporting base. The objective of the design is to determine the value of damping ( $C$ ) and elastic and plastic stiffness of the bi-linear spring ( $k_e, k_p$ ), such that the absolute value of the maximum absolute acceleration is minimum, while the maximum relative displacement of the mass  $M$  is less than a specified value. Finally the effects of varying the mass  $M$  and yield deformation of the bi-linear spring are discussed.

### INTRODUCTION

The specific problem is the optimum design of the single-degree-of-freedom system undergoing ground shock as shown in Fig. 1. A linear spring of stiffness  $k$  and a dashpot  $c$  are in parallel with a bi-linear spring. The bi-linear spring load deflection curve is shown in Fig. 2, where  $k_e$  is the elastic stiffness and  $k_p$  the plastic stiffness. The input is applied as a known base motion  $y_0(t)$  and the absolute displacement of the mass  $m$  is  $y(t)$ . The practical problem is to choose  $c$ ,  $k$ ,  $k_e$ , and  $k_p$  such that the relative displacement  $y_r(t) = y(t) - y_0(t)$  will be within specified bounds and the transmitted acceleration  $\ddot{y}(t)$  is a minimum. The paper is based on Ref. [18].

### BACKGROUND

The problem mentioned in the introduction is a type of mathematical programming problem, which are generally specified as follows: Determine a vector  $Z^* = (Z_1, \dots, Z_n)^T$  that minimizes the cost function  $\phi_0(Z)$  while satisfying the constraints of the form  $\psi_i(Z) > 0$   $i = 1, \dots, m$  and zeroing the surface equations  $\zeta_j(Z) = 0$ ,  $j = 1, \dots, p$ . If all the problem functions  $\phi_0$ ,  $\psi_i$  and  $\zeta_j$  are linear, the problem is called a linear programming problem; if any of these are nonlinear, the problem is called a nonlinear programming problem [2].

The method used in the paper is an extension of the State Space Method of

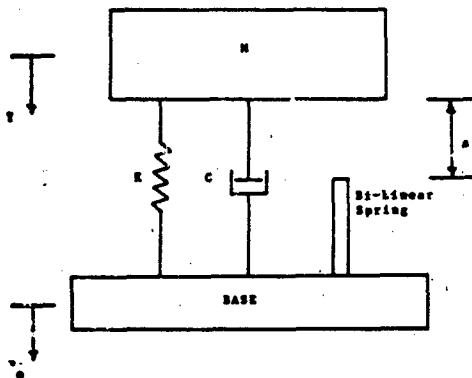


Fig. 1 - One degree of freedom representation of a Machine and Foundation

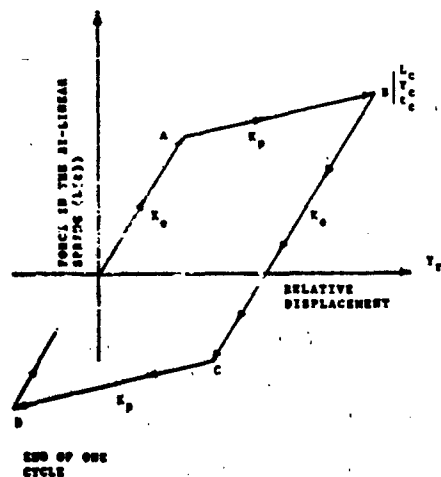


Fig. 2 - Theoretical force-displacement curve for the bi-linear spring

Ref. [1]. The field of nonlinear programming is evolving rapidly with a complete historical survey of mathematical programming given in Ref. [2]. A review of the literature in optimum design of structures since Galileo to 1963 can be found in Ref. [3] and from 1963 to mid-1968 in Ref. [4]. Structural optimization subjected to dynamic constraint from 1968 to 1972 is reviewed in Ref. [5].

Schmit and Fox [6] addressed the ground shock problem for a mass on a linear spring and dashpot. One approach is to formulate the dynamic problem to fit into the class of mathematical pro-

gramming problems. Schmit and Fox use the synthesis concept and the nonlinear programming method is called the Steep-Descent Alternate Step Method. Karnopp and Trikha [7] pointed out the difficulties in selecting the performance criteria for optimum performance of shock and vibration isolators. They represent the force on the mass by  $f(t)$  and then try to minimize the function  $c = g(f_m) + p_1 h(x_m)$  where  $f_m = \max |f(t)|$  and  $x_m = \max |(x(t))|$ , the relative displacement.

Willmert and Fox [8] studied the optimization of linear multi-degree-of-freedom shock isolation systems. They dealt with optimization of the system, but also the number of elements in the system. First a system with only one element is optimized and the results stored. Then having in mind that increasing the size of the system will make it less desirable (more expensive; requires more space) the objective function for a system with two elements is compared with that for one element. If the reduction in the objective function for the larger system compensates for its less desirability, the second system is optimized and compared with a system with three elements, etc. Otherwise the process terminates. They also showed that for multi-degree-of-freedom-systems the optimum mass, stiffness and damping coefficients are not necessarily unique. In addition they related the number of elements in the system to the number of degrees of freedom.

The writers of [8] have successfully demonstrated the feasibility of their technique to the problem of topology of the linear shock isolation systems and use the basic approach of the determination of the topology of the system to improve the optimization technique for a fixed number-of-degrees-of-freedom shock isolation system. Still their technique fails to separate the time minimization or maximization from space parameter optimization and consequently it is not economical for a system with more degrees of freedom. In addition as they have mentioned in their paper, it required a considerable amount of computer time to optimize a three-degree-freedom shock isolation system.

In 1974, Afimiwala and Mayne [9], adopted nonlinear programming to study the optimum design of a nonlinear shock absorber with  $n$ th order stiffness and  $m$ th order damping due to an acceleration impulse imposed by the

support motion, with the objective function being maximum acceleration, having an upper limit on the maximum relative displacement. Through a non-dimensional curve they have shown that the optimum system can be achieved with  $n = 0$ , regardless of  $m$ , or  $m = 0$  regardless of  $n$ . And also for large  $n$  and  $m$  the optimum system becomes less desirable and poorly performed. Also through this study they have shown the comparison between the approximate design method suggested by Sevin and Pilkey and more advanced mathematical programming technique. They point out the computer time needed for a simple unconstrained optimization required by Sevin and Pilkey method was less than one second while using their technique it was one minute.

Other writers such as Sevin and Pilkey [10] presented a mathematical statement of the problem of optimum design of shock isolator systems and discuss the two computational methods applicable to the problem (direct and indirect methods). They also gave an extensive bibliography related to the literature published in this field.

Julian Wolkovitch [11] reviewed some of the published optimization techniques applicable to the optimization of the mechanical system to shock and vibration and pointed out the gap between the theories of relatively new field of optimization of mechanical system to shock and vibration, and, their application to the practical systems.

In 1971, D. L. Bartel, E. J. Haug and K. Rim [12] introduced a new technique called The Method of Constrained Steepest Descent With State Equations, CSDS, to the field of optimum design of spatial frames. Following that they optimized several three member frames each of which had nine design variables, 18 state variables and 27 constraints, and successfully demonstrated the feasibility of the new technique to the field of structural optimization.

In the same year, D. L. Bartel and A. I. Krauter [13] applied the method of constrained steepest descent with state equations to the problem of optimum design of a vibration absorber system. Through two examples of the effectiveness of the method to the field of optimum design of dynamic systems was shown.

In 1972, E. J. Haug, Jr., K. C. Pan and T. C. Streeter [14]

presented a computational method for optimal structural design, using the steepest descent method with state equations. Through extensive numerical examples they removed any doubt about applicability of the CSDS method to more practical systems.

In 1976, J. S. Arora and E. J. Haug, Jr. [15], presented some refinements to the State Space Optimization Technique and carried out three test problems and compared the computational time of these three test problems with the computational time reported in the literature for the same problems. They reported that using the State Space Optimization Technique, computer time needed for the first test problem (25 member transmission tower) was reduced by 16 to 37%; time for the second test problem (72 member tower) was reduced by a factor of 2.3 to 2.5 and finally for the third test problem (200 member plane truss), computational time was reduced by a factor of 14 to 18.

In 1977, T. T. Feng, J. S. Arora and E. J. Haug, Jr. [16] presented an algorithm for optimal design of elastic structures, subjected to dynamic loading.

Following that in 1978, E. J. Haug and J. S. Arora [17] employed the adjoint variable methods to develop a unified method of sensitivity analysis for mechanical system design. And also they presented some numerical examples.

In 1979, M. H. Hasiao, E. J. Haug, Jr. and J. S. Arora [1] developed a State Space Method for Optimal Design of Vibration Isolators and applied it to two test problems and pointed out that computational time required to achieve the optimum systems was one tenth of the time reported in the previous studies [8,9].

#### STATEMENT OF THE PROBLEM

First the general mathematical formulation will be presented and then it will be applied to the specific one-degree-of-freedom system of Fig. 1.

The parameters of the system are identified by a state parameter vector  $b = [b_1, b_2, \dots, b_m]^T$ , where

$$\begin{aligned} b_1 &= c & b_3 &= k_e \\ b_2 &= k & b_4 &= k_p \end{aligned} \quad (1)$$

The differential equations are of the form

$$P(b) \dot{Z} = F(t, Z(t), b, \alpha(b)) \quad (2)$$

$$0 \leq t \leq T$$

where  $P(b)$  is a square matrix and  $Z$  and  $F$  are column matrices. The usual second order differential equations are reduced to this form by defining additional variables, such as

$$Z_2 = \dot{y} \quad \text{and} \quad Z_1 = y.$$

Here

$$\alpha(b) = \beta(Z(t_c)) \quad (3)$$

meaning that  $\alpha$  is a function of  $Z$  at time  $t_c$  at the floating boundary, which is the time when the first maximum relative displacement is reached.

The initial conditions are

$$Z_1(0) = 0 \quad (4)$$

and there are additional conditions at  $t_c$  such that

$$c(Z(t_c), Z(t_c), t_c, b) = 0 \quad (5)$$

The cost function  $\phi_0$ , which in this case is the maximum transmitted acceleration of the mass, is to be minimized and is represented as

$$\phi_0 = \max f_0(t, Z(t), b, \alpha(b)) \quad 0 \leq t \leq \tau \quad (6)$$

There are performance constraints, representing the maximum relative displacements  $\phi_i$  of the form

$$\begin{aligned} \phi_i &= \max f_i(t, Z(t), b, \alpha(b)) \\ -\phi_i &\leq 0 \quad 0 \leq t \leq \tau \end{aligned} \quad (7)$$

and explicit bounds on the system parameters of  $b_i$  of the form

$$b_i^L \leq b_i \leq b_i^U \quad i = 1, \dots, m \quad (8)$$

requiring the system parameters to be in a certain range. For example, for practical damping  $c$  is greater or equal to zero, and since  $b_1 = c$ , the bounds on  $b_1$  are

$$0 \leq b_1 \leq \infty \quad (9)$$

Now the following the idea of Ref. [1], the maximum value of the cost function is designated  $b_{m+1}$ , so that Eq. (6) may be restated as

$$\begin{aligned} f_0(t, Z(t), b, \alpha(b)) - b_{m+1} &\leq 0 \\ 0 \leq t \leq \tau \end{aligned} \quad (10)$$

The inequalities (10, 7) may be expressed in integral form by Eqs. (11) and (12), where the  $H(\cdot)$  are the

unit step functions:

$$\begin{aligned} \psi_0 &= \int_0^\tau (f_0(t, z, b, \alpha(b)) - b_{m+1})^2 dt = 0 \\ H(f_0 - b_{m+1}) dt &= 0 \end{aligned} \quad (11)$$

and

$$\begin{aligned} \psi_i &= \int_0^\tau (f_i(t, z, b, \alpha(b)) - \theta_i)^2 dt = 0 \\ H(f_i - \theta_i) dt &= 0 \end{aligned} \quad (12)$$

Recall that the unit step function  $H(r)$ , for example, is such that

$$\begin{aligned} H(r) &= 0 & r < 0 \\ H(r) &= 1 & r > 0 \end{aligned} \quad (13)$$

so, in Eq. (11), if  $f_i < \theta_i$ , then  $H(f_i - \theta_i) = 0$  and the integral  $\psi_i = 0$ . If  $f_i > \theta_i$ , then  $\psi_i \neq 0$  and the inequality is not satisfied.

Now the equivalent problem is summarized as: Minimize the cost function  $b_{m+1}$ , subject to the constraint of Eqs. (8), (11), and (12), the differential equations (2), initial conditions (4) and the surface equations (5).

Next it is necessary to calculate the derivatives of the constraint integrals with respect to the design parameters and eliminate their dependence on the state variables. To do this the adjoint variables vector  $\lambda^T$  is introduced as in ref. [1], through the identity

$$\int_0^\tau \lambda^T [P\dot{Z} - F(t, z, b, \alpha(b))] dt = 0 \quad (14)$$

A small change  $\delta b$  in the state parameters will cause a change  $\delta Z$  in  $Z$  and  $\delta \alpha$  in  $\alpha$ . Expanding the left side of Eq. (14) to the first order, we obtain

$$\begin{aligned} \int_0^\tau \lambda^T [P\delta Z - \frac{\partial F}{\partial Z} \delta Z + \frac{\partial(P\dot{Z})}{\partial b} \delta b - \frac{\partial F}{\partial b} \delta b \\ - \frac{\partial F}{\partial \alpha} \delta \alpha] dt = 0 \end{aligned} \quad (15)$$

where

$$\frac{\partial F}{\partial Z} = \begin{bmatrix} \frac{\partial F_1}{\partial Z_j} \end{bmatrix}_{n \times n} \quad \frac{\partial F}{\partial b} = \begin{bmatrix} \frac{\partial F_1}{\partial b_j} \end{bmatrix}_{n \times m}$$

$$\frac{\partial F}{\partial \alpha} = \begin{bmatrix} \frac{\partial F_1}{\partial \alpha_1} & \dots & \frac{\partial F_1}{\partial \alpha_n} \\ \frac{\partial F_n}{\partial \alpha_1} & \dots & \frac{\partial F_n}{\partial \alpha_n} \end{bmatrix} \quad (16)$$

$$\delta \alpha = \begin{bmatrix} \frac{\partial \alpha_1}{\partial b_1} & \dots & \frac{\partial \alpha_1}{\partial b_m} \\ \frac{\partial \alpha_n}{\partial b_1} & \dots & \frac{\partial \alpha_n}{\partial b_m} \end{bmatrix} \begin{bmatrix} \delta b_1 \\ \vdots \\ \delta b_m \end{bmatrix}$$

The last of Equations (16) involves a "floating boundary matrix", defined as  $n \times m$ , or  $\delta \alpha$  may be written as

$$\delta \alpha = \eta_{n \times m} \delta b_{m \times 1} = \begin{bmatrix} \frac{\partial \alpha_i}{\partial b_j} \end{bmatrix}_{n \times m} \quad (\delta b) \quad (17)$$

Now Eq. (15) becomes

$$\int_0^T \lambda^T \left[ P \delta \dot{Z} - \frac{\partial F}{\partial Z} \delta Z + \frac{\partial(P\dot{Z})}{\partial b} \delta b - \frac{\partial F}{\partial b} \delta b - \frac{\partial F}{\partial \alpha} \eta \delta b \right] dt = 0 \quad (18)$$

Integrating (18) by parts, noting from initial condition Eq. (4) that  $\epsilon(Z(0)) = 0$ , and requiring  $\lambda(T) = 0$ , Eq. (18) becomes

$$\int_0^T \left( P^T \dot{\lambda} + \frac{\partial F^T}{\partial Z} \lambda \right)^T \delta Z dt = \int_0^T \lambda^T \left[ \frac{\partial(P\dot{Z})}{\partial b} - \frac{\partial F}{\partial b} - \frac{\partial F}{\partial \alpha} \eta \right] \delta b dt \quad (19)$$

Now due to changes  $\delta b$  in  $b$ , we have small changes in  $\psi_0$  and  $\psi_1$  as follows:

$$\psi_0 + \delta \psi_0 \equiv \int_0^T \left[ \langle f_0 - b_{m+1} \rangle^2 + \langle f_0 - b_{m+1} \rangle \left( \frac{\partial f_0}{\partial Z} \delta Z + \frac{\partial f_0}{\partial b} \delta b + \frac{\partial f_0}{\partial \alpha} \eta \delta b + \delta b_{m+1} \right) \right] dt = 0 \quad (20)$$

and

$$\psi_1 + \delta \psi_1 \equiv \int_0^T \left[ \langle f_i - \theta_i \rangle^2 + 2 \langle f_i - \theta_i \rangle \left( \frac{\partial f_i}{\partial Z} \delta Z + \frac{\partial f_i}{\partial b} \delta b + \frac{\partial f_i}{\partial \alpha} \eta \delta b \right) \right] dt = 0 \quad (21)$$

To eliminate the explicit dependence of Eqs. (20) and (21) on  $\delta Z$ , we can use the identity of Eq. (19) as the following:

$$P^T \dot{\lambda}_0 + \frac{\partial F^T}{\partial Z} \lambda_0 = 2 \langle f_0 - b_{m+1} \rangle \frac{\partial f_0^T}{\partial Z} \quad (22)$$

$$P^T \dot{\lambda}_i + \frac{\partial F^T}{\partial Z} \lambda_i = 2 \langle f_i - \theta_i \rangle \frac{\partial f_i^T}{\partial Z} \quad i=1, \dots, k \quad (23)$$

$$\text{and } \lambda_i(\tau) = 0 \quad i = 0, 1, \dots, k$$

Then Eqs. (20) and (21) reduce to

$$\psi_0 + \int_0^T \left[ \lambda_0^T \left[ \frac{\partial(P\dot{Z})}{\partial b} - \frac{\partial F}{\partial b} - \frac{\partial F}{\partial \alpha} \eta \right] \delta b + 2 \langle f_0 - b_{m+1} \rangle \left( \frac{\partial f_0}{\partial b} + \frac{\partial f_0}{\partial \alpha} \eta \right) \delta b \right] dt \quad (24)$$

$$- \int_0^T 2 \langle f_0 - b_{m+1} \rangle \delta b_{m+1} dt = 0$$

and

$$\psi_1 + \int_0^T \left[ \lambda_i^T \left[ \frac{\partial(P\dot{Z})}{\partial b} - \frac{\partial F}{\partial b} - \frac{\partial F}{\partial \alpha} \eta \right] \delta b + 2 \langle f_i - \theta_i \rangle \left( \frac{\partial f_i}{\partial b} + \frac{\partial f_i}{\partial \alpha} \eta \right) \delta b \right] dt = 0 \quad (25)$$

Now, if we let

$$L_0 = \int_0^T \left[ 2 \langle f_0 - b_{m+1} \rangle \left( \frac{\partial f_0}{\partial b} + \eta^T \frac{\partial f_0^T}{\partial \alpha} \right) + \left( \frac{\partial(P\dot{Z})}{\partial b} - \frac{\partial F}{\partial b} - \eta^T \frac{\partial F^T}{\partial \alpha} \right) \lambda_0 \right] dt \quad (26)$$

and

$$L_1 = \int_0^T \left[ 2 \langle f_i - \theta_i \rangle \left( \frac{\partial f_i}{\partial b} + \eta^T \frac{\partial f_i^T}{\partial \alpha} \right) + \left( \frac{\partial(P\dot{Z})}{\partial b} - \frac{\partial F}{\partial b} - \eta^T \frac{\partial F^T}{\partial \alpha} \right) \lambda_i \right] dt \quad (27)$$

then Eqs. (24) and (25) become:

$$\psi_0 + L_0^T \delta b - \int_0^T 2 \langle f_0 - b_{m+1} \rangle dt \delta b_{m+1} = 0 \quad (28)$$

and

$$\psi_1 + L_1^T \delta b = 0 \quad (29)$$

Equations (28) and (29) written in matrix form as

$$\begin{bmatrix} \psi_0 \\ \psi_1 \end{bmatrix} + \begin{bmatrix} L_0^T \\ L_1^T \end{bmatrix} \delta b - \int_0^T \begin{bmatrix} 2 \langle f_0 - b_{m+1} \rangle dt \\ 0 \end{bmatrix} \delta b_{m+1} = \begin{bmatrix} 0 \\ 0 \end{bmatrix} \quad (30)$$

where the sensitivity matrix A of reference [1] is

$$A = [A] = \begin{bmatrix} L_0^T & -\int_0^{t_c} \langle f_0 - b_{m+1} \rangle dt \\ L_1^T & 0 \end{bmatrix}^T \quad (31)$$

and Eq. (30) may be written

$$\Psi + A\delta b = 0 \quad (32)$$

#### Algorithm for Systems with Floating Boundaries

The gradient projection method of Reference [1] may now be presented, as modified to account for floating boundary at  $t_c$ .

Step 1. Start the iteration by selecting an estimated design  $b(j)$  and solve equation (5) for  $Z(t_c)$ .

Step 2. Using equation (3), calculate  $\alpha(b)$  for the design vector  $b(j)$  and state vector  $Z(t_c)$ .

Step 3. Knowing  $\alpha(b)$  from step 2, solve equation (2) for  $Z(t)$ .

Step 4. For the design vector  $b(j)$ , calculate the Floating Boundary Matrix  $n$  of the equation (17).

Step 5. Proceed as step 2 of reference [1] by evaluating the constraints of equations (11) and (12) and set up the index set

$$I = \{i \geq 0: f_i(t_2 Z(t), b, \alpha(b)) \geq \theta_i\}$$

for some  $t \leq t_c$

Step 6. For each  $i \in I$ , calculate the adjoint variable of equations (22) and (23).

Step 7. For each  $i \in I$ , calculate  $L_i$  using equations (26) and (27) and construct the sensitivity matrix A of equation (31).

Step 8. Reduce  $\Delta J$  (the objective function) and calculate

$$y_0 = \frac{1}{2\Delta J} e^T [I - A(A^T A)^{-1} A^T] e \quad (33)$$

where

$$e = [0, 0, \dots, 1]^T$$

Step 9. Compute

$$\mu = -(A^T A)^{-1} (2y_0 \Psi - A^T e) \quad (34)$$

Step 10. Compute

$$\delta b = \frac{1}{2y_0} \delta b_1 + \delta b_2 \quad (35)$$

where  $\delta b_1 = [I - A(A^T A)^{-1} A^T] e$  (36)

$$\delta b_2 = -A(A^T A)^{-1} \Psi \quad (37)$$

and put  $b(j+1) = b(j) + \delta b$

Step 11. If all constraints are satisfied, terminate. Otherwise, return to step 1 with the new design estimate  $b(j+1)$ .

#### Application to the Simple Shock Absorber

Now the modified State Space Method of optimal design of shock absorbers will be used to design a bi-linear single-degree-of-freedom shock absorber, as shown in Fig. 1 and 2, for optimum performance during loading and unloading.

The design objective is to minimize the acceleration of the mass  $m$  from a shock of finite duration,  $y_0(t)$ , such that the relative displacement between the mass  $m$  and the base will not exceed a given limit. The design parameters (or space parameters) are  $k$ ,  $k_e$ ,  $k_p$ , and  $c$ .

Using the free-body and inertia diagrams of Fig. 3, the differential equation of motion is:

$$m\ddot{y} + c(\dot{y} - \dot{y}_0) + k(y - y_0) + L(t) = W \quad (38)$$

with initial conditions

$$y(0) = 0 \quad \dot{y}(0) = 0 \quad (39)$$

Letting  $y_r = y - y_0$ , Eq. (38) becomes

$$m\ddot{y}_r + c\dot{y}_r + ky_r + L(t) = W - m\ddot{y}_0 \quad (40)$$

To reduce to the first order form of Eq. (2), let

$$\begin{aligned} Z_1(t) &= y_r(t) \text{ and } Z_2(t) = \dot{y}_r(t) \\ \text{with } \dot{Z}_2(t) &= \ddot{y}_r(t) \end{aligned} \quad (41)$$

Substituting into Eq. (40) and setting in matrix form

$$\begin{bmatrix} 1 & 0 \\ 0 & m \end{bmatrix} \begin{bmatrix} \dot{Z}_1 \\ \dot{Z}_2 \end{bmatrix} = \begin{bmatrix} -Z_2 \\ -(Z_2 - kZ_1 - m\ddot{y}_0 + W - L(t)) \end{bmatrix} \quad (42)$$

with initial conditions

$$\begin{bmatrix} Z_1(0) \\ Z_2(0) \end{bmatrix} = \begin{bmatrix} 0 \\ 0 \end{bmatrix} \quad (43)$$

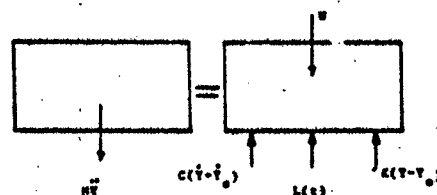


Fig. 3 - Force Mass Inertia Diagram for a Single-Degree-of-Freedom Shock Absorber

Note that Eqs. (42) and (43) are of the form of Eqs. (2) and (4) respectively.

From Fig. 2, the force  $L(t)$  in the nonlinear spring is as follows:

$$\begin{aligned} L_1(t) &= k_e y_r \quad 0 \leq y_r \leq y_e \\ L_2(t) &= (k_e - k_p) y_e + k_p y_r \\ &\quad \dot{y}_r > 0; y_t \leq y_r \leq y_c \\ L_3(t) &= (k_e - k_p)(y_e - y_c) + k_e y_r \\ &\quad \dot{y}_r < 0; y_t \leq y_r \leq y_c \end{aligned} \quad (44)$$

where  $y_t = (y_c - y_e) \left(1 - \frac{k_p}{k_e}\right) - y_d$

$$L_4(t) = (k_e - k_p)(y_e - y_c - y_t) + k_2 y_r \quad \dot{y}_r < 0 \quad y_r < y_t$$

Using the idea of the unit step function, Eqs. (44) may be written as one, Eq. (45).

$$L(t) = [L_1 + (L_2 - L_1)H(y_r - y_e)]H(y_r) + [(L_4 - L_3)H(y_t - y_r) + L_3][1 - H(y_r)] \quad (45)$$

The Eq. (45) is good for only one cycle. The end of one cycle is determined by noting that after  $y_c$  occurs,  $L(t)$  is decreasing and a cycle ends when  $L(t)$  changes sign.

The equations may then be cast in terms of the system parameters  $b_i$ , as in Eq. (1). Then Eqs. (42) and (45) become:

$$\begin{bmatrix} 1 & 0 \\ 0 & m \end{bmatrix} \begin{bmatrix} Z_1 \\ Z_2 \end{bmatrix} = \begin{bmatrix} Z_2 \\ -b_1 Z_2 - b_2 Z_1 - m y_0 + W - L(t) \end{bmatrix} \quad (46)$$

with

$$\begin{aligned} L(t) &= [(b_2 - b_1)(y_e - Z_1)H(Z_1 - y_e) + b_3 Z_1] \\ &\quad H(Z_2) + [(b_3 - b_1)(y_c - y_e) \left(1 - \frac{b_2}{b_3}\right) - y_d - Z_1] \\ &\quad H((y_c - y_e) \left(1 - \frac{k_2}{k_1}\right) - y_d Z_1) - (b_3 - b_1) \\ &\quad (y_e - y_c) + b_3 Z_1] [1 - H(Z_2)] \end{aligned} \quad (47)$$

Therefore  $\alpha_1(b) = 0$  and  $\alpha_2(b) = y_c$

For the problem on hand, it is desired to minimize the maximum absolute acceleration, so an artificial design parameter  $b_3$  is defined by

$$\frac{1}{m} [-b_1 Z_2 - b_2 Z_1 + W - L(t)] - b_3 \leq 0 \quad (49)$$

The cost function to be minimized is  $J = b_3$ . Finally, a constraint on extreme value of relative displacement is imposed as

$$|Z_1(t)| - Z_{1\max} \leq 0, \quad 0 \leq t \leq \tau \quad (50)$$

Therefore, for the problem on hand, one has the following:

$$p(b) = \begin{bmatrix} 1 & 0 \\ 0 & m \end{bmatrix} \quad (51)$$

$$F(t, Z_1, b_1, \alpha(b)) = \begin{bmatrix} Z_2 \\ -b_1 Z_2 - b_2 Z_1 - m y_0 + W - L(t) \end{bmatrix} \quad (52)$$

and

$$f_0(t, Z_1, b_1, \alpha(b)) = \frac{1}{m} [-b_1 Z_2 - b_2 Z_1 + W - L(t)] \quad (53)$$

One now has to find the derivatives of  $F(t, Z_1, b_1, \alpha(b))$  with respect to state variable  $Z(t)$ , design parameter vector  $b$  and  $\alpha(b)$  as follows:

$$\frac{\partial F}{\partial Z} = \begin{bmatrix} \frac{\partial F_1}{\partial Z_j} \\ \frac{\partial F_2}{\partial Z_j} \end{bmatrix}_{2 \times 2} = \begin{bmatrix} \frac{\partial F_1}{\partial Z_1} & \frac{\partial F_1}{\partial Z_2} \\ \frac{\partial F_2}{\partial Z_1} & \frac{\partial F_2}{\partial Z_2} \end{bmatrix} \quad (54)$$

The result is:

$$\frac{\partial F}{\partial Z} = \begin{bmatrix} 0 & 1 \\ -b_2 + \frac{\partial L(t)}{\partial Z_1} & -b_1 \end{bmatrix} \quad (55)$$

$$\begin{aligned} \text{where } \frac{\partial L(t)}{\partial Z_1} &= [(b_3 - b_1)H(Z_1 - y_e) + b_3] \\ &\quad H(Z_2) + [(b_3 - b_1)H(y_c - Z_1) + b_3] \\ &\quad (1 - H(Z_2)) \end{aligned} \quad (56)$$

The derivative  $\frac{\partial F}{\partial b}$  is:

$$\frac{\partial F}{\partial b} = \left[ \frac{\partial F_j}{\partial b_i} \right]_{2 \times 3} = \begin{bmatrix} \frac{\partial F_1}{\partial b_1} & \frac{\partial F_1}{\partial b_2} & \frac{\partial F_1}{\partial b_3} & \frac{\partial F_1}{\partial b_4} \\ \frac{\partial F_2}{\partial b_1} & \frac{\partial F_2}{\partial b_2} & \frac{\partial F_2}{\partial b_3} & \frac{\partial F_2}{\partial b_4} \end{bmatrix} \quad (57)$$

$$\frac{\partial F_2}{\partial b} = \begin{bmatrix} 0 & 0 & 0 & 0 \\ 0 & -Z_1 & \frac{\partial F_2}{\partial b_3} & \frac{\partial F_2}{\partial b_4} \end{bmatrix} \quad (58)$$

where

$$\begin{aligned} \frac{\partial F_2}{\partial b_3} &= -[(y_e - Z_1)H(Z_1 - y_e) + Z_1]H(Z_2) \\ &\quad - [(y_c - Z_1 + (y_c + y_d) \frac{b_2}{b_3})H(y_c - Z_1) + \\ &\quad (y_e - y_c) + Z_1][1 - H(Z_2)] \end{aligned} \quad (59)$$

and

$$\frac{\partial F_2}{\partial b_2} = - \left[ (Z_1 - y_e) H(Z_1 - y_e) H(Z_2) - \left[ (Z_1 - y_r - y_d) H(y_r - Z_1) + (y_c - y_e) \right] (1 - H(Z_2)) \right] \quad (60)$$

For  $\frac{\partial F}{\partial \alpha}$  the result is

$$\frac{\partial F}{\partial \alpha} = \begin{bmatrix} \frac{\partial F_1}{\partial \alpha_1} & \frac{\partial F_1}{\partial \alpha_2} \\ \frac{\partial F_2}{\partial \alpha_1} & \frac{\partial F_2}{\partial \alpha_2} \end{bmatrix} \quad (61)$$

$$= \begin{bmatrix} 0 & 0 \\ 0 & - \frac{(b_2 - b_1)^2}{b_1} H(y_r - Z_1) + (b_1 - b_2) \end{bmatrix} (1 - H(Z_2)) \quad (62)$$

The next step is to calculate the partial derivatives of  $f_0$  and  $f_1$  with respect to the state variable vector  $Z$ , state parameter vector  $b$  and function vector  $\alpha(b)$ . To do that, one has to use equation (53) and differentiate it with respect to  $Z$ ,  $b$ , and  $\alpha(b)$  as follows:

$$\frac{\partial f_0}{\partial Z_1} = \frac{1}{m} (2 H(f_0) - 1) \left[ -b_2 - \left[ (b_1 - b_2) H(Z_1 - y_e) + b_1 H(Z_2) + (b_1 - b_2) H(y_r - Z_1) + b_1 (1 - H(Z_2)) \right] \right] \quad (63)$$

$$\frac{\partial f_0}{\partial Z_2} = - \frac{b_1}{m} (2 H(f_0) - 1) \quad (64)$$

$$\frac{\partial f_0}{\partial b_1} = - \frac{Z_1}{m} (2 H(f_0) - 1) \quad (65)$$

$$\frac{\partial f_0}{\partial b_2} = - \frac{Z_2}{m} (2 H(f_0) - 1) \quad (66)$$

$$\frac{\partial f_0}{\partial b_3} = \frac{1}{m} (2 H(f_0) - 1) \left[ (y_e - Z_1) H(Z_1 - y_e) + Z_1 H(Z_2) + \left[ (y_r - Z_1 + (y_c + y_d) \frac{b_1}{b_2}) H(y_r - Z_1) + (y_e - y_c) + Z_1 \right] (1 - H(Z_2)) \right] \quad (67)$$

$$\frac{\partial f_0}{\partial b_4} = - \frac{1}{m} (2 H(f_0) - 1) \left[ (Z_1 - y_e) H(Z_1 - y_e) H(Z_2) + \left[ (Z_1 - y_r - y_d) H(y_r - Z_1) + (y_c - y_e) \right] (1 - H(Z_2)) \right] \quad (68)$$

$$\frac{\partial f_0}{\partial \alpha_1} = 0 \quad (69)$$

$$\frac{\partial f_0}{\partial \alpha_2} = - \frac{1}{m} (2 H(f_0) - 1) \left[ \frac{(b_2 - b_1)^2}{b_1} H(y_r - Z_1) + (b_1 - b_2) \right] (1 - H(Z_2)) \quad (70)$$

Now, if we define

$$f_1(t, Z, b) = [Z_1(t)] - (2 H(Z_1) - 1) Z_1(t) \quad (71)$$

Then the condition on the extreme value of relative displacement can be written as

$$f_1(t, Z, b) - \theta_1 = [Z_1(t)] - Z_{1, \max} \leq 0, 0 \leq t \leq \tau \quad (72)$$

Defining

$$\theta = Z_{1, \max} \quad (73)$$

then equation (72) becomes

$$(2 H(Z_1) - 1) Z_1(t) - \theta_1 \leq 0, 0 \leq t \leq \tau \quad (74)$$

Therefore, partial derivatives of  $f_1(t, Z, b, \alpha(b))$  with respect to state variable vector  $Z$ , state parameter vector  $b$  and  $\alpha(b)$  become

$$\frac{\partial f_1}{\partial Z_1} = 2 H(Z_1) - 1 \quad \frac{\partial f_1}{\partial Z_2} = 0 \quad (75)$$

$$\frac{\partial f_1}{\partial b_1} = \frac{\partial f_1}{\partial b_2} = \frac{\partial f_1}{\partial b_3} = \frac{\partial f_1}{\partial b_4} = \frac{\partial f_1}{\partial \alpha_1} = \frac{\partial f_1}{\partial \alpha_2} = 0 \quad (76)$$

Thus the differential equations for the adjoint variables

$$\lambda_0 = \begin{bmatrix} \lambda_{0,1} \\ \lambda_{0,2} \end{bmatrix} \quad \text{and} \quad \lambda_1 = \begin{bmatrix} \lambda_{1,1} \\ \lambda_{1,2} \end{bmatrix} \quad (77)$$

become

$$\begin{bmatrix} 1 & 0 \\ 0 & m \end{bmatrix} \begin{bmatrix} \dot{\lambda}_{0,1} \\ \dot{\lambda}_{0,2} \end{bmatrix} + \begin{bmatrix} 0 & \frac{\partial f_2}{\partial Z_1} \\ 1 & -b_1 \end{bmatrix} \begin{bmatrix} \lambda_{0,1} \\ \lambda_{0,2} \end{bmatrix} = \quad (78)$$

$$2(1 - \theta_1 - b_1) H(1 - \theta_1 - b_1) (2 H(f_0) - 1) \begin{bmatrix} \frac{\partial f_0}{\partial Z_1} \\ -b_1 \\ m \end{bmatrix}$$

and

$$\begin{bmatrix} 1 & 0 \\ 0 & m \end{bmatrix} \begin{bmatrix} \dot{\lambda}_{1,1} \\ \dot{\lambda}_{1,2} \end{bmatrix} + \begin{bmatrix} 0 & \frac{\partial f_2}{\partial Z_1} \\ 1 & -b_1 \end{bmatrix} \begin{bmatrix} \lambda_{1,1} \\ \lambda_{1,2} \end{bmatrix} = 2H(f_1 - \theta_1)(f_1 - \theta_1) \begin{bmatrix} \frac{\partial f_1}{\partial Z_1} \\ 0 \end{bmatrix} \quad (79)$$

The cases studied are listed in Table 1. Case 16 is that of Schmit and Fox [6] for a linear system, with the base input the rectangular pulse of Fig. 5, designated Input II. Cases 1 thru 15 are for the nonlinear system and the excitation used is shown in Fig. 7, with  $\ddot{y}_0(t)$  specified as follows, and designated Input I:

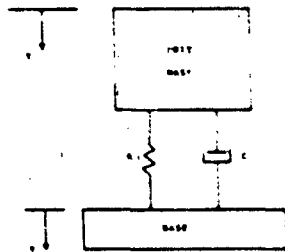


Fig. 4. The Simple System

$$\begin{aligned} \ddot{y}_0(t) &= -414.0g & 0 < t < 0.00075 \text{ sec.} \\ \ddot{y}_0(t) &= 6.3g & 0.00075 < t < 0.050 \text{ sec.} \\ \ddot{y}_0(t) &= 0 & t > 0.050 \text{ sec.} \end{aligned}$$

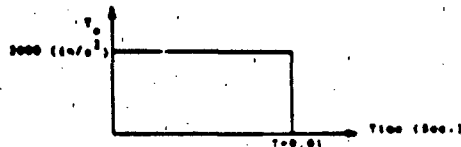


Fig. 5-The Square Pulse, Input No. II.

#### Linear System with Damping

The linear system with damping, Case 16, is a special case of the nonlinear system with  $k_n = k_p = 0$ . The input acceleration is, as in Fig. 5:

$$\begin{aligned} \ddot{y}_0(t) &= 2000 \text{ in./sec} & 0 < t < 0.01 \text{ sec.} \\ \ddot{y}_0(t) &= 0 & t > 0.01 \text{ sec.} \end{aligned}$$

In Table 2, the results of Schmit and Fox [6] are compared with results obtained with the present method. For both optimizations, the initial values of the parameters are:  $k=1000 \text{ lb./in.}$  and  $c=3.0 \text{ lb./sec./in.}$ . The specified  $(y_r)_{\max} = 0.6 \text{ inches}$ . The final design, representing the optimum values, are also listed in Table 2. In Fig. 6

Table 1. List of the Design Cases 1 to 16.

Case No.	Yield Deflection (in.)	Weight (lb.)	Maximum Relative Displacement (in.)	Upper and Lower Bounds	Loading Case
1	0.3	100	2.0	C-C=0.0	1
2	0.3	100	2.0	C-C=0.0	1
3	0.3	100	2.0	1, None	1
4	0.3	100	2.0	1, None	1
5	0.3	100	2.0	1, None	1
6	0.3	1000	2.0	1, None	1
7	0.3	10000	2.0	1, None	1
8	0.1	100	2.0	1, None	1
9	0.1	100	2.3	1, None	1
10	0.3	100	2.0	1, None	1
11	1.0	100	2.0	1, None	1
12	1.0	100	2.0	1, None	1
13	2.0	100	2.0	1, None	1
14	0.3	100	2.0	C-C=0	1
15	0.3	1.0	2.0	1, None	1
16	---	100.0	0.0	Spk=0, Spk=0	11

a design graph is shown as a plot of  $k$  versus  $c$ . The curve with the shading shows the displacement constraint of 0.6 inches. The arch-shaped curves are maximum acceleration,  $\ddot{y}(t)$ , curves with units of  $\text{in./sec.}^2$ . The initial design point is marked and the design paths followed by the two different methods are plotted. The more direct path is that of the State Space Optimization Method, so it appears to be more efficient than that of [6].

#### Nonlinear System with No Damping

For Cases 2 and 14, the value of damping constant was specified as  $c=0$ . In addition, it happened that for Case 15, where the bounds excluded only negative  $c$ , the computer program chose  $c=0$ , because the mass was very small.

For all the nonlinear cases, since the linear spring stiffness  $k$  could be combined with  $k_n$  and  $k_p$ , the program was run with  $k_n = k_p = 0$ . Thus, for no damping, the only parameters remaining were  $k_n$  and  $k_p$ .

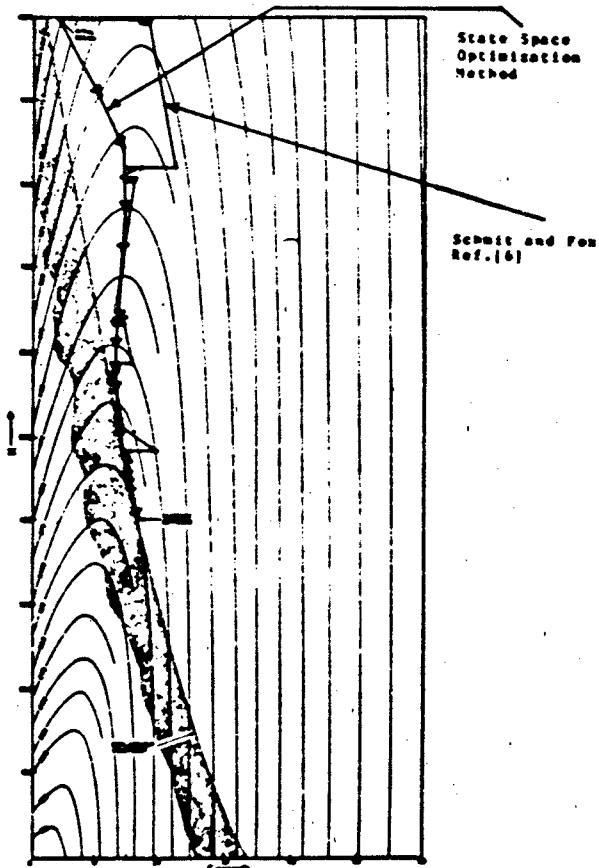


Fig. 6. Comparison Between the Design Path For Case A of Ref. [6] and the Path Taken by the State Space Optimization Method.

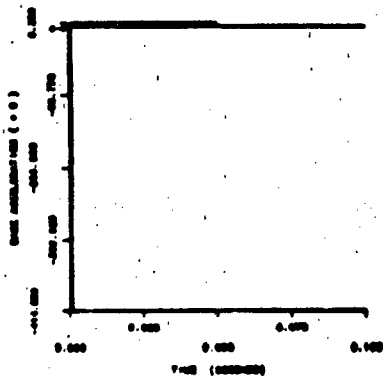


Fig. 7. Plot of the Base Acceleration Versus Time For the Impulse Loading No.1

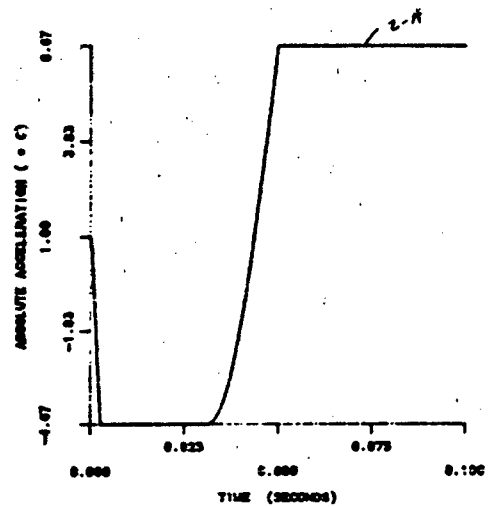


Fig. 8. Plot of the Absolute Acceleration Versus Time for the Design Case No. 2-A.

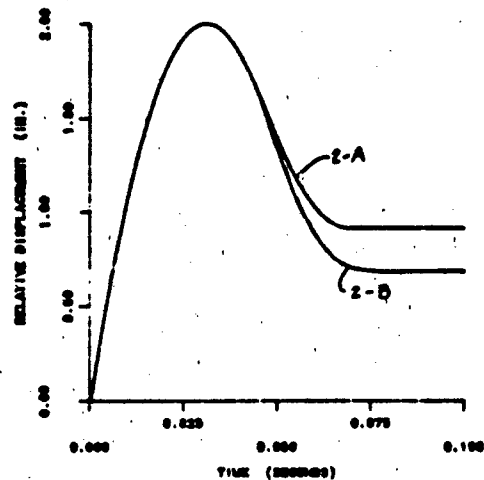


Fig. 9. Plot of the Relative Displacement Versus Time for the Design Case No. 2-A and 2-B.

Table 2. Comparison of the Results Obtained by the Writers of (6) and the Results Obtained by Using State Space Optimization Method - Case 16.

TYPE OF THE PROBLEM: Minimize Maximum Acceleration such that Max. Relative Displacement be less than 0.6 (In.)								
METHOD USED	INITIAL DESIGN				FINAL DESIGN			
	K	C	(Yr)max.	(Acc.)max.	K	C	(Yr)max.	(Acc.)max.
Schmit and Fox Method	1000.	3.0	---	580	410	15.9	0.6	366.4
State Space Method	1000.	3.0	0.567	590	414	15.9	0.6	368.8

M=336.4 lbs.  
Displacements are in inches  
Accelerations are in inches/Second<sup>2</sup>:

In Table 3 the optimum values are given for Cases 2-A and 2-B. First for Case 2-A the acceleration was minimized at the initial peak only or during the loading phase of the nonlinear spring. For this situation the optimum  $k_e=1889$  lb./in. and optimum  $k_p=0$ . The initial peak acceleration was  $-4.67g$  but an extension of the timewise solution showed the second maximum acceleration at  $6.67g$  as seen in Fig. 8. The timewise relative displacement is given in Fig. 9, which shows the bound of  $+2$  inches was reached. To minimize the maximum positive acceleration the program was re-run through both the loading and unloading phase of the non-linear spring, or one complete cycle, for Case 2-B. The resulting acceleration-time curve is shown in Fig. 10. The new peak values were  $-5.31g$  and  $6.57g$ , so by producing the minimum acceleration over one whole period, the negative peak was increased and the positive peak decreased slightly. It should be noted that for Case 2-B, the optimum value of  $k_p=70$ , rather than zero. The load-deflection curve for the non-linear spring for Case 2-A is shown in Fig. 11.

For Case 14 the best value of  $k_p=0$  as summarized in Table 4. Case 14 differs from Case 2-A in the size of the mass and the maximum relative displacements. For Case 14, and all the Cases except 2-A, the optimization was over a complete cycle.

Design Case 15 was done to study effect of weight variation. Again  $k_p=0$ , as shown in Table 5 and the case is discussed further under effect of variation of mass.

#### Nonlinear System with Damping

As a proof of the validity of the method for the general system, Case 1 was done two ways: first by a long process of trial and error and then by the computer programs. The value of damping was set at  $c=4.0$  lb.s./in.. Then a design graph was plotted as  $k_e$  versus  $k_p$ , with lines of constant  $(y_r)_{max}$  and  $(\ddot{y})_{max}$ , as in Fig. 12. From these curves it can be seen that for  $(y_r)_{max}=2$  inches, the minimum  $(\ddot{y})_{max}$  lies between  $4.4$  and  $4.5g$ , and further analysis showed that

Table 3. A Comparison Between the Optimum Quantities Obtained for Case No. 2 Based on:  
a) Optimum Performance During Loading Only  
b) Optimum Performance During Loading and Unloading

Case No. 2	Optimum	Maximum Acceleration/g		
		$k_e$	$k_p$	Loading
Case 2-A Design Based on Optimum Performance During Loading Only	1889	0	-4.67	6.67
Case 2-B Design Based on Optimum Performance During Loading and Unloading	1708	70	-5.31	6.57

$k_e$ : Lb./In.  
 $k_p$ : Lb./In.

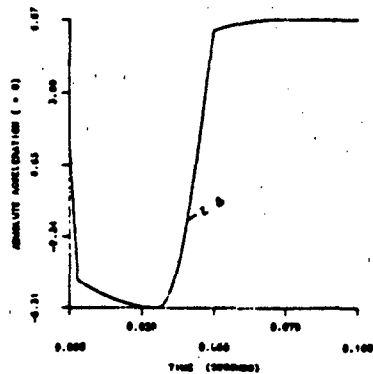


Fig. 10. Plot of the Absolute Acceleration Versus Time for the Design Case No. 2-b

the 4.46g curve just touched the  $(y_r)_{max} = 2$  inches curve. The computer program based on the State Space Method followed the design path indicated by the line with arrows, in the direction of decreasing displacement until it reached the 2 inch bound.

For Design Case 3, a design graph was also made, as in Fig. 13, for  $(y_r)_{max} = 2$  in., but for various  $c$ . The arrows on the "constant  $c$  lines" are in the direction of decreasing  $(y_r)_{max}$ . In addition, two computer design paths are shown with the arrows indicating the direction of decreasing  $(y_r)_{max}$ . In Fig. 14, a three-dimensional design plot is shown. As summarized in Table 4, optimum  $c = 4.04$  and  $k_e = 164.7$  lb./in. with  $k_p = 189.8$  lb./in. for Case 3. Since  $k_p$  is greater than  $k_e$ , a hardening spring system is required, as shown in the load-deflection curve for Case 3, Fig. 15. One important point is that the

Table 4. Initial and Optimum Design For the Design Case No. 14

Case No.	Initial Design					Optimum Design				
	B1	B3	B4	(Yr)max.	(Acc.)max./g	B1	B3	B4	(Yr)max.	(Acc.)max./g
14	B1=0	2400	130	2.93	1.76	0.0	2433	0	3.0	1.27
	B1=0									

slope of the unloading curve was taken as  $k_e$ , recalling Fig. 2, which results in a load-displacement curve in Fig. 15 which may be difficult to achieve in practice, after the maximum deformation has occurred. In Figs. 16 and 17 the  $y_r$  versus  $t$  and  $\ddot{y}$  versus  $t$  curves are given for Case 3.

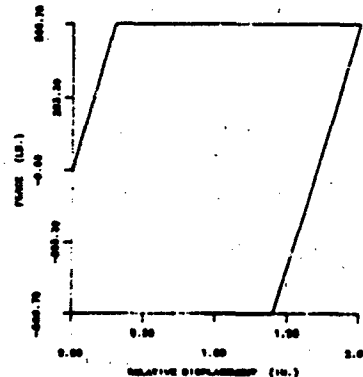


Fig. 11. Plot of the Force in Elastic-Spring VS. Relative Displacement-Case 2-A

The effect of variation of mass is shown by comparing Cases 3, 4, 5, 6, 7 and 15 (see Table 1), where the bounds set for  $c$  are only that  $c$  be non-negative, that is  $c \geq 0$ . Plots of  $c$ ,  $k_e$ , and  $k_p$  versus  $W$  are given in Figs. 18, 19 and 20 respectively. Note that the plots show almost linear variation. The value of  $c$  goes to zero at about  $W = 6$  lb., and then stays at zero for  $0 < W < 6$  lb. The results are summarized in Table 5. Note that the transmitted acceleration is practically constant, except for very small mass, when  $c = 0$ .

Table 5. Optimum Quantities For Cases 3 to 7 and 15.

Case No.	W (lb.)	c (lb./in.)	$k_e$ (lb./in.)	$k_p$ (lb./in.)	(Yr)max.	(Acc)max./g
15	1	1.0	118.8	0	2.0048	6.640
3	100	14.04	164.7	189.8	2.0003	4.461
4	200	18.36	223.5	389	2.0001	4.456
5	300	12.68	279.5	589	1.9999	4.454
6	1000	142.9	1680	1988	2.0001	4.45
7	10,000	1431.5	15848	19966	2.0001	4.47

For Case 3 and Cases 8 thru 13, the yield deformation  $y_e$  was varied from 0 to 2 inches (see Table 6). The situation for  $y_e = 0$  and  $y_e = 2$  are exactly the same, with the same linear load-deflection curve. The optimum  $c$  increases and then decreases as  $y_e$  increases. The transmitted maximum acceleration is minimum when  $y_e = 1$  inch, which is one-half

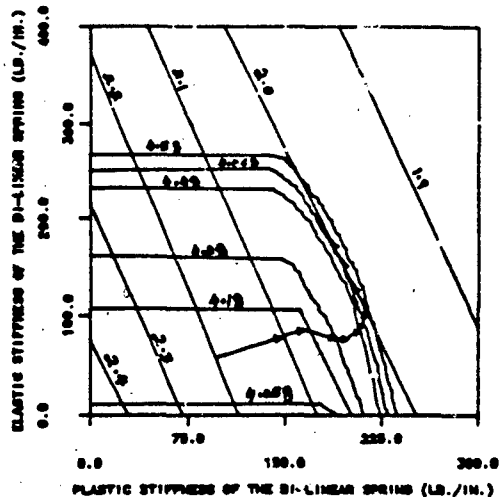


Fig. 12. Geometrical Paths of Constant Acceleration and Maximum Relative Displacement for the Design Case No. 1

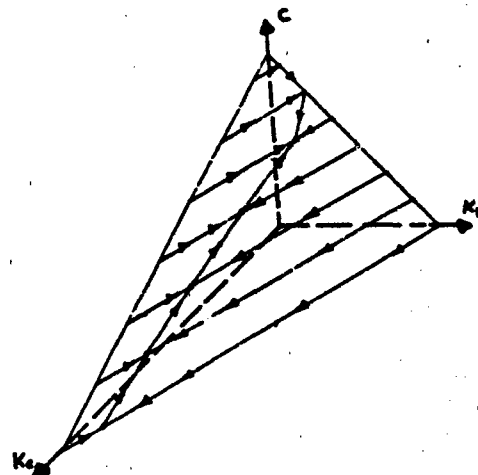


Fig. 14. Three Dimensional Presentation of a Four Dimensional Design Space and Path of the Optimum Points for the Design Case No. 3. The Arrows Show the Direction of Decreasing Maximum Acceleration.

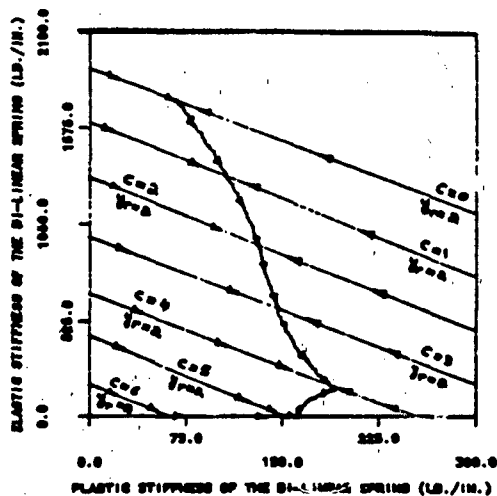


Fig. 13. Plot of the Optimum Points for the Design Case No. 3. The Arrows on Each  $\alpha$ -line Show the Direction of Decreasing Maximum Acceleration for that Line and Arrows Between the  $c$ -line show the Direction of Decreasing Maximum Acceleration in going from one  $\alpha$ -line to the next  $c$ -line.

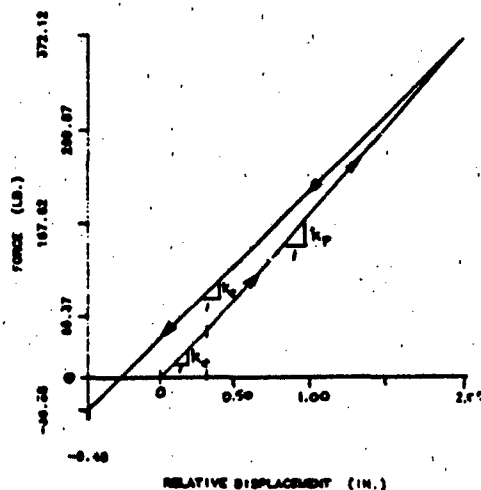


Fig. 15. Plot of the Force in Elastic-Plastic Spring Versus Relative Displacement for the Design Case No. 3.

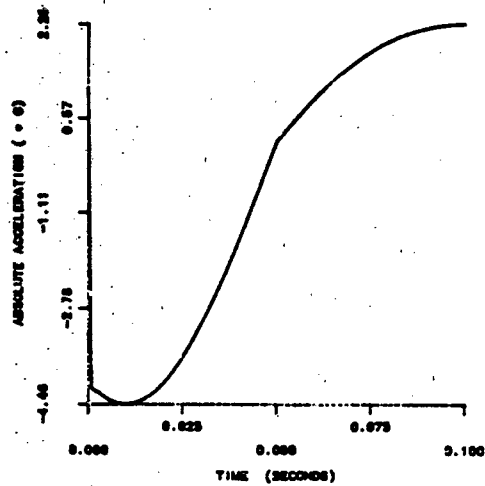


Fig. 16. Plot of the Absolute Acceleration Versus Time for the Design Case No. 3.

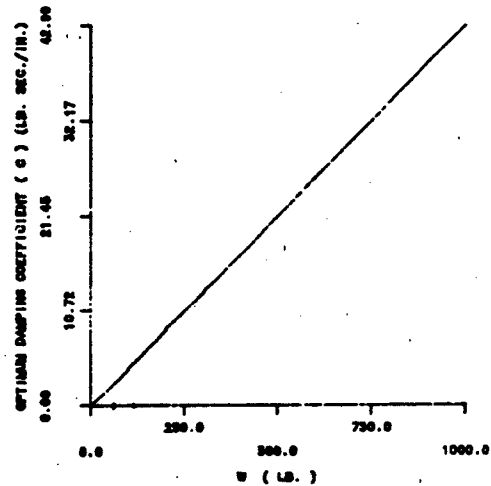


Fig. 18. Plot of the Optimum Damping Coefficient Versus Weight of the Mass ( $\mu$ ) for the Design Cases 3 to 7 and 13.

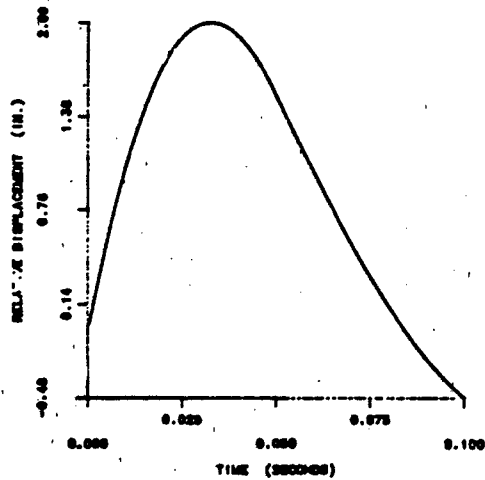


Fig. 17. Plot of the Relative Displacement Versus Time for the Design Case No. 3.

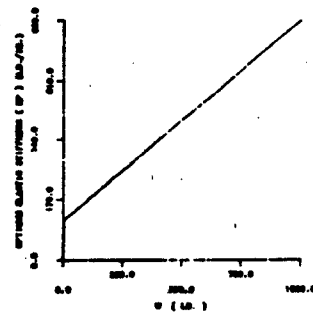


Fig. 19. Plot of the Optimum Elastic Stiffness of the Bi-linear Spring Versus Weight of the Mass ( $\mu$ ) for the Design Cases 3 to 7 and 13.

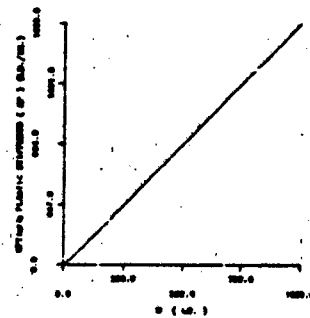


Fig. 20. Plot of the Optimum Plastic Stiffness of the Bi-linear Spring Versus Weight of the Mass ( $\mu$ ) for the Design Cases 3 to 7 and 13.

the maximum relative displacement. In general, a hardening spring is required when the spring is nonlinear.

Table 6. Optimum Quantities For Cases 3 and 8 to 13.

Case No.	$\mu_e(\%)$	C	$k_e$	$k_p$	$(Yr)_{max}$	$(Acc)_{max}/g$
8	0	13.96	189.01	2.0007	4.462	
9	0.1	13.997	189.11	2.0000	4.465	
3	0.3	14.04	189.81	2.0003	4.461	
10	0.5	14.258	1107.51	2.0001	4.424	
11	1.0	14.16	1149.71	2.9001	4.351	
12	1.5	13.97	1180.61	2.0002	4.390	
13	2.0	13.96	189.01	2.0007	4.462	

#### Summary and Conclusion

The theory is outlined for the State Space Method as extended to include floating boundaries and applied to a shock mounting system having four unknown parameters:  $k$ ,  $c$ ,  $k_e$  and  $k_p$ . Since the linear spring is in parallel with the nonlinear spring, the stiffnesses may be combined, so most of the practical results are given for  $k=0$ , for the nonlinear system. A computer program was developed such that, in one computer run, the optimum values of  $c$ ,  $k_e$ , and  $k_p$  are determined such that the transmitted acceleration  $(y)_{max}$  is a minimum while the relative deformation remains within specified upper and lower bounds, say  $\pm 2$  inches. The following conclusions are offered:

(1) The State Space Method seems to be more efficient than the Steep-Descent Alternate Step Method used by Schmit and Fox [6] when applied to the same linear one-degree-of-freedom systems in that the path followed is more direct.

(2) For the excitation designated as the Input I, which includes a very severe initial impulse, the optimum values of  $k_e$ ,  $k_p$  and  $c$  vary almost linearly with the size of the supported mass, while the maximum transmitted acceleration remains nearly constant. For very small mass,  $c=0$  and  $k_p$  approaches zero. For larger masses,  $c=0$  and a hardening spring is best.

When the ratio of yield deformation to maximum deformation is varied from zero to one, it is found that the  $(y)_{max}$  is least when the ratio is one-half.

(3) The computer time for each run depends on the nearness of the initial guess to the final design values.

The method could be applied to more complex problems, such as multi-degree-of-freedom systems on nonlinear mounts.

#### Acknowledgments

The study was supported in part by the Defense Nuclear Agency under Contract DNA 001-78-C-0036 and by the Office of Naval Research thru Contract N00014-79-C-1049.

#### BIBLIOGRAPHY

- (1) M. H. Hsiao, E.J. Haug, Jr., and J. S. Arora, "A State Space Method for Optimal Design of Vibration Isolators", Journal of Mech. Design, Trans. ASME, Vol. 101, pp. 309-314, 1979.
- (2) A.V. Fiacco and G.P. McCormick, "Non-linear Programming: Sequentially Unconstrained Minimization Techniques", Wiley, New York, 1968.
- (3) Z. Wasitowski and A. Branbt, "The Present State of Knowledge in the Field of Optimum Design of Structures", Appl. Mech. Rev., 16, pp. 341-350, 1963.
- (4) C. Y. Sheu and W. Prager, "Recent Developments in Optimal Structural Design", Appl. Mech. Rev. 21, pp. 985-992, 1968.
- (5) B.L. Pierson, "A Survey of Optimal Structural Design Under Dynamic Constraints", Int. J. Num. Meth. Engng., Vol. 4, pp. 491-499, 1972.
- (6) L. A. Schmit and R. L. Fox, "Synthesis of a Simple Shock Isolator", NASA Contractor Report, NASA CR-55, June, 1964.
- (7) D. C. Karnopp and A. K. Trikha, "Comparative Study of Optimization Techniques for Shock and Vibration Isolation", ASME, Journal of Engineering for Industry, Vol. 91, pp. 1128-1132, Nov., 1969.
- (8) K. D. Willmert and R. L. Fox, "Optimum Design of a Linear Multi-Degree-of Freedom Shock Isolation System", ASME, Journal of Engineering for Industry, Vol. 94, pp. 465-471, May, 1972.
- (9) K. A. Afimiwala and R. W. Mayne, "Optimum Design of an Impact Absorber", ASME, Journal of Engineering for Industry, Vol. 96, pp. 124-130, Feb., 1974.
- (10) E. Sevin and W. D. Pilkey, "Optimization of Shock Isolation Systems", S.A.E. Paper No. 680749, 1968.
- (11) J. Wolkovitch, "Techniques for Optimizing the Response of Mechanical Systems to Shock and Vibration", S.A.E. Paper No. 680748, 1968.

(12) D. L. Bartel, E. J. Haug, Jr. and K. Rim, "The Optimum Design of Spatial Frames Using the Method of Constrained Steepest Descent With State Equations", Journal of Engineering for Industry, Transaction of the ASME, pp. 1261-1267, 1971.

(13) D. L. Bartel and A. I. Krauter, "Time Domain Optimization of a Vibration Absorber", Journal of Engineering for Industry, Transaction of the ASME, pp. 799-804, Aug., 1971.

(14) E. J. Haug, Jr., K. C. Pan and T. C. Streeter, "A Computational Method for Optimal Structural Design: I. Piecewise Uniform Structures", Int. Journal Num. Meth. Engng., Vol. 5, pp. 171-184, 1972.

(15) J. S. Arora and E. J. Haug, Jr., "Efficient Optimal Design of Structures by Generalized Steepest Descent Programming", Int. J. Num. Meth. Engng., Vol. 10, pp. 747-766, 1976.

(16) T. T. Feng, J. S. Arora and E. J. Haug, Jr., "Optimal Structural Design Under Dynamic Loads", Int. J. Num. Meth. Engng., Vol. 11, pp. 39-52, 1977.

(17) E. J. Haug, Jr. and J. S. Arora, "Design Sensitivity Analysis of Elastic Mechanical Systems", Computer Methods in Applied Mechanics and Engineering, Vol. 15, pp. 35-62, 1978.

(18) K. Kasraie, "State Space Method For Optimal Design of Shock Absorbers With Floating Boundaries", Doctoral Thesis, The Pennsylvania State University, Aug., 1983.

## The development of a method for the shock-resistant securing of large batteries in submarines

By:  
**A. Jansen,**  
Royal Netherlands Navy, The Hague  
Project-officer, Shock, Noise and Vibration

The paper describes the different tests carried out for the development of an adhesive material (polyurethane) for bonding a hook-construction to the deck and the battery, to prevent the upwards movement of large batteries in a submarine during an underwater explosion. Test results are presented and discussed. This bonding method can be a powerful tool in specific situations for reducing (labour) cost, to improve the shock resistance and for simplification of structures. Some examples are given.

### Introduction

In the course of time several navies have developed their own system for the securing of large batteries in submarines, to prevent the vertical movement during an underwater explosion. If there is insufficient clearance between the top of the battery and the ship's structure and no securing device, the vertical shock motion will cause a short circuit: a disaster for the submarine.

Due to a design modification of the batteries, the Royal Netherlands Navy had to reconsider the securing of the batteries for her new submarines under construction. The height of the battery increased considerably and reduced the available clearance to a few centimetres. The existing securing system of vertically placed wedges, which give only friction between the batteries, became unacceptable and a modification was necessary. The Royal Netherlands Navy, together with Bolidt B.V. Alblasserdam (NL) and with assistance of Varta, Hagen (FRG), developed a bonded polyurethane (PU) joint, which fully meets all requirements.

### Securing methods

- A) A resiliently mounted battery storage compartment is the solution which has been applied [1].  
The resilient mountings decoupled the batteries from the ship and the acceleration levels transmitted via the mountings are too low to cause a vertical displacement of the batteries relative to the resiliently mounted compartment.
- B) An old method, which has been applied many times, is the use of wedges, which press the batteries to each other and to the bulkheads and prevent horizontal movements during seaway and shock motions. It gives no vertical protection. The friction, between the batteries and the compartment bulkheads, reduces the vertical displacement only a little during an underwater explosion.

In 1978 the Royal Netherlands Navy did a number of shock tests on the IWECO-TNO medium weight shock testing machine (figure 1) with batteries fastened with wedges.

This shock testing machine can simulate rather accurately nearly all shock motions, submarine shock motions as well, by adjusting the stiffness of the acceleration and deceleration springs.

For the shock test the batteries and wedges were positioned and pressed to each other in exactly the same arrangement as on board (figure 2) [2].

High speed cameras and measurements indicated already displacements up till about 250 mm, at moderate shock motions (figure 3). These large movements are unacceptable and dangerous. Notice the large difference in acceleration level between top and bottom of the battery.



Figure 2: Batteries with wedges on medium weight shock testing machine

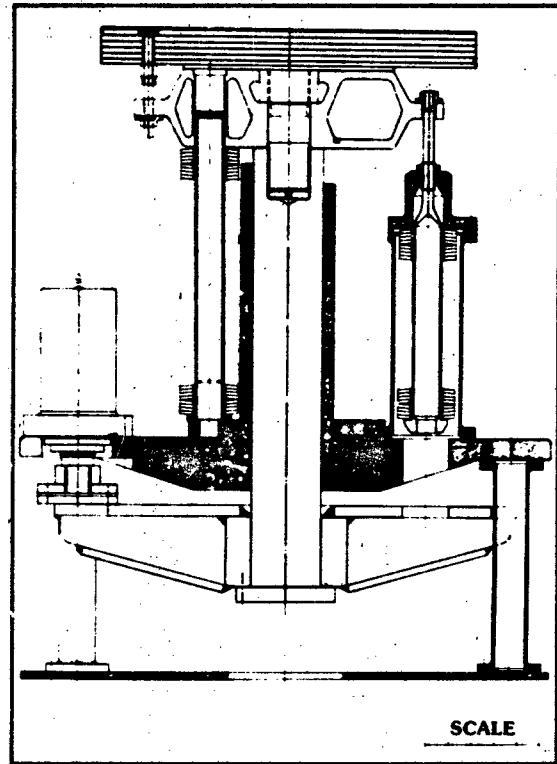


Figure 1: Medium weight shock testing machine

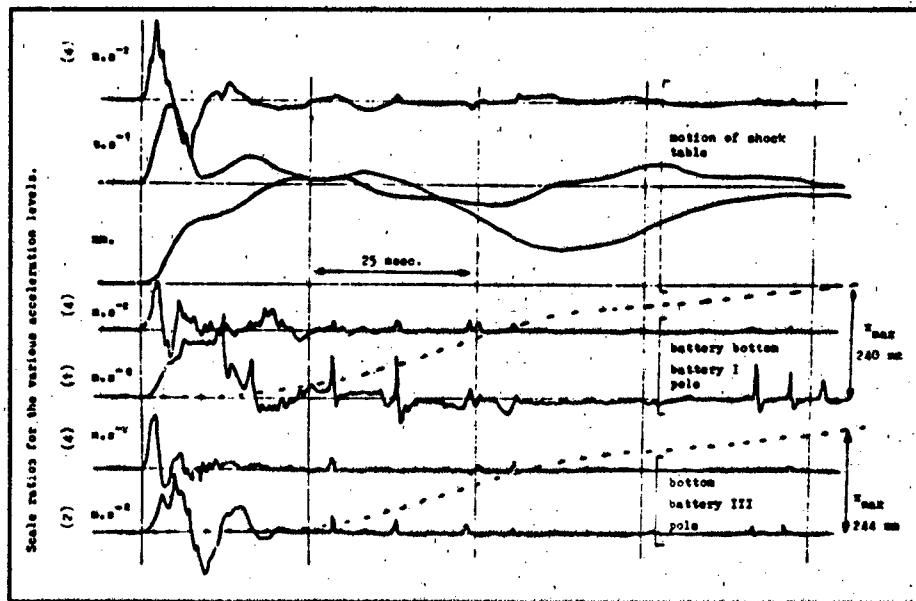


Figure 3: Shock measuring results

- C) Holding down straps between the top of the battery and the compartment's bottom were studied, but found to be unacceptable and unpractical.
- D) A good and practical solution is a hook, bolted to the ship's structure, and counterhook, bolted to the battery bottom (figure 4). Shock testing in a submarine test section, to a level just without plastic deformation of the hull, proofed its rather good shock resistance [3].

Together with Varta Batterie A.G., Hagen (FRG), who provided the batteries, the Royal Netherlands Navy investigated a hook construction (figure 5) on the medium weight shock testing machine [4].

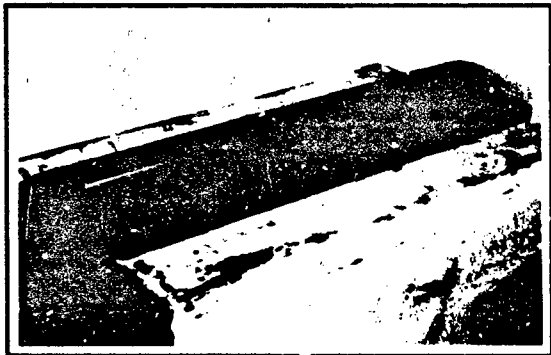


Figure 5: Bottom view of the fixing hook

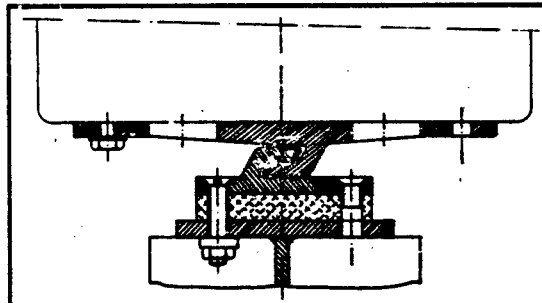


Figure 4: Hook construction

The battery met the maximum shock requirements without any damage and expected hull lethal levels with some damage (figure 6).

This hook construction was in principle adopted by the Royal Netherlands Navy. However, it was not possible to apply bolted hooks to the ship's structure because the compartment was already nearly finished, the increased chance of a short-circuit via the bolts was not accepted, the required puncture-voltage for the (whole) compartment was very difficult to reach and the risk of corrosion problems was too high. In connection with the available space the height of the hook had to be reduced.



Figure 6: Damaged battery housing

### Development of a bonded joint

Except for the modern GRP minehunters, it is not common in ordinary naval ship design to apply adhesives like epoxy, polyurethane and such in the ship's structure or for heavily loaded constructions. But in this situation it could solve most of the problems at the same time; if an adhesive could be found which met the requirements.

### Purpose of the R&D programme

The purpose was to select an adhesive, in combination with the (re-)design of the hook construction and the given ship's structure (i.e. the nearly completed battery compartment), which fulfils the requirements at a minimum of costs.

### R&D programme

With the emphasis on the mechanical aspects, the R&D programme was in broad outlines as follows:

- A) The selection of one or more adhesives.
- B) Static strength tests to determine:
  1. tensile strength of adhesive with appropriate primer;
  2. influence of plate stiffnesses and layer thickness;
  3. bonding strength of the primer to stainless steel, High Tensile Steel and GRP.
- C) Dynamic tests, i.e. shock tests, to determine:
  1. dynamic tensile strength of adhesive;
  2. dynamic/static strength ratio;
  3. weakest link in the chain: steel-primer-adhesive-primer-steel.
- D) Re-design of the hook construction:
  1. to reduce height, available space is 50 mm;
  2. to reduce costs;
  3. to obtain a uniform load distribution over the total bonded area.
- E) Shock testing of the battery with possible solutions of the hook construction.
- F) Shock testing of final hook construction bonded to battery and simulated deck structure.

### Selection of the adhesive

The possible adhesives were selected on a number of criteria, like:

- A) Applicable in thick layers (5 - 10 mm) to level the unevenness of the compartment deck;

- B) Resistance against battery-acid, water, aging and such;
- C) Suitable to meet severe shock loads and large deck deformations, causing high stresses and high peel forces;
- D) Highly flexible (elongation: > 100%) to average the differences in stresses, caused by the large differences in deck stiffnesses and adhesive layer thickness, and to prevent high shear stresses caused by the hull deformation, due to the high waterpressure;
- E) High puncture-voltage value;
- F) Long life-time, preferably equal to the ship's life-time.

After a first selection of different types of adhesives it was decided to continue with polyurethane-type adhesives. Generally speaking, PU has a lower shear and tensile strength than epoxies, but a considerably higher peel strength (2-5x) and, depending on the specific type, an extremely high elongation at break, up till about 800%. However, the mechanical and chemical "strength" decreases with an increasing elongation percentage; an optimum has to be found.

Finally 3 PU adhesives were chosen for further investigations. These three were: Bolidt LP2578, Bolidtec and Bolidt LP2711. The most important mechanical properties are presented in table A.

PU type	tensile strength <sup>†)</sup> (N/mm <sup>2</sup> )	elongation at break <sup>†)</sup> (%)	shore hardness
Bolidt LP 2711	2 (280 psi)	250	55 A
Bolidt LP 2578	14 (2000 psi)	60	60 D
Bolidtec	13 (1840 psi)	400	77 A

Table A: Mechanical properties of tested PU adhesives.

<sup>†)</sup> In accordance with DIN 53.455.

It should be noted that each PU requires different primers for a good bonding to different materials.

### Static strength tests

Taking into account mechanical and chemical properties, the Bolidtec PU seemed to be the most appropriate adhesive and as next best Bolidt LP2578. The properties of LP2578 were better than Bolidtec, but the strain was considerably lower.

Bolidt LP2711 had lower mechanical and chemical properties, but the strain was about twice as high as Bolidtec. Sealing of this adhesive by a better acid resistant PU would be necessary. Therefore most of the tests were concentrated on Bolidt LP2578 and Bolidtec.

A) The static tensile strength was determined for: three different types of testpieces and with different PU layer thicknesses, see figures 7 and 8.

The mean ultimate tensile strength about  $4,7 \text{ N/mm}^2$  for Bolidt LP2578 is somewhat better than Bolidtec with about  $4,2 \text{ N/mm}^2$  tensile strength. [5]

The influence of layer thickness and steel end-plates stiffness is neglected. Relative to the mass of the battery (assumed to be completely rigid) and the available area for the bonded joint, these values were sufficient.

3) To get some insight in the relative importance of the stiffnesses of the steel end-plates, the thicknesses were changed for the different testpieces (figure 7). Test results showed that a relatively low stiffness of both end-plates decreased the tensile strength with about 10-20% and with "infinite" stiff end-plates the tensile strength increased about 15-25%, both values relative to the mean ultimate tensile strength.

C) The influence of the layer thickness was considerable, which could be expected. Figure 9 shows the trend, ignoring some other possible parameters.

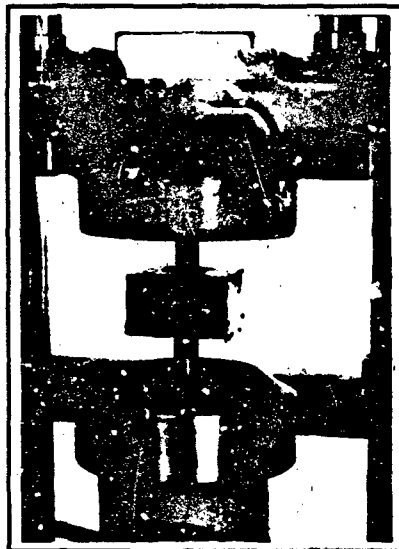


Figure 8: Testpiece during tensile test

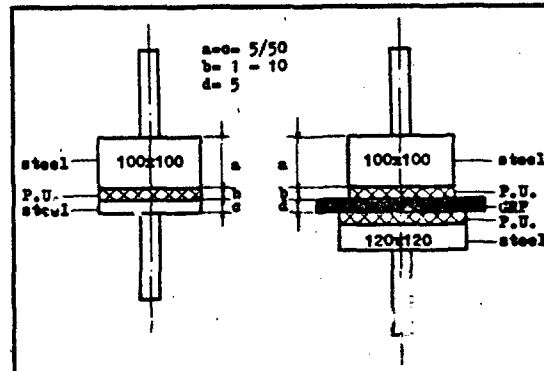


Figure 7: Testpieces for tensile test

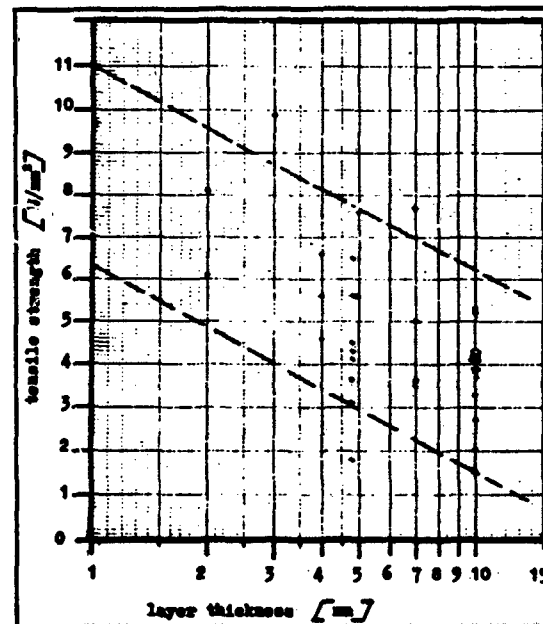


Figure 9: Influence of layer thickness on tensile strength

D) Extensive tests with dolleys were carried out with different types of primers on various materials (stainless steel, GRP, high tensile steel, etc.) to be sure that the bonding strength of the PU to the various materials was higher than the tensile strength of the PU itself (see figure 10).

The static tensile strength of the different primers was about  $6 - 9 \text{ N/mm}^2$ .

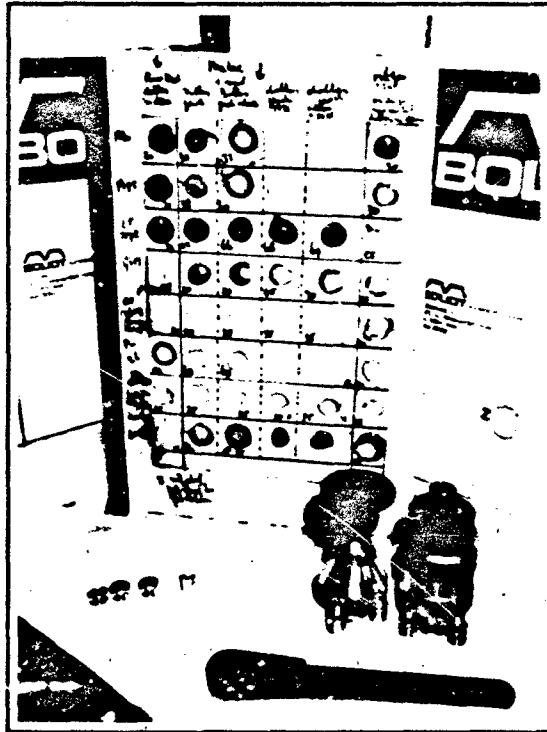


Figure 10: Testing of primers with dolleys

### Dynamic testing of adhesives

- A) It is well known that under a dynamic load the material's properties can differ largely from data determined statically.
- To determine the dynamic properties of the adhesive, a small mass (10 kgs) was bonded (layer thickness 5 mm) to a steel plate (figure 11) and shock tested on the light weight shock testing machine of IWECO-TNO. This machine is identical to the medium weight shock testing machine. From the measured accelerations and the given mass the stresses in the adhesive were calculated. E.g. for the Bolidtec PU they varied between 12 - 15 N/mm<sup>2</sup>.
- B) The dynamic/static ratio varied between 2.5 - 4, depending on the type of PU. It means that either the area of the bonded joint can be reduced or that there is a large safety factor comparing the required (calculated) minimum strength and the (dynamic) allowable stress.
- C) The weakest link in the chain is the bonding between steel and PU. In particular the combination stainless steel - PU requires attention (the hook will be made of stainless steel). By means of hammer drop tests (figure 12) this has been investigated. This investigation was necessary because the primer is a brittle material (strain about 1%).

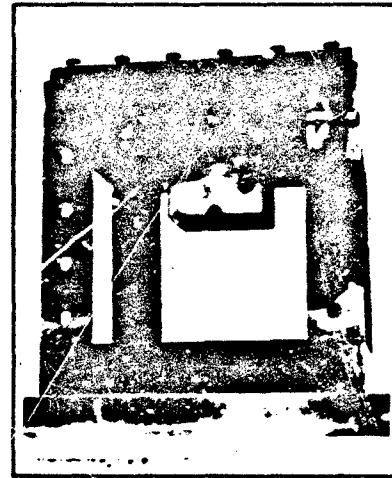


Figure 11: Shock testing with small mass

From these tests it could be concluded that with an increasing stiffness of the PU layer the fracture will shift from the PU to the primer. This was found after the first shock test series, with the dummy batteries on a simulated deck structure, on the medium weight shock testing machine. During these shock tests some hook constructions failed, due to the brittleness of the very thin (20 - 30  $\mu$ ) primer layer. The fracture started and remained in the primer itself.

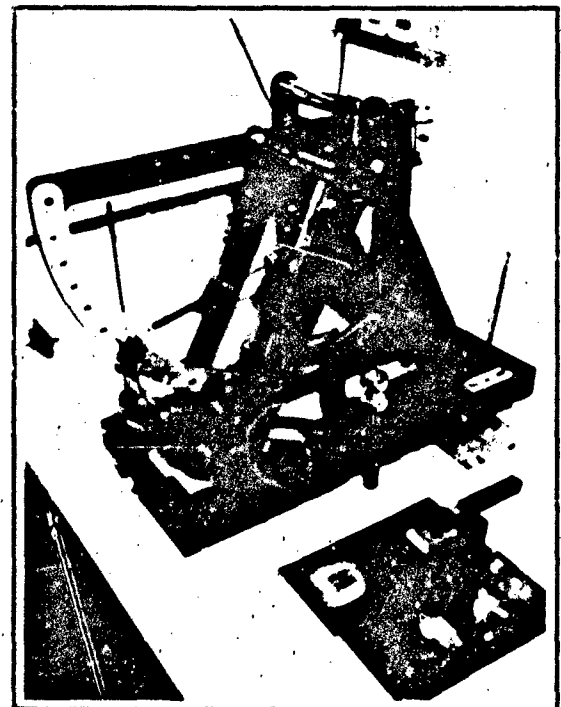


Figure 12: Hammer drop test for testing of primer

### Re-design of the hook construction

In this specific situation (a modification of the batteries during the construction phase) it was necessary to re-design the hook construction because only a very limited space was available. The hook construction, as normally provided by the battery supplier, Varta, was too large as far as height is concerned and, due to the manufacturing process (extrusion), rather expensive.

Optimisation of the hook by means of finite element stress analysis reduced the height from 19 mm to 14 mm (figure 13). In the final design two hooks instead of one will be used. The advantage of two hooks is that a more uniform load distribution can be obtained and the "bottom plate" of the hook can be thinner. If the hook construction could be bonded to the battery bottom the height of the nut in this bottom could be gained as well.

On the basis of a stress analysis, with two small hooks welded to a thin steel bottom plate, the Royal Netherlands Navy decided to design, to fabricate and to (shock)test a number of different hook constructions; it was cheaper and more reliable information could be obtained. In total 7 different designs were tested [6].

For these tests old submarine batteries were used. The hooks were bonded to the batteries and bolted to the shock testing machine (figures 14 and 15).

Six of the batteries failed at moderate shock levels. The (GRP) battery bottoms appeared to be severely weakened by water and acid and some minor structural damage (due to transport).

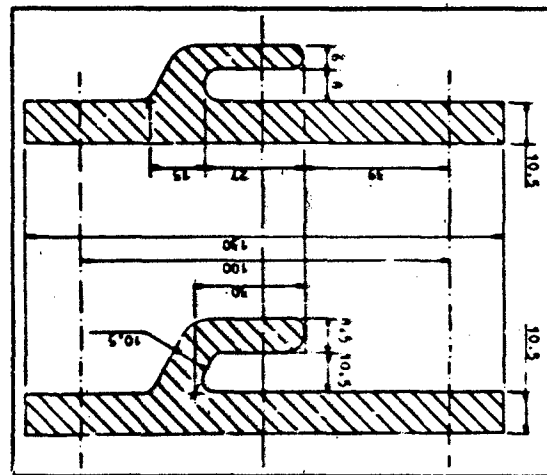


Figure 13: Original hook and optimised hook

Design no. 7 (figure 16) survived above hull lethal levels, without any damage as far as the "hook" concerned. The bonding of the hook to the battery consisted of 580 gr/m<sup>2</sup> glass roving mat and the PU adhesive Bolidt LP2578.

This PU will protect the battery bottom against mechanical damage and weakening (due to its flexibility and resistance against impact loading), acid and water, and guarantees the shock resistance over the battery life time. The bonded hook was at least 2 times stronger than the bolted hook, concerning the connection to the battery.

A hook bonded to the battery, compared to a bolted hook, gives also an increase of 1 - 1.5% in the battery's capacity for the same height. The battery bottom becomes thinner by leaving out the nuts.

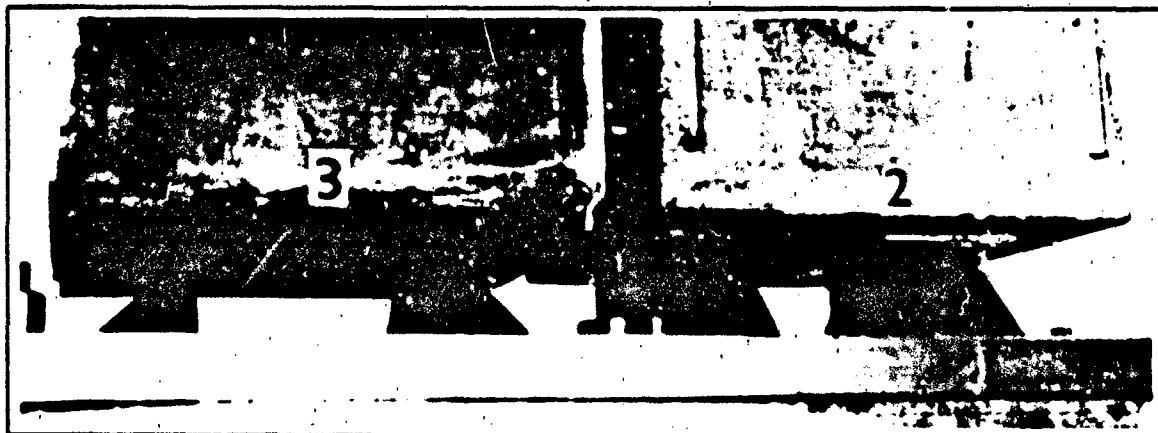
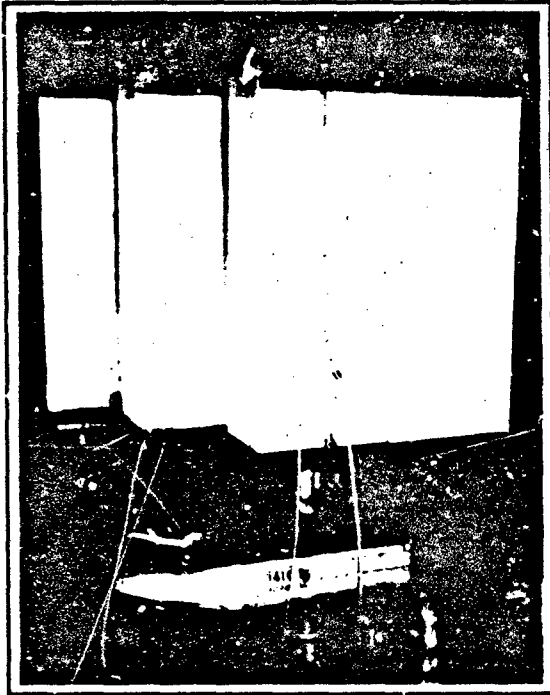
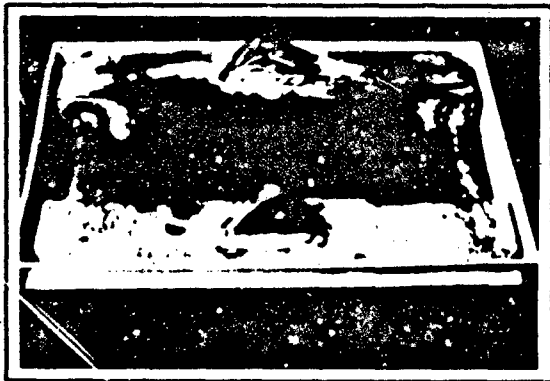


Figure 14: Detail of attachment batteries 3 and 2





**Figure 18:** Dummy batteries with final hook construction on shock testing machine



**Figure 19:** Dummy mass in the GRP battery housing

For the first shock series some, and for the second considerable, overtesting was introduced, due to the rigid mass. It was known from previous tests that the flexibility of the battery housing and the flexibly mounted battery poles and lead plates reduce the shock loading considerably. Acceleration levels on the bottom were 2 - 4 higher than the levels on top of the battery.

For the first series the PU adhesive Bolidt LP2578 and for the second series Bolidt LP2711 had been applied.

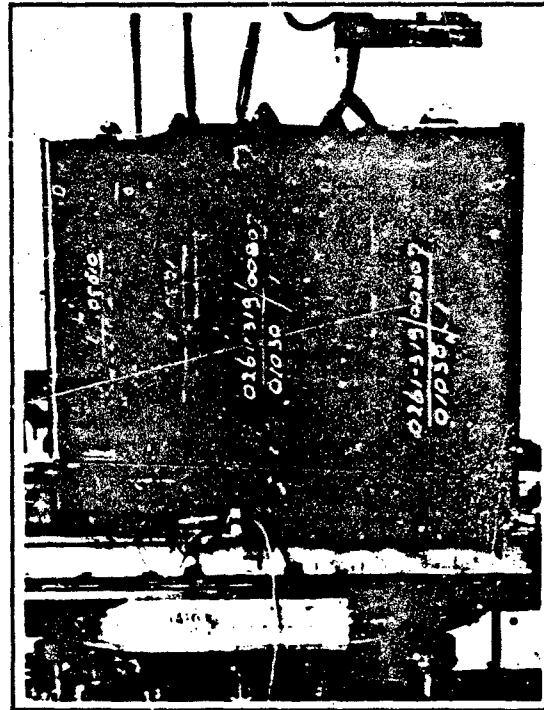


**Figure 20:** Masses welded to hook on shock testing machine

The PU Bolidtec was preferred, because it has the best mechanical and chemical properties for the bonding layer, but it has two disadvantages as far as bonding process concerns:

- A) the very short pot-life (about 15 sec.);
- B) it requires special equipment for injection (at that time not available).

The short pot-life makes it sensitive for defects in the bonding-layer, due to the small thickness (5 - 10 mm).

When the pot-life can be extended without loss of properties, it will be the most suitable PU for this application.

For the first shock test series 3 plates with 2 hook constructions, suitable for 2 batteries and a plate with one hook construction for one battery, were bonded to a simulated deck structure. Different PU layer thicknesses (3 - 6 - 9 mm) were used. The thinnest layer at the most flexible (centre) part of the deck structure. The 6 and 9 mm layers were on locations with about equal stiffnesses (figure 21).

As expected the centre hook bonded joint failed first, due to the high deck flexibility and the rather low strain (about 60%) of the Bolidt PU LP2578. But it met the minimum shock requirement. The bonded joint of the other two double hook constructions failed at the maximum required shock level.

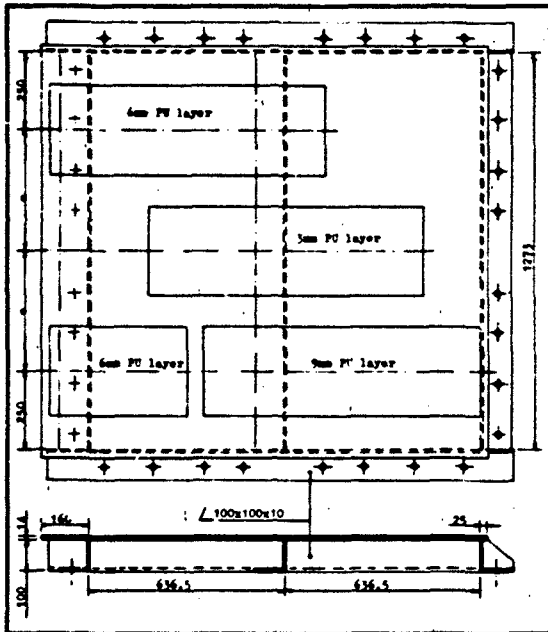


**Figure 21:** Top view on simulated ship structure

All three bonded joints failed in the primer layer and not in the PU due to the brittleness of the primer and the limited capability of this PU to flatten the stresses in the bonded joint.

The single mounted original battery, on a stiff location of the deck, remained in position and the bonded joint met above hull lethal shock levels.

Four dummy batteries were severely damaged. During the last shock test, the hook plate punched out the bottom of the battery housing (figure 22). Comparing this result with the shock test result of the original battery (also the original battery of figure 8) it will be clear that the four dummy batteries and the bonded joint were overtested. The hook construction showed no damage.

Although the first shock test series demonstrated that the PU Bolidt LP2578 adhesive met the requirements, three out of four joints failed. The second series with the far more flexible PU Bolidt LP2711 was very convincing. The shock levels were far above the expected hull lethal levels.

The centre hook construction on the simulated deck structure deformed (bended) about 12 mm over a distance of 900 mm, the bonded joint was not affected by this deformation. The hook construction was deformed as well (figure 23).

No peel-off effect could be determined, even with an asymmetric loading of the hook construction at the most severe shock.

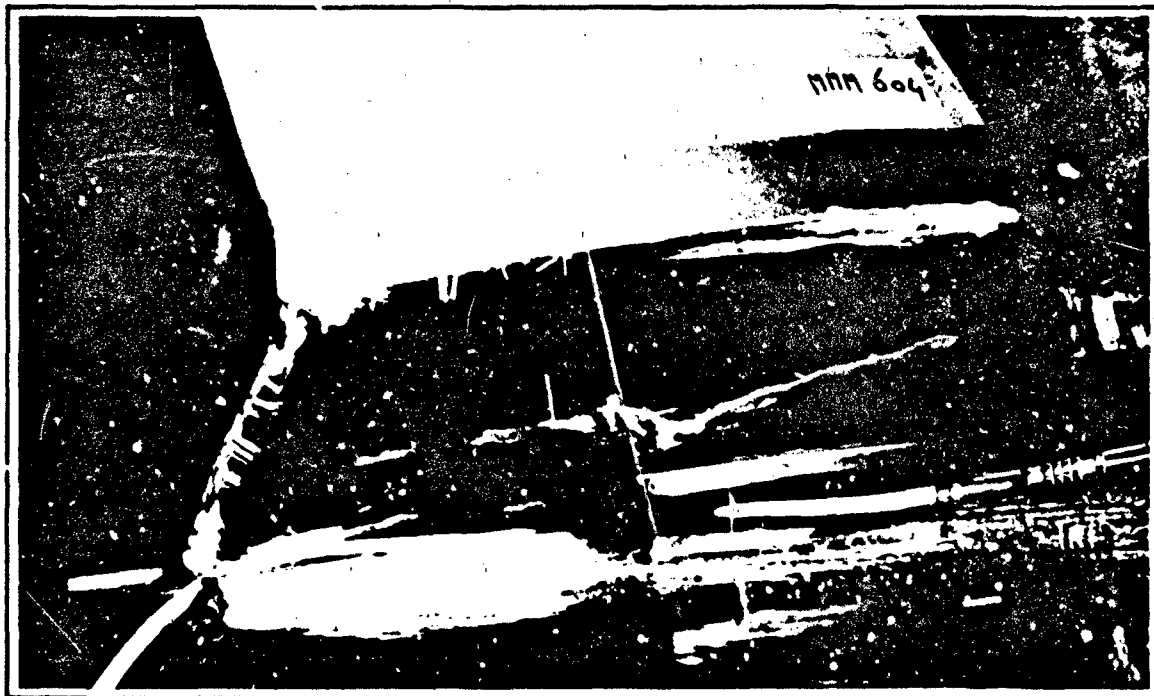


**Figure 22:** Crashed bottom of battery housing after shock test



Figure 23: Detail of deformed deck hook

The average tensile stress in the bonded joint was about 60% of the "dynamic" ultimate tensile stress derived from the shock tests with small masses. Comparison of the shock test results and the shock requirements indicates a safety factor far above 3.

Shock testing will proceed with the 500 kgs masses to determine the ultimate strength of the Bolidt LP2711 PU.

### Evaluation and conclusions

Except for its acid resistance the PU Bolidt LP2711 meets all requirements and is fully acceptable when covered with a flexible protecting layer like the PU Bolidtec or equal. In principle this system will be applied on board of the submarine. The battery compartment bulkheads and topdeck will be covered with (2 mm) PU Bolidt LP2578, which replaces at the same time the 2x3 mm rubber layer at the bulkheads.

The manufacturing process will be carefully controlled. Bond strength tests for the primer and the first thin PU-coating layer will be carried out on each hook. The bonded joint, metal-PU-metal, will be checked on bonding by means of echo-acoustic. This method also will be applied to check a possible decrease in bonding during the life-time of the ship. A development programme is planned to investigate the possibility to apply echo-acoustic for determination of the bonding-strength.

From the cost point of view it has been calculated that a bonded joint between hook and battery will be 40-60% cheaper than a bolted hook, under the condition that it is incorporated in the manufacturing process of the battery. The bonded joint between compartment deck and hook construction can be 25-40% cheaper than a bolted hook.

The "battery-hook" is re-usable, it can easily be cut off and cleaned. The counterhook to the deck is difficult to remove, only by electric heating or such. However, the expectations and the experiences in other applications are such, that the PU will have sufficient strength during the whole ship's life-time. Besides that a very large safety factor has been built in and if deterioration takes place, then it will most probably start at the

surface coating between two hooks and the PU there can easily be repaired.

The hook bonded to the battery bottom, compared to the bolted hook, has the following advantages:

- A) An increase in the battery capacity of 1 - 15% for the same battery height.
- B) The shock resistance is at least two times better, at less cost (more severe testing was not possible due to failure of the battery lid).
- C) The PU layer (1mm) around the bottom part of the battery gives an extra protection against the influence of water, acid and possible mechanical impact.

The bonded joint of the hook construction to the compartment deck has the advantage of:

- A) A high electrical insulation value of the hook from the deck (the deck has a puncture voltage value of about 20 kV/mm).
- B) A shock resistance, which is superior to the existing bolted hook.
- C) A good protection of the ship structure against water and acid (the chemical stability of the PU assures a long life-time and can easily be repaired).
- D) The space underneath the battery can be used for oil storage tanks or such, instead of seatings for the bolted hooks.

The experience with this R&D programme enabled the Royal Netherlands Navy to solve other problems. E.g. the GRP fairing of the bow-thruster of a new GRP minehunter, delaminated from the hull during the shock trials and also due to slamming. It was not possible to add bolts or other

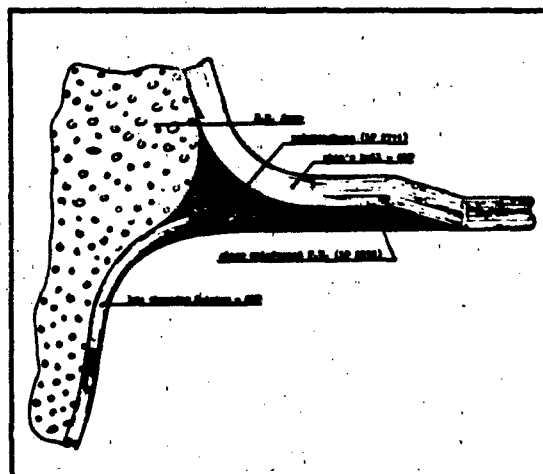


Figure 24: Fairing of bow-thruster bonded to hull by means of PU

fasteners to make a mechanical joint, because the fairing was too thin. Figure 24 shows how this problem has been solved.

The shape of the fairing has a built-in start for delamination. The flexible layer (5 mm) of PU prevents this.

A ship's shock trial is planned to prove the shock resistance of this solution.

Another example is the porcelain toilet. Previous shock tests and ship shock trials showed fractures at very low shock levels (about 25 g). Bonded with a 10 mm PU LP2711 layer to a steel plate, which can be bolted to a deck or bulkhead, shock tests showed an improvement of about a factor 4. High enough to meet the most severe shock levels for tweendecks and superstructures of surface ships.

Shock testing with a toilet on a 50 mm PU layer (figure 25) showed an improvement of about a factor 6.

The savings compared to the stainless steel lavatories, in use at this moment, are about Dfl. 1.500,- (US dollar 550,-) per item.



**Figure 25:** Porcelain toilet bonded with 50 mm PU to steel plate

Under study at this moment are a joint between bulkheads (sandwich) and deck structures and the replacement of a bolted water-tight hatch cover, with a complex and expensive sealing, by a PU bonded joint.

Continued research will be necessary to improve the quality and properties of bonded joints and to investigate profitable application possibilities. Still it can be concluded that once the use of adhesives in naval ship design has been accepted it can be a powerful and cost-effective tool for specific areas.

## References

- [1] "Shock and vibration Bulletin No. 51", page 129 - 136.  
By: K. Hellqvist, May 1981
- [2] "Shock testing of submarine batteries on the medium weight shock testing machine", December 1978. IWECO-TNO 5072024-C02-78.  
By: F.J. van Bragt
- [3] "Bleiakkumulatoren als Fahrbatterie im U-Boot", Marine Rundschau 9/1980.  
By: Hans-Joachim Lawrenz
- [4] "Shock testing of submarine batteries, manufacturer Varta", March 1982. IWECO-TNO 5072312-059-82.  
By: F.J. van Bragt
- [5] "Strength of polyurethane-rubber adhesives to steel and to glass reinforced polyester", MOD No. SB 51-08.  
By: T.H. Smits, January 1983
- [6] "Shock testing of the attachment of submarine batteries to the ship's foundation by means of polyurethane", June 1983. IWECO-TNO 5075403-082.  
By: F.J. van Bragt

**DISCUSSION**

Mr. Herman (Naval Sea Systems Command): In looking at your shock test machine set-up, it looked like the blow was primarily in the vertical direction. Did you ever load these glued on, or epoxied on, hooks in the horizontal direction to get a shear load on them?

Mr. Jansen: It is not necessary because we have the compartment bulkheads in the transverse and the axial directions. There are still gaps between the batteries. We have certain gaps to remove the batteries from the hooks which are filled by wooden pieces or something like that. So in the transverse direction you don't need the hook construction.

SHIPBOARD SHOCK RESPONSE OF THE MODEL STRUCTURE DSM;  
EXPERIMENTAL RESULTS VERSUS RESPONSES PREDICTED BY EIGHT PARTICIPANTS

R. Regoord, TNO-IWECO  
Delft, the Netherlands

A simple structure has been shock tested. Both the input and the three dimensional response have been measured. Using only the input, the response was predicted as well by eight suppliers, shipyards, etc. The results of this participation which were obtained with different methods and computer programmes, are described in this paper. They throw some light on the state of the art. This may be useful for the renewal of shock design specifications of naval equipment which must resist the effect of noncontact underwater explosions.

INTRODUCTION

The Netherlands naval shipbuilding specifications for shipboard equipment require a certain resistance against the effect of noncontact underwater explosions. Emphasis in these specifications is laid on passing a shock test. As soon as possible and prior to this test the supplier of the equipment is obliged in most cases to examine this resistance by performing calculations which must be made available to the purchasing authority. Even if this analysis is approved the supplier can be held responsible later on for possible damage during the test. In those cases where for practical reasons no shock test is held, shock calculations only should prove the shock resistance.

The supplier up till now is free in choosing his favourite analysis method out of the two or three methods mentioned in these specifications for shipboard equipment:

(A) Static g-method.

The distributed mass of the equipment is multiplied with a specified acceleration in a specified direction. The resulting load distribution should be examined statically. This method is chosen in over 90% of all cases.

(B) Dynamic analysis in the time domain.

The shock is specified as a prescribed shock motion of the foundation points. The equations of motion are solved numerically step by step in the time domain. To include the effect of various types of strongly non-linear shock reducing mountings, the programme SHOCK3D is available [7], which is combined with the general purpose finite element programme ASKA.

(C) Spectral response analysis.

Recent specifications also present shock response spectra as an input for a spectral (or modal) response analysis. Such a method is mentioned in the relevant NATO standardization agreement. It is essentially the same method as widely applied by the US Navy under the name DDAM. Some theoretical background is presented in Appendix 2.

In the future Netherlands shock specifications will be reconsidered in order to reflect the capabilities of the more accurate and powerful methods now available. Such a revision should be prepared carefully because it may have great impact on cost and delivery schedules of equipment. Undoubtedly the simple static g-method will be maintained for most of the equipment. The difficulty is to describe in what cases a more accurate but more expensive analysis of equipment seems to be of so much interest that such an analysis is mandatory.

As a preparation to this revision pieces of equipment have to be both shock-tested and to be analysed by methods of varying complexity in order to gain the necessary insight and experience. The first of these exercises was done on a very simple structure made up from beams and rigid masses, which looks a bit like ship's davit. Because so far it has been solidly mounted on top of the shock testing machine, the structure is named DSM (see Fig. 1). Once having compared (see [1]) the experimental results and the predictions as obtained by TNO with the afore mentioned methods, the question arose if suppliers of naval equipment are also able to perform such calculations. To get informed about the state of the art the Department of Ships of the R.N.I.N. invited a number of suppliers, ship-

yards and universities to carry out shock response calculations of whatever kind for this same test structure DSM with the same shock input as measured on top of the shock table. The paper summarises the contributions of the participants as reported in [3].

#### THE MODEL STRUCTURE DSM

The prime interest being the comparison of results from various analysis methods and not the merits of a very large finite element model, the test structure should be a rather simple one in order to avoid large modelling efforts. It should respond in a multidirectional way to a unidirectional excitation as most structures tend to do.

Fig. 1 shows the steel structure which consists of two identical welded frames (IPE 120) erected in parallel vertical planes and interconnected by means of bolts to a long and a short horizontal beam. Mass plates can be attached to the frames and to the long beam at various places by means of threaded rods. The plates cause large local inertia forces. By changing their location the dynamic characteristics of the structure can be varied. Two different configurations have been investigated. In addition to the one shown in Figures 1 and 3 during shock test no. L 1543, a second configuration has been tested during shock L 1540. In the latter case the mass plates were attached to the vertical ends of the frame as is shown schematically in Figure 2. For both configurations there is a plane of symmetry. The total mass is the same and amounts to about 100 kg. The largest dimension is 1,15 m.

The way in which the frames are mounted on the shock table is shown in Figures 4 and 6.

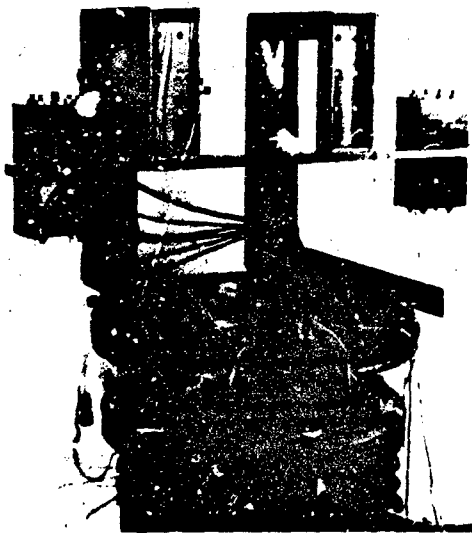


Fig. 1 DSM on top of the shock table during test L 1543.

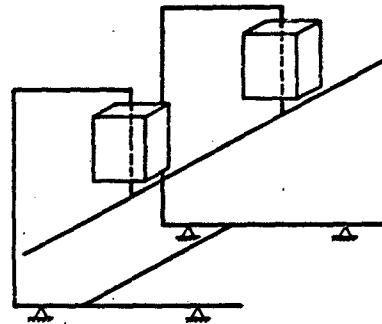


Fig. 2 L 1540-configuration

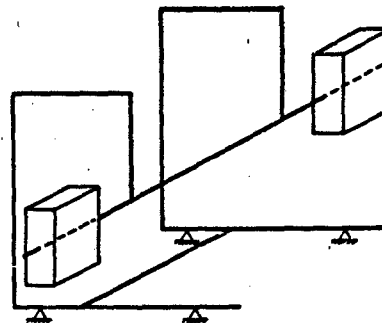


Fig. 3 L 1543-configuration

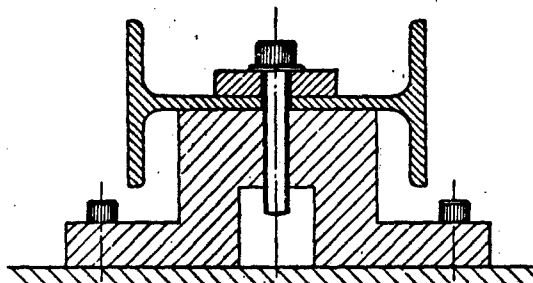


Fig. 4 Attachment of the frame

#### THE SHOCKS APPLIED

DSM has been mounted on the light weight shock testing machine as designed by TNO and installed since 1972 for normal acceptance tests of shipboard equipment. It can be adjusted to simulate shock motions of the ship's bottom, the decks and the superstructure. Some figures illustrating the maximum damaging potential for a test mass of 100 kg are: maximum acceleration 6000 m/s<sup>2</sup>, maximum velocity 11 m/s, time to max. velocity 3 ms, displacement at max. velocity 30 mm. Full particulars are in a report [5] presenting the calibration as required by the relevant Nato Standardisation Agreement.

After preliminary calculations, DSM appeared to be a rather weak structure. Therefore, to avoid plastic deformation, a mild shock was simulated. One that could occur in the superstructure during a fairly mild attack. The motion of the shock table is not necessarily a pure vertical translation. Small rotations of the table and small translations in a horizontal plane may occur. These motions may be induced when the center of gravity of the equipment to be tested is eccentric and/or when the dynamic reaction forces have horizontal components. Normally these small motions are of no interest whatsoever but for these particular tests they were measured as well, to obtain complete input data. Locations of 8 accelerometers A1-A8 on the shock table are shown in Figures 5 and 6. In the horizontal x-direction (see Fig. 5) the acceleration signals appeared to be very small. They therefore were

neglected. For both the configurations during shocks L 1540 and L 1543 the signals 5 and 6 were at a guess of some importance (see Fig. 7). The vertical acceleration signals are almost identical in pairs: signals 2 and 4 and signals 1 and 3 (see Fig. 8). Apparently the yz-plane is a plane of symmetry for the excitation and DSM causes the table to rotate a little around an axis parallel to the x-axis. There was no rotation during a third shock test L 1544 with an empty table as shown in Fig. 6. For all three tests the adjustment of the machine was precisely the same. Shock motions of the table, however, were rather different as can be seen from the integrated acceleration signals 2 (see Fig. 9). Consequently shock response spectra (see Fig. 10) as derived from these signals also differ considerably. Appendix 1 presents some comments on these feed-back effects.

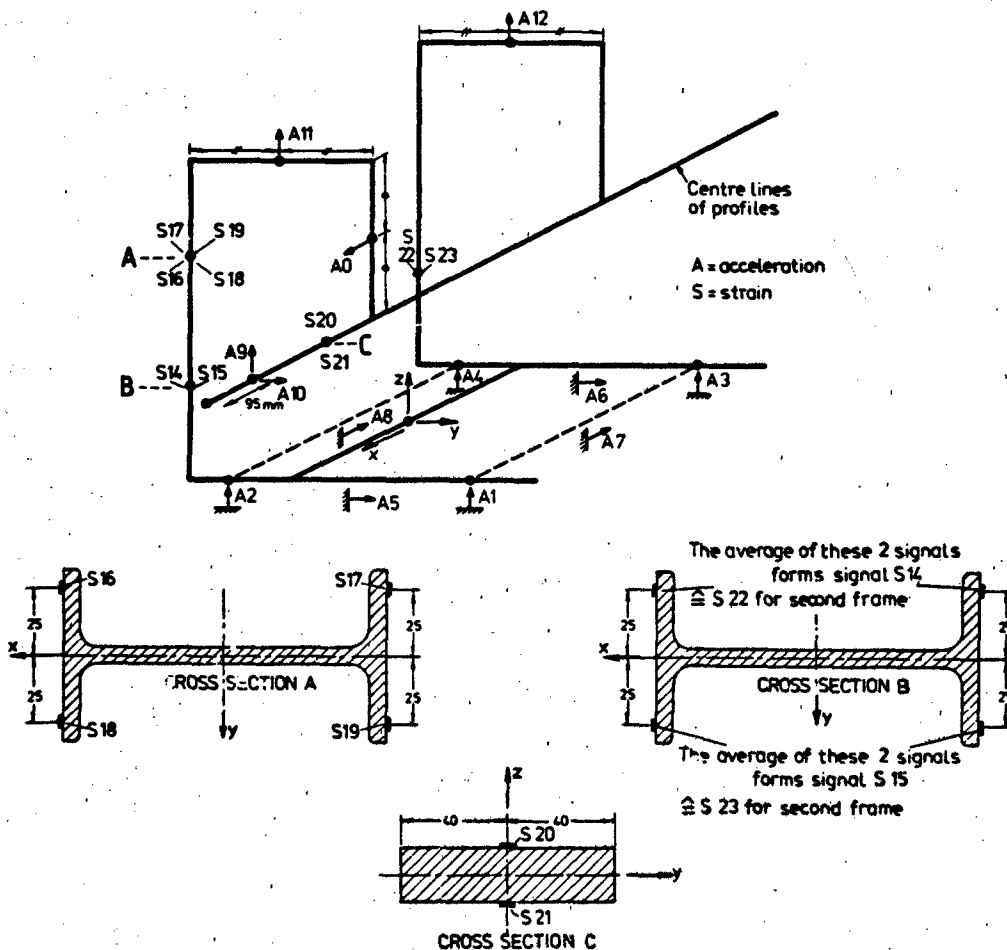


Fig. 5 Position of all 23 transducers

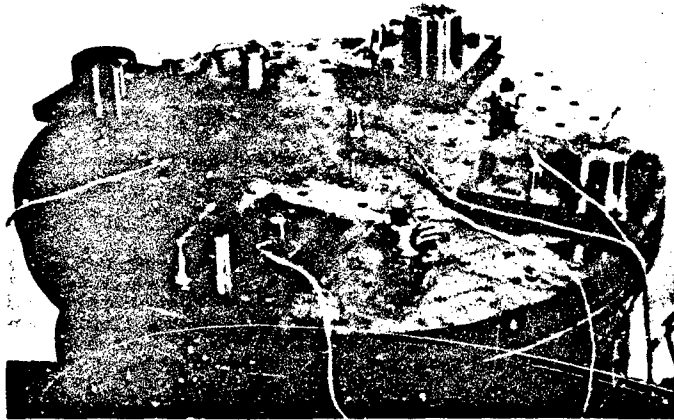


Fig. 6 The supports during test L 1544

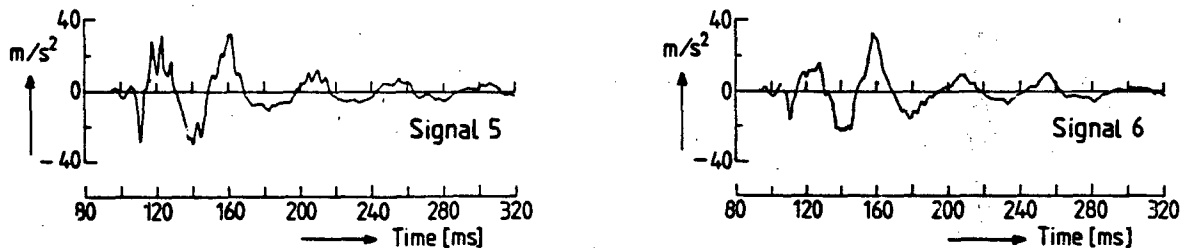


Fig. 7 Acceleration in y-direction of the shock table during test L 1540

#### INVITATION FOR PARTICIPATION

Once the predicted response had been compared [1] with the measured response it was decided to invite other parties to also predict the shock response of DSM. They were not informed in advance on the measured response or the predictions of TNO.

The information as distributed comprised i.a.:

- (1) Detailed drawings of the model structure DSM.
- (2) Description of transducer locations (Fig. 5).
- (3) For both configurations of DSM the shock input information in three different ways:
  - (3.1) For a dynamic analysis in the time domain the signals 1 and 2 as prescribed motions of the two support points in the vertical direction. Moreover the signal 5 as the prescribed motion of both support points in the horizontal y-direction. The sampling frequency is 1010 Hz.
  - (3.2) For a quasi-static analysis the following shock design numbers in the vertical direction.

Shock	Acceleration [m/s <sup>2</sup> ]	Deceleration [m/s <sup>2</sup> ]
L 1540	44	51
L 1543	44	56

These are maxima from signal 2 after having been multiplied by a factor of 0,82, which is a rather arbitrary value which stems from a more or less established procedure of interpreting shock signals by the R.Nl.N. (and also other Navies). Instead of taking the maximum acceleration which cannot be representative because it lasts only for an infinitesimal short time, some sort of average value is taken. Prescribing specific shock design numbers as given above seems to be a better starting point, instead of letting every participant free in interpreting the acceleration signals. The weight of the structure was not to be taken into account additionally.

(3.3) For a spectral response analysis 44 maxima, undamped, shock spectral values (pseudo velocities) as derived from signal 2 were given for frequencies between 10 and 195 Hz (see Fig. 10).

(4) Some suggestions [6]:

(4.1) Participants were recommended to analyse only that part of DSM for which x-coordinates are positive, if they agreed with the almost symmetry of the structure and the excitation.

(4.2) They were recommended to neglect damping.

(4.3) They were told that in case of a spectral response analysis the most interesting mode summation procedures were

$$\text{ROOTSUM} = \sqrt{\sum_j f_{ij}^2} \quad \text{and}$$

$$\text{NLRSUM} = f_{ij\max} + \sqrt{\sum_j f_{ij}^2 - f_{ij\max}^2}$$

in which  $f_{ij}$  are the elements of a response matrix containing as columns the contributions of the various modes to strains, accelerations, etc.  $f_{ij\max}$  is the largest element in the  $i$ -th row of the response matrix.

(4.4) Participants were told that the experimental results available for comparison are the strain signals 14-21, the acceleration signals 0, 9, 10 and 11 and their derived velocity and displacement signals.

(4.5) They were left completely free in choosing their own methods and their favourite computer programme(s).

(5) Some forms to be filled in by participants concerning the programme used, the finite element model, number of degrees of freedom, etc. as well as the predicted first peak and second peak of a signal. Natural frequencies of vibration modes of DSM were also asked for, because they can be considered important interim results.

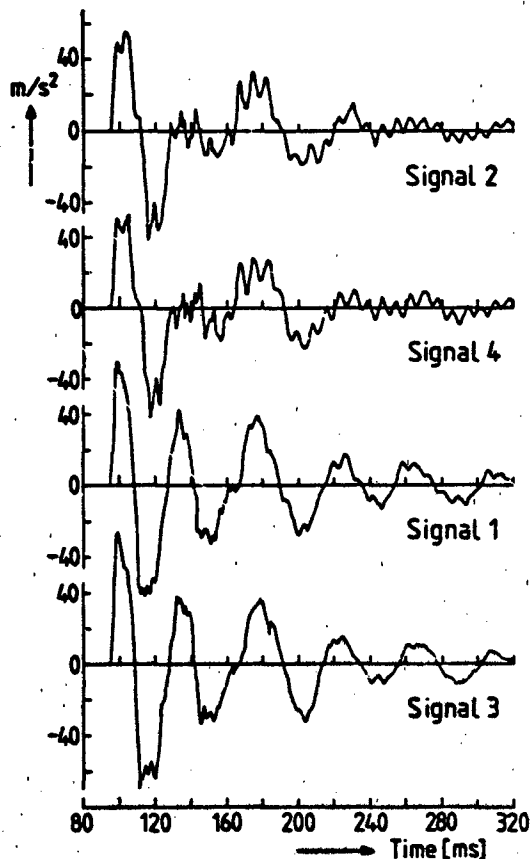


Fig. 8 Acceleration in z-direction of the shock table during test L 1540

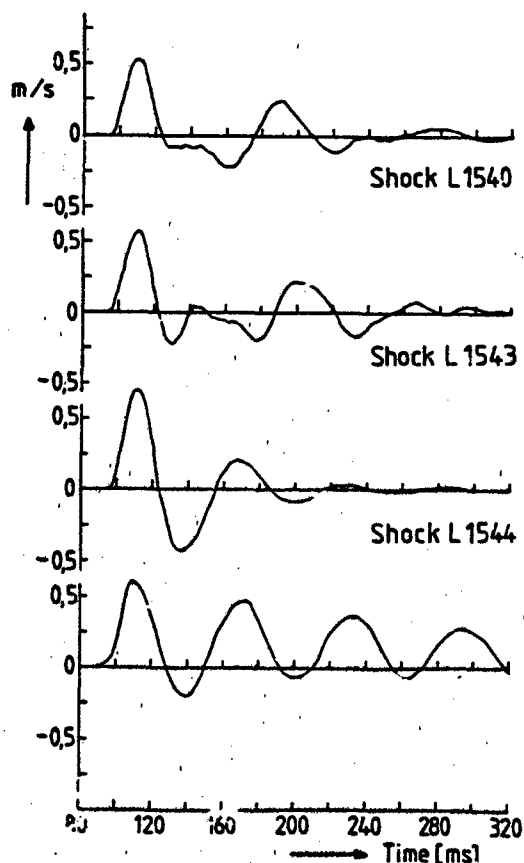


Fig. 9 Measured vertical velocity signal 2 and "equivalent" standardized shock motion

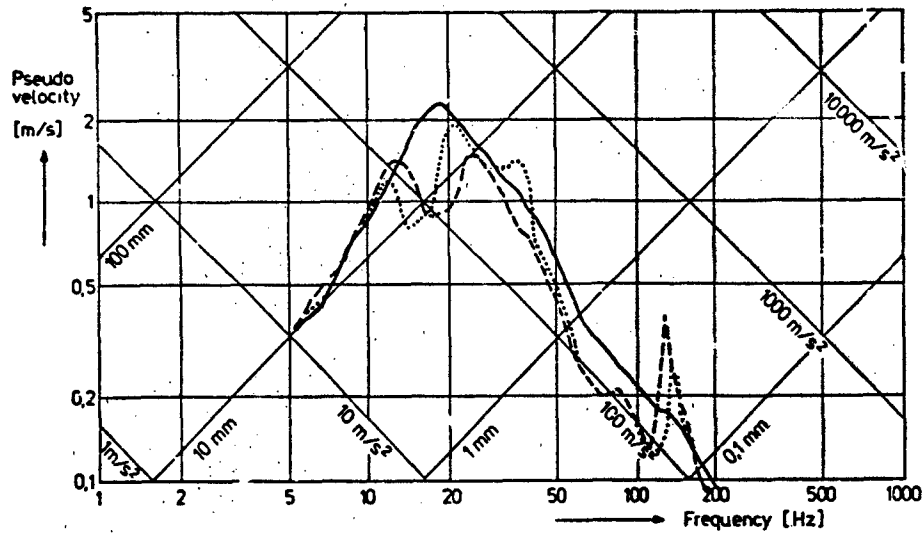


Fig. 10 Shock spectra of signal 2

----- SHOCK L 1540  
 \_\_\_\_\_ SHOCK L 1544  
 ..... SHOCK L 1543

Table 1  
 Survey of replies

	Shipyards	Suppliers	Research
Number of invitations	5	22	9
Written replies	2	6	3
of which were positive	2	4	2

#### THE RESPONSE OF THOSE INVITED TO PARTICIPATE

Invitations have been sent to 36 addresses, almost all of them in the Netherlands. They can be grouped into three categories:

- The main shipyards which are building naval ships.
- Suppliers of all types of equipment. Nearly all of the larger firms were included. However also some smaller firms have been invited which have hardly any knowledge about dynamic analysis methods.
- Three technical universities, some research institutes and engineering bureaus.

The total number of participants appeared to be 8. They are mentioned in Table 2, together with letters A to I, denoting the solutions. The original prediction by TNO-IWECO, as reported in [1], is included for comparison under the letter H.

Regrettably there were only a few replies mentioning the reason for not participating. In most cases there seemed to be no sufficient knowledge of dynamic analysis methods and in some cases it was caused by a lack of time. Anyway there was a ten month period for preparing solutions.

A	P. Lamsens CRIF, Heverlee, Belgium
B	J. Thomas BV Kon. Mij. "De Scheide", Vlissingen
C	R. van Tijn, U. v.d. Wal Hollandse Signaalapparaten NV, Hengelo
D	A.A.M. Ranke Philips - ISA TIS/CARD, Eindhoven
E	P.A.M. Bracké, H.J. Kempes Holec Smit, Slikkerveer
F	W.A.M. Brekelmans, F.P.T. Ezayens Eindhoven Univ., Dept. of Mech. Eng.
G	J. van Geldre, J.L. v. Kuyvenhoven Rietachoten en Rouvens, Rotterdam
H	T.H. Korse, R. Regoord TNO-IWECO
I	P. Pruijssers, D. Stapersma Neth. United Shipb. Bureau, The Hague

Table 2 List of participants

## THE APPLIED METHODS AND MODELS

Recommendations regarding the symmetry, absence of damping and shock input were accepted by all the participants. Table 3 shows the methods. Fortunately all those (A, C, D, E) who analysed only a single configuration have chosen shock L 1543.

Participant G calculated by simple formulae the deformations and strains. All other solutions were obtained with finite element programmes as listed in Table 4.

All participants, except B, used beam elements, deforming under the action of normal forces, of bending, of St. Venant torsion and mostly also of shear effects in bending. This shear stiffness was neglected by Z and W. Participant D, having solved the problem twice with and without shear stiffness, reports the influence of shear deformation to be negligible. Participant B used plate elements which can take membrane forces, bending and shear. Consequently the total number of degrees of freedom (d.o.f.), the unknowns, is about 10 times larger than for the more simple beam models. Examples of models are shown in Figures 11 and 12.

At the points of attachment to the shock table, the assumed boundary conditions are somewhat different. Suppressed and/or prescribed degrees of freedom are listed in Table 4. 1, 2 and 3 denote the translations in the x-, y- and z-directions; 4, 5 and 6 the rotations around these axes. The differences only concern the rotations, which were left free by most participants. In model B rotations are locally suppressed at a single nodal point of the cross section, coinciding with the connecting bolt. So in this model the whole cross section of the frame need not necessarily be prevented from rotating. Contemplating the actual attachment (Fig. 4), one might conclude that the plate model offers better opportunities to simulate the boundary conditions than the models made up from beam elements do.

For each of the respective contributions the following details and peculiarities seem worth mentioning:

- A The shortest horizontal beam simply was not modelled because its presence was assumed to have no effect at all on the response. By static condensation the system was reduced to 34 d.o.f. For the spectral response analysis vibration modes 1-9 were considered.
- B This model, being much more detailed than the others offers the opportunity for more correct modelling certain parts of the structure, for instance, the connection of the frame to the long beam. See Fig. 13. Points  $e_i$  and  $f_i$  ( $i = 1, \dots, 4$ ) were forced to have the same displacements and rotations. A similar technique was applied for the attachment of the small mass plates.

No static condensation was applied. For the dynamic response in the time domain a 3-point integration scheme was used with a time step of 0.99009 ms. Though all 1325 vibration modes were determined, only the response of the modes 1-25 were superimposed in the time domain.

- C No static condensation was applied. For the spectral response analysis vibration modes 1-8 were used.
- D That part of the long beam which is clamped to the frame was given a much larger stiffness by specifying a separate beam element over that length. No static condensation was applied. For the spectral response analysis vibration modes 1-9 were used.
- E Neither static nor dynamic condensation was applied.
- F No static condensation was applied. Vibration modes were only determined to compare natural frequencies with those of other participants. The response of the separate modes was not determined because of problems with the mode superposition part of the computer programme. So the coupled equations were solved by means of the Houbolt integration procedure. The time step is 1 ms.
- H Static condensation was applied, resulting in 48 d.o.f. for the spectral response analysis and 18 d.o.f. for the dynamic response analysis in the time domain. For the spectral response analysis modes 1-8 were combined. For the analysis in the time domain a Runge Kutta integration procedure was used with a time step of 0.2 ms. More details are reported in [1].
- I That part of beam No. 2 which was clamped to the frame was given an infinite stiffness by specifying a separate beam element (RBAR) over that length. Neither static nor dynamic condensation was applied. For the dynamic response in the time domain a 3-point integration scheme was used with a time step of 0.99009 ms.

## NATURAL FREQUENCIES AND VIBRATION MODES

Fixed base natural frequencies of DSM as they were calculated for the symmetric modes are collected in Tables 5 and 6. Apparently frequencies for all beam models for modes 1-5 are rather close. Differences may have been caused by the various boundary conditions, the introduction of some stiff elements, a slightly different mass distribution, etc. Vibration modes are more difficult to compare because only a limited amount of information was made available. As an example for the L 1543 configuration Figures 14 to 17 show the lower modes as calculated by TNO [1]. The modes from

Participant	Shock L 1540					Shock L 1543				
	static	spectral			dynamic	static	spectral			dynamic
		ABS-SUM	ROOT-SUM	NRL-SUM			ABS-SUM	ROOT-SUM	NRL-SUM	
A								X		
B	X				X	X				X
C						X	X		X	
D						X	X		X	
E						X				X
F					X					X
G	X					X				
H	X	X	X	X	X	X	X	X	X	X
I	X				X	X				X

Table 3 Used methods

Participants	Programme	Model composition	Element type	Suppressed and prescribed d.o.f. at support points	Number of d.o.f. before static or dynamic condensation
A	SUPERB	beams	BEAM	1, 2, 3	201
B	NASTRAN	plates	QUAD4 QUAD8	1, 2, 3 4, 5, 6	1325
C	ANSYS	beams	STIFF4	1, 2, 3	90
D	ASKA	beams	BECOC BECOCX	1, 2, 3	180
E	NASTRAN	beams	BAR	1, 2, 3 5, 6	84
F	MARC	beams		1, 2, 3	98
H	ASKA + SHOCK3D	beams	BECOS	1, 2, 3	127
I	NASTRAN	beams	BAR RBAR	1, 2, 3	192

Table 4 Model description

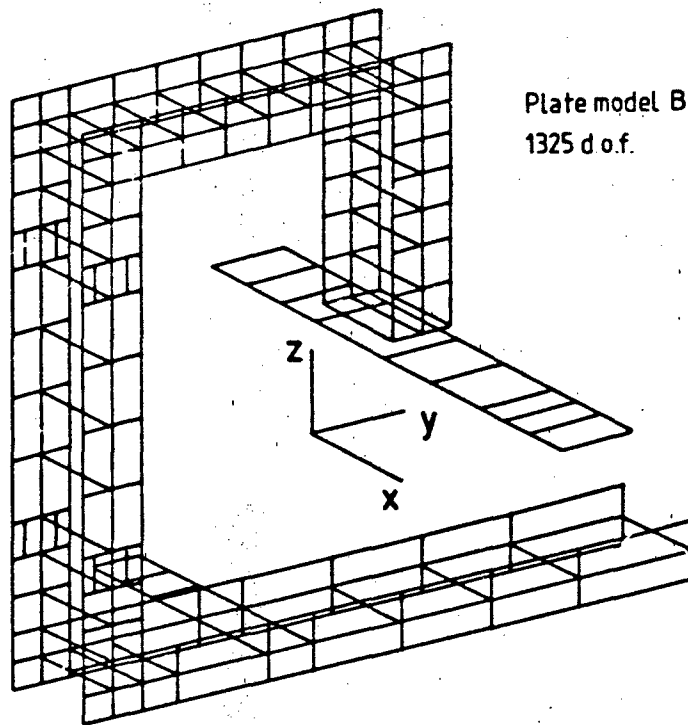


Fig. 11 Finite element model of participant B

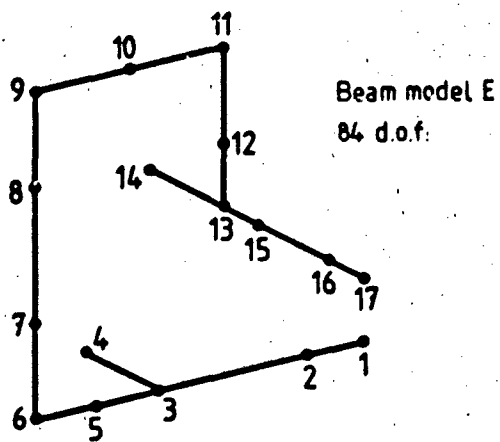


Fig. 12 Finite element model of participant E

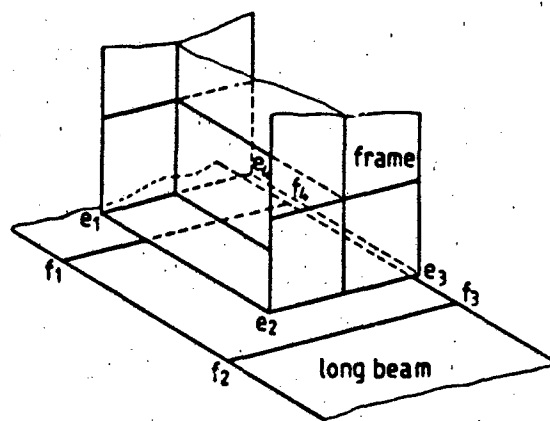


Fig. 13 Detail of model B

	Vibration mode no.						
	1	2	3	4	5	6	7
B	15,7	28,2	38,0	121,4	130,1	195	264
F	15,9	20,6	27,8	38,4	62,4	97	122
H	15,8	20,6	27,7	38,4	59,0	118	157
I	15,6	22,5	27,3	41,4	72,9	120	167

Table 5 Natural frequencies (Hz) for the L 1540 configuration

	Vibration mode no.						
	1	2	3	4	5	6	7
A	14,1	20,8	22,0	37,9	90,7	125	132
B	15,5	22,8	37,4	77,2	105,5	145	166
C	14,3	21,5	22,8	38,2	85	118	128
D	15,3	21,8	23,0	40,3	87,2	96	135
E	15,0	24,2	28,8	39,3	83,1	116	137
F	14,3	21,6	22,8	37,8	84,2	97	117
H	14,3	21,5	22,9	37,6	83,4	116	128
I	14,7	21,4	23,0	39,6	93,0	125	135
T	14,4	21,7	31,0	61,6	84,3	127	129
TT	15,6	21,8	39,8	83,2	97,6	127	168

Table 6 Natural frequencies (Hz) for the L 1543 configuration

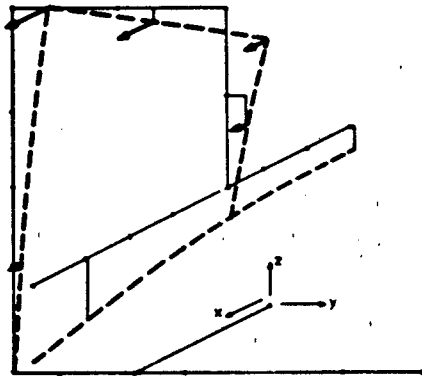


Fig. 14 Vibration mode 1, 14,3 Hz, Shock L 1543

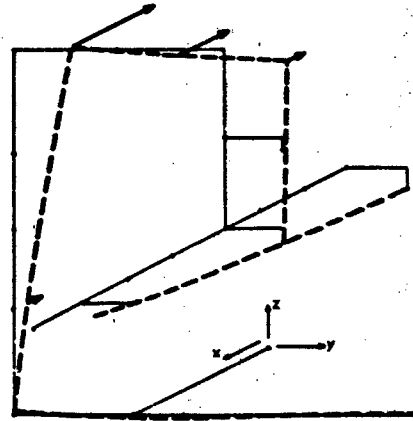


Fig. 15 Vibration mode 2, 21,5 Hz, Shock L 1543

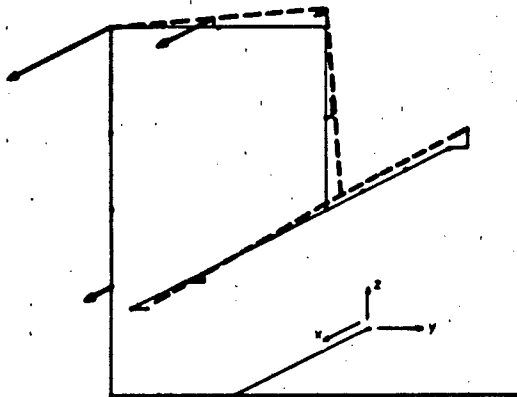


Fig. 16 Vibration mode 3, 22,9 Hz, Shock L 1543

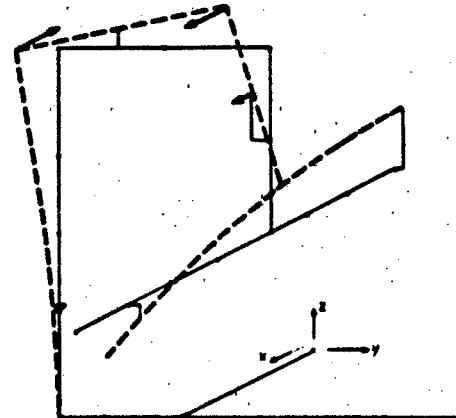


Fig. 17 Vibration mode 4, 37,6 Hz, Shock L 1543

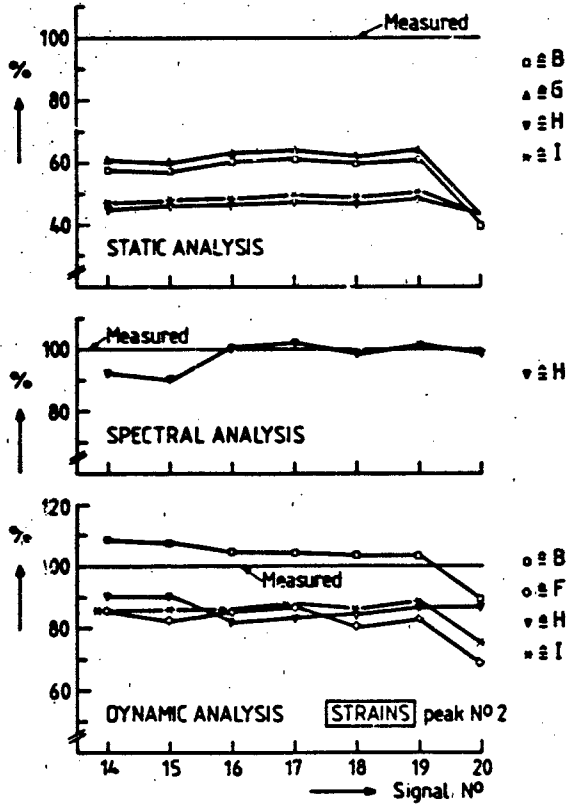


Fig. 18 Predictions of strains (peak no. 2) in percentages of the measured values for shock L 1540

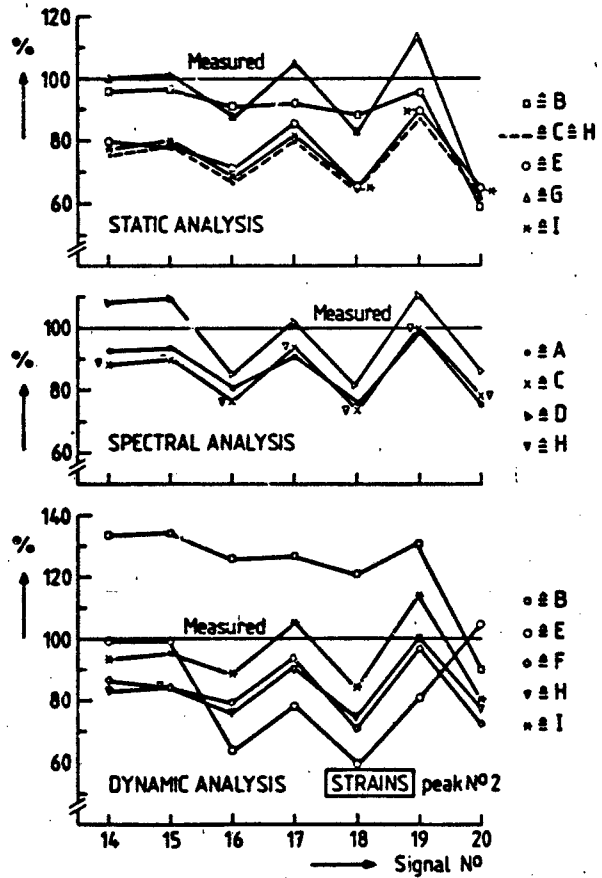


Fig. 19 Predictions of strains (peak no. 2) in percentages of the measured values for shock L 1543

Measurements		Participants								
		A	B	C	D	E	F	G	H	I
Signal		•	○	×	▷	◊	◇	△	▽	*
Max. rel. displ.	[mm]									
	9	6,4	54,7					45,3	56,2	56,3
12	2,4		66,7				54,2	66,7	66,7	
Max. abs. displ.	[mm]									
	(0)	0,8	6,2					0,0	10,0	8,7
(10)	2,5		3,2				20,0	0,8	1,2	

Table 7 Static analysis. Predictions in percentages of measured values. Shock L 1540.

Measurements		Participants								
		A	B	C	D	E	F	G	H	I
Signal		•	◻	x	▷	◦	◊	△	▽	*
<u>Max. rel. displ.</u> 9 (11)	[mm]									
	7,6 2,0		72,4 90,0	84,2 85,0		80,3 80,0		77,6 75,0	85,5 85,0	79,0 85,0
<u>Max. abs. displ.</u> 0 (10)	[mm]									
	2,0 1,3		25,0 2,3	55,0 2,3		60,0 30,8		0,0 46,1	55,0 2,3	50,0 3,1

Table 8 Static analysis. Predictions in percentages of measured values. Shock L 1543.

Measurements		Participants								
		A	B	C	D	E	F	G	H	I
Signal		•	◻	x	▷	◦	◊	△	▽	*
<u>Acc.</u> 0 peak 3 9 peak 2 10 peak 2 3 11 peak 2	[m/s <sup>2</sup> ]									
	13 -32 40									
			62,5		47,5	97,5			72,5	
	44 -78		79,5		83,3	92,3			82,1	
	-13 28 -31		190,3		109,7	112,9			112,9	
48 -64		45,3		35,9	54,7			43,8		
<u>Max. rel. displ.</u> 9 11	[mm]									
	7,6 2,0	100,0 95,0		102,6 100,0	101,3 115,0				102,6 95,0	
<u>Max. abs. displ.</u> 0 10	[mm]									
	2,0 1,3	165,0 238,5		80,0 138,5	67,0 116,9				85,0 123,1	

Table 9 Spectral analysis. Predictions in percentages of measured values. Shock L 1543

Measurements		Participants								
		A	B	C	D	E	F	G	H	I
Signal		•	◻	x	▷	◊	◊	△	▽	*
<u>Acc.</u>	[m/s <sup>2</sup> ]									
1	2		100,0				100,0		150,0	50,0
0 peak 2	- 5		120,0				100,0		160,0	80,0
3	8		87,5				75,0		87,5	37,5
1	56		100,0				96,4		128,6	94,6
9 peak 2	-120		90,0				80,0		86,7	73,3
1	- 28		125,0				107,1		107,1	100,0
10 peak 2	62		109,7				79,0		88,7	75,8
3	- 68		151,5				101,5		132,3	98,5
1	36		113,9				263,9		105,6	102,8
11 peak 2	- 60		103,3				286,7		78,3	68,3
<u>Vel.</u>	[m/s]									
1	-0,05		40,0						60,0	20
0 peak 2	0,06		50,0						50,0	33,3
1	0,76		93,4						92,1	90,8
9 peak 2	-0,87		77,0						79,3	73,6
1	-0,12		100,0						91,7	91,7
10 peak 2	0,31		116,1						103,2	106,4
1	0,49		102,0						102,0	104,1
11 peak 2	-0,42		85,7						81,0	78,6
<u>Max. rel. displ.</u>	[mm]									
9	6,4		81,2						84,4	79,7
12	2,4		100,0						100,0	95,8
<u>Max. abs. displ.</u>	[mm]									
(0)	0,8		12,5						25,0	25,0
(10)	2,5		100,0						96,0	104,0

Table 10 Dynamic analysis in the time domain. Predictions in percentages of measured values. Shock L 1540

Measurements		Participants								
		A	B	C	D	E	F	G	H	I
Signal		•	□	×	▷	○	◊	△	▽	*
<u>Acc.</u>	[m/s <sup>2</sup> ]									
1	13		92,3			96,1	84,6		92,3	76,9
0 peak 2	- 32		100,0			101,2	87,5		118,8	84,4
3	40		87,5			104,2	55,0		60,0	42,5
1	44		97,7			98,2	93,2		95,5	97,7
9 peak 2	- 78		94,9			102	78,2		76,9	76,9
1	- 13		69,2				53,9		61,5	46,2
10 peak 2	28		96,4				75,0		82,1	82,1
3	- 31		135,5				93,6		96,8	96,8
1	48		87,5			91,7	225,0		91,7	91,7
11 peak 2	- 64		107,8			71,7	211,0		87,5	78,1
<u>Vel.</u>	[m/s]									
1	0,07		100,0			42,8			128,6	114,3
0 peak 2	-0,24		70,8			62,5			79,2	66,7
1	0,66		100,0			104,6			97,0	97,0
9 peak 2	-0,75		96,0			100,0			81,3	88,0
1	-0,09		55,6			166,7			55,6	55,6
10 peak 2	0,19		105,3			168,4			89,5	94,7
1	0,50		104,0			100,0			102,0	102,0
11 peak 2	-0,32		100,0			62,5			78,1	71,9
<u>Max. rel. displ.</u>	[mm]									
9	7,6		94,7			109,2			89,5	89,5
(11)	2,0		110,0			90,0			80,0	95,0
<u>Max. abs. displ.</u>	[mm]									
0	2,0		60,0			110,0			90,0	85,0
(10)	1,3		146,1			223,1			138,5	146,1

Table 11 Dynamic analysis in the time domain. Predictions in percentages of measured values. Shock L 1543

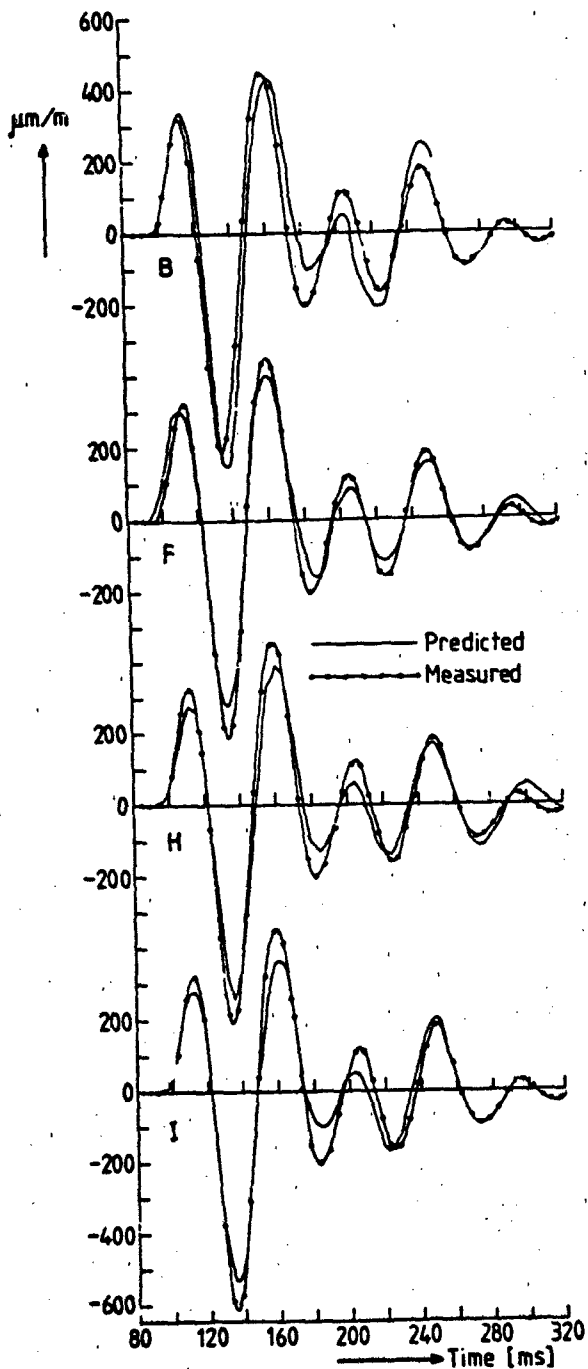


Fig. 20 Predicted versus measured strain signal 14 for shock L 1540

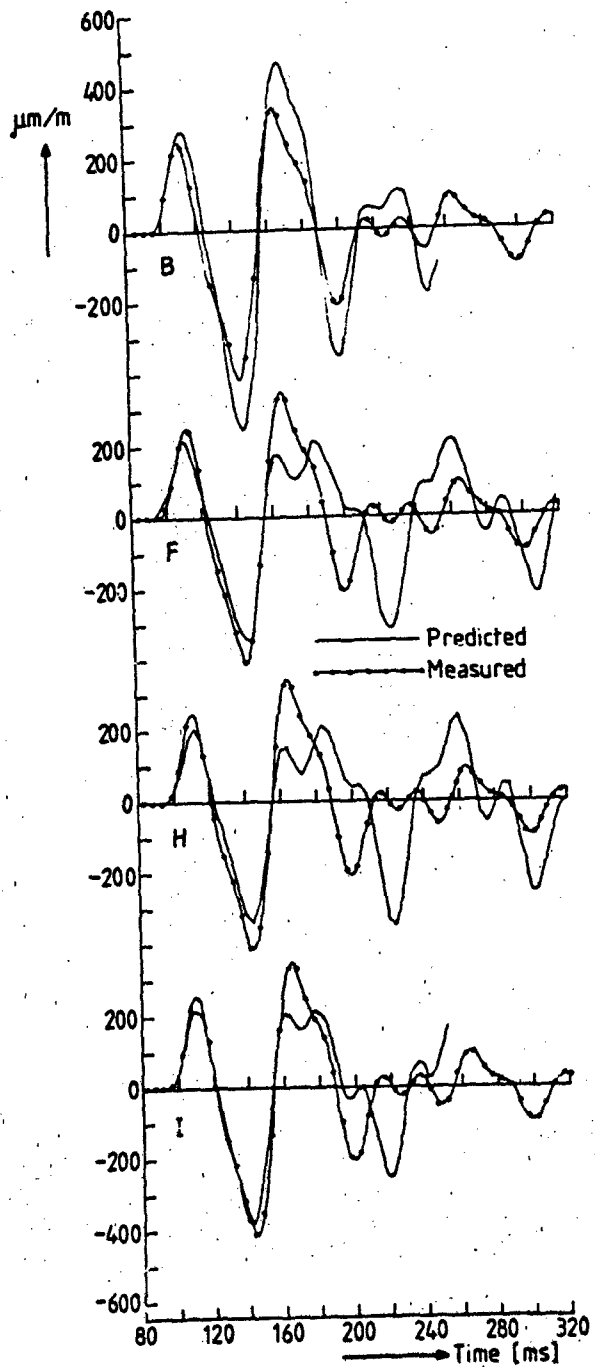
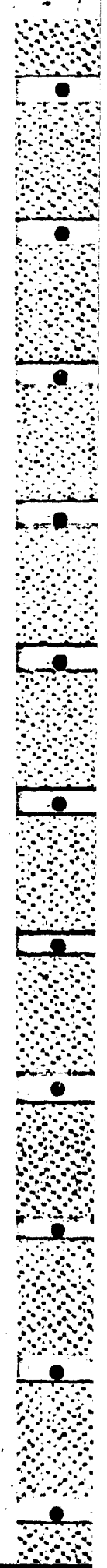


Fig. 21 Predicted versus measured strain signal 14 for shock L 1543



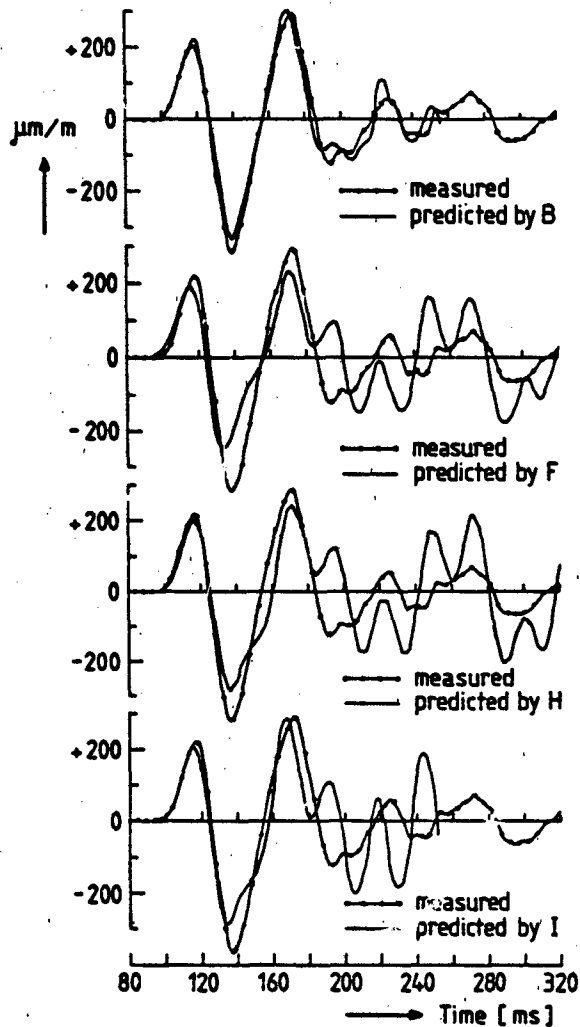


Fig. 22 Predicted versus measured strain signal 20 for shock L 1543

participants A, E and I look very similar. The plate model from participant B, however, does not possess a vibration mode comparable to the second mode of the beam models for the L 1540 configuration and the third mode of the beam models for the L 1543 configuration. In these beam models the deformation by torsion is very large. Appendix 3 shows that in fact the torsional stiffness of the beam models is much too low because the rigidity against warping has been wrongfully neglected.

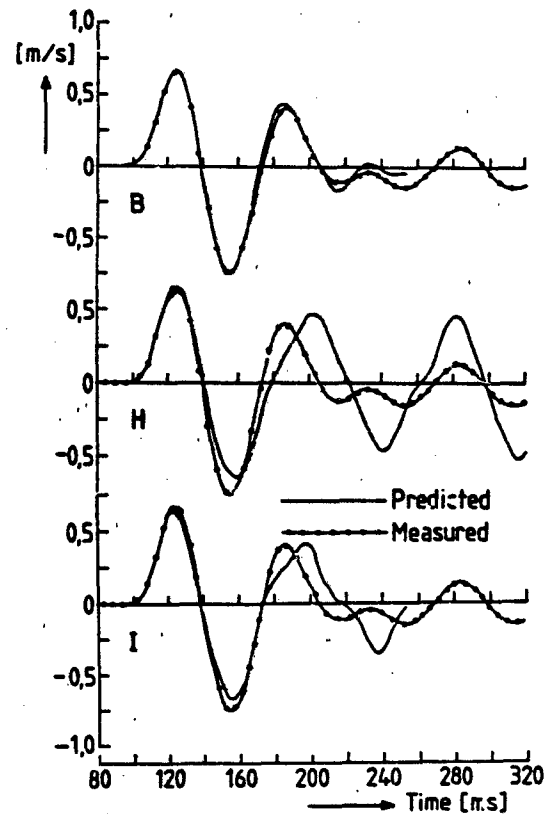


Fig. 23 Predicted versus measured velocity signal 9 for shock L 1543

#### THE ACTUAL SHOCK RESPONSE

Peak values of the signals as predicted in the various entries have been compiled partly in figures and partly in tables.

Strains, which are considered to be the most important response quantities, have been collected in Figures 18 and 19 for shocks L 1540 and L 1543 resp. Predictions are expressed as percentages of the measured peak values. The second peak of the measured strains always appeared to be larger than the first peak and for that reason Figures 18 and 19 are related to the second peak. In these Figures signal numbers are shown horizontally. Symbols indicate the various participants. Lines connecting equal symbols are merely for sake of reading.

Predicted peak values of motions, i.e. accelerations, velocities and (relative) displacements, show more spread and they are presented here only in Tables 7-11. They contain the prediction as obtained by the static method, the spectral analysis and the dynamic analysis in the time domain.

Some examples of predicted time histories, together with the actual recordings, are shown in Figures 20 to 24.

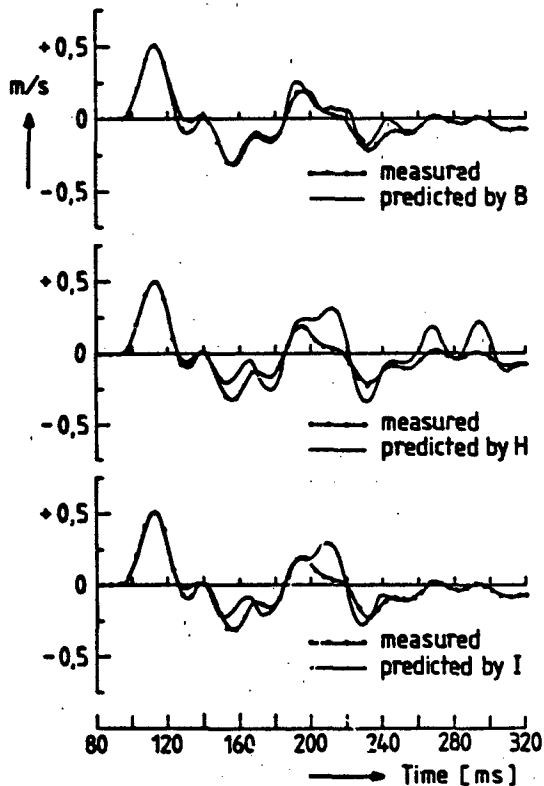


Fig. 24 Predicted versus measured velocity signal 11 for shock L 1543

## DISCUSSION OF THE RESULTS

### Accuracy of static analysis

At first sight it is rather striking that participant G, using only the simple formulae instead of a finite element model, has obtained the best strain predictions. However, in checking G's calculations, it was found that the results for signals 14-19 are related to the outer fibres of the beam, 32 mm from the neutral axis, whereas the strain gauges are 25 mm from the neutral axis. Because bending is the dominant deformation G's results should still be multiplied by a factor of approx. 0,8. This correction however, which would lead to approximately the same strain levels as found for all other beam models, was not carried through. If so, all other solutions should have to be scrutinized as well which was neither the intention nor practical. It is now to be noted that all the beam models have led to strains which mutually differ only a few per cent. However, the predictions are much too low. They are about 50% of the measured values for shock L 1540 and 75% for shock L 1543.

As far as the strains in the frame are concerned, plate model B shows somewhat better results than the beam models.

It is worth noting that for shock L 1543 the prediction percentages of the strain signals 16-19, which are all in the same cross-section, show a typical zigzag line (see Fig. 19). This persistent deviation occurs for all beam models but not for the plate model. The same holds for the results of the spectral response analysis and the analysis in the time domain. Appendix 3 throws light upon this phenomenon.

The predicted displacements are also too low. The horizontal ones in particular have been poorly predicted.

### Accuracy of spectral response analysis

From the entries received it is concluded that the NROLSUM procedure gives results mostly far in excess of the measured values. Strains lie between 100 and 140% of the measured ones. The ROOTSUM procedure produces better results for this test structure and therefore the following is related to the ROOTSUM values.

When we look at the calculated strains, for the L 1543 configuration, three of the four solutions, viz. A, C and H are very close with differences of only a few per cent. For these solutions the average prediction of strain is about 90% of the measured response, with percentages varying between 75% and 100%.

The fourth solution from participant D shows the best results with an average percentage of 98% and values ranging from about 85% to 110%. Though both contributions D and H were produced by the same computer programme, the strains of D are roughly 10% higher than the ones produced by H. A possible explanation might be that the natural frequency of the first vibration mode (15,3 Hz) is roughly 1 Hz higher than those of the three other participants A, C, and H (14,3 Hz) (see Table 6). This first vibration mode dominantly contributes to the deformation of the frame. But at 15,3 Hz the excitation in the form of a shock spectral value is about 10% larger than at 14,3 Hz, which may explain the larger shock response as found by participant D.

One of the main reasons for this higher natural frequency is supposed to be the difference in modelling the connection between the frame and the long horizontal beam. That part of the beam which is clamped to the frame is supposed to behave rather rigidly, and was consequently allocated a modulus of elasticity 100 times larger than the real modulus. D reported this stiffening to increase the lowest natural frequency from 14,0 to 15,3 Hz. Other participants A, C, and H neglected this local stiffening. The plate model of participant B takes into account this local stiffening and as a result produces also a rather high first natural frequency of 15,5 Hz, though there may be also other reasons for this.

Very close results were obtained, as far as the displacements in the vertical direction are concerned. Mostly they differ less than 5% from the measured values. In horizontal direction

the differences are larger, but, in contrast to the static analysis, they agree much better with the measured values. The acceleration is the quantity which differs most from the measurements, probably because a rather large number of vibration modes is needed for a good prediction of accelerations. For instance the spectral analysis from TNO resulted in the following mode contributions at the location where the acceleration signal 11 was measured: 15,0 0,3 11,1 5,9 10,4 0,0 0,1 12,3 2,7 1,3 10,5 0,3 2,7 4,5 3,1 0,0 0,0 and 0,0 m/s.

#### Accuracy of dynamic analysis in the time domain

For the L 1540 configuration the best strain predictions are from the plate model, exceeding the measured values only by some 5%. The three beam models produce strains which are generally some 15% too low. The results of these three models are very close with differences often less than 5%. When we look at the predicted time histories of which Fig. 20 is a typical example, there is a striking similarity with the measured signals during the initial phase of the shock (about 150 ms).

For the L 1543 configuration this picture differs. The best results as far as strains are concerned have now been produced by the beam model of participant I with percentages between 80% and 115%. The other beam models produced values mostly between 70% and 100%. Most of the strains as produced by the plate model B exceed the measured values by some 30%. When we consider the full signals, of which Figures 21-24 are examples, and leaving the actual peaks out of the consideration, the plate model B nevertheless shows a better similarity with the measured signals than all beam models. It seems as if vibration modes of DSM are represented more accurately in the plate model than in the beam models. Again the shape of the signals as produced by the three beam models is very similar. As far as peak values of accelerations, velocities and displacements are concerned, the spread in results is slightly wider than for the strains. About 3/4 of all peak values of both shocks is within the range of 75% to 110% of the measured values.

It is a remarkable fact that for the signals 10 and 11 there are some 4 exceptionally high prediction percentages (over 150%). They are obtained by the spectral and the dynamic method. The reason for these deviations, produced by different participants (A, E, F and H) and different computer programmes, is still unknown.

#### PREFERENCE

It is concluded that the spectral and the dynamic method produce much better results than the static method. It is clear that the amplification in the response, due to the near coincidence of the main excitation frequency and a natural frequency of a vibration mode, cannot be taken into account by a purely static ana-

lysis. For an arbitrary piece of equipment to be placed on board of a naval ship, it would be helpful to know approximate values for the lowest fixed base natural frequencies of the equipment. A comparison with the expected excitation frequencies for the particular shipboard location together with other relevant aspects may then lead to the decision whether or not to carry out a spectral or a dynamic analysis. The number of participants using a spectral method and those using the dynamic analysis in the time domain is about the same. So from that point of view there does not seem to be a preference for one of these two methods. Probably most participants are only familiar with the method they used.

When we compare both methods, the results of the spectral method that uses the ROOTSUM procedure are slightly better than those of the analysis in the time domain. This is rather surprising because the response analysis in the time domain in general is expected to produce more accurate results. For other structures or pieces of equipment the picture may very well be the opposite. Anyhow the spectral response analysis has some advantages. In general it will be somewhat cheaper and the amount of response data will be not so large and lead to a better survey. Interim results can show to what extent the various vibration modes are sensitive to excitation.

#### STATE OF THE ART

Most participants are rarely doing a shock analysis and some of the persons involved had not much experience in doing finite element calculations. Against that background we consider the results of the calculations to be very good. It is to be noted that in fact there is not a single contribution which has to be judged inferior.

In general the people involved were quite enthusiastic though in some cases it must have taken them quite some time to master the method and programme.

It is difficult, if not impossible, to extrapolate this positive experience from a limited number of parties to the wide range of suppliers and shipyards. That there is scope for improvements in the shock design of naval equipment is affirmed by this investigation, which showed good prediction possibilities with various programmes and methods.

#### RECOMMENDATIONS

- a) The creation of training possibilities. An example is the "shock course" which was recently prepared at TNO. It offers an opportunity for trainees to become familiar with the principles of these analysis methods.
- b) A carefully considered description in manuals and specifications as to what type of equipment is worthwhile to be analysed dynamically.
- c) Guidelines for reporting the modelling, and interim and final results.

#### ACKNOWLEDGEMENT

This work is part of a program performed for the Netherlands Ministry of Defence (Navy). The contract technical manager was Lt. Cdr. E.W.H. Keizer. The author wishes to thank all participants in this investigation and his colleague T.H. Korse for improving the beam model.

#### REFERENCES

- [1] R. Regoord, Shipboard shock response of the model structure DSM. Part 1. Results of a static, a spectral and a dynamic analysis compared with experimental results, TNO-IWECO report 5071202-81-1, May 1981.
- [2] Part 2. Predicted grade curve response versus shock test response, TNO-IWECO report 5071202-81-2, Dec. 1981. Restricted.
- [3] Part 3. Comparison between experimental results and the shock responses as predicted by eight participants using different methods and computer programmes, TNO-IWECO report 5071302-82-1, Dec. 1982.
- [4] T.H. Korse, Part 4. The influence of some alternative boundary conditions of an improved beam model on the calculated response, TNO-IWECO report 5071302-82-2, Dec. 1982.
- [5] F.J. Benedictus, F.J. van Bragt, Calibration test report of TNO-shock machines according to shock requirements for GRP mine counter measure vessel. Part 1: light weight shock machine, TNO-IWECO report 12217/001/1, May 1977. Restricted.
- [6] G.J. O'Hara, Effect upon shock spectra of the dynamic reaction of structures, Experimental Mechanics, May 1961.
- [7] C.J.M. Gelten, R. Regoord, Description of SHOCK3D, a computer programme for nonlinear shock response, TNO-IWECO report 5071021-78-1, Sept. 1978.
- [8] R.J. Roark, W.C. Young, Formulas for stress and strain, Chap. 9.3. Fifth edition. McGraw-Hill.

#### APPENDIX 1

##### Accuracy of testing

Shock specifications for equipment consisting of either calculations and/or acceptance tests are based on the existence of standardized analytical shock motions, which depend on the location in the ship, the weight of the equipment, etc. These motions increase linearly with the so-called shock level factor  $\beta$  ( $\beta \leq 1$ ). After a shock acceptance test which is aimed at simulating such a specific motion, the  $\beta$ -value is determined in an approximate way by a procedure in which the measured maximum acceleration, deceleration, the peak velocity and the first peak of displacement are compared with the required analytical ones. When passing the test, the equipment is said to be shock resistant for that location up to the  $\beta$ -value thus obtained.

For the tests L 1540, L 1543 and L 1544, for which there were no differences in adjusting the machine, these  $\beta$ -values were determined. It appeared that for shock L 1544, the shock table being unloaded, the  $\beta$ -value is slightly higher than for the two other shocks. For these two shocks the "equivalent" standardized shock motion is shown as part of Fig. 9. The shock spectrum of that motion has been used as an input for a spectral response analysis of DSM using the ROOTSUM mode summation. Having in mind the good experience with this method and the finite element model in predicting for instance peak strains which are roughly 90% of the real strains, we expected that the predictions of that new analysis should be at least obtained during the tests. However, Fig. 25, in which are now presented the measured values as percentages of the required theoretical strains, shows serious undertesting. For signals 14 and 15 the test level is only some 40% of the required level. For this discrepancy there are two equally important reasons. During the test the table motion decays more rapidly than the standardized shock motion. Consequently, as shown by the corresponding shock spectra (Fig. 26) the response in the frequency range between roughly 10 and 20 Hz is lower than it should be. The lowest vibration mode of DSM which contributes for the major part to the strain response has a frequency in the middle of this range.

The second reason is the feed-back effect from the equipment to the shock table, producing the shock spectrum dip as discussed earlier by O'HARA [6]. In this case they are of considerable depth (Fig. 27 and 28) and they occur very close to the lowest fixed base natural frequency of DSM. It should be noted that in those rare cases in which shock spectra were produced during normal acceptance tests with this shock machine, such important dips have not been found.

From this study [2] it is concluded that for this particular test structure the accuracy of testing is far less than the accuracy of an analysis. Shock spectra should be derived during acceptance tests as a standard procedure.

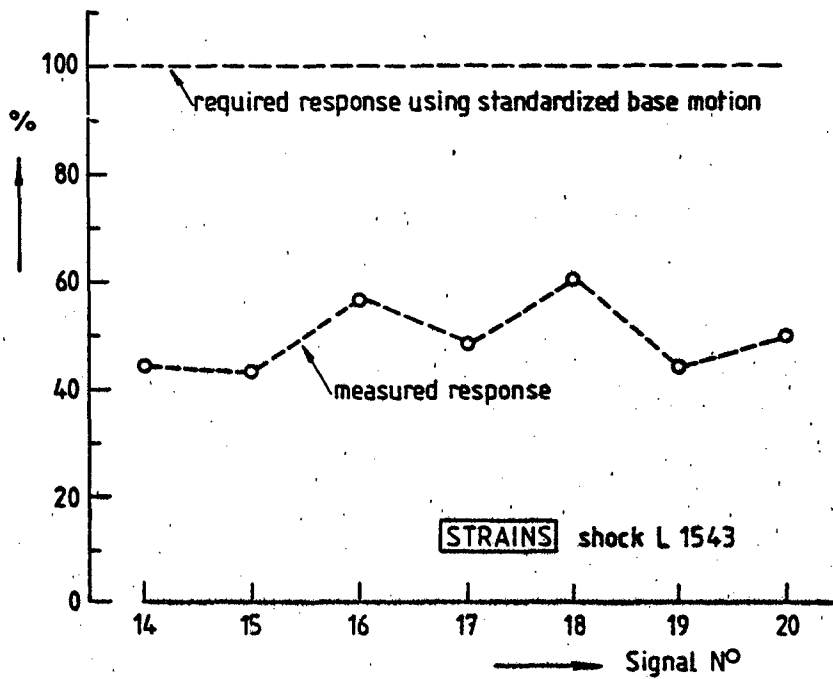
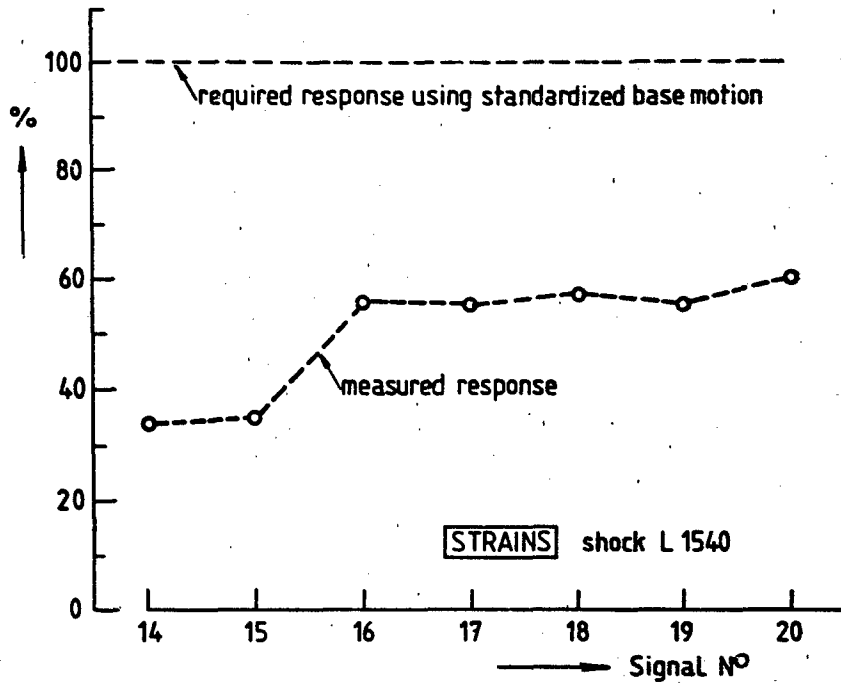


Fig. 25 Measured versus required strains as calculated with a spectral response analysis (ROOTSUM) using standardized base motion

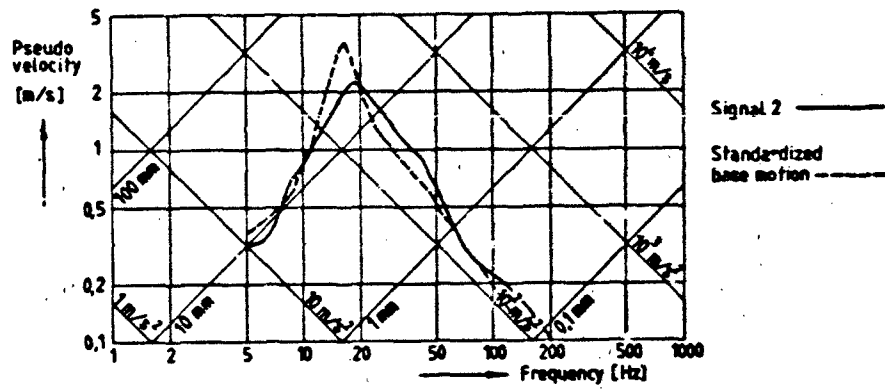


Fig. 26 Shock spectra for shock L 1544

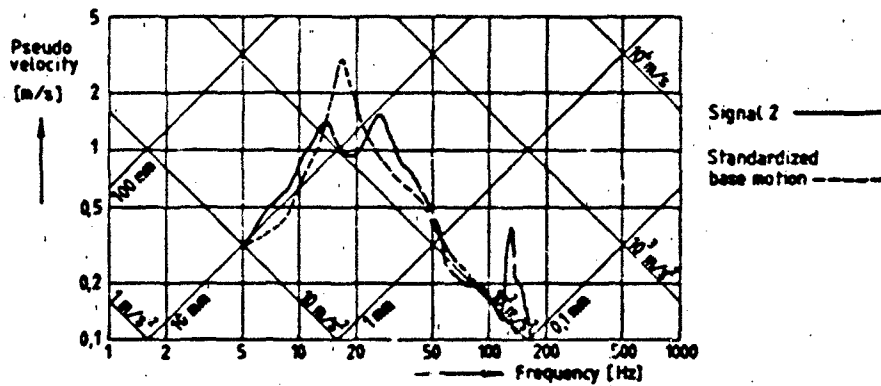


Fig. 27 Shock spectra for shock L 1540

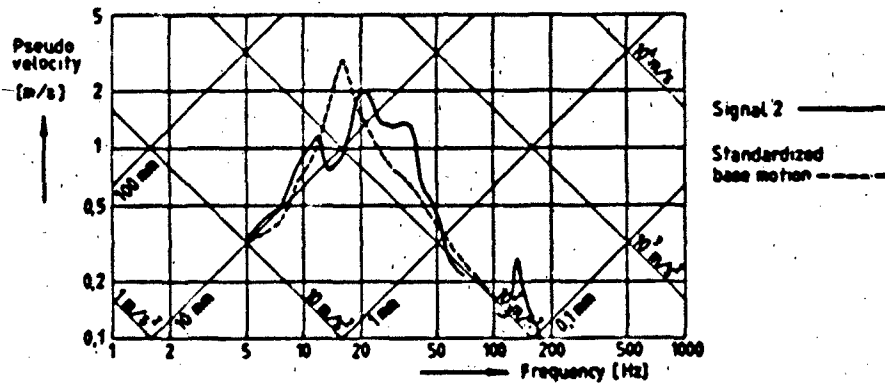


Fig. 28 Shock spectra for shock L 1543

APPENDIX 2

Theory of spectral response analysis

General matrix equations governing the forced response of an undamped system are

$$\begin{bmatrix} M_{uu} & M_{up} \\ M_{pu} & M_{pp} \end{bmatrix} \begin{bmatrix} \ddot{q}_u \\ \ddot{q}_p \end{bmatrix} + \begin{bmatrix} K_{uu} & K_{up} \\ K_{pu} & K_{pp} \end{bmatrix} \begin{bmatrix} q_u \\ q_p \end{bmatrix} = \begin{bmatrix} P \\ R \end{bmatrix} \quad (1)$$

in which matrices are partitioned according to the freedom families,

- u for unconstrained d.o.f. or unknowns
- and p for prescribed d.o.f.
- M is the mass matrix
- K is the stiffness matrix
- q is the vector of absolute displacements and rotations of nodal points of the structure
- R is the vector of reaction forces at the prescribed d.o.f.
- P is the vector of given external forces.

In order to simplify these equations the excitation should meet the following requirements which are typical for a spectral response analysis

- (1) External forces are absent or  $P = 0$  (2)
- (2) The structure is connected to a single rigid foundation which translates according a given function of time  $p(t)$  in a certain fixed direction defined by the unit direction vector  $1$  having as components  $c_1, c_2$  and  $c_3$ . Consequently the vector  $q_p$  only contains translations which are connected to the time function  $p(t)$  by the formula

$$q_p = B_p 1 p(t) \quad (3)$$

in which  $B_p$  is a Boolean matrix. The introduction of motions relative to the foundation is also typical for a spectral response analysis. They are defined by

$$z_u = q_u - q_u^r \quad (4)$$

in which  $q_u^r$  is a rigid body motion of the structure given by

$$q_u^r = B_u 1 p(t) \quad (5)$$

in which  $B_u$  is another Boolean matrix. For such a rigid body motion

$$\begin{bmatrix} K_{uu} & K_{up} \\ K_{pu} & K_{pp} \end{bmatrix} \begin{bmatrix} q_u^r \\ q_p \end{bmatrix} = 0$$

and thus  $K_{uu} q_u^r + K_{up} q_p = 0$  (6)

Substituting (2) through (6) into the upper part of Equation (1) gives

$$M_{uu} \ddot{z}_u + K_{uu} z_u = -(M_{uu} B_u + M_{up} B_p) 1 p(t) \quad (7)$$

Once the eigenvalue problem as defined by the matrices  $M_{uu}$  and  $K_{uu}$  has been solved the vibra-

tion modes  $\phi^s$  are collected as columns in the matrix X. The intensity of the modes is chosen such that

$$X^T K X = I \text{ (unit matrix)}$$

Angular natural frequencies  $\omega_s$  are presented in the diagonal matrix

$$Q^2 = \begin{bmatrix} \omega_1^2 & & \\ & \omega_2^2 & \\ & & \omega_n^2 \end{bmatrix}$$

Now the Equations (7) are decoupled by substituting  $z = X \eta$ , in which  $\eta$  is the column vector of principal coordinates, and by premultiplying by the transposed matrix X

$$\ddot{\eta} + Q^2 \eta = -Q^2 X^T (M_{uu} B_u + M_{up} B_p) 1 p(t) \quad (8)$$

For vibration mode s we have

$$\ddot{\eta}_s + \omega_s^2 \eta_s = -\omega_s^2 \left( \sum_{i=1}^3 \tau_{si} c_i \right) p(t)$$

in which  $\tau_{si}$  are coefficients of the so-called participation matrix

$$\Gamma = X^T (M_{uu} B_u + M_{up} B_p)$$

For each vibration mode s the three participation factors  $\tau_{s1}, \tau_{s2}$  and  $\tau_{s3}$  reveal how sensitive this mode is for excitation. Equation (8) is very similar to the Equation (9) for a simple one mass spring system subjected to the same base motion  $p(t)$ .

$$\ddot{z} + \omega^2 z = -p(t) \quad (9)$$

This problem is solved for a variety of frequencies by the shock spectrum concept, giving for instance the maximum values of the relative motion  $z$  and the absolute acceleration  $\ddot{z} = \omega^2 z$ . For corresponding natural frequencies of the multi degree of freedom system we can directly use these shock spectral values:

$$\eta_s^{\max} = z^{\max} \omega_s^2 \left( \sum_{i=1}^3 \tau_{si} c_i \right)$$

$$\eta_s^{\text{abs max}} = \omega_s^2 z^{\max} \left( \sum_{i=1}^3 \tau_{si} c_i \right)$$

For each separate vibration mode the maximum response in terms of stresses, strains, etc. can now be determined because the maximum value of the principal coordinate  $\eta_s$  is known. Inherent in the shock spectral analysis, is the loss of information regarding the time of occurrence of maximum mode intensities. This appears from the final step when mode contributions are added according to some sort of summation procedure as ROOTSUM or NRLSIM.

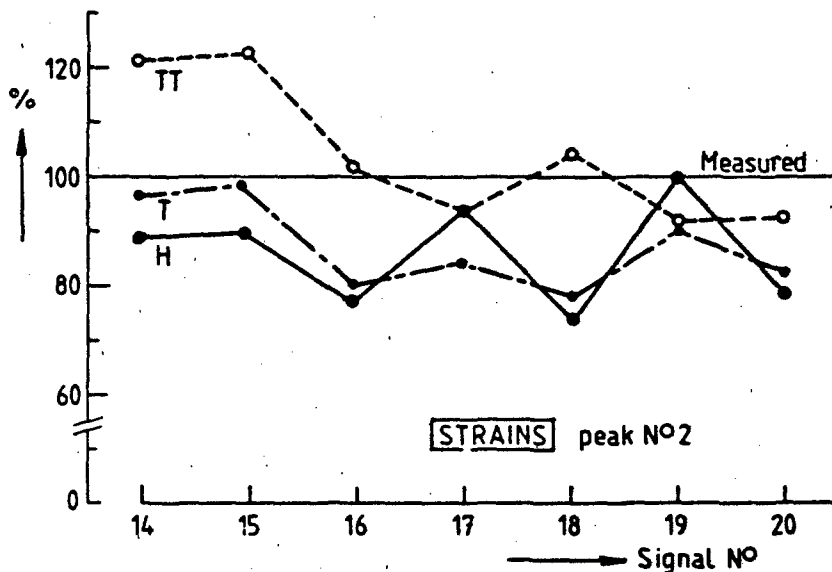


Fig. 29 Effect of modified boundary conditions on strain predictions for shock L 1543

### APPENDIX 3

#### Modified boundary conditions

The persistent deviation of strains in cross section A predicted by all beam models (sawtooth line in Fig. 19) as well as the better prediction of full time signals by the plate model B (see Fig. 21-24), was a challenge to improve the beam model. For shock L 1543 spectral response calculations with model H have been repeated under several different assumptions [4]. It was found that in addition to the St. Venant torsional stiffness of the frame the stiffness due to constrained warping is of some influence. If a bar with a non-circular cross-section is twisted, the cross-sections do not remain plane, but they warp. If this warping is prevented the torsional stiffness is increased as explained for instance in [8]. This warping rigidity of the frame was taken into account by the BRCOP element of ASKA, which has a seventh degree of freedom at each nodal point, the first derivative  $\phi'$  of the angle of twist of the cross section. At that end of the frame which is connected to the long horizontal beam  $\phi'$  has been suppressed.

Natural frequencies for this modified model are presented in Table 6 under the letter T. Modes 1 and 2 hardly changed their frequency as com-

pared to the original solution H. Also the shape is similar. The frequency of the third mode increased, however, from 22.9 Hz to 31.0 Hz and the shape is now more like that of the former mode 4 (Fig. 17). Due to the introduction of warping rigidity, beginning with the third mode, the frequencies deviate from those of all other beam models. There is a better agreement now with the frequencies of the plate model B. Strains for solutions H and T are shown in Fig. 29. The sawtooth effect now appears to be much less pronounced. Signal 14 in cross section B of course is not affected by bending due to constrained warping because at the two strain gauge locations (see Fig. 5) the effects are equal and of opposite sign, leaving no effect when averaging. The same holds for signal 15.

Having improved the model by the introduction of warping rigidity an additional second modification was carried through. The rotation of the frame at the points of support (see Fig. 4) is now suppressed around the y-axis, as was also done by participants B and E. The solution is indicated by TT. Natural frequencies are rather close now to those of the plate model B (see Table 6). Fig. 29 shows that strains also changed significantly. Though it is felt that suppressing this rotation is better than leaving it free, it is only by a much more detailed finite element mesh that the real boundary conditions could be simulated.

DIRECT ENERGY MINIMIZATION APPROACH TO WHIPPING  
ANALYSIS OF PRESSURE HULLS

Kenneth A. Bannister  
Naval Surface Weapons Center  
White Oak, Silver Spring, MD 20910

This paper addresses the large deformation behavior of cylindrical shells executing low frequency, but large amplitude, whipping-type vibrations. This problem is important in the practical design of cylindrical shell structures to resist failure due to in-service bending loads combined with pressure. Submarine pressure hulls, aircraft fuselages, and industrial piping applications fall into this category of structure/loading combination. A new methodology is described for dealing with such nonlinear shell analysis problems. A symbolic manipulation system is first applied alone and then coupled with two appropriate minimization algorithms to solve for the local large deformation response as the cylinder undergoes whipping. A previous potential energy based analysis of the problem has been extended for the purpose and the mathematical labor is greatly expedited with the aid of the symbolic manipulation system. It is shown that in cases where explicit algebraic solutions for, say, the moment-curvature relation of the shell are impractical to generate, only a potential energy expression and its first derivatives need to be constructed. From the energy and derivative expressions, nonlinear optimization algorithms can be brought to bear to minimize directly the potential energy by methodically and efficiently adjusting the displacements (or other appropriate basic quantities). Having solved for the basic quantities, derived quantities, such as strains, stresses, and moments can then be computed.

INTRODUCTION

This paper is concerned with the development and demonstration of a new methodology to aid in the solution of nonlinear problems in mechanics. The particular application discussed here is a very specific case of nonlinear shell response connected with whipping motions of a submarine pressure hull. The underlying methodology actually has a much broader range of application for both shell vibration problems and in structural mechanics at large. It is shown how the methodology can be used to extend a previous nonlinear shell analysis and then facilitate practical solutions, exact and approximate (numerical), of the resulting equations. The large amount of

mathematical labor typically associated with obtaining nonlinear shell solutions is greatly reduced and the analyst has much greater freedom to modify or extend the analysis without the penalty of tedious, time-consuming algebraic manipulations.

We consider the large deformation behavior of a cylindrical shell executing low-frequency, but large amplitude, whipping motions. This problem is important in the practical design of cylindrical shell structures to resist failure caused by combined in-service bending and pressure loads. Submarine pressure hulls, aircraft fuselages, and piping systems are included in this category of structure-loading combination.

## BRIEF REVIEW OF WHIPPING

An earlier paper [1] gave a fairly detailed discussion of explosion bubble-induced whipping of surface ships and submarines. Basically, whipping is defined as the transient beam-like response of a ship to some form of strong hydrodynamic loading, in this case the accelerating fluid flow field surrounding a pulsating and migrating explosion gas products bubble. Figures 1-8, taken from [1], show typical whipping response histories for a uniform elastic beam floating in the free surface and subjected to bubble loadings from a 100 kg TNT charge placed at a depth of 30.48m (100 ft) directly below the C.G. of the beam. Figures 2-4 show the bubble parameters while Figures 5-8 show the various vertical whipping responses induced in the beam. These whipping analyses were performed with a simple lumped mass-elastic finite element structural model coupled to the bubble equations of motion. Typically, only the first few modes of vibration of the ship are needed to satisfactorily capture the whipping response, i.e., the heave and pitch rigid body modes and the first 2-3 distortion modes.

If the whipping motions achieve large amplitudes, then any attempt at predicting the local hull plating response (that is, shell response) must account for possible large out-of-plane displacements of the shell which cannot be handled within the context of elementary beam theory. Fortunately the motions are low frequency, at least at locations remote from where the bubble loads impinge, hence a quasistatic shell analysis is appropriate. In the region of intense bubble loading, because of the high frequency shell motions, shell inertia terms become important and thus a more sophisticated transient analysis is required. In this paper we will focus on the problem of analyzing the large deformation behavior of a submarine pressure hull in response to low frequency whipping-type motions.

## ENERGY ANALYSIS OF SHELL UNDER BENDING AND PRESSURIZATION

We consider the large deformation response of an elastic thin-walled circular cylindrical shell subjected to pure bending and either internal or external pressure. Figure 9 shows the cross section of the shell and defines pertinent geometric and pressure parameters used in the analysis. By "thin" we mean that  $a/t > 50$  and since

most pressure hulls are of the order  $a/t=100$  we can regard them as thin shell structures. Because the shell is thin, we say that the state of affairs in the shell wall can be adequately represented by conditions in the middle surface ( $r=a$ ). For the sake of convenience, we further assume that moment and curvature do not vary over the shell length so that all cross sections deform in the same manner. A side view of the shell is shown in Figure 10. The shell's neutral axis is bent into an arc of circle with radius  $\rho$  due to the terminal moments. Figure 10 also defines  $d$ , distance from the neutral surface to a given point on the deformed shell middle surface. This parameter is used in computing stress and strain quantities in the shell wall. Linearly elastic material behavior is assumed, thus  $E$  (Young's modulus) and  $\nu$  (Poisson's ratio) completely characterize the material response.

The thinness of the shell wall relative to other shell dimensions leads to large (when compared to the thickness  $t$ ) displacements normal to the shell wall during bending, rendering the problem geometrically nonlinear. Therefore, any attempt to accurately determine the shell response must account for these geometric nonlinearities. There is a smooth transition from small to large displacements in this problem. Thus, nonlinear effects must be anticipated starting at fairly low load levels compared to the peak (maximum possible) moment that the shell can carry. Furthermore, pressure has a remarkable effect on the load-displacement response, as will be shown. Internal pressure tends to stiffen the shell in a way that increases the peak moment while external pressure weakens the shell's ability to withstand bending.

The problem will be analyzed by an energy minimization approach, facilitated by the use of a symbolic manipulation system (MACSYMA, developed at the MIT Computer Laboratory). The total potential energy function is formulated for the shell with loads and is cast in terms of middle surface displacements at a cross section of the shell. The shell is assumed to be infinitely long and moreover that no variation of conditions occurs along its length. Truncated Fourier series terms with a priori unknown coefficients are included in the displacement functions to account for nonlinear effects. The goal of the analysis is then to determine the coefficients of these additional terms

which minimize the potential energy. The strategy followed is to generate an expression for the potential energy involving the unknown coefficients and the curvature parameter defined by  $\epsilon = a/\rho$ .  $\epsilon$  will also be unknown for given values of moment and pressure. Then, for each choice of bending moment and pressure, the minimizing set of unknown displacement coefficients and curvature parameter is found by two methods:

(1) Use of MACSYMA to obtain explicit solutions for the coefficients in terms of  $\epsilon$  and subsequently  $M(\epsilon)$ ; this we will call the "exact" solution; and

(2) Generation of the nonlinear moment-curvature relation by direct application to the potential energy of two different computer algorithms designed to minimize nonlinear multivariate unconstrained functions; that is, the potential energy will be minimized directly with the aid of optimization algorithms.

The purpose for the second method is to show that if an "exact" moment-curvature cannot easily be obtained by the first method, then accurate numerical results can be produced through direct energy minimization. This notion has broader implications for situations where a large number of unknowns, say 200, are involved in a particular nonlinear mechanics problem.

As in most nonlinear shell analyses, the sheer amount of mathematical manipulation can be enormous. In the present case, the symbolic algebraic manipulation language MACSYMA is used to substantially reduce the mathematical labor. This is, to the author's knowledge, the first time such a tool has been applied in a comprehensive manner to a nonlinear shell analysis. MACSYMA is excellently suited to the task as it can handle all of the necessary mathematical operations involved such as functional evaluation, trigonometric expansion and reduction, differentiation, integration, and equation solving. It has a syntax very similar to other standard programming languages such as ALGOL, PL/1, and FORTRAN, along with file manipulation features. These properties make MACSYMA extremely convenient to apply to the problem at hand.

Using a powerful mathematical tool such as MACSYMA, it is now possible to carry out analyses of nonlinear structural mechanics problems and avoid

many ad hoc simplifications authors in the past found necessary to make the effort tractable. In the present work, a MACSYMA code has been constructed which reproduces step-by-step the mathematical analysis of the shell bending problem beginning with displacement function generation, derivation of stress and strain quantities, proceeding with construction of the potential energy function, and finally ending with solution for the unknown Fourier coefficients and generation of a moment-curvature parameter relation. It is possible, within this code, to include or exclude quite readily certain nonlinear displacement terms that previous authors felt compelled to drop due to mathematical complexity. Thus, the usual simplifications invoked in shell work suggested by the phrases "neglect quantities of small magnitude" and "neglect cross product and squared quantities" can be freely adopted, ignored, or modified as the analyst wishes. The extra calculational burden is carried by the computer, not the analyst. As an example of the savings in time and labor that can be realized with such a symbolic language tool, the author applied FORMAC-73, an older language, to a two-term Fourier series displacement function analysis based on a nonlinear shell theory in order to obtain the integrand of the strain energy (bending and stretching of the shell middle surface) expression. Manually, this effort required two weeks with a considerable amount of time consumed in checking for and correcting errors. With FORMAC-73, the same exercise required less than one day with the algebraic operations done correctly throughout. For three, four, or more Fourier terms or, let us say, alternative displacement functions of greater complexity, it was clear that hand-computations would become very costly in time and the likelihood for errors very great. In addition, the coding could be stored if desired and modified and re-run for different cases and the results retained on files for listing or for later applications.

One of the earliest studies of the cylindrical shell in pure bending (without pressurization) was the classic paper by Brazier [2]. Brazier simplified the analysis greatly by the accurate assumption that the shell middle surface is extensible. He also pointed out that the problem becomes fundamentally nonlinear due to the thinness of the shell wall relative to other dimensions of the shell. Thus the linear relationship between moment and curvature derived from St. Venant's

theory of bending of beams of solid cross section is invalidated since local wall deformations are large and thus strain cannot be a linear function of original position. Figure 11 shows the disparity between the linear (St. Venant) and large deformation (nonlinear) predictions of moment vs. curvature. Also, in Figure 12 we see the ovalization mode that the shell cross section takes on; this mode was assumed by Brazier in his analysis.

In the small displacement range, superposition holds, hence the moments and pressure can be applied in any order. Then, following the approach of Brazier [2] and Wood [4], the possibility of nonlinear deformations is allowed by introducing truncated Fourier series terms in the displacement components  $v$  and  $w$  (defined in Figure 9). These terms have undetermined coefficients which are to be found by application of the Theorem of Minimum Potential Energy.

The potential energy  $V$  is given by

$$V = U + W. \quad (1)$$

$U$  is the strain energy stored in the shell due to bending and  $W$  represents the work of the pressure and bending loads. In order to account for the bending strain energy, the change of curvature at any point on the shell must be computed. Brush and Almroth [3] show this to be given by (after accounting for a sign change due to use of a different convention for  $w$ )

$$\chi_{\phi\phi} = \frac{1}{a^2} \left( \frac{dv}{d\phi} + \frac{d^2w}{d\phi^2} \right). \quad (2)$$

Next, the strain energy  $U$  is given by

$$U = \frac{a}{2} \int_0^{2\pi} \left[ D \chi_{\phi\phi}^2 + t(\sigma_{xx}\epsilon_{xx} + \sigma_{\phi\phi}\epsilon_{\phi\phi} + \bar{\sigma}_{\phi\phi}\bar{\epsilon}_{\phi\phi} + \bar{\sigma}_{xx}\bar{\epsilon}_{xx} + 2\bar{\sigma}_{xx}\bar{\epsilon}_{xx} + 2\bar{\sigma}_{\phi\phi}\bar{\epsilon}_{\phi\phi}) \right] d\phi. \quad (3)$$

An important geometric parameter is  $d$ , the distance from the shell neutral surface to a given fiber in the shell middle surface (as shown in Figure 10). The usual assumption of thin shell theory is applied here, namely, that stresses and strains do not vary through the wall thickness and that the normal stress through the thickness vanishes. Therefore, the middle surface stress-strain state adequately represents the response of the shell. The parameter  $d$  is given by

$$d = (a - w) \cos\phi - v \sin\phi.$$

The circumferential and axial stresses and strains in the small displacement range are given by Wood [4] for bending and pressure as follows:

for bending

$$\epsilon_{xx} = \frac{d}{\rho},$$

$$\sigma_{xx} = \frac{Ed}{\rho},$$

$$\epsilon_{\phi\phi} = -\frac{Kd}{\rho}, \quad (4)$$

$$\sigma_{\phi\phi} = 0;$$

and for pressure

$$\bar{\epsilon}_{xx} = \frac{a}{2}(1-2\nu),$$

$$\sigma_{xx} = \frac{Ea}{2}, \quad (5)$$

$$\bar{\epsilon}_{\phi\phi} = \frac{a}{2}(2-\nu),$$

$$\sigma_{\phi\phi} = Ea.$$

Although the deformations may become large, strains remain small; this is typical in thin shell structures. A large strain analysis would require

accounting for plastic material response-this problem is not considered here.

In these equations, the pressure enters through the parameter  $\alpha$  given by

$$\alpha = \frac{Pa}{Et} \quad (6)$$

Sokolnikoff [5] reports the linear  $w$  and  $v$  displacement components for bending and pressure are given by:

for  $w$

$$w_0 = \frac{\sqrt{ea}}{2} \cos \phi, \quad (7)$$

$$\bar{w} = -\frac{(2-\nu)}{2} \alpha a;$$

and for  $v$

$$\bar{v} = 0 \text{ (symmetry)}, \quad (8)$$

$$v_0 = -\frac{\sqrt{ea}}{2} \sin \phi.$$

We have introduced the curvature parameter  $c$  in Equations (7) and (8). It is defined by

$$c = \frac{a}{\rho}. \quad (9)$$

The total displacements  $v$  and  $w$  are then the sum of bending, pressurization, and additional terms  $v_1, w_1$  needed to account for large deformations of the shell. Thus we have

$$v = v_0 + v_1 \quad (10)$$

$$w = \bar{w} + w_0 + w_1.$$

Following Brazier [2], we assume that the additional displacements  $v_1, w_1$  are inextensional; thus we have

$$w_1 = \frac{dv_1}{d\phi}. \quad (11)$$

According to Wood [4],  $v_1$  and  $w_1$  can be expressed as the infinite series given by

$$v_1 = \sum_{n=2}^{\infty} A_n \sin n\phi \quad (12)$$

and, following Equation (11), we must have

$$w_1 = \frac{dv_1}{d\phi} = \sum_{n=2}^{\infty} nA_n \cos n\phi. \quad (13)$$

Note that  $v$  and  $w$  do not vary with position along the shell axis, that is, all cross sections must deform in the same manner. Also note that the choice for  $v_1$  satisfies displacement continuity and symmetry conditions on  $v$ . Hence, the total displacements become

$$v = -\frac{\sqrt{ea}}{2} \sin \phi + \sum_{n=2}^{\infty} A_n \sin n\phi$$

$$w = -\frac{(2-\nu)}{2} \alpha a + \frac{\sqrt{ea}}{2} \cos \phi \quad (14)$$

$$+ \sum_{n=2}^{\infty} nA_n \cos n\phi.$$

The work done by the pressure and applied moments is given by Wood [4] as

$$W = -\frac{P\pi}{2} (\nu^2 a^2 c^2 \quad (15)$$

$$- \sum_{n=2}^{\infty} (n^4 - n^2) A_n^2) - \frac{M}{a} c.$$

We see then that the potential energy  $V$  can ultimately be written as a nonlinear function of the coefficients  $A_n$  and the current curvature parameter  $\epsilon$  in the general form

$$V = V(A_2, A_3, \dots, \epsilon). \quad (16)$$

The strategy followed from this point is to seek values for the coefficients  $A_2, A_3, \dots$  which minimize the total potential energy of the shell and the loading.

Wood [4] proceeded with the solution by neglecting certain terms in  $V$  involving  $v_1^2, w_1^2, v_1 w_1$ , then expanding  $V$  and applying the theorem of Minimum Potential Energy:  $V$  is stationary when

$$\frac{\partial V}{\partial A_2} = \frac{\partial V}{\partial A_3} = \dots = \frac{\partial V}{\partial A_n} = 0. \quad (17)$$

Wood [4], for example, has carried out the simplification (or linearization) of  $V$  just mentioned and has found that the coefficients  $A_2$  and  $A_3$  become

$$A_2 = \frac{a\epsilon^2(1-\nu^2) \left[ 1 + \frac{(1-\nu)}{2} \right] \alpha}{2(t/a)^2 + 8(1-\nu^2)\alpha} \quad (18)$$

$$A_3 = \frac{-a\epsilon^3(1-\nu^2)}{48(t/a)^2 + 72(1-\nu^2)\alpha}$$

The remaining coefficients vanish, i.e.,

$$A_4 = A_5 = \dots = A_n = 0. \quad (19)$$

However, these terms do not vanish if the linearization is not carried out, as will be shown later. Unfortunately, the amount of algebraic manipulation associated with including squared and cross product terms grows enormously as more terms in the Fourier expansions are taken. This difficulty is greatly lessened by use of symbolic manipulation system such as MACSYMA.

It is useful to derive a general form for the moment-curvature relation of the shell. We have seen earlier that the coefficients  $A$  can be expressed as functions of the curvature parameter; hence, the potential energy  $V$  may be written

$$V = G(A_2(\epsilon), A_3(\epsilon), \dots, \epsilon). \quad (20)$$

For  $V$  to be stationary with respect to  $\epsilon$ , we must have

$$\frac{\partial V}{\partial \epsilon} = \frac{\partial G}{\partial A_2} \frac{\partial A_2}{\partial \epsilon} + \dots \quad (21)$$

$$+ \frac{\partial G}{\partial \epsilon} = 0.$$

But since

$$\frac{\partial V}{\partial A_2} = \frac{\partial V}{\partial A_3} = \dots = \frac{\partial V}{\partial A_n} = 0, \quad (22)$$

i.e.,

$$\frac{\partial G}{\partial A_2} = \frac{\partial G}{\partial A_3} = \dots = \frac{\partial G}{\partial A_n} = 0. \quad (23)$$

Equation (21) reduces to

$$\frac{dG}{d\epsilon} = 0. \quad (24)$$

This last equation may be rewritten quite easily in the following form

$$\frac{dG}{d\epsilon} = f(A_2, A_3, \dots, \epsilon) \quad (25)$$

$$- \frac{M}{a} = 0$$

or, solving for  $M$ , we have

$$M = a f(A_2, A_3, \dots, A_n, \epsilon). \quad (26)$$

Wood has found in his linearized analysis [4] that Equation (26) becomes

$$M = \frac{EI_{xx}}{2a} \left\{ c \left[ 2 + \frac{\nu^2 (t/a)^2}{6(1-\nu^2)} \right] + 2 \frac{(2-\nu)^2}{2} \alpha^2 + \dots \right.$$

$$+ 4 \frac{(2-\nu)}{2} \alpha - 2\nu^2 \alpha \quad (27)$$

$$+ \epsilon^3 \left[ \nu^2 - \frac{3(1-\nu^2) \left(1 + \frac{(2-\nu)}{2} \alpha\right)^2}{(t/a)^2 + 4(1-\nu^2)\alpha} \right]$$

$$+ \epsilon^5 \left[ \frac{-\nu^2 (1-\nu^2)}{24(t/a)^2 + 36(1-\nu^2)\alpha} \right] \Bigg\}.$$

Equation (27) may be written, for convenience, in the simpler form

$$M = c_1 \epsilon + c_2 \epsilon^3 + c_3 \epsilon^5. \quad (28)$$

Note that peak moment values are readily found corresponding to roots of the quartic given by

$$5c_3 \epsilon^4 + 3c_2 \epsilon^2 + c_1 = 0. \quad (29)$$

Since Equation (29) has four possible roots, the root desired must be real and positive. This value of  $\epsilon$  can then be substituted in Equation (28) to get the corresponding peak moment. Other quantities of interest, such as the deformed cross section profile and stress and strain dependence on angle  $\phi$  can also be generated at this peak moment value.

This analysis has been extended with the aid of MACSYMA to include the quadratic terms in  $v_1$  and  $w_1$  which Wood neglected in his energy function. It is shown also that Wood's entire analysis can be reproduced by use of MACSYMA. By including the quadratic terms previously neglected, we show that these terms have significant effects on the moment-curvature behavior of the shell. Explicit solutions, in algebraic form, are given for two, three, and four term trigonometric expansions of  $v_1$  and  $w_1$  (see Equation (4)). It turns out that the coefficients  $A_4$  and  $A_5$  calculated in this case do not vanish as Wood found in his linearized analysis. As an alternative to straight-forward solution for the moment-curvature relationship through the use of MACSYMA, two different gradient method-based optimization algorithms are applied directly to the potential energy functional. These algorithms were designed for the minimization of nonlinear unconstrained multivariate functions. They require only explicit

expressions for the function to be minimized (in this case the potential energy) and its first derivatives with respect to the independent variables ( $A_2, \dots, A_5, \epsilon$ ). We show that both algorithms give excellent agreement with the "exact" moment-curvature results calculated through MACSYMA-generated expressions. Thus in situations where it may not be practical to solve directly for a moment-curvature relation, useful and accurate numerical results can be obtained by direct minimization so long as expressions for the potential energy functional and its derivatives can be obtained.

## RESULTS

By use of the MACSYMA symbolic manipulation system, quadratic and cross-product displacement terms can easily be retained in the energy expression (Equation (3)) and the necessary algebraic operations carried out. To do this by hand would prove to be a formidable task, even for a few terms in the Fourier expansions. Such routine mathematical operations as trigonometric reduction, expansion of products, differentiation, and integration can be done with MACSYMA. A further useful application of this tool, equation solving, is illustrated in Appendix A.

A useful way to characterize the shell response is to display its moment-curvature behavior similar to the generic curve given in Figure 11. Two computational procedures are available: Direct generation of an explicit equation relating moment  $M$  and the curvature parameter  $\epsilon$ ; or direct minimization of the total potential energy expression by numerical minimization (i.e., optimization) methods. MACSYMA-generated solutions for the coefficients  $A_1, \dots, A_n$  have been obtained for the fully nonlinear energy expression. With these coefficients, we can then compare plots of  $M(\epsilon)$  for Wood's linearized analysis with results from the present nonlinear analysis. This will show clearly whether neglecting the quadratic terms (as Wood did) affects the moment-curvature behavior. Figures 13 and 14 show respectively comparisons of  $M(\epsilon)$  for Wood's analysis with the present analytical results for moderate internal and external pressure (300 psi). The shell is made of steel and has dimensions typical of a submarine pressure hull. The curves for the fully nonlinear analyses (two, three, and four-term Fourier expansions) are

very nearly the same; hence, all three curves appear to coalesce to a single line (upper curves in Figures 13 and 14). Computations for the nonlinear cases were done with the MACSYMA code listed in Appendix B. Additional comparisons like those in Figures 13 and 14 can be found in [6] for other pressure values and shell geometries.

As an alternative to explicit generation of the moment-curvature equation, the energy expression for the system can be minimized directly through use of a numerical optimization technique. In this case, of course, we must forego seeing the explicit algebraic solution form and must instead settle for "approximate" answers, albeit with a controllable accuracy. The purpose here is to demonstrate that in those cases of nonlinear shell analysis where even the assistance of a tool such as MACSYMA is not completely effective in obtaining "exact" solutions, extremely accurate numerical results can be easily be gotten if the energy functional can at least be generated. This situation could arise in the present work, for example, if a large number of Fourier expansion terms were desired or if the underlying shell theory formulation was made more complex. We will, without loss of generality, illustrate this approach for only the simplest of the Fourier expansions (i.e., two terms); more terms could easily be accommodated but with a greater expenditure of computer time in performing the MACSYMA manipulations.

Two gradient method-based algorithms have been used to minimize the energy functional. Both are designed to minimize quite general nonlinear unconstrained multivariate functions. At present  $V$ , the total potential energy functional, is the objective function for which a global minimum is sought for given moment and pressure. The minimum is found by systematically adjusting  $\epsilon$  and the coefficients  $A_n$  until  $V$  is minimized. The user must supply explicit expressions for  $V$  and its first partial derivatives with respect to  $\epsilon, A_1, \dots, A_n$ . Also, reasonable starting values must be supplied for these parameters from which the algorithms begin with iterative search for the minimum of  $V$ . Both algorithms are conveniently contained within the FORTRAN subroutines CONMIN developed by Shanno and Phua [7].

The first algorithm incorporates a variable metric technique, i.e., initially it resembles the Steepest

Descent Method in performance while resembling the Newton-Raphson method as the minimum is approached [8]. The second algorithm is based on the conjugate gradient method. In this case, the procedure is to seek the minimum by successive linear searches along mutually conjugate directions. Of course a major task then becomes the generation of sets of such directions. The particular implementation used here is one due to Shanno [9]. As is shown in [6], both algorithms were first "put through their paces" by testing them against suitably difficult functions; both were found to be satisfactory. FORTRAN routines were then written, built around MACSYMA-generated FORTRAN coding for the energy expression, and coupled with the CONMIN subroutine to compute moment-curvature results similar to the previous "exact solution" procedure.

Moment-curvature plots, similar to Figures 13 and 14, were computed for the same shell geometry but for an internal pressure of 3000 psi by use of both algorithms. Results for the conjugate gradient and variable metric methods are shown in Figures 15 and 16, respectively. The upper line in both figures was generated from the exact solution for  $M(\epsilon)$  discussed earlier while the triangles represent the discrete points where the algorithms supplied approximate values. Both algorithms gave excellent agreement with the exact solution, typically to three or four digits' accuracy on moment values. Further calculations of this kind are given in [6]. It is expected that the excellent performance obtained for the simple two-term expansion carries over to the higher expansions as well. In general, in both the test problems and in the moment-curvature calculations, the conjugate gradient method required more function evaluations (of  $V$  and its partial derivatives), that is, more computer time, than the variable metric method to converge to a solution.

#### CONCLUSIONS, RECOMMENDATIONS FOR FUTURE WORK

A new methodology has been developed for the solution of geometrically nonlinear shell problems and is illustrated by application to the specific case of a large deformation analysis of a thin elastic circular cylindrical shell subjected to pure bending and pressurization. We have shown that a symbolic manipulation language, such as MACSYMA, is a powerful analytical tool. The massive algebraic

work attendant with nonlinear shell work is greatly expedited with the aid of such tools. It is demonstrated that two optimization algorithms (one conjugate gradient, one variable metric) originally designed for minimization of nonlinear unconstrained multivariate functions can be used to compute extremely accurate results where MACSYMA-generated explicit solutions may be impractical. The function minimized in this case is the total potential energy of the shell and external loads.

Several assumptions and limitations are inherent in the shell analysis considered here. The main assumptions are that: (1) The possibility for bifurcation (buckling) from the nonlinear deformation states leading up to the limit moment is omitted; (2) Initial imperfections, or deviations from the true circular form, are not considered; (3) The shell is infinitely long and thus all cross sections deform the same way (also the influence of end boundary conditions are neglected; and (4) The additional displacements  $w_1$ ,  $w_2$  are assumed to be inextensible. These effects can all be considered by reformulating the analysis from the start. It was felt that the complexity associated with analyzing these effects would unnecessarily obscure the purpose here which is to illustrate clearly a new methodology. Of these assumptions, perhaps the most important to relax in extending the work, is the assumption concerning bifurcation. Other investigators have pointed out that bifurcation into a pattern of axial wrinkles on the compression side of the shell occurs just before the limit moment. In real shells, this wrinkling behavior is greatly affected by the presence of imperfections. Also, material nonlinearity (plasticity) may become important as the wrinkles increase in amplitude.

There are several avenues for further research. Clearly, the entire subject of shell buckling analysis can benefit from the introduction of tools such as MACSYMA--this applies to finite element-type work as well. An interesting alternative to starting with the displacement-based energy approach of Brazier and Wood is to begin with strains as discussed by Reissner. This would allow the use of series of polynomial functions such as Legendre or Chebyshev polynomials. In fact, Chebyshev polynomials appear very attractive for this application as they are known to possess certain optimal properties.

The analysis can also be extended to include stretching of the shell middle surface, influence of the axial dimension (i.e., three dimensional analysis), the presence of stiffeners, or plasticity effects. Again, the strain energy functional may turn out to be very nonlinear, including non-smooth behavior if plasticity rules are invoked; but practical solutions may be computed by treating the problem as one in constrained minimization or if need be, an equivalent succession of unconstrained problems.

#### REFERENCES

1. Bannister, K. A., "Whipping Analysis Techniques for Ships and Submarines," The Shock and Vibration Bulletin, Bulletin 50, Part 3 (September, 1980): 83-98.
2. Brazier, L. G., "On the Flexure of Thin Cylindrical Shells and Other Sections," Proceedings of the Royal Society of London, Series A CVXI (1927): 104-14.
3. Brush, D. O., and Almroth, B. O., Buckling of Bars, Plates, and Shells, New York: McGraw-Hill, 1975.
4. Wood, J. D. "The Flexure of a Uniformly Pressurized, Circular, Cylindrical Shell," Journal of Applied Mechanics 25 (1958): 453-58.
5. Sokolnikoff, I. S., Mathematical Theory of Elasticity, New York: McGraw-Hill Book Company, 1956.
6. Bannister, K. A. "Large Deformation Analysis of a Cylindrical Shell Under Pure Bending and Pressurization," Ph.D Dissertation, The Pennsylvania State University, 1983.
7. Shanno, D. F., and Phua, K. H. "Remark on Algorithm 500: Minimization of Unconstrained Multivariate Functions," Association for Computing Machinery Transactions on Mathematical Software 6, No. 4 (December 1980): 618-22.
8. Shanno, D. F., and Phua, K. H., "Matrix Conditioning and Nonlinear Optimization," Mathematical Programming 14 (1978): 149-60.

9. Shanno, D. F., "Conjugate Gradient Methods with Inexact Searches," Mathematics of Operations Research 3 (1978): 244-56.

10. Mathlab Group, MACSYMA Reference Manual Version 10, Massachusetts Institute of Technology, Laboratory for Computer Science, Cambridge, Massachusetts, 1982.

DISCUSSION

Voice: The triangle seems to stop at the end of the curve.

Mr. Bannister: It turns out that the last point I showed is very close to peak. In fact I had hoped to find the actual peak value, but unfortunately, time ran out at that point, and I was not able to do that. But I think it could be easily done by bracketing and going beyond the peak and then going back and forth. This is something that I hope to do later.

Voice: The depth of your explosive charge was 30 meters. What happens to the radiation damping if the depth of the charge goes down to the depth of the bubble? How does that affect the hull whipping?

Mr. Bannister: You mean if the depth of the bubble is very large?

Voice: No. Suppose the same explosive charge was deeper, say 500 meters or 1000 meters. How does that affect your whipping analysis?

Mr. Bannister: I showed some results like that in an earlier paper, the 50th Shock and Vibration Bulletin, but at a shallower depth. The bubble frequency goes way up. I would say it is very fast and very high frequency, particularly at 1,000 meters,

Voice: How does the bubble load the target?

Mr. Bannister: There are two effects. There is the radial oscillation that the bubble contributes to, and there is also the upward migration. At great depth migration is minimal. So all you have is the very high frequency oscillation. Also, because the whipping response of the target usually involves as low as four or five modes of vibration, there is a problem with the tuning between these modes and the high frequency bubble motion. Therefore, you get very low whipping amplitudes.

Voice: Hull whipping occurs at the lower end of the spectrum.

Mr. Bannister: That is correct.

Voice: Would the whipping damage the target?

Mr. Bannister: When you get to a situation where you have high frequency bubble loading, then the problem comes in predicting motion because you have to have higher and higher modes in the whipping model. After about the tenth mode you will have trouble with this particular model that I used, which was a simple lumped mass elastic beam model.

Voice: As you go deeper, you might have the effects of radiation damping. Did you analyze for the effects of the greater depths?

Mr. Bannister: No, I did not consider those depths.

APPENDIX A

APPLICATION OF MACSYMA TO ROOT-FINDING

Brazier's analysis [2] leads to an Euler equation for the circumferential displacement component  $v$  in the following form

$$\frac{d^6 v}{d\phi^6} + 2 \frac{d^4 v}{d\phi^4} + \frac{d^2 v}{d\phi^2} \quad (A-1)$$

$$= - \frac{18a^5}{\rho^2 t^2} \sin 2\phi$$

The solution to Equation (A-1) can easily be obtained by the theory of ordinary differential equations, but it is instructive to employ MACSYMA in obtaining the homogeneous solution. Although MACSYMA can solve ODE's by the Laplace Transform method, it turns out that sixth-order differential equations exceed the present capability. However, by inspection we can write down the characteristic equation for (A-1) as

$$R^6 + 2R^4 + R^2 = 0 \quad (A-2)$$

which obviously has the repeated roots

$$R = 0 \quad (A-3)$$

$$R = \pm \sqrt{-1}.$$

MACSYMA can be used to obtain the same roots. The input commands and replies to these commands are shown next,

This is a MACSYMA 303

FIX303 1 DSK MACSYM being loaded  
Loading done

(C1) EQU:R\*\*6+2\*R\*\*4+R\*\*2;

(D1) R^6 + 2R^4 + R^2

(C2) SOLVE(EQU,R);

SOLVE FASL DSK MACSYM being loaded  
Loading done

(D2) [R = - 1I, R = 1I, R = 0]

After a preliminary message, the righthand side of the characteristic equation is input to MACSYMA on the line (C1) and is stored in the variable named EQU. After this point, any reference to EQU is equivalent to referencing the polynomial expression in R. In line (D1), MACSYMA merely "plays back" or displays the contents of EQU in standard algebraic format. On line (C2), MACSYMA is instructed to solve for the roots of the R-expression; it is assumed EQU = 0 in this case. After printing a brief message concerning loading of files to perform the root search, the roots are computed and then are displayed on line (D2). Note that MACSYMA uses the convention

$$1I = \sqrt{-1} = i. \quad (A-4)$$

Having found the roots, the homogeneous solution can be written

$$v(\phi) = (B_1 + B_2\phi) + (B_3 + B_4\phi)\cos\phi + (B_5 + B_6\phi)\sin\phi. \quad (A-5)$$

APPENDIX B

LISTING OF MACSYMA CODE USED TO GENERATE NONLINEAR SOLUTION  
FOR THREE-TERM FOURIER EXPANSION

```

N:3$
MATCHDECLARE(ZZ,TRUE)$
DEFRULE(R1,SIN(ZZ),0)$
DEFRULE(R2,COS(ZZ),0)$
EBOTH(XX,YY):=BLOCK([RESULT],
RESULT:TRIGREDUCE(EXPAND(XX),YY),
RESULT:APPLY1(RESULT,R1,R2),
RETURN(RESULT))$
ARRAY(AA,10)$
V:V0+V1$
W:W0+W1+WBAR$
D:(A-W)*COS(PHI)-V*SIN(PHI)$
DD:D*D$
V0:V0*SIN(PHI)$
W0:W0*COS(PHI)$
WBAR:WBAR$
V1:0$
W1:0$
V1:V1+SUM(AA[I]*SIN(I*PHI),I,2,N)$
W1:W1+SUM(I*AA[I]*COS(I*PHI),I,2,N)$
V:EV(V)$
W:EV(W)$
D:EV(D)$
DD:EBOTH(EV(DD),PHI)$
CHI:(DIFF(W,PHI,2)+DIFF(V,PHI))/(A*A)$
U1:DC*EBOTH(CHI*CHI,PHI)*A$
ST:E*D*EPS/A$
SP:0$
STB:E*AL/2$
SPB:E*AL$
ET:D*EPS/A$
EP:-NU*D*EPS/A$
FTB:AL*(1-2*NU)/2$
EPB:AL*(2-NU)/2$
U2I:DD*E*EPS**2/A**2*A*T$
U3I:0$
U4I:SPB*EPB*A*T$
U5I:STB*ETB*A*T$
U6I:EBOTH(STB*ET*A*T,PHI)$
U7I:A*T*EBOTH(SPB*EP,PHI)$
UI:(U1+U2I+U3I+U4I+U5I)/2+U6I+U7I$
U:2*PI-UI$
TT:((AL*E*T/A)*PI/2)*((A*NU*EPS)**2-SUM((I**4-I**2)*AA[I]**2,
I,2,N))$
WW:M*EPS/A$
VV:U-TT-WW$
STORE([KBAN,ENERGY,DSK,USERS4],VV,U1,U2I,
U3I,U4I,U5I,U6I,U7I,TT,WW,V,W,ST,SP,STB,
SPB,ET,EP,ETB,EPB,N)$

```

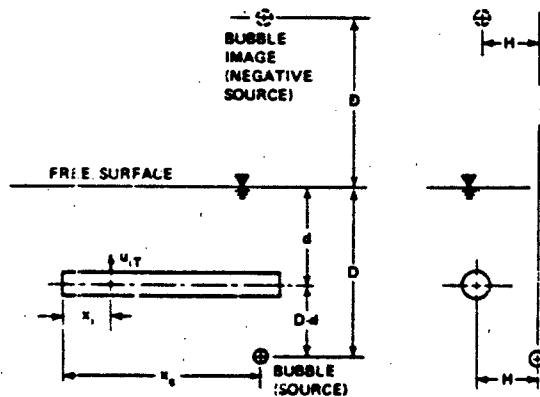


Figure 1. Floating Uniform Elastic Beam Subjected to 100 Kg TNT Explosion Bubble Loading (charge at 30.48 m depth)

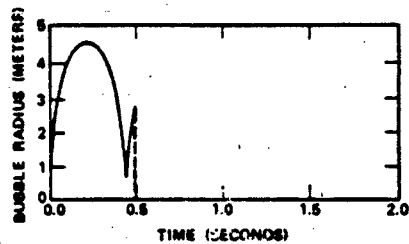


Figure 2. Bubble Radius vs. Time

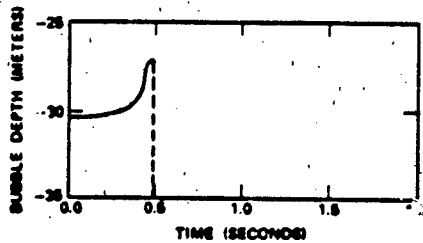


Figure 3. Bubble Center Depth vs. Time

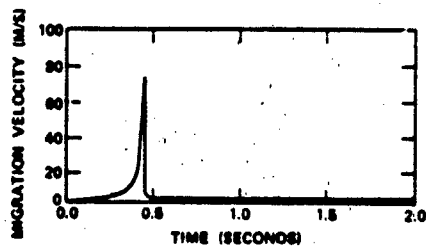


Figure 4. Bubble Migration Velocity vs. Time

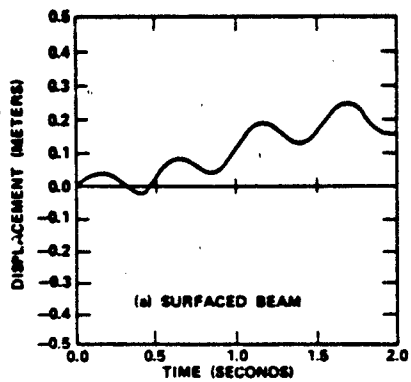


Figure 5. Beam Whipping Response: Vertical C.G. Displacement vs. Time

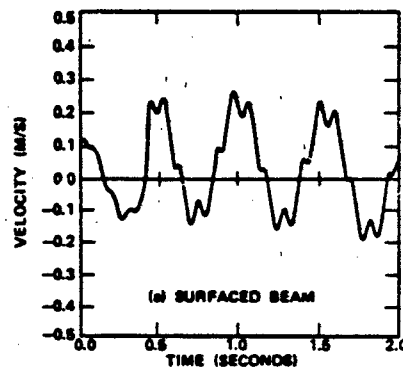


Figure 6. Vertical C.G. Velocity vs. Time

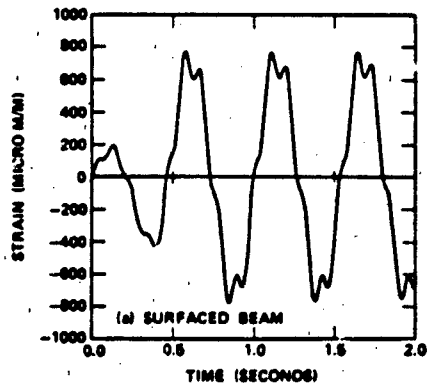


Figure 7. Bending Moment vs. Time

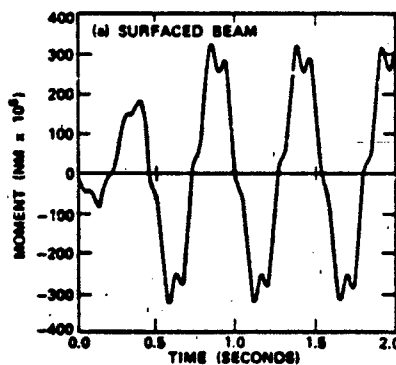
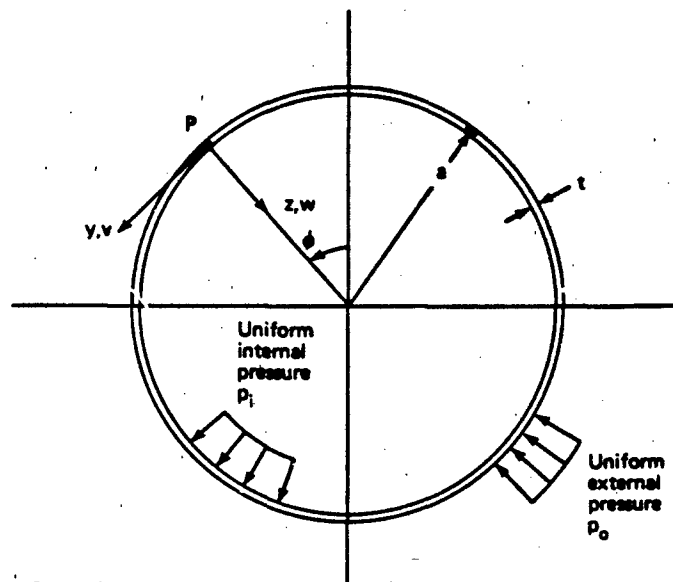


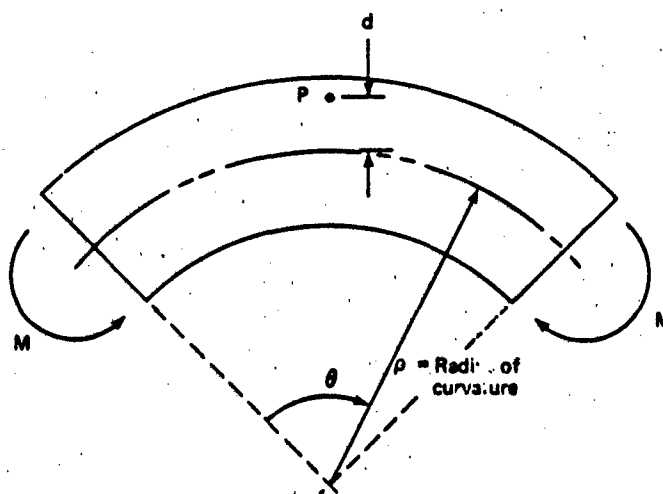
Figure 8. Bending Strain vs. Time



$y, z$  = Circumferential and normal coordinates

$v, w$  =  $y$  and  $z$ -direction displacement components at the point  $P$  of the shell middle surface

Figure 9. Definition of Cross Section Parameters and Coordinates for Circular Cylindrical Shell



$d$  = Distance from neutral axis to point  $P$  of shell middle surface

Figure 10. Cylindrical Shell in Pure Bending

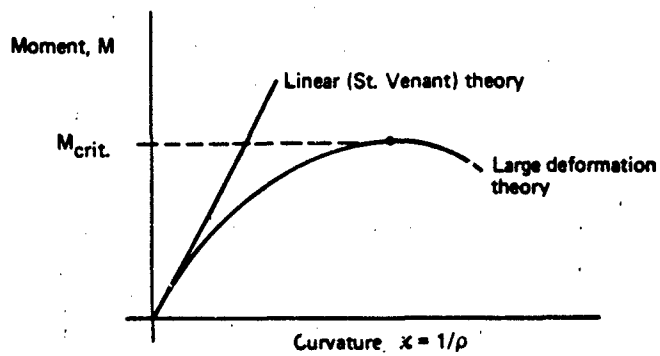


Figure 11. Moment-Curvature Behavior as Predicted by Linear (St. Venant) Theory and Large Deformation (Brazier-type) Theory

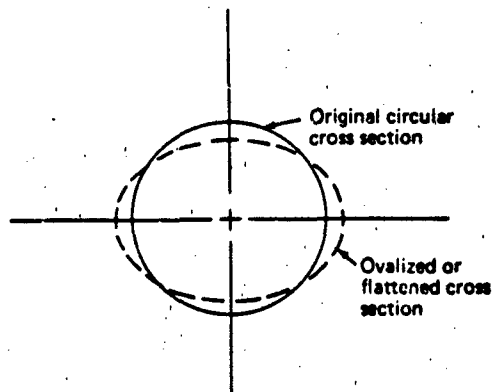


Figure 12. Brazier's Ovalization Mode for the Circular Cylindrical Shell in Pure Bending

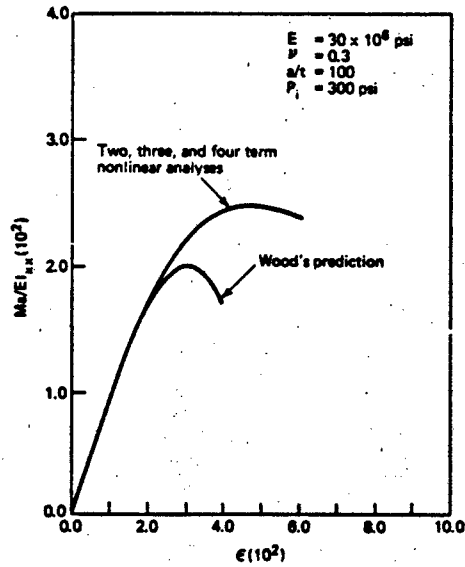


Figure 13. Comparison of Nondimensional Moment-Curvature Predictions (Thin shell, moderate internal pressure)

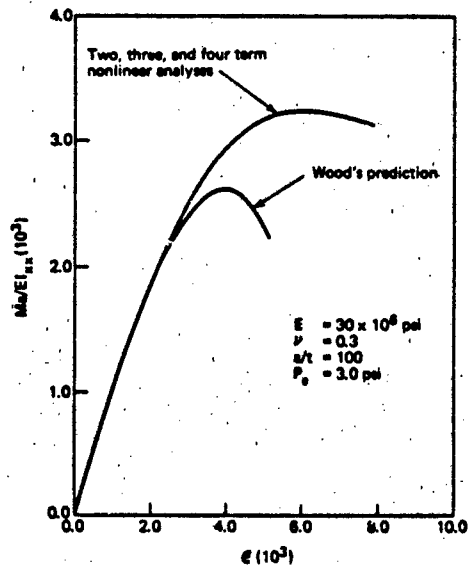


Figure 14. Comparison of Nondimensional Moment-Curvature Predictions (Thin shell, moderate external pressure)

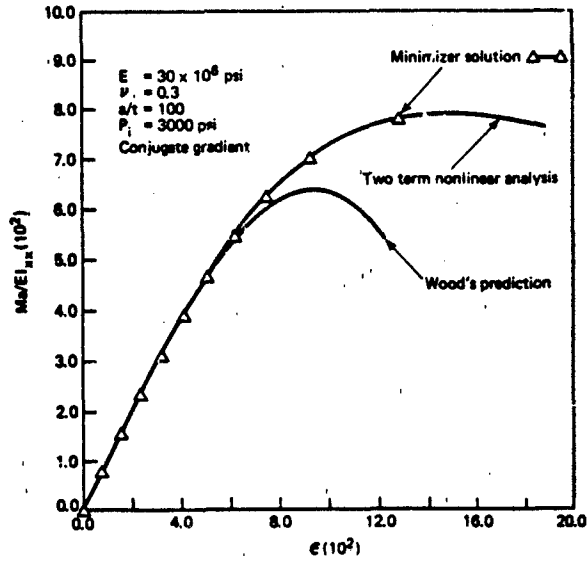


Figure 15. Comparison of Conjugate Gradient, Exact, and Wood's Prediction for 3000 psi Internal Pressure

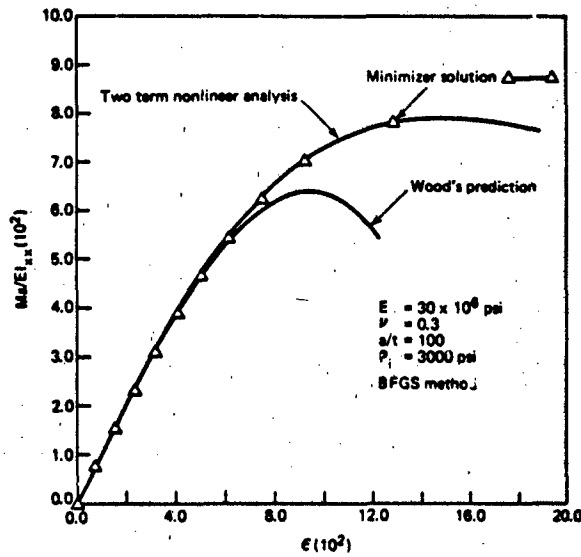


Figure 16. Comparison of Variable Metric (BFGS Algorithm), Exact, and Wood's Prediction for 3000 psi Internal Pressure

## SHOCK

### WATER IMPACT LABORATORY AND FLIGHT TEST RESULTS FOR THE SPACE SHUTTLE SOLID ROCKET BOOSTER AFT SKIRT

D. A. Kross  
NASA/Marshall Space Flight Center  
Marshall Space Flight Center, Alabama

N. C. Murphy  
United Space Boosters, Inc.  
Huntsville, Alabama

E. A. Rawls  
Chrysler Corporation  
New Orleans, Louisiana

A series of water impact tests has been conducted using full-scale segment representations of the Space Shuttle Solid Rocket Booster (SRB) aft skirt structure. The baseline reinforced structural design was tested as well as various alternative design concepts. A major portion of the test program consisted of evaluating foam as a load attenuation material. Applied pressures and response strains were measured for impact velocities from 40 feet per second (ft/s) to 110 ft/s. The structural configurations, test articles, test results, and flight results are described.

#### INTRODUCTION

A significant cost saving feature of the Space Shuttle launch vehicle is the recovery, retrieval, refurbishment, and subsequent reuse of its two SRB's. To date, SRB hardware value at over 450 million dollars has been successfully retrieved. This demonstrates that the overall SRB recovery approach of first decelerating the booster by deployment of parachutes and then entering the ocean in a tail-first attitude is sound. The majority of the primary structural elements of the boosters have sustained only minor damage due to water impact. In the case of the SRB aft skirt, however, major structural damage has been experienced. Specifically, the aft skirt internal stiffener rings have been cracked and, on occasion, have had portions completely blown off due to the tremendous water impact pressures.

Subsequent to the first Shuttle launch, efforts were initiated to design, fabricate, and install structural reinforcements to the SRB aft skirt internal stiffener rings. Due to manufacturing schedule and installation accessibility constraints, these reinforcements were added in varying degrees

with the sixth flight set of boosters being the first with a complete complement of reinforcements. These boosters contain about 1,000 lb of aft skirt ring reinforcements. As structural modifications were being developed, a parallel effort was started with the objectives of quantifying the effect of these design improvements and identifying alternative, more cost effective means of solving the aft skirt water impact damage problem. The primary results obtained from the test program portion of this evaluation effort will be discussed herein.

#### STRUCTURAL CONFIGURATION

The general SRB configuration at water impact is illustrated in Figure 1. Each booster weighs approximately 166K lb when it impacts the water tail-first at a nominal vertical velocity of 88 ft/s. The aft skirt of each SRB contains three internal stiffener rings as shown in Figure 2. Detail dimensions are given in Figure 3 for the three baseline design rings as well as a new proposed candidate mid-ring design. The aft skirt is constructed of 2219-T87 aluminum with a skin thickness varying from 0.42 to

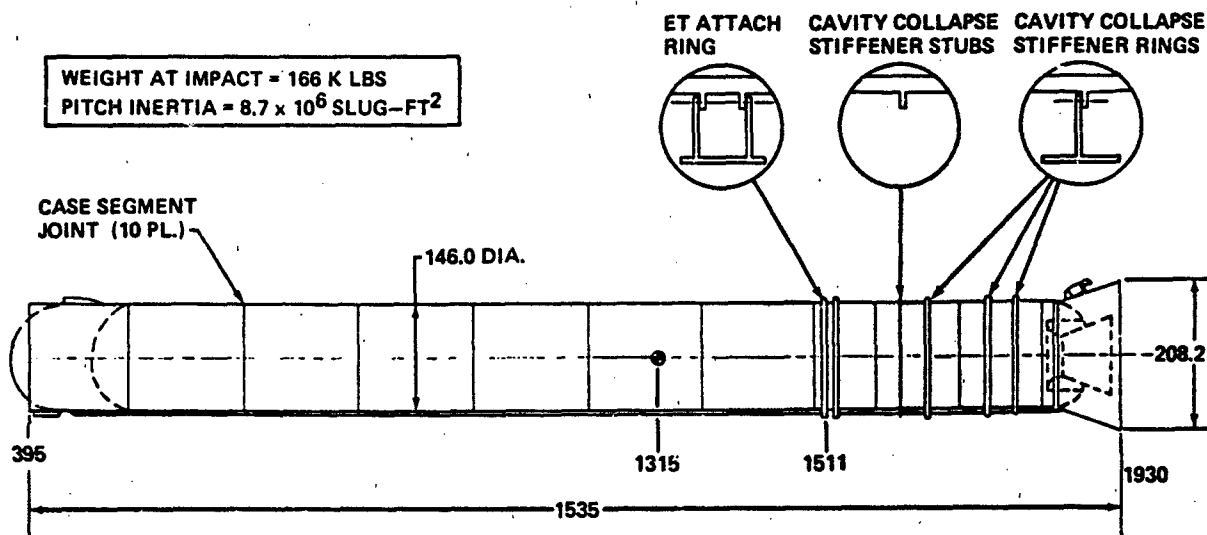
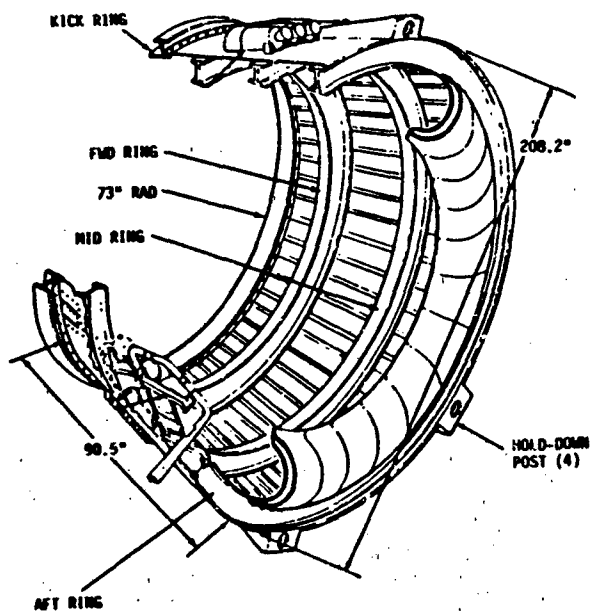


FIGURE 1

SRB WATER IMPACT CONFIGURATION



SRB AFT SKIRT GEOMETRY  
FIGURE 2

to 0.50 inch and contains integrally milled internal stiffeners located every 5° circumferentially. The original first flight boosters had gussets located between the rings and aft skirt stiffeners located at every third stiffener (15°). Subsequently, for strength improvement purposes, additional gussets were added

at each stiffener which had no previous gusset. In addition, clips were added between the ring web and ring flanges.

FULL SCALE AFT SKIRT SEGMENT TEST PROGRAM

As part of the aft skirt structural modification evaluation, a series of water impact tests was conducted using full-scale SRB aft skirt segment test articles. The primary objectives of these tests were as follows:

- o Obtain applied pressures and associated structural dynamic strain response data at full-scale water impact conditions.
- o Evaluate effects of foam and foam contour shape on the dynamic response.
- o Assess effects of removing selected structural ring reinforcements such as clips and gussets.
- o Study a proposed mid-ring alternative design.
- o Test the aft ring segment to failure.

Two test articles were used in this test program. The first simulated a segment of the aft skirt mid-ring structure, whereas the second test article represented a full-scale segment of the aft ring structure. Both test articles were constructed of 2219-T87 aluminum

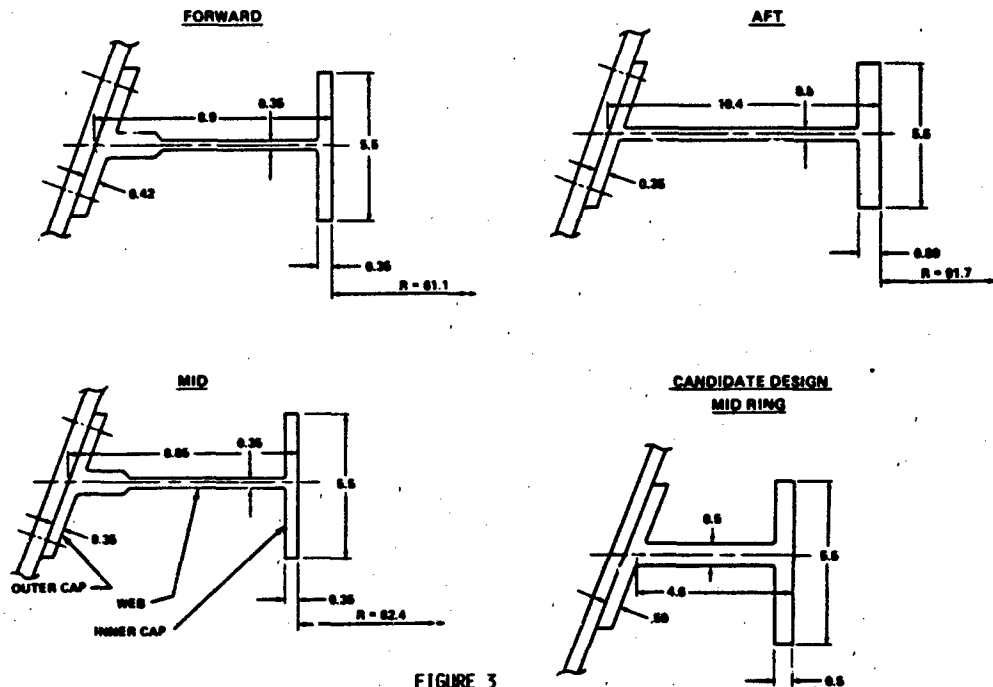


FIGURE 3  
SRB AFT SKIRT RINGS

material and included flight-type mechanical fasteners between the ring, clips, gussets, and skin structure. The mid-ring test specimen, shown in Figure 4, consisted of a wedge-shaped structure which represented a 15° arc segment of the aft skirt, but without curvature. Located approximately half-way up on one side of the edge was a full-scale aft skirt mid-ring segment configured with structural reinforcements similar to the current baseline SRB design. The other side of the wedge contained an alternative candidate design for the mid-ring. The skin panels were flight design configured to include the integrally milled stiffeners above and below the mid-ring. The test article weighed approximately 725 lb. The aft ring test article represented a 30° arc segment of the aft ring/skirt skin/stiffener configuration, but, again without curvature. As shown in Figure 5, the aft ring segment included both the original gussets, which were present on every third stringer on the first flight boosters, and the smaller gussets, which were added for additional support at every vacant stringer location. The aft ring test article weighed 435 lb.

Instrumentation consisted of pressure, strain, and accelerometer measurements. The mid-ring test specimen had 12 pressure transducers, 3 accelerometers, 57 uniaxial strain gauges, and 28 rosette strain gauges installed for a total of 153 channels of data. The aft ring test article contained 12 pressure transducers, 3 accelerometers, 27 uniaxial strain gauges, and 31 rosette strain gauges for a total of 135 data measurements. On each individual test, however, only 130 channels of data, in addition to time code, were recorded.

The SRB aft skirt segment water impact test program was conducted at the Hydroballistic Facility of the Naval Surface Weapons Center located in White Oak, Maryland. An air gun launch system was used to accelerate the test article to the desired initial impact velocities which ranged from 40 to 110 ft/s. Instrumentation, trailing wires and arresting cables were attached between the test article and the tank structure. A total of 20 mid-ring and 25 aft ring tests were performed.

FIGURE 4 MID RING TEST ARTICLE CONFIGURATION

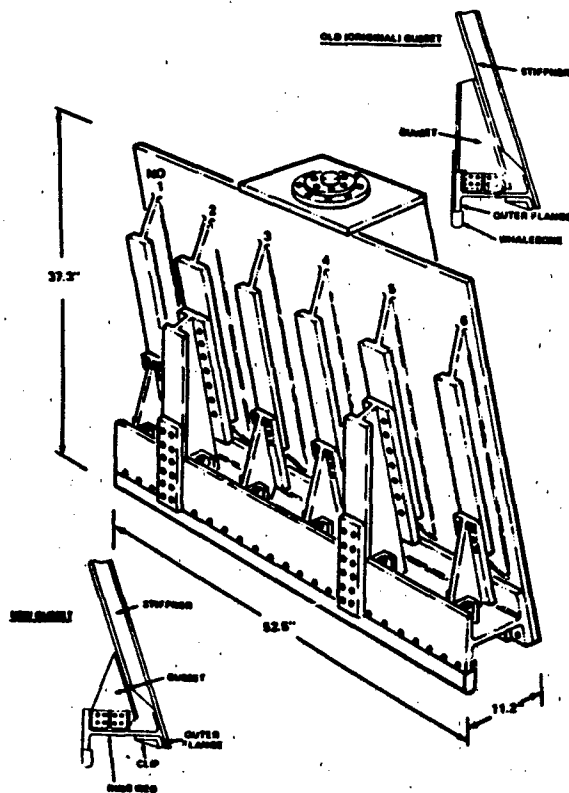
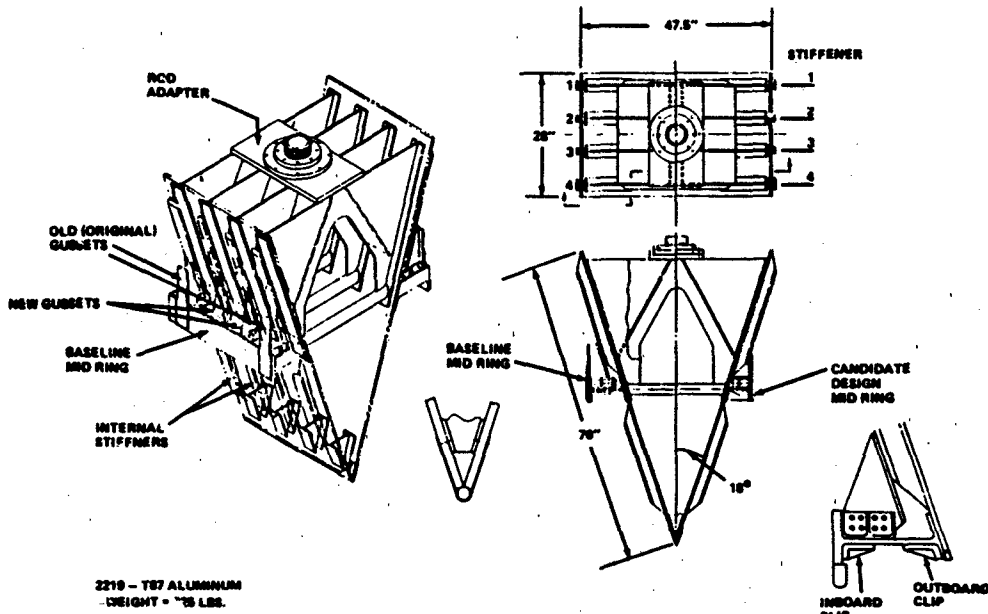


FIGURE 5. AFT RING TEST ARTICLE CONFIGURATION

MID-RING TEST RESULTS

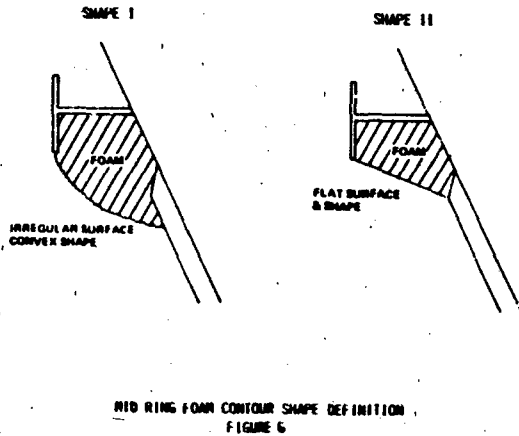
The mid-ring segment test condition, summarized in Table 1, included variations in impact velocity, impact angle, foam shape, and structural configuration. The impact angle coordinate system is defined such that a negative angle corresponds to tilting the wedge side with the baseline design ring segment down toward the water. Foam contour shapes that were tested are shown in Figure 6. The foam used was a 2.7 lb/ft<sup>3</sup> density sprayable Instafoam. Two types of structural modifications were tested in addition to the fully reinforced configuration. The first consisted of removing the inboard and outboard clips near stiffener 2 and 3 on the baseline design ring and removing the gussets at stiffener 2 and 3 on the new design ring. The second structural modification included those made on the first plus the removal of gussets at stiffener 2 and 3 on the baseline design ring.

The effects of initial entry angle on pressures are shown in Figure 7 for both the baseline design ring and new design ring. Maximum pressures were measured on the ring inner flange followed by the ring web, ring outer flange, and, finally, the skirt skin which had the lowest pressure values, as expected.

TABLE 1  
MID RING SEGMENT TEST MATRIX

RUN NO.	V (FPS)	θ (DEG)	FOAM SHAPE	TEST ARTICLE STRUCTURAL CONFIGURATION															
				BASELINE RING DESIGN												NEW RING DESIGN			
				INBOARD CLIPS				OUTBOARD CLIPS				GUSSETS				GUSSETS			
				1	2	3	4	1	2	3	4	1	2	3	4	1	2	3	4
10	22.5	0	NO	ON				ON				ON				ON			
11	40.9	0	NO	ON				ON				ON				ON			
12	41.0	0	NO	ON				ON				ON				ON			
13	60.1	0	NO	ON				ON				ON				ON			
14	59.7	0	II	ON				ON				ON				ON			
16	81.1	0	II	ON				ON				ON				ON			
17	60.0	-8	NO	ON				ON				ON				ON			
18	60.1	0	II	ON				ON				ON				ON			
19	58.7	+8	NO	ON				ON				ON				ON			
24	68.8	-8	I/NO	ON				ON				ON				ON			
27	63.0	-8	II	ON				ON				ON				ON			
28	70.9	-8	NO	ON				ON				ON				ON			
29	60.4	-8	II	ON				ON				ON				ON			
30	60.4	+8	NO	ON				ON				ON				ON			
33	60.1	-8	II	ON				ON				ON				ON			
36	60.8	-8	II	ON	OFF	OFF	ON	ON	OFF	OFF	ON	ON	OFF	OFF	ON	ON	OFF	OFF	ON
37	60.9	-8	I	ON	OFF	OFF	ON	ON	OFF	OFF	ON	ON	OFF	OFF	ON	ON	OFF	OFF	ON
38	66.3	-8	I	ON	OFF	OFF	ON	ON	OFF	OFF	ON	ON	OFF	OFF	ON	ON	OFF	OFF	ON
40	92.4	0	I	ON	OFF	OFF	ON	ON	OFF	OFF	ON	ON	OFF	OFF	ON	ON	OFF	OFF	ON
46	69.9	-8	I/NO	ON	OFF	OFF	ON	ON	OFF	OFF	ON	ON	OFF	OFF	ON	ON	OFF	OFF	ON

FIGURE 7  
MID RING MODEL PRESSURES  
ENTRY ANGLE COMPARISON



As the skirt skin becomes less vertical, on a given ring side, the associated ring and skin pressures increase. For example, the web pressure experienced by the baseline design ring increases from about 200 psi to nearly 500 psi as the impact angle is varied from +8 to -8 degrees. With the addition of foam, this angular effect is also present as shown in Figure 8. This figure also illustrates the significant reduction in pressure with the addition of foam. Shape I foam is seen to be superior to Shape II in that pressures are lower for the latter case. Figure 9 presents the

VELOCITY: 80 FT/SEC NO FOAM

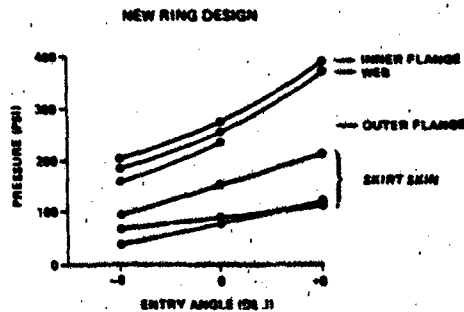
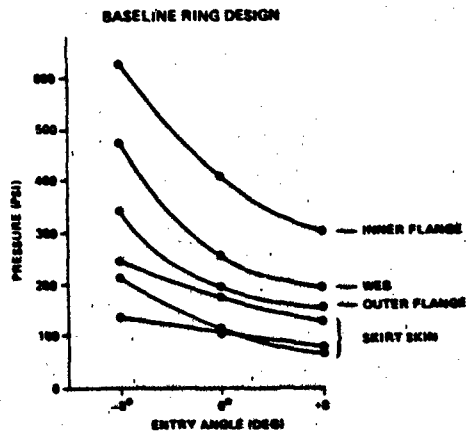


FIGURE 8  
MID RING MODEL PRESSURES  
FOAM/NO FOAM COMPARISON  
BASELINE RING DESIGN  
ANGLE: -4 DEG.

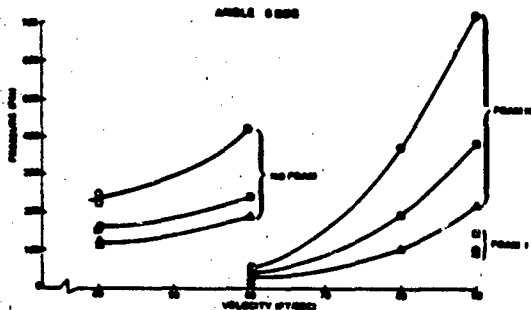
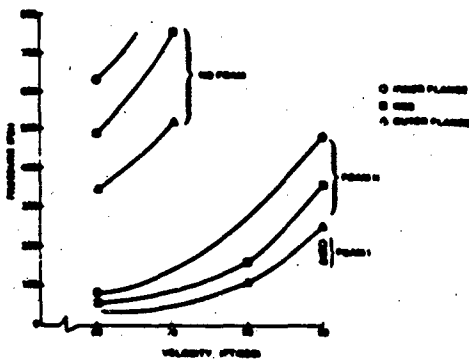
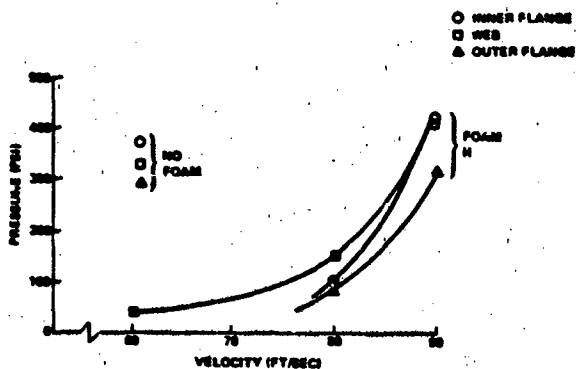


FIGURE 9  
MID RING MODEL PRESSURES  
FOAM/NO FOAM COMPARISON

NEW RING DESIGN  
ENTRY ANGLE: 0 DEG.



effect of foam on measured pressures for the new design ring. It should also be noted that, in general, the pressures experienced by the new design ring are lower on the inner flange area than for the baseline design ring at comparable initial conditions.

Relative maximum normal stress levels are plotted as a function of initial impact velocity in Figure 10. The addition of foam is seen to significantly reduce the peak stresses and foam contour Shape I is superior to Shape II in reducing stresses. Figure 11 illustrates the relative stress distribution through the ring with and without foam. The ring web experiences the highest stresses, whereas the gusset stresses are lowest for the no foam condition. With the addition of foam, the peak stresses occur in the inner and outer caps of the ring.

The effects of removing selected structural reinforcements from the mid-ring segment test article are presented in Figure 12. These results indicate that removal of four clips increases the stresses from 10 to 30 percent, whereas removing the four clips and two gussets causes an additional increase of 20 to 70 percent. A comparison of stresses between the baseline design and the new design rings without foam is given in Figure 13. In general, the baseline design ring stresses are at least double those experienced by the new design ring.

#### AFT RING TEST RESULTS

The aft ring segment test conditions are summarized in Table 2. In addition to varying foam contour shapes, different combinations of foam and cork were tested as illustrated in Figure 14. The cork had been applied to the flight booster aft ring for thermal protection prior to identifying foam as a load attenuating medium. Therefore, cork was included in the test program to assist in evaluating flight-type configurations. Also, the foam application method was varied between layered and poured. The layered technique consisted of spraying approximately one-inch-thick laminations, whereas the poured method used a single spray application with molds to define the shape.

Peak pressures are shown in Figure 15 as a function of impact velocity for the no foam configuration. Maximum values over 4,000 psi were measured at the higher velocities. A comparison of peak pressures with various foam shapes

**FIGURE 10**  
**FOAM/NO FOAM COMPARISON - BASELINE MID RING**

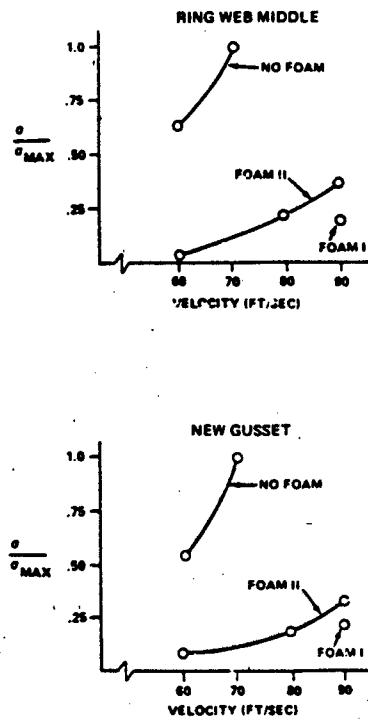


**FIGURE 11**  
**MID RING MODEL**  
**FOAM II VS. NO FOAM**

VELOCITY: 80 FPS ANGLE: -8 DEGREE STRUCTURAL CONFIGURATION: 1

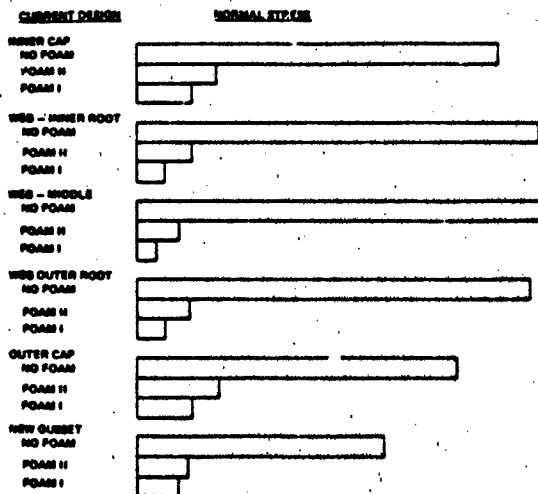


**FIGURE 12**  
**MID RING MODEL - CURRENT DESIGN**  
**STRUCTURAL CONFIGURATION COMPARISON**

1. ALL CLIPS INSTALLED VELOCITY: 80 FPS  
 2. FOUR CLIPS REMOVED ANGLE: -8 DEG.  
 3. FOUR CLIPS, TWO GUSSETS REMOVED FOAM: I

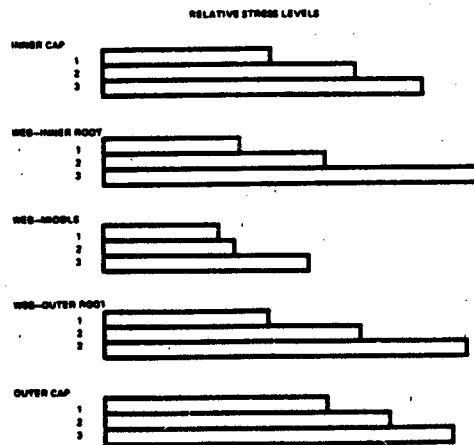


**FIGURE 13**  
**MID RING MODEL**  
**RING DESIGN COMPARISON**

VELOCITY: 80 FT/SEC ANGLE: 8 DEGREE EFFECTIVE  
 A: STRUCTURAL CONFIGURATION 1, NO FOAM, CURRENT DESIGN  
 B: STRUCTURAL CONFIGURATION 1, NO FOAM, NEW DESIGN

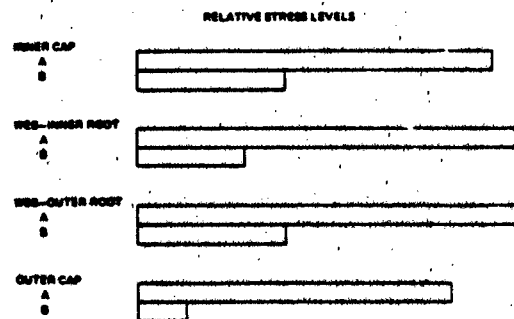


TABLE 2  
AFT RING SEGMENT TEST MATRIX

RUN NO.	V (FPS)	θ (DEG)	FOAM SHAPE	FOAM APPLIC.	STRUCTURAL CONFIGURATION											
					CLIPS							GUSSETS				
					1	2	3	4	5	6	7	1	2	3	4	5
1	37.8	0	NO	---	OFF							ON				
2	57.7	↓	NO	NO	OFF							ON				
3	57.7		V	L												
4	57.0		V	P												
5	66.4		V	P												
7	80.1		V	P												
8	88.4		V	P												
9	90.0		V	L												
15	87.7		VI	L												
20	84.5		VII	L												
21	84.7		VIII	L												
22	38.8		NO	NO												
23	57.6		NO	NO												
25	57.5		IX	L												
26	79.7		IX	L												
31	78.4		IX	L												
32	79.3	IX	P													
34	80.0	IX	L													
36	85.2	IX'	L													
39	88.0	-10	IX	L												
41	86.4	+10	IX	L												
42	80.2	0	NO	NO												
43	89.0	↓	↓	↓												
44	100.7	↓	↓	↓												
45	111.3	0	NO	NO	OFF							ON				

FIGURE 14  
AFT RING FOAM CONTOUR SHAPE DEFINITION

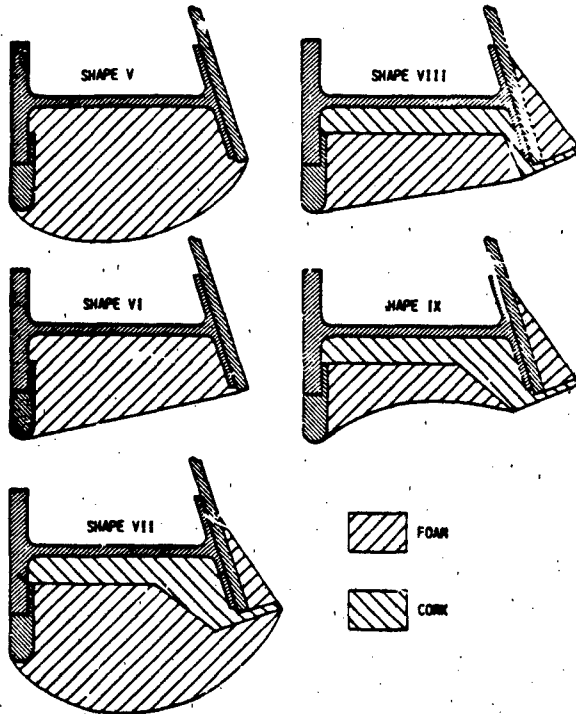
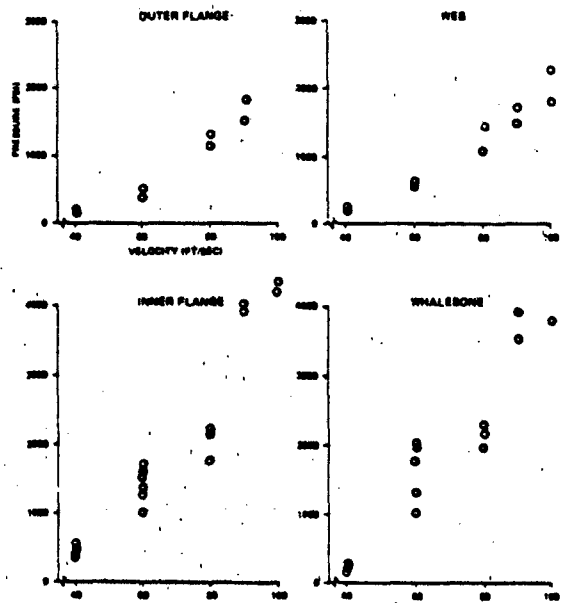
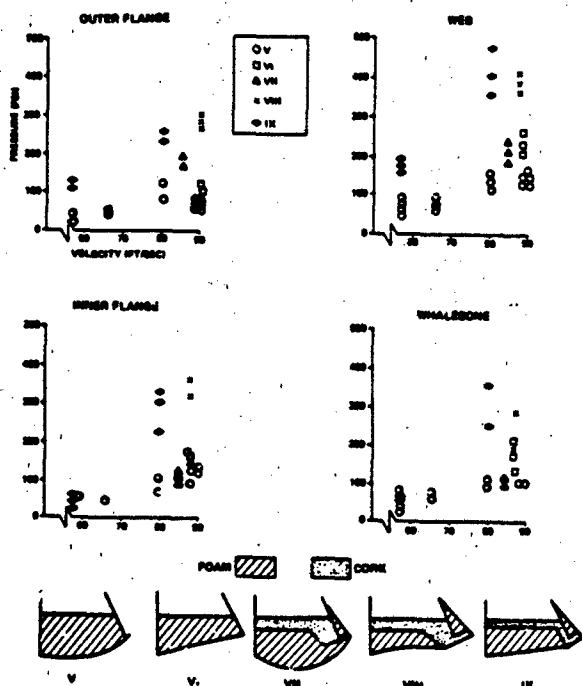


FIGURE 15  
AFT RING PRESSURES  
NO FOAM



is presented in Figure 16. It is seen that a significant reduction in pressures occurs with any of the foam contours tested. As expected, the convex contour Shape V is superior to the other shapes. The present flight configuration closely resembles Shape VII which indicates that the anticipated peak pressure is between 175 to 250 psig on the aft ring web. It is noted that the external contours of Shape V and Shape VII are similar, yet the peak pressures for Shape V are lower. This is most likely due to the presence of the incompressible cork in the Shape VII configuration, which does not act as a load attenuator as the highly compressible foam does.

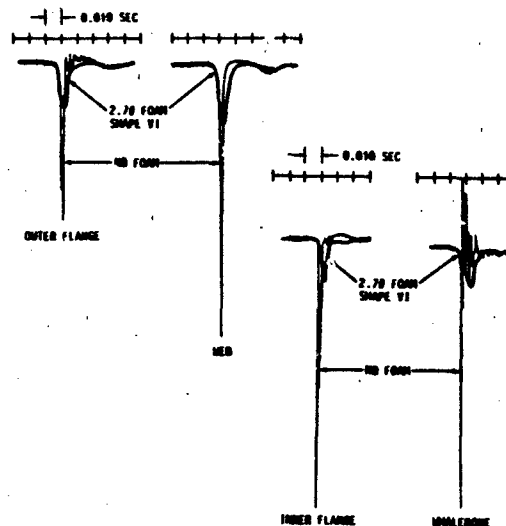
FIGURE 16  
AFT RING MODEL PRESSURES  
FOAM SHAPE COMPARISON



A comparison of pressure time histories with and without foam is shown in Figure 17. The amplitudes are seen to be reduced and the frequency of the applied shock load is lowered with the addition of foam.

Maximum relative normal stresses through the aft ring segment are summarized in Figure 18. The difference between the poured and layered application technique is seen to not cause a significant difference in peak stresses. Foam shape has a strong

FIGURE 17  
FULL SCALE SEGMENT RING PRESSURES

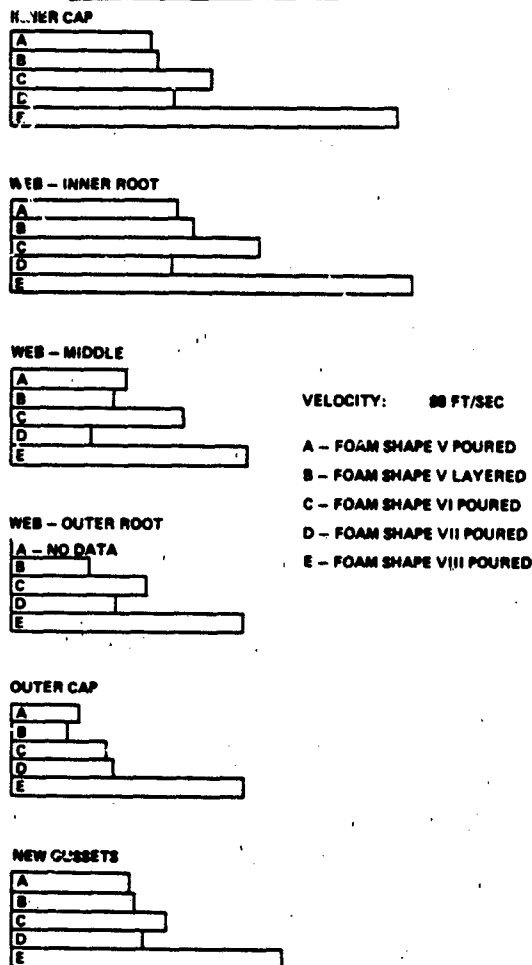


influence on the maximum stresses with Shapes V and VII proving to be the best. Strain time histories measured on a gusset and inner flange are presented in Figure 19. The peak strain amplitudes are seen to be significantly reduced, the response frequency lowered, and the ringout-type response eliminated with the addition of foam.

Relative peak stress levels for various aft ring structural configurations without foam are shown in Figure 20. The removal of some of the clips and gussets tends to reduce the maximum stresses since additional flexibility is being introduced. The area of the aft ring between gussets did experience somewhat higher stresses when the clips and gussets were removed, but this was not nearly as significant as the stress reductions noted in the area of the gussets.

One of the objectives of the air ring segment water impact test program was to increase the impact velocity until a structural failure occurred. This was accomplished at a velocity of 110 ft/s with the primary failure occurring in the outboard flange as illustrated in Figure 21. A similar failure was experienced on the third flight of an SRB during water impact at the same velocity. This higher impact velocity was due to a failed main parachute.

FIGURE 18  
AFT RING TEST MODEL RELATIVE STRESS LEVELS



FLIGHT RESULTS

Foam was added to the SRB aft skirt rings beginning with the seventh flight set of boosters. The foam contour shape was similar to Shape I on the mid-ring and Shape VII on the aft ring. Although some foam was missing from the rings after SRB retrieval, post-flight inspections indicate that the majority of foam was intact just prior to water impact.

Flight instrumentation consisted of two pressure transducers located approximately 130° apart on the aft, mid, and forward rings of each booster. These measurements were present starting with the seventh Space Shuttle launch (STS-7). Figure 22 contains some typical water impact pressure time history data obtained from the flights. Table 3 summarizes the flight results obtained to date. The pressure values

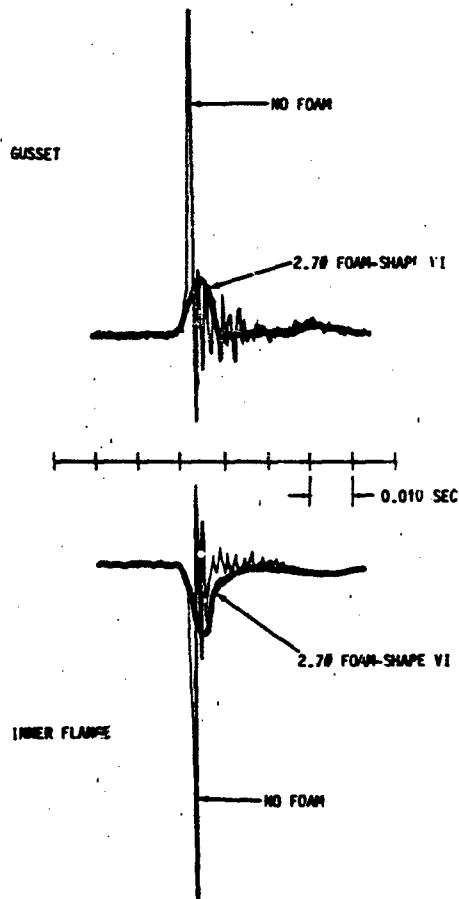


FIGURE 19  
FULL SCALE SEGMENT STRAINS

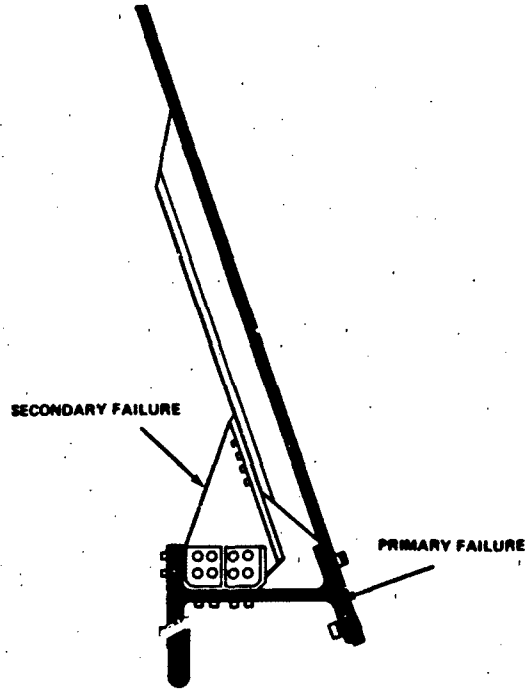
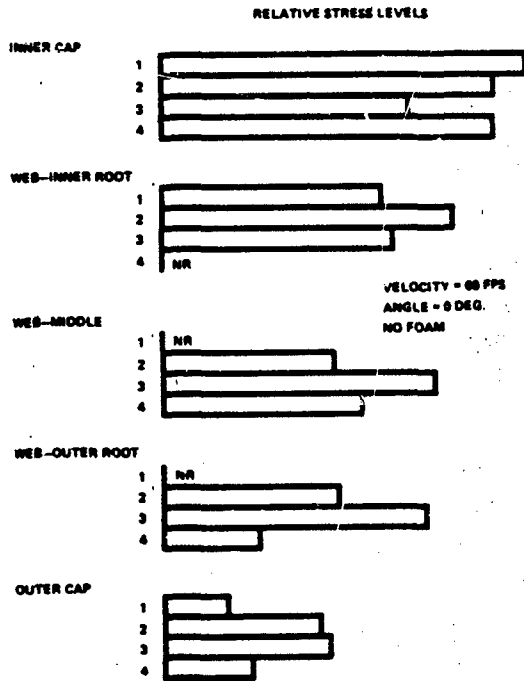
are seen to vary greatly, which is indicative of a highly asymmetric circumferential distribution. Also, the exact amount and shape of foam present at water impact is not accurately known since the major portion of foam is often missing when the boosters are retrieved.

SUMMARY AND CONCLUSIONS

In summary, a total of 45 water impact tests have been conducted on SRB full-scale aft skirt ring segment test articles at impact velocities from 40 to 110 ft/s. Pressure and strain measurements were recorded to evaluate the applied loads and associated dynamic structural response. Significant trends have been identified and are presented herein.

1. ALL CLIPS AND GUSSETS IN
2. ALL CLIPS OUT, ALL GUSSETS IN
3. ALL CLIPS OUT, GUSSETS 3 AND 4 OUT
4. CLIPS 3 AND 6 OUT, ALL GUSSETS IN

FIGURE 21. AFT RING FAILURE MODE



AFT RING TEST ARTICLE  
STRUCTURAL CONFIGURATION COMPARISON

FIGURE 20

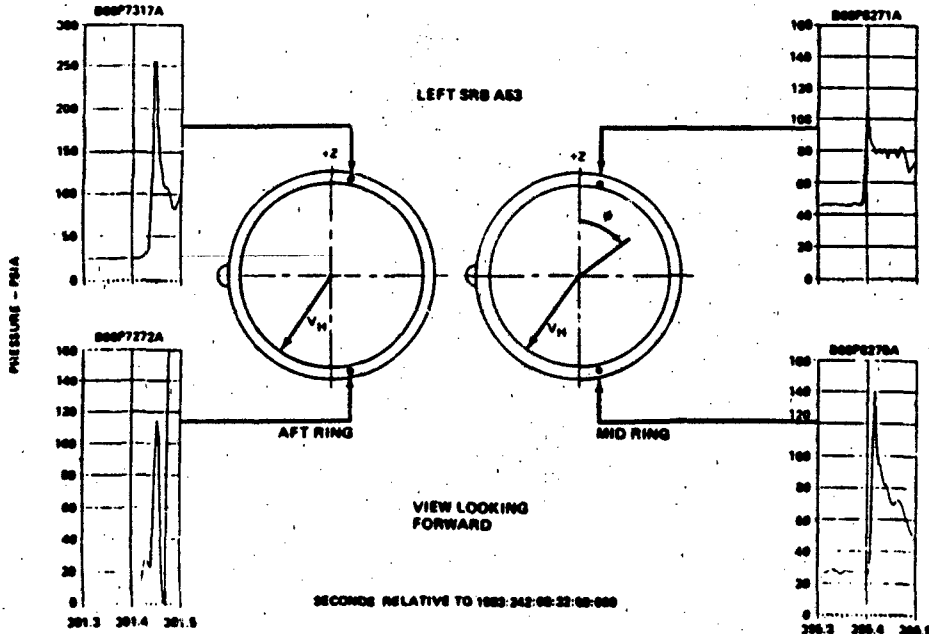


FIGURE 22  
AFT AND MID RING  
FLIGHT PRESSURES

TABLE 3  
 S.S.J AFT SKIRT PRESSURES (PSIG)  
 FLIGHT EXPERIENCE

AFT SKIRT RING	AXIS	FLIGHT AND BOOSTER						
		STS-7		STS-8		STS-9	STS-11	
		LEFT	RIGHT	LEFT	RIGHT	LEFT	LEFT	RIGHT
FWD	~ +Z	300	506	140	570	166	529	262
FWD	~ -Z	286	250	240	290	270	-	219
MID	~ +Z	270	475	506	125	600	-	386
MID	~ -Z	275	290	106	480	256	619	233
AFT	~ +Z	166	334	425	186	320	480	-
AFT	~ -Z	125	96	320	280	184	283	148
V <sub>V</sub> (FT/SEC)		~ 88	~ 88	88	~ 88	90	110	104
V <sub>H</sub> (FT/SEC)		~ 15	~ 15	20	20	46	47	47
ROLL -> (DEG)		106	180	210	20	46	316	136

The following conclusions may be drawn based on the results discussed herein.

- o Initial entry angle has a significant effect on maximum pressures and stresses. For example, a change in angle of 8 degrees doubles the pressure and associated stress levels experienced by the baseline design mid-ring without foam.

- o The addition of foam to the baseline design ring reduces the peak pressures and dynamic stresses by 75 to 90 percent for both the mid- and aft rings.

- o Pressures and stresses increase with velocity at a greater rate than the commonly used velocity squared ratio. For instance, the pressure and stress values double with an increase in velocity from 80 to 90 ft/s.

- o A convex foam shape is superior to a relatively flat wedge shape from a viewpoint of structural loads and responses. The convex shape reduces the pressures and stresses on the baseline ring by 50 percent.

- o Removal of the structural reinforcement clips from the baseline design mid-ring causes an increase in maximum stress levels up to a factor of two. In the case of the aft ring, however, stress reductions were noted when some clips and gussets were removed.

- o A structural failure occurred on the aft ring outer flange and small gusset in a fashion similar to that experienced on the STS-3 flight.

- o Flight results consisting of pressure measurements indicate that the aft skirt ring web pressure environment is asymmetric circumferentially and is, it appears, highly dependent on the exact amount as well as shape of foam present at water impact.

AN OBJECTIVE ERROR MEASURE FOR THE COMPARISON OF  
CALCULATED AND MEASURED TRANSIENT RESPONSE HISTORIES

Thomas L. Geers  
Lockheed Palo Alto Research Laboratory  
Palo Alto, California

A simple error measure is proposed for the objective comparison of a calculated transient response history with its measured counterpart. The measure assigns a single numerical value to the discrepancy between the two histories over a specified comparison period. Computation of the measure involves the integration in time of squares and/or products of the calculated and measured histories. Representative results are shown for both idealized and actual response histories.

INTRODUCTION

Computer codes are now widely used to perform response calculations for transiently excited structures. Often, experiments are performed to evaluate the accuracy of the calculations, which inevitably raises questions concerning evaluation criteria. The criteria used to date have generally been subjective in nature, focusing on the size of nearly simultaneous peaks, the magnitudes of pronounced oscillations, apparent decay rates, and other general-appearance characteristics. The impreciseness of these criteria has made it difficult to incorporate them into systematic evaluations and, as a result, to establish consensus positions.

This paper describes a simple, objective error measure for assessing the discrepancy between a calculated and a measured transient response history. The measure is based on two "correspondence histories", each of which involves the integration in time of squares and/or products of computed and measured response histories. These correspondence histories possess the following attributes:

1. Each approaches a constant value at late time.
2. One is sensitive to magnitude, but insensitive to phase, discrepancy.
3. One is sensitive to phase, but insensitive to magnitude, discrepancy.

The first attribute allows one to compare two response histories on the basis of two numbers. The second and third attributes assure that these numbers describe orthogonal discrepancies, which allows one to construct a single "comprehensive error-factor" by the vector addition of a "magnitude error-factor" and a "phase error-factor".

There is a vast amount of information involved in a typical direct comparison of transient-response calculations with corresponding experimental data. Use of the comprehensive error-factor substantially reduces the comparison effort. For example, a direct comparison of two different sets of medium-scale calculations with corresponding experimental data might require examination of three sets of 50 response histories, each with 200 time steps needed for adequate response resolution; such a comparison therefore, would involve the assimilation of 30,000 data points. Use of the comprehensive error factor reduces the number of data points to be assimilated from 30,000 to 100.

COMPREHENSIVE ERROR-FACTOR

Consider the temporal functions

$$\Phi_{cm}(T, \tau) = \int_{-\tau}^T c(t+\tau) m(t) dt \quad (1)$$

$$\Phi_{c^2}(T, \tau) = \int_{-\tau}^T c^2(t+\tau) dt$$

where  $c(t)$  and  $m(t)$  are piecewise continuous functions of time. It is usually convenient to define  $c(t)$  and  $m(t)$  such that they are zero for  $t < 0$ , in which case the lower limits of these integrals are zero and  $-\tau$  for  $\tau > 0$ , and are both  $|\tau|$  for  $\tau < 0$ . In terms of the functions of (1), the "correspondence histories"  $G(T, \tau)$  and  $H(T, \tau)$  are defined by the relations

$$G^2(T, \tau) = \frac{\Phi_{c^2}(T, \tau)}{\Phi_{m^2}(T, 0)}; \quad |\tau| \ll T \quad (2)$$

$$H^2(T, \tau) = \frac{|\Phi_{cm}(T, \tau)|}{[\Phi_{c^2}(T, \tau) \Phi_{m^2}(T, 0)]^{1/2}}; \quad |\tau| \ll T$$

where  $c(t)$  is a calculated response history,  $m(t)$  is the corresponding measured response history, and  $\tau$  is the (generally uncertain) delay between starting times for the two histories. As shown below,  $G(T, \tau)$  is sensitive to magnitude discrepancy between  $c(t)$  and  $m(t)$ , but is not sensitive to phase discrepancy between the two. In contrast,  $H(T, \tau)$  is sensitive to phase discrepancy, but is not sensitive to magnitude discrepancy.

If both  $G(T, \tau)$  and  $H(T, \tau)$  are virtually constant between the times  $T/2$  and  $T$ , where  $0 < T < \bar{T}$ , it is reasonable to calculate the "correspondence averages"

$$\begin{aligned} \bar{G}(\tau) &= \frac{2}{\bar{T}} \int_{T/2}^{\bar{T}} G(T, \tau) dT, \\ \bar{H}(\tau) &= \frac{2}{\bar{T}} \int_{T/2}^{\bar{T}} H(T, \tau) dT \end{aligned} \quad (3)$$

from which one can readily compute the magnitude, phase and comprehensive error averages

$$\bar{E}_m(\tau) = \bar{G}(\tau) - 1 \quad \bar{E}_p(\tau) = 1 - \bar{H}(\tau) \quad (4)$$

$$\bar{E}_c(\tau) = [\bar{E}_m^2(\tau) + \bar{E}_p^2(\tau)]^{1/2}$$

It is readily seen that both  $\bar{E}_m(\tau)$  and  $\bar{E}_p(\tau)$  are unaffected by uncertainty regarding the polarities of  $c(t)$  and  $m(t)$ . It is also readily determined that  $\bar{E}_m(\tau)$  is virtually unaffected by uncertainty in  $\tau$ , but that  $\bar{E}_p(\tau)$  may be substantially affected by such uncertainty. Inasmuch as the comparison of two transient-response histories should be unaffected by modest translations of those histories along the time axis, it is appropriate to define the comprehensive error-factor as

$$e_c = \text{MIN} \{ \bar{E}_c(\tau) \} \quad (5)$$

In addition, if  $\hat{\tau}$  is the value of  $\tau$  at which  $\bar{E}_c(\tau)$  reaches its minimum, the magnitude and phase error-factors are given as

$$e_m = \bar{E}_m(\hat{\tau}) \quad e_p = \bar{E}_p(\hat{\tau}) \quad (6)$$

Equation 5 defines the comprehensive error-factor for the comparison of a calculated response history with its experimental counterpart. For an ensemble of  $N$  such comparisons, one may calculate an average comprehensive error-factor as

$$\bar{e}_c = \frac{1}{N} \sum_{n=1}^N (e_c)_n$$

Because the  $(e_c)_n$  are all positive, this ensemble average is not undermined by the cancellation of positive and negative contributions. This alleviates the need to calculate and interpret higher-order statistical quantities, such as standard deviations, although such quantities may be worth calculating in some situations. Similar ensemble averages  $\bar{e}_m$  and  $\bar{e}_p$  may also be calculated; the former is helpful in assessing whether the calculated response histories in a particular ensemble tend to overestimate or underestimate their measured counterparts.

#### DISCUSSION

The comprehensive error-factor defined in (5) assigns a single numerical value to the discrepancy between a calculated response history and its measured counterpart. Information as to the nature of this discrepancy is provided by the magnitude and phase error-factors defined in (6).

$G(T, \tau)$  and  $H(T, \tau)$  are closely related to quantities commonly used in time-series analysis (see, e.g., [1]). In this regard, the former might be termed the "normalized energy history" for  $c(t)$  and the latter might be termed the "normalized correlation history" for  $c(t)$  and  $m(t)$ . Note that  $H(T, \tau)$  is defined such that its numerator and denominator are of the same metric as those of  $G(T, \tau)$ ; this is appropriate for vector addition of  $\bar{E}_m(\tau)$  and  $\bar{E}_p(\tau)$  to obtain  $\bar{E}_c(\tau)$  [see (4)].

Some interesting aspects of the preceding development are discussed in the Appendix; they may be summarized as follows:

1.  $\Phi_{mc}(t, \tau) = \Phi_{cm}(T+\tau, -\tau)$  and  $\Phi_{c^2}(T, \tau) = \Phi_{c^2}(T+\tau, 0)$ ; the former indicates that it matters little whether  $c(t)$  or  $m(t)$  is shifted by  $\tau$  in (2), as  $\tau \ll T$ .

2. The second relation in the preceding item may be used for efficient computation of  $\Phi_c^2(T, \tau)$ ;  $\Phi_{cm}(T, \tau)$  may be efficiently computed as  $\Phi_{cm}(T, \tau) = F^{-1}\{\tilde{c}_T(\omega)\tilde{m}_T(-\omega)\}$ , where  $F^{-1}$  denotes inverse Fourier transformation, and where  $\tilde{c}_T(\omega)$  and  $\tilde{m}_T(\omega)$  are the Fourier transforms of  $c(t)$  and  $m(t)$ , respectively, both truncated at  $t = T$ .
3.  $0 < H(T, \tau) < 1$  for any  $c(t)$  and  $m(t)$ .
4. If  $c(t) = (1+\epsilon)m(t)$ , where  $\epsilon > -1$  is a constant,  $e_m = \epsilon$ ,  $e_p = 0$  and thus  $e_c = |\epsilon|$ .
5. If  $m(t) = \sin 2\pi t$  for  $t > 0$  and  $c(t) = (1+\epsilon) \sin [2\pi(1+\gamma)t - \phi]$  for  $t > \phi/2\pi(1+\gamma)$ ,  $e_m = \epsilon$ ,  $e_p = 0$  and thus  $e_c = |\epsilon|$  for  $\epsilon > -1$ ,  $\gamma T \ll 1$  and  $T^2 \gg 1$ .
6. If  $m(t) = \sin 2\pi t$  for  $t > 0$  and  $c(t) = (1+\epsilon) \sin [2\pi(1+\gamma)t - \phi]$  for  $t > \phi/2\pi(1+\gamma)$ ,  $e_m = \epsilon$ ,  $e_p = 1$  and thus  $e_c = (1 + \epsilon^2)^{1/2}$  for  $\epsilon > -1$ ,  $\gamma T \gg 1$  and  $T^2 \gg 1$ .
7. A previously considered error measure is the root-mean-square error history  $E_r(T, \tau)$ , defined as

$$E_r^2(T, \tau) = [\Phi_m^2(T, 0)]^{-1} \int_0^T [c(t+\tau) - m(t)]^2 dt \quad (7)$$

It is informative to compare this with the magnitude-, phase- and comprehensive-error histories, defined as [cf. (4)]:

$$E_m(T, \tau) = G(T, \tau) \quad E_p(T, \tau) = 1 - H(T, \tau) \quad (8)$$

$$E_c(T, \tau) = [E_m^2(T, \tau) + E_p^2(T, \tau)]^{1/2}$$

For  $E_m^2(T, \tau) \ll 1$  and  $E_p^2(T, \tau) \ll 1$ , it is readily shown that

$$E_r^2(T, \tau) = E_c^2(T, \tau) + 4E_p(T, \tau), \quad \Phi_{cm}(T, \tau) > 0 \quad (9)$$

$$E_r^2(T, \tau) = E_c^2(T, \tau) + 4[1 + E_m(T, \tau) - E_p(T, \tau)],$$

$$\Phi_{cm}(T, \tau) < 0$$

Hence  $E_r(T, \tau)$  greatly exceeds  $E_c(T, \tau)$  due to the terms of order unity,  $E_m(T, \tau)$  and  $E_p(T, \tau)$ . This characteristic makes an rms-error factor given by  $e_r = E_r(\tau)$  too stringent an error measure, as seen below.

The comprehensive error-factor is the result of many iterations. The proposal for comparing calculated and measured transient response histories on the basis of integral functions originated with the author in 1978 [2]. O'Hara [3] responded by pointing out the value of  $G(T, 0)$  and  $H(T, 0)$  as magnitude-sensitive and phase-sensitive correspondence measures, respectively. This prompted the author [4] to formulate a comprehensive error measure as the vector sum of a magnitude error measure and a phase error measure and, noting the undesirable dependence of  $H(T, \tau)$  on  $\tau$ , to introduce the error minimization operation of (5). Belsheim [5] proposed the Fourier-transformation technique of Aspect 2 in the interest of computational efficiency. Finally, Baladi and Barnes [6] have enhanced some of the author's intermediate results [7] and have applied the error-factor concept to ground-shock problems.

This iteration process has yet to converge, especially with respect to two rather arbitrary aspects. The first of these is the averaging of  $G(T, \tau)$  and  $H(T, \tau)$  over the latter half of the comparison period  $T$  [see (3)]. The second is the definition of  $H(T, \tau)$  in (2) such that its numerator and denominator are of the same metric as those of  $G(T, \tau)$ ; in a previous iteration,  $H(T, \tau)$  was defined as the present  $H^2(T, \tau)$ , which relaxes the requirement for taking the absolute value of the numerator. The author hopes that the present paper will encourage analysts to use the comprehensive error-factor as a comparison tool and to propose further improvements in the methodology.

#### IDEALIZED TRANSIENT RESPONSE HISTORIES

It is informative to examine some magnitude, phase, comprehensive and root-mean-square error-factors generated by a comparison of idealized transient-response histories. Consider, for example, the idealized measured response history

$$m(t) = e^{-t} \sin 2\pi t \quad (10)$$

Imagine that a transient-response calculation is performed that is supposed to yield a result identical to (10); instead, however, the calculation yields

$$c(t) = 0.8 e^{-t/0.8} \sin 2\pi t \quad (11)$$

These two response histories are shown, along with the associated error-factors, in Figure 1. As would be expected, the phase error-factor is very small, the magnitude error-factor reflects both the smaller peak amplitude and more rapid decay of  $c(t)$  relative to  $m(t)$ , and the root-mean-square error-factor is only slightly larger than the comprehensive error-factor.

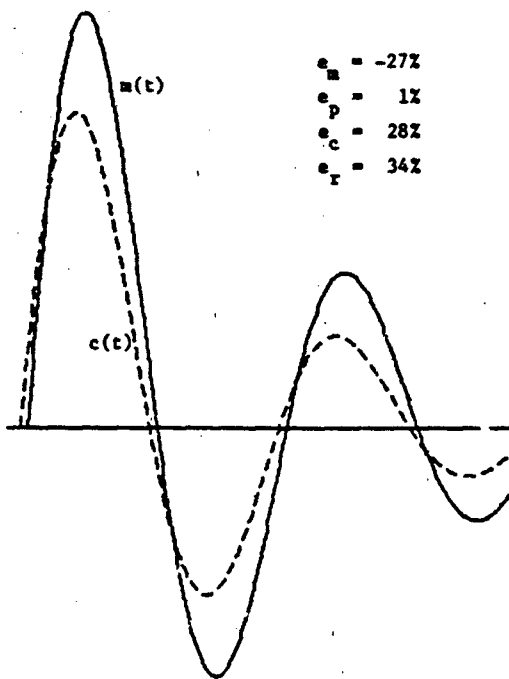


Figure 1. Idealized Response Histories with Amplitude and Decay Discrepancies

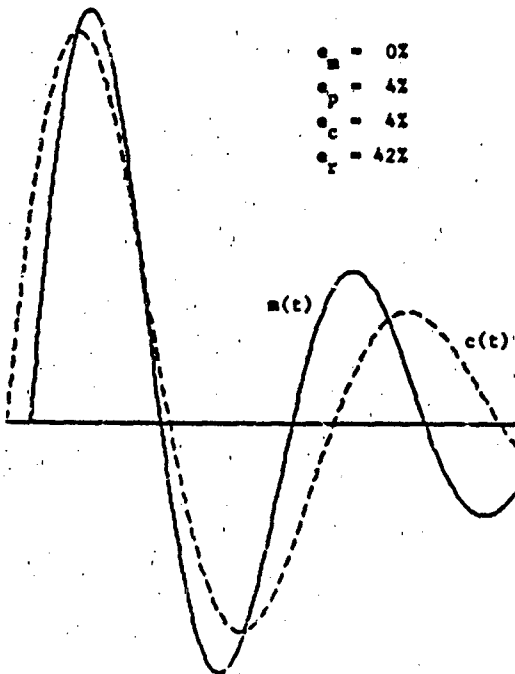


Figure 2. Idealized Response Histories with Frequency Discrepancy

Imagine now that another transient-response calculation, which is supposed to yield a result identical to (10), produces instead

$$c(t) = e^{-t} \sin 1.6\pi t \quad (12)$$

The response histories given by (10) and (12) are shown, along with the associated error-factors, in Figure 2. It is seen that the magnitude error-factor vanishes and that the phase error-factor is small, too small, perhaps, for some. The aforementioned previous iteration in which  $H(T, \tau)$  was defined as the present  $H^2(T, \tau)$  would have given  $e_c = e_p = 0.09$  for this comparison. Finally, the root-mean-square error-factor seems unacceptably large as a measure of discrepancy for the visually satisfying agreement exhibited by the two histories.

Finally, imagine a third transient-response calculation that produces, instead of (10),

$$c(t) = 1.2 e^{-t/1.2} \sin 1.6\pi t \quad (13)$$

This response history, along with (10) and the associated error-factors, appear in Figure 3. It is seen that magnitude error is the dominant contributor to comprehensive error, phase error having been minimized by a suitable shift of  $c(t)$  in time. Visual comparison of the areas beneath corresponding half-sine segments of the two response histories lends support to the magnitude error-factor shown, while the value for the root-mean-square error-factor appears too large.

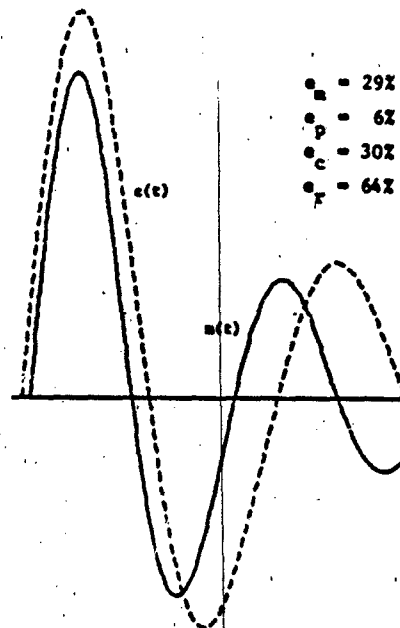


Figure 3. Idealized Response Histories with Amplitude, Decay and Frequency Discrepancies

RESPONSE HISTORIES FOR A HARDWARE TEST

Figures 4-7 show comparisons between calculated and measured transient response histories associated with a hardware test series. The figures are ordered in terms of increasing values of  $e_c$ . Virtual constancy of  $G(T, \tau)$  and  $H(T, \tau)$  during the latter half of the comparison period  $\bar{T}$  was monitored through examination of the deviational functions

$$G_+(\hat{\tau}) = \text{MAX}(G(T, \hat{\tau})) - \bar{G}(\hat{\tau}) ; \frac{1}{2} \bar{T} < T < \bar{T}$$

$$G_-(\hat{\tau}) = \bar{G}(\hat{\tau}) - \text{MIN}(G(T, \hat{\tau})) ; \frac{1}{2} \bar{T} < T < \bar{T}$$

$$H_+(\hat{\tau}) = \text{MAX}(H(T, \hat{\tau})) - \bar{H}(\hat{\tau}) ; \frac{1}{2} \bar{T} < T < \bar{T}$$

$$H_-(\hat{\tau}) = \bar{H}(\hat{\tau}) - \text{MIN}(H(T, \hat{\tau})) ; \frac{1}{2} \bar{T} < T < \bar{T}$$

None of these functions exceeded 0.12 for any of these comparisons.

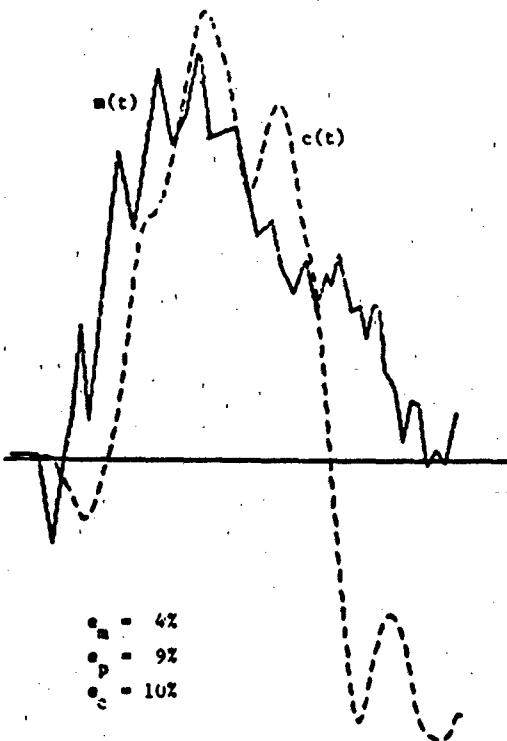


Figure 4. First Pair of Response Histories for a Hardware Test

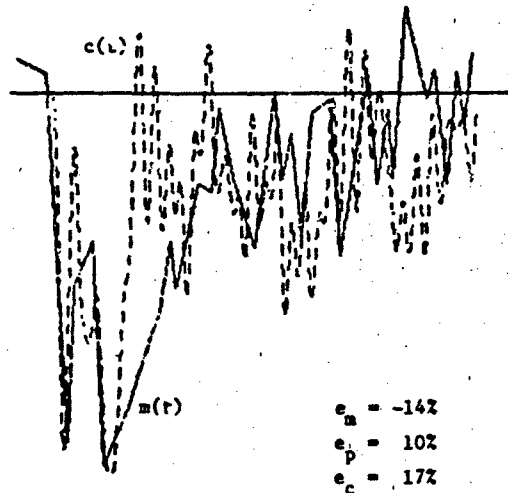


Figure 5. Second Pair of Response Histories for a Hardware Test

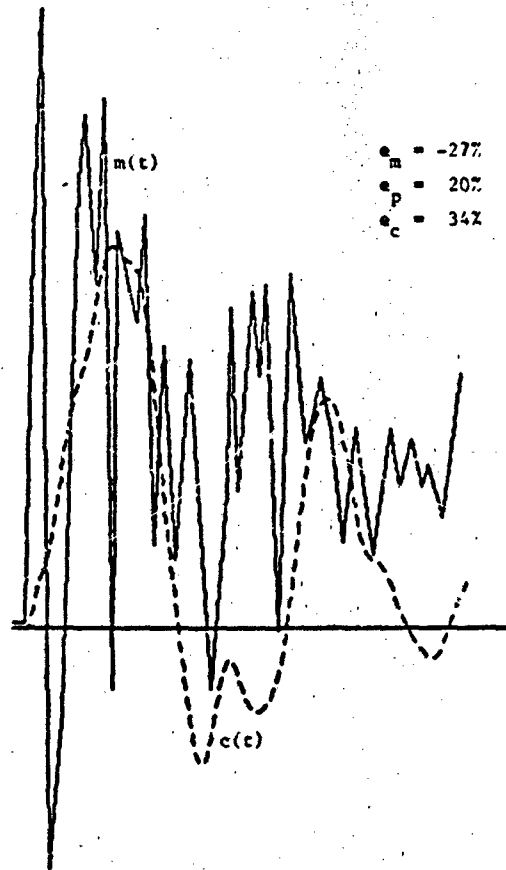


Figure 6. Third Pair of Response Histories for a Hardware Test

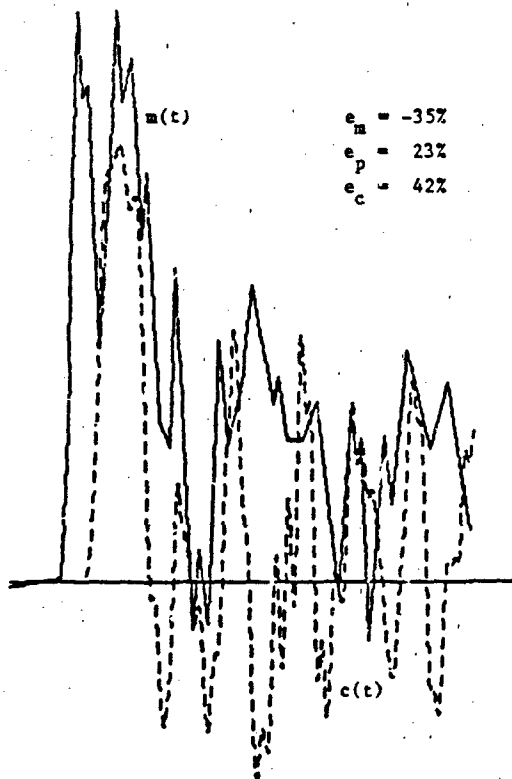


Figure 7. Fourth Pair of Response Histories for a Hardware Test

#### CONCLUSION

In this paper, the comprehensive error-factor  $e_c$  has been proposed as a simple, objective error measure for assessing the discrepancy between a calculated and a measured transient response history. This error-factor assigns a single numerical value to the discrepancy existing over a specified comparison period. Information regarding the nature of the discrepancy is provided by the magnitude and phase error-factors  $e_m$  and  $e_p$ , which constitute orthogonal components of  $e_c$ .

#### ACKNOWLEDGEMENTS

Three investigators in addition to those already mentioned have contributed directly to this paper: Mr. R. L. Eort of the Naval Research Laboratory has provided valuable insight through his familiarity with Weiner filtering, and Messrs. G. L. Fox and E. F. Hirt of NKF Engineering Associates generated Figures 1-7 with their program COMPARE. This work was carried out under Contracts DNA001-78-C-0029 and DNA001-81-C-0135 with the Defense Nuclear Agency, Washington, D.C.

#### REFERENCES

1. Y. W. Lee, *Statistical Theory of Communication*, John Wiley & Sons, New York, 1961.
2. T. L. Geers, "Some Recent Developments in Underwater Shock Analysis", Proceedings of the Defense Nuclear Agency Strategic Structures Division Biennial Review Conference, Menlo Park, CA, 20-22 March 1979.
3. G. J. C'Hara, informal communication, October 1978.
4. T. L. Geers, "A Simple Error Measure for the Comparison of Calculated and Measured Transient Response Histories", presented at the 52nd Shock and Vibration Symposium, New Orleans, LA, 27-29 October 1981.
5. R. O. Belsheim, informal communication, March 1981.
6. G. Y. Baladi and D. E. Barnes, "An Objective Waveform Comparison Technique", Tech. Rpt. SL-83-4, U.S. Army Engineer Waterways Experiment Station, Vicksburg, MS, October 1983.
7. T. L. Geers; letter (w/encl) to G. Y. Baladi dated 6 February 1981.

#### APPENDIX

This Appendix contains derivations of results summarized in the Discussion Section above.

$$1. \quad \Phi_{mc}(T, \tau) = \Phi_{cm}(T+\tau, -\tau)$$

$$\Phi_{mc}(T, \tau) = \int_{-T}^T m(t+\tau)c(t)dt$$

$$= \int_{-T+\tau}^{T+\tau} c(t'-\tau)m(t')dt' = \Phi_{cm}(T+\tau, -\tau)$$

$$\Phi_{c^2}(T, \tau) = \Phi_{c^2}(T+\tau, 0)$$

$$\Phi_{c^2}(T, \tau) = \int_{-T}^T c^2(t+\tau)dt = \int_{-T+\tau}^{T+\tau} c^2(t')dt'$$

$$= \Phi_{c^2}(T+\tau, 0)$$

$$2. \quad \underline{\Phi_{cm}(T, \tau) = F^{-1} \{ \tilde{c}_T(\omega) \tilde{m}_T(-\omega) \}}$$

From (1):

$$\Phi_{cm}(T, \tau) = \int_{-\infty}^{\infty} c_T(t+\tau) m_T(t) dt$$

where the subscript T denotes truncation at  $t = T$ . Now  $c_m(t+\tau)$  may be written as an inverse Fourier transform to obtain, with  $\tilde{c}_T(\omega)$  denoting the Fourier transform of  $c_T(t)$ ,

$$\Phi_{cm}(T, \tau) = \int_{-\infty}^{\infty} \frac{1}{2\pi} \int_{-\infty}^{\infty} \tilde{c}_T(\omega) e^{j\omega(t+\tau)} d\omega m_T(t) dt$$

Interchange of the order of integration then yields

$$\Phi_{cm}(T, \tau) = \frac{1}{2\pi} \int_{-\infty}^{\infty} \tilde{c}_T(\omega) e^{j\omega\tau} \int_{-\infty}^{\infty} m_T(t) e^{j\omega t} dt d\omega$$

But

$$\int_{-\infty}^{\infty} m_T(t) e^{j\omega t} dt = \int_{-\infty}^{\infty} m_T(t) e^{-j(-\omega)t} dt = \tilde{m}_T(-\omega)$$

Hence

$$\Phi_{cm}(T, \tau) = \frac{1}{2\pi} \int_{-\infty}^{\infty} \tilde{c}_T(\omega) \tilde{m}_T(-\omega) e^{j\omega\tau} d\omega$$

which proves the statement.

$$3. \quad \underline{0 < H(T, \tau) < 1}$$

Consider the quantity

$$\int_{-\infty}^{\infty} \left[ \frac{c(t+\tau)}{\Phi_{c2}^{1/2}(T, \tau)} + \frac{m(t)}{\Phi_{m2}^{1/2}(T, 0)} \right]^2 dt > 0$$

Expansion of the integrand and utilization of (1) gives  $1 + 2H^2(T, \tau) + 1 > 0$ , which yields  $H^2(T, \tau) < 1$  and  $-H^2(T, \tau) < 1$ . Hence, because

$H^2(T, \tau) > 0$  by definition, use of the positive square root proves the statement.

$$4. \quad \underline{c(t) = (1+\epsilon) m(t), \quad \epsilon > -1}$$

$$\Phi_{cm}(T, \tau) = (1+\epsilon) \Phi_{mm}(T, \tau)$$

$$\Phi_{c2}(T, \tau) = (1+\epsilon)^2 \Phi_{m2}(T, \tau)$$

From No. 1, above,  $\Phi_{m2}(T, \tau) = \Phi_{m2}(T+\tau, 0)$ ; hence

$$G^2(T, \tau) = (1+\epsilon)^2 \frac{\Phi_{m2}(T+\tau, 0)}{\Phi_{m2}(T, 0)}$$

$$H^2(T, \tau) = \frac{|\Phi_{mm}(T, \tau)|}{\Phi_{m2}^{1/2}(T+\tau, 0) \Phi_{m2}^{1/2}(T, 0)}$$

But  $\Phi_{mm}(T, 0) = \Phi_{m2}(T, 0)$ , so  $H(T, 0) = 1$ , which, from No. 3, above, is the maximum value of  $H(T, \tau)$ , yielding the minimum value of  $E_p(T, \tau) = 1 - H(T, \tau)$ . Hence  $\tau = 0$  and

$$e_m = \epsilon, \quad e_p = 0, \quad e_c = |\epsilon|$$

$$5, 6. \quad m(t) = \sin 2\pi t, \quad t > 0;$$

$$\underline{c(t) = (1+\epsilon) \sin [2\pi(1+\gamma)t - \phi], \quad t > \phi/2\pi(1+\gamma)}$$

$$\Phi_{m2}(T, 0) = \int_0^T \sin^2 2\pi t dt = \frac{1}{2} T \left( 1 - \frac{\sin 4\pi T}{4\pi T} \right)$$

$$\Phi_{c2}(T, \tau) = \Phi_{c2}(T+\tau, 0)$$

$$= (1+\epsilon)^2 \int_{\phi/2\pi(1+\gamma)}^{T+\tau} \sin^2 [2\pi(1+\gamma)t - \phi] dt$$

$$= \frac{1}{2} (1+\epsilon)^2 T^* \left[ 1 - \frac{\sin 4\pi(1+\gamma)T^*}{4\pi(1+\gamma)T^*} \right]$$

where  $T^* = T + \tau - \phi/2\pi(1+\gamma)$ .

$$\Phi_{cm}(T, \tau) = (1+\epsilon) \int_{t_0}^T \sin[2\pi(1+\gamma)(t+\tau)-\phi] \sin 2\pi t dt$$

where  $t_0$  is the larger of zero and  $\phi/2\pi(1+\gamma) - \tau$ . With  $t' = t+\tau$ , this becomes

$$\begin{aligned} \Phi_{cm}(T, \tau) &= (1+\epsilon) \int_{t_0}^{T+\tau} [\sin 2\pi(1+\gamma)t' \cos \phi \\ &\quad - \cos 2\pi(1+\gamma)t' \sin \phi] \\ &\quad \times (\sin 2\pi t' \cos 2\pi\tau \\ &\quad - \cos 2\pi t' \sin 2\pi\tau) dt' \end{aligned}$$

where  $t_0'$  is the larger of  $\tau$  and  $\phi/2\pi(1+\gamma)$ . Evaluation of this integral yields

$$\begin{aligned} \frac{2\Phi_{cm}(T, \tau)}{(1+\epsilon)T'} &= \cos \phi \cos 2\pi\tau \{f[2\pi\gamma T'] - f[2\pi(2+\gamma)T'] \\ &\quad - \frac{t_0'}{T'} f[2\pi\gamma t_0'] + \frac{t_0'}{T'} f[2\pi(2+\gamma)t_0']\} \\ &\quad - \sin \phi \sin 2\pi\tau \{f[2\pi\gamma T'] + f[2\pi(2+\gamma)T'] \\ &\quad - \frac{t_0'}{T'} f[2\pi\gamma t_0'] - \frac{t_0'}{T'} f[2\pi(2+\gamma)t_0']\} \\ &\quad - \sin \phi \cos 2\pi\tau \{g[\pi\gamma T'] - g[\pi(2+\gamma)T'] \\ &\quad - \frac{t_0'}{T'} g[\pi\gamma t_0'] + \frac{t_0'}{T'} g[\pi(2+\gamma)t_0']\} \\ &\quad - \cos \phi \sin 2\pi\tau \{g[\pi\gamma T'] + g[\pi(2+\gamma)T'] \\ &\quad - \frac{t_0'}{T'} g[\pi\gamma t_0'] - \frac{t_0'}{T'} g[\pi(2+\gamma)t_0']\} \end{aligned}$$

where  $f(x) = \frac{\sin x}{x}$ ,  $g(x) = \frac{\sin^2 x}{x}$ , and  $T' = T+\tau$ .

For  $T^2 \gg 1$ ,  $T \gg \tau$  and  $T \gg \phi/2\pi(1+\gamma)$ ,

$$\Phi_{m2}(T, 0) = \frac{1}{2} T \quad \Phi_{c2}(T, \tau) = \frac{1}{2} (1+\epsilon)^2 T$$

$$\begin{aligned} \Phi_{cm}(T, \tau) &= \frac{1}{2} (1+\epsilon) T (\cos(\phi+2\pi\tau) f[2\pi\gamma T] \\ &\quad - \sin(\phi+2\pi\tau) g[\pi\gamma T]) \end{aligned}$$

If, in addition,  $\gamma T \ll 1$ , then  $H^2(T, \tau) \approx |\cos(\phi+2\pi\tau)|$ ; but if, instead,  $\gamma T \gg 1$ , then  $H^2(T, \tau) \ll 1$ .

From the preceding, if  $T^2 \gg 1$ ,  $T \gg \tau$ ,  $T \gg \phi/2\pi(1+\gamma)$  and  $\gamma T \ll 1$ , the error-factors are, for  $\epsilon > -1$ ,

$$e_m = \epsilon, \quad e_p = 0, \quad e_c = |\epsilon|$$

On the other hand, if  $T^2 \gg 1$ ,  $T \gg \tau$ ,  $T \gg \phi/2\pi(1+\gamma)$  but  $\gamma T \gg 1$ , the error-factors are, for  $\epsilon > -1$ ,

$$e_m = \epsilon, \quad e_p = 1, \quad e_c = (1+\epsilon^2)^{1/2}$$

7.  $E_T^2(T, \tau)$  for  $E_m^2(T, \tau) \ll 1$  and  $E_p^2(T, \tau) \ll 1$

From (2) and (7)

$$E_T^2(T, \tau) = G^2(T, \tau) + 1$$

$$-2 \begin{cases} G(T, \tau) H^2(T, \tau), \Phi_{cm}(T, \tau) > 0 \\ -G(T, \tau) H^2(T, \tau), \Phi_{cm}(T, \tau) < 0 \end{cases}$$

The introduction of (8) into this then yields

$$E_T^2(T, \tau) = E_c^2(T, \tau) - [3+2E_m(T, \tau)] E_p^2(T, \tau)$$

$$+ 4[1+E_m(T, \tau)] E_p(T, \tau) \text{ for } \Phi_{cm}(T, \tau) > 0$$

$$E_T^2(T, \tau) = E_c^2(T, \tau) + [1+2E_m(T, \tau)] E_p^2(T, \tau)$$

$$+ 4[1+E_m(T, \tau)] [1-E_p(T, \tau)] \text{ for } \Phi_{cm}(T, \tau) < 0$$

which produces, for  $E_m^2(T, \tau) \ll 1$  and  $E_p^2(T, \tau) \ll 1$ , (9).

## DISCUSSION

Mr. Coulter (Ballistic Research Laboratory): If you had a single pulse, would your magnitude error be proportional to the impulse? You seemed to imply that it would be proportional to the magnitude part of the error. I am thinking about applying this to a single blast pulse. We have records just like yours, only they are single blast pulses. Would you use the same kind of acceptable errors, (5%, 10% or 20%) as you would with other measures? I am searching for something that would be acceptable.

Mr. Geers: That is where the subjectivity comes in. At least you can make the subjectivity whatever you want. You can bring it in at one point with this technique, because once you have chosen an error measure that you consider acceptable, then the computer does the rest. But it is up to the person to make that subjective judgement. That is strictly a judgement call. My personal reaction has been that anything better than 20% is really good. When you get to around 20 or 30%, it is getting fair. When you get above the 30 to 40% range, that is rather poor.

Mr. Coulter: So if you shoot for 30%, or maybe 20%, you are doing well?

Mr. Geers: If you get within 20%, you are close.

Mr. Strauss (Rocketdyne): I'd like to go back to your next to the last sample of data. In this example it looks like your phasing was very close, and your amplitude was way off. In a case like this, or in general, wouldn't it make sense to separate the phase and the amplitude? If you have the phase right, it is a simple error to correct. Whereas if your phase is off, you have to recalculate something.

Mr. Geers: Yes, that is a good point. I am glad you mentioned that. That is why I show all three. But when we have many, many comparisons to make, we cannot do it on a global basis with multiple errors. I was seeking one single number for a given comparison, and that is the top level. You can go down to the next level, and you can look at the magnitude and the phase errors separately. You can go down to various levels, and I think that is a good idea.

Mr. Barsoum (U.S. Army Materials and Mechanics Research Center): If you are looking at responses in various locations in a structure, you will have hundreds of numbers. Perhaps one should look at energy which has the same kinds of norms as these. From an engineering point of view, you are looking at the response of most critical locations. How do you find these in the experiments?

Mr. Geers: You could set up a critical group. If you had transducers that showed responses that were large, or that would subject the

structure to incipient failure, perhaps you could select those as a subgroup of special interests. Then you could make the comparisons between the calculations and the measurements for that group and draw the histograms that I showed. You could say this is for subgroup critical, and this is an evaluation of the errors made by the calculations at the critical points. So you can make any kind of selection that you want in the subgroups and evaluate the error.

Mr. Frydman (Harry Diamond Laboratories, Session Chairman): This kind of technique seems to be very useful for shaker waveform synthesis operations. We spend an enormous amount of time trying to compare responses with predicted results, and we essentially rely on manual techniques. This would enable us to do it electronically.

Mr. Geers: This doesn't suit everybody. Some people don't like it because they like to look at peaks. They are only interested in the peak response. But what worries me about peaks is that you can have a measured response. You can imagine a case where the calculated response would just go flat, up a spike, down, and then hit the peak right on the nose, and that is one hundred percent accurate? That wouldn't satisfy me. The first thing I considered was just looking at peaks. But I ruled that out because I saw too many cases where a person could do well on hitting the peak, but the frequency content just was not there. The time of the peak wasn't any good. It gets flakey fast with peaks.

Voice: Have you considered applying this to random vibration which may have a coherent component to it?

Mr. Geers: No, but it's your pleasure. I was interested in the transient response problem and that is what I focused on.

ALTERNATIVE SHOCK CHARACTERIZATIONS  
FOR CONSISTENT SHOCK TEST SPECIFICATION\*

Thomas J. Baca  
Sandia National Laboratories  
Albuquerque, New Mexico

Mechanical shock environments must be characterized in the most complete manner possible if they are to be successfully simulated in the shock test laboratory. The objective of the research described in this paper is to evaluate three methods of analyzing transient acceleration time histories which represent promising alternatives to shock response spectra as the basis for deriving consistent shock test specifications. A shock test specification is defined to be consistent if it meaningfully relates the operational and laboratory shock environments. The limitations of shock spectra are discussed in this regard before presenting the advantages of the new alternative characterizations. These shock analysis techniques include: 1) ranked peaks in the acceleration time history; 2) root-mean-square acceleration as a function of time; and 3) root-mean-square acceleration as a function of frequency. These shock characterizations provide the parameters necessary to develop a new shock test specification technique which can replace the current practice of enveloping shock spectra. Data from a simulated field shock environment are analyzed using all three shock characterizations as well as shock spectra. The new method of shock test specification is demonstrated using drop table and decaying sinusoid shock test inputs. Test specifications using the standard method of shock spectra enveloping are also derived. The resulting shock test specifications are compared and the implications of using alternative shock characterizations in deriving consistent test specifications are identified. Beneficial aspects of utilizing these alternative shock analysis techniques instead of shock spectra are presented with particular emphasis being placed on the evaluation of conservatism associated with different shock test specification techniques.

INTRODUCTION

Shock tests are specified to simulate operational shock environments. Aerospace components are shock tested in the laboratory to develop confidence that they will survive the flight shock environment. The adequacy of the shock test as a consistent substitute for the field shock can only be judged if both shock environments are characterized properly. Shock spectra are currently used in the aerospace industry to characterize shock environments and to subsequently specify shock tests. A shock test input is taken to be acceptable if its shock spectrum envelops the shock spectrum of the field data. The objective of this paper is to develop an alternative to shock spectrum

enveloping for shock test specification. The proposed method of shock test specification requires a more complete characterization of both laboratory and field shock data. This method requires calculation of root-mean-square acceleration as a function of frequency and time, as well as the sorting of peak acceleration values in the shock time history. This new test specification technique is implemented for decaying sinusoid and and haversine shock test inputs which are two widely used types of laboratory excitation. A comparison of this method with the standard shock spectrum approach will finally be undertaken through a study of both the test inputs and analytically derived responses from a simple structure.

\*This work was supported by the United States Department of Energy.



LIMITATIONS OF SHOCK SPECTRA IN DERIVING  
CONSISTENT SHOCK TEST SPECIFICATIONS

A discussion of the limitations of using shock spectrum enveloping as the sole means of specifying shock tests is useful in motivating the development of a test specification technique based on alternative shock characterizations. An absolute acceleration shock spectrum (SAA) is a plot of the maximum value of the absolute acceleration response of a single degree of freedom system (SDOF) having a specified critical damping ratio versus the natural frequency of the SDOF system. The concept of shock spectra was conceived by Biot [1,2] as a means of characterizing the strong ground motion of earthquakes by their effects on simple SDOF models of buildings. The key aspect of the shock spectrum is that it reflects the effects of a transient on a certain class of structures (i.e., SDOF structures with a certain damping ratio). It does not retain information about the specific characteristics of the shock. In spite of this intended use of the shock spectrum concept, shock spectra are widely used in the aerospace community as an acceptable means of characterizing a shock environment [3]. Shock test specification has been implemented through the selection of laboratory test inputs having shock spectra which exceed the shock spectra of available field data [4]. Objections to this procedure have been raised previously [5-8], particularly in the context of assessing shock test conservatism [6-8]. The principal reason for the acceptance of shock spectrum enveloping as a test specification technique is that component structures which can survive tests specified in this manner, generally perform well in the operational shock environment.

The implications of shock spectrum enveloping can be demonstrated through the following example. Consider the shock time history shown in Figure 1a which was measured as the input to the fixed end of a 12.7 cm (5 inch) long metal cantilever beam mounted in a support structure. Given that this is the operational shock environment, what kind of test pulse should be applied in the shock laboratory? The most common answer would be the 1300 g x 0.33ms haversine pulse shown in Figure 1b.

A haversine pulse is defined by the following equation:

$$\ddot{x}(t) = \begin{cases} \frac{A}{2} (1 - \cos \frac{2\pi t}{TH}) & , 0 < t < TH \\ 0 & \text{elsewhere} \end{cases} \quad (1)$$

where A is the amplitude of the haversine pulse and TH is the duration. These haversine pulse parameters are derived by selecting the haversine pulse having a shock spectrum that envelops the shock spectrum of the field data, as shown in Figure 2.

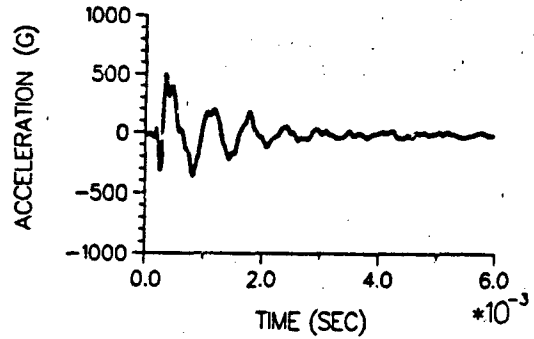


Figure 1a Time History for Field Data.

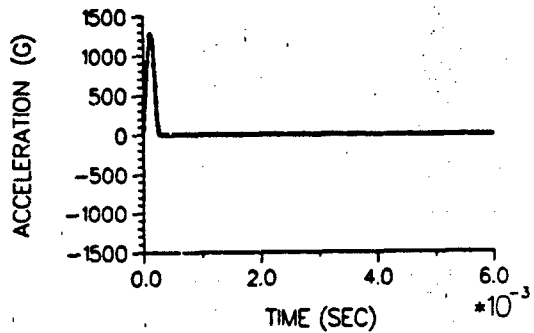


Figure 1b Time History for 1300 g x 0.33 ms Haversine Shock Test Specification.

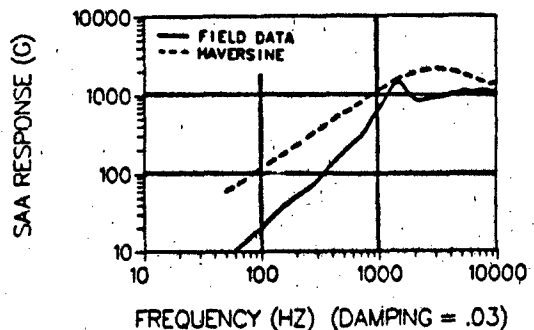


Figure 2 Comparison of Shock Spectra for Field Data and 1300 g x 0.33 ms Haversine Shock Data.

While the main advantage of the haversine pulse is that it can be created repeatedly on a drop table shock machine, the obvious disadvantage is that it does not resemble the field shock data in terms of its peak acceleration, two-sidedness, or duration. These observations can be made by an inspection of the time histories in Figures 1a and 1b. Since the shock spectrum (Figure 2) is not a measure of frequency content, it is necessary to look at a comparison of the energy spectra (Fourier amplitude spectrum squared) to see that the two shock excitations vary markedly in terms of frequency content (see Figure 3). One final approach to evaluating these two shock pulses is to calculate the response at the end of a finite element model of the beam when it is excited by each pulse. The results of this calculation performed using MSC/NASTRAN are shown in Figures 4a and 4b. A much higher response is produced by the haversine pulse than by the field data pulse.

#### ALTERNATE SHOCK CHARACTERIZATIONS

The alternative shock characterizations to shock spectra employed in this paper were originally introduced as significant descriptors of field and laboratory shock environments which could be used to meaningfully quantify and actually control shock test conservatism [6,8]. These characteristics of shock transients aim to describe the distinctive features of a particular shock environment so that these same characteristics will be preserved in a laboratory test shock pulse. Consequently, these alternative shock characterizations are unlike the shock spectrum which quantifies only the effects of a shock on SDOF structures.

Three main characteristics of the shock time history have been preserved in the alternative shock characterizations:

- 1) the variation of the average amplitude of the acceleration time history as a function of time.
- 2) the frequency content of the shock excitation.
- 3) the magnitude of the peaks in the acceleration time history.

Time domain root-mean-square acceleration,  $TRMS(\tau)$ , is defined as a measure of the first of these characteristics:

$$TRMS(\tau) = \left[ \frac{1}{\tau} \int_0^{\tau} \ddot{x}^2(t) dt \right]^{1/2} \quad (2)$$

$0 < \tau \leq TD$

where TD is the duration of the shock transient.

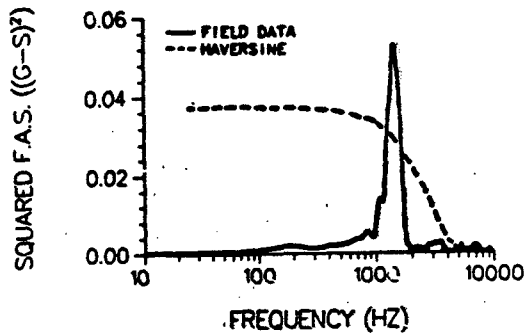


Figure 3 Comparison of Squared Fourier Amplitude Spectra for Field Data and 1300 g x 0.33 ms Haversine Shock.

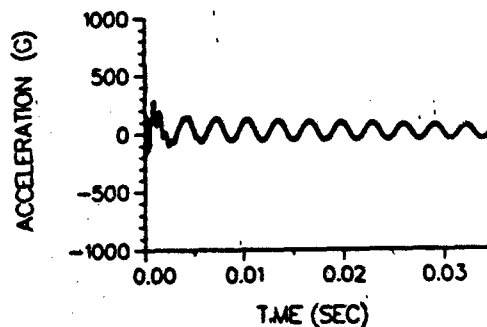


Figure 4a Time History of Calculated Response at End of Cantilever Beam to Field Data Input (Figure 1).

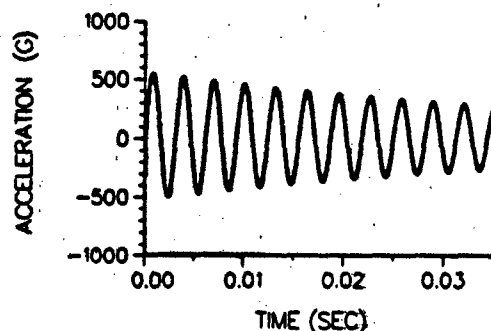


Figure 4b Time History of Calculated Response at End of Cantilever Beam to 1300 g x 0.33 ms Haversine Shock Input (Figure 2).

At time  $\tau = TD$ , the overall RMS acceleration for the time history, TRMSO, is an overall indicator of the average acceleration level experienced during the shock event. It is important to remember that each TRMSO value must have a duration, TD, associated with it to be meaningful. Overall TRMS values from two different shock events must have the same analysis duration before any comparison can be made between the two time histories. A plot of TRMS versus time for the field data time history in Figure 1 is shown in Figure 5.

It was shown previously [6] that the contribution to the overall TRMS acceleration (TRMSO) by all frequencies less than the frequency of interest F is given by a frequency domain RMS acceleration:

$$FRMS(F) \approx \frac{2}{TD} \left[ \int_0^F |\ddot{X}(f)|^2 df \right]^{1/2} \quad (3)$$

where  $\ddot{X}(f)$  is the Fourier transform of  $\ddot{x}(t)$ :

$$\ddot{X}(f) = \int_{-\infty}^{\infty} \ddot{x}(t) e^{-j2\pi ft} dt \quad (4)$$

and  $j = \sqrt{-1}$ .

Figure 6 shows a plot of FRMS for the field data shock (Figure 1). Note that a sharp increase in the FRMS level is indicative of substantial frequency content at that frequency (e.g., ~1500 Hz in Figure 6). The FRMS plot has the advantage over the Fourier amplitude spectrum that it not only reflects frequency content, but also retains a readily interpretable numerical value. The numerical value at a given frequency of the Fourier amplitude spectrum is not as directly amenable to physical interpretation. It should again be emphasized that the FRMS plots of two shocks can only be compared if they both have a duration equal to TD. Keeping track of the duration of a transient helps to retain an important characteristic of the shock time history. (No more effort is involved than that of specifying the critical damping ratio associated with a particular shock spectrum.) Finally, calculation of FRMS is accomplished efficiently. Fast Fourier Transform techniques [9] allow the rapid solution of Equation (4), while the integration specified in Equation (3) can be accomplished numerically.

An acceleration peak is defined to be the maximum value between changes in sign of the time history. Once positive and negative peaks have been identified, a sorting algorithm [8] can be applied to rank: all of the peak values; the positive peak values; and the negative peak values. The ranked peak accelerations for all peaks in the field data time history in Figure 1 are shown in Figure 7. This plot serves as a summary of the extreme acceleration values of the shock time history. Plotting the positive

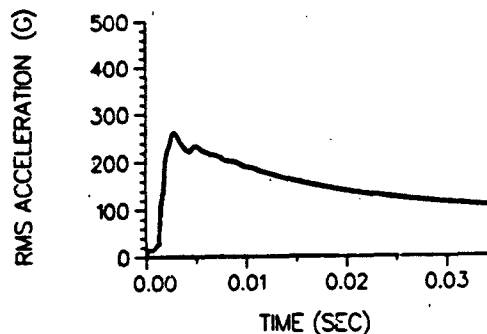


Figure 5 Time Domain RMS for Field Data (Figure 1).

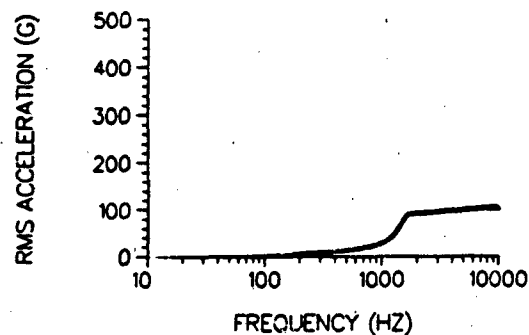


Figure 6 Frequency Domain RMS for Field Data (Figure 1).

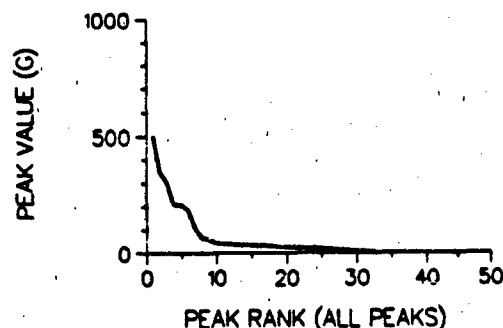


Figure 7 Ranking of Absolute Peaks for Field Data (Figure 1).

and negative ranked peaks on the same curve (see Figure 8) provides valuable insight into the two-sidedness of the shock time history. Comparisons of ranked peaks from two time histories should be done only if both records have been filtered to ensure that each will have the same bounds on their frequency content.

#### ALTERNATIVE SHOCK TEST SPECIFICATION METHOD

It is important to emphasize that a complete understanding of a shock excitation requires study of all three of the alternative shock characterizations. The goal of consistent shock test specification is to match the shock characterizations of the field data and the laboratory test shock input to the greatest extent possible. Knowledge of the failure mechanisms of the structure being tested may be of use in judging the significance of each of the shock characterizations, but the approach taken in this paper is to consider each of them to be equally important. It is also assumed that the time histories of the field shock data are available to the engineer responsible for shock test specification. The three parameters used in the proposed shock test specification require calculation of the overall RMS acceleration (TRMSO), FRMS(F), and the maximum peak acceleration. Normally, it would be expected that all of the shock characterizations previously mentioned would have been determined for the field data.

Test specification procedures are given in the following paragraphs for decaying sinusoid and haversine shock test inputs. A decaying sinusoid shock pulse is composed of a sum of decaying sinusoids of the form:

$$\ddot{x}(t) = \begin{cases} A e^{-2\pi t Z/T} \sin \frac{2\pi t}{T} & t \geq 0 \\ 0 & t < 0 \end{cases} \quad (5)$$

Methods exist for specifying decaying sinusoid shock test inputs on the basis of enveloping shock spectra [10]. The intuitively attractive feature of the decaying sinusoid pulse is that it allows the shock input to be more "realistic looking" when one is attempting to simulate pyrotechnic shocks which are two-sided, decaying types of shocks (e.g., Figure 1). The main restriction on the use of the decaying sinusoid shock pulses is that they are limited to the force capability of the shaker system on which they are implemented. Haversine shock test inputs (as given by Equation (1)) are commonly generated on drop table shock machines. This test technique has the advantage of being able to achieve higher peak acceleration levels than those of decaying sinusoid pulses produced on shakers. The widespread use of haversine shock test inputs motivates development of a test specification technique for these simple pulses in this paper.

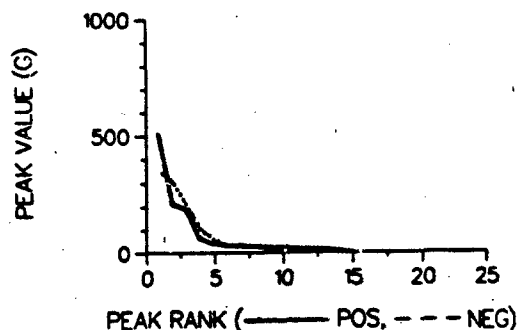


Figure 8 Ranking of Positive and Negative Peaks for Field Data (Figure 1).

The parameters of interest in the test specification processes discussed next are as follows:

- Z = Decay rate of the exponential term in the decaying sinusoid component
- A = Amplitude of decaying sinusoid or haversine pulse
- T = Period of decaying sinusoid component ( $T=1/f$ , where  $f$  is the frequency of the sinusoid)
- TH = Baseline duration of the haversine pulse
- TD = Analysis duration of both field shock and test shock
- TP = Time for the exponential factor in the decaying sinusoid to decay to P percent of its original amplitude
- TRMSO = Overall RMS acceleration for duration TD.

#### Decaying Sinusoid Test Specification:

Selecting an appropriate decaying sinusoid shock requires that values of A, Z, and T be selected for each frequency which is judged to be significant in the FRMS plot. The procedure described here is for a single component, but the method applies to any number of decaying sinusoid components. (Note that a low frequency and low amplitude compensating pulse [10] must be included to make the shock pulse have zero final velocity and displacement.)

The value of T is first selected by looking at a plot of FRMS for the field data. The predominant frequency of the field data will be indicated by a sharp increase in slope in the FRMS plot. More than one frequency may be evident in the field data, so that more decaying sinusoid frequency components may be needed. The contribution to the overall TRMSO value of each predominant frequency can be measured from the FRMS plot as well.

Observation of the field shock data will yield the time at which the shock has decreased

to P percent of its peak level. Defining the ratio of TP to T as:

$$RP = \frac{TP}{T} \quad (6)$$

the value of P is controlled by the exponential decay rate, Z.

$$P = 100 \cdot (e^{-Z2\pi \cdot RP}) \quad (7)$$

so that in general,

$$RP = \frac{-1}{2\pi Z} \ln \left( \frac{P}{100} \right) \quad (8)$$

Figure 9 shows plots of Equation (8) for P=1,2,10,20. These curves can be used to select a value of Z which will give approximately the same effective duration of the shock for a decaying sinusoid component having period T.

Once Z is selected, a value of A is sought based on the TRMSO value. This can be accomplished in a general way by first defining a

normalized duration for the decaying sinusoid pulse:

$$R = \frac{TD}{T} \quad (9)$$

Solving Equation (2) in terms of R for a decaying sinusoid as defined in Equation (5) gives a normalized TRMSO:

$$\frac{TRMSO(R)}{A} = \frac{1}{\sqrt{8\pi R}} \left[ \left( \frac{1}{Z} - \frac{Z}{Z^2+1} \right) + e^{-4\pi ZR} \left( \frac{1}{Z} + \frac{\sin 4\pi R - Z \cos 4\pi R}{Z^2+1} \right) \right]^{1/2} \quad (10)$$

. R > 0.

This equation is plotted in Figure 10 for several damping values. Knowing the desired TRMSO value, Z, and R for the field data, A can be found once the value of TRMSO(R)/A is determined from Figure 10.

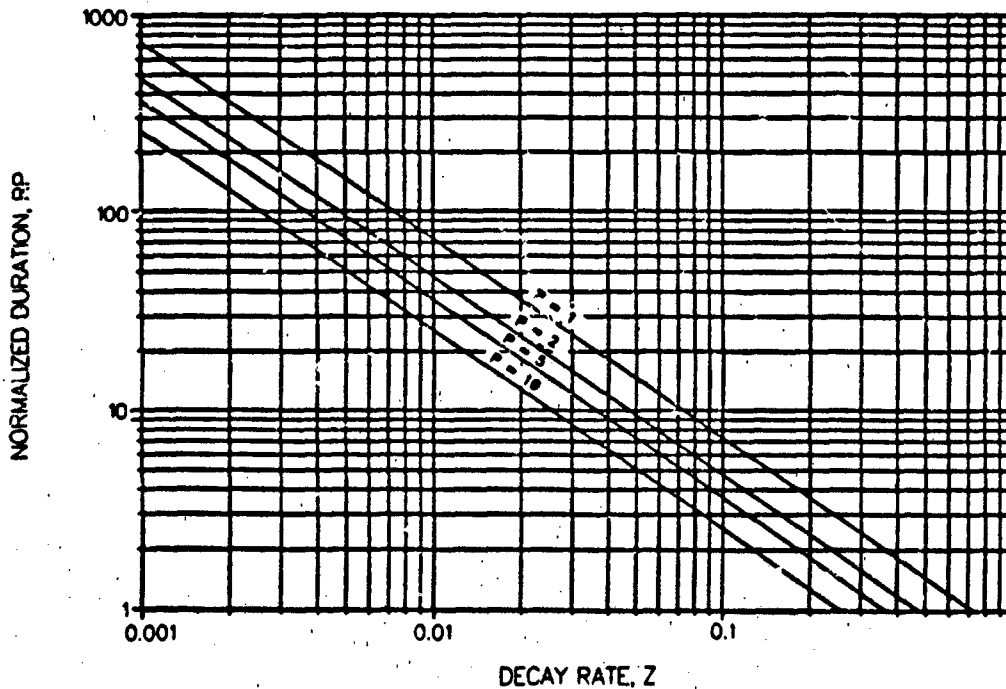


Figure 9 Normalized Duration (RP=TP/T) of a Decaying Sinusoid vs Decay Rate (Z) of a Decaying Sinusoid for Different Values of P.

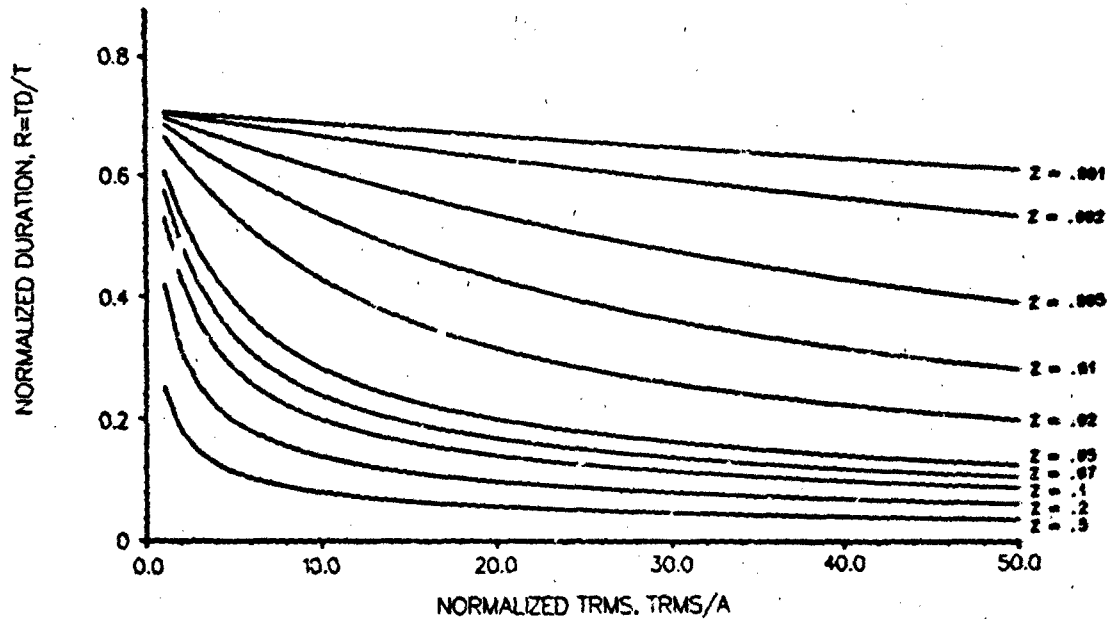


Figure 10 Normalized TRMS (TRMS/A) vs Normalized Duration (R=TD/T) at Different Decay Rates (Z) for a Decaying Sinusoid Pulse with Amplitude A, Period T, and Duration TD

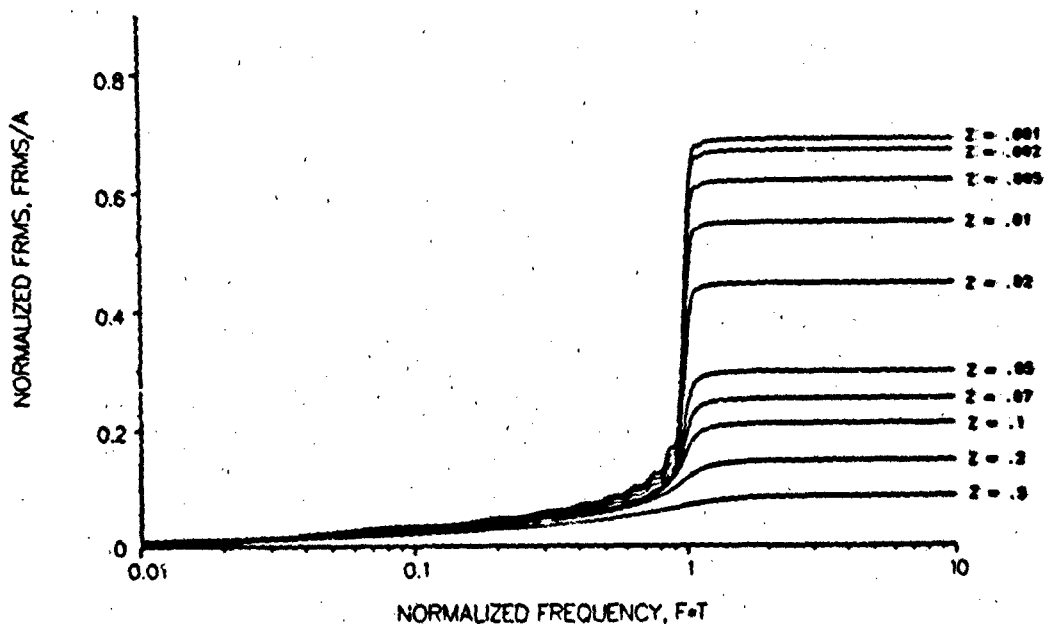


Figure 11 Normalized FRMS (FRMS/A) vs Normalized Frequency (F\*T) at R=9 and at Various Decay Rates (Z) for a Decaying Sinusoid Pulse.

The frequency domain RMS for the decaying sinusoid pulse can be found by first solving Equation (4) analytically to get:

$$|\ddot{X}(f)| = \frac{AET}{4\pi} \left[ C_1 \cos C_3 - \frac{C_1}{E} + C_2 \sin C_3 - D_1 \cos C_4 + \frac{D_1}{E} - D_2 \sin C_4 \right] + j \left[ \frac{AET}{4\pi} - C_1 \sin C_3 + C_2 \cos C_3 - \frac{C_2}{E} + D_1 \sin C_4 - D_2 \cos C_4 + \frac{D_2}{E} \right] \quad (11)$$

where,

$$C_1 = \frac{(fT - 1)}{(fT - 1)^2 + Z^2} \quad C_2 = \frac{Z}{(fT - 1)^2 + Z^2}$$

$$C_3 = 2\pi R (fT - 1) \quad C_4 = 2\pi R (fT + 1)$$

$$D_1 = \frac{(fT + 1)}{(fT - 1)^2 + Z^2} \quad D_2 = \frac{Z}{(fT + 1)^2 + Z^2}$$

$$E = e^{-2\pi ZR}$$

and then solving Equation (3) numerically to produce a plot of normalized FRMS versus normalized frequency for a specified R value such as that shown in Figure 11 for various values of Z and R=9. The values of T, Z, and A are now determined for this decaying sinusoid component. The procedure is repeated if other components are necessary.

One final step in the definition of the entire decaying sinusoidal pulse is required if the peak acceleration of the test input is different from the peak acceleration of the field data. Should this be the case, the values of A are scaled by a constant factor so that the peak acceleration of the decaying sinusoid test pulse matches the peak acceleration of the field data.

#### Haversine Test Specification:

The duration of the haversine pulse is selected by taking TH as the period corresponding to the frequency below which all contributions to the overall RMS are made in the FRMS plot. If there is a single predominant frequency, F, in the FRMS plot, one would take TH as 1/F.

Once TH is selected, then the normalized duration for the haversine pulse can be calculated:

$$RH = \frac{TD}{TH} \quad (12)$$

Solving Equation (2) for a haversine pulse as defined in Equation (1), the following expression for normalized TRMSO versus RH is obtained:

$$\frac{\text{TRMSO}(RH)}{A} = \begin{cases} \frac{1}{2} \left[ \frac{3}{2} + \frac{C_5}{\pi RH} \right]^{1/2} & 0 < RH \leq 1 \\ \frac{1}{2} \left[ \frac{3}{2RH} \right]^{1/2} & RH > 1 \end{cases} \quad (13)$$

where,

$$C_5 = \left( \frac{1}{8} \sin 4\pi RH - \sin 2\pi RH \right)$$

Figure 12 provides a plot of Equation (13) which can be used to find TRMSO(RH)/A for a given value of RH determined from Equation (12). The value of A necessary to match the TRMSO value from the field data can now be found by simple multiplication.

A normalized FRMS plot as a function of normalized frequency for various values of RH is given in Figure 13. This plot was generated by first finding the Fourier transform (Equation (4)) of the haversine pulse (Equation (1)):

$$|\ddot{X}(f)| = A \cdot K [\sin 2\pi fTH] + j A \cdot K [\cos 2\pi fTH - 1] \quad (14)$$

where,

$$K = \frac{1}{4\pi f} \left[ \frac{1}{1 - (fTH)^2} \right]$$

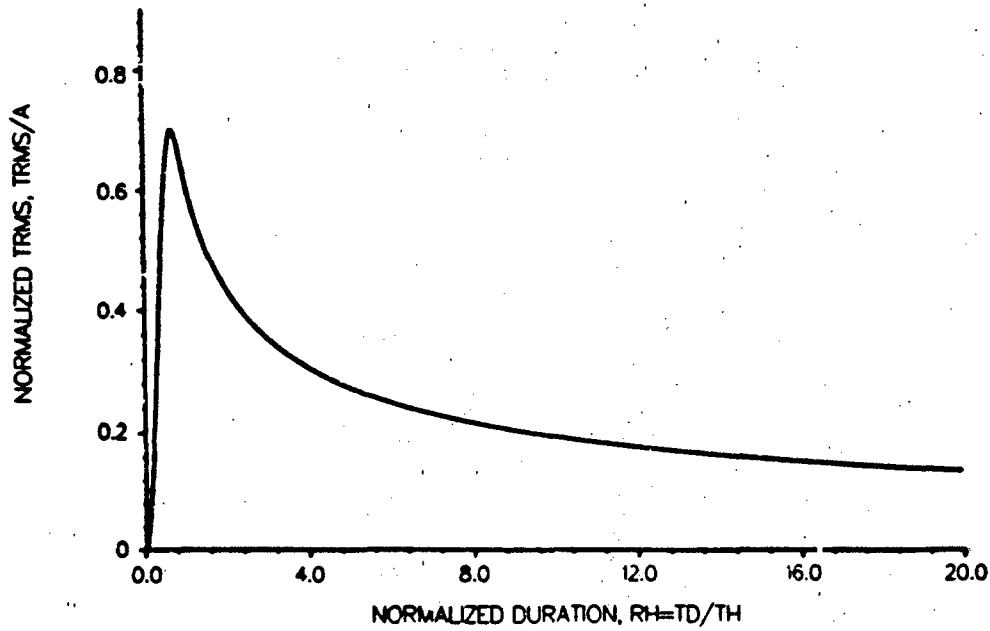


Figure 12 Normalized TRMS (TRMS/A) vs Normalized Duration (RH=TD/TH) for a Haversine Pulse with Amplitude (A) and Baseline Duration (TH). (TD = Duration of Input Time History.)

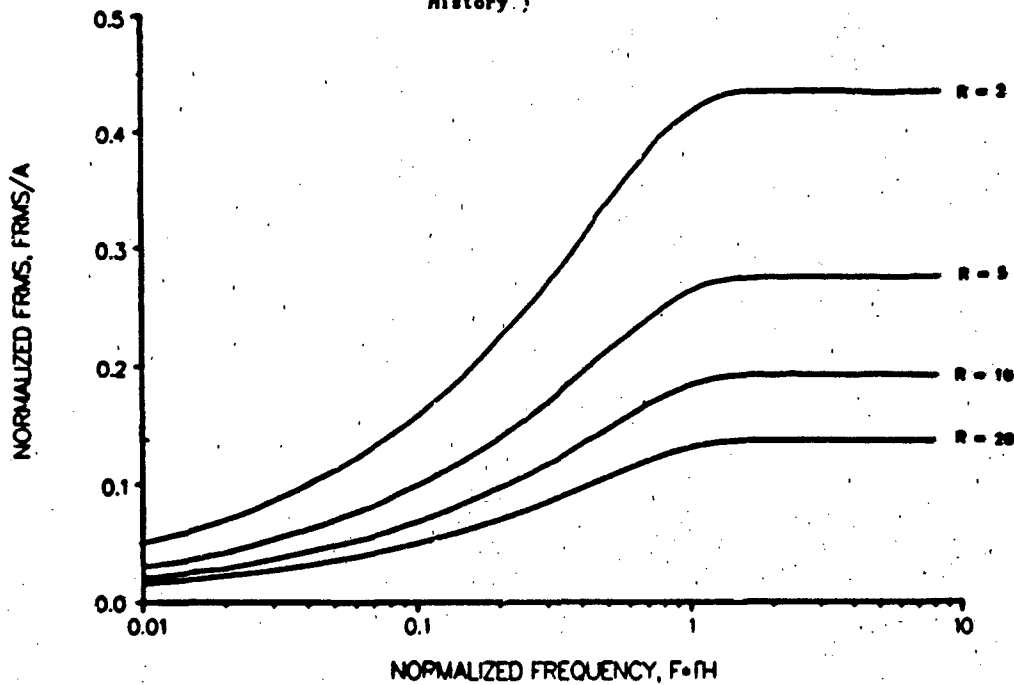


Figure 13 Normalized FRMS (FRMS/A) vs Normalized Frequency (F\*TH) at Various RH Values (RH=TD/TH) for a Haversine Pulse with Amplitude (A) and Baseline Duration (TH). (TD = Duration of Input Time History.)

This result was then used in Equation (3) and the integration was carried out numerically.

A final modification to the value of A is necessary if the value determined by matching TRMSO differs from the peak value seen in the field data. The two peak values are made identical in this circumstance.

#### COMPARISON OF SHOCK TEST SPECIFICATION METHODS

A comparison of the shock test specification method introduced above and the standard method of shock spectrum enveloping was completed. The time history in Figure 1 was taken as the field data having the following parameters

$$\text{TRMSO} = 108 \text{ g}$$

$$\text{TD} = 0.006 \text{ s}$$

$$\text{T} = 0.00067 \text{ s (1 / 1500 Hz)}$$

$$\text{TP} = 0.0035 \quad (\text{P} = 10)$$

$$\text{MAXIMUM PEAK} = 505 \text{ g}$$

Three test specifications were evaluated and were denoted methods A, B, and C. Method A uses the proposed method without the final modification for the peak value. Method B includes the final modification for the peak value. Finally, Method C derives test inputs by shock spectrum enveloping. The test specifications are given in Table I. The resulting shock test inputs are shown in Figures 14 and 15. The corresponding shock characterizations are shown in Figures 16-19. For purposes of comparison with shock spectrum techniques, the shock spectra for the derived shock test inputs are shown in Figures 20a-c.

Two approaches were taken in judging the consistency of the three test specification methods. First, the shock characteristics in Table II were compiled for the shock inputs derived by each method. For ease of visualization, Figure 21 was created to show the shock input characteristics normalized with respect to the field data. Figure 21 shows that

- Only Method B using a decaying sinusoid input is consistent in all categories.
- Method C generally produces conservative results except with regard to the maximum negative peak criterion.
- Methods A and B more closely match the field data than Method C in general.

Table I. Test Specifications for Methods A, B, and C.

Method**	Shock Test Technique				
	Decaying Sinusoid*			Haversine	
	A (g)	1/T (Hz)	Z	A (g)	TH (s)
A	432	1500	0.07	577	0.0067
B	570	1500	0.07	505	0.0067
C	296 1300	1550 4000	0.05 0.4	1300	0.0033

\* A compensating pulse must be added to ensure that the shaker displacement and velocity are zero at the end of the test (see Reference 10).

\*\* Method A - Matched FRMS and TRMSO.  
Method B - Method A modified to match maximum peak value.  
Method C - Current method of shock spectrum enveloping.

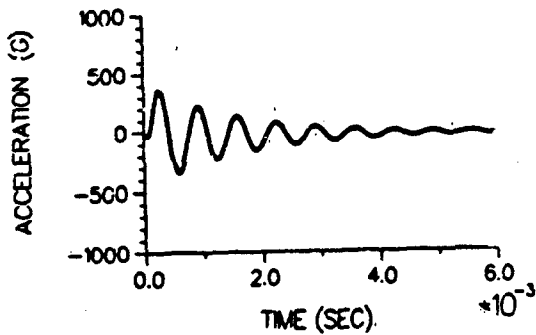


Figure 14a Test Input Derived by Method A Using Decaying Sinusoid Pulses (AD is designation in succeeding characterizations of this pulse).

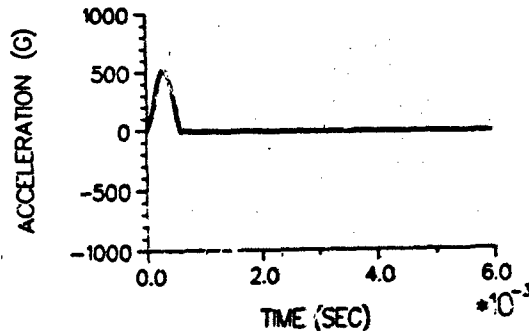


Figure 15a Test Input Derived by Method A Using a Haversine Pulse (AH is designation in succeeding characterizations of this pulse).

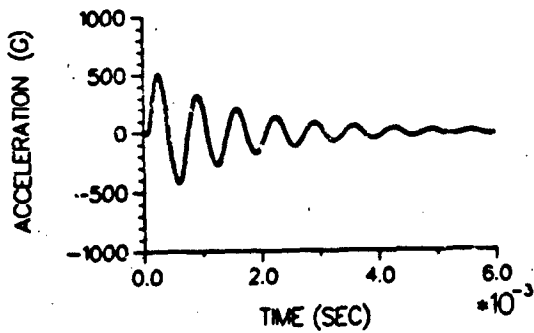


Figure 14b Test Input Derived by Method B Using Decaying Sinusoid Pulses (BD is designation in succeeding characterizations of this pulse).

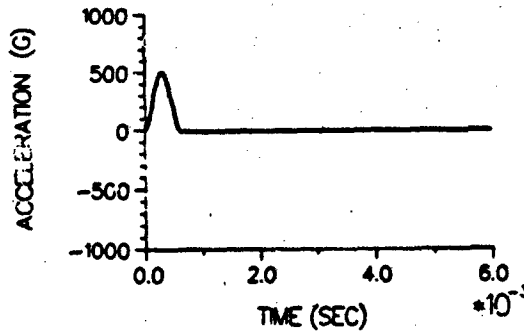


Figure 15b Test Input Derived by Method B Using a Haversine Pulse (BH is designation in succeeding characterizations of this pulse).

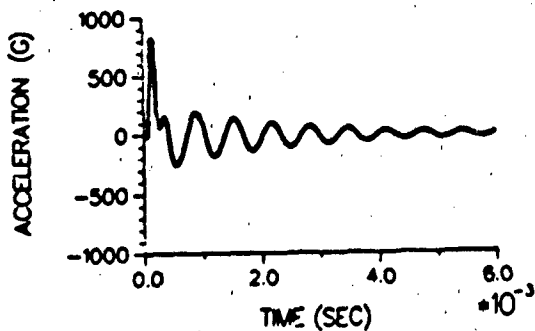


Figure 14c Test Input Derived by Method C Using Decaying Sinusoid Pulses (CD is designation in succeeding characterizations of this pulse).

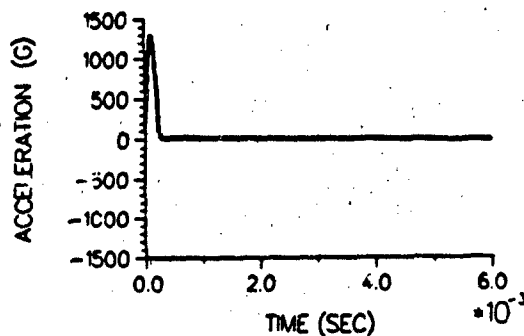


Figure 15c Test Input Derived by Method C Using a Haversine Pulse (CH is designation in succeeding characterizations of this pulse).

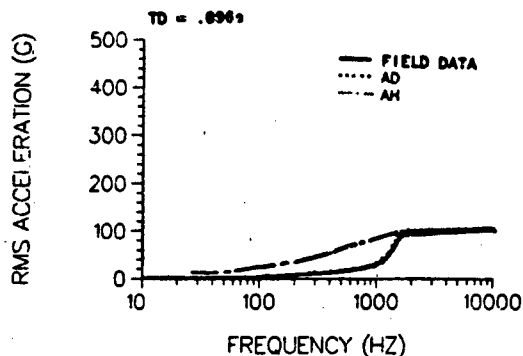


Figure 16a RMS Acceleration vs Frequency Comparison between Field Data and Method A Test Inputs.

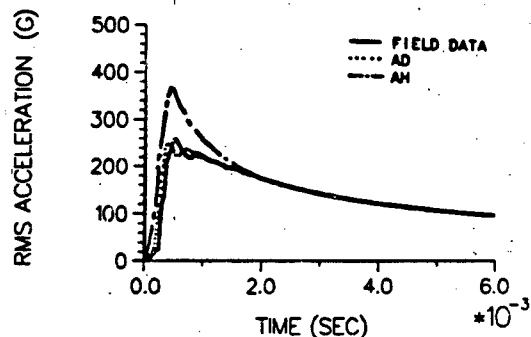


Figure 17a RMS Acceleration vs Time Comparison between Field Data and Method A Test Inputs.

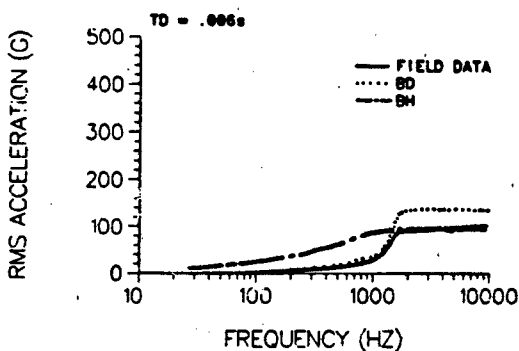


Figure 16b RMS Acceleration vs Frequency Comparison between Field Data and Method B Test Inputs.

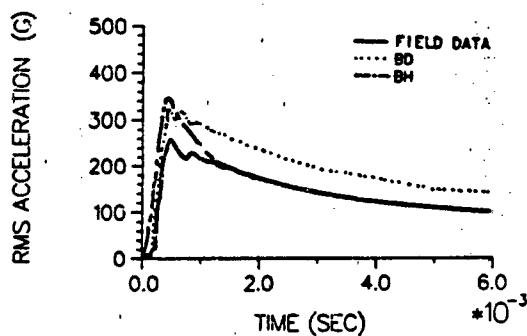


Figure 17b RMS Acceleration vs Time Comparison between Field Data and Method B Test Inputs.

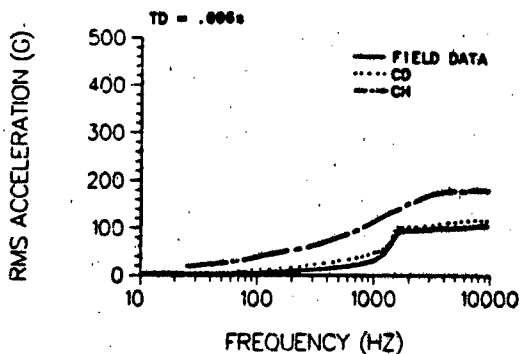


Figure 16c RMS Acceleration vs Frequency Comparison between Field Data and Method C Test Inputs.

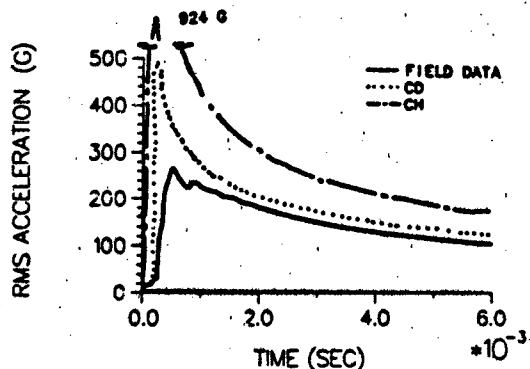


Figure 17c RMS Acceleration vs Time Comparison between Field Data and Method C Test Inputs.

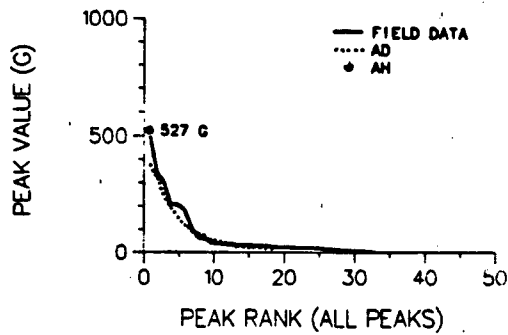


Figure 18a Ranked Absolute Peak Value Comparison between Field Data and Method A Test Inputs.

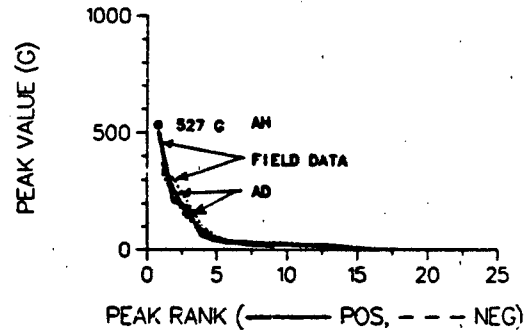


Figure 19a Ranked Positive and Negative Peak Value Comparison between Field Data and Method A Test Inputs.

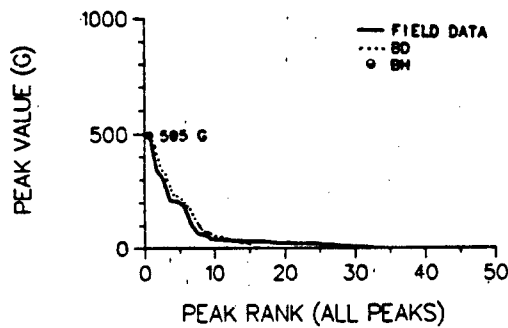


Figure 18b Ranked Absolute Peak Value Comparison between Field Data and Method B Test Inputs.

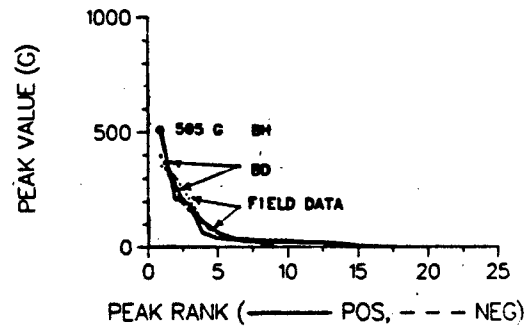


Figure 19b Ranked Positive and Negative Peak Value Comparison between Field Data and Method B Test Inputs.

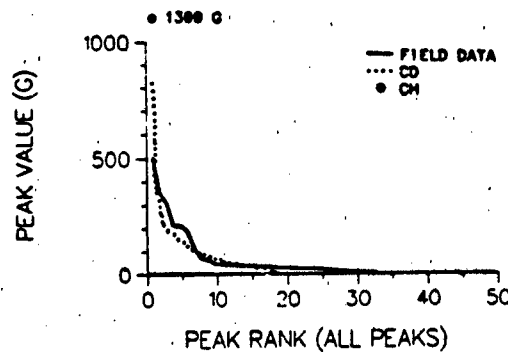


Figure 18c Ranked Absolute Peak Value Comparison between Field Data and Method C Test Inputs.

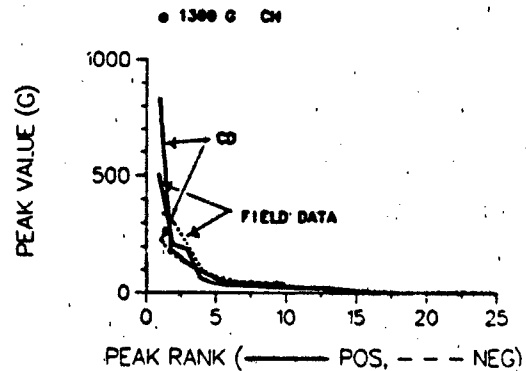


Figure 19c Ranked Positive and Negative Peak Value Comparison between Field Data and Method C Test Inputs.

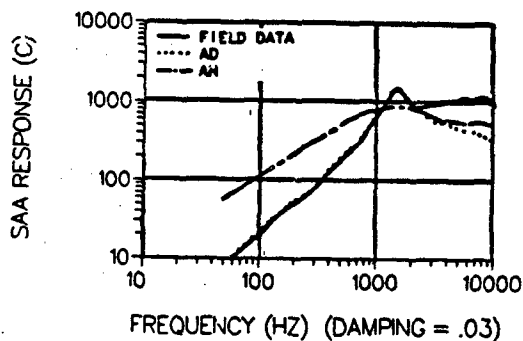


Figure 20a Shock Spectrum Comparison between Field Data and Method A Test Inputs.

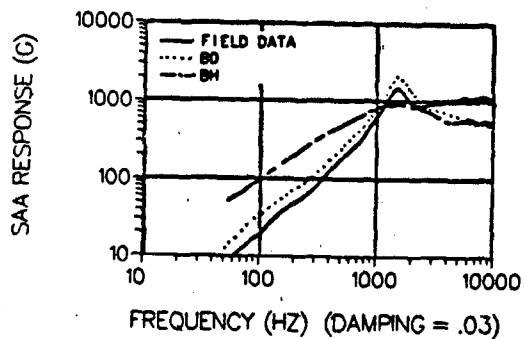


Figure 20b Shock Spectrum Comparison between Field Data and Method B Test Inputs.

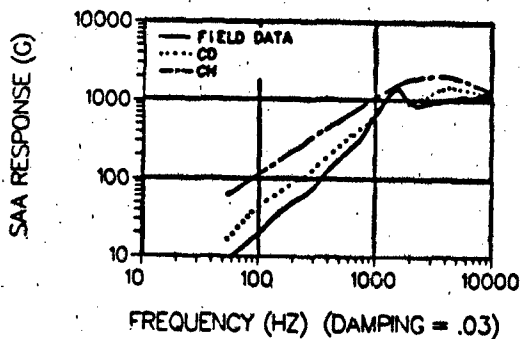
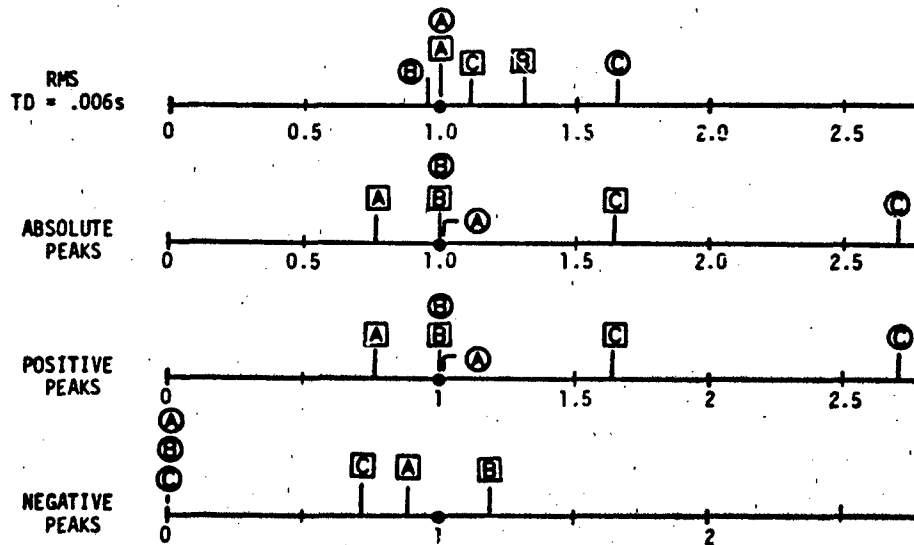


Figure 20c Shock Spectrum Comparison between Field Data and Method C Test Inputs.

Table 11. Comparison of Shock Input Characteristics (TD = .006s).

Test Spec Method*	Shock Excitation	Shock Characteristics			
		TRMSO (g)	Max Peak (g)	Max Positive Peak (g)	Max Negative Peak (g)
—	Field Data	108	505	505	352
A	Decaying Sinusoid (AD)	108	383	383	315
	Haversine (AH)	108	527	527	0
B	Decaying Sinusoid (BD)	142	505	505	418
	Haversine (BH)	104	505	505	0
C	Decaying Sinusoid (CD)	121	822	822	250
	Haversine (CH)	178	1300	1300	0

- \* Method A - Matched FRMS and TRMSO.
- Method B - Method A modified to match maximum peak value.
- Method C - Current method of shock spectrum enveloping.



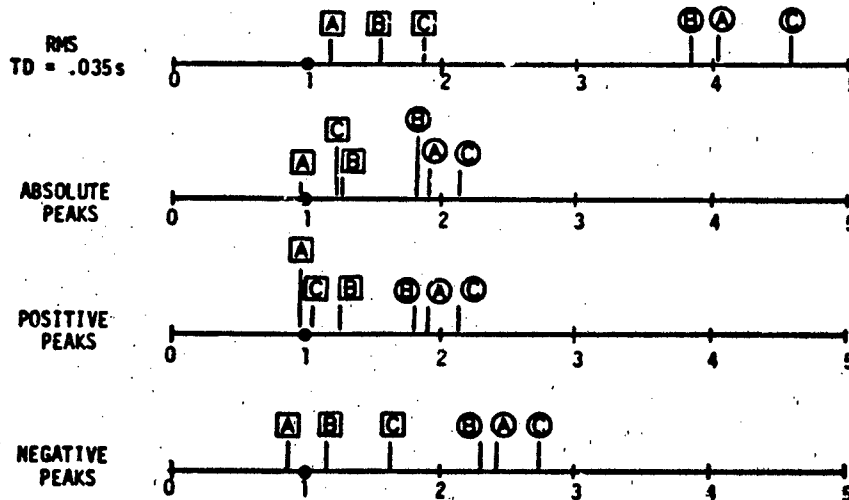
METHOD	DECAYING SINUSOD	HAVERSINE
A (FREQ/RMS)	A	A
B (FREQ/RMS/PKS)	B	B
C (SHOCK SPECTRA)	C	C

Figure 21 Normalized Shock Input Characterization. (Test Specification Value / Field Data Value).

Table III. Comparison of Shock Response Characteristics (TD = .035s).

Test Spec Method*	Shock Excitation	Shock Characteristics			
		TRMSO (g)	Max Peak (g)	Max Positive Peak (g)	Max Negative Peak (g)
—	Field Data	60	242	242	185
A	Decaying Sinusoid (AD)	70	232	232	165
	Haversine (AH)	242	463	463	448
B	Decaying Sinusoid (BD)	92	306	306	218
	Haversine (BH)	231	442	442	428
C	Decaying Sinusoid (CD)	112	301	257	301
	Haversine (CH)	274	521	521	505

\* Method A - Matched FRMS and TRMSO.  
 Method B - Method A modified to match maximum peak value.  
 Method C - Current method of shock spectrum enveloping.



METHOD	DECAYING SINUSOID	HAVERSINE
A (FREQ/RMS)	A	A
B (FREQ/RMS/PKS)	B	B
C (SHOCK SPECTRA)	C	C

Figure 22 Normalized Model Response Characterization (Test Model Response Value / Field Data Model Response Value).

As a second means of judging the consistency of the shock test inputs with the field data, each input was used to excite a MSC/NASTRAN model of a ~12.7cm (5 inch) long cantilever beam. Response time histories at the end of the beam model as well as shock characterizations are shown in the Appendix. These data are summarized in Table III and Figure 22, and correspond to the data in Table II and Figure 21. The main observations from these data are that:

- All methods are consistent in being higher than the field data except Method A which produces response peaks slightly lower than the field data.
- Responses produced by haversine inputs are always higher than those produced by decaying sinusoid inputs.

#### CONCLUSIONS

A new method of specifying decaying sinusoid and haversine shock tests has been developed and demonstrated. The method is based on the more complete characterization of both field and laboratory shock environments. These shock characterizations include time and frequency domain RMS acceleration and ranked acceleration peaks. These characterizations are shown to be very useful alternatives to shock spectrum characterizations which fail to retain valuable information about the field shock time history. Such information is essential if the field shock environment is to be simulated to the greatest extent possible in the shock laboratory.

Decaying sinusoidal shock tests specified according to the proposed method are found to produce both shock test inputs and responses which are consistent with actual field shock data. This claim cannot be made by the single shock test inputs produced by the standard method of shock test specification based on shock spectrum enveloping. The characterizations in this paper show that decaying sinusoidal shock test inputs may be below field environment levels while those produced using haversines may be considerably higher. The degree of conservatism associated with all of these test specification needs to be studied in more detail. The methods of Reference 6 provide the basis for this type of analysis.

#### REFERENCES

1. Biot, M. A., "Theory of Elastic Systems Vibrating Under Transient Impulse with an Application to Earthquake-Proof Buildings," Proceedings of the National Academy of Science, Vol. 19, No. 2, 1933, pp. 262-268.
2. Biot, M. A., "A Mechanical Analyzer for the Prediction of Earthquake Stresses," Bulletin of the Seismological Society of America, Vol. 31, 1941, pp. 151-171.
3. Rader, W. P., and W. F. Bang, "A Summary of Pyrotechnic Shock in the Aerospace Industry," Shock and Vibration Bulletin, Vol. 41, Part 5, 1970, pp. 9-15.
4. Kelly, R. D., and G. Richman, Principles and Techniques of Shock Data Analysis, The Shock and Vibration Information Center, USDOD, SVM-5, 1969.
5. Smallwood, D. O., "Time History Synthesis for Shock Testing on Shakers," Seminar on Understanding Digital Control and Analysis in Vibration Test Systems, Greenbelt, Maryland, June 1975, pp. 23-41.
6. Baca, T. J., "Characterization of Conservatism in Mechanical Shock Testing of Structures," Ph.D. Dissertation, Department of Civil Engineering, Stanford University, September 1982.
7. Spanos, P-T, D., "Digital Synthesis of Response-Design Spectrum Compatible Earthquake Records for Dynamic Analyses," The Shock and Vibration Digest, Vol. 15, No. 3, March 1983, pp. 21-30.
8. Baca, T. J., "Evaluation and Control of Conservatism in Drop Table Shock Tests," Shock and Vibration Bulletin, Vol. 53, Part 1, 1983, pp. 163-176.
9. Cooley, J. W., and J. W. Tukey, "An Algorithm for the Machine Calculation of Complex Fourier Series," Mathematics of Computation, Vol. 19, April 1965, pp. 297-301.
10. Smallwood, D. O., and A. R. Nord, "Matching Shock Spectra with Sums of Decaying Sinusoids Compensated for Shaker Velocity and Displacement Limitations," Shock and Vibration Bulletin, Vol. 44, Part 3, 1974, pp. 43-56.

#### APPENDIX

This appendix includes the time histories and response characterizations which were calculated using a MSC/NASTRAN finite element model of a 12.7 cm (5 inch) long cantilever beam excited by the test inputs derived from all three test specifications techniques using decaying sinusoid and haversine inputs. The responses are calculated at the free end of the beam.

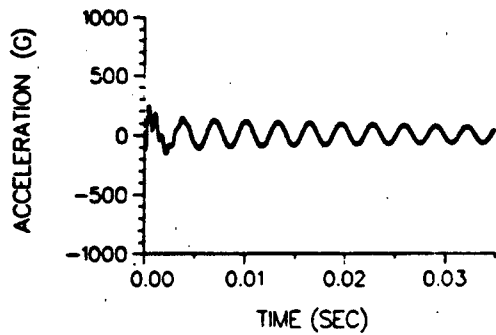


Figure A1a Calculated Model Response from Test Input Derived by Method A Using Decaying Sinusoid Pulses (AD).

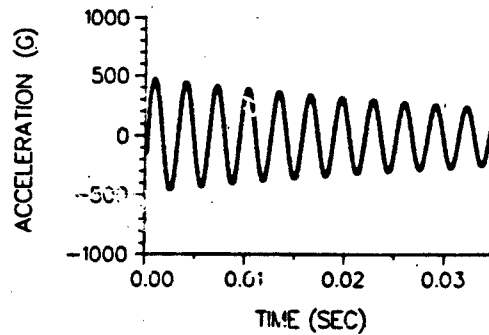


Figure A2a Calculated Model Response from Test Input Derived by Method A Using a Haversine Pulse (AH).

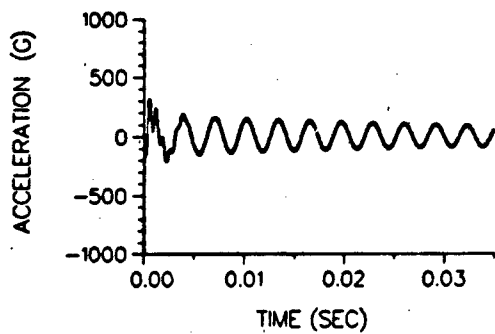


Figure A1b Calculated Model Response from Test Input Derived by Method B Using Decaying Sinusoid Pulses (BD).

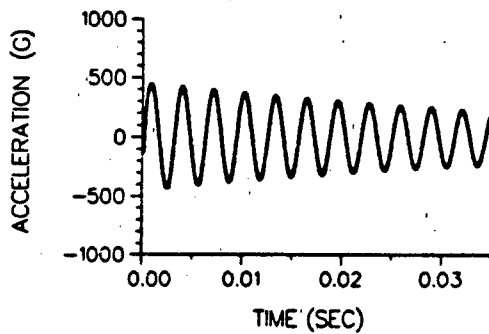


Figure A2b Calculated Model Response from Test Input Derived by Method B Using a Haversine Pulse (BH).

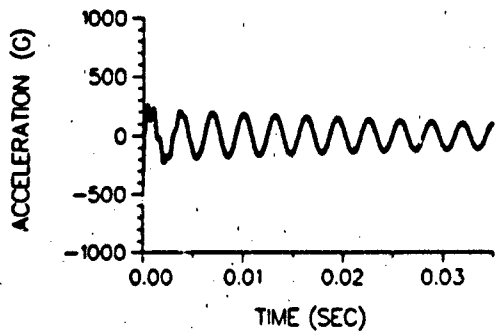


Figure A1c Calculated Model Response from Test Input Derived by Method C Using Decaying Sinusoid Pulses (CD).

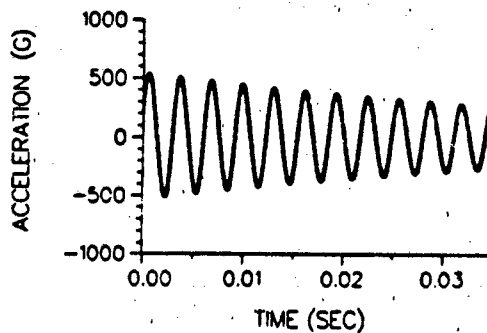


Figure A2c Calculated Model Response from Test Input Derived by Method C Using a Haversine Pulse (CH).

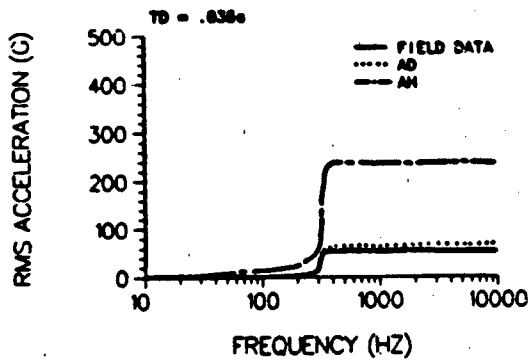


Figure A3a RMS Acceleration vs Frequency Comparison between Field Data and Method A Test Responses (Model Calculations).

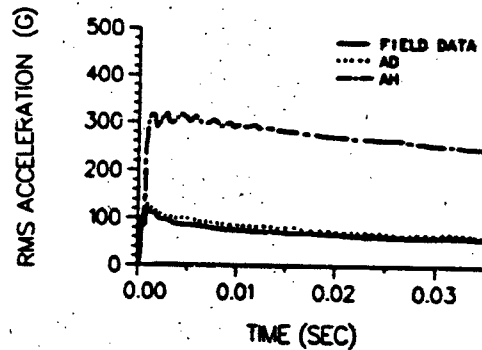


Figure A4a RMS Acceleration vs Time Comparison between Field Data and Method A Test Responses (Model Calculations).

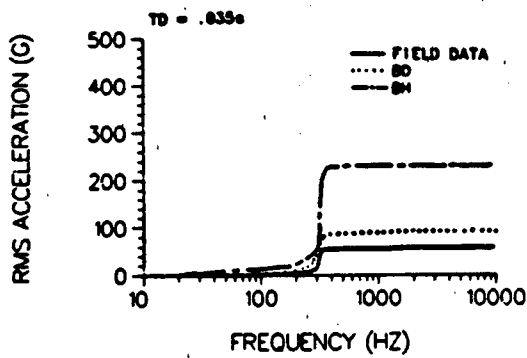


Figure A3b RMS Acceleration vs Frequency Comparison between Field Data and Method B Test Responses (Model Calculations).

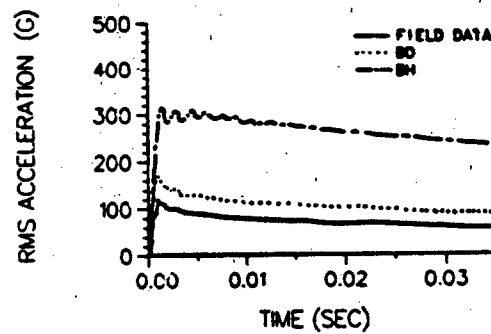


Figure A4b RMS Acceleration vs Time Comparison between Field Data and Method B Test Responses (Model Calculations).

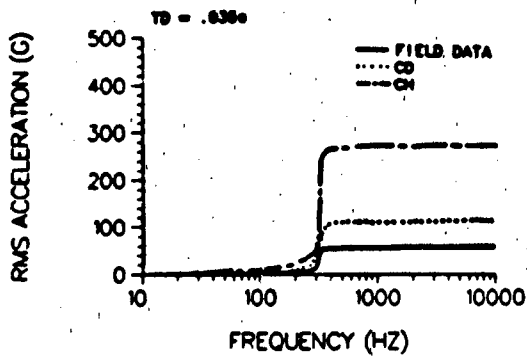


Figure A3c RMS Acceleration vs Frequency Comparison between Field Data and Method C Test Responses (Model Calculations).

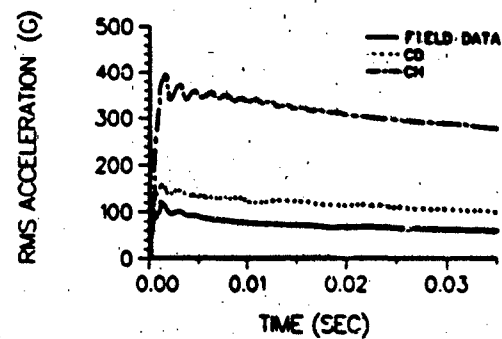


Figure A4c RMS Acceleration vs Time Comparison between Field Data and Method C Test Responses (Model Calculations).

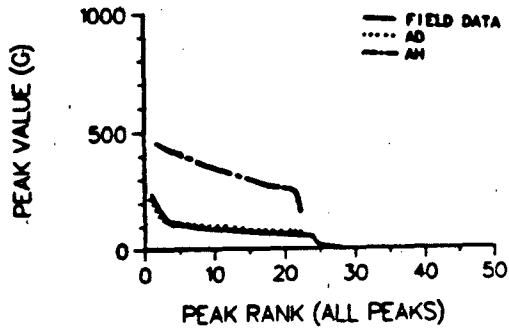


Figure A5a Ranked Absolute Peak Value Comparison between Field Data and Method A Test Responses (Model Calculation).

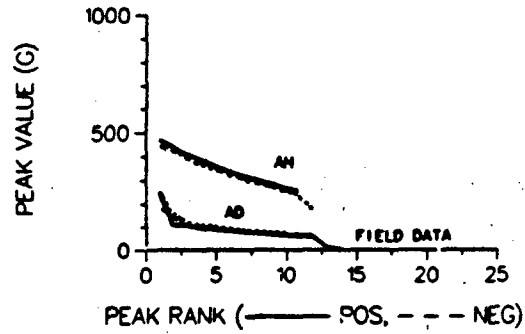


Figure A5a Ranked Positive and Negative Peak Value Comparison between Field Data and Method A Test Responses (Model Calculation).

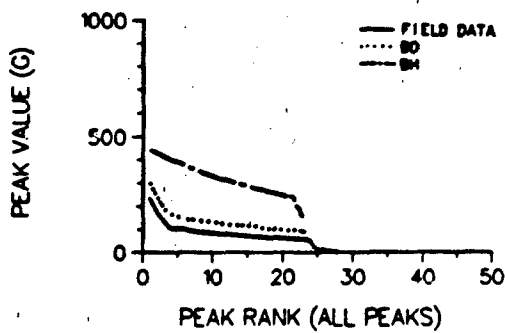


Figure A5b Ranked Absolute Peak Value Comparison between Field Data and Method B Test Responses (Model Calculation).

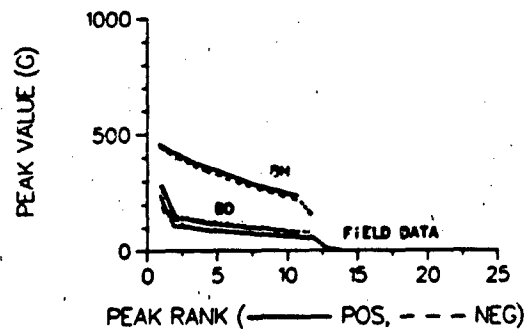


Figure A5b Ranked Positive and Negative Peak Value Comparison between Field Data and Method B Test Responses (Model Calculation).

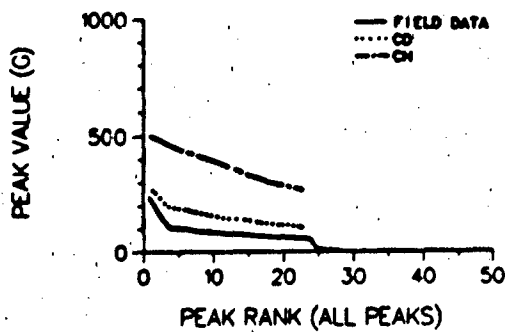


Figure A5c Ranked Absolute Peak Value Comparison between Field Data and Method C Test Responses (Model Calculation).

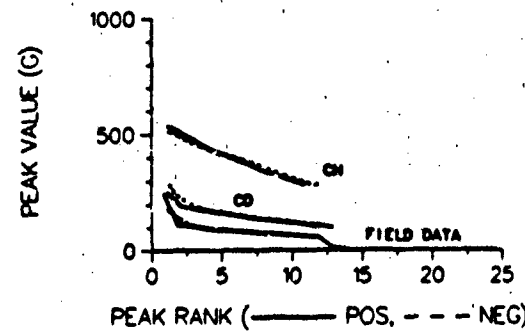


Figure A5c Ranked Positive and Negative Peak Value Comparison between Field Data and Method C Test Responses (Model Calculation).

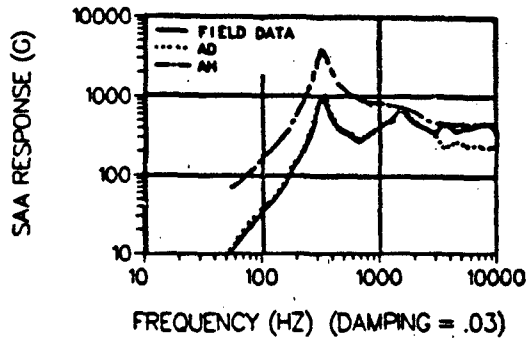


Figure A7a Shock Spectrum Comparison between Field Data and Method A Test Responses (Model Calculation).

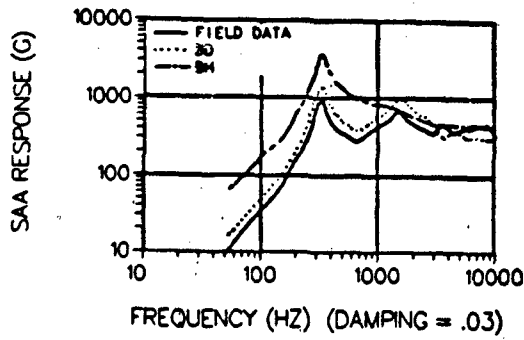


Figure A7b Shock Spectrum Comparison between Field Data and Method B Test Responses (Model Calculation).

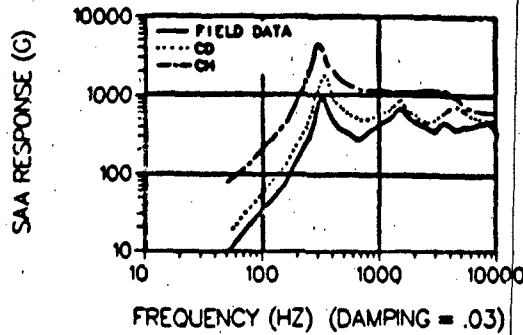


Figure A7c Shock Spectrum Comparison between Field Data and Method C Test Responses (Model Calculation).

## DISCUSSION

Mr. Strauss (Rocketdyne): Does it apply primarily to shock or transient pulses that are primarily a single frequency? Many times transient pulses have a broad band frequency content.

Mr. Baca: No, it can be applied for multiple frequencies. The example I showed was for one frequency for simplicity, but it is possible to pick out which frequencies are making the contributions to the overall rms level.

Mr. Strauss: Would you then apply multiple decaying sinusoids superimposed on each other?

Mr. Baca: Yes. Currently, when we synthesize a decaying sinusoid pulse, we are selecting different sinusoidal components to match the peaks in our shock spectra. I would match this particular frequency where I see significant energy applied in field data.

Mr. Strauss: One of the papers this morning addressed some overtest and undertest problems by using decaying sinusoids, or shaker type tests, as opposed to pyrotechnic devices which are the real source. Have you compared the different kinds of results from actual test cases on hardware?

Mr. Baca: We are currently gathering data, and we are applying both this method and the shock spectra to try to come up with some kind of an evaluation.

Mr. Coers (Lockheed): I assume the field data in these comparisons looked more like a decaying sinusoid than a haversine. Is that right?

Mr. Baca: That first plot is field data.

Mr. Coers: That is why the decaying sinusoid looked much better in this case. You have to look at the nature of the field data and make a judgment as to whether you will take a single pulse type representation or a decaying sinusoid. Is that right?

Mr. Baca: In my experience the decision is often made for you. First of all, you do have that judgment to make just because you know it is a pyrotechnic type shock versus maybe a transportation shock which has that one-sided nature, or maybe a blast shock. Even though we would like to use a decaying sinusoidal pulse, many times the G levels are such that we cannot reach that on a shaker. So, we are forced to go to a drop table type technique just to reach some of the G levels we are concerned about. That is why I feel it is important to at least address the issue of how to specify a test using the simple pulses, even though you know that is not the best way to do it.

Mr. Coers: But you try to do the best with what you have.

SHOCK RESPONSE ANALYSIS BY PERSONAL COMPUTER  
USING THE EXTENDED IFT ALGORITHM

Charles T. Morrow, Consultant  
Encinitas, California

This is the third in a series of papers on the development of the Indirect Fourier Transform algorithm for spectral analysis and shock response analysis. The first presented the basic theory and explored computation times and memory requirements. The second reported the development of a program for shock spectral analysis by computer and disclosed that the phase characteristic of the undamped residual shock spectrum could be expressed in terms of an Apparent Starting Time for shock transients. The present paper extends the algorithm to response analysis by computer for single- and multiple-degree-of-freedom systems, with specific mathematical development through two degrees.

In his report THE ENVIRONMENTAL SPECIFICATION AS A TECHNICAL MANAGEMENT TOOL, the author first recommended, on the subject of shock fundamentals, that description and specification of a shock be accomplished by the undamped residual shock spectrum. (Note that damped residuals are not uniquely defined for shocks that do not have a definite ending.) Lack of a commercial instrument to do this led to the publication of a paper on the IFT algorithm implemented on a personal computer. In the same report, the author also recommended that response computation be carried out by a computer with stored programs for various configurations of interest, so as to permit convenient exploration of benefits of proposed design changes in shock transmission paths. Again, no commercial instrument for the purpose is available -- the analog shock spectrum computer is limited to the simulation of only one degree of freedom and does not come to grips with the design problem. Extension of the IFT algorithm, as in the present paper, can permit a personal computer to compute and display responses of an arbitrary mechanical system to a shock excitation.

In multiple-degree-of-freedom systems, it is possible for the response to increase after shock termination, to levels that may cause failure or malfunction.

Once the response has become negligible, and the user has made an exit from the plotting routine, the computer displays the plot duration, the extreme values for the plot, the difference between them, and a fatigue factor that is an indication of the number of cycles of increasing stress. This display is referred to as the Fatigue Summary.

## INTRODUCTION

THE ENVIRONMENTAL SPECIFICATION AS A TECHNICAL MANAGEMENT TOOL, based on a survey of the state of shock and vibration design as influenced by organizational considerations resulting inadvertently from environmental specifications as now written, had primarily a nontechnical message. However, it did contain two technical recommendations concerning shock. The first, that description and specification of shocks be accomplished by the undamped residual shock spectrum rather than a damped maxmax spectrum, was intended to provide a better indication of shock effect on multiple-degree-of-freedom systems. (At the higher frequencies, a maxmax spectrum cannot fall below the maximum acceleration of the shock.) The second technical recommendation, that mechanical system response

computations be carried out on a computer with built-in subroutines for various equipment dynamical configurations, was intended to make it easier to carry out a systematic approach to design, especially when this must involve the crossing of organizational lines. Taken together, these recommendations amount to saying that shock description and response computation have somewhat different objectives and should be optimized accordingly.

However, both can be accomplished by variations of the same algorithm. The Indirect Fourier Transform algorithm, based in part on early papers by Southworth and O'Hara, takes its name from the facts that the undamped residual shock spectrum can be computed by sequential consideration of data points in a shock time history and that the Fourier transform, if desired, can

be computed indirectly from this, with consequent saving in computer memory requirements. Extension of the algorithm permits computation of the shock response of any linear mechanical system to an arbitrary shock, without making an inverse Fourier transformation. The most basic fundamentals for both applications and the development of a computer program for spectral analysis have been discussed in depth in two previous papers.

In brief, if a shock excitation can be approximated by a finite series of RAMPs plus possibly a few STEPs, and if the response of a linear mechanical system to both RAMPs and STEPs is known, then the response of the system to the shock can be computed in terms of a general equation with several coefficients, which are updated as time passes through the data points. Should the mechanical system be an undamped simple resonator, the final values of the trigonometric coefficients determine an undamped residual shock spectrum, simply related in both magnitude and phase (if a time shift is made from  $t-t_k$  to  $t$  in the exponentials and trigonometric functions) to the Fourier transform of the shock.

The theory starts with the differential equations for the mechanical system. Laplace transforms are taken, term by term. The resulting simultaneous equations are solved algebraically for the transform of the variable of interest, in relation to that of the acceleration of the base. This transform is evaluated for both RAMP and STEP. Inverse Laplace transforms are then obtained by the Heaviside expansion theorem. An equation sufficiently general to express the response after time  $t_k$  to any succession of RAMPs and STEPs is

$$a(t, t_k) = B_k + C_k(t-t_k) + \sum_{i=1}^n D_{i,k} e^{-\alpha_i(t-t_k)} \cos 2\pi f_i(t-t_k) + \sum_{i=1}^n E_{i,k} e^{-\alpha_i(t-t_k)} \sin 2\pi f_i(t-t_k). \quad (1)$$

For response evaluation at  $t = t_k$ , this reduces to:

$$a(t=t_k) = B_k + \sum_{i=1}^n D_{i,k} \quad (2)$$

In this form, the equation, with  $t-t_k$  in the arguments of the exponential and trigonometric functions, is suitable for a constant-time-increment  $\Delta t = t_k - t_{k-1}$  version of the algorithm, or for a hybrid version with data inputs for some but not all values of the integer  $k$ . The difference between constant and hybrid is not primarily in the spectral or response computations but in the data inputs required by the computer and the prompts supplied to the user. For hybrid-time-increment inputs, there are prompts for both the integer  $k$  and the corresponding acceleration. For constant-time-increment inputs,  $k$  is incremented automatically as needed, provided the user identifies the input as a RAMP or STEP by adding, for a STEP, an S immediately after the number representing the acceleration. Only acceleration prompts and acceleration inputs are required for constant-increment time. A variable-time-increment version of the algorithm is also available in the program, for spectral analysis only, so that any significant spectral error produced by confining data inputs to multiples of a constant time increment can be

observed.

In the absence of further data inputs, Equation (1) would still be valid after  $t_{k+1}$ . To benefit from the simplicity of Equation (2), it at least receives a time shift before evaluation of the next instantaneous response, except when there is an initial STEP or a STEP after a RAMP. A shift from  $t-t_k$  to  $t-t_{k+1}$  is accomplished by the equations:

$$B_{k+1} = B_k + C_k \Delta t \quad (3)$$

$$C_{k+1} = C_k \quad (4)$$

$$D_{i,k+1} = D_{i,k} e^{-\alpha_i \Delta t} \cos 2\pi f_i \Delta t + E_{i,k} e^{-\alpha_i \Delta t} \sin 2\pi f_i \Delta t \quad (5)$$

and

$$E_{i,k+1} = D_{i,k} e^{-\alpha_i \Delta t} \sin 2\pi f_i \Delta t - E_{i,k} e^{-\alpha_i \Delta t} \cos 2\pi f_i \Delta t \quad (6)$$

which follow from the obvious properties of the exponential and from the formulas for trigonometric functions of sums and differences of angles.

If a STEP or the beginning of a RAMP occurs at time  $t_k$ , there must be a corresponding updating of the coefficients of Equation 1. Neither this operation nor the time-shift operation appreciably slows down response computation or plotting as system complexity increases. However, for each mechanical system there must be a determination of system natural frequencies and system decrements and a determination of the amounts by which the coefficients must be changed for each RAMP or STEP input. This one-time computation, which rapidly becomes more complicated with increasing complexity in the mechanical system of interest, is the primary focus of the present paper.

#### GENERAL CONSIDERATIONS concerning complex systems

Fortunately, there are a number of a-priori requirements that can be used to check the validity of numerical responses if not always the formulas on which the computations are based:

1. A RAMP response is always the time integral of the corresponding STEP response.
2. A STEP response is always the time derivative of the corresponding RAMP response.
3. A STEP of acceleration can not produce in response an absolute acceleration term proportional to time.
4. All steady absolute acceleration responses in response to a unit STEP are unity.
5. A RAMP of acceleration can not produce a steady response acceleration.
6. All absolute accelerations proportional to time in response to a unit-slope RAMP have unit slope.
7. In any response to a STEP, the sum of the cosine coefficients must sum to zero with the steady response term in order to avoid a discontinuity. (For a simple resonator, the cosine coefficient and the steady response term must sum to zero.)

8. In any response to a RAMP, the derivatives of all response terms must sum to zero at time zero in order to avoid a slope discontinuity. In other words, the sum of the sine coefficients, each divided by the corresponding system angular frequency, minus the sum of the cosine coefficients, each divided by the corresponding system decrement, must equal the coefficient of the time-proportional term. (For the simple resonator, this reduces to a relationship among three coefficients.)

9. In any response to a STEP, the total described in Requirement 8 must be zero, to avoid a change of slope.

10. In any response to a RAMP, the sum of the cosine coefficients must be zero in order to avoid a discontinuity. (For the simple resonator, the cosine coefficient must be zero.)

11. For a simple resonator or terminal resonator in a series, the steady relative displacement produced by a unit STEP is  $m_j/k$  or  $1/\omega_{pj}^2$  or  $1/2\pi f_{pj}^2$ , where  $f_{pj}$  is the undamped part resonance frequency. There is no term proportional to time. Requirement 9 also applies.

12. For a simple resonator or terminal resonator in a series, the acceleration proportional to time produced by a unit-slope RAMP has the coefficient  $1/\omega_{pj}^2$  or  $1/2\pi f_{pj}^2$ . There is no constant term. Requirement 8 also applies.

13. For the j'th resonator along a linear transmission path with n resonators, the steady relative displacement produced by a unit STEP is

$$(1 + \sum_{j=1}^n m_j/m_j) / \omega_{pj}^2 = (1 + \sum_{j=1}^n m_j/m_j) / 4\pi^2 f_{pj}^2, \quad (7)$$

where  $f_{pj}$  is the undamped natural frequency of the j'th resonator. Requirement 9 also applies.

14. For the j'th resonator along a linear transmission path with n resonators, the relative displacement proportional to time has as a coefficient the expression of Equation (7). Requirement 8 also applies.

Requirements 1 and 2 are two ways of expressing the same relationship. In checking the validity of results, differentiation may often be more convenient than integration, but integration may be more suitable in deriving some relationships. These requirements lead in turn to Requirements 3 and 5. Requirement 4 is a matter of statics, which apply after a shock is over and any response transients have decayed. Any discontinuity of response or response slope would require at least a discontinuity in the displacement of the base, to make a sudden compression of a spring. This does not happen with a RAMP or STEP. Requirement 6 follows from Requirements 5 and 1. Requirements 11 and 13 are again a matter of statics. With Requirement 1, they lead to Requirements 12 and 14. Requirement 13 demands only that the resonators through the j'th be in a linear transmission path. For special cases that do not comply with this, analogous but more complicated expressions can be devised.

In practical implementation of the algorithm, the computer inserts a RAMP to zero slope after each STEP. Should the actual excitation slope be otherwise, this will be corrected by the next RAMP input.

#### RESPONSE LAPLACE TRANSFORMS for damped simple resonator

If the displacement differential equation for the simple damped resonator is differentiated through twice to express it in terms of acceleration,

$$m_1 d^2 a_1 / dt^2 + c_1 d(a_1 - a_0) / dt + k_1 (a_1 - a_0), \quad (8)$$

where  $a_1$  is the response acceleration of the mass and  $a_0$  is the excitation of the base. Take the Laplace transform term by term and solve for  $L_1$ , the transform of  $a_1$ , in terms of  $L_0$ , the transform of  $a_0$ :

$$L_1 = [(m_1^2 + 2\alpha_{p1}s) / (s^2 + 2\alpha_{p1}s + \omega_{p1}^2)] L_0 \\ = [1 - s^2 / (s^2 + 2\alpha_{p1}s + \omega_{p1}^2)] L_0. \quad (9)$$

Obtain the transform of the relative displacement by subtracting  $L_0$  and dividing by  $s^2$  to express the effect of double integration with respect to time:

$$L_{d10} = -[1 / (s^2 + 2\alpha_{p1}s + \omega_{p1}^2)] L_0. \quad (10)$$

The roots of denominator are:

$$s_1 = -\alpha_1 + j\omega_1, \quad s_1^* = -\alpha_1 - j\omega_1, \quad (11)$$

with

$$\alpha_1 = \alpha_{p1}, \quad (12)$$

and

$$\omega_1^2 = \omega_{p1}^2 - \alpha_{p1}^2. \quad (13)$$

These roots represent the natural frequencies of the simple system.

For unit STEP

$$L_0 = 1/s, \quad (14)$$

and for unit-slope RAMP

$$L_0 = 1/s^2. \quad (15)$$

#### RESPONSES of damped simple resonator

For the unit STEP, substitute  $1/s$  in Equations (9) and (10) and apply the Heaviside expansion theorem to obtain:

$$a_1 = 1 - e^{-\alpha_1 t} \cos \omega_1 t + (\alpha_1 / \omega_1) e^{-\alpha_1 t} \sin \omega_1 t \quad (16)$$

and

$$x_1 - x_0 = -1/\omega_{p1}^2 + (1/\omega_{p1}^2) e^{-\alpha_1 t} \cos \omega_1 t \\ + (\alpha_1 / \omega_{p1}^2 \omega_1) e^{-\alpha_1 t} \sin \omega_1 t. \quad (17)$$

For the unit-slope RAMP, substitute  $1/s^2$  for  $L_0$  in Equations (9) and (10) and apply the Heaviside expansion theorem to obtain:

$$a_1 = t - (1/\omega_1) e^{-\alpha_1 t} \sin \omega_1 t \quad (18)$$

and

$$x_1 - x_0 = -t/\omega_{p1}^2 - (2\alpha_1/\omega_{p1}^4)e^{-\alpha_1 t} \cos \omega_1 t + [(\omega_1^2 - \alpha_1^2)/\omega_{p1}^4 \omega_1] e^{-\alpha_1 t} \sin \omega_1 t. \quad (19)$$

Replace  $t$  in the exponential and trigonometric arguments by  $t-t_k$  for a RAMP or STEP starting at  $t_k$ . The resulting equations, multiplied by the actual step or change of slope, show how much the coefficients  $D_1$  and  $C_1$  in Equation (1), for absolute acceleration or relative displacement, must be changed to reflect the addition of the new response.

#### LAPLACE TRANSFORMS for damped double resonator

The differential equations for the damped two-degree-of-freedom mechanical system are:

$$m_2 d^2 a_2 / dt^2 + c_2 d(a_2 - a_1) / dt + k_2 (a_2 - a_1) = 0 \quad (20)$$

and

$$m_1 d^2 a_1 + c_1 d(a_1 - a_0) / dt + c_2 d(a_1 - a_2) + k_1 (a_1 - a_0) + k_2 (a_1 - a_2) = 0. \quad (21)$$

Taking the Laplace transform term by term yields:

$$m_2 s^2 L_2 + c_2 s(L_2 - L_1) + k_2 (L_2 - L_1) = 0 \quad (22)$$

and

$$m_1 s^2 L_1 + c_1 s(L_1 - L_0) + c_2 s(L_1 - L_2) + k_1 (L_1 - L_0) + k_2 (L_1 - L_2) = 0. \quad (23)$$

Solving these two simultaneous equations algebraically yields as the transforms of the absolute accelerations:

$$L_2 = [(\omega_{p1}^2 + 2\alpha_{p1} s)(\omega_{p2}^2 + 2\alpha_{p2} s) / DJL_0] \quad (24)$$

and

$$L_1 = [(\omega_{p1}^2 + 2\alpha_{p1} s)(\omega_{p2}^2 + 2\alpha_{p2} s^2) / DJL_0]. \quad (25)$$

The Laplace transforms of the relative displacements are obtained by subtracting  $L_1$  from  $L_2$  and  $L_1$  from  $L_0$ , and then dividing the two resulting equations by  $s^2$  to express the effect of a double integration:

$$L_{d21} = -[(\omega_{p1}^2 + 2\alpha_{p1} s) / DJL_0] \quad (26)$$

and

$$L_{d10} = -[(1 + m_2/m_1)(\omega_{p2}^2 + 2\alpha_{p2} s + s^2) L_0 / D]. \quad (27)$$

The denominator of the last four equations is:

$$D = [(\omega_{p1}^2 + 2\alpha_{p1} s + (1 + m_2/m_1)s^2)(\omega_{p2}^2 + 2\alpha_{p2} s) + (\omega_{p1}^2 + 2\alpha_{p1} s + s^2)s^2] \\ = (s - s_1^*)(s - s_1^*)(s - s_2^*)(s - s_2^*) \\ = (s + \alpha_1 - j\omega_1)(s + \alpha_1 - j\omega_1)(s + \alpha_2 - j\omega_2)(s + \alpha_2 + j\omega_2), \quad (28)$$

where the roots represent the system natural or resonance frequencies and the asterisk denotes a complex conjugate. The mass ratio,  $m_2/m_1$ , which for small values can lead to dangerously large responses in  $m_2$ , appears only in the relationships between part and system complex frequencies. After evaluation of  $L_1$  for STEP or RAMP, according to Equations (12) and (13), in the inverse Laplace transformation of these equations by the Heaviside expansion theorem, each root leads to an exponential term of form

$$e^{(-\alpha + j\omega)t} = e^{-\alpha t} e^{j\omega t} \quad (29)$$

or

$$e^{(-\alpha - j\omega)t} = e^{-\alpha t} e^{-j\omega t}, \quad (30)$$

with the same complex coefficients for complex conjugate frequencies, so that the relationships

$$e^{-\alpha t} (e^{j\omega t} - e^{-j\omega t}) = 2e^{-\alpha t} \cos \omega t \quad (31)$$

and

$$e^{-\alpha t} (e^{j\omega t} + e^{-j\omega t}) = 2e^{-\alpha t} \sin \omega t \quad (32)$$

may be applied to yield responses in the form of exponentially decaying sinusoids. The variable  $t$  may be replaced by  $t-t_k$  to express the effect of a RAMP starting or a STEP occurring at time  $t_k$ .

#### INVERSE TRANSFORMATIONS for the double resonator

In the performance of the inverse transformation, the double resonator presents the problems of more complicated mechanical systems. Yet it is simple enough for two limiting cases to provide some valuable insight. If the mass ratio  $m_2/m_1$  is negligible, the transfer function (ratio of transforms of input acceleration and output acceleration) reduces to the product of the transforms for the individual resonators. (A similar limiting relationship holds for a series of resonators arranged sequentially along a shock transmission path.) The system resonances are the same as the part resonances. This can be used as a check on the validity of computer results for more complicated cases. Of greater interest is the fact that the roots can be found in closed form, algebraically, if  $L_{d21}$  resonators are undamped. Setting the denominator  $D$  equal to zero still yields a fourth-power equation, but the third-power and first-power terms are zero. The system decrements  $\alpha_1$  and  $\alpha_2$  are zero. The system angular frequencies may be obtained from the formula

$$\omega_2^2 = b/2 + (1/2)(b^2 - 4c)^{1/2} \quad (33)$$

and

$$\omega_1^2 = b/2 - (1/2)(b^2 - 4c)^{1/2}, \quad (34)$$

where

$$b = \omega_{p1}^2 + \omega_{p2}^2 (1 + m_2/m_1) \quad (35)$$

and

$$c = \omega_{p1}^2 \omega_{p2}^2. \quad (36)$$

(Note that the roots are actually of imaginary form

$s = j\omega$ . This is allowed for in the signs in the above equations.)

In Laplace transform theory, it is pointed out that the Heaviside expansion theorem has problems if two complex roots are identical, but this need not be a concern. The frequencies given by Equations (33) and (34) can not be identical unless the mass ratio  $m_2/m_1$  is zero, and a similar behaviour may be expected for more complicated mechanical systems. The smaller the ratio (as in the case of a small sliding contact within a massive potentiometer) the closer the system frequencies can be in the event of bad design, and the larger the consequent shock response in the second mass.

In the shock response program as it now stands, the computer prints out the numerical coefficients for the various powers of  $s$  in  $D$  after the part frequencies and  $Q$ 's have been put in by the user, so that the roots can be found by an independent purchased BASIC program. If this has already been done or the roots have been measured, on continuation the coefficients disappear from the video screen to provide a more compact data record, and prompts appear for the system frequencies and decrements.

#### SAMPLE RESPONSES for simple and double resonators

Figures 1 and 2 show the data inputs, except for a one-millisecond time increment already selected but not illustrated, with hybrid time increment data processing, for a 100-g 10-millisecond terminal peak sawtooth, which is verified for accuracy in Figure 3. The shock-end marker at the left, marking the last data input, will also appear on all response plots. Figure 4 shows the fatigue summary that would be applicable if the plot were representative of the actual stress in the test item. The fatigue factor is obtained by summing the absolute values of all acceleration changes that would increase stress and dividing by the difference of the extreme values. If there were two sawtooths in succession, the fatigue factor would be two. On the other hand, if the second sawtooth were in the negative direction, the difference of the extreme values would double, but the fatigue factor would be unity. For the response plots to follow, the fatigue factors are only approximate, as responses were not completely negligible by the ends of the plots. It should be possible later to devise a computer correction for termination error. Response fatigue factors tend to be more characteristic of the damping of the test item than of the character of the shock, but they serve to remind one that a single large stress may not cause failure or malfunction. (Have you ever tried to break an obsolete credit card by a single folding?)

One can at this point examine the undamped residual shock spectrum of Figure 5 to obtain some feeling for the probable effect of the shock on the test item and, if one wishes, examine the Apparent Starting Time of Figure 6 to be sure that there is a degree of simultaneity of the effects of the shock at various frequencies.

Figure 7 shows data inputs for a sample test item with a single resonance at 100 Hz and a  $Q$  of 20. The absolute acceleration response of the mass is plotted in Figure 8. Most of the response of interest occurs well after the shock is over. If the plot is allowed to scroll upward to provide a frame such as Figure 9, the

response eventually decreases. The fatigue summary of Figure 10 shows a fatigue factor approaching 7 because of the continuing oscillations. The relative displacement response is shown in Figure 11, with a Fatigue Summary in Figure 12. Note that, even at 100 Hz, the displacement amounts to a significant fraction of an inch.

This version of the extended algorithm could readily be made to yield maximax shock spectra in absolute acceleration or relative displacement. Computation time would be somewhat longer than for the undamped residual, and maximax spectra are less indicative of the continuing response after shock termination, especially in multiple-degree-of-freedom systems. However, maximax relative displacement spectra could be useful in the design of shock isolators for adequate sway space.

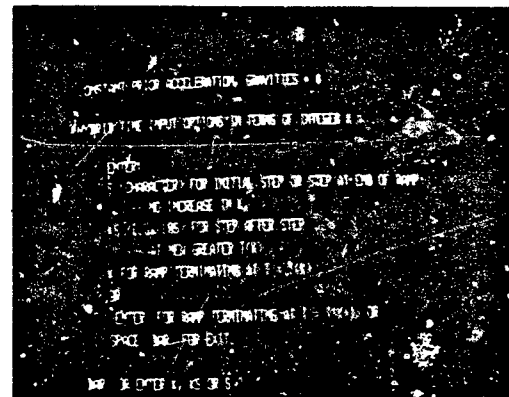


Figure 1. Data for Sawtooth Shock, Prompt

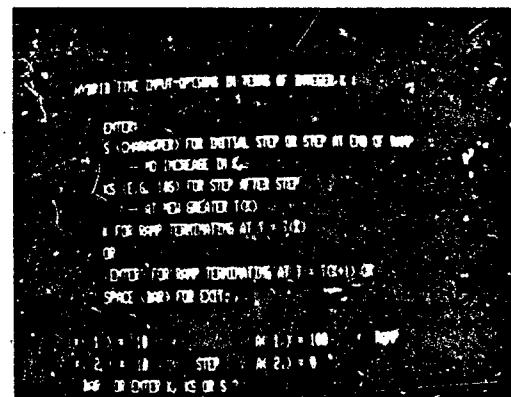


Figure 2. Data for Sawtooth Shock



Figure 3. Plot of Sawtooth Shock

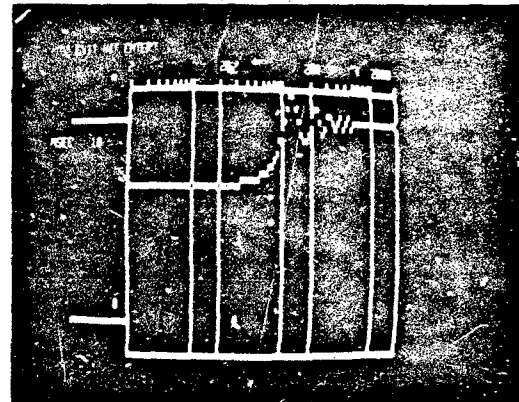


Figure 6. Residual Apparent Starting Time

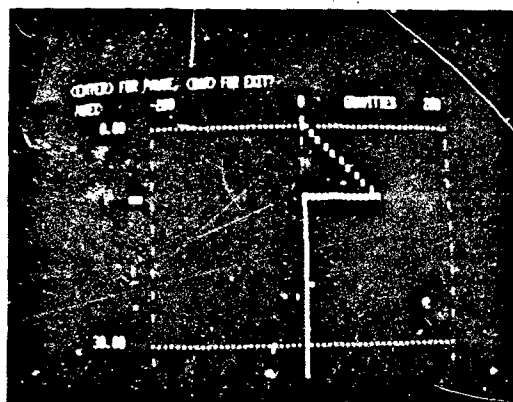


Figure 4. Fatigue Summary, Sawtooth Shock

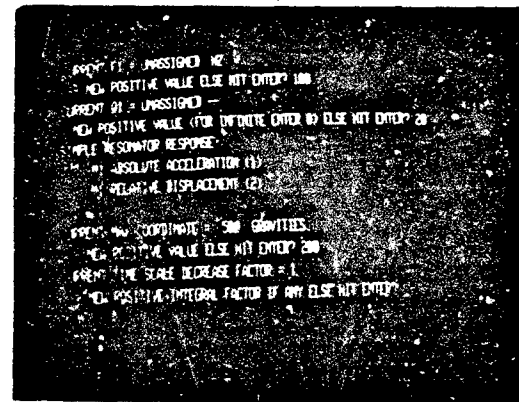


Figure 7. Description of Simple Resonator

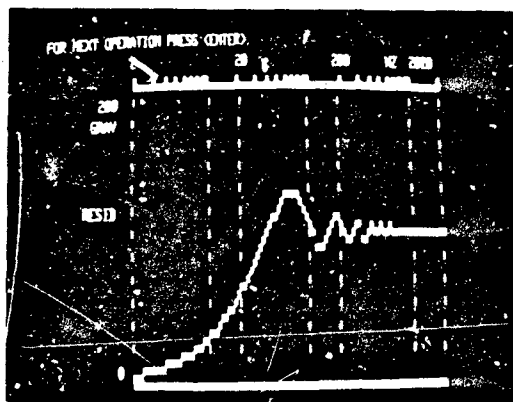


Figure 5. Undamped Residual Shock Spectrum

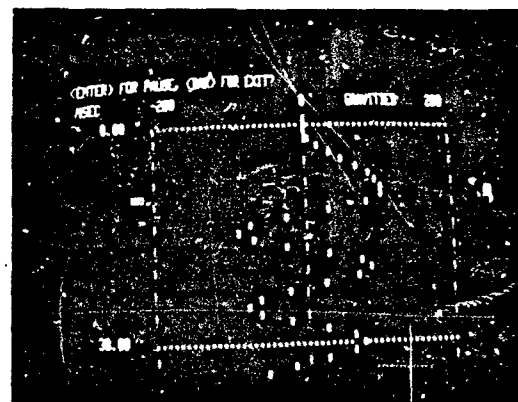


Figure 8. Resonator Initial Response

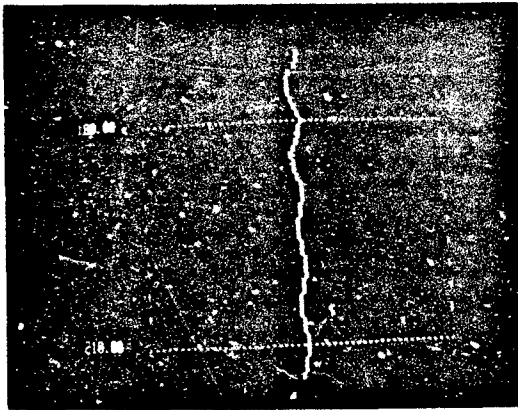


Figure 9. Later Response of Resonator

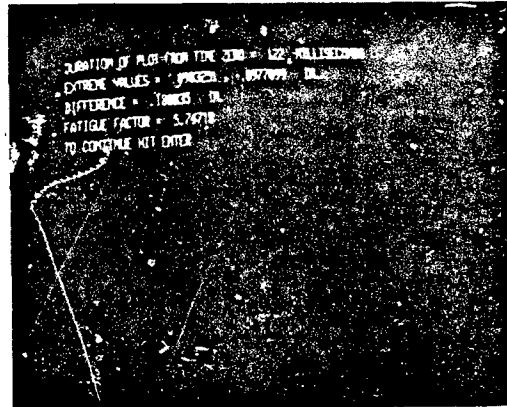


Figure 12. Fatigue Summary, Relative Displacement

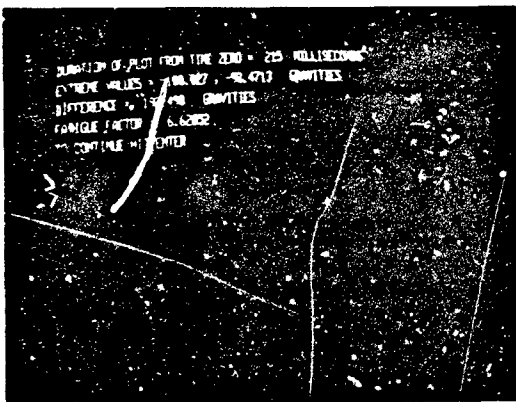


Figure 10. Fatigue Summary, Absolute Acceleration

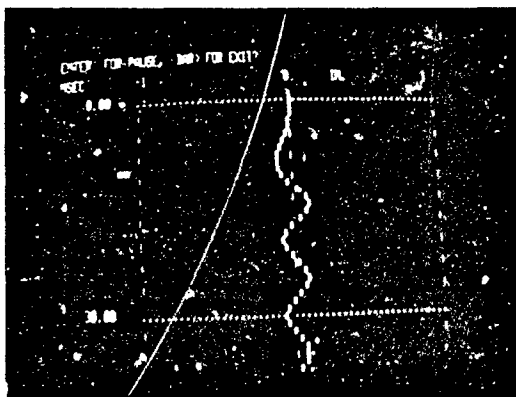


Figure 11. Relative Response in Simple Resonator

Before proceeding to two-degree-of-freedom systems, the scale is changed as in Figure 13, to permit plotting larger responses. Figure 14 and 15 show data inputs for a double resonator with a frequency of 100 Hz and a Q of 20 for both resonators and a mass ratio  $m_2/m_1$  of 1/40. The angular frequency and decrement values are supplied by the computer. After the mass ratio is ENTERed, the computer immediately computes and displays, as in Figure 15, the coefficients for the various terms in the denominator of the Laplace transforms. These can be put into an independent root computation; or if this has already been done or the system complex frequencies have been measured, pressing the ENTER key clears away the coefficient information and provides prompts for the root values. In Figure 16, these have been inserted, the computer displays also the system frequencies in Hz and the Q values, and the user has selected the absolute acceleration of the second mass for plotting. This is shown in Figure 17 as a paper printout obtained as the plot scrolled up the video screen. To make the curve more readable, some of the points have been connected by pencil lines. Note that the response amplitude actually increases after the shock is over, then decreases and increases again, and so on. This is a beating effect resulting from the fact that there are two nearly equal system frequencies in the response with very nearly equal initial amplitudes. The energy for increased response in the second resonator comes from decreased response in the first resonator -- the decrease does not have to be very much because  $m_1$  is much larger than  $m_2$  and can hold more energy. Figure 13 shows the Fatigue Summary.

Figures 17 and 18 should be convincing evidence that shock spectral analysis and response estimation have been too obsessed with the simple resonator and with response during a shock. The application of damping in shock spectra has blurred the fundamentals of shock description while not necessarily yielding more realistic estimates of test hardware stress. Excessive emphasis on the shock spectrum as a general response estimate has diverted attention from beneficial design changes that might be carried out with negligible cost and schedule penalties.

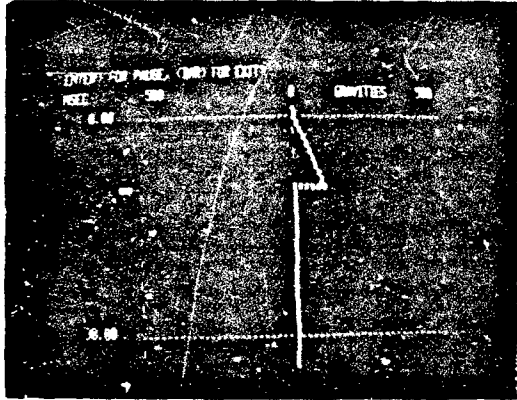


Figure 13. Change of Scale



Figure 16. System Roots Entered

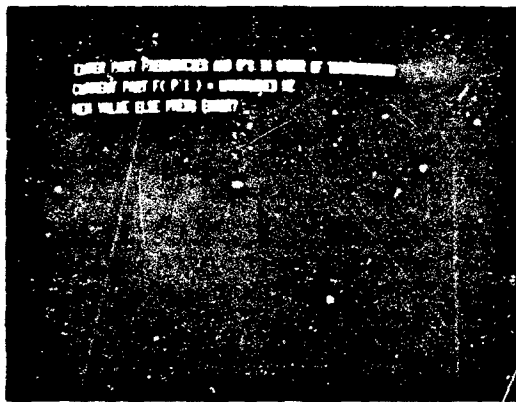


Figure 14. Description of First Double Resonator

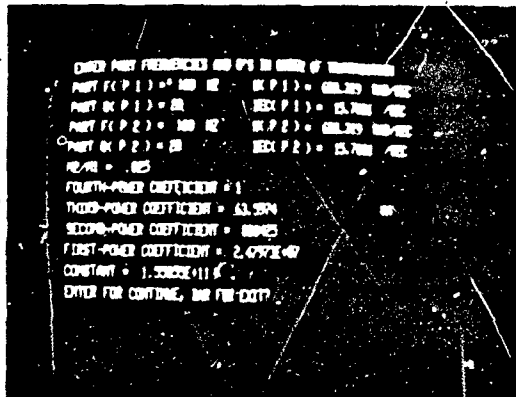


Figure 15. Polynomial Coefficients Computed

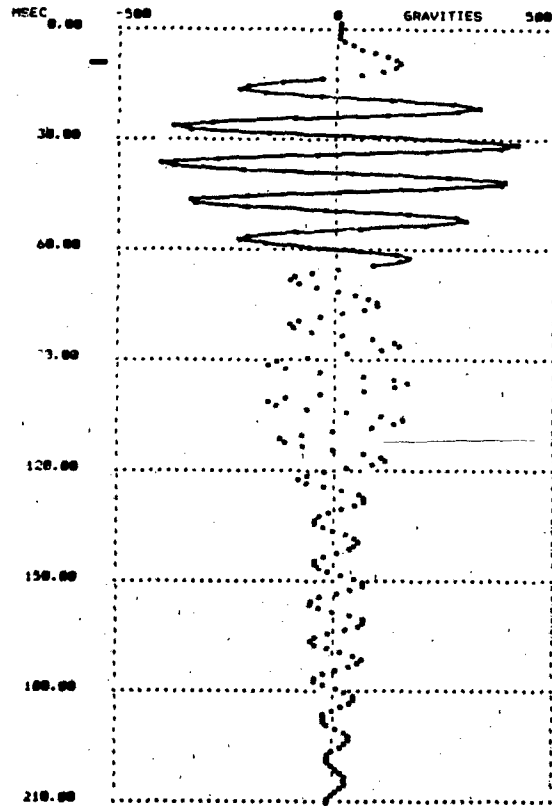


Figure 17. Absolute Response of Second Mass

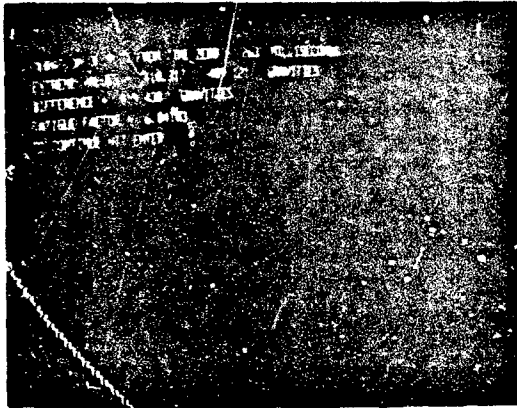


Figure 16. Fatigue Summary, Second Mass

To decrease the shock transmission in this case, damping would be attractive in principle. It would lower the fatigue factor, which would be beneficial if the method of damping did not decrease the fatigue resistance. But damping might be difficult to carry out in practice. Figure 19 shows data inputs for a detuning of the part frequency of the second resonator to 200 Hz. Figure 20 shows the resulting plot and Figure 21 shows the Fatigue Summary. Almost the same results would be obtained if the first resonator rather than the second were detuned to 200 Hz -- the response plots would be almost undistinguishable. Depending on the circumstances, either approach could result in a beneficial redesign, which could be carried out with confidence in the benefit to be obtained. If the second mass should not be accessible for instrumentation during shock, there might be no other way to obtain a quantitative estimate of the benefit than to use a computation algorithm like the IFT.

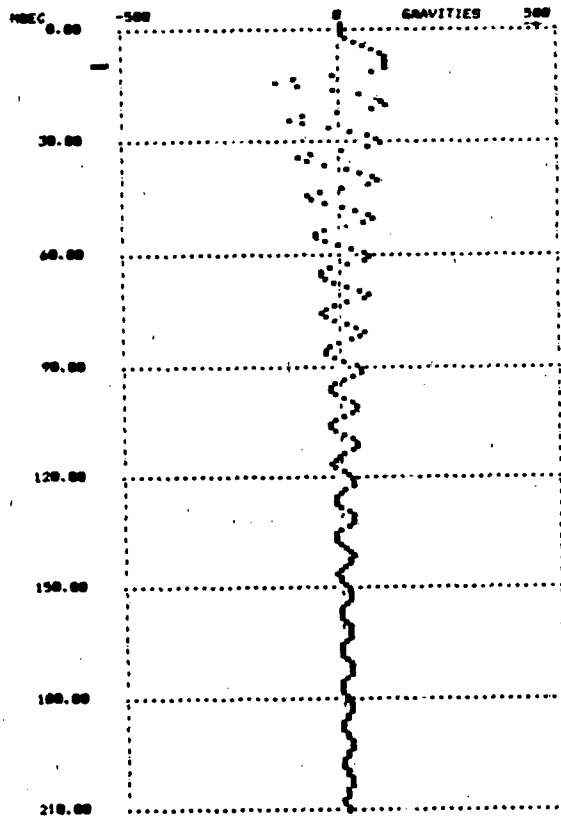


Figure 20. Response of Detuned Second Mass

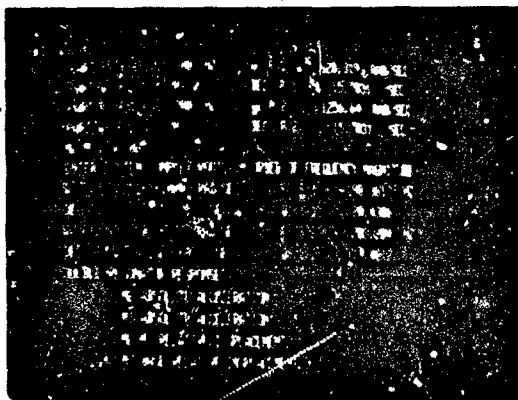


Figure 19. Description of Detuned Resonator

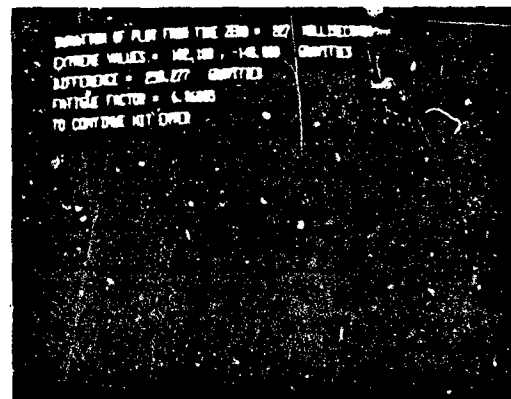


Figure 21. Fatigue Summary, Detuned Mass

Terminal resonators at the ends of shock transmission paths are potentially most vulnerable to damage or malfunction, and therefore they tend to be the most interesting resonators. However, the algorithm is capable of yielding absolute accelerations and relative displacements throughout a dynamical system. Within a multiple-resonator transmission path, relative displacements are more indicative of potential damage.

#### FURTHER DEVELOPMENT

Many things remain to be done to the program, some important and some more cosmetic in nature, before it is suitable for use by other engineers. Of course, more subroutines need to be added for more equipment dynamical configurations, so that redesign explorations can be extended to configuration as well as parameter changes. It would be a great convenience to have a built-in program for finding the roots of the denominator of the response transforms, preferably using the parts decrements and angular frequencies as initial values so as to increase the computation speed. For the two-degree-of-freedom system, interpolation from tables of complex roots could be faster, but the memory requirements would rapidly become excessive with increasing mechanical system complexity.

The program still needs further improvement of user interaction and some general cleanup, together with provision for more efficient RAM utilization in anticipation of added subroutines. The present interpretive BASIC program was achieved in part by combining on disk three separate programs (variable-time-increment spectra, constant-time-increment spectra and hybrid-time-increment responses) that had been subject to the limitations of 16 bytes of RAM memory, in a Radio Shack Model 1 personal computer, and of tape storage. Together with disk operating system and extended BASIC, it is now running into the limitations of 48 bytes of RAM. Most of the this memory is not involved directly in the algorithm but in the program routines for printing, plotting and user interaction. Editing will help some to decrease the memory requirement. Compiling may help even more, while speeding up operations that are not handled by machine-language subroutines. It has recently become possible to compile machine code directly from programs written in interpretive BASIC. Before the IFT algorithm is completely reduced to practice for the Z-80 (8-bit) microprocessor, it will undoubtedly be necessary to use some overlays in memory. This will be unnecessary for a computer with a 16-bit microprocessor and ample memory.

The author has compilers for several computer languages, for exploration, measurement of computation times etc. So far, it has been more important to develop the program further than to translate it. Compared to PASCAL, BASIC presents problems in the development and debugging of large programs; but it remains the language best adapted to interaction between computer and user. At the other extreme, ASSEMBLY language, in the hands of an expert programmer, generates the most efficient code, but it is extremely tedious and, except for occasional subroutines, entirely unsuited to a program development whose features are still somewhat exploratory.

The response plots of this paper have intentionally been made with few points along the time axis in order

to make the illustrations compact. Higher-resolution graphics, now available as an expansion kit for TRS-80 Model III and 4 computers, would ease this problem and provide more resolution in acceleration. However, as equipment designers are often off by a factor of two or more in their impressions of shock and vibration response, and sometimes off by a factor of ten, the present resolution should be adequate for most purposes.

When this work was first carried past the restrictions of a programmable calculator, the TRS-80 was almost the only personal computer available. Even now, there is more information readily available on programming it than for any other personal computer. Alternate computers, perhaps more common in industrial laboratories, may be considered after the program is more fully developed, if user interest warrants it.

For complete reduction of the IFT algorithm to practice, it is necessary that a computer be able to accept into an array shock data from an A/D converter. This can be very nearly the last refinement. It is much more satisfactory to develop and debug the programming with the aid of simple combinations of RAMP's and STEP's from the keyboard, whose responses are more predictable, at least for limiting cases of the mechanical system.

#### CONCLUSION

This paper demonstrated the feasibility of using the Indirect Fourier Transform algorithm both for spectral analysis of an arbitrary shock and for exploring any benefit, in decreased shock transmission, of possible design changes in a mechanical system. The extended algorithm may be considered a supplement to popular modal analysis techniques now applied primarily to structural problems. As the work still to be done is mostly too detailed for effective reporting, the present paper may be the last of the series for a while. In the meantime, the work reported here on the two-degree-of-freedom mechanical system will provide a programming approach for more complicated system responses.

After a sufficient number of subroutines for additional mechanical systems have been added, it should be possible to consider multiple excitations or the effect of a nonlinearity such as a blowoff valve in an automobile suspension or shock isolator. The latter would require changes of mechanical system configuration in the course of shock response computation, according to the velocity response of the damper.

The present paper should be a convincing demonstration that there are potentially much more powerful tools and techniques for practical shock and vibration engineering, with minimal cost and schedule penalties, than have been used to date. Part of the challenge facing the aerospace and avionics industries is to establish closer cooperation between engineers concerned with functional aspects of equipment and engineers concerned with shock and vibration. One of the findings of the author's previous report was that environmental specifications as now written have inadvertently tended to separate these two groups of engineers in such a way that the approvals required for the crossing of organizational lines constitute a major roadblock for efficient shock and vibration design. Reduction of

algorithms such as the extended IFT to practice should, by permitting graphic low-cost illustration of benefit from a possible design change, make approvals easier, so that organizational boundaries become less of an obstacle.

**REFERENCES:**

1. C. T. Morrow, THE ENVIRONMENTAL SPECIFICATION AS A TECHNICAL MANAGEMENT TOOL, 59-62, The Shock and Vibration Information Center, November, 1981.
2. H. Southworth, Jr., "Derivation of the Relationship between the "Residual" Shock Spectra and the Fourier Integral Spectra", SHOCK AND VIBRATION BULLETIN 29, Part 4, 408-411, The Shock and Vibration Information Center, 1961.
3. G. J. O'Hara, "A Numerical Procedure for Shock and Fourier Analysis", NRL Report 5772, June 5, 1962.
4. C. T. Morrow, "Indirect Fourier Transform and Shock Response", SHOCK AND VIBRATION BULLETIN 52, Part 4, 37-45, The Shock and Vibration Information Center, 1982.
5. C. T. Morrow, "Shock Spectral Analysis by Personal Computer, Using the IFT Algorithm, SHOCK AND VIBRATION BULLETIN 53, Part 1, 97-102, The Shock and Vibration Information Center, 1983.

## LEAST FAVORABLE RESPONSE OF INELASTIC STRUCTURES

Fashin Craig Chang, Thomas L. Paez, Frederick Ju  
The University of New Mexico  
Albuquerque, NM 87131

In the design of a structural system, a test input is sought to conservatively represent an ensemble of measured field inputs. When a structure survives the test input, it is assumed that it would survive the field inputs. The method of shock response spectra is a technique for specifying conservative test inputs, but it has some disadvantages. In this investigation a technique is developed for the specification of test inputs. It is based on the method of least favorable response, and it overcomes some of the shortcomings of the method of shock response spectra. Numerical examples show that the present technique can be used in practical applications.

### 1.0 INTRODUCTION

In the design of a structural system the engineer attempts to provide a plan for a structure that will survive one or more input excitations. To do this the engineer must have some means for analyzing structural response, and for judging whether the system can survive an excitation or a class of excitations. Most realistic situations involve environments that are random, and in such cases design techniques are sought to specify structures with pre-established probabilities of failure.

Short duration, strong motion excitations excite extreme responses, and structural failure can occur due to peak response; consequently it is desirable to know what maximum response can be caused in a structural system by a dynamic load. For reasons of conservatism and design safety, it is desirable to establish a procedure for computing a bound on the maximum structural response caused by a shock input. Buildings designed to survive an upper bound on the peak response should respond satisfactorily to the actual input.

A structural input excitation used in an analysis or physical test is considered conservative if it excites a more severe response in a structure than the individual inputs it is meant to represent. Therefore, when measured environments representing a real shock source are available, and it is necessary to design a structure to survive that source, a conservative input representing the measured shock is sought.

The method of shock response spectra provides a technique for the analysis and design of structures subjected to short duration shock excitations. The method of shock response spectra is used to establish a test input that can represent an ensemble of inputs conservatively, in the sense that the peak response excited by the test input is greater than the peak response excited by any of the underlying measured inputs. References 1 through 5 provide reviews and some recent applications of the method of shock response spectra in structural analysis and design.

The method of least favorable response was established by Drenick and Shinozuka in References 6 and 7. Its applicability was extended to use in analytical and physical testing by Smallwood in Reference 8. The method of least favorable response provides an alternate method for the specification of test inputs. The technique allows the engineer to specify a test input based on an ensemble of measured shock inputs. The test input will cause a response in a linear structure that is a bound on the response excited by the underlying measured inputs. Therefore, this method is equivalent, in concept, to the method of shock response spectra. Reference 9 compares the methods of least favorable response and shock response spectra and shows that the former has some considerable advantages over the latter.

One of the main disadvantages of the methods discussed above is that shock environments are often represented using test inputs

that are different in character from the original shocks. This problem is discussed in detail by Baca in Reference 10. He shows that this problem can lead to overconservative tests, especially in the case of the method of shock response spectra where simple waveform test inputs can be used.

Another disadvantage is that the techniques discussed above are mainly for use with linear structures. Of course, the techniques are used in connection with failure analysis of structures, but the theoretical developments are usually concerned with linear equations. One exception occurs with the method of shock response spectra; a few papers concerned with test specification for nonlinear structures have been written. (See, for example, References 11, 12, 13.)

In view of these problem areas, it is desirable to develop a technique for the specification of test inputs for the analysis and design of structures that 1) yields inputs similar in form to the underlying measured inputs, 2) accounts for the potential for nonlinear response in a structure, and 3) can be used when failure is related to peak response.

The objective of this study is to establish a method for the specification of a test input based on an ensemble of measured inputs. The input will have the three properties listed in the previous paragraph. The approach is based on the method of least favorable response; therefore, the linear theory of least favorable response is reviewed in the following section. Next, the peak response of bilinear hysteretic single-degree-of-freedom (SDF) structures is investigated. Finally, a method is established for specifying a test input that will cause maximum displacement response in a structure.

## 2.0 THE LINEAR THEORY OF LEAST FAVORABLE RESPONSE

The method of least favorable response provides a means for defining an upper bound on the response of a linear structure excited by a sequence of shock inputs. Consider a linear dynamical structure. When it is excited by a single input, the response at a point on the structure can always be expressed using the convolution integral. This is

$$y(t) = \int_0^t h(t-\tau) x(\tau) d\tau \quad (2-1)$$

where  $x(t)$  is the input excitation,  $y(t)$  is the response, and  $h(t)$  is the system impulse response function. If the system response

starts at time zero, then it is assumed that the initial conditions are zero velocity and displacement.

Now assume that the structure has positive viscous damping and the input can be Fourier transformed. Then the response has a Fourier transform, and the input and response Fourier transforms are denoted  $X(\omega)$  and  $Y(\omega)$ , respectively. These functions can be inverse Fourier transformed to obtain the input and response,  $x(t)$  and  $y(t)$ . The convolution integral in Equation (1) can be Fourier transformed. The result is

$$Y(\omega) = H(\omega) X(\omega) \quad (2-2)$$

where  $H(\omega)$  is called the frequency response function and is the Fourier transform of the impulse response function.

Equation (2-2) can be inverse Fourier transformed to obtain a frequency domain expression for the structural response. This is

$$y(t) = \frac{1}{2\pi} \int_{-\infty}^{\infty} H(\omega) X(\omega) e^{i\omega t} d\omega \quad (2-3)$$

The objective is to bound the maximum value in the absolute value of the response; therefore, the absolute value is taken in Equation (3). This yields

$$|y(t)| = \frac{1}{2\pi} \left| \int_{-\infty}^{\infty} H(\omega) X(\omega) e^{i\omega t} d\omega \right| \quad (2-4)$$

Parseval's theorem can be used to show that when the absolute value signs are taken inside the integral on the right, above, the absolute value of the response is bounded, as follows.

$$|y(t)| \leq \frac{1}{2\pi} \int_{-\infty}^{\infty} |H(\omega)| |X(\omega)| d\omega = I \quad (2-5)$$

The expression on the right is a constant, independent of time; this constant is denoted  $I$ . Since the absolute value of the response is equal to or less than  $I$ , this implies that the maximum value in the absolute value of the response is equal to or less than  $I$ . Let

$$Y = \max_t |y(t)| \quad (2-6)$$

then

$$Y \leq I \quad (2-7)$$

The quantity,  $I$ , is known as the least favorable response (LFR) of the system, corresponding to the input with Fourier transform given by  $X(\omega)$ .

The LFR forms a bound on all the peak responses of the system whose frequency response function is  $H(\omega)$  where the input has Fourier transform modulus bounded by  $|X(\omega)|$ . A test input is known as a least favorable input (LFI) if it produces a response whose absolute maximum is equal to 1.

Let  $x_T(t)$  denote a test input with Fourier transform  $X_T(\omega)$ . This input excites a response  $y_T(t)$ , in the system of interest, whose Fourier transform is  $Y_T(\omega) = H(\omega)X_T(\omega)$ . A bound on the absolute maximum of the test response is given by

$$\max_t |y_T(t)| = \frac{1}{2\pi} \int_{-\infty}^{\infty} |X_T(\omega)| |H(\omega)| d\omega \quad (2-8)$$

The Fourier transforms of the test input and the frequency response function can be expressed in their polar forms,  $X_T(\omega)$

$$X_T(\omega) = |X_T(\omega)| e^{i\theta_T(\omega)} \quad \text{and} \quad H(\omega) = |H(\omega)| e^{i\phi(\omega)}$$

When the expressions are used in Equation 2-3, the response function  $y_T(t)$  is given by

$$y_T(t) = \frac{1}{2\pi} \int_{-\infty}^{\infty} |X_T(\omega)| |H(\omega)| e^{i(\theta_T(\omega) + \phi(\omega) - \omega t)} d\omega \quad (2-9)$$

At time  $t = 0$ , the above expression can be made equal to 1, the LFR, by taking

$$\theta_T(\omega) = -\phi(\omega) \quad \text{and} \quad |X_T(\omega)| = |X(\omega)| \quad (2-10)$$

In this case the test response at time zero is

$$y_T(0) = \frac{1}{2\pi} \int_{-\infty}^{\infty} |X(\omega)| |H(\omega)| d\omega = 1 \quad (2-11)$$

This shows that the test response can be made equal to the LFR by choosing the Fourier transform modulus of the test input equal to the Fourier transform modulus of the actual input, and by choosing the complex phase of the test input equal to minus the phase of the frequency response function. The effect of this choice of phase is to cause the response Fourier components to add constructively at time  $t = 0$ .

In view of Equation 2-10, the Fourier transform of the test input is given by

$$X_T(\omega) = |X(\omega)| e^{i\phi(\omega)} \quad (2-12)$$

This function can be inverse Fourier transformed to obtain a time domain expression for the test input. This input is the LFI.

$$x_T(t) = \frac{1}{2\pi} \int_{-\infty}^{\infty} X_T(\omega) e^{i\omega t} d\omega \quad (2-13)$$

This input could be used in a physical test of the structure. Since the response it excites is equal to or greater than the response excited by the input  $x(t)$ , the test input produces a conservative test, in the peak response sense. If a structure survives  $x_T(t)$ , then it would also survive  $x(t)$ .

The procedure outlined above provides a means for computing the LFR and specifying a shock test based on one measured input,  $x(t)$ . The procedure can be modified to define an LFR and shock test input when several measured inputs are available. Let  $x_j(t)$ ,  $j=1, \dots, n$ , be a sequence of measured shock signals from one or more shock sources, and assume that a structure of interest will be subjected to one or more shocks from each source in the field. Then an LFR based on the sequence of inputs can be constructed as follows. Compute the Fourier transform of each shock and denote the results  $X_j(\omega)$ ,  $j=1, \dots, n$ . Compute the complex modulus of each Fourier transformed signal,  $|X_j(\omega)|$ ,  $j=1, \dots, n$ . Let  $X_e(\omega)$  define the envelope of the Fourier transformed moduli; then  $X_e(\omega)$  is

$$X_e(\omega) = \max_j |X_j(\omega)| \quad (2-14)$$

The LFR based on the sequence of inputs is given by

$$I = \frac{1}{2\pi} \int_{-\infty}^{\infty} X_e(\omega) |H(\omega)| d\omega \quad (2-15)$$

This is a bound on the peak response excited by the inputs,  $x_j(t)$ ,  $j=1, \dots, n$ , individually, since  $X_e(\omega)$  bounds the Fourier transform moduli of the individual inputs.

A test input which will excite the LFR, at time  $t = 0$ , is given by

$$x_T(t) = \frac{1}{2\pi} \int_{-\infty}^{\infty} X_e(\omega) |H(\omega)| e^{i\omega t} d\omega \quad (2-16)$$

This input could be used in a physical test of the structure. It is conservative with respect to each of the individual inputs in a peak response sense.

The method of least favorable response has a few features that make it practically important. First, it generates test inputs and responses that are conservative with respect to a collection of underlying inputs and the responses they excite. Second, it generates test inputs that have the same oscillatory quality as the underlying inputs. Third, it preserves the power of the underlying input by matching  $X_e(\omega)$  to the moduli of the Fourier transforms of the underlying inputs and simply rearranging the phase of the response.

### 3.0 A DISPLACEMENT RESPONSE BOUND FOR BILINEAR HYSTERETIC SYSTEMS

It was shown in Section 2.0 that for a linear system the least favorable response (LFR) can be obtained from Equation 2-8. The LFR is a bound on the individual responses excited by a sequence of inputs. The least favorable input (LFI) given in Equation 2-16 is a test input which generates the LFR in a linear system. In this section a technique is developed to compute the LFR of a nonlinear single-degree-of-freedom (SDF) structure.

The capacity to generate the LFR of an SDF structure is important since it can be used by the designer to establish a bound on the displacement response of a multi-degree-of-freedom (MDF) structure in its fundamental mode. In many practical cases the fundamental mode of response contributes most significantly to the overall response. Beyond this, the results of this investigation may prove useful for application in the definition of inputs at several characteristic frequencies, simultaneously.

The technique to be considered is based on the method of least favorable response. The LFI is an input characterized in terms of the complex modulus and phase of its Fourier transform. The modulus of the Fourier transform of an LFI reflects an envelope on the moduli of the Fourier transforms of the underlying inputs. When the shock sources represented in the ensemble of inputs are very similar, then the moduli of the Fourier transforms of the inputs are very similar and the envelope very nearly matches these. The complex phase functions of the Fourier transforms of actual inputs are random, at least in part. And the complex phase of the Fourier transform of the LFI is chosen to cause the components of the response to superpose

constructively at time  $t = 0$ . The phase is chosen as minus the complex phase of the frequency response function of the structure under consideration.

In this investigation it is assumed that the bilinear hysteretic structure possesses an LFR and an LFI which generates that response. It is assumed that the LFI of the bilinear system has the same general form as the LFI of the linear system. The parameters of this LFI must be determined.

Consider a base excited, linear SDF system. The frequency response function for the system is given by

$$H(\omega) = \frac{1}{(\omega_n^2 - \omega^2) + 2i\zeta\omega_n\omega} \quad -\infty < \omega < \infty \quad (3-1)$$

where  $\omega_n$  is the natural frequency of the system and  $\zeta$  is the damping factor of the system. This function can be interpreted in terms of its real and imaginary parts or its complex modulus and phase. The phase of the frequency response function is

$$\phi(\omega) = \tan^{-1} \frac{-2\zeta\omega_n\omega}{\omega_n^2 - \omega^2} \quad -\infty < \omega < \infty \quad (3-2)$$

This is plotted in Figure 3.1 as a function of circular frequency,  $\omega$ . Note that  $\phi(\omega)$  is an odd function and varies rapidly in the vicinity of  $\omega_n$  and slowly elsewhere.

It is assumed in this study that the complex phase of the Fourier transform of the LFI of a bilinear hysteretic system is given by

$$\phi(\omega) = \tan^{-1} \frac{-2\zeta_e\omega_e\omega}{\omega_e^2 - \omega^2} \quad -\infty < \omega < \infty \quad (3-3)$$

where  $\omega_e$  is the characteristic frequency and  $\zeta_e$  is the characteristic damping factor. These parameters are chosen to maximize the response of the bilinear system. The parameters must be determined. This form is chosen for the phase in the hope that it will yield a response in a bilinear hysteretic structure that is near the LFR.

For a specific bilinear hysteretic system and ensemble of inputs, the parameters in the phase of the Fourier transform of the LFI can be determined by searching the peak response values as a function of  $\omega_e$  and  $\zeta_e$  to obtain a maximum. The response of a bilinear hysteretic

SDF system is governed by the equation

$$\ddot{y} + 2\zeta\omega_n \dot{y} + \frac{1}{m} R(y) = -\ddot{x}_0 \quad (3-4)$$

where  $\zeta$  and  $\omega_n$  are the damping factor and small displacement natural frequency of the system,  $m$  is the SDF system mass,  $\ddot{x}_0$  is the base motion input excitation of the system,  $R(y)$  is the bilinear hysteretic restoring force function. The restoring force is a function with an infinite number of realizations. When  $y$  is small,  $R(y)$  is a linear function of  $y$  with stiffness  $k$ . When the yield displacement,  $D$ , is surpassed, then permanent set accumulates in the system and the stiffness reduces to  $k_y$ . When the velocity reverses sign, the stiffness increases to  $k$  and oscillations occur about a new equilibrium displacement (reflecting the permanent set) until yielding occurs again, etc. Figure 3-2 shows a potential realization of the spring restoring force function for a bilinear hysteretic system. Equation 3-4 can be solved using a numerical procedure. For example, the numerical procedure given in Reference 14 can be used to solve Equation 3-4.

Let  $x_j(t)$ ,  $j=1, \dots, n$  be an ensemble of measured inputs from one or more shock sources to which a structure will be exposed. The LFR and LFI of a bilinear hysteretic structure corresponding to these inputs are defined as follows. Compute the Fourier transforms of the inputs and denote these  $X_j(\omega)$ ,  $j=1, \dots, n$ . Then compute the complex moduli of the inputs and find the envelope of the moduli. This is

$$X_e(\omega) = \max_j |X_j(\omega)| \quad -\infty < \omega < \infty \quad (3-5)$$

This is the modulus of the Fourier transform of the LFI. The form of the complex phase of the LFI is given in Equation 3-3. When specific values of  $\omega_e$  and  $\zeta_e$  are used in Equation 3-3, an input whose Fourier transform has the form of the LFI can be established. This is

$$X_T(\omega) = X_e(\omega) \exp \left[ i \tan^{-1} \left[ \frac{-2\zeta_e \omega_e \omega}{\omega_e^2 - \omega^2} \right] \right] \quad -\infty < \omega < \infty \quad (3-6)$$

A time domain test input can be established by inverse Fourier transforming this function. The result is

$$x_T(t) = \frac{1}{2\pi} \int_{-\infty}^{\infty} X_T(\omega) e^{i\omega t} d\omega, \quad -\infty < t < \infty \quad (3-7)$$

This function of time can be used as input in Equation 3-4 and the response can be computed numerically and denoted  $y_T(t, \omega_e, \zeta_e)$ .

Dependence of the response function on the parameters of the input is emphasized by inclusion of these parameters as arguments in the response expression.

The peak value, in time, of the response is

$$Y(\omega_e, \zeta_e) = \max_t y_T(t, \omega_e, \zeta_e) \quad (3-8)$$

The peak response can be maximized with respect to  $\omega_e$  and  $\zeta_e$  by solving for the values of  $\omega_e$  and  $\zeta_e$  which satisfy the following equations.

$$\frac{\partial Y}{\partial \omega_e} = 0, \quad \frac{\partial Y}{\partial \zeta_e} = 0 \quad (3-9)$$

Denote the solution to these equations  $\omega_e^*$  and  $\zeta_e^*$ . Use of these values in Equations 3-7 yields the LFI. Evaluation of Equation 3-8 at  $\omega_e = \omega_e^*$  and  $\zeta_e = \zeta_e^*$  yields the LFR.

Equations 3-9 can be solved in any of a number of ways. In the present investigation they are solved using a simple search procedure.

#### 4.0 NUMERICAL EXAMPLES

In the previous section, methods for the approximate determination of the least favorable input (LFI) and least favorable response (LFR) of a bilinear hysteretic system were developed. A computer program named LFIR has been written to execute the computations required to determine the LFI and LFR. Some numerical examples are solved in this section using the computer program.

Two types of problems are solved. First, the LFI and the response it excites are determined for a single input applied to a single structural system. Second, the parameters of the complex phase of the LFI are determined for a sequence of increasingly severe inputs. This problem is solved for three bilinear hysteretic systems.

The type of input used in all cases is an oscillatory random input with decaying exponential amplitude. The input is denoted  $x_0(t)$  and its specific form is given by

$$x_0(t) = e^{-\alpha t} \sum_{j=1}^N c_j \cos(\omega_j t - \phi_j), \quad 0 < t < T \quad (4-1)$$

$\alpha$  is the amplitude decay rate of the input;  $N$  is the number of components in the input;  $c_j$ ,  $j=1, \dots, N$  are the input amplitudes;  $\omega_j$ ,  $j=1, \dots, N$ , are the frequencies where the input has power;  $\phi_j$ ,  $j=1, \dots, N$  are mutually independent, uniform

random variables distributed on the interval  $(-\pi, \pi)$ . The input is an approximately normally distributed, nonstationary random process.

#### 4.1 Example One

Consider the response of a bilinear hysteretic SDF structure, whose parameters are given in Table 4.1, to the shock input whose parameters are given in Table 4.2. The input is shown in

Table 4.1

#### Bilinear Hysteretic System Parameters

$m = 1.0$  mass  
 $k = (2\pi)^2$  stiffness  
 $k_y = 0.5$  yield stiffness  
 $c = 1.256$  damping  
 $D = 0.0813$  yield displacement  
 $\omega_n = 2\pi$  natural frequency

Table 4.2

#### Shock Input Parameters

$N = 30$   
 $c_j = 2.0 \quad j=1, \dots, 30$   
 $\omega_j = 0.1 + 0.238(j-1) \quad j=1, \dots, 30$   
 $\alpha = 0.628$

Figure 4.1; the response to the input is shown in Figure 4.2. Since the yield displacement is 0.0813, the response is clearly in the plastic region, in this example. The peak response caused by the actual input is 0.1651.

The LFI and LFR were computed using program LFIR. The parameters of the complex phase of the Fourier transform of the input were found to be  $\omega_e = 5.056$  and  $\zeta_e = 0.109$ .

The modulus of the Fourier transform of the input is shown in Figure 4.3. The LFI, computed using Equation 3-7, is shown in Figure 4.4. The response excited by this input is shown in Figure 4.5. This time history shows that the LFI is 0.3012.

This example demonstrates the process used in finding the LFI and LFR of a bilinear hysteretic structure when a single input is considered.

#### 4.2 Example Two

In this numerical example several problem sequences are solved. In order for the

techniques developed in this study to be useful in the practical specification of tests, it is necessary to express the results in a form that is easy to use. Specifically, when the engineer needs to test an equipment item, it is desirable to specify a test sequence where he can run a few tests on the equipment item, and use the results to specify the LFI. The results of this numerical example will show that such a sequence can be defined.

In the first part of this example, the bilinear hysteretic structure whose parameters are given in Table 4.1 is subjected to a sequence of 16 inputs. The inputs all have the same form, Equation 4-1, and only one of the input parameters is varied; this is the amplitude. The input parameters are listed in Table 4.3 and the amplitudes for all the inputs are given. The  $c_{ij}$  is the amplitude of the  $j^{\text{th}}$  component of the  $i^{\text{th}}$  input.

Table 4.3

#### Shock Input Parameters

$N = 30 \quad \alpha = 0.628$   
 $\omega_j = 0.1 + 0.238(j-1) \quad j = 1, \dots, 30$   
 $c_{ij} = 0.2(i-1) + 1 \quad j = 1, \dots, 30, i = 1, \dots, 16$

The actual structural response to each input was computed. Based on the responses, the actual peak displacement responses were determined. The ratio between each peak response and the yield displacement was taken to establish the ductility ratio,  $U$ , of each response. Next, the parameters of the complex phase of the Fourier transform of the LFI (using peak displacement criterion) were determined for each input. These parameters are graphed versus the ductility ratio and are shown in Figures 4.6 ( $\omega_e$  parameter) and 4.7 ( $\zeta_e$  parameter).

The LFR was computed for each input. This quantity was normalized by dividing by the actual maximum response, and is graphed as a function of ductility ratio in Figure 4.8.

This entire process was repeated for two more yield stiffness to elastic stiffness ratios. These are  $k_y/k = 0.3$  and  $k_y/k = 0.1$ . The results of these analyses are also shown in Figures 4.6, 4.7, and 4.8.

All the results show the same general trends. Consider first Figure 4.6. When the ductility ratio is low, the frequency parameter decreases. All the curves exhibit an erratic behavior. The reason is that the inputs are random.

The plots in Figure 4.6 raise a question of interest. That is, do the curves asymptotically approach limits? The answer is probably yes, and each limit is related to the ratio between the yield stiffness and the elastic stiffness. As the structural response displacement increases far beyond the yield limit, each SDF system has a spring force versus displacement diagram that resembles a linear system response with stiffness,  $k_y$ . Since the natural frequency of an SDF system, with mass  $m$  and stiffness  $k$ , is  $\sqrt{k/m}$ , the parameter  $\omega_e$  must approximately approach the value,  $\sqrt{k_y/m}$ , in the limit. And the ratio  $\omega_e/\omega_n$  must approach  $\sqrt{k_y/k}$ .

An analysis was performed to establish a smooth curve for each sequence of data in Figure 4-6. Each data sequence was fitted to the mathematical model

$$\frac{\omega_e}{\omega_n} = \sqrt{\frac{k_y}{k}} + A - \frac{k_y}{k} e^{-\gamma U}$$

where  $\omega_e/\omega_n$  is the ordinate of the curve,  $U$  is the abscissa,  $\sqrt{k_y/k}$  is the asymptote, and  $A$  and  $\gamma$  were evaluated using the least squares method. The results of the analyses are given in Table 4.4

Table 4.4  
Curve Parameters for Data in Figure 5.8

$\sqrt{k_y/k}$	0.5	0.3	0.1
A	1.125	0.995	0.966
$\gamma$	0.572	0.226	0.112

The smooth curves are shown in Figure 4.9. The results show that the curves are relatively close to one another over the range of  $U$  values considered. This implies that the frequency parameter,  $\omega_e$ , of the LFI can be chosen, approximately, even when the yield stiffness to elastic stiffness ratio is not known accurately.

Now consider Figure 4.7. Based on these curves a few statements can be made. All the curves exhibit erratic variation. More important, the damping parameter,  $\gamma$ , of the LFI, appears to remain small when the damping in the actual system is small.

Figure 4.8 shows that the ratio between the LFR and the actual peak response displays a certain degree of unpredictable variation. This variation is due to the fact that the inputs are random. However, the ratio appears to be constant, on the average, and the average is about 1.4. This indicates that an LFR about 40 percent greater than the actual peak response can usually be expected.

It was stated that the procedure outlined in this numerical example would make it easy for the test engineer to find the LFI for an equipment item. One procedure a test engineer might follow is now presented.

When an equipment item will be subjected to a class of field inputs similar in character to the input of Equation 4-1, the test engineer can specify an LFR test using a sequence of experiments. First, the test item must be instrumented. Base input is assumed, and the response at a critical point is monitored. Using a low amplitude sine sweep (or equivalent method) the fundamental frequency must be determined. The frequency response function near the fundamental frequency must be established, and this information must be used to determine the damping factor in the fundamental mode. For example, this can be inferred from the half power bandwidth.

Next, the yield point must be established. This can be done using a sequence of experiments. In each experiment the actual input is multiplied by a factor  $q$ .  $q$  is varied from a small value (say 0.05) to the value 1.0. The structure is excited using the modified input. The response at the point of interest is monitored and the peak value is determined. The values of peak response are plotted versus  $q$ . The curve generated using this approach remains linear until yielding occurs. After yielding, the slope of the curve increases. The value of  $q$  corresponding to the yield point and the peak value of the response where the yield displacement is realized can be determined from the curve.

Now the test engineer applies the actual input to the equipment item and observes the peak value of the response at the point of interest. The ratio between this quantity and the peak value of the response where yielding first occurs is the ductility ratio. This ductility ratio can be used to enter Figure 4.6 (or 4.9) to determine the frequency parameter for the LFI.

The test engineer determines the modulus of the Fourier transform of the actual input, then uses this with frequency parameter given above and the actual system damping factor to establish the LFI. The test input is computed using the above information in Equations 3-6 and 3-7.

The technique described above can be used to establish the LFI parameters for other classes of random inputs. The analysis sequence is simply repeated using the other input in place of Equation 4-1.

## 5.0 SUMMARY AND CONCLUSION

The objective of this paper was to establish a method to search for a test input that excites a conservative response in an equipment item capable of inelastic response. A method for specifying a conservative test input based on measured field inputs was established. The criterion of peak displacement response was used.

The technique developed here was based on the linear theory of least favorable response (LFR). It was assumed that when an equipment item is subjected to a severe excitation, the response may be inelastic. An equipment item executing inelastic response displays a diminished stiffness. Therefore, the characteristic frequency of an inelastic structure is lower than its fundamental frequency. This study specified a method to search for the input that causes the inelastic system response to be a maximum. The input has the same form as the linear least favorable input (LFI).

Equations 3-6 and 3-7 establish the form of the LFI. The intensity of the actual shock input is accurately reflected in the test since the LFI preserves the modulus of the Fourier transform of the actual input. Comparison of Figures 4.1 and 4.4 shows that the general character of the actual input is preserved in the LFI.

The potential for inelastic response is accounted for in this study since Equation 3-4 is assumed to govern the response of the systems under consideration.

Example One demonstrates how the techniques developed in this investigation can be applied in the definition of an actual test input. Example Two shows that the results can be generalized for easy application in the specification of test inputs.

An important result of this study is shown in Figure 4-6. This shows the frequency parameter to be used in specification of an LFI as a function of ductility ratio. The numerical investigations show that the frequency parameter is the most important factor in the definition of the LFI. Figure 4-6 permits the easy identification of this parameter for test definition.

The damping which corresponds to the maximum displacement response was also determined. The damping variation is shown in Figure 4-7. It is concluded from the computations that the change of damping does not significantly affect the LFR. Hence, it is recommended that the damping parameter in the LFI be defined as the damping in the actual system.

The procedures developed in this study can be useful in practical applications. Example 2 can be simplified even further. For example, note that the LFI depends not on the form of the actual input, but rather on the complex modulus of the Fourier transform of the input. In view of this, the frequency parameters of the LFI can be written as a function of the ductility ratio for an input whose Fourier transform modulus has certain characteristics, such as "increasing with frequency near  $\omega_n$ " or "decreasing with frequency near  $\omega_n$ " or "constant with frequency near  $\omega_n$ ". Using this approach the parameters of an LFI would not be tied to a specific input form, but rather to an input whose Fourier transform modulus has a specific form. Other simplifications and generalizations may also be possible.

The results obtained during this investigation are limited by the assumptions of the study. Most important, only single-degree-of-freedom, bilinear hysteretic systems were studied. Further, random inputs were used, but the probabilistic character of the response was not investigated. Only one form for the LFI was used.

Future studies may seek to improve the present analyses in several areas. For example, an alternate form for the LFI may be sought; specifically, inputs which generate more severe responses may be developed. Other forms of inelastic behavior may be considered. Probabilistic studies may be performed; these can be used to predict the probability of conservatism of a shock test. Most important, a shock test specification procedure which explicitly accounts for the characteristics of inelastic multi-degree-of freedom systems must be pursued.

REFERENCES

1. Matsuzaki, Yuji, "A Review of Shock Response Spectrum," The Shock and Vibration Digest, 9(3), pp. 3-12, March 1977.
2. Morrone, A., "Analysis of Seismic Testing Motions with Instantaneous Response Spectra," Nuclear Engineering and Design, 51, (3), pp. 445-451, February 1979.
3. Nelson, F. C., "Shock and Seismic Excitation of Mechanical Equipment," ASME Paper 74-DE-3, presented at the Design Engineering Conference and Show, Chicago IL, April 1-4, 1974.
4. Hadjian, A. H., "Seismic Response of Structures by the Response Spectrum Method," Nuclear Engineering and Design, 66, pp. 179-207, 1981.
5. Trubert, M., and Salama, M., "Generalized Modal Shock Spectra Method for Spacecraft Loads Analysis," AIAA Journal, 18 (3), pp. 988-994, August 1980.
6. Drenick, R. F., "Model Free Design of Aseismic Structures," Journal of the Engineering Mechanics Division, Proceedings, ASCE, 96, pp. 483-493, August 1970.
7. Shinozuka, M., "Maximum Structural Response to Seismic Excitations," Journal of the Engineering Mechanics Division, Proceedings ASCE, 96, pp. 483-493, August 1970.
8. Smallwood, "A Transient Vibration Test Technique Using Least Favorable Responses," Shock and Vibration Bulletin, No. 43, Part 1, pp. 151-164, June 1973.
9. Paei, Thomas L., "Conservatism in Least Favorable Response Analysis and Testing," The Shock and Vibration Bulletin, Bulletin 51, Part 2, pp. 93-109, May 1981.
10. Baca, Thomas Joseph, Characterization of Conservatism in Mechanical Shock Testing of Structures, Ph.D. Dissertation, Stanford University, Stanford, CA, September 1982.
11. Kawakatsu, T., Kitade, K., Takemori, T., Kuwabara, Y., and Ogiwara, Y., "Floor Response Spectra Considering Elasto-Plastic Behavior of Nuclear Power Facilities," Paper K9/4, Transactions of the International Conference on Structural Mechanics in Reactor Technology, 5th, K(5): Seismic Response Analysis of Nuclear Power Plant Systems, Berlin, Germany, August 13-17, 1979.
12. Mahin, Stephen A., and Bertero, Vito V., "An Evaluation of Inelastic Seismic Design Spectra," Journal of the Structural Division, Proceedings ASCE, 107(ST9), pp. 1777-1795, September 1981.
13. Iwan, W. D., "Estimating Inelastic Response Spectra from Elastic Spectra," Earthquake Engineering and Structural Dynamics, 8, pp. 375-388, 1980.
14. Clough, R. W., Penzien, J., Dynamics of Structures, McGraw-Hill, Inc., New York, 1975.

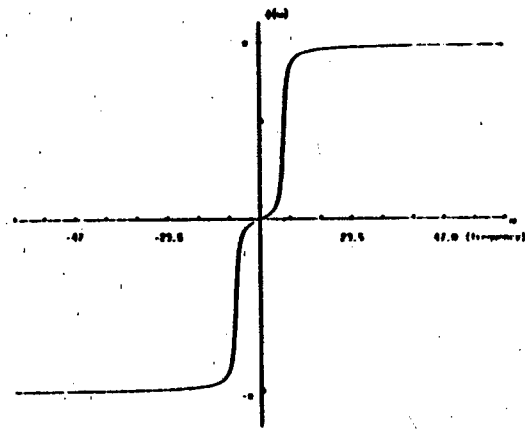


Figure 3.1. Complex Phase of SDF System Frequency Response Function.

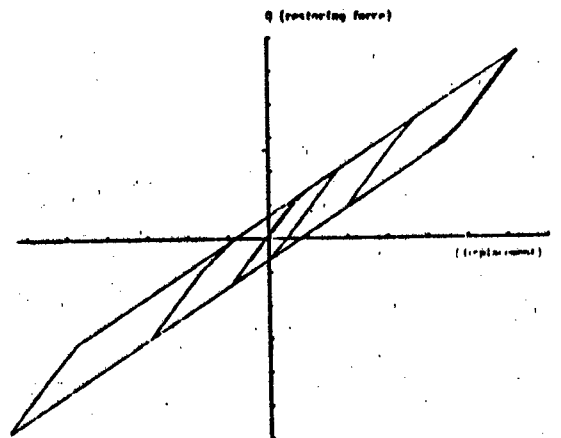


Figure 3.2. Realization of Restoring Force Function of Bilinear Hysteretic Spring.

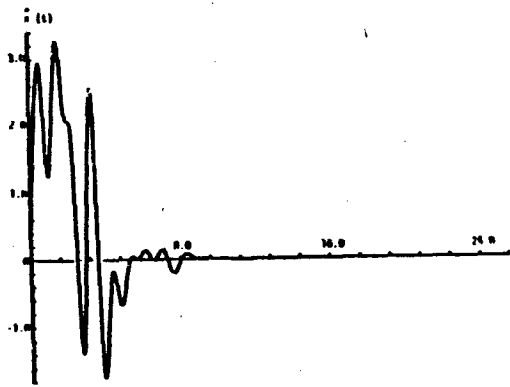


Figure 4.1. Input Time History.

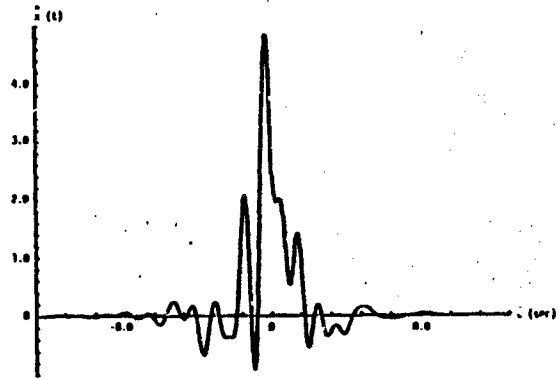


Figure 4.4. LFI Based on Maximum Displacement Criterion.

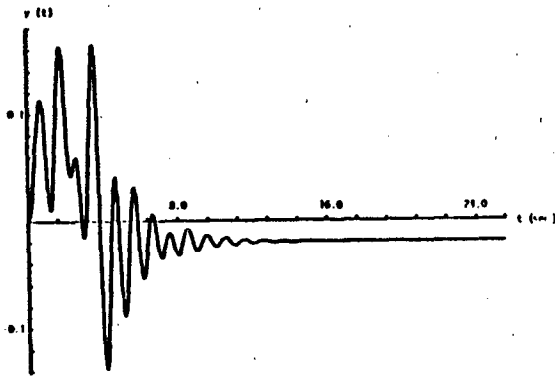


Figure 4.2. Response of Bilinear Hysteretic Structure to Input in Figure 5.1.

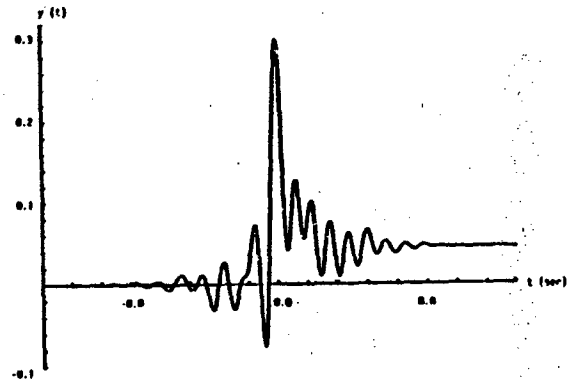


Fig. 4.5. Response of Bilinear Hysteretic System to Input in Figure 5.4.

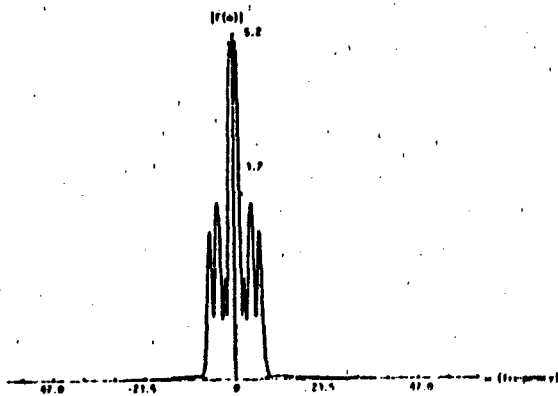


Figure 4.3. The Modulus of the Fourier Transform of the Input.

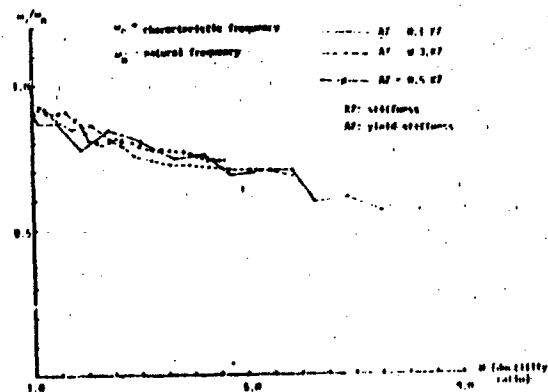


Figure 4.6. LFI Parameter versus Ductility Ratio (Displacement).

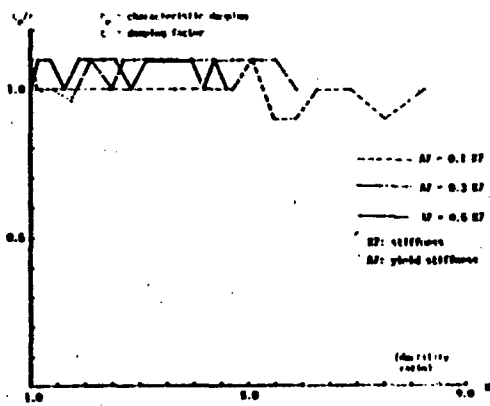


Figure 4.7. LFI Damping Parameter versus Ductility Ratio.

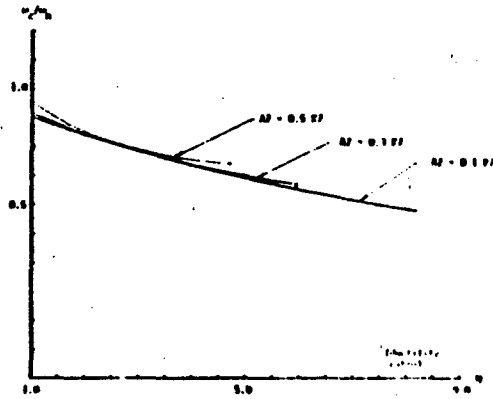


Figure 4.9. Smooth Curves Corresponding to Figure 5.8.

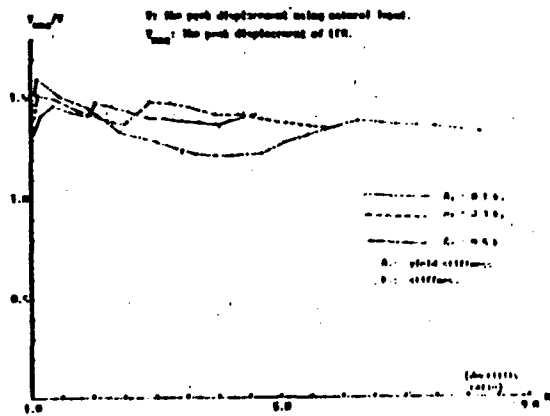


Figure 4.8. Ratio of LFR to Actual Peak Response versus Ductility Ratio.

LOW VELOCITY, EXPLOSIVELY DRIVEN FLYER PLATE DESIGN FOR  
IMPACT FUZE DEVELOPMENT TESTING

R. A. Benham  
Sandia National Laboratories  
Albuquerque, New Mexico

A new design of an explosive system to propel a thick, aluminum flyer plate into a reentry vehicle warhead contact fuze system has been designed and tested. This design produces a "reverse ballistic" impact environment used to study the function of contact sensors at impact velocities of around 1525 mps (5000 fps). The paper presents the explosive design, calculations of shock wave damage to the flyer plate, and results of an experiment in which this design was utilized. Use of nitromethane explosive permitted achievement of impact, with a thick aluminum plate, without serious plate spall damage while other widely used explosives cause considerable damage in the plate.

INTRODUCTION

Fuzing options for ballistic missile warheads may include a contact sensor to provide surface bursts. Development of these contact fuzes requires laboratory test methods which provide a wide variety of impact velocity and target conditions. Rocket flight tests, rocket sled tests, and explosively driven flyer plate tests have produced realistic impact environments for observing the performance of fuzing designs. The explosively driven flyer plate method provides a less expensive alternative to rocket flight tests in the velocity ranges above those currently attainable with rocket sled techniques [1830-2440 mps (6000-8000 fps)]. Flyer plates provide a "reverse ballistic" test in which the nose tip fuze system is held stationary while the plate (target) material is driven into it at velocities from 2350-3660 mps (7700-12,000 fps). These tests produce representative impact velocity vectors (therefore stresses) while allowing high quality data recovery using hard wire instrumentation. Previous papers [1-3] described the experimental concepts and developed an analytical approach useful in predicting the behavior of the particular explosive flyer plate system currently being used at Sandia National Laboratories.

A new requirement to explosively drive a thick aluminum flyer plate to low velocity [1220-1870 mps (4000-6000 fps)] has prompted the investigation of a different explosive design. These flyers are to be used in experiments which investigate detailed fuze system operation as well as subsequent nose tip crush-up.

The same explosive and design of thick plate systems will not work for thin plate systems because the driving pressure pulse becomes short with respect to the plate thickness, and plate spallation may result. The plate damage may range from microcracks to major fractures dividing the plate into several separate layers. The plate must be intact to produce a proper impact test.

The hydrodynamic shock wave computer code WONDY V [4] was used to calculate the spall damage for various plate thickness/velocity combinations and for different explosive types. These calculations lead to the choice of nitromethane liquid as an explosive that can drive the plate to lower terminal velocity without causing serious spall damage. The lower density and detonation velocity (therefore detonation pressure), as well as homogeneity of the nitromethane, increase the desirability of this explosive material.

A small-scale experiment was designed and conducted to verify proper operation. This paper presents the results of this experiment and describes the analytical method for predicting the explosive system performance. The success of the small experiment led to the design of a large explosive system using 68.1 kg (150 lb) of nitromethane to drive a 12.7 mm (5 in.) thick aluminum plate [.292 M (11.5 in.) in diameter] to impact a nose tip fuze system at 1585 mps (5200 fps).

The explosive design currently used to propel metallic flyer plates consists of a large, thick walled barrel partially packed with explosive. The flyer plate is placed in one end of the barrel, usually with a foam rubber cushion between it and the explosive. The flyer plate has a machined guard ring around it to aid in preventing plate breakup. The plate thickness may also be tapered across a diameter to cause end-over-end rotation, thus allowing impact at any desired angle between 0 and 70 degrees (between the nose tip axis and the flyer plate surface normal). Figure 1 shows the barrel design; the system is detailed in another document [2].

#### THEORY

Shock wave damage caused in the plate during explosive launch may be calculated using the one-dimensional computer code WONDY V [4]. For formulating the WONDY calculation (which does not consider lateral effects), the explosive thickness was reduced so that the calculated terminal velocity would match the final velocity state obtained during an actual test, thus making the calculated driving forces in the plate similar to actual forces experienced during a test. Figure 2 shows the results of a WONDY calculation for a high velocity, small scale design consisting of an 8.5 mm (.335 in.) thick aluminum (6061-T6) flyer plate, driven to a terminal velocity of 3200 mps (10,500 fps) by 1.42 kg (3.125 lb) of Composition C-4 explosive in a 28.4 kg (62.5 lb) tamping barrel. The plot shows the state of stress (pressure) at points in the explosive gases that drive the plate as well as points within the plate. The flyer plate had reached terminal velocity by the time of the plot, and there are no spall planes evident, as desired.

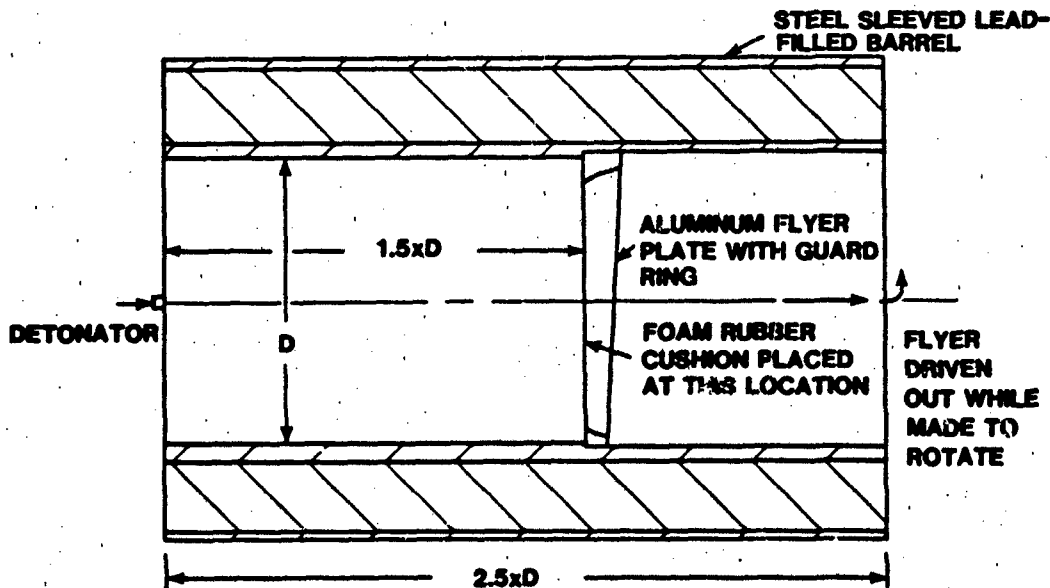
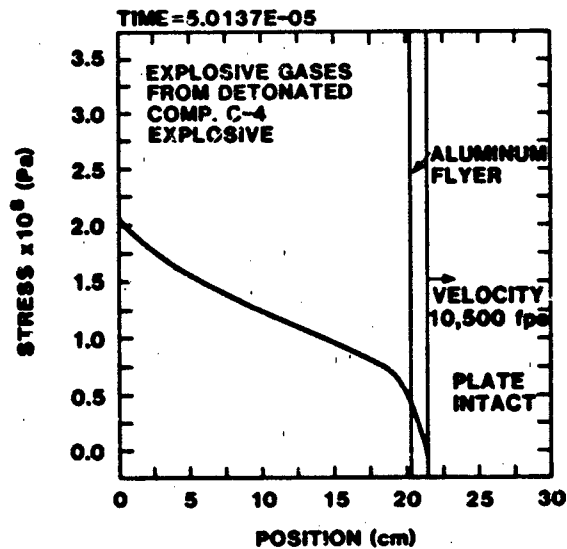


Fig. 1 - Barrel Tamped Explosive Flyer Plate System



1/4 SCALE, AL PLATE, 0.062 IN GAP 10500FPS 7/27/83

Fig. 2 - One-Dimensional Calculation of Shock Driving Pressures for Standard High Velocity Design

If the same explosive design is used (same explosive type and same barrel) but the flyer plate thickness is increased to reduce the terminal velocity to 1830 mps (5000 fps), calculations show that spall planes result. Figure 3 shows the pressure-position plot for the shock wave calculations of this configuration. The overall thickness of the plate has increased (indicating that the front spall plates are moving faster than the back plates). A plate in this condition would not produce an adequate impact fuze test.

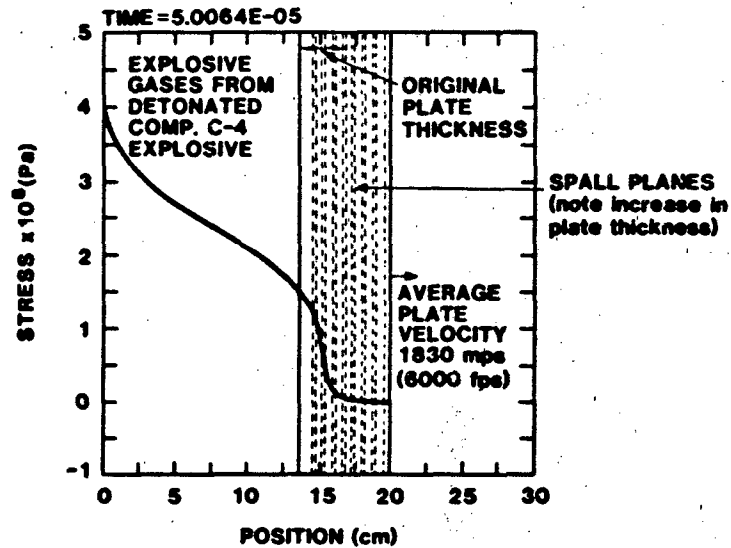
The spall planes in the flyer plate are generated by tensile waves reflecting from the free face (opposite the explosive loaded face) of the flyer back into the plate. Simple spall failure models generate a spall plane when the reflected tensile wave reaches a threshold value, while other more sophisticated models [5] are based on accumulated damage generated whenever the tensile pressures rise above a threshold value. The local density is lowered to reflect the damage. For the purposes of this paper, only relative spall damage is of importance, so the spall model is not extremely important. A spall damage threshold of  $20 \times 10^8$  Pa (20 kbars) in simple tension was chosen after the work of Jones [6].

One approach to lessen spall damage in a chosen material is to lower the driving pressure which must then "push" longer to obtain the same flyer velocity. Lower stress gradients in the plate cause reduced reflected tensile stresses and therefore a reduced tendency to spall. The detonation pressure (C-J pressure) of the explosive is indicative of the plate driving pressure and is related to explosive properties:

$$P_{C-J} = \frac{\rho D^2}{1 + \gamma}$$

From this equation it is readily seen that reducing  $\rho$  (the density) and  $D$  (the detonation velocity) will decrease the C-J pressure ( $P_{C-J}$ ). The ratio of specific heats ( $\gamma$ ) for most explosives is between 2.5 and 3. The C-J pressure for Composition C-4 is  $278 \times 10^8$  Pa (278 kbar) ( $\rho = 1.59$  gm/cm<sup>3</sup>,  $D = 3040$  mps,  $\gamma = 2.7$ ).

Nitromethane, a liquid explosive with both a low density (1.14 gm/cm<sup>3</sup>) and detonation velocity (6240 mps) and a gamma of 2.45 [the C-J pressure is  $128 \times 10^8$  Pa (128 kbars)] [7,8] is a possible alternative explosive for driving thick plates to lower velocities. Table 1 shows comparative properties of explosives considered as an



1/4 SCALE, AL PLATE, 0.062 IN GAP 6000 FPS 7/27/83

Fig. 3 - One-Dimensional Calculation of Shock Driving Pressures with Comp. C-4 Explosive for Low Velocity Design

TABLE 1  
Properties of Candidate Explosives  
for Driving Low Velocity Flyer Plates

Explosive	Density (gm/cm <sup>3</sup> )	Detonation Velocity (mps)	$\gamma$ Range	C-J Pressure ( $\times 10^8$ Pa) (Kbar)	Comment
Nitromethane	1.14	6240	2.45	128	Liquid
Amatol 60/40 (Ammonium nitrate/TNT)	1.50	5760	2.70-3.00	134-124	Solid
Nitroguanidine	1.55	7650	"	245-227	"
TNT	1.56	6640	"	186-172	"
Cyclotol 70/30 (RDX/TNT)	1.73	8060	"	304-281	"
Comp. C-4	1.59	8040	2.70	278	"

Properties obtained from Army Material Command pamphlet "AMCP 706-177 Engineering Design Handbook - Properties of Explosives of Military Interest," January 1971.

alternative to Composition C-4. The explosive performance data used along with nominal barrel dimensions indicated an expected velocity in the range between 1524-1830 mps (5000-6000 fps). WONDY V calculations show that only minor spall damage may occur. Figure 4 shows the results of the shock wave calculations. Note that some spall cracks exist; however, the plate thickness is closer to the initial thickness (compare with Figure 3), and there is no appreciable velocity gradient across the plate thickness. The result is not exactly as desired but may be acceptable.

For proper initiation of nitromethane, a shock pressure of greater than the C-J pressure [ $128 \times 10^8$  Pa (128 kbars)] is needed. Calculations indicate that detonation of Composition C-4 explosive into nitromethane should generate a pressure of  $150 \times 10^8$  Pa (150 kbars) thus causing initiation of the nitromethane. Composition C-4 is easily initiated with a standard detonator and booster pellet. The design of the system, shown in Figure 5, was expected to meet the test requirements. A pad of Composition C-4 was placed at the end of the barrel with a thin aluminum barrier to separate it from the nitromethane. The barrel

contained two holes near the barrier for fill and vent of the nitromethane.

The calculation of design performance was accomplished by determining the equivalent length of nitromethane which would cause the same effect as the Composition C-4 initiator. This length was then used to replace the Composition C-4 to give a simple, single explosive barrel system as required for calculation [2]. Lateral and aft gas expansion is empirically accounted for in the method prescribed. The equivalent length was determined by using the barrel calculation method to determine the length of nitromethane [47 mm (1.85 in.)] which would drive the aluminum plate to the same terminal velocity as the 25.4 mm (1.00 in.) Composition C-4 initiator. The calculated terminal velocity for the all nitromethane equivalent system was 1612 mps (5287 fps).

#### EXPERIMENTAL VERIFICATION

The small-scale explosive system (Figures 5 and 6) was fabricated and test fired in order to determine if the method for predicting final velocity was adequate and if the driving pressures were indeed low enough to cause

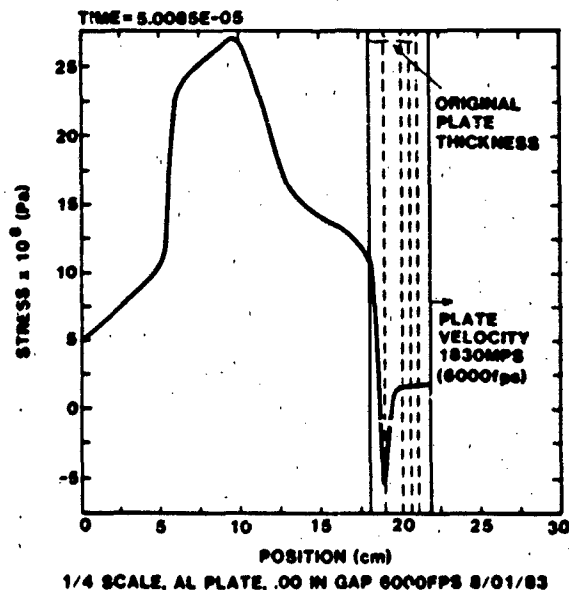


Fig. 4 - One-Dimensional Calculation of Shock Driving Pressures with Nitromethane Explosive for Low Velocity Design

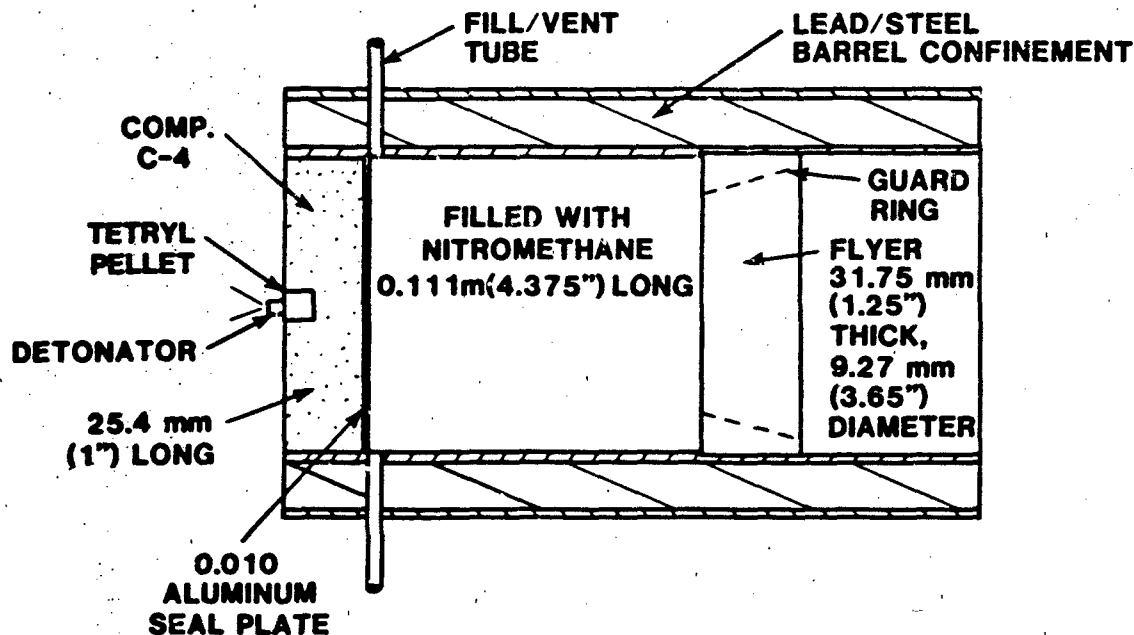


FIG. 5 - Explosive System

only minor spall damage. The barrel axis was oriented vertically with the nitromethane fill and vent tubes at the top of the cavity volume. Nitromethane was carefully poured into the barrel cavity to insure that no air bubbles were trapped within the barrel. A single bridge wire detonator (Reynolds RP-2) was attached to the tetryl pellet booster within the pad of Composition C-4. The flyer plate was accelerated downward for 1.19 m (47 in.) where a normal impact with a simulated nose tip occurred. Flash x-ray exposures were made at three equally spaced positions along the flyer trajectory. The x-ray source was directed perpendicularly across the trajectory onto three x-ray films housed within protective cassettes. The film was located 0.46 m (18 in.) away from the trajectory. Figure 7 shows the test setup. The x-ray pulse length was 70 ns, which produces clear x-ray shadow graphs of the flyer during transit. Figure 8 shows one x-ray exposure taken after the flyer had traveled half the trajectory length. The x-ray data allowed accurate measurement of the flyer velocity [1573 mps (5160 fps)] as well as documentation of the flyer plate condition. The measured terminal velocity was within 2.5 percent of the calculated value, which is accurate enough for velocity predictions. Evidence of spall damage is visible at the edges of the flyer plate; however, the plate thickness remains unchanged (within

measurements resolution). Spall cracks may exist but no large voids are apparent, which agrees with the spall calculations shown in Figure 4. The results of this test are documented in a test report [9].

#### CONCLUSION

A method has been devised for calculating the performance of an explosive system designed to drive thick aluminum plates to relatively low velocities [1573 mps (5160 fps)] for conducting impact fuze studies. An experiment was designed based on this method and was conducted to produce velocity and flyer plate condition measurements. Calculation predicted the terminal velocity within 2.5 percent, and the flyer had some spall damage as expected (based on shock code prediction) but was intact and the plate thickness remained unchanged. These results support the design of a 68.1 kg (150 lb) nitromethane explosive system\* which will drive a .127 m (5 in.) thick plate to a velocity of 1585 mps (5200 fps) before impacting a contact fuze system.

\* Scaling laws for complete spall are not fully developed; however, Ref. [10] indicates that relative spall damage may not be much worse than in the small scale systems.

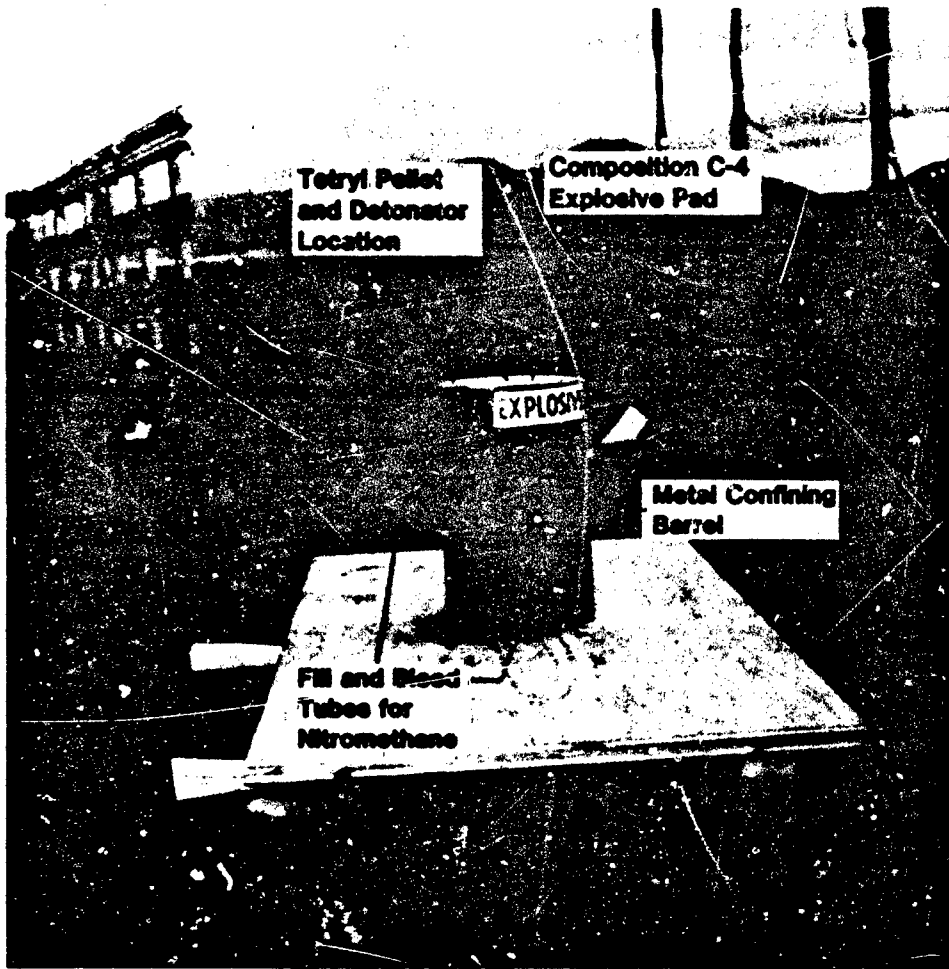


Fig. 6 - Explosive System

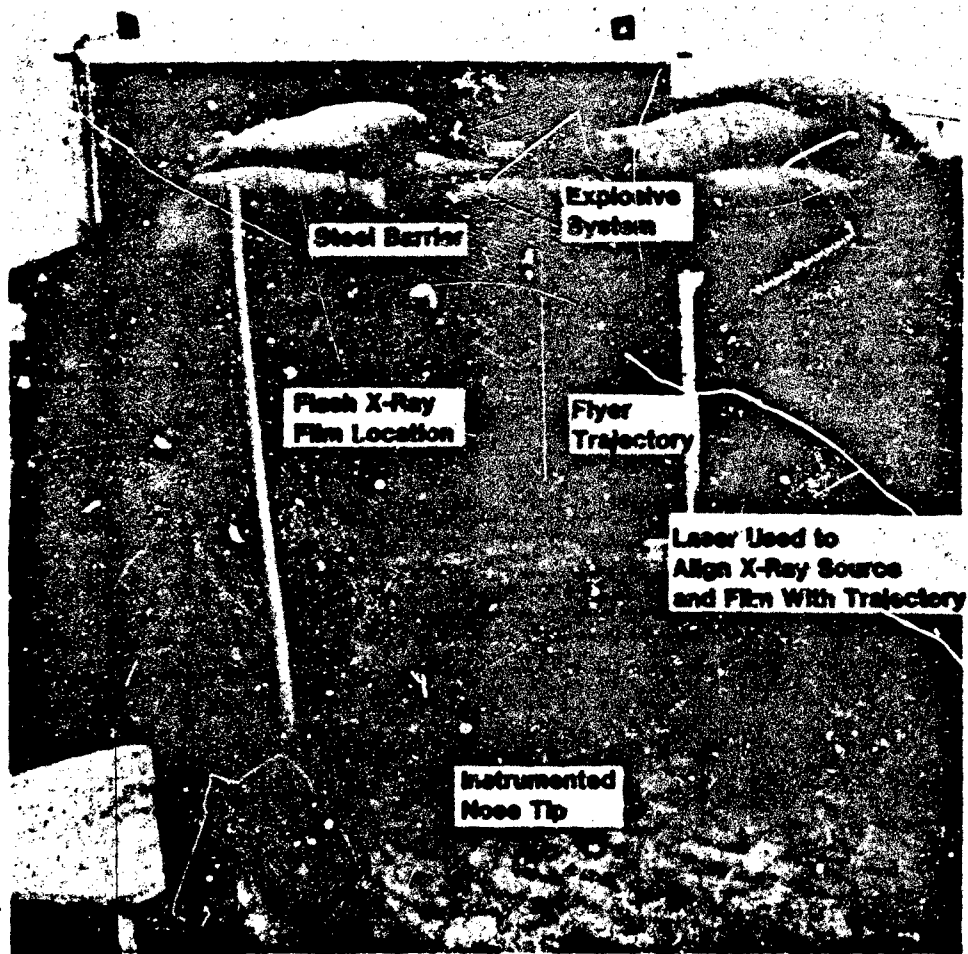


Fig. 7 - Test Setup for Low Velocity Design

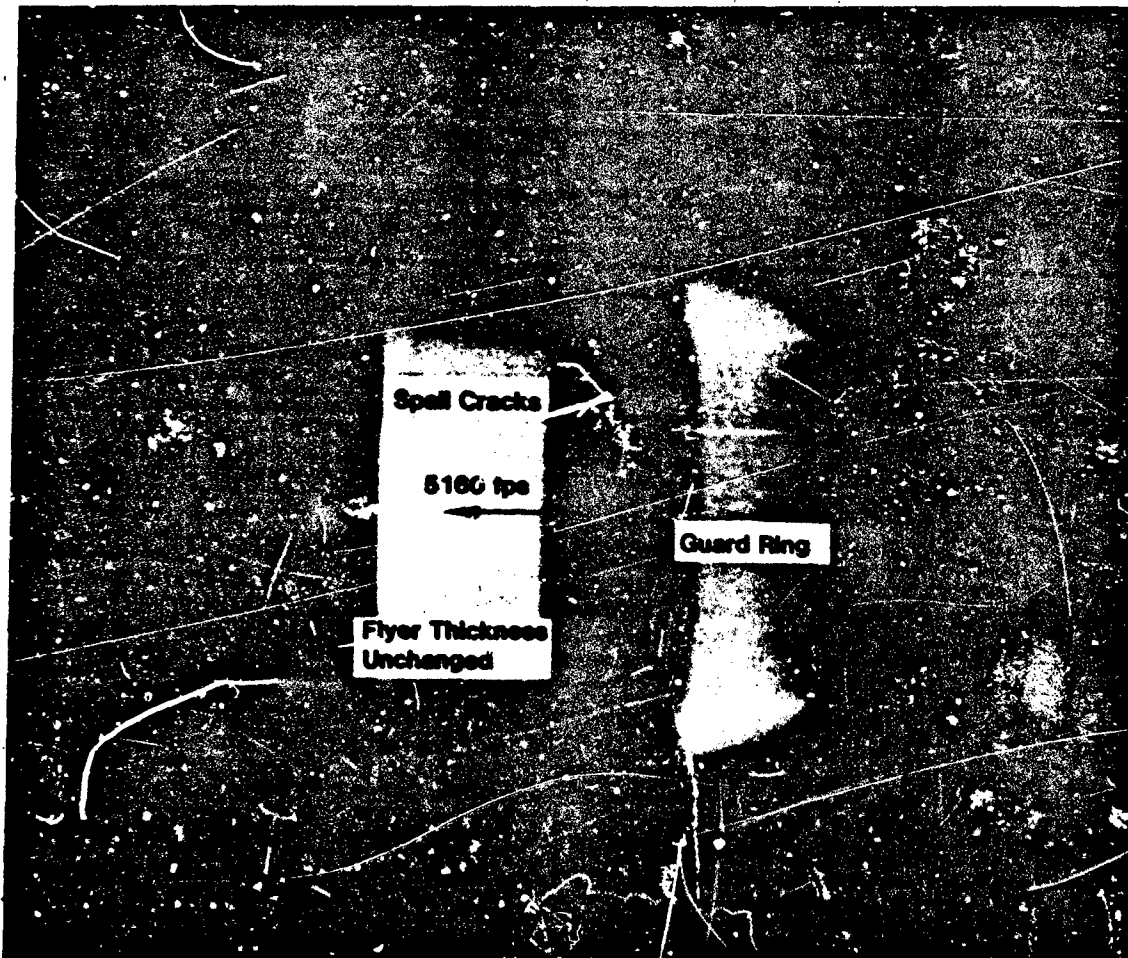


Fig. 8 - Flash X-Ray Exposure of Flyer Plate  
During Transit to Impact (5160 fps)

#### ACKNOWLEDGEMENTS

The author would like to thank Ben Duggins, Dale Hill and Louis Perea for conducting the experiment, Marlin Kipp for consultation on WONDY V, and Jeana Pineau for preparing this report.

#### REFERENCES

1. F. H. Mathews and B. W. Duggin, "Barrel-Tamped, Explosive Propelled Plates for Oblique Impact Experiments," Shock and Vibration Bulletin, No. 46, Part 2, pp. 145-154, Aug. 1976.
2. R. A. Benham, "Terminal Velocity and Rotation Rate of a Flyer Plate Propelled by a Tube-Confined Explosive Charge," Shock and Vibration Bulletin, No. 49, Part 2, pp. 193-201, Sept. 1979.
3. R. A. Benham, "A Technique Combining Heating and Impact for Testing Reentry Vehicle Impact Fuzes at High Velocity," Shock and Vibration Bulletin, No. 52, Part 3, pp. 53-63, May 1982.
4. M. E. Kipp and R. J. Lawrence, "WONDY V - A One-Dimensional Finite-Difference Wave Propagation Code," Sandia National Laboratories Report SAND81-0930, June 1982.
5. F. R. Tuler and B. M. Butcher, "A Criterion for the Time Dependence of Dynamic Fracture," Intl. Journal of Fracture Mechanics, Vol. 4, pp. 431-437, 1968.
6. O. E. Jones, "Metal Response Under Explosive Loading," Proceedings of 12th Annual ASME Symposium at UNM, March 2-3, 1972, subject: Behavior and Utilization of Explosives in Engineering Design, pp. 125-148.
7. D. R. Hardesty and P. C. Lysne, "Shock Initiation and Detonation Properties of Homogeneous Explosives," Sandia National Laboratories Report SLA74-0165, pp. 70-87, May 1974.
8. J. W. Nunziato and M. E. Kipp, "Numerical Studies of Initiation, Detonation and Detonation Failure in Nitromethane," Sandia National Laboratories Report SAND81-0669, pp. 33 and 96-97, Apr. 1983.
9. Sandia National Laboratories letter report from R. A. Benham to G. E. Clark and D. R. Henson, subject: "Low Velocity, Explosive Flyer Plate System Test," Aug. 8, 1983.
10. J. Lipkin and M. E. Kipp, "Wave Structure Measurement and Analysis in Hypervelocity Impact Experiments," Journal of Applied Physics, Vol. 47, No. 5, pp. 1979-1986, May 1976.

## EXPERIMENTAL INVESTIGATION OF VIBROIMPACT OF TWO CANTILEVER BEAMS

C.N. Bapat and S. Sankar  
Department of Mechanical Engineering  
Concordia University  
Montreal, Quebec, Canada

The damping effect of collisions occurring at only one point along the length between two cantilever beams in free and forced vibrations were experimentally investigated. The use of a snubber made from neoprene pad instead of a steel stud at the impact location had little effect on the free vibrations. In forced vibrations with one sided clearance, displacement amplitudes were reduced considerably when the resonant frequencies of beams differed. The performance with steel stud and a neoprene pad looked like that of a highly damped system with positive shift in the resonant frequencies. The maximum displacement amplitude with steel stud was approximately 25% smaller than that for the neoprene pad. However, the noise level, on average, was 10 dBA higher. The forced vibration response with two sided clearance looked like that of a single oscillator and displacement amplitudes were larger than that with one sided clearance. The tip of the beam as an impact point and smallest possible one sided clearance produced minimum displacement amplitudes in the forced vibrations and fastest decay of displacement in the free vibrations.

### NOMENCLATURE

- $d$  = gap between secondary beam and impact point, mm.  
 $l$  = distance of impact point from base, mm.  
 $S_0$  = base displacement, mm.  
 $\Omega$  = excitation frequency, Hz.  
 $X$  = tip displacement, mm.  
 $X_0$  = initial tip displacement, mm.  
 $X_{rms}$  = rms value of tip displacement, mm.

### 1. INTRODUCTION

Damping of resonant vibration can be achieved by attaching an auxiliary oscillator such as a conventional dynamic neutraliser to the main system. However, some of the problems associated with this arrangement during forced vibrations are: a. excessive displacement of the secondary system and b. the need for precise control of damping stiffness and auxiliary mass to achieve the best performance. This system is also extremely sensitive in the resonant range and hence there is a possibility of large displacements due to either increase or decrease in the excitation frequency. This is also not a good damper in free vibration.

Many of the disadvantages can be alleviated by fixing the properly designed secondary unit to the base of the primary unit, in such a way that during vibrations these oscillators collide producing an intermittent force which results in reduction of the displacement amplitude of the main mass [1]. There are many practical applications of this arrangement: in controlling displacement amplitudes of piping systems [2,3] and, in printed circuit boards [4] where snubbers with small clearances are used between two systems. The machines used in compacting [5], vibratory feeding [6], and pile driving [7], and the problems such as dynamic drift due to impacts leading to mismeasurement [8], high stresses in gear trains and collisions between independent structures [9], can be modelled in the first approximation, as vibroimpacts of two oscillators.

In the vibration control aspect considered theoretically by Cempel [1], only one unit is forced excited while in Ref. 4, the simplified design procedure is given for the particular application without theoretical or experimental verification. Masri studied a similar system, theoretically for massless secondary, and experimentally [2,3] for a quite stiff secondary system.

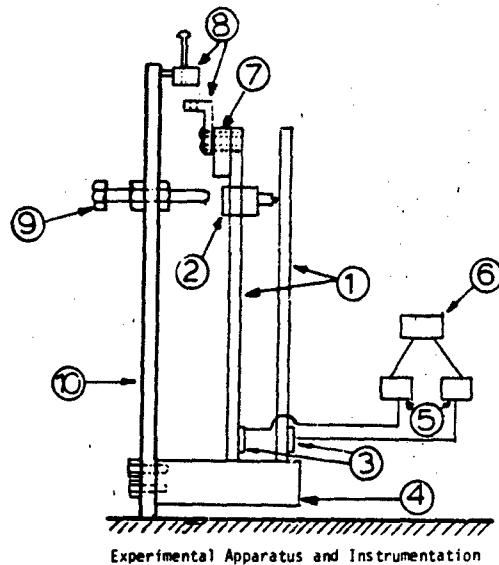
The aim of the experimental investigation is to study only the displacement control aspect of the vibroimpact system in detail. The effect of excitation frequency and amplitude, different snubbers made from steel or a neoprene pad, position of impact point from the base and one or two sided clearance on the free and forced vibration will be considered.

## 2. FREE VIBRATIONS

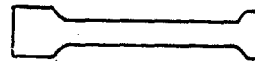
A schematic diagram of the experimental apparatus and measuring equipment is shown in Fig. 1(a). Two identical beams each weighing 0.230 kg machined from spring steel with the dimensions 30.23 x 2.54 x 0.3175 cm (11.9 x 1.0 x 0.125 in) in a particular shape of I shown in Fig. 1(b) were fixed to an aluminium block at the base. A specially designed slider weighing 0.054 kg. was used to adjust the position of the impact point along the beam (Fig. 1(c)). It could also accommodate a pointed steel bolt or a neoprene snubber shown in Fig. 1(d) having contact area 645.16 mm (1 x 1 in.) and thickness 12 mm (0.5 in.) glued to the stud. For convenience, the beam with slider will be called the primary beam and the other a secondary beam. The gap between the secondary beam and the top portion of the snubber can be adjusted. It can be seen from Fig. 1(c) that during vibration impacts can occur only on one side of the secondary beam and hence this is called an one sided clearance case. Whereas a two sided clearance case is one in which device shown in Fig. 1(e) is fixed to the primary such that impacts occur on both sides of the secondary beam.

The behaviour of beams with two sided clearance will be considered only in the forced vibration case. Additionally an aluminium block weighing 0.087 kg was attached to the top portion of the primary beam intentionally to achieve the difference in their natural frequencies. Both beams were tightly clamped to the aluminium base, item 4, as shown in Fig. 1(a). Two temperature compensated strain gauges were glued to the beams at the base and strains were recorded on the dual channel strip chart recorder and were calibrated to measure the displacement. The initial displacement  $X_0$ , at the tip of the primary beam was set to a certain value by using screw, item 9, and the system was allowed to vibrate freely by using a release mechanism, item 8.

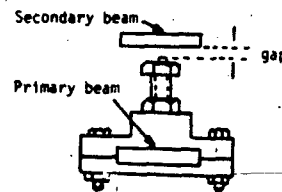
Primary beam impacted the secondary beam whenever initial deflection was greater than the gap and impact ceased to exist only when maximum deflection was less than the gap. The best impact location is one which produces fastest reduction in the maximum displacement during free vibration. To find this location, the distance of the impact point from the base was varied in steps and the results are shown in Fig. 2 for constant  $X_0 = 8.3$  mm. The top and bottom trace represents the deflection of the secondary and primary beam respectively. Careful examination of Fig. 2(a) through 2(d) indicates that the damping effect of impacts



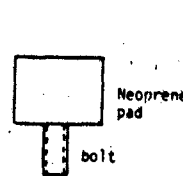
- |                     |                        |
|---------------------|------------------------|
| 1. Beams            | 6. Stripchart Recorder |
| 2. Slider           | 7. Aluminium Block     |
| 3. Strain Gauge     | 8. Release Mechanism   |
| 4. Aluminium Base   | 9. Adjusting Screw     |
| 5. Strain Indicator | 10. Heavy Beam         |



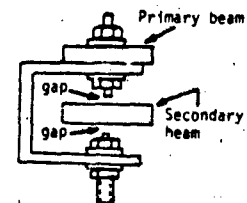
(b) Beam Details



(c) Slider details



(d) Neoprene pad



(e) Two Sided Clearance

Figure 1.

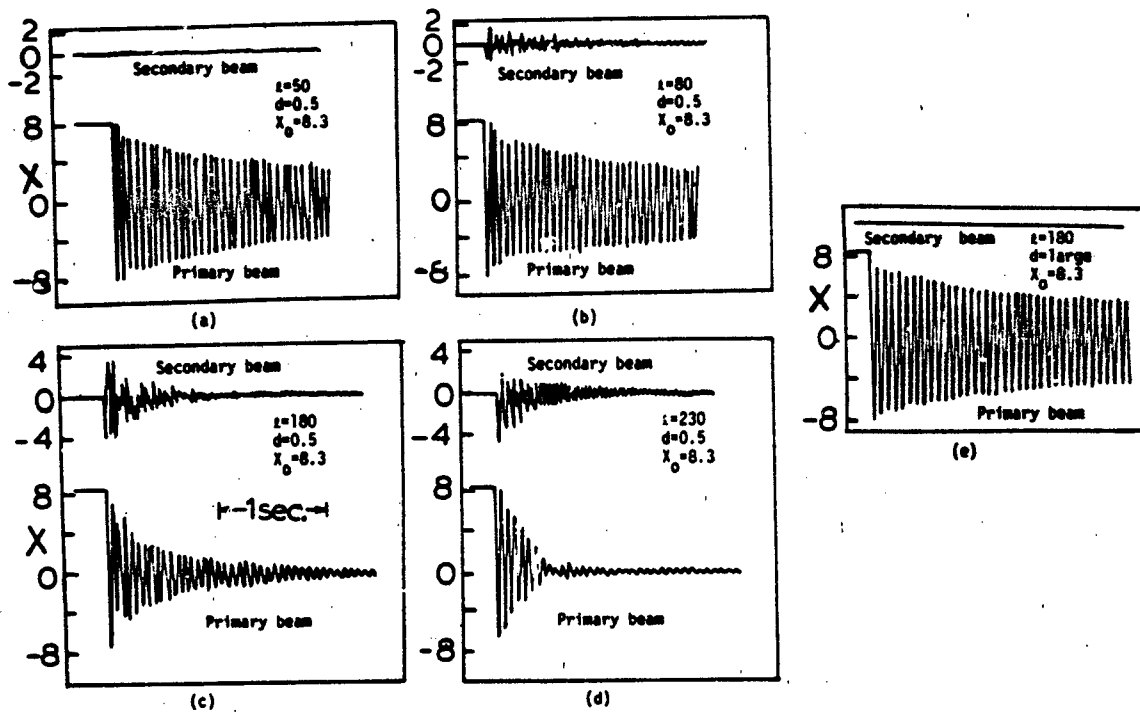


Figure 2. Effect of position of impact point on the free decay of beams using elastomer snubber.

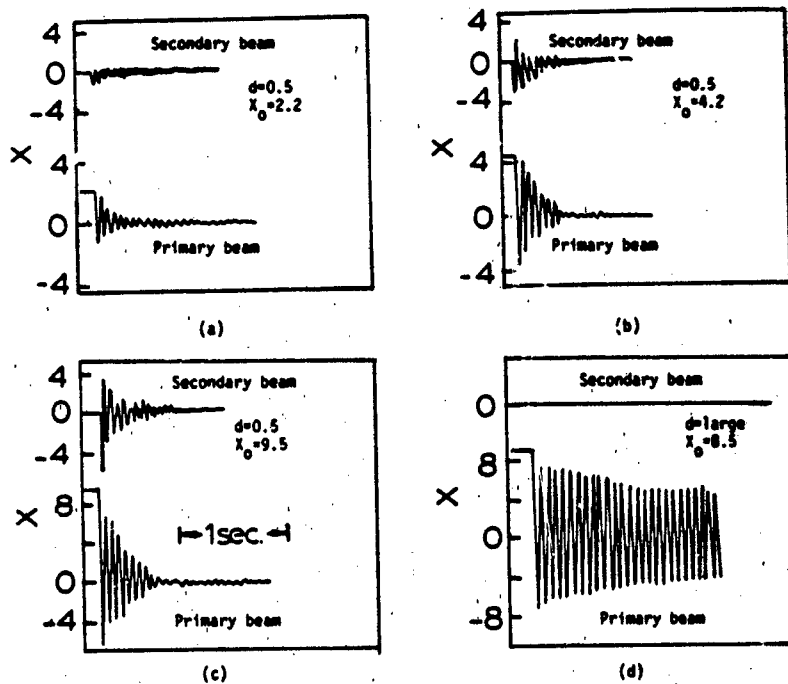


Figure 3. Effect of initial deflection on the free decay using steel bolt as a snubber. Distance from base=230.

increases, as compared to the nonimpact case of Fig. 2(e), as impact point moves away from the base i.e. towards the tip of the cantilever. The damping produced is largely due to energy lost at impact. The energy loss increases with the increase in the relative velocity at impact which increases as impact point moves towards the point of maximum velocity, i.e. tip of the beam. The effectiveness of damping can be seen as a difference in Fig. 2(e) and Fig. 2(a), (b), (c), and (d). Energy is transferred from one system to another due to impacts and inherent internal damping of both beams consume some of the energy. Noise produced during impact and frictional energy loss due to rubbing between the snubber and the secondary beam also adds to the energy loss. The decrease of displacement is quite fast till impacts occur and afterwards in the impactless time interval systems vibrate freely with very little damping. Hence the amplitude in the impactless vibration region decreases with the decrease in the gap as impacts continue occurring till the maximum deflection becomes less than the gap. The effect of initial deflection when impact point was 230 mm from the base shown in Fig. 3(a), (b) and (c) indicate that the damping produced depends on the initial deflection. However, in all cases deflection decrease was very fast initially when impacts occurred. The time required to reduce amplitude to the small level, and the displacement amplitudes of the secondary, increase with initial deflection,  $X_0$ . However, the system still maintains good amplitude reduction characteristics as evident from the comparison of Fig. 3(a) through (c) with Fig. 3(d) where, due to a large gap, impacts do not occur at all. The behavior of system with neoprene and steel snubber was found very similar and hence separate figures are not given.

### 3. FORCED VIBRATIONS

A schematic diagram of the experimental model and measuring equipment is shown in Fig. 4. The previously discussed setup was fixed to a hydraulic shaker, having large inertia, to reduce the effect of impacts on the shaker. Sinusoidal displacement of the base,  $S_0 \sin \Omega t$ , was produced and was monitored. The impact patterns were monitored by observing the acceleration of the tip which showed a large spike at impact which is clearly seen in the second trace from top in Fig. 5(b) and 5(d). The base displacement, acceleration, and the tip displacements of two beams were monitored on a four channel oscilloscope and typical waveforms of these are shown respectively from top to bottom in Fig. 5 for two different frequencies of 15.5 Hz and 23 Hz and with impacts (Fig. 5(b) and 5(d)) and without impacts (Fig. 5(a) and 5(c)). The occurrence of impact can be monitored very easily, which in Fig. 5(d) is somewhat erratic while in Fig. 5(b) is nearly regular. The comparison of tip displacement of both beams at 23 Hz in Fig. 5(c) and (d) indicate that the amplitude of the primary beam was reduced by a substantial amount while the displacement of secondary was slightly increased due to impacts. However

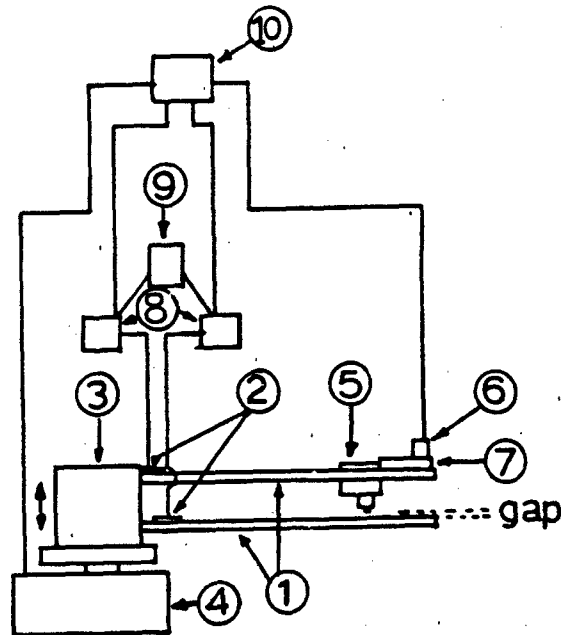


Figure 4: Experimental Set-Up for Forced Vibrations

#### Key:

- |                    |                               |
|--------------------|-------------------------------|
| 1. Beams           | 2. Strain Gauges              |
| 3. Aluminium Base  | 4. Hydraulic Shaker           |
| 5. Slider          | 6. Accelerometer              |
| 7. Aluminium Block | 8. Strain Indicator           |
| 9. FFT Analyser    | 10. Four Channel Oscilloscope |

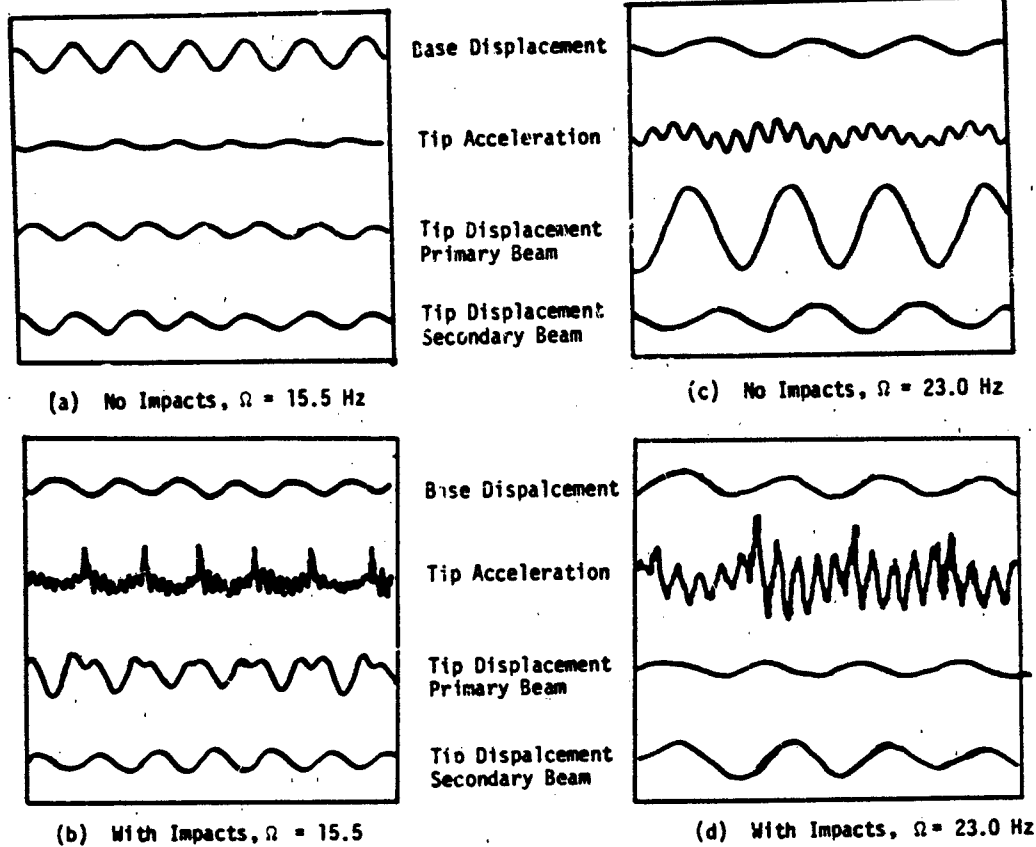


Figure 5: Waveforms of Base Displacement, Tip Acceleration and Displacement  
Base Amplitude = 0.254 mm, gap = 0.5 mm

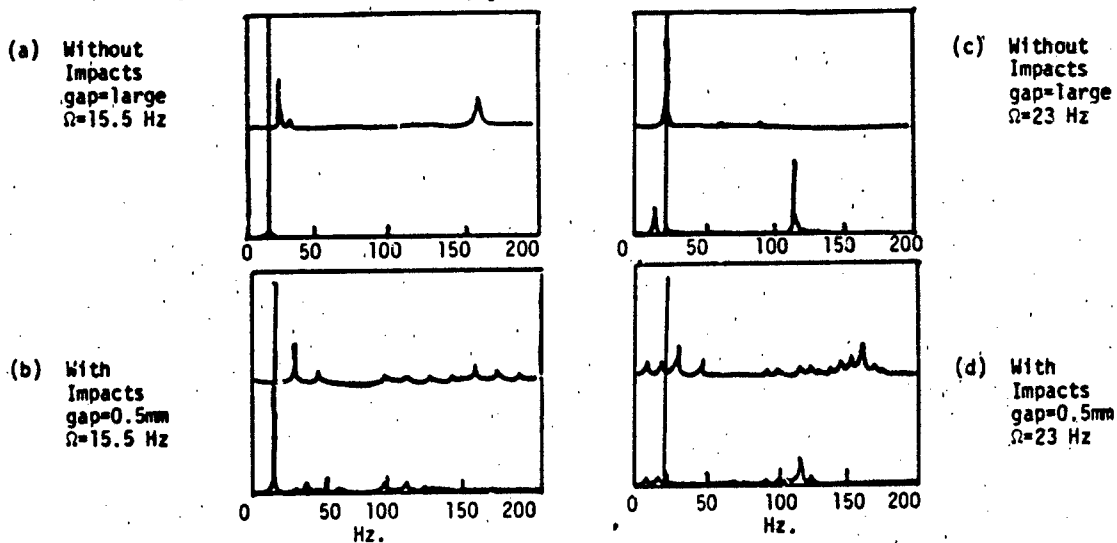


Figure 6: FFT Spectrum Without and With Impacts  
Base Amplitude = 0.254 mm, Impact Point 230 mm from Base

due to impacts, there was slight increase and distortion of displacement waveform at 15.5 Hz. The waveform with impacts are nearly periodic but not exactly sinusoidal and hence the FFT analyser was used to find out the rms values of displacement. These rms values of displacements,  $X_{rms}$ , were obtained after initial transients had died and the time period was selected as 8 seconds in which at least 120 excitation cycles were complete. Doubling the time duration had very little effect on the rms values and hence 8 seconds was considered adequate. The acceleration at the tip showed increase due to impacts as compared to the non-impact case. The corresponding FFT spectrums of displacements of the beams are shown in Fig. 6 without and with impacts. The largest peaks which match in the top and the bottom figures correspond to the excitation frequencies or the resonant frequencies of the beams. However, the creation of many other frequencies in Fig. 5(b) and (d) was solely due to impacts which excited higher modes of the beams due to broad impact spectrum.

The first resonant frequency and damping ratio of the primary and secondary beam was found to be approximately 14.25 Hz, 23.25 Hz, and 0.0052, 0.0082 respectively. The usual method of free decay and sinusoidal resonant tests were used. Thus systems were lightly damped.

The arrangement considered here is basically used to suppress the resonant displacement amplitudes of both beams. The variation of rms values of displacements in the frequency range of 10 to 35 Hz which covers the first resonance of both the beams, with and without impacts is shown in Fig. 7(a) and 7(b) for the primary and secondary beam respectively with one sided gap of 0.5 mm and base displacement of 0.254 mm. The impact point was 230 mm away from the base. The Fig. 7 shows that the resonant amplitudes in the frequency range of 14-16 Hz and 22-24 Hz of the primary and secondary beams respectively are drastically reduced. However a pseudo resonance with peaks of fairly small amplitudes of about 2.15 mm and 2.0 mm occur at 16.1 Hz in case of primary and secondary beams respectively. A small peak of 1.25 mm at 28.5 Hz can be seen in the response curve of the secondary beam. The vibro-impact system considered was highly nonlinear and the nonlinearity is of hardening type. And this is reflected by the pseudo peaks at somewhat higher than the natural frequencies of the beams. Otherwise the displacement amplitudes remain fairly small compared to the resonant displacements of impactless beams. The effect of excitation level on the displacements clearly shows the complex nonlinear behaviour (see Fig. 8). The  $X_{rms}$  for both beams at the base displacement of 0.508 mm are not twice that of a 0.254 mm and these are compared for selected values of excitation frequencies for both the cases of impact point at 180 mm and 230 mm in Table 1. This table indicates that due to highly nonlinear hardening type behaviour the deflections at 0.508 mm base displacement in

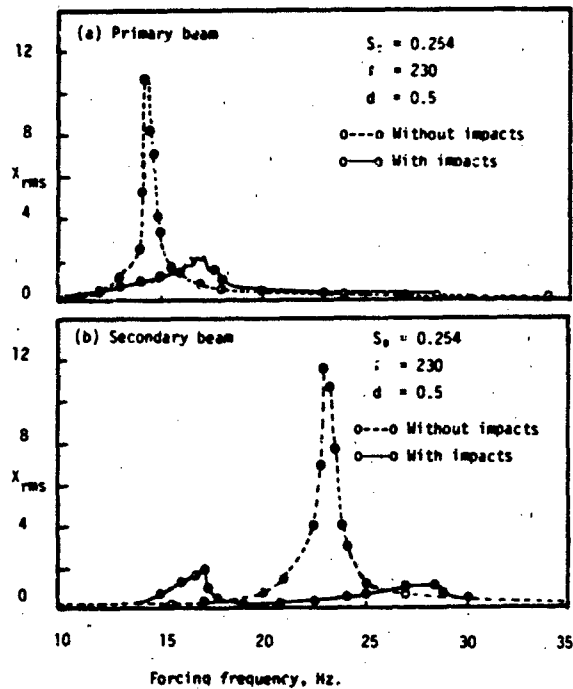


Figure 7. RMS displacement amplitudes of beams with steel connector.

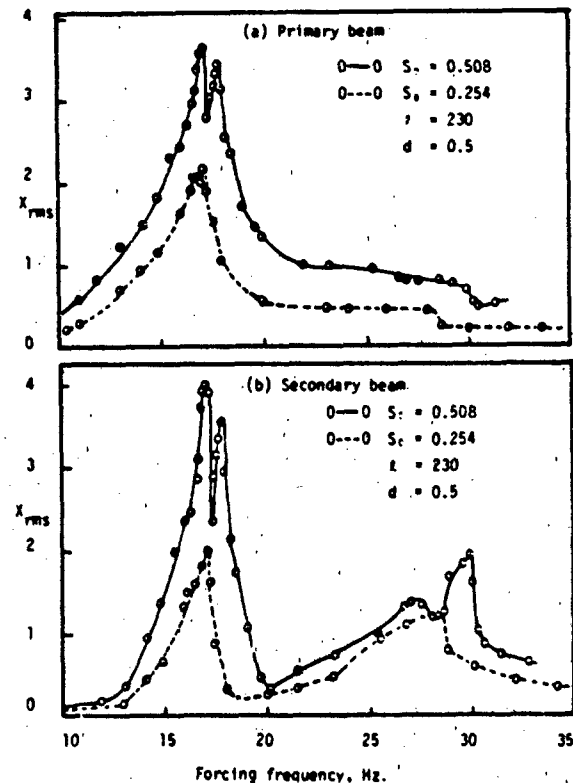


Figure 8. Effect of amplitude of excitation on the response using steel connector.

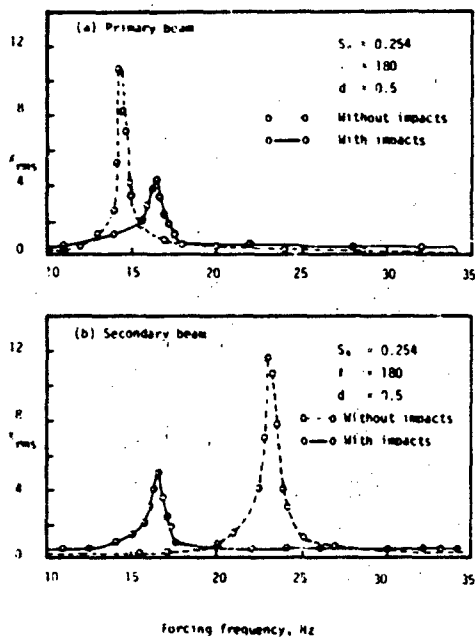


Figure 9. Effect of impact point from base on the RMS displacement using steel connector.

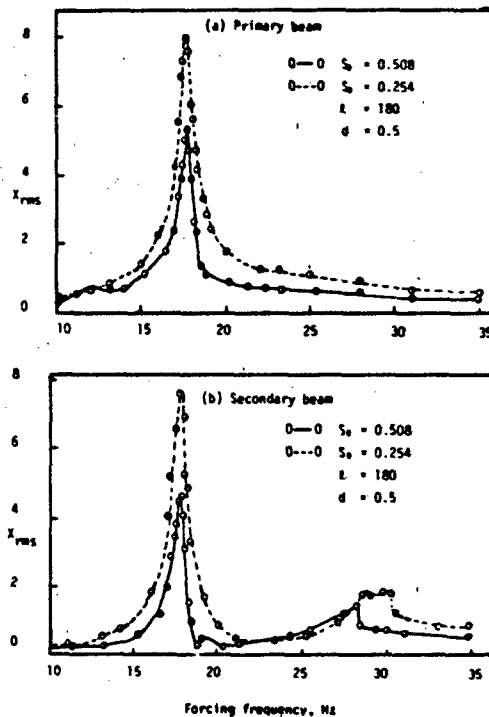


Figure 10. Effect of amplitude of excitation on response using steel connector.

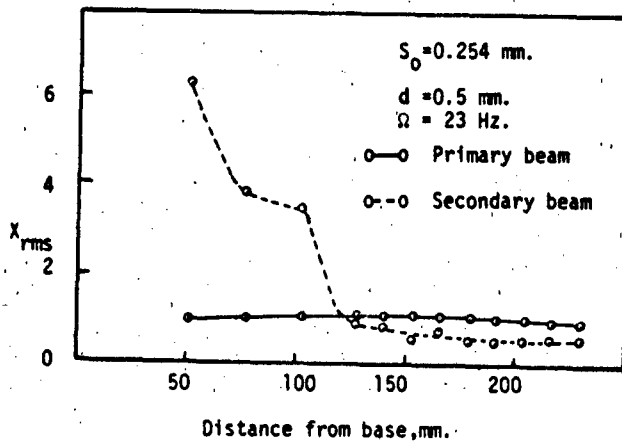
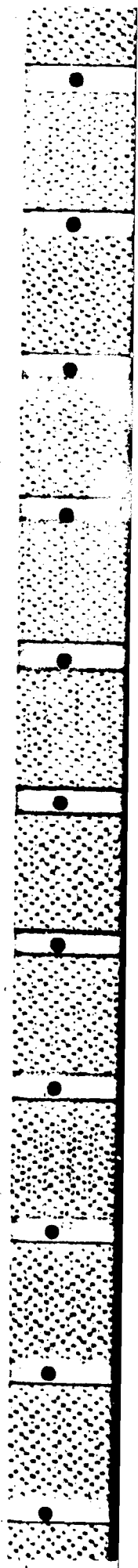


Figure 11. Effect of position of impact point from base on the response using steel connector.



most of the cases are less than twice the value at base displacement of 0.254 mm.

Table 1: Comparison of  $X_{rms}$  at different  $S_0$  and  $l$  for Steel Snubber

	$l = 230$				$l = 280$			
	Primary		Secondary		Primary		Secondary	
	0.254	0.508	0.254	0.508	0.254	0.508	0.254	0.508
			$X_{rms}$					
15	1.20	1.8	0.73	1.50	1.06	1.38	0.53	1.07
16.25	1.80	2.76	1.62	2.30	3.84	5.46	3.46	6.53
25	0.46	0.92	0.84	0.96	0.61	1.07	0.53	0.69
30	0.19	0.67	0.61	1.61	0.46	0.69	0.69	1.84

The two peak behaviour not so clear between 16 to 17 Hz. for 0.254 mm base displacement is quite clear at 0.508 mm. In Fig. 8 the phenomenon similar to the jump in the nonlinear hardening spring can be seen around 28.5 and 30 Hz for 0.254 and 0.508 mm base displacement. The effect of reducing the distance from the base of an impact point,  $l$ , from 230 mm to 180 mm is shown in Fig. 9. Comparing Fig. 7 with Fig. 9 indicates that the maximum displacement amplitude of the primary and secondary beam has increased from 2.1 mm to 5.5 mm and from 2 mm to 4.7 mm respectively and the frequency at which this occurs has also increased from 16.1 Hz to 17.8 Hz. This increase in frequency is due to the decrease in the effective mass as the pointer moves towards the base while effective stiffness remains nearly constant. The maximum displacement amplitude has increased because the energy lost at impact is decreased due to the decrease in the relative velocity at impact. The effect of amplitude of base excitation on the response when impact point was 180 mm from base is shown in Fig. 10. Comparison of results for  $l = 230$  and  $l = 180$  shown in Fig. 8 and 10 indicates that the two peak behaviour in the frequency range of 16 to 17 Hz for the former has disappeared and the maximum  $X_{rms}$  has nearly doubled. It seemed that the position of the impact point has substantial effect on the response.

The effect of the position of impact point on the response of beams excited in the resonant range of the secondary beam at 23 Hz is shown in Fig. 11. It indicates that the tip rms displacement of the secondary beam increases with the decrease in the distance of the impact point from the base. However, the response of the primary nonresonant beam remains nearly constant. The behaviour studied here indicates that the tip, which is the point of maximum displacement in this frequency range is the most suitable impact point from the point of view

of amplitude reduction. Similar performance was observed when the excitation frequency was in the resonant range of the primary system. Hence in most of the cases studied the connector was fixed to the beam at 230 mm from the base which was the most practically possible position of maximum distance from the base.

A successful attempt was made to reduce the noise level, produced due to metals contacting during impacts, by using neoprene pad of 625.25 mm<sup>2</sup> area, as an impacting connector. The effect of using the hard neoprene, similar to the neoprene pads used in the bearings for bridges, on the displacement performance can be seen in Fig. 12(a) and (b) for the primary and secondary beams respectively. The double peak region not so clear in the metal stud case becomes quite clear even at 0.254 mm base displacement. The displacement amplitudes here are in general larger than that in case of a steel stud for the primary as well as secondary beam. The two peaks at 15.5 Hz and 17.5 Hz are quite clear in Fig. 12 in the response of the primary system. Similar two peaks exactly at the same frequencies were observed in the response of the secondary beam. However an additional peak of approximately 1.5 mm is observed at 31.25 Hz. The effect of base amplitude on the response shown in Fig. 13 is similar to the case of a steel stud.

The comparison of noise level, measured using A weighting network of the sound level meter, for the steel and neoprene connector is shown in Fig. 14. The microphone of the sound level meter was 25 cm away from the point of impact. The noise level when neoprene connector was used is slightly higher than the noise level produced in the impactless system and the maximum difference is less than 3dBA. However, the noise level when steel connector is used is quite high reaching 82 dBA maximum and on an average is 10 dBA higher than the neoprene

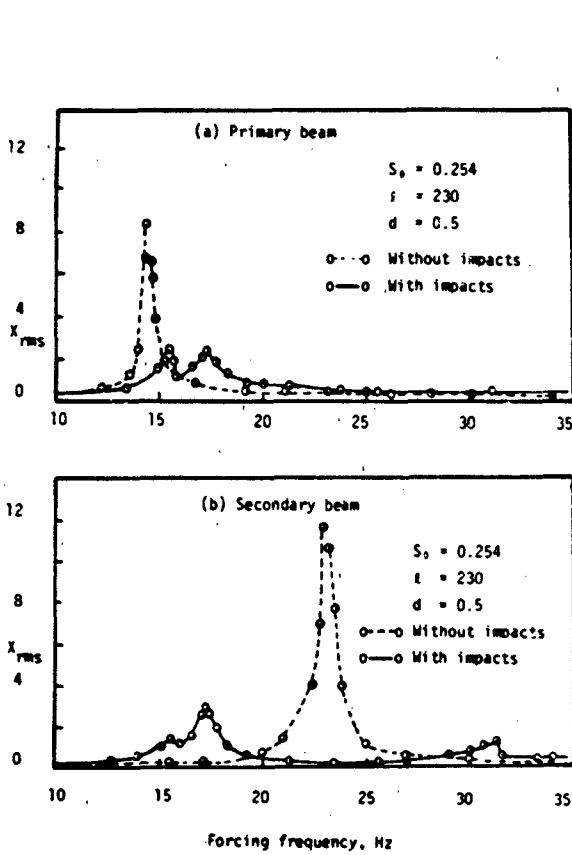


Figure 12. Effect of neoprene connector on the beam response

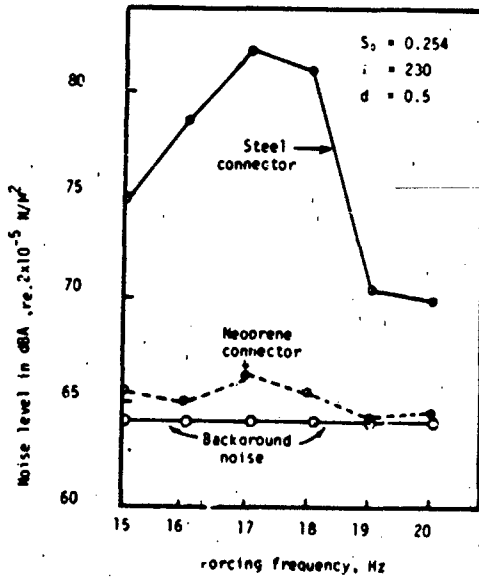


Figure 14. The comparison of noise produced using steel and neoprene connector

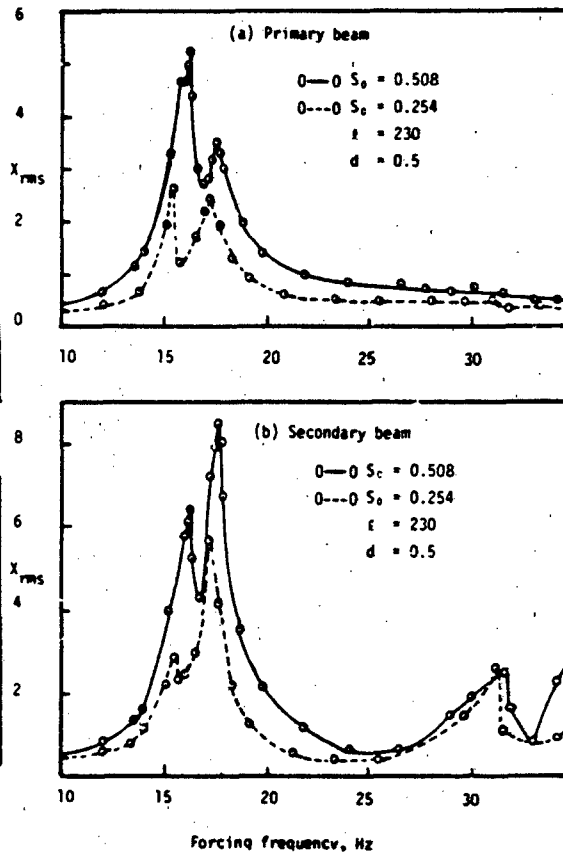


Figure 13. Effect of amplitude of excitation on the response using neoprene connector

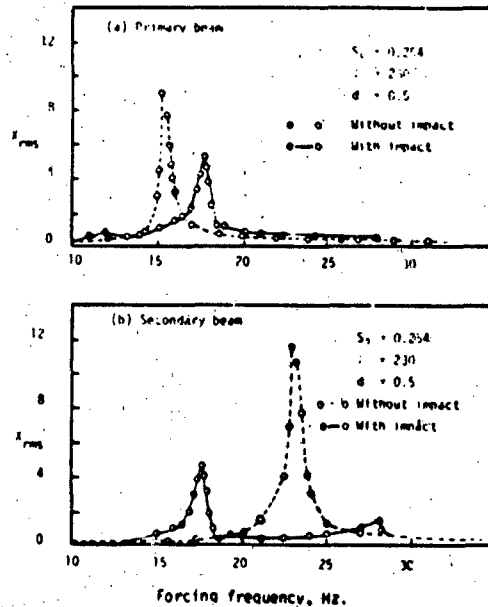


Figure 15. Effect of two sided gap of 0.5mm on the response

connector. Hence, the partial disadvantage of slightly higher displacement amplitudes is compensated by the substantial reduction in the noise level.

The experimental results presented above are for one sided clearance. However it was possible to attach a connector to the primary beam, as shown in Fig. 1(e), and secondary beam could be placed maintaining a gap of 0.5 mm on both sides. In this case impacts occurred on both sides of the secondary beam and so this had a two sided clearance. The displacement reduction, with two sided clearance, with steel stud and base displacement of 0.254 mm, can be seen as a difference between full and dotted lines in Fig. 16(a) and (b) for primary and secondary beam respectively. The large peaks occurring at 13.75 and 23.25 Hz are replaced by peaks of 4.2 and 4.8 mm at 16.5 Hz for the primary and secondary beams. This frequency of 16.5 Hz was found to correspond to the natural frequency of the system when both beams were connected rigidly at the tip. The maximum displacement amplitude in this case of two sided clearance is nearly twice that of one sided clearance. Hence from the point of view of amplitude reduction the one sided clearance system seems to be superior to the two sided clearance system.

#### 4. CONCLUSIONS

The vibration control aspect of vibroimpact of two beams was experimentally investigated. The system is found to work effectively in the free and forced vibrations. The performance from the point of view of displacement reduction of the system with one sided clearance was found to be superior to the system with two sided clearance. Loud noise produced during impact between metal surfaces can be substantially reduced by using a hard neoprene type material. The resonant displacement amplitudes of both beams were minimum when the impact point was near the tip of the beam.

#### ACKNOWLEDGEMENT

The authors acknowledge the assistance rendered by Mr. Anthony Gee (Mechanical Engineering Department, Concordia University) during this study.

#### REFERENCES

1. Cz. Cempel, 1971, *Rozprawy Inzynierskie* 19, 301-307. The percussive vibration of two independent systems (in Polish).
2. S.F. Masri, 1978, *Journal of Mechanical Design*, Transactions of the American Society of Mechanical Engineers 100, 480-486. Analytical and Experimental Studies of a Dynamic System with a Gap.
3. S.F. Masri, Y.A. Mariamy and J.C. Anderson, 1981, *Journal of Applied Mechanics*, Transactions of the American Society of Mechanical Engineers, 48, 404-410. Dynamic Response of a Beam with a Geometric Non-linearity.
4. D.S. Steinberg, 1977, *Machine Design* 71-73. Snubbers Calm PCB Vibration.
5. V.S. Metrikin, 1975, *Mechanics of Solids* 10, 36-41. Stability of Periodic Motion of a System with Impactive Interaction.
6. W.H. Park, 1967, *Journal of Engineering for Industry*, Transactions of the American Society of Mechanical Engineers 89, 587-596. Mass-Spring-Damper Response to Repetitive Impact.
7. T. Irie and K. Fukaya, 1972, *Bulletin of the Japan Society of Mechanical Engineers* 15, 299-306. On the Stationary Impact Vibration of a Mechanical System with Two Degrees of Freedom.
8. A. Ye Kobrinskii, 1969, NASA Technical Translation TTF-534. Mechanisms with Elastic Couplings, Dynamics and Stability.
9. R.K. Miller and B. Fatemi, American Society of Mechanical Engineers, 81-DET-16. An Efficient Technique for the Approximate Analysis of Vibroimpact.

## DISCUSSION

r. Lee (Ohio State University): Obviously, you used similar materials. Have you tried it with different materials, one aluminum beam and one steel beam?

r. Bapat: If the resonant frequencies are different, this system will work. It does not matter what type of materials are used in the same. Even if one beam is made from aluminum, and one beam is made from steel, you will not get much damping if their resonance frequencies are the same. But, if you have similar beams, but with differences in their resonance frequencies, you will get more damping.

r. Geers (Lockheed): I would think different materials would reduce the effectiveness of the system. For example, what if one of the beams were so light that it had no feedback effect on the steel beam? If I had a large discrepancy in the mass density, for example, the other beam doesn't damp the first one.

r. Bapat: Instead of mass density we found the most important parameter is the ratio of the stiffnesses of the systems. We found this in a computer simulation when the beams were considered as a single degree of freedom system. If you consider one system is very stiff compared to the other system, then the response of each system will be considerably reduced.

Ir. Geers: Clearly, when I make one of the masses zero, I have suddenly lost everything. Is that right?

Ir. Bapat: That is not so. If you make one mass zero, that means one beam acts purely as a spring. The effectiveness of the system depends more on the stiffness of the beams than on their mass, but it is not totally independent of their mass.

Ir. Geers: Yes, I see. So the stiffness is the most important parameter?

Ir. Bapat: Stiffness is the most important parameter, but mass will have an effect.

## MODELS FOR SHOCK DAMAGE TO MARINE STRUCTURAL MATERIALS

David W. Nicholson, Code R14  
Naval Surface Weapons Center  
White Oak, MD 20910

This paper presents a simple discussion of various types of strain rate embrittlement thought to occur in marine structural materials under shock loading. A constitutive model is briefly sketched which illustrates how material flow and damage are measured, their thresholds, how they compete to dissipate available elastic and kinetic energy, and conditions under which their governing processes become unstable.

### I. INTRODUCTION

This paper provides a very simple discussion of constitutive models suitable for describing various forms of strain rate embrittlement in marine structural materials. The ultimate concern is the capability of the finite element codes to predict structural response, including rupture, to severe transient loads. Unfortunately, the predictions can be no better than the underlying constitutive models. In this regard, the major finite element codes appear to have limitations in respect to the treatment of strain rate dependence.

### II. STRAIN RATE EMBRITTEMENT

In many instances, strain rate has a stiffening effect on structures. This means that the load to attain a given deformation is higher if the loading rate is increased. Strain rate may also have a strengthening effect in the sense that the failure loads are also increased. These features are faithfully accommodated in a number of viscoplastic constitutive models [1-6]. Of these, the models discussed in [1-3] appear to be the primary ones implemented in the major finite element codes such as MARK, ABAQUS and ADINA.

However, there are important instances of strain rate embrittlement for which it appears that suitable constitutive models have not yet been implemented. Three examples of this are given in the next section.

#### 1. Direct Embrittlement

It is well known that some materials, particularly steels, undergo a transition from ductile to brittle fracture as the temperature is lowered below a critical temperature  $T_c$ . It appears [7] that this transition is promoted, i.e. the effective critical temperature is raised, by high strain rates. Some direct evidence in this respect is provided in [8], which shows the dynamic fracture toughness of a steel alloy decreasing abruptly in the high strain rate range.

The mechanism is illustrated in Fig. (1a,b). Note that yield stress increases when fracture toughness decreases. This illustrates how fracture and plastic flow compete to dissipate stored elastic and kinetic energy. That is, if the loading occurs in times small compared with the characteristic retardation times for flow, the stored elastic energy may instead be dissipated by fracture or some other inelastic process.

#### 2. Damage Softening

In ductile materials, final catastrophic crack propagation is preceded by various microscopic damage processes, among which we focus on the nucleation, growth and coalescence of microvoids. Figures 2(a,b,c) illustrate a possible version of this process as follows. Initially, voids are formed by detachment of inclusions. Next, they grow at

a steady rate. Finally, after sufficient growth they interact in an unstable manner. That is, the material between the voids is so severely stretched that it fails, with the result that the voids are linked.

The strain rate effect on this process is as follows. Nucleation and growth of microvoids appear to occur by a sort of elastic cavitation process [9]. The thresholds may be high, but the processes appear to occur rapidly (in times limited by elastic wave speeds). For low strain rates, plastic flow efficiently dissipates stored elastic energy. But plastic flow is slow (retarded), and thus high strain rates lead to high instantaneous values of stored elastic energy. It is easy to imagine that void nucleation and growth thresholds can be exceeded under such conditions, leading to rapid dissipation by damage.

### 3. Thermoplastic Instabilities

It is well known that the energy dissipated by plastic flow is largely turned into heat. Also, metals show thermal softening, thus reducing the threshold for further plastic flow. But, as the threshold is reduced, further plastic flow is promoted, with the effect of greater heating and thus greater softening. Thus, the strains and temperatures continue to rise until a critical condition is reached, for example producing a phase transformation. This is clearly an unstable process, and it is thought to be manifested in the form of shear bands.

The role of strain rates may be described as follows. First, the situation is more nearly adiabatic since loading times are short compared to heat transfer times. Secondly, the stresses and therefore the rate of plastic work, and hence the rate of heating, are increased by strain rate.

### III. ELEMENTARY MATHEMATICAL MODELS

For the sake of illustration, we now offer simple examples of constitutive models for describing some mechanisms for strain rate embrittlement. Strains are assumed to be small and the material is assumed to be isotropic.

The main features of the models are as follows. The mechanisms are viewed as inelastic processes which dissipate appropriate parts of the excess stored (elastic and kinetic) energy relative to a threshold energy. The rate of dissipation is controlled by a retardation time.

This situation is evident in conventional viscoplastic formulations. The flow work is given by

$$\dot{w}_f = s_{ij} \dot{e}_{ij}^f \quad (1)$$

where

$$s_{ij} = \sigma_{ij} - \sigma_{kk} \delta_{ij} / 3$$

$$\begin{aligned} \dot{e}_{ij}^f &= \dot{e}_{ij} - \dot{e}_{kk} \delta_{ij} / 3 \\ &= \dot{e}_{ij}^f \end{aligned}$$

where  $\sigma_{ij}$  and  $\dot{e}_{ij}^f$  are the stress and the flow strain, with deviatoric parts  $s_{ij}$  and  $\dot{e}_{ij}^f$ . We are assuming flow incompressibility, so that  $\dot{e}_{kk} = 0$ . Also, repeated indices imply summation.

The constitutive equation for flow strain is

$$\dot{e}_{ij}^f = \eta_f \langle w_{ef} - \theta_f \rangle s_{ij} / \mu_{mn} \mu_{mn} \quad (2)$$

Here

$$w_{ef} = s_{ij} s_{ij} / 4\mu$$

is the elastic strain energy associated with shear, while  $\mu$  is the elastic shear modulus. Also, the symbols  $\langle \cdot \rangle$  are defined by

$$\langle x \rangle = \begin{cases} x & x > 0 \\ 0 & x \leq 0 \end{cases}$$

and the quantity  $\theta_f$  is a threshold energy related to the conventional yield stress.

Combining (1) and (2) furnishes

$$\dot{w}_f = \eta_f \langle w_{ef} - \theta_f \rangle \quad (3.1)$$

and hence flow dissipates excess elastic energy at a rate determined by  $\eta_f$ , which may be called the (reciprocal of the) retardation time.

We represent damage as an internal state variable which manifests itself by modifying the values of material properties such as  $\theta_f$ . In analogy with flow, we assume that the energy absorbed (dissipated) by damage is given by

$$\dot{w}_d = \eta_d \langle w_{ed} - \theta_d \rangle \quad (3.2)$$

where  $w_{ed}$  is a part of the stored elastic energy driving the damage process. For the sake of illustration we assume that

$$w_{ed} = (\langle s \rangle)^2 / 3\kappa \quad (4)$$

where  $s$  is the isotropic stress and  $\kappa$  is the bulk modulus. Equation (4) is suitable for cases in which damage is caused by hydrostatic tension, which may be characteristic of void mechanisms.

Finally, to describe thermal effects we invoke the conventional assumption [10] that all flow work is converted into heat. Accordingly,

$$\dot{w}_f = \rho c \dot{T}$$

and hence

$$\dot{T} = \frac{\eta_f}{\rho c} \langle w_{ef} - \theta_f \rangle \quad (5)$$

where  $\rho$  is the mass density and  $c$  is the specific heat, assumed constant.

#### IV. SIMPLE STABILITY ANALYSIS

For the sake of illustration we now assume that  $\eta_f$ ,  $\eta_d$ ,  $\mu$ ,  $\kappa$  and  $\rho$  are all constants, but that  $\theta_f$  and  $\theta_d$  depend on flow work, damage and temperature:

$$\theta_f = \theta_f(w_f, w_e, T) \quad (6.1)$$

$$\theta_d = \theta_d(w_f, w_e, T) \quad (6.2)$$

We also assume that  $w_{ef}$  and  $w_{ed}$  are imposed and maintained at constant values indefinitely. Under some conditions to be investigated shortly,  $w_{ef}$  and  $w_{ed}$  will always exceed the flow and damage thresholds. The result is that flow and damage will continue indefinitely and the temperature will rise monotonically. A condition will eventually be reached which represents some type of failure, such as void coalescence to form cracks, or shear band formation.

Such a process represents failure of bounded input - bounded output (BIBO) stability. That is, finite values of  $w_{ef}$  and  $w_{ed}$  lead to infinite values of  $w_f$ ,  $w_d$  and  $T$ .

Technically there are four possible cases:

- i.  $w_{ef} < \theta_{fo}$        $w_{ed} < \theta_{do}$
- ii.  $w_{ef} > \theta_{fo}$        $w_{ed} < \theta_{do}$
- iii.  $w_{ef} < \theta_{fo}$        $w_{ed} > \theta_{do}$
- iv.  $w_{ef} > \theta_{fo}$        $w_{ed} > \theta_{do}$

where  $\theta_{fo}$  and  $\theta_{do}$  are the initial values of  $\theta_f$  and  $\theta_d$ .

Nothing happens in (i), while (ii) only involves flow and has been treated elsewhere [10]. The case (iii) seems unlikely since damage thresholds are typically higher than flow thresholds. Thus (iv) appears to be the most interesting case.

Ignoring inertia, equations (3.1, 3.2) can be integrated, at least numerically. The resulting values of  $w_f$  and  $w_d$  may then be substituted into (6.1, 6.2) to furnish functions of the form

$$\theta_f = \lambda_f(t; w_{ef}, w_{ed})$$

$$\theta_d = \lambda_d(t; w_{ef}, w_{ed})$$

Clearly, BIBO fails for  $w_{ef}$  and  $w_{ed}$  such that

$$w_{ef} > w_{ef}^*$$

$$w_{ed} > w_{ed}^*$$

where  $w_{ef}^*$  and  $w_{ed}^*$  are the solutions, assumed to exist, of

$$w_{ef}^* = \max_t \lambda_f(t; w_{ef}^*, w_{ed}^*)$$

$$w_{ed}^* = \max_t \lambda_d(t; w_{ef}^*, w_{ed}^*)$$

A similar stability analysis for flow alone was presented in [10], in which specific examples were considered.

#### V. CONCLUSION

Various types of strain rate embrittlement have been discussed. A simple constitutive model has been sketched, which illustrates measures of flow and damage, their thresholds and rates, how they compete to dissipate available elastic and kinetic energy, and conditions under which their governing processes become unstable.

REFERENCES

1. Bohemesser, K. and Prager, W., "Über die Ansätze der Mechanik Isotroper Kontinua," ZAMM, 12, 1932.
2. Perzyna, P., "Fundamental Problems of Viscoplasticity," Advances in Applied Mechanics, 9, Academic Press, N.Y., 1966.
3. Nicholson, D. W., and Phillips, A., "On the Structure of the Theory of Viscoplasticity," Int'l J. Sol. Structures, 10, 1974.
4. Bodner, S. R., and Partom, Y., "Constitutive Equations for Elastic Viscoplastic Strain Hardening Materials," J. Appl. Mech, June 1975.
5. Valanis, K. C., "A Theory of Viscoplasticity without a Yield Surface," Archives of Mechanics, 23, 1971.
6. Chernocky, E. P., and Krempl, E., "A Theory of Thermoviscoplasticity for Uniaxial Mechanical and Thermal Loading," Kennesauer Polytechnic Institute Report CS79-3, July 1979.
7. Rolfe, S. T., and Barsom, J. M., Fracture and Fatigue Control in Structures, Prentice-Hall, Inc., Englewood Cliffs, New Jersey, 1977.
8. Freund, L. B., "Dynamic Fracture Initiation in Metals," ASME Paper 81-PVP-15, 1981.
9. Nicholson, D. W., "A Constitutive Model for Rapidly Damaged Structural Materials," Acta Mechanica, 39, 1981.
10. Nicholson, D. W., and Kiddy, K. C., "A Rate Sensitive Plasticity Model with Thermal Softening," PVP-70, ASME, 1982.

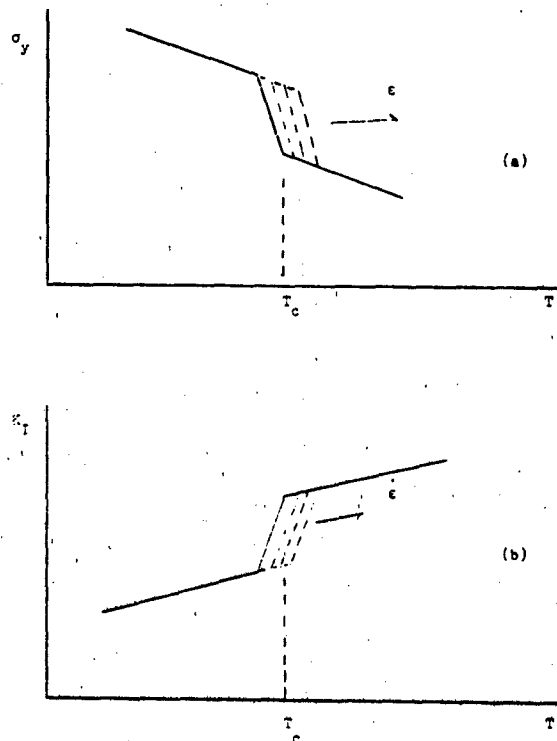


FIG 1: EFFECT OF TEMPERATURE AND STRAIN RATE ON FLOW STRESS AND FRACTURE TOUGHNESS

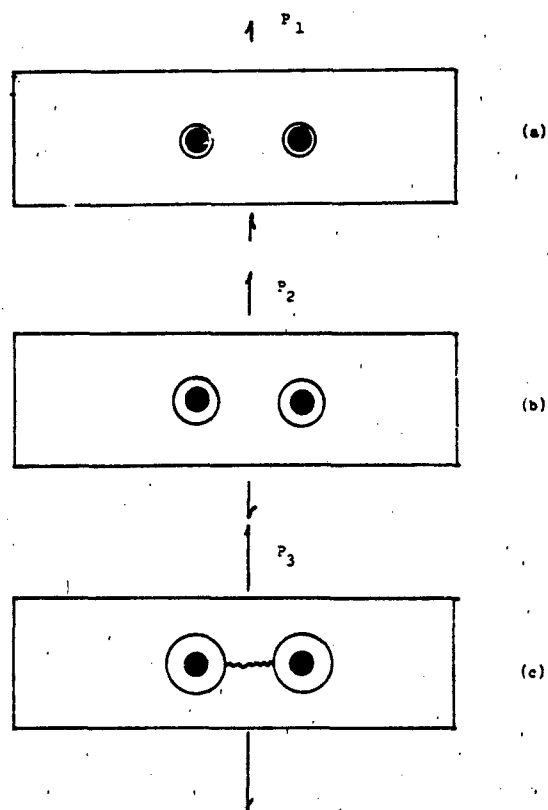


FIG 2: VOID NUCLEATION BY DETACHMENT OF INCLUSIONS, SUBSEQUENT GROWTH, AND COALESCENCE



## DISCUSSION

Mr. Lee (Ohio State University): I guess a lot depends on how you define the damage. In my mind I thought plasticity is also a kind of damage, but it looks like you tried to separate them into a flaw and the damage. Isn't changing the elastic modulus, due to damage, in conflict with the facts of basic elasticity? I can see, physically, if you stretch a rubber band for a long time and let it go, then its elasticity has changed from the original elasticity. But, that is due to the irrecoverable process of the motion that was piled up inside. When that went through, obviously you can characterize that as damage, or it is because of a plastic deformation.

Mr. Nicholson: We are taking the same point of view as you have in composite materials. If you have voids forming in a material, you can calculate an effective elastic bulk modulus where you smear out the voids. You are not saying that the elastic behavior is changing point-wise within the material. You are not talking about a point-wise property. You are talking about a property of regions of material that are large compared to the voids. So when we say that elastic modulus tensor is changing, we say that the effective elastic modulus tensor is changing. That is, it is a modulus which refers to volumes of material that are large compared to the characteristic size of the defects. So I agree with you. In a proper statement of a point-wise constitutive relationship, we shouldn't say the elastic moduli are changing. But I am not really saying that; I say that the effective moduli are changing. I think that is an important difference. As far as plasticity versus damage is concerned, I am talking from the specialized language of the people who play this game. Plasticity contributes to residual strain so it can be measured microscopically, in principle. Damage is something that doesn't necessarily have an effect on the permanent strain. If you introduce a small crack to a material and then reduce the loads, the length of the material will not be affected by that; but still the defective material properties are different. In some respects I was just defining damage. I think of it more this way. Physically, damage means defects, and I know the defects have some effect on the effective material properties. I would like to use that effect to obtain a macroscopic measure of damage; I smear out a lot of the details of damage by doing that. But, I would like to use that effect to measure the damage, rather than do what some other people have done. They actually cut up the material and count the voids, which is impossible, and then try to characterize the orientations and so forth. I am trying to avoid that whole operation by consolidating all of the effects of damage and the effect of the elastic moduli.

Mr. Lee: Would you consider embrittlement due to entrapped hydrogen and chemical reactions,

such as rusting out, as damage?

Mr. Nicholson: I was trying to confine my attention to stress-induced damage. In some cases, chemical effects have a relationship to stresses. Hydrogen embrittlement, as I know it, tends to be a long term process of hydrogen migrating through materials and accumulating in cracks, and so forth, where they reduce the thresholds for further crack propagation. That kind of effect changes the elastic properties, but not mechanically. So I am not considering that damage for the purpose of formulating a constitutive model. I am talking about the kind of damage that occurs in very short times under very high stresses, and generally, I assume these times are small compared to chemical times.

Mr. Lee: Do you consider that as a form of damage?

Mr. Nicholson: Yes, definitely. Material is degraded by it, and its function is changed by it. But, it is not a damage where strain rates are particularly relevant. I am trying to deal with a case where you take two pieces of material, one which you test statically to failure, and you find it exhibits ductile failure. You test another piece of material dynamically to failure, and by examining the cracked surface, you find it looks like a brittle failure. But the question is why are those two different? Ordinarily, that difference is not due to chemical effects but some sort of strain rate embrittling effect which I have been trying to talk about here.

## A STUDY OF THE EFFECT OF MASS LOADING ON THE SHOCK ENVIRONMENT

Qi-Zheng Wang  
Beijing Institute of Strength and Environment Engineering  
Beijing, China

and  
Hua-Bao Lin  
Chinese Academy of Space Technology  
Beijing, China

The weight variations in mounted subassemblies have relatively little effect on the pyrotechnic shock environment at the mounting point. This is the so-called mass loading effect. This paper presents a mechanical model which attempts to explain theoretically the mechanism of the mass loading effect. A drop test and a structural striking test are conducted to simulate the pyrotechnic shock. The experimental results agree well with the predictions of the model analysis. A local and an entire body shock environment of a system and their shock test specifications are briefly discussed.

### INTRODUCTION

There is a problem often encountered in drawing up shock specifications of a system, whether the weight variations in mounted subassemblies affect the shock environment of the system, and how it affects. This problem has prompted many pyrotechnic shock measurements and analysis (1-8)

It is believed that mass loading, in general, will affect the shock environment. But the experimental results show that actually the contrary is the case. The weight variations in mounted subassemblies have relatively little effect on the pyrotechnic shock environment at the mounting point. This is the so-called mass loading effect. To make an investigation on this problem will help to make prediction of the shock environment from the weight variations by conducting only a few firing tests. The investigation of the effect of mass loading on the shock environment will help greatly in the design work of equipment mounting configuration and in drawing up shock specifications.

While dealing with the shock specification of a subassembly, we must distinguish between local and entire shock specifications. Generally speaking, if an entire shock of the subassembly is taken to be a local shock, the specification would be under-test. On the other hand, if a local shock environment is taken as an entire shock, the shock specifications would be over-test. However, at the present local shock environment

is often confused with the entire, leading to some troubles.

In view of the above mentioned, this paper presents a mechanical model which attempts to explain the mechanism of the mass loading effect theoretically. The dynamic model consists of three masses connected in series by two springs, i.e. "mass 0 -spring 1 -mass 1 -spring 2 -mass 2" system. The system has free-free boundary conditions. The mass 0, 1 and 2 represent the supporting structure, the mounting structure and the mass loading respectively. The springs 1 and 2 represent the connecting stiffness of the masses. When the supporting structure (mass 0) is shocked by a single impulse, the response at the mounting point (mass 1) is the shock environment of mass loading (mass 2). The maximum response of the mass 1 can be estimated using Laplace Transformation method. Several special cases are calculated, and the results are assembled and tabulated.

Because of the scatter of pyrotechnic shock data, a structural striking test was conducted in the laboratory to simulate the pyrotechnic shock together with a drop test. Both tests generate approximately the same shock environment at the mounting point. The test specimen is a cylindrical shell with stringers and ring frame. The pyrotechnic shock environment is practically a local shock of the system. However, the routine shock test according to general shock specification is usually an entire shock of the system. In fact, the shock spectra

method has the conception of the entire shock. There may be the same shock environment at the mounting point for both local and entire shock of the system, but the responses of the mass loading itself are quite different from each other.

#### MODEL ANALYSIS

For simplicity, we shall assume that the actual structure can be regarded as a three-mass system which consists of three masses  $m$ ,  $m_1$ , and  $m_2$  tied in series by two springs shown in Figure 1, where  $m$  and  $m_1$  are connected structural masses and  $m_2$  the mass loading,  $k_1$  and  $k_2$  are connected stiffness. The shock source may be characterized by momentum  $mV$ . Hence, the equations of motion of the three-mass system ignoring damping are written

$$\begin{aligned} m\ddot{X} - k_1(X_1 - X) &= 0 \\ m_1\ddot{X}_1 + k_1(X_1 - X) - k_2(X_2 - X_1) &= 0 \\ m_2\ddot{X}_2 + k_2(X_2 - X_1) &= 0 \end{aligned} \quad (1)$$

with initial conditions

$$\begin{aligned} X(t) \Big|_{t=0} &= X_0 = 0, \quad \dot{X}_0 = V \\ X_1 = \dot{X}_1 = X_2 = \dot{X}_2 &= 0 \end{aligned} \quad (2)$$

setting  $\delta_1 = X_1 - X$  and  $\delta_2 = X_2 - X_1$ , Equation (1) becomes

$$\begin{aligned} \delta_1 + k_1\delta_1 / (m+m_1) - k_2\delta_2 / m &= 0 \\ -k_1\delta_1 / m + \delta_2 + k_2\delta_2 / (m_1+m_2) &= 0 \end{aligned} \quad (3)$$

with initial conditions

$$\begin{aligned} \delta_1(t) \Big|_{t=0} &= \delta_{10} = 0, \quad \dot{\delta}_{10} = -V \\ \delta_{20} = \dot{\delta}_{20} &= 0 \end{aligned} \quad (4)$$

By using the Laplace Transformation method the maximum values of variables  $\ddot{X}(t)$ ,  $\ddot{X}_1(t)$ ,  $\ddot{X}_2(t)$ ,  $\ddot{\delta}_1(t)$ ,  $\ddot{\delta}_2(t)$  are obtained as follows:

$$\ddot{X}_m = \omega_1 C_1 V (C_6 + C_7) / (C_8 C_9) \quad (5)$$

$$\ddot{X}_{1m} = \omega_1 V (C_5 + C_6) / (C_8 C_9) \quad (6)$$

$$\ddot{X}_{2m} = \omega_2 V / (C_8 C_9) \quad (7)$$

$$\ddot{\delta}_{1m} = V (C_6 + C_7) / (\omega_1 C_8 C_9) \quad (8)$$

$$\ddot{\delta}_{2m} = V / (\omega_2 C_8 C_9) \quad (9)$$

where  $\omega_1 = (k_1/m_1)^{1/2}$ ,  $\omega_2 = (k_2/m_2)^{1/2}$ ;

$$C_1 = m_1/m, \quad C_2 = m_2/m, \quad C_3 = m_2/m_1,$$

$$C_4 = k_2/k_1, \quad C_5 = \omega_2/\omega_1, \quad C_6 = (1+C_1 C_2)^{1/2},$$

$$C_7 = (1+C_3) C_4, \quad C_8 = (1+C_1+C_4+C_2^2+2C_3 C_4)^{1/2},$$

$$C_9 = (1+C_1+C_4+C_2^2-2C_3 C_4)^{1/2}$$

From above general formulas the following special cases can be derived:

Case 1,  $m \gg m_1, m_2$

$$\ddot{X}_m = \omega_1 V (1+C_7) / C_{10} \quad (10)$$

$$\ddot{X}_{1m} = \delta_{10} C_{11} \quad (11)$$

$$\delta_{10} = V (1+C_7) / (\omega_1 C_{10}) \quad (12)$$

$$\ddot{\delta}_{2m} = V / (\omega_2 C_{11}) \quad (13)$$

Case 2,  $m_1, m_2 \gg m$

$$\ddot{X}_m = \delta_{10} C_{12} \quad (14)$$

$$\delta_{10} = V / (C_{12} C_{10}) \quad (15)$$

$$\ddot{X}_{1m} = \omega_1 V / C_{12} \quad (16)$$

$\delta_{10}$  and  $\ddot{X}_{1m}$  both depend on the equations (7) and (9).

Case 3,  $m+m_1 \ll m_2$

$$\ddot{X}_m = \delta_{10} C_{13} \quad (17)$$

$$\ddot{X}_{1m} = \omega_1 V / C_{14} \quad (18)$$

$$\delta_{10} = V / (C_{14} C_{17}) \quad (19)$$

$$\ddot{\delta}_{2m} = V / (C_{13} C_{18}) \quad (20)$$

where  $C_{10} = [(1+C_7)^2 + C_7^2 C_2]^{1/2}$ ,

$$C_{11} = [(1+C_7)^2 + C_7^2 C_2]^{1/2}, \quad C_{12} = (k_1/m)^{1/2},$$

$$C_{13} = (k_2/m)^{1/2}, \quad C_{14} = (1+C_1)^{1/2}, \quad C_{17} = (1+C_1)^{1/2},$$

$$C_{18} = [1+(C_1^2+C_2^2)]^{1/2}, \quad C_{19} = [1+1/(C_1^2+C_2^2)]^{1/2},$$

$$C_{20} = [1+(C_1^2-C_2^2)]^{1/2}$$

The maximum  $\ddot{X}_m$ ,  $\ddot{X}_{1m}$  and  $\ddot{X}_{2m}$  are tabulated in table 1 for various cases combined with  $m$ ,  $m_1$ ,  $m_2$ ,  $k_1$ , and  $k_2$ .

#### LOCAL AND ENTIRE SHOCK TESTS

A cylinder structure with skin-stringer-ring-frame is shown in Figure 2. The two ends of an aluminum beam are fixed on the ring-frame of the cylinder. The mass loading  $m$  is located at the center of the aluminum beam. The weight variations of the mass loading  $m_2$  are 0, 1, 2, 5, 7, 10 and 12 kilograms. The schematic of the striking test is shown in Figure 3. B and C are hang points at the ring-frame of the cylinder.  $X_1$  and  $X_2$  are the acceleration measurement points (axial direction). S is the striking point. The shock source is produced by suddenly releasing a strong beam to S point. The releasing distance are kept the same so that the shock source can be reproduced.

The cylinder structure also was conducted a free drop test as shown in Fig. 4. The cylinder was fixed on a heavy drop hammer. The hammer was dropped freely on the anvil. The hammer and anvil both are rigid. The drop height was kept the same

5.5ms). This is an entire shock test.

The accelerometers at the mounting points  $X_1$  and  $X_2$  are fixed on the top of the bolts. For convenience, the maxima of  $\dot{X}_1(t)$  and  $\dot{X}_2(t)$  were read out. Each test is repeated by three to five times. The average of the measurement data is used. The experimental results of the striking and drop tests are listed on the table 2. The typical time histories are shown in Figures 5-18.

It is known from [1],[8] and our own research information, if the transient waveforms are similar, their shock spectra are similar too. Thus, the differences between the local and entire shock environment is not identified by the transient waveforms or the shock spectra themselves.

#### DISCUSSION AND CONCLUSION

1. The weight variations of the mass loading, in general, have some effects on the shock environment at the mounting point, see equation (6).

2. If  $m \gg m_1, m_2$ , no matter how the connecting stiffness  $k_1$  and  $k_2$  may be,  $\dot{X}_{1m}$  holds the order of  $V\omega_0$ , i.e. the weight variations in mounted subassemblies have relatively little effect on the shock environment at the mounting point.

3. If  $m \gg m_1$  and  $k_1 \gg k_2$ , regardless of the variations of  $m_2$ ,  $\dot{X}_{1m}$  holds the order of  $V\omega_0$ . In this case, the weight variations in mounted subassemblies has relatively little effect on the shock environment too.

4. If  $m \gg m_1 + m_2$ , the shock test reveals the characteristics of entire shock.

5. If  $m \ll m_1 + m_2$ , the shock test reveals the characteristics of local shock.

6. The differences between the local and the entire shock environment is not identified by the transient waveforms or the shock spectra themselves.

7. When the locations of the measurement points for shock environment are chosen, or the results of the shock measurement are adjudged, not only will the rigidity around the measurement point be taken account of, but the size of masses around the measurement location must be taken note of too.

8. The shock specifications are not only determined by the shock spectra and by the waveform, but the impedance method has to be taken into consideration also.

#### REFERENCES

1. W. J. Kacern, M. B. McGrath, and W. P. Rader, "Aerospace Systems Pyrotechnic Shock Data, Ground Test and Flight." Volume I, N71-17900.
2. W. P. Rader, "Investigation of Mass Loading Effects" N71-19250.
3. M. B. McGrath, "A Discussion of Pyrotechnic Shock Criteria." The Shock and Vibration Bulletin, No.41, Part 5, December 1970.
4. W. P. Rader, and W. P. Bangs, "A Summary of Pyrotechnic Shock in Aerospace Industry." The Shock and Vibration Bulletin, No.41, Part 5, 1970.
5. W. B. Keegan and W. P. Bangs, "The Effects of Various Parameters on Spacecraft Separation Shock." The Shock and Vibration Bulletin, No.42, Part 3 January 1972.
6. H. W. Luhrs, "Pyrotechnic Shock Transmission in Component versus S/C testing." Proceedings of 2nd Aerospace Testing Seminar, IES, March 1975.
7. D. R. Powers, "Simulation of Pyrotechnic Shock in a Test Laboratory." The Annual Technical Meeting Proceedings, IES, 1976.
8. W. P. Rader, "Pyrotechnic Shock Sources and Environments." The Annual Technical Meeting Proceedings, IES, 1976.

Table 1  
Results of Theoretical Model Analysis ( $\bar{X}_{im}$ )

CASES	CONDITIONS			MAXIMUM
	$k_1, k_2$	$m_1, m_2$	$\omega_1, \omega_2$	$\bar{X}_{im}$
General				Eq. (6)
Case 1	$k_1 \approx k_2$	$m_1 \gg m_2$		Eq. (10)
		$m_1 \approx m_2$	$\omega_1 \approx \omega_2$	$0.89V\omega_1$
		$m_1 \gg m_2$	$\omega_1 \ll \omega_2$	$V\omega_1$
		$m_1 \ll m_2$	$\omega_1 \gg \omega_2$	$0.71V\omega_1$
	$k_1 \gg k_2$	$m_1 \approx m_2$	$\omega_1 \gg \omega_2$	$V\omega_1$
		$m_1 \gg m_2$	$\omega_1 \approx \omega_2$	$V\omega_1$
			$\omega_1 \ll \omega_2$	$V\omega_1$
			$\omega_1 \gg \omega_2$	$V\omega_1$
	$k_1 \ll k_2$	$m_1 \approx m_2$	$\omega_1 \ll \omega_2$	$0.71V\omega_1$
		$m_1 \gg m_2$	$\omega_1 \ll \omega_2$	$\omega_2^2/\omega_1^2 \gg k_2/k_1$ $V\omega_1$
		$m_1 \ll m_2$	$\omega_1 \approx \omega_2$	$2V\omega_1(k_1/k_2)^{1/2}$
			$\omega_1 \ll \omega_2$	$\omega_2^2/\omega_1^2 \ll k_2/k_1$ $V\omega_2(k_1/k_2)^{1/2}$
			$\omega_1 \gg \omega_2$	$V\omega_1(k_1/k_2)^{1/2}$
Case 2		$m_1 \gg m_2$		Eq. (16)
		$m_1 \approx m_2$		$0.71V\omega_1$
		$m_1 \gg m_2$		$V\omega_1$
		$m_1 \ll m_2$		$V\omega_1(m/m_1)^{1/2}$
Case 3		$m_1 \gg m_2$		Eq. (18)
	$k_1 \approx k_2$	$m_1 \approx m_2$		$0.45V\omega_1$
		$m_1 \gg m_2$		$0.71V\omega_1$
		$m_1 \ll m_2$		$V\omega_1(m/m_1)^{1/2}$
	$k_1 \gg k_2$	$m_1 \approx m_2$		$0.71V\omega_1$
		$m_1 \gg m_2$		$V\omega_1$
		$m_1 \ll m_2$		$V\omega_1(m/m_1)^{1/2}$
	$k_1 \ll k_2$	$m_1 \approx m_2$		$V\omega_1(k_1/k_2)^{1/2}$
		$m_1 \gg m_2$		$V\omega_1(k_1/k_2)^{1/2}$
$m_1 \ll m_2$			$\approx 0$	
Case 4	$k_1 \approx k_2$	$m_1 \approx m_2$	$\omega_1 \approx \omega_2$	$0.50V\omega_1$
	$k_1 \gg k_2$	$m_1 \approx m_2$	$\omega_1 \gg \omega_2$	$0.71V\omega_1$
	$k_1 \ll k_2$	$m_1 \approx m_2$	$\omega_1 \ll \omega_2$	$0.41V\omega_1$

Table 2

Results of Striking Test and Drop Test (Fig. 5-18)

$m_2 R$ kg	$\ddot{x}_{1m}$		$\ddot{x}_{2m}$			
	High Frequency Peak R		High Frequency Peak R		Low Frequency Peak R	
	Striking Test	Drop Test	Striking Test	Drop Test	Striking Test	Drop Test
0	130.2	131.3	45.8	47.1		21.7
1	120.2	107.7	12.8	16.3	2.2	11.5
2	119.2	127.3	8.4	11.4	2.3	7.5
5	114.2	107.1	3.9	15.2	1.1	12.7
7	123.4	113.6	11.7	13.6	0.7	12.6
10	119.5	122.8	3.6	12.5	0.7	11.0
12	122.8	128.6	2.9	14.0	0.7	13.1

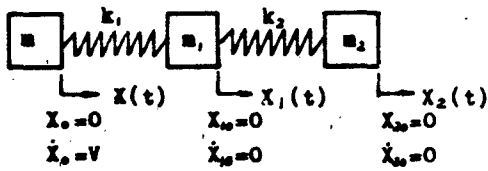


Fig.1- Three-Mass System

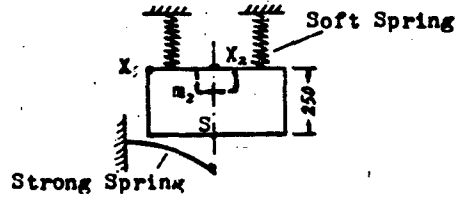


Fig.3- Striking Test

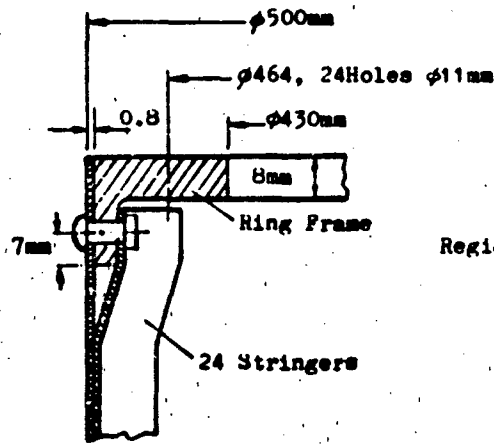


Fig.2- Cylinder Structure

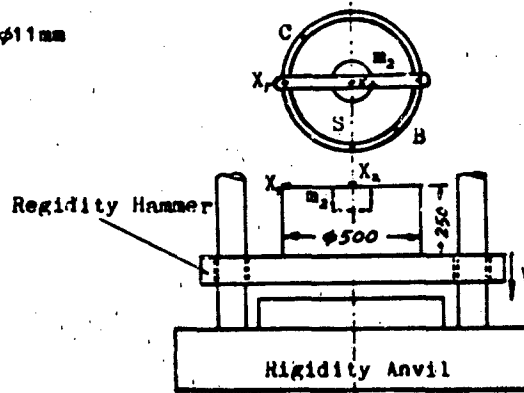


Fig.4- Drop Test

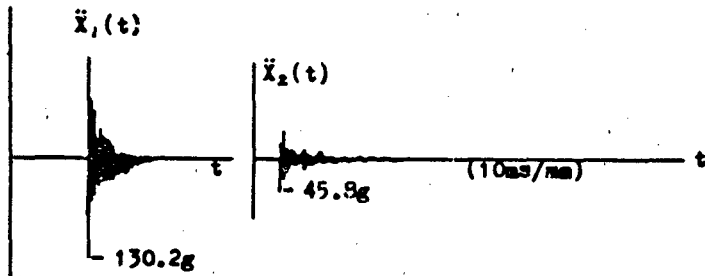


Fig.5- Striking Test  
 $m_2=0$

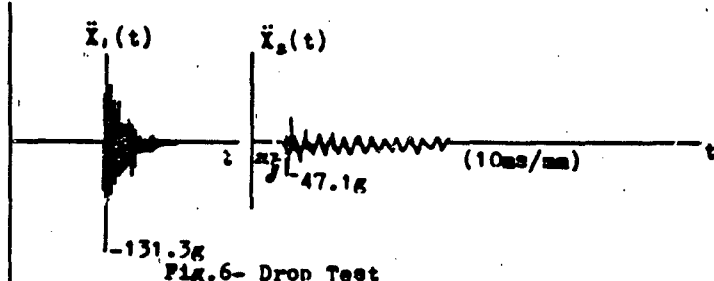


Fig.6- Drop Test  
 $m_2=0$

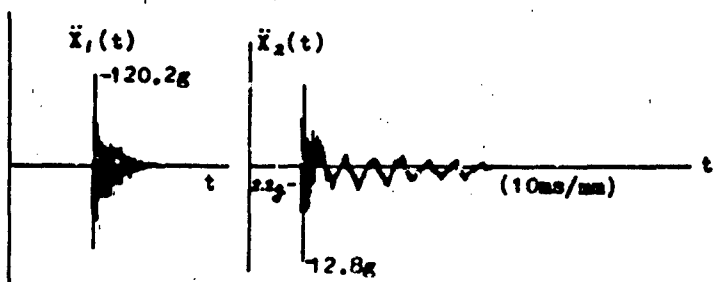


Fig.7- Striking Test  
 $m_2=1kg$

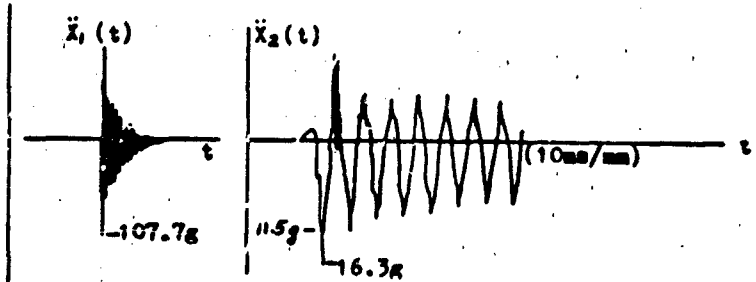


Fig.8- Drop Test  
 $m_2=1kg$

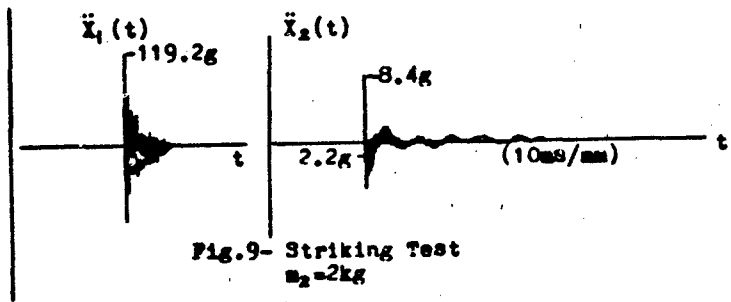


Fig. 9- Striking Test  
 $m_2=2kg$

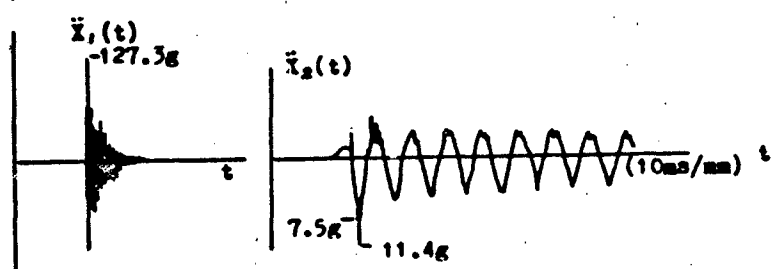


Fig. 10- Drop Test  
 $m_2=2kg$

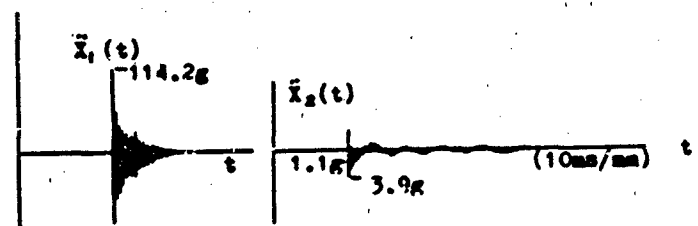


Fig. 11- Striking Test  
 $m_2=5kg$

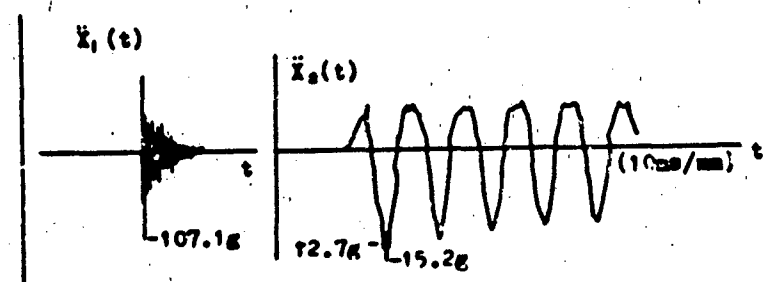


Fig. 12- Drop Test  
 $m_2=5kg$

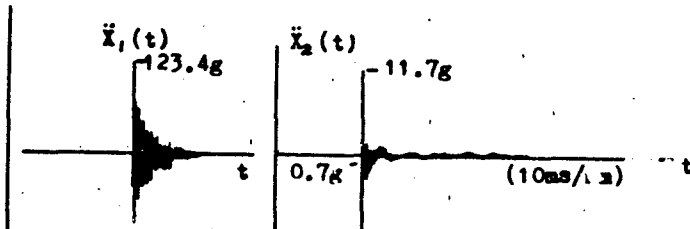


Fig.13- Striking Test  
 $m_2=7\text{kg}$

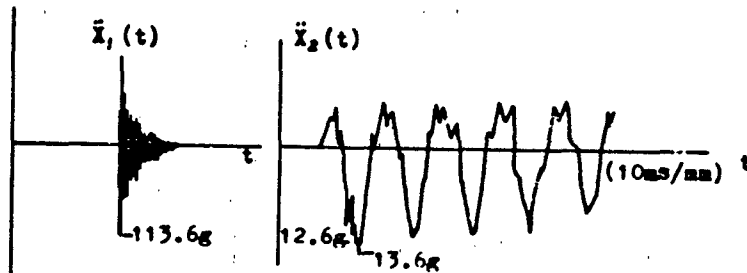


Fig.14- Drop Test  
 $m_2=7\text{kg}$

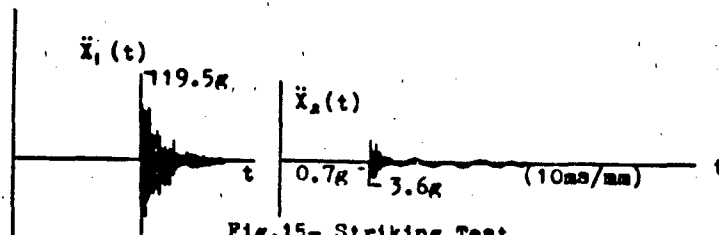


Fig.15- Striking Test  
 $m_2=10\text{kg}$

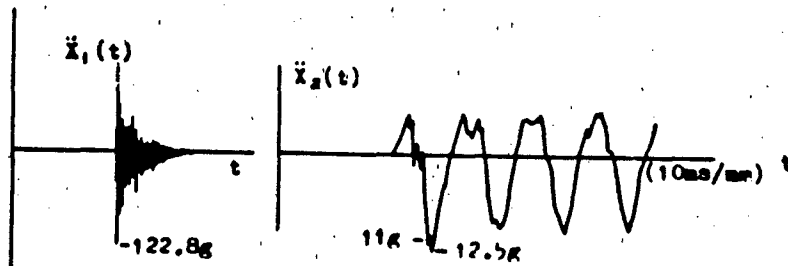


Fig.16- Drop Test  
 $m_2=10\text{kg}$

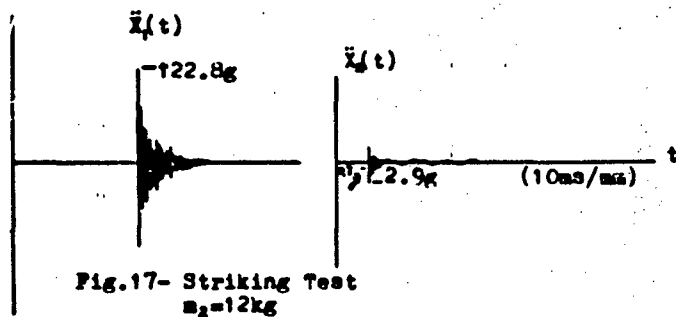


Fig. 17- Striking Test  
 $m_2=12kg$

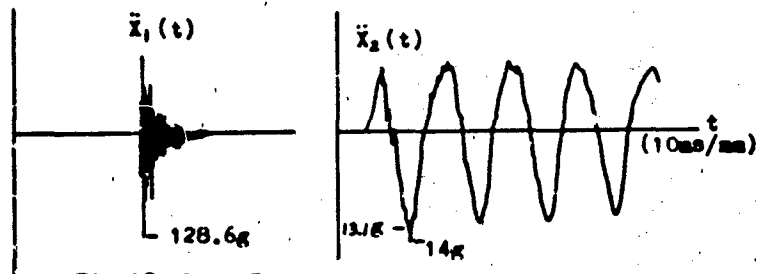


Fig. 18- Drop Test  
 $m_2=12kg$

# BLAST AND GROUND SHOCK

## ASSESSMENT OF SEISMIC SURVIVABILITY

by

Robert E. McClellan\*

The 1971 San Fernando earthquake showed that modern civil-architectural structures, designed to the same legal code requirements, can have seismic survivabilities which vary from near 100% to exactly zero. Codified seismic design procedures (however disguised as dynamics) actually use static lateral loads with assumed linear properties for materials and structures. Rigorous assessment of seismic survivability, although not required by existing codes for civil-architectural structures, is possible by rational analytical methods which enable derivation of a structure's time history of distortion when it is subjected to base motion of given displacement time history. The methods, which account for real non-linear material and structure properties, as well as the effects of previous earthquakes on structure ductility, are demonstrated in application to high-rise buildings, and inferences regarding the effect of some commonly used structural details on seismic survivability of high-rise buildings are discussed.

### ACTION

### STRUCTURE DUCTILITY

Ductility is the property possessed by civilly designed structures enabling them to sustain inelastic deflection without failure. Load-deflection curves of practical structures have an initial essentially linear (elastic) load-deflection relation up to the yield deflection followed by a non-linear (elasto-plastic) load-deflection relation to failure. The inelastic part of a load-deflection relation curve, depending on the structural materials and configuration, may be represented by many continuous curve representations; however, for configurations normally used in civil-architectural structures, the inelastic part of the load-deflection curve can be approximated by a straight line of suitable slope, and the total load-deflection relation can be represented by one of the two bi-linear approximations as shown in Figure 1.

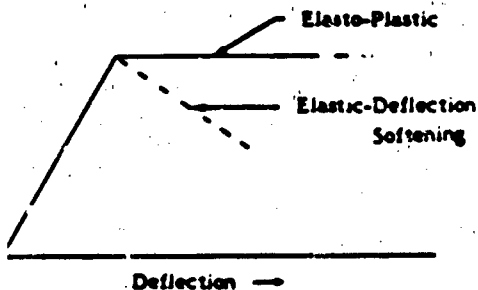


Figure 1. Bi-Linear Approximations of Structure Load-Deflection Curves

\*Registered Structural Engineer - California  
Senior Engineer - Strategic Studies  
Energy and Resources Division  
Aerospace Corporation

The deflection in Figure 1 refers to the coordinate of maximum deflection with regard to the governing failure mechanism, e.g., the mid-span deflection of a uniformly loaded simple beam, or the total drift, roof to base, of a high-rise building in first mode seismic response. The area under the load-deflection curve has the units of force times distance; therefore, the total area under the load-deflection curve to the failure deflection relates to a structure's total work absorption capability to failure. Where structures are found to respond in the elastic-deflection softening manner, it is almost always required that they be modified to achieve elasto-plastic response in order to upgrade their survivability.

Ideal elasto-plastic behavior is shown on Figure 2. The load-deflection curve has an initial elastic line up to yield, after which the curve is purely plastic (constant load resistance for continued deflection). If deflection goes past yield, unloading and reloading follow lines parallel to the initial elastic line. Elasto-plastic behavior is a good approximation of the response of well designed steel or reinforced concrete structures to earthquakes.

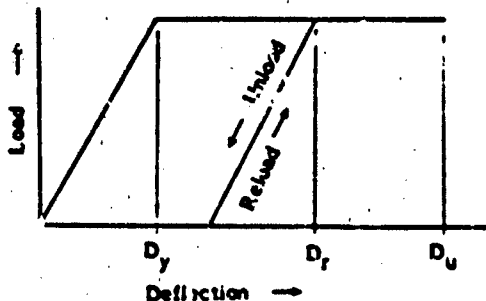


Figure 2. Elasto-Plastic Load-Deflection Relation

Response, in elasto-plastic behavior, is described in terms of the dimensionless ductility ratio,  $\mu$ . This ratio is defined as

$$\mu = \frac{\text{maximum response deflection}}{\text{deflection at incipient yield}} = \frac{D_r}{D_y} \quad (1)$$

It is emphasized that  $\mu$  is referenced to deflection, not to stress or strain. The values of  $\mu$  from 0 to 1 measure energy stored elastically and recoverable by rebound;  $\mu$  values in excess of 1 measure non-recoverable plastic work on a structure. The deflection defining  $\mu = 1$  for any given response of an elasto-plastic structure has a unique value that is independent of the number of responses, short of failure, into the inelastic region.

There is a maximum amount of plastic work, characteristic of any given structure configuration and material, that can be absorbed before failure. It is therefore seen that an ideal elasto-plastic structure fails when either single or multiple responses into the inelastic region are such that

$$1 + \sum (\mu - 1) \geq \text{Failure } \mu \quad (2)$$

$$\begin{aligned} \text{where Failure } \mu &= \frac{\text{deflection at incipient failure}}{\text{deflection at incipient yield}} \\ &= \frac{D_u}{D_y} \end{aligned}$$

Failure  $\mu$  values, based on rupture or collapse, can range from near 1 for brittle structures to more than 20 for structures designed to respond in a ductile manner. Some degree of inelastic response occurs for any civil-architectural structure in a severe earthquake. Hence it is important for survivability that structures be designed to achieve large Failure  $\mu$ .

#### THE DUCTILITY OF HIGH-RISE TOWERS

Evidence of damage to buildings which have survived severe lateral distortion indicates that, as built, they had load-deflection curves as shown on Figure 3. Such curves show that brittle elements, e.g., masonry curtain walls or concrete elevator shafts, were connected in parallel with flexible structural frames. Under light loads, they responded along line 0 - 1. Under severe loads, their stiff-

† The structural term "stage" refers to primary horizontal members and the vertical and lateral load resisting members which frame into them, in this case a girder and its immediate supporting columns. The architectural terms "story" and "floor" do not unambiguously define the corresponding structure.

nesses were abruptly softened when responses reached  $D_{pu}$ , the rupture distortion of the brittle elements or their connections to the flexible frames. This softening is detected as a lengthening of the natural period of vibration after a building's exposure to lateral motion. After brittle elements are once ruptured, future elastic responses follow line 0 - 2, or if response exceeds  $D_y$ , unloading and reloading follow lines parallel to 0 - 2.

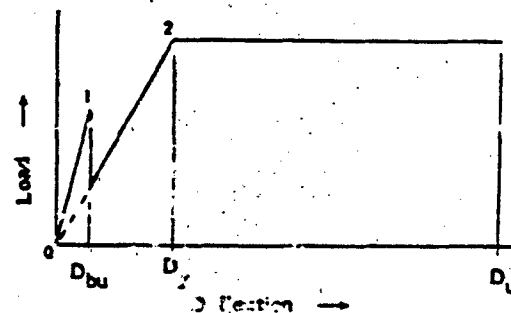


Figure 3. Typical Building Load-Deflection Curve

Buildings without brittle and flexible members connected in parallel (as with some newer buildings) exhibit a single linear load-deflection relation to yield. In either case, new buildings or previously exposed old buildings, the load-deflection curve is essentially elasto-plastic, and the survivability now is a function of the previous history of cumulative inelastic distortion and of  $D_u$ , the cumulative distortion at incipient failure. Stated in general, a structure can have only a finite number of inelastic responses before the cumulative work absorbed will result in unforewarned failure, and that finite number can be as small as 1.

Seismic survivability is increased as Failure  $\mu$ ,  $D_u/D_y$ , is increased. Design of high-rise buildings for large Failure  $\mu$  requires attention to problems which are inherent in series type structures, of which frames of high-rise towers are a type. Practical high-rise towers have only a narrow range within which the relative values of their floor to floor structural parameters vary, so it is possible to examine their inherent problems in achieving large Failure  $\mu$  by using reasonable choices of the parametric relations involved.

Consider a high-rise tower of  $m$  stages in number with all stage heights and stage masses identical, and where the lateral stiffness ( $K$ ) of each stage is proportional to the load tributary to it. Taking first mode lateral distortion as the critical response makes the forces at each floor act in phase, and each force will have a magnitude which is, to a good approximation, proportional to the distance of its floor above the base of the structure. The preceding conditions are illustrated in Figure 4.

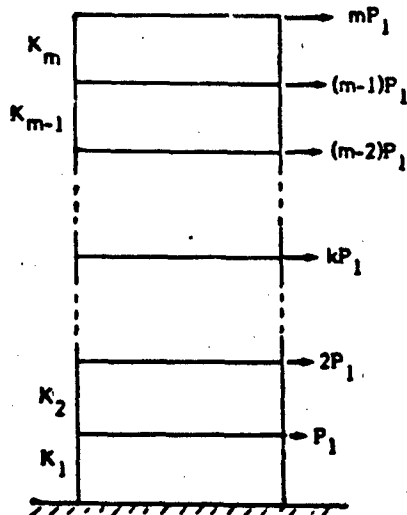


Figure 4. Example Tower Frame

The lateral force at the \$k^{th}\$ stage floor is \$P\_{k,k} = kP\_1\$ and the total load tributary to the \$k^{th}\$ stage (the shear at the \$k^{th}\$ stage) is

$$mP_1 = (m-1)P_1 + (m-2)P_1 + \dots + kP_1$$

Letting \$k = 1\$ gives the total tributary load to the first stage (the base shear) as

$$(m^2 + m) \frac{P_1}{2}$$

With the assumed conditions on stage stiffness and lateral force distribution, the drift in each stage is the same. The drift in the first stage is

$$d_1 = \frac{(m^2 + m) P_1}{2 K_1}$$

and the total displacement of the free end is

$$D_m = m d_1 = \frac{m(m^2 + m) P_1}{2 K_1} \quad (3)$$

The preceding expression relates free end displacement and base shear during first mode elastic response of the example tower.

If the response of the tower goes inelastic due to yielding in the \$k^{th}\$ stage, then the tributary load to the \$k^{th}\$ stage at incipient yield can be expressed as

$$mP_1(y_k) + (m-1)P_1(y_k) + \dots + kP_1(y_k)$$

where the subscript \$(y\_k)\$ designates the value of \$P\_1\$ at this condition. The \$k^{th}\$ stage drift at incipient yield is

$$d_{k(y_k)} = \frac{(m^2 + m) P_1(y_k)}{2 K_1}$$

and the free end deflection of the tower at incipient yield, \$D\_y\$, is

$$D_y = D_{m(y_k)} = \frac{m(m^2 + m) P_1(y_k)}{2 K_1} \quad (4)$$

Yield in the \$k^{th}\$ stage limits drift in the stages above it to that occurring at \$k^{th}\$ stage yield. Stages below the \$k^{th}\$ can still receive increasing drift.

If the elastic drift below the \$k^{th}\$ stage is small during the interval from \$k^{th}\$ stage yield to its failure (this is equivalent to saying the \$k^{th}\$ stage is low in the structure or that the \$k^{th}\$ stage plastic drift to failure is small), then the free end deflection at incipient tower failure can be expressed as

$$D_u = D_y + (d_{kf} - d_{k(y_k)}) \quad (5)$$

where \$d\_{kf} = k^{th}\$ stage drift at \$k^{th}\$ stage failure.

The tower failure ductility ratio is then

$$\text{Failure } \mu = \frac{D_u}{D_y} = \frac{D_y + (d_{kf} - d_{k(y_k)})}{D_y} \quad (6)$$

It is seen that as more stages are placed in series (as more stories are added to a tower),  $D_y$  becomes large compared to  $[d_{kf} - d_k(y_k)]$  and the Failure  $\mu$  approaches the limiting value of 1. That is to say, if a high-rise tower contains a sub-strength stage, the load-deflection curve of the tower will be elasto-plastic, but the plastic deformation region will be essentially limited to the plastic drift in the yielding stage. Before yield, all stages receive work due to lateral distortion; after yield, the yielding stage alone receives essentially all further work. For a high-rise tower to be given a reasonable degree of ductility, care must be taken to design all stages to have individually large plastic drifts before failure and to assure that no weak links (sub-strength stages) exist, particularly that they do not exist low in the structure.

A schematic representation of a tower frame with yield in the  $k^{\text{th}}$  stage is given in Figure 4a. If yield occurs, it is usually low in the structure, often in the first stage (e.g. Olive View Medical Center, San Fernando 1971).

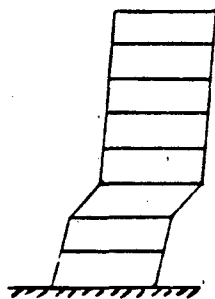


Figure 4a. Yielding Frame Schematic

## STRUCTURAL RESPONSE TO GROUND MOTION

### The Response Spectrum

The cyclic motion of earthquakes contains components of many frequencies. If the recorded amplitude of ground motion is plotted against frequency, the resulting graph is the ground motion spectrum. In general, the amplitude-frequency plot is highly irregular (shows sharp peaks and valleys) with largest displacements occurring at low frequencies and largest accelerations at high frequencies. As a practical matter, the highly irregular plot is often smoothed by substitution of a curve enveloping its peaks, or, alternatively, running through its mean values. It is apparent that choice of smoothing process strongly affects the smoothed spectrum values, and furthermore, that the ground motion spectrum gives no information on time history of motion as required for dynamic analysis.

With a given ground motion spectrum, the corresponding spectrum for single mode linear elastic response is constructed with amplitudes as simple multiples, between one and two, of the ground spectrum. The response spectrum is extremely useful as a rational formalism for deriving loads to be used for aseismic design. However, attempts to use it for "dynamic analysis" of response of real structures to real earthquakes involve several necessary assumptions as follows:

- 1) Time is not a parameter of concern in dynamics problems.
- 2) The various response modes are uncoupled; i.e., response in any one mode will not excite response in other modes.
- 3) The effect of phasing of modal responses on over-all response can be accounted for by an arbitrary formalism; e.g., the over-all response is assumed equal to the square root of the sum of the squares of the modal responses.

In fact, the preceding assumptions are seriously violated in the non-linear response region of interest for survivability assessment, so while the response spectrum provides a useful means for deriving loads to be used for design, its use does not constitute an analysis of the response which will actually occur in any given earthquake.

### Time Domain Response Analysis

#### The Lumped Parameter Method

Rigorous solution of multi-mode structural response to ground motion requires analysis in the time domain. Time domain analysis is often attempted by use of the lumped parameter method. This consists essentially of "lumping" the structural parameters of mass, spring rate, and damping and then determining the equations of motion for the system. In matrix form, the equations are expressed as

$$[M]\{\ddot{x}\} + [C]\{\dot{x}\} + [K]\{x\} = \{F(t)\}$$

where, for response to ground motion, the vector  $\{F(t)\}$  is obtained by applying the time history of ground motion as a boundary condition.

If the preceding matrix equation is linear, it can be solved by computer. Unfortunately, the responses of interest for earthquakes result in severe non-linearity in the stiffness and damping matrices and preclude use of matrix analysis for structural response, unless the problem can be segmentally linearized, a costly procedure.

Lumped parameter analysis has sometimes been used for after-the-fact investigation of damaged structures, in which cases "equivalent linear" damping and stiffness matrices were devised which, used in the matrix equation, would correctly predict the observed results. Determining "equivalent viscous damping" or "equivalent spring rate" can be informative for research, but it is not an analysis of response.

#### The Distortion Wave Method

When the base of a structure is subjected to a pulse of transverse motion, a signal of the time-history of that motion is transmitted up the structure as a transverse wave of distortion whose velocity, for wave lengths exciting first mode seismic response, can be related to the structure configuration by the expression

$$V_s = \frac{4H}{T} \quad (7)$$

where  $V_s$  = velocity of transverse wave propagation in the structure, meters/sec  
 $H$  = structure height, meters  
 $T$  = first mode period, sec

The amplitude of the structure wave induced by base motion is the same as that of the base motion; however, the wave length in the structure is different from that of the medium in which the base motion occurs by the ratio of the wave velocities in the structure and the base medium, i.e.,

$$L_s = \frac{V_s}{V_m} L_m \quad (8)$$

where  $L_s$  = wave length in structure, meters  
 $V_m$  = wave velocity in base medium, meters/sec  
 $L_m$  = wave length in base medium, meters

It is apparent that, for a given amplitude, the slope of the distortion wave (the drift between floors) is increased as its wave length is decreased. A wave reaching the free end of a structure is reflected toward the base unchanged except in sign. Structural wave amplitudes are reduced exponentially with distance traversed (i.e., with time) as determined by damping.

Structural damage in earthquakes begins in local zones of inelastic response. Considering multi-story buildings, such a "local zone" would be a sub-strength stage in yield at its points of maximum moment (the column to girder connections), and it is apparent that inelastic response at any stage limits the seismic shear load which can be transmitted by that stage. The presence of a zone of inelastic response is a boundary condition separating the elastic response regions on either side. Whatever the signal transmitted to the inelastic response zone, the signal propagated through that zone to the elastic region beyond consists of a nearly constant force for the duration of inelastic response.

The general steps of determining a structure's response to a given earthquake ground motion, using the distortion wave method, are as follows:

- 1) The lateral wave propagation velocity of the structure is calculated.
- 2) The structural waves induced by the known ground motion time-history (ground displacement versus time) and reflection from the free end are determined.
- 3) The amplitudes of the structural waves are reduced exponentially with time as determined by appropriate damping.
- 4) The instantaneous frame distortion at any time is found as the algebraic sum of the separate wave distortions (including reflected waves) present in the frame at the given time.
- 5) If local inelastic response occurs, the over-all structure response is determined step-wise for the time intervals before and after the onset of inelastic response.

The response obtained by the preceding technique yields the floor to floor drift, including any inelastic drift, in the time domain. The distortion wave method conforms to the real physical nature of structural response to cyclic base motion. Survivability assessment requires that the effect of each seismic wave capable of inducing inelastic response be considered; however, this often only requires use of a single critical cycle of ground motion which can be found by inspection of the ground displacement - time history for the earthquake of interest. †

#### SURVIVABILITY ASSESSMENT

##### THE CONCEPT OF SURVIVABILITY

The terms "vulnerability" and "survivability", which are used in a qualitative sense in informal conversation, require precise and quantitative definitions when used in systems analysis. General definitions are as follows:

Vulnerability is the degradation of system capability, expressed as a fraction, expected to occur when the system is exposed to a defined hostile environment for a defined period of time.

Survivability is the portion of system capability, expressed as a fraction, expected to be retained when the system is exposed to a defined hostile environment for a defined period of time.

† That the damaging distortion of a tall building tends to appear during response to a single critical cycle of ground motion occurring at the building's first mode period is Derrick's observation (C. J. Derrick, Structural Engineer) based on evidence of damage in the Long Beach 1933 and subsequent events in Southern California. Derrick's observation can be supported by statistical argument based on the randomness of earthquake ground motion. Distortion wave analysis for seismic response was first discussed by Derrick ca 1930, but its acceptance was limited by the then lack of displacement-time history data for strong ground motion (Housner's analysis of El Centro 1940 was still 10 years in the future). Current use of distortion wave analysis is primarily for weapons effects, e.g., to obtain the time-domain elasto-plastic response of structures subjected to combined vertical and horizontal ground shock. Most such work cannot reach the open literature.

It is seen that these concepts are related as

$$\text{Survivability} = 1 - \text{Vulnerability}$$

Either concept can be used for analysis, but since structural engineers are more interested in "how much is left" than in "how much is used up", the remaining discussion will emphasize survivability.

Considering civil-architectural structures and earthquakes, "system capability" is a structure's as-built ability to accept inelastic deflection without failure, i.e., system capability is precisely the previously defined "Failure  $\mu$ ". The "defined hostile environment" is the expected intensity and recurrence times of earthquakes for the locale of the structure. The "defined period of time" is, as a minimum, whatever is the intended lifetime of the structure; however, longer times might be chosen in particular cases. Accordingly, survivability is estimated as

$$\text{Survivability} = \frac{\text{Failure } \mu - \sum(\mu - 1)}{\text{Failure } \mu} \quad (9)$$

where Failure  $\mu$  for any structure is a calculable number, and the term  $\sum(\mu - 1)$  includes the effects of any inelastic response which has occurred as well as anticipated responses in the remaining expected life of the structure.

The concept of survivability can be illustrated by comparison of example structures in a given seismic environment. Assume a region of seismicity such that there can be expected four "major" earthquakes and one "great" earthquake in a 100 year time period of interest. "Major" and "great" are arbitrarily assumed, for this comparison, as inducing response deflections,  $D_r$ , of 30 centimeters and 40 centimeters respectively in the example structures.

Assume three tower structures, architecturally identical, but with different yield deflection,  $D_y$ , and failure deflection,  $D_u$ , as tabulated below. The survivabilities were assessed for the 100 year time period with the expected five earthquakes.

	<u>Tower 1</u>	<u>Tower 2</u>	<u>Tower 3</u>
$D_y$	20 cm	20 cm	30 cm
$D_u$	60 cm	100 cm	60 cm
Failure $\mu$	3	5	2
"Major" $\mu$ (4 times)	1.5	1.5	1
"Great" $\mu$ (1 time)	2	2	1.33
$\Sigma(\mu-1)$	3	3	0.33
Survivability	0	0.4	0.84

The example survivabilities indicate that Tower 1 cannot survive the defined 100 year environment, although it could survive a shorter time period with a reduced number of events. Tower 2 retains 40% of its original capability; i.e., it can still survive one more "major" event, but a second major event or a single great event would cause its collapse. Tower 3, however, can survive several centuries of the example seismic environment, if not razed to make way for a parking lot.

It is apparent that a structure's survivability is reduced by its every inelastic response to lateral distortion. The point at which survivability becomes unacceptably low logically depends on several factors, including the structure's use and planned remaining life. It can be argued that an unsuspecting public has a right to structures which will protect them unharmed through the most severe earthquake credible during the public's exposure. Notice that this argument does not require that the structure itself remain undamaged. In any event, as far as building codes are concerned, speculation regarding minimum allowable survivability is academic, since design by codified static loads to codified allowable stresses gives no clue to survivability, nor is survivability assessment required by code.

#### THE HOSTILE ENVIRONMENT

##### Regional Seismicity

Seismicity refers to the magnitudes and recurrence intervals of earthquakes historically characteristic of any region. The concept of seismicity is implicitly recognized in the "seismic zone" categories defined in building codes. More direct statement of seismicity is given in empirical relationships of magnitude and recurrence time such as reported by Dr. G. W. Housner for California and presented in the following table.

#### PROBABLE NUMBER OF EARTHQUAKES IN CALIFORNIA

Of magnitude	Per 25	Per 50	Per 100	Per 200
M greater than	years	years	years	years
6.0	25	50	99	198
6.2	18	36	73	146
6.4	13	26	53	106
6.6	9.3	19	37	74
6.8	6.4	13	26	51
7.0	4.3	8.6	17	34
7.2	2.6	5.2	10	21
7.4	1.7	3.4	6.7	13
7.6	0.97	1.9	3.9	7.8
7.8	0.51	1.0	2.0	4.1
8.0	0.28	0.56	1.1	2.2
8.2	0.13	0.26	0.51	1.0
8.4	0.06	0.08	0.17	0.34

Regional seismicity descriptions, such as the preceding, help define the "hostile environment" required for assessment of seismic survivability. Full definition of the hostile environment must include description of the expected ground displacement time history (which is related to Modified Mercalli Intensity) for the building site of interest.

##### Ground Motion Intensity

The "magnitude" of an earthquake is a numerical grading, on a logarithmic scale, of the energy released during the event. The Modified Mercalli Intensity of an earthquake is a numerical grading of the damage potential of ground motion at a specific site during a seismic event. It is apparent that the intensity at a given site is a function of the magnitude of the earthquake, of the distance of the site from the center of energy release, of the local site geology, and of the intervening geology between the site and the origin of the earthquake.

The most useful quantitative description of intensities of past earthquakes at any site would be strong-motion seismograms recorded at the site. Local site geology is the parameter of major influence on the ground motion amplitude and period relation, so such records, along with the corresponding information on earthquake magnitude and location of origin, could be extrapolated to describe expected future site ground motion. Unfortunately, as of 1984 such site specific records are rarely available, so it is usually necessary to use records of ground motion from sites of similar local geology and seismicity to define expected future ground motion at any specific site. Past ground motion at any site can be similarly estimated, and such estimates should be supported by recorded evidence of damage to structures of known properties, if such evidence is available.

#### RESPONSE PARAMETER EVALUATION

The structure response parameters required for survivability assessment of high-rise buildings were explained in the section THE DUCTILITY OF HIGH-RISE TOWERS. Evaluation of these parameters requires equating the drift in each stage to the stage column and girder end moments. This permits identification of the stage in which yielding occurs, and, if yielding occurs in the  $k^{\text{th}}$  stage, it permits quantification of

$d_k(y_k)$  =  $k^{\text{th}}$  stage drift at  $k^{\text{th}}$  stage incipient yield,

$d_{kf}$  =  $k^{\text{th}}$  stage drift at  $k^{\text{th}}$  stage incipient failure,

and the corresponding  $D_y$  and  $D_u$  can be found if the over-all shape of the structure's seismic distortion curve is known at incipient yield in the  $k^{\text{th}}$  stage.

A frequently used assumption is that the elastic response seismic distortion curve of a high-rise tower is linear, i.e. has a constant slope. A theoretically better assumption is that the distortion curve is sinusoidal with zero slope at the roof line, and the slope at the  $k^{\text{th}}$  stage level, at  $k^{\text{th}}$  stage incipient yield, is equal to  $d_k(y_k)/h_k$  where  $h_k$  is the height of the  $k^{\text{th}}$  stage.

Yield in the  $k^{\text{th}}$  stage occurs when the  $k^{\text{th}}$  stage drift and  $k^{\text{th}}$  stage shear relationship loses linearity. Failure in the  $k^{\text{th}}$  stage occurs at the  $k^{\text{th}}$  stage drift where instability or rupture (whichever occurs first) begins.

#### STRUCTURAL DETAIL EFFECTS

Regarding yield and failure of structures, it is well to recall that most failures start in connections rather than in under-designed members. For steel high-rise frames, the column-girder connection details can be critical, particularly so for welded connections.

An example of potentially a problem connection is shown in Figure 5. Unless the column flange is stiffened (5a), or thick enough to preclude significant column flange bending, stress concentration in the girder flange weld can result in progressive tearing (5b) and an elastic-deflection softening response. If stiffeners are used, they must be clipped as shown to prevent inducing the tri-axial tension stress and consequent loss of ductility which would occur at the welded intersection point of three orthogonal plates.

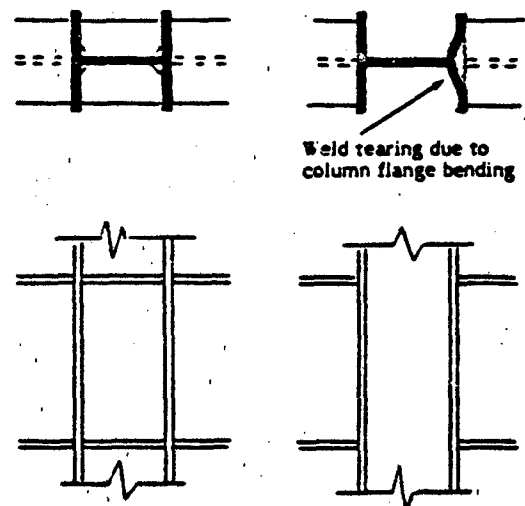


Figure 5. Column-Girder Weld Examples

Many high-rise buildings with welded rigid frames, recently built or being built in California, utilize the unstiffened girder-column connection as shown in 5b. Considering that these buildings have usually not been given a lateral distortion analysis and were designed with various degrees of appreciation for problems of stress concentration and fracture mechanics, it is reasonable to conclude that they will exhibit large differences in survivability during future earthquakes.

As with steel, concrete structure survivability depends on details of design. An unreinforced concrete member in flexure will fail brittly when its ultimate strength in tension is reached. However, reinforced concrete in flexure can attain an elasto-plastic load-deflection relation if failure is governed by tension steel yield rather than by concrete compression rupture.

Accordingly, the traditional "balanced" design of tension steel in flexural concrete, which provides for nearly simultaneous compression yield in concrete and tension yield in steel, is not conducive to achievement of a significant "plastic" component of response before failure. Published values of Failure  $\mu$  for concrete beams are as follows:

Governing Failure Mode      Approximate Failure  $\mu$

Reinforced Concrete in Flexure       $\frac{10}{\phi}$  but  $\leq 10$   
(no compression steel)

Reinforced Concrete in Flexure       $\frac{10}{\phi - \phi'}$  but  $\leq 20$   
(tension plus compression steel  
tied against buckling)

where       $\phi$  = percentage of tension reinforcement,  
             $\phi'$  = percentage of compression reinforcement.

For comparison, the Failure  $\mu$  for structural steel WF shapes in flexure (restrained against lateral buckling) is approximately 26, and structural steel in pure tension has a Failure  $\mu$  of approximately 50.

In general, the Failure  $\mu$  ( $D_u/D_y$ ) for a structural system such as a high-rise tower is lower than the Failure  $\mu$  of its component members. This must cause concern regarding the seismic survivability of reinforced concrete towers with "balanced" design flexural reinforcing.

\*\* Newmark, N. M., et al, Design of Protective Structures to Resist the Effects of Nuclear Weapons, Air Force Special Weapons Center TDR-62-138, December 1962.

SUMMARY

Elasto-plastic response is described in terms of ductility ratio  $\mu$ ; that is

$$\mu = \frac{\text{maximum response deflection}}{\text{deflection at incipient yield}} = \frac{D_r}{D_y} \quad (1)$$

where  $D_r$  and  $D_y$  are total drift, roof to base, of high-rise structures in first mode response. Response  $\mu \leq 1$  represents elastic response. Response  $\mu > 1$  represents elasto-plastic response whose inelastic component is  $\mu - 1$ .

As built, structures have a maximum amount of inelastic response which they can accept without failure. This is described in terms of ductility ratio as

$$\text{Failure } \mu = \frac{\text{deflection at incipient failure}}{\text{deflection at incipient yield}} = \frac{D_u}{D_y}$$

The effects of inelastic responses are cumulative; therefore, a structure will fail when either single or multiple responses into the inelastic region are such that

$$1 + \sum (\mu - 1) \geq \text{Failure } \mu \quad (2)$$

A structure's seismic survivability is that fraction of its ductility it is expected to retain after exposure to the seismic environment of its geological locale for a defined period of time. Survivability is estimated as

$$\text{Survivability} = \frac{\text{Failure } \mu - \sum (\mu - 1)}{\text{Failure } \mu} \quad (9)$$

where Failure  $\mu$  is the as-built (undamaged) ductility of the structure. Survivability is a function of the history of cumulative inelastic response deflection and of  $D_u$ , the cumulative deflection at incipient failure. A structure can have only a finite number of inelastic responses before failure will result. Historically, for brand new multi-story buildings this number can be as small as 1 (e.g. Olive View Medical Center, San Fernando, 1971).

It is characteristic of series structures that Failure  $\mu$  tends to decrease toward 1 ( $D_u/D_y \rightarrow 1$ ) as the number of stages is increased. Accordingly, high-rise towers require particular care in design to assure achievement of a reasonable degree of ductility.

Failures usually begin in connections rather than in under-designed members. Modern welded connections can develop the full ductility of the members they connect, if designed with concern for problems of stress concentration and fracture mechanics. Similarly, reinforced concrete connections and members can be given the characteristics of elasto-plastic response if designed for failure governed by steel tension yield rather than by concrete rupture.

Although often categorically maligned regarding their safety in earthquakes, the pre-1933 steel frame office buildings in Southern California were built with nearly "fool-proof" riveted connections. This, and the high damping provided by their masonry filler walls, can give them seismic survivability superior to that of some of the newer high-rise buildings designed in conformance with post-1933 codes.

#### BIBLIOGRAPHY

1. Blume, J. A., Newark, N. M., Corning, L. H., Design of Multistory Reinforced Concrete Buildings for Earthquake Motions, Portland Cement Association, 1961.
2. Hudson, D. E., Response Spectrum Techniques in Engineering Seismology, Proceedings, World Conference on Earthquake Engineering, Berkeley, Calif., 1956.
3. Housner, G. W., Behavior of Structures During Earthquakes, Journal, Engineering Mechanics Division, ASCE, No. EM4, Oct. 1959.
4. Blume, J. A., A Reserve Energy Technique for the Earthquake Design and Rating of Structures in the Inelastic Range, Proceedings, Second World Conference on Earthquake Engineering, Tokyo, 1960.
5. Clough, R. W., Benuska, K. L., Nonlinear Earthquake Behavior of Tall Buildings, Journal, Engineering Mechanics Division, ASCE, EM3, Jun 1967.
6. Derrick, C. J., Elements of Aseismic Design, Part 1, Physical and Theoretical Background, Univ. of So. Calif., 1955.

## GROUND SHOCK EFFECT ON SOIL FIELD INCLUSIONS

R. E. McClellan\*

The Aerospace Corporation, El Segundo, California

The displacement response of a high density inclusion to ground shock is different from that of the surrounding soil field. An expression for inclusion-soil field peak relative displacement is derived in terms of the soil, inclusion, and ground shock parameters of interest. The magnitude of peak relative displacement is examined using reasonable values of soil and inclusion parameters, and for ground shock strengths commensurate with hardened design against nuclear weapons effects. It is found that high density inclusion ground shock response displacement can be large enough to damage or cut nearby buried power or communication cables responding with the soil field.

### INTRODUCTION

Most soil is the product of weathering and erosion of rock and has been transported by wind or water some distance from its place of origin. Depending on its geological history, a soil field can contain rocks (high density inclusions) of sufficient size that their displacement response to ground shock can be significantly different from that of the surrounding soil.

Relative displacement of a soil field and high density inclusion during ground shock occurs due to impedance mismatch and inertial effects. Inertial effects relative displacement is stated to govern at high overpressures, e.g., those of interest in survivable basing of weapons systems. Air blast induced (vertical) ground shock dominates at high overpressures, and the corresponding vertical relative displacement of inclusion and soil field can endanger cables buried over inclusions and responding with the soil field. Buried cables for power or communications are necessary components of most systems hardened against nuclear weapons effects. Accordingly, the survivability of buried cables, as affected by the presence of high density inclusions in the soil field, can be a limiting factor on attainable system hardness.

### IMPEDANCE MISMATCH

Impedance mismatch affects relative displacement in two ways:

- 1) Distortion of the soil stress wave leeward of the inclusion.
- 2) The difference in compressibility of the inclusion and the adjacent soil.

The soil stress wave distortion includes both change in shape of the stress front and change in soil stress magnitude occurring leeward of the inclusion. This is shown schematically in Figure 1 for one-dimensional wave propagation vertically downward from a horizontal ground surface.

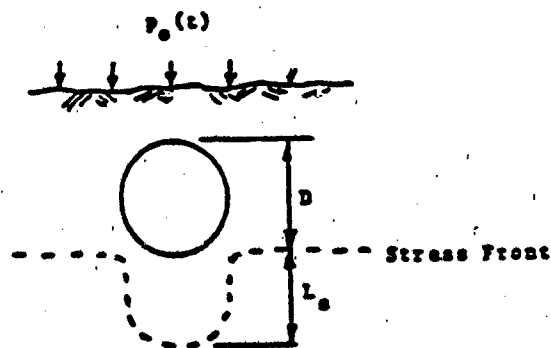


Figure 1. Stress Front Distortion Below High Density Inclusion for One-Dimensional Wave Propagation

In Figure 1, the stress front transit time difference over inclusion height  $D$  is

$$\Delta t = \left[ \frac{1}{c_1} - \frac{1}{c_2} \right] D \quad (1)$$

\* Manager - Strategic Studies  
Energy and Resources Division

where  $C_1$  is the stress front speed in the soil and  $C_2$  is the stress front speed in the inclusion. The length of the soil block,  $L_s$ , distorting the stress front is then

$$L_s = C_1 \Delta t = \left[ 1 - \frac{C_1}{C_2} \right] D \quad (2)$$

Reference 1 presents an approximation to the peak relative displacement due to stress front distortion as

$$\xi_s = \epsilon L_s = \frac{\eta \alpha_2 P_0}{E_s} \left[ 1 - \frac{C_1}{C_2} \right] D \quad (3)$$

where  $\epsilon$  = average strain of distorting soil block in  $L_s$

$P_0$  = peak air blast overpressure

$\alpha_2$  = attenuation factor to midheight of inclusion

$E_s$  = soil constrained modulus corresponding to stress  $\alpha_2 P_0$

$\eta$  = stress concentration factor

$$\eta = \frac{\rho_2 C_2 \rho_1 C_1}{(\rho_2 C_2 + \rho_1 C_1)^2}$$

$\rho_1$  = soil density

$\rho_2$  = inclusion density

The factor  $\eta$  gives the fraction of shock strength transmitted by the inclusion to the soil below. For soil and inclusion impedances of interest,  $\eta$  usually falls somewhere in the range of 0.35 to 0.45, and, of course,  $\eta \rightarrow 1$  as  $\rho_2 C_2 \rightarrow \rho_1 C_1$ . The stress front distortion effect illustrated in Figure 1 causes the inclusion to move downward relative to the soil field.

The peak relative motion of the soil field and inclusion due to differences in compressibility can be estimated as

$$\xi_c = \alpha_2 P_0 \left[ \frac{1}{E_s} - \frac{1}{E_i} \right] D \quad (4)$$

where  $E_i$  is the constrained modulus of the inclusion. For both the soil and inclusion modulus,  $E \propto \rho C^2$ . In most cases of interest  $E_s \ll E_i$ , and  $\xi_c$  can be approximated by

$$\xi_c = \frac{\alpha_2 P_0}{E_s} D \quad (5)$$

The compressibility effect on peak relative displacement,  $\xi_c$ , occurs at the top of the inclusion which moves upward relative to the soil stratum at the same depth. There is no relative motion between the soil field and the bottom of the inclusion due to difference in compressibility. The relative displacement due to difference in compressibility varies linearly over the height of the inclusion.

#### INERTIAL EFFECT

The inertial effect on relative displacement is due to the difference in mass of the inclusion and displaced soil. To examine this effect, consider a bi-linear ground shock as shown on Figure 2.

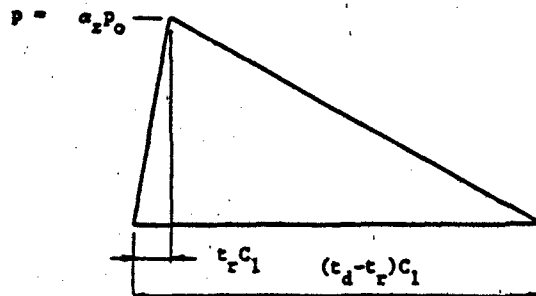


Figure 2. Bi-Linear Ground Shock Wave

The parameters of the bi-linear ground shock include  $t_r$ , the rise time,  $t_d$ , the positive phase duration, and  $P_0$ , the air blast peak overpressure. These and other parameters affecting inclusion response are referenced in the SOIL AND WEAPON PARAMETERS section. With the ground shock defined, inertia effect on relative displacement is found as the soil field inertial displacement minus the inclusion inertial displacement.

The differential pressure over a small vertical length of soil,  $\Delta Y$ , during ground shock rise can be expressed as

$$\Delta P = \frac{P}{t_r C_1} \Delta Y \quad (6)$$

and during decay

$$\Delta P = \frac{P}{(t_d - t_r) C_1} \Delta Y \quad (7)$$

For soil field inertial displacement, integrate the acceleration of a soil block of length  $\Delta Y$  over time  $t_d$ . During the pressure rise, the differential pressure on the soil block

$$\Delta P = \frac{\alpha_z p_o}{t_r C_1} (\Delta Y) = \rho_1 (\Delta Y) a_r \quad (8)$$

where  $p$  is expressed in newtons/m<sup>2</sup>,  $\rho$  in kg/m<sup>3</sup>,  $Y$  in meters, and  $a$  in m/sec<sup>2</sup>. The soil block acceleration during pressure rise is constant with a value

$$a_r = \frac{\alpha_z p_o}{\rho_1 C_1 t_r} \text{ m/sec}^2 \quad (9)$$

The peak velocity attained is

$$v_r = a_r t_r = \frac{\alpha_z p_o}{\rho_1 C_1} \text{ m/sec} \quad (10)$$

and the rise time displacement of the soil block is

$$s_r = \frac{1}{2} a_r (t_r)^2 = \frac{\alpha_z p_o}{\rho_1 C_1} \times \frac{t_r}{2} \text{ meters} \quad (11)$$

Similarly, during pressure decay

$$\frac{-\alpha_z p_o}{(t_d - t_r) C_1} (\Delta Y) = \rho_1 (\Delta Y) a_d \quad (12)$$

and the soil block acceleration during pressure decay is

$$a_d = \frac{-\alpha_z p_o}{(t_d - t_r) \rho_1 C_1} \quad (13)$$

The soil block displacement during pressure decay is

$$\begin{aligned} s_d &= v_r (t_d - t_r) + \frac{1}{2} a_d (t_d - t_r)^2 \\ &= \frac{\alpha_z p_o}{\rho_1 C_1} \times \frac{(t_d - t_r)}{2} \text{ meters} \quad (14) \end{aligned}$$

and the total soil block inertial displacement during time  $t_d$  is  $s_r + s_d$  which is

$$s_1 = \frac{\alpha_z p_o}{\rho_1 C_1} \times \frac{t_d}{2} \text{ meters} \quad (15)$$

The inclusion inertial displacement can be found by proportioning as

$$s_2 = K \frac{\rho_1}{\rho_2} s_1 \text{ meters} \quad (16)$$

where  $K$  is an inclusion configuration factor and  $\rho_1/\rho_2$  is the ratio of soil and inclusion densities. The configuration factor is examined in the INCLUSION CONFIGURATION FACTOR section.

The peak relative displacement due to inertia effect is then

$$s_i = s_1 - s_2 \quad (17)$$

$$= \frac{\alpha_z p_o}{\rho_1 C_1} \times \frac{t_d}{2} \left[ 1 - K \frac{\rho_1}{\rho_2} \right] \text{ meters} \quad (18)$$

This relative displacement represents the amount by which the inclusion moves up relative to the surrounding soil field.

#### TOTAL PEAK RELATIVE DISPLACEMENT

To obtain the total peak relative displacement, the separate relative displacements must be added with due consideration for time phasing and direction of motion. In this regard, the peak relative displacement due to difference in compressibility occurs early in time, approximately when the peak of the stress wave reaches the level of the bottom of the inclusion and represents upward relative motion of the inclusion. Similarly, the peak relative displacement due to stress front distortion occurs even earlier, when the stress front reaches the bottom of the inclusion, and represents downward relative motion of the inclusion. Both of these impedance mismatch induced relative displacements are related to soil compression which achieves a peak strain and, on load removal, retains between 20% and 30% of the peak strain as residual strain. The inertial effects peak relative displacement occurs late in time, at  $t = t_d$ , when for conservative estimate the impedance mismatch effects are reduced to 30% of their peak values. Accordingly, assigning positive to designate upward

relative motion of the inclusion, the total peak relative displacement can be estimated as

$$\xi_r = \xi_1 + 0.3(\xi_c - \xi_1) \quad (19)$$

$$\text{which is } \xi_r = \frac{\alpha_2 p_0}{\rho_1 C_1} \frac{t_d}{2} \left[ 1 - K \frac{\rho_1}{\rho_2} \right] + 0.3 \frac{\alpha_2 p_0}{E_s} D \left[ 1 - \eta \left( 1 - \frac{C_1}{C_2} \right) \right] \quad (20)$$

In Equation 19 it is seen that the second expression on the right gives the impedance mismatch effects relative displacement (correct with regard to direction) occurring at the time of peak inertial effects relative displacement given by the first expression on the right.

#### SOIL AND WEAPON PARAMETERS

The derived formula for peak relative displacement ( $\xi_r$ ) contains the soil parameters dilatation wave speed,  $C_1$ , soil density,  $\rho_1$ , soil constrained modulus,  $E_s$ , and depth attenuation factor,  $\alpha_2$ , which is a function of the soil properties and the weapon parameters of yield and overpressure. These parameters, the ground shock rise time,  $t_r$ , and the positive pressure phase duration,  $t_d$ , are discussed in Reference 2.

#### INCLUSION CONFIGURATION FACTOR

The configuration factor,  $K$ , is related to inclusion shape and acoustic impedance,  $\rho_2 C_2$ , as they affect the acceleration of the inclusion. Considering a square section soil field block of height  $D$ , it has been found that the net accelerating force on the soil block during overpressure rise is a constant such that

$$\Delta p = \frac{p}{t_r C_1} D \quad (21)$$

where, as before,  $p$  is the peak overpressure attained at the depth of the inclusion. Then the acceleration of the soil block during overpressure rise is

$$a_1 \propto \frac{p D}{t_r C_1 \rho_1 D^2} \quad (22)$$

To find  $\Delta p$  for an inclusion, consider an example with square section and height  $D$  as for

the preceding soil block. The inclusion  $\Delta p$  varies during overpressure rise. Its value at any time is the instantaneous difference between ground shock pressure on top of the inclusion and the pressure transmitted to the soil field below, i.e.

$$\Delta p = p_a - p_b \quad (23)$$

where  $p_a$  and  $p_b$  are instantaneous values. The transmitted pressure,  $p_b$ , is a function of  $p_a$ , the pressure gradient in the inclusion, and the stress concentration factor in the form

$$p_b = \left[ p_a - \frac{p}{t_r C_2} D \right] \eta \quad (24)$$

which gives

$$\Delta p = p_a (1 - \eta) + \eta \frac{p}{t_r C_2} D \quad (25)$$

where  $p$  is the peak overpressure at the depth of the inclusion. The second term on the right is a constant. The term  $p_a$  varies linearly with time from zero to  $p$  during  $t_r$ . Taking the average value of  $p_a$  during  $t_r$  gives

$$\Delta p \approx \frac{p}{2} (1 - \eta) + \eta \frac{p}{t_r C_2} D \quad (26)$$

in which it is seen, for usual values of soil and inclusion acoustic impedances, that the first term on the right dominates. Conversely, if the soil and inclusion properties approach each other, then  $\eta \rightarrow 1$ ,  $C_2 \rightarrow C_1$ , and  $\Delta p$  goes to that found for the example soil block.

The acceleration of the square inclusion during  $t_r$  is then

$$a_2 \propto \left[ \frac{p}{2} (1 - \eta) + \eta \frac{p}{t_r C_2} D \right] \frac{1}{\rho_2 D^2} \quad (27)$$

Considering that  $\eta \approx 0.4$  and the product  $t_r C_2 \approx 4$  meters,  $a_2$  during  $t_r$  can be estimated as

$$a_2 \approx \frac{0.3p + 0.1p D}{\rho_2 D^2} \quad (28)$$

Similarly, for a soil block of height D and recognizing  $t_p C_1 \sim 1$  meter,

$$a_1 = \frac{pD}{\rho_1 D^2} \quad (29)$$

The inertial effect displacements of soil block and inclusion during  $t_p$  are proportional to their accelerations; accordingly the soil block displacement,  $s_1$ , and inclusion displacement,  $s_2$ , are related as

$$s_2 = \frac{a_2}{a_1} s_1 \quad (30)$$

which is

$$s_2 = \left[ \frac{0.3}{D} + 0.1 \right] \frac{\rho_1}{\rho_2} s_1 \quad (31)$$

In this relation, the parenthetical term is K, the configuration factor for an inclusion of square cross section.

Applying the same argument to an inclusion of circular cross section, and assuming sinusoidal distribution of ground shock pressure on the projected area of the inclusion, give

$$s_2 = \frac{0.637}{\pi/b} \times s_2 \text{ for square} \quad (32)$$

Then, for a circular inclusion

$$s_2 = 0.8 \left[ \frac{0.3}{D} + 0.1 \right] \frac{\rho_1}{\rho_2} s_1 \quad (33)$$

and the configuration factor, K, for a circular section is approximately 80% of that for a square section.

The preceding arguments for estimating K were based on the overpressure rise phase of the ground shock. Parallel arguments for the overpressure decay phase of a bi-linear ground shock lead to the same estimates for K. It will be recognized that the presented derivation of K suppresses the effects of variation of soil and inclusion physical parameters and weapon parameters whose values, for examples of practical interest, lie within limits having a secondary effect on estimated response.

#### EXAMPLE

To examine the order of relative displacement occurring between a soil field and inclusion subjected to ground shock, consider a stone of approximately cylindrical shape and 2 m diameter buried horizontally in densely compacted granular soil with 1 m of cover. Assume a peak air-blast overpressure of  $6.895 \times 10^6$  newtons/m<sup>2</sup> from a 1 Mt bomb. Then approximately

$$\begin{aligned} \rho_1 &= 1810 \text{ kg/m}^3 \\ \rho_2 &= 2643 \text{ kg/m}^3 \\ C_1 &= 579 \text{ m/sec} \\ C_2 &= 3353 \text{ m/sec} \\ \alpha_2 &= 0.95 \\ E_s &= 1.034 \times 10^9 \text{ n/m}^2 \\ \eta &= 0.38 \\ \tau_d &= 0.016 \text{ sec} \\ K &= 0.2 \end{aligned}$$

Substituting the preceding values in the expressions for  $t_s$ , one obtains

$$\begin{aligned} t_s &= \frac{0.38 \times 0.95 \times 6.895 \times 10^6 \left[ 1 - \frac{579}{3353} \right] \times 2}{1.034 \times 10^9} \\ &= 0.004 \text{ meters} \end{aligned}$$

$$t_c = \frac{0.95 \times 6.895 \times 10^6}{1.034 \times 10^9} \times 2 = 0.013 \text{ meters}$$

$$\begin{aligned} t_1 &= \frac{0.95 \times 6.895 \times 10^6}{1810 \times 579} \times \frac{0.016}{2} \left[ 1 - 0.2 \frac{1810}{2643} \right] \\ &= 0.043 \text{ meters} \end{aligned}$$

and

$$\begin{aligned} t_t &= 0.043 + 0.3 (0.013 - 0.004) \\ &= 0.0457 \text{ meters (1.8 inches)} \end{aligned}$$

The soil properties used in the preceding example are near the upper limits of those that could reasonably be expected in naturally compacted soils. For an example of inclusion response in a less favorable natural soil consider

$$\begin{aligned} \rho_1 &= 1762 \text{ kg/m}^2 \\ C_1 &= 305 \text{ m/sec} \\ E_s &= 310 \times 10^6 \text{ n/m}^2 \\ \eta &= 0.22 \end{aligned}$$

with the other parameters unchanged.

Then

$$\begin{aligned} \xi_t &= 0.084 + 0.3 (0.043 - 0.008) \\ &= 0.0947 \text{ meters (3.7 inches)} \end{aligned}$$

It is apparent that, in either of the example cases, the inertial effects govern. However, with larger inclusions, for example  $D \geq 10$  meters, the compressibility effects can approach or exceed inertial effects, particularly in poorly compacted soil.

#### PROTECTION OF BURIED CABLE

Buried cable is a line target which, for consistent survivability, must be designed for the effects of higher overpressure than for the point targets in which it terminates. It would not be unusual to require that buried cable survive ground shock effects an order of magnitude higher than estimated in the preceding example. That is, a  $\xi_t > 1$  meter may sometimes have to be considered in protecting cable against the response of soil field inclusions.

The derivation and examples considered air blast induced vertical ground shock. Parallel analysis shows that contact surface bursts or penetration bursts can induce horizontal ground shock effects, in the near cratering region, as large or larger than air blast vertical ground shock effects at the same distance from the point of burst.

Protection of buried cable from high density inclusions requires over-excavating the cable trench and back filling with soil free of rocks of damaging size. The amount of over-excavation required depends on the expected size and distribution of inclusions and the intended hardness of the cable.

Design of cable protection also requires consideration of factors outside the scope of this paper, e.g., cable distortion by vertical ground shock due to air blast propagating parallel to the cable, cable distortion by horizontal ground shock intersecting the cable. Analysis of these and other factors affecting cable survival is found in the literature.

#### REFERENCES

1. Summary of Soil - Structure Interaction (U), Allgood, J., Naval Civil Engineering Laboratory Technical Report R-771, July 1972.
2. Principles and Practices for Design of Hardened Structures (U), Air Force Design Manual, Technical Documentary Report AFSWC-TDR-62-138, December 1962.

#### BIBLIOGRAPHY

Foundation Analysis and Design, Bowles, J. E., McGraw-Hill, 1968.

Buckling of Soil-Surrounded Tubes, Luscher, U., ASCE Proceedings, Journal of the Soil Mechanics and Foundations Division, Vol. 92, No. SM6, November 1966.

Static and Dynamic Constrained Moduli of Frenchman Flat Soils, Hendron, A. J. and Davisson, M. T., Proceedings of the Symposium on Soil-Structure Interaction, University of Arizona, September 1964.

Pre-Dice Throw II-I Structures Experiments (U), McClellan, R. E., POR 6097, Space and Missile Systems Organization (AFSC), January 1976.

PENETRATION OF SHORT DURATION AIRBLAST INTO  
PROTECTIVE STRUCTURES

J. R. Britt\* and J. L. Drake†  
Applied Research Associates, Southern Division  
Vicksburg, Mississippi

This paper describes a combined analytical and experimental effort to study blast wave propagation into the interior of rooms from short duration airblast produced by conventional weapons detonated near entrances to these facilities. Twenty-seven small-scale high-explosive tests were conducted to study the effects of opening size, incident blast pulse duration and peak pressure levels on the blast transmitted into structures. Two structures with square openings were used in the program. Peak entrance pressures ranged from 0.07 to 1.5 MPa (10 to 220 psi). A computer code--CHAMBER--was developed based upon a modified ray theory combined with empirical formulae derived from the experiment and non-linear shock propagation and shock or shock addition rules to describe the diffracted shock at any point in the room. An existing jet-fill code was incorporated to account for the quasi-steady flow. The CHAMBER code represents the end product of the analysis of over 300 records of blast inside the test structures. Comparisons of calculated waveforms using CHAMBER with measurements are given. The code reproduces the blast pressure-time records, including high order reflections, with an accuracy comparable with the best 3-D hydrocode calculations. Since fill is included, the code can also compute the complete pressure pulse (diffracted and quasi-steady flow) for long duration blast.

INTRODUCTION

Personnel areas and equipment within hardened military facilities must be protected against the blast produced by explosions outside entrances and openings to these facilities. Methods for predicting the interior blast pressures are not well developed for short duration pulses characteristic of those from conventional weapons. Previous research by others [1] emphasized the quasi-steady gas flow (fill) through openings into rooms for long duration pulses, simulating airblast from nuclear weapons. Because the short duration diffracted pulses that accompany the filling process are not included in this technique, interior peak blast pressures can be grossly underestimated for conventional size threats.

The transmission of the blast environment starts with the diffraction of the incident shock wave through the opening of the

building. This wave expands into the structure with a corresponding drop in pressure due to geometrical expansion and rarefactions. The pressure differential between the exterior and interior causes an inflow of air which results in an eventual equalization of the interior pressure with the exterior blast environment--so-called "filling". It is convenient to consider the shock propagation and subsequent internal reflections separately from the filling and mass flow, even though they occur simultaneously. The injury to personnel and damage to equipment within a structure associated with each of these components is dependent upon the position within the building, the magnitude and duration of the incident pressure, the room dimensions (volume), and size of the openings into the facility.

Airblast "filling" or "leakage" into chambers from long duration blast loads has been studied extensively and is well understood, particularly for large structures with

\*Formerly Research Physicist, U. S. Army Engineer Waterways Experiment Station, Vicksburg, Mississippi.

†Formerly Research Civil Engineer, U. S. Army Engineer Waterways Experiment Station, Vicksburg, Mississippi.

small openings. Filling is essentially a quasi-steady process where a jet of air flows through the opening due to the difference in the interior and exterior pressure. Initially, the abrupt rise in exterior pressure causes a high velocity jet to enter the chamber. The average interior pressure gradually builds as additional air is forced into the structure until it eventually attains a near equilibrium condition with the outside blast environment. The time at which equalization occurs (fill time) may be estimated by the formula [1],

$$T_{fill}(\text{msec}) = \frac{V}{2A} (\text{ft})^{\frac{1}{2}} \quad (1)$$

where  $V$  is the chamber volume and  $A$  is the area of the opening. Thus for small chamber volumes, equilibrium occurs almost immediately. An excellent review of the important research for the filling problem is given in Ref. [1] (Chapter 4). Coulter [2-6] performed experiments in a shock tube using model rooms to study the filling process. The volumes and entrance areas as well as the incident pressure and opening geometries were widely varied. Primary interest in most of these studies was on long duration pulses (typical of nuclear explosions) against civil defense-type structures such as basements and parking garages.

Several theoretical treatments of the filling process are available [1, 7-9, 16]. Most of these ignore the shock wave interaction problem and focus on the jet that forms at the entrance. Experimental verification of these computations is quite good for simple room and entrance geometries and for relatively small openings [1]. However, for large openings and for locations near the entrance, the interior pressure may be dominated by the shock propagation into the facility.

The incident shock generates a pressure wave at the opening that subsequently propagates into the facility. This wave expands geometrically into the interior, decays in amplitude, and reflects from internal surfaces. Decay rate and pulse duration of this wave are governed by the size of the openings into the structure. The attenuation of the peak is inversely proportional to the opening diameter (or mean opening dimension), while its duration is proportional to the opening diameter.

The shock diffraction and interior reflection problem was recognized in early studies [1-9], but little experimental data were obtained on the propagation and attenuation of this wave into structures. Some data were reported for the expansion of a blast wave from underground tunnels [10-12], but offer no

convincing data to verify theoretical computations for the complex interaction of the multiple internal reflections, particularly for the short duration pulses transmitted through blast valves and small openings.

In this paper, a combined analytical and experimental effort is described that studied blast wave propagation into the interior of rooms from airblast waves incident to openings in rooms. Twenty-seven small-scale high-explosive tests were conducted to study the effects of opening size, incident blast pulse duration and peak pressure levels on the blast transmitted into a structure. Interiors of the model rooms were heavily instrumented to measure both the blast entering the room and the subsequent reflections at several locations on the walls. An analytical method was developed based upon a modified ray theory combined with non-linear shock propagation and shock on shock addition rules to describe the diffracted shock at any point in the room. Empirical formulae for the non-linear shock propagation were derived from fits to experimental data. An existing jet-fill theory was incorporated to account for the quasi-steady flow.

Comparisons of calculated waveforms with measurements are given. The described method reproduces the blast pressure-time records, including high order reflections, with an accuracy comparable with the best 3-D hydrocode calculations. Since fill is included, the technique can also compute the complete pressure pulse (diffracted and quasi-steady flow) for long duration blast.

## EXPERIMENTS

### Test Setup

A series of high-explosive experiments was conducted during the period of July 1980 through September 1983 at the J. S. Army Waterways Experiment Station Big Black Test Site to study the propagation and subsequent multiple reflections of a diffracted shock into a room [13,14]. It was desired to model the short duration but high amplitude diffracted shock that would be present downstream from blast valves or transmitted through small penetrations from large explosions as well as the interior airblast produced by conventional size weapons detonated near entryways. In all, twenty-seven tests were conducted using C-4 and TNT charges ranging from 0.11 to 12.3 kg detonated outside small-scale instrumented rooms. The charge mass and stand-off distances were selected to provide the desired peak pressure and duration of the incident airblast at entrances to the test article. Entrance blast peak pressures from 0.07 to

\*This equation can be made dimensionally correct by replacing the coefficient 2 by an equivalent factor containing the sound speed in air.

1.5 MPa and pulse durations just outside the entrance ranging from 0.6 to 2.8 msec were achieved.

Two structures were used during the course of the testing program. The first low pressure series of twenty tests used a heavily reinforced plywood box--designed to represent a prototype room with a central opening in one wall--as the test structure. Pressure entering the box ranged from .07 to .26 MPa. The room was 0.95 meters high, 0.95 meters wide, and 2.19 meters long. (See Fig. 1 for details of the box configuration.) Because the blast wave propagation was symmetrical about planes that bisected the entrance wall and are parallel to the side walls, the tests were conducted in quarter-space. The opening was located in a corner of the end wall, simulating an opening and end wall of twice the test dimensions. An entrance section consisting of a plywood tunnel, 1.22 meters long, was placed outside the opening. This "tunnel" provided a uniform section to measure the shock conditions at the entrance to the room. The tunnel was constructed so that inserts could be placed inside to vary the tunnel cross section. Side dimensions of the square openings were varied from 76 mm, 152 mm, and 304 mm.

For these tests Kulite XT-190 series air-blast transducers were flush-mounted in a regular grid along a wall adjacent to the opening (a plane of symmetry) and on the opposite wall. In all, 20 gages were monitored--18 at locations within the box, one to provide entrance conditions, and a free-field gage.

The second test series used a cubical steel box with each interior side 1.2 meters in length. Seven tests were conducted in this series with entrance pressure levels ranging from .2 to 1.5 MPa. A 0.285-meter exit tunnel was centered on an adjacent side wall to determine the blast as it vented from the room. Kulite XT-190 and Kulite HKS-375 series air-blast gages were flush-mounted on three walls to measure reflected pressure. On these tests, 13 gages were monitored within the chamber and four gages to provide entrance conditions. (See Fig. 2 for details of the chamber configuration.)

#### Results

Typically, the interior pressure history consisted of a rapid succession of short duration pressure pulses corresponding to superposition of multiple reflections from the

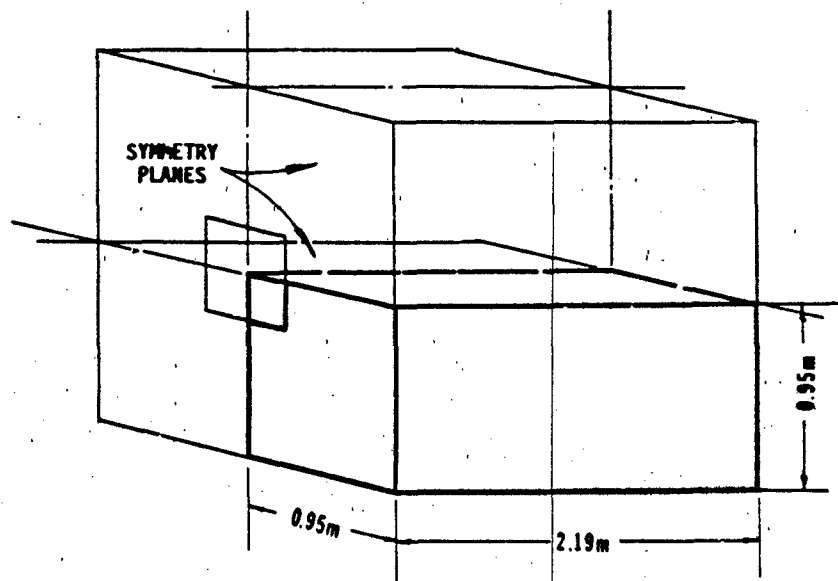


Figure 1. Quarter space test structure layout with planes of symmetry.

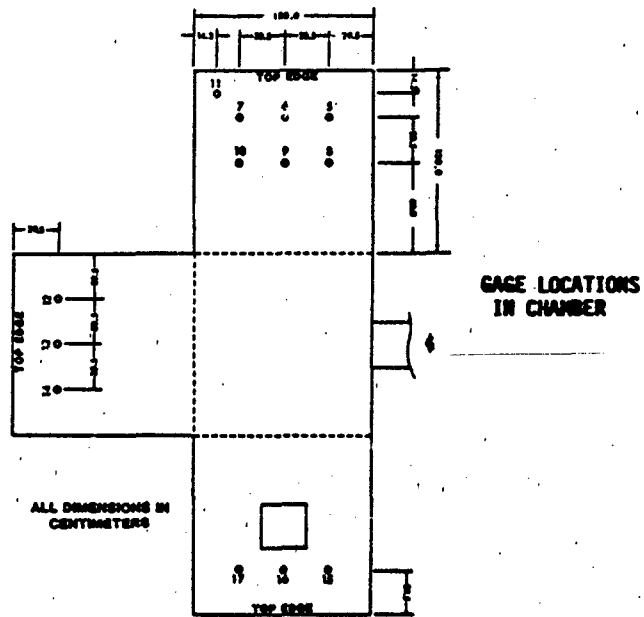
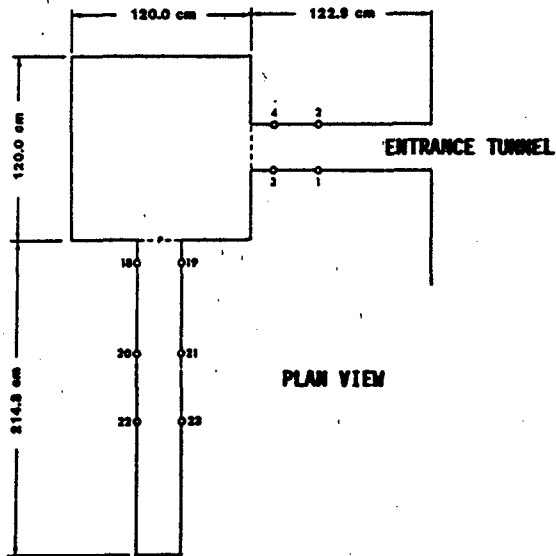


Figure 2. Test setup and gage locations for steel test structure.

interior walls (Fig. 3). Normally, the first peak associated with the direct wave produced the greatest pressure. However, at some locations, constructive interference between reflected waves produced peak pressures greater than the direct pulse, as shown by the pressure history in Fig. 4. Fig. 5 shows records taken inside the steel structure. Gage 1 shows the pressure pulse entering the room, and gages 2-6 illustrate the dramatic variation of the waveform at different locations in the facility.

A plot of the side on peak pressures from the first test series normalized by the peak incident pressure in the tunnel is shown in Fig. 6 plotted as a function of the

distance in tunnel diameters from the opening to the gages. The relationship between normalized pressure and range is

$$\frac{P_{\max}}{P_0} = C(R/D) - 1.35 \quad (2)$$

where  $P_{\max}$  is the peak side on pressure in the test structure,  $P_0$  is the entrance pressure,  $R$  is the distance from the center of the opening to the gage, and  $D$  is the entrance tunnel diameter. The coefficient  $C$ , shown in Fig. 7, was found to be a function of the angle  $\alpha$ , between the normal to the center of the opening and the gage location as given by the expression,

$$C = 0.65 (1 - 0.25 \alpha) \quad (3)$$

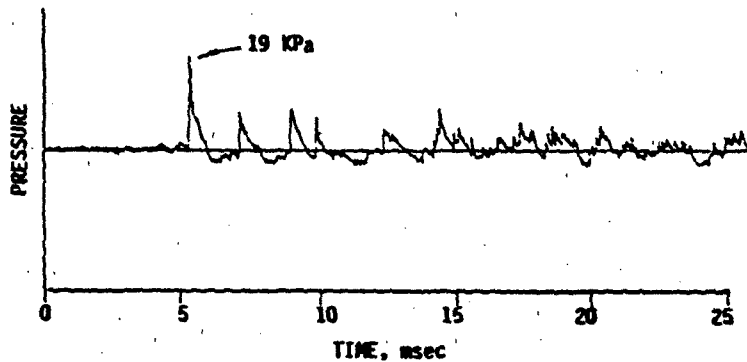


Figure 3. Typical interior pressure-time history at low pressure.

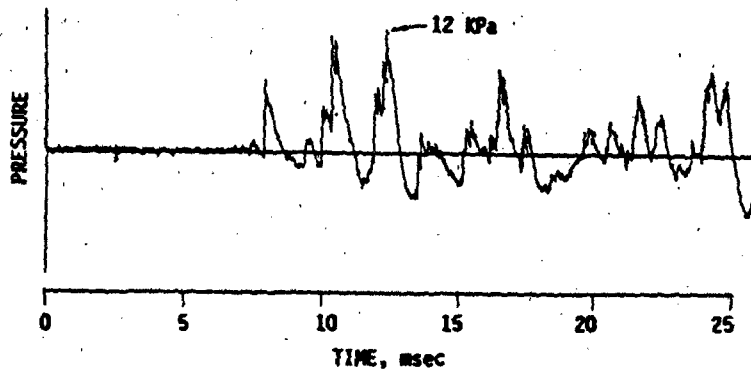


Figure 4. Typical interior time history showing constructive influence of reflections.

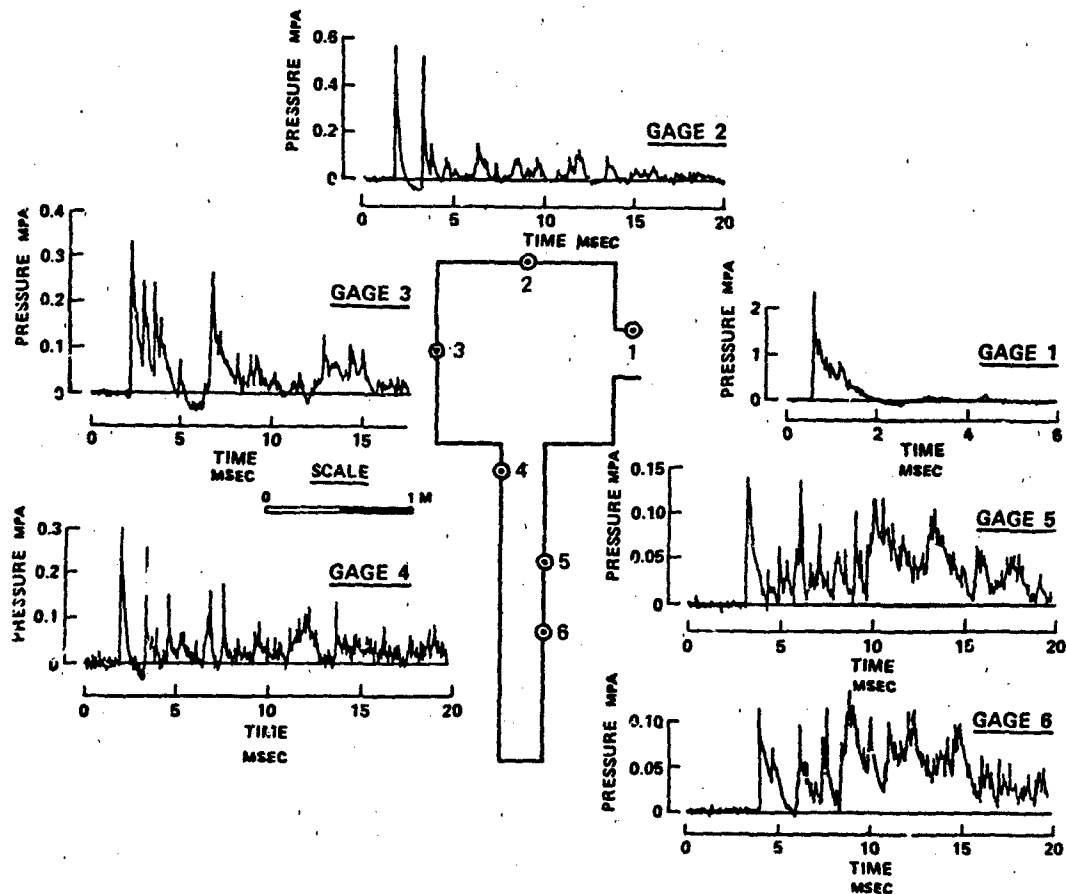


Figure 5. Typical pressure-time histories inside the steel structure and interconnecting tunnel.

for  $\alpha$  in radians.

The duration of the input shock was found to be controlled by the size of the opening. Rarefaction waves are developed at the edges of the opening that propagate across the entrance and drop the pressure behind the incident shock. This effect can be measured by the time the rarefaction wave takes to transit the opening. Fig. 8 shows a plot of the positive duration versus the opening length. A linear relationship for the positive duration,  $t_+$ , was obtained as

$$t_+ = \frac{D}{C_0} \quad (4)$$

where  $C_0$  is the sound speed in air. If the exterior pulse duration,  $t_p$ , is less than  $D/C_0$ , then  $t_+ = t_p$ .

Eq. 2 fits the side-on pressure measurements within about  $\pm 20$  percent. Because of instrumentation limitations associated with measurements of explosively generated airblast, such as the frequency response of gages and the

recording system, gage overshoot, and vibration of gage mounts, this accuracy is within normal experimental scatter. Measurements of pulse duration have a much larger random scatter which is characteristic of most airblast data.

The analysis above treats only side-on blast which is equivalent to the free field blast in a chamber before reflections occur. All of the test records from the steel chamber and many from the wood chamber are reflected blast requiring a much more complex analysis procedure as discussed below.

#### SHOCK DIFFRACTION MODEL

A semi-empirical modified ray tracing procedure was developed to model shock wave diffraction through an opening into a room of rectangular cross-section. The blast at the opening is treated as originating from a point source located at the center of the entrance. Interior walls are assumed to be perfectly rigid reflecting planes. Each encounter with a wall

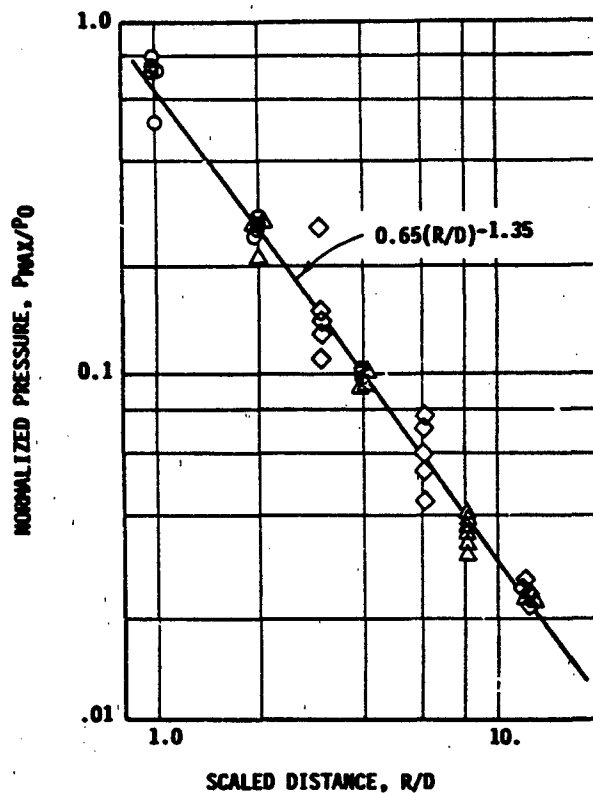


Figure 6. Peak pressure transmitted into the chamber normalized by the incident pressure as a function of distance from the entrance in opening diameters.

generates a reflection which can be treated as a pulse originating from an "image source" located behind the wall. The pressure at any location in the room is then a non-linear superposition of the direct shock and a contribution from an "image source" for each of an infinite series of reflections.

The outline of steps for computing a waveform is as follows: First, path lengths for rays of successively higher order reflections are generated. Arrival times are calculated by integrating the pressure dependent shock propagation velocity along the path. The shock wave pressure attenuation with distance for each ray is assumed to be the same as for the direct shock expressed by Eq. 2. Orders of reflections having arrival times greater than the times of interest do not contribute and are not computed. Next, pressure, particle velocity and density waveforms for each ray are calculated neglecting the presence of other rays. Finally, the pressure waveforms are combined

using non-linear shock addition rules to produce the total diffracted pulse. Each of these steps is treated in detail below.

#### Path Lengths

An infinite number of ray paths are possible within the room due to combinations of reflections from the six walls. The order of the ray is defined as

$$N = \sum_{i=1}^3 n_i \quad (5)$$

where  $n_i$  is the order of the reflection in each of the rectangular coordinate directions,  $i = 1, 2, \text{ and } 3$ . Let  $r_{N_i}$  be the components of the  $N$ th order ray, then

$$r_{N_i} = x_i^i - (-1)^{n_i} x_i^0 \pm n_i L_i \quad (6)$$

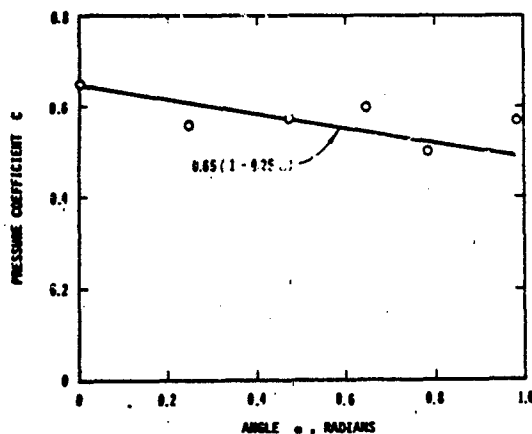


Figure 7. Pressure coefficient  $C$  as a function of angle from normal to the opening.

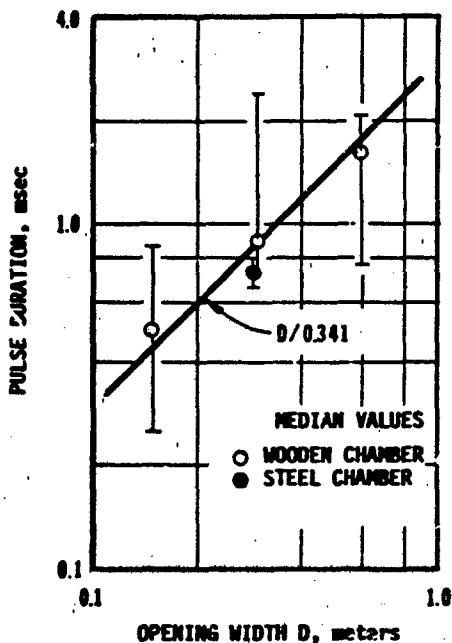


Figure 8. Pulse duration as a function of width of entrance opening.

where  $x_1^0$  and  $x_1^1$  are the coordinates of the source and receiver, respectively, and  $L_1$  is the dimension of the room in the  $i$ 'th direction. Note that for each non-zero order of reflection,  $n_1 \neq 0$ , two values of the ray component are possible; one from each of the opposite walls of the room in that plane, for

example, floor and ceiling. When  $n_1=0$ , then only one value is possible for the  $i$ 'th ray component. The total ray length is found from all combinations of  $r_{n_1}$  as

$$R_N = \left( \sum_{i=1}^3 r_{n_i}^2 \right)^{1/2} \quad (7)$$

In general, six ray lengths are possible when  $n_1 > 0$ , for  $i = 1, 2, \text{ and } 3$ .

#### Arrival Time

The arrival time,  $t_0$ , for each ray is evaluated by integrating

$$t_0 = \int_0^R \frac{dR}{U(R, \alpha)} \quad (8)$$

where  $U$  is the pressure dependent shock wave propagation velocity. Using a polytropic equation of state for air with a pressure dependent ratio of heat capacities,  $\gamma = C_p/C_v$ , the Rankine-Hugoniot conditions at the shock front give

$$U = C_0 \left[ P_{\max} / [P_a \gamma_0 (1 - \rho_a / \rho_{\max})] \right]^{1/2} \quad (9)$$

where the density ratio is

$$\frac{\rho_a}{\rho_{\max}} = \left\{ \frac{\frac{P_a}{\gamma_0 - 1} + \frac{P_{\max} + 2P_a}{2}}{\frac{P_{\max} + P_a}{\gamma - 1} + \frac{P_{\max} + 2P_a}{2}} \right\} \quad (10)$$

$P_{\max}$  is the peak shock overpressure at distance  $R$  and angle  $\alpha$ , given by Eq. 2,  $P_a$  is the atmospheric pressure,  $\gamma_0$  is the value of  $\gamma$  at atmospheric pressure (approximately 1.4),  $\rho_{\max}$  is the density of air at pressure  $P_{\max}$ ,  $\rho_a$  is the density of air at pressure  $P_a$ , and  $C_0$  is the sound speed in air at pressure  $P_a$ . At pressures up to about 2 MPa,  $\gamma = \gamma_0$  is a good approximation.

#### Pressure Histories

An examination of the measurements indicated that pressure histories for any ray can be adequately computed from the commonly used exponential formula

$$P_i(R, t) = \begin{cases} 0 & \text{for } t < t_0 \\ P_{\max}(R, \alpha) [1 - (t - t_0)/t_+] & \text{for } t > t_0 \\ x \exp[-(t - t_0)/t_+] & \text{for } t > t_0 \end{cases} \quad (11)$$

where  $t_+$  is the positive phase duration given by Eq. 4, and  $P_{\max}$  is the peak overpressure given by Eq. 2. Peak pressure,  $P_{\max}(R, \alpha)$ , is the only factor which changes in this expression for different rays and observation points. The total waveform is constructed by superposition of these pressure histories for all rays using the following non-linear shock addition formulae.

### Shock Combining Rules

Non-linear shock rules were postulated by Needham [15] combining shocks at a point from multiple sources and incorporated into the LAMB model. While these shock addition rules cannot be supported from first principles, they have proved to be accurate in comparisons with measurements and hydrocode calculations for many shock combining situations. In this method the waveform for each ray is computed ignoring the presence of other shocks. These results are then combined using the three shock addition rules as follows:

#### Shock Addition Rule Number 1 - "Conservation of Mass"

It is assumed that at a point in space, the density,  $\bar{\rho}$ , is the ambient density,  $\rho_a$ , plus the sum of the overdensities,  $\Delta\rho_i$ , due to all shocks that have passed that point at a given time

$$\bar{\rho} = \rho_a + \sum_{i=1}^{N_s} \Delta\rho_i \quad (12)$$

where  $N_s$  is the number of shocks,

#### Shock Addition Rule Number 2 - "Conservation of Momentum"

$$\bar{V} = \frac{\sum_{i=1}^{N_s} \rho_i \vec{V}_i}{\bar{\rho}} \quad (13)$$

where  $\bar{V}$  is the total material velocity,  $\rho_i$  is the density for shock  $i$ , and  $\vec{V}_i$  is the particle velocity for shock  $i$ .

#### Shock Addition Rule Number 3 - "Conservation of Energy"

The total overpressure from  $N_s$  shocks is

$$\bar{p} = \sum_{i=1}^{N_s} P_i + \left(\frac{\gamma_0+1}{2}\right) \left(\frac{1}{2} \sum_{i=1}^{N_s} \rho_i |\vec{V}_i|^2 - \frac{1}{2} \bar{\rho} |\bar{V}|^2\right) \quad (14)$$

where  $P_i$  is overpressure for shock  $i$ .

#### Other Shock Wave Parameters

These shock combination rules require not only pressure,  $P_i(t)$ , waveforms, but also velocity,  $V_i(t)$ , and density,  $\rho_i(t)$ , waveforms. Experimental measurements provided only  $P_i(t)$ . Hydrocode calculations were performed for this project in order to develop  $V_i(t)$  and  $\rho_i(t)$  formula, but these calculations were not completed in time to be used in this paper.

Particle velocity,  $V_{max}$ , and density,  $\rho_{max}$ , at a shock front are related to the pressure,  $P_{max}$ , through the Rankine-Hugoniot conditions. The density,  $\rho_{max}$ , is given by Eq. 10 while the particle velocity relation is

$$V_{max} = C_o \left[ \frac{(1-\rho_a/\rho_{max})P_{max}}{\rho_a \gamma_o} \right]^{1/2} \quad (15)$$

These conditions do not hold exactly behind the shock front.

In the current analytical model of the measured blast environment in a room at low to moderate overpressures ( $0.07 < P_o < 1.5$  MPa) the following approximations (whose accuracies are supported by comparison of the calculated pressures with measurements) have been made. First, assume adiabatic expansion behind the shock front to obtain the density

$$\rho_i(t) = \rho_{max} \left[ \frac{P_i(t)+P_a}{P_{max}+P_a} \right]^{1/\gamma} \quad (16)$$

where  $P_i$  is obtained from Eq 11 for each shock wave. Next, assume that the Rankine-Hugoniot relation for particle velocity applies, approximately, behind the shock front to obtain

$$V_i(t) = C_o \left[ \frac{(1-\rho_a/\rho_i)P_i(t)}{\rho_a \gamma_o} \right]^{1/2} \quad (17)$$

These approximations, along with the shock addition rules, provide a reasonable procedure for calculating the shock waveforms produced by the many reflections from the walls of a room. In the following section, the accuracy of this procedure is evaluated by comparison with measurements.

### WAVEFORM CALCULATIONS

Using modified ray theory model discussed above for the diffracted pulse and the fill code of Ref. [5] a computer code, CHAMBER, was developed to calculate the combined pressure pulse in a room. This code was written in FORTRAN, originally for mainframe computers, but has been converted to run on a micro-computer. CHAMBER is an outgrowth of an earlier code, WESFILL, reported in Ref. [13] which treated only the low-pressure region where reflections can be treated acoustically.

Fig. 9 is a comparison of the CHAMBER computed values of the initial peak reflected shock wave overpressure with the data measured in the steel chamber. The 45-degree line represents perfect agreement. The maximum deviations from this line for 90 percent of the data is about 35 percent which is within the normal experimental scatter for measurements of this type. Since the code uses

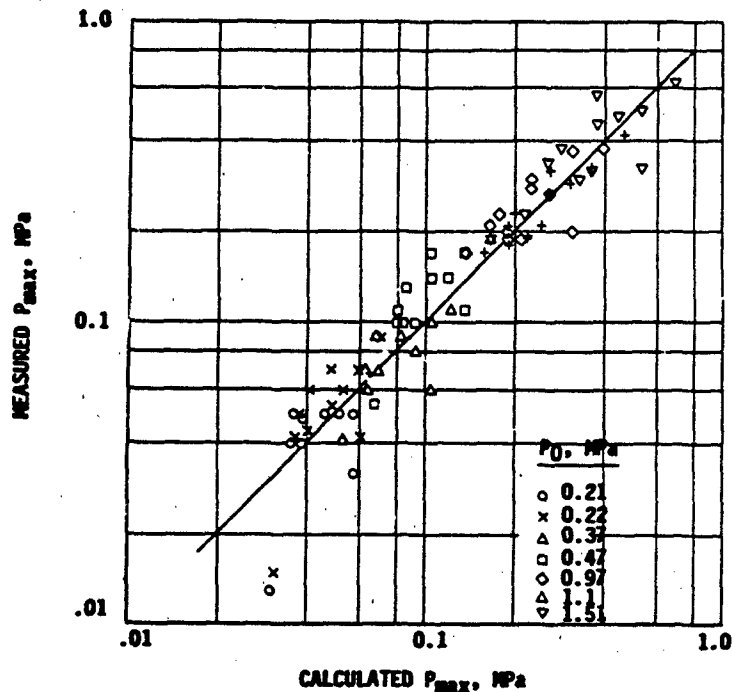


Figure 9. Calculated versus measured peak initial reflected pressures in steel test chamber.

Eqs. (2)-(4) derived from the measurements in the wood test structure, this comparison with data from the steel chamber provides an independent check on the generality of these formulae. Several test cases were run to verify the accuracy of the waveform computations. Fig. 10 is an example of the low pressure measurements made in the wooden structure. Agreement between the amplitude of the peaks, the time of the peaks, and apparent reverberations within the structure are reproduced well by the code. Fig. 11 is an example of comparisons with the high pressure measurements made in the steel chamber. Measured records from two symmetrically located gages are shown with the computed waveform. The calculated values are intermediate between the two measurements. Fig. 12 shows another comparison between calculated and measured records. The calculated curve and the input data at the top of the figure are from an actual CHAMBER run. In this case the second peak resulting from higher order reflections is greater than the first peak.

#### CONCLUSIONS

The explosive tests discussed in this paper provided an experimental basis for developing and verifying a semi-empirical calculational procedure for short duration blast

entering a room through an opening. The code CHAMBER based on this procedure reproduces the blast pressure-time records, including high order reflections, with an accuracy comparable with the best 3-D hydrocode calculations. Further improvement of the procedure will require incorporating more experimental data and more accurate formulae for density and particle velocity histories.

The analysis presented in this paper -- embodied in the CHAMBER code -- is in excellent agreement with measurements obtained in two experimental structures. While this analysis may not be applicable to all openings, the measurements on which the analysis is based cover a fairly broad range of parameters as follows: (a) the pressure pulse just outside the entrance ranged from 0.07 to 1.51 MPa, (b) the positive phase durations of the incident pulse ranged from 0.9 to 4.3 acoustic transit times across the opening, (c) the ratio of opening area to entrance wall area varied from .006 to 0.1, (d) the ratio of room volume to opening area ranged from 20 to 750 m, (e) the angle  $\alpha$  with the entrance, described in Eq. (3), ranged from 0 to 69 degrees for the first arrival at gages.

For the short duration blast in our tests, the quasi-static fill contributed only a small fraction to the total internal pressure.

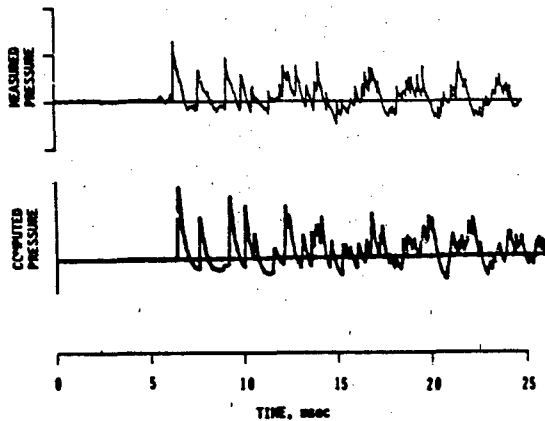


Figure 10. Example of the diffraction/reflection calculation with measured pressure history at mid-point of the midplane wall for low pressures ( $P_{max} \sim 14 \text{ KPa}$ ).

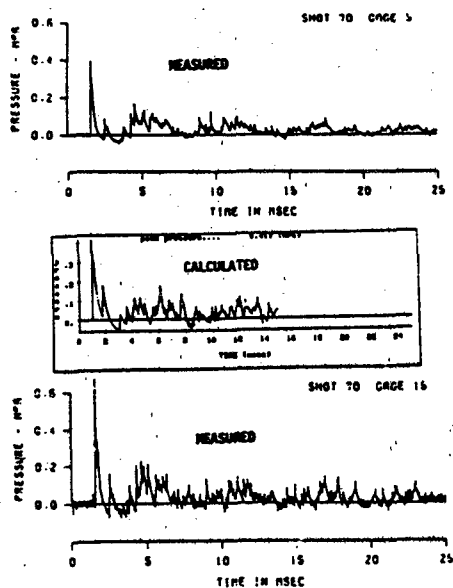


Figure 11. Comparison of calculations with measurements from symmetrically located gages in steel chamber with non-linear reflections.

However, for long duration blast incident on the entrance, fill will become a more dominant part of the total waveform. Since Coulter's fill model [5] is included in CHAMBER, calculations can be performed for long duration pulses. Fig. 13 is an example of computations compared with airblast measurements in a test structure on Operation Prairie Flat [17], a 500-ton (453,600-kg) surface tangent detonation. The dimensions of the test article are shown at the top of the figure. In this case the entrance area was 31 percent of the wall area, or three times greater than the openings used in our tests. The pressure pulse at the entrance had a peak of 4.7 psi (.032 MPa) and a duration of 250 msec, which is about 50 acoustic transit times across the opening. The circles on Fig. 13 were computed assuming an opening size equal to the square root of the entrance area, i.e., 4.5 ft on a side. The calculated values follow the shape of the measured curve, but the peak is 35 percent lower. The triangles, computed using an opening 5.5 ft on a side, are in better agreement with the peaks. This result suggests that for long, rectangular openings an effective opening size greater than the square root of the area should be used for the refracted shock calculations. The quasi-static fill contribution to the calculated pulse gradually rises to a maximum value of 3.7 psi at 30 msec and is approximately equal to the input record for later times. This part of the total pulse appears to be accurately computed.

The model of this paper is intended for use with relatively small square or round openings; but, as the previous example shows, the code can also be used successfully for some rather large rectangular entrances. Additional comparisons between calculations and measurements are needed to fully delineate the range of application of the model.

#### ACKNOWLEDGEMENTS

The experimental work and much of the analysis were performed by the authors while employees of the U. S. Army Engineer Waterways Experiment Station (WES). Support for the project at WES was provided by the Air Force Engineering and Services Center and the Army Office, Chief of Engineers. The authors gratefully acknowledge the assistance of C. D. Little of WES in the data analysis and preparation of figures.

#### REFERENCES

1. A. R. Kriebel, "Airblast in Tunnels and Chambers," DASA 1200-II Supplement 1, Defense Nuclear Agency, Washington, DC, Oct 1972
2. G. A. Coulter, "Air Shock and Flow in Model Rooms," BRL NR 1987, U. S. Army Ballistics

AIRBLAST PENETRATION INTO STRUCTURES

units (if metric, 2-U.S.) = 1

room dimensions (m) ...  
 length (l) = 1.2  
 height (h) = 1.2  
 width (w) = 1.2

opening location and size (m) ...  
 x = 0.2  
 y = 0.2  
 area of opening (m<sup>2</sup>) = 0.04

peak pressure (MPa) = 1.05  
 pulse duration (msec) = 1.5  
 maximum time (msec) = 15.

target location (m) ...  
 x = 1.2  
 y = 0.2  
 z = 0.2

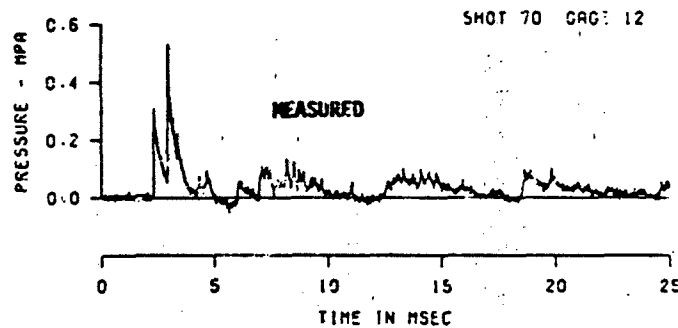
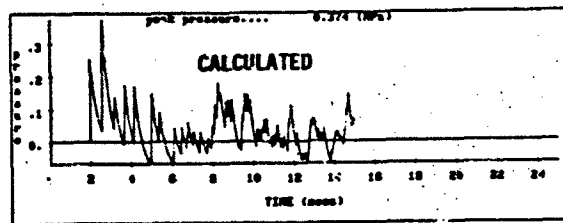
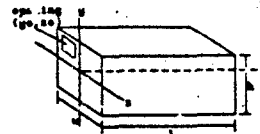


Figure 12. Comparison of calculated pressure with measurement showing constructive non-linear reflections.

- Research Laboratory, Aberdeen Proving Ground, MD, June 1969
3. G. A. Coulter, "Flow in Model Rooms Caused by Air Shock Waves," BRL MR 2044, U. S. Army Ballistics Research Laboratory, Aberdeen Proving Ground, MD, July 1970
4. G. A. Coulter, "Air Shock Loading of Exterior Walls of Shelter Models," BRL MR 2118, U. S. Army Ballistics Research Laboratory, Aberdeen Proving Ground, MD, Aug. 1971
5. G. A. Coulter, "Blast Loading in Existing Structures - Basement Models," BRL MR 2208, U. S. Army Ballistics Research Laboratory, Aberdeen Proving Ground, MD, Aug. 1972
6. G. A. Coulter, "Blast Loading of Objects in Basement Shelter Models," BRL MR 2348, U. S. Army Ballistics Research Laboratory, Aberdeen Proving Ground, MD, Jan. 1974
7. R. O. Clark and W. M. McMurtry, "Shock Wave Filling of Chambers," AFWL-TR-70-73, Air Force Weapons Laboratory, Albuquerque, NM, Sept. 1970
8. Dennis Keefer, "Model of Room Response to Air Blasts," ARO 16395.1-A-E Army Research Office Contract DAAG 29-79-G-0049, The University of Tennessee Space Institute, Tullahoma, TN, Aug. 1979
9. J. F. Melichar, "The Propagation of Blast Wave into Chambers," BRL MR 1920, U. S. Army Ballistics Research Laboratory, Aberdeen Proving Ground, MD, Mar. 1968
10. A. T. Skjeltorp, et al, "Blast Propagation Outside a Typical Underground Ammunition Storage Site," 5th International Symposium on Military Applications of Blast Simulation, Stockholm, Sweden, May 1977
11. D. R. Smith, "Effects of Explosions in Underground Magazines," Draft Report to DOD Explosive Safety Board, USAE Waterways

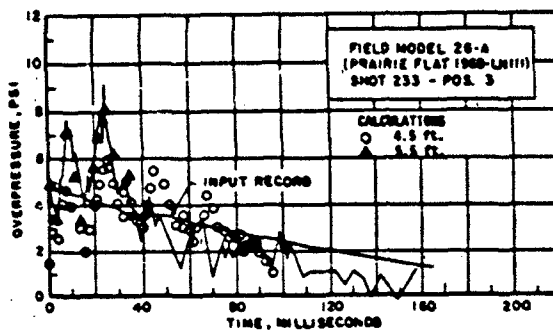
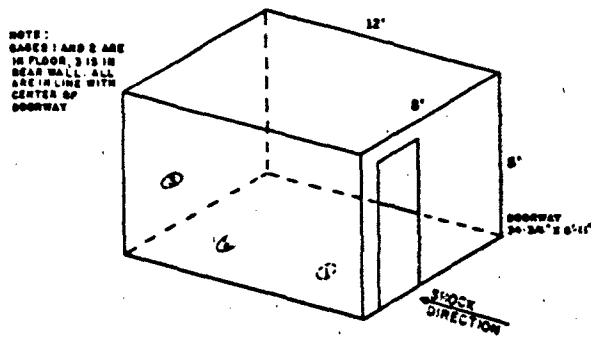


Figure 13. Test structure and pressure history for Prairie Flat structure.

- Experiment Station, Vicksburg, MS, Apr. 1979
12. G. Gurke and G. Scheklinski, "Underground Ammunition Storage Model Tests," Report E 12/T7, Ernst-Mach Institut, Freiburg, Germany
13. J. L. Drake and J. R. Britt, "Airblast Penetration into Semihardened Structures," ESL-TR-80-60, Air Force Engineering and Services Center, Tyndall AFB, FL, Oct. 1980
14. J. R. Britt and C. D. Little, "Airblast Attenuation in Entranceways and Other Typical Components of Structures: Small Scale Tests Data Report 1," Draft, USAE Waterways Experiment Station, Vicksburg, MS, 1983
15. S. Hikida and C. E. Needham, "Low Altitude Multiple Burst (LAMB) Model; Volume 1: Shock Description," DNA 58637, S-Cubed, Albuquerque, NM, June 1981
16. K. Kaplan, "Accidental Explosions and Effects of Blast Leakage into Structures."
- ARLDCR-79009, ARRADCOM, Dover, NJ, 1979
17. G. A. Coulter and R. L. Peterson, "Blast Fill Time of a One-Room Structure," Operation Prairie Flat Project Officers Report - Project LN 111, PGR-2102, U. S. Army Ballistics Research Laboratory, Aberdeen Proving Ground, MD, Nov. 1964

A COMPUTATIONAL PROCEDURE FOR PEAK INSTRUCTURE MOTIONS AND  
SHOCK SPECTRA FOR CONVENTIONAL WEAPONS

S. A. Kiger, J. P. Balsara, J. T. Baylot  
USAR Waterways Experiment Station  
P. O. Box 631, Vicksburg, Mississippi 39180

A semiempirical procedure for computing maximum values of structural displacement, velocity, and acceleration is presented. The simplified methods take into account, at least approximately, the large attenuation of the conventional weapon shock front as it traverses the structure, by using an integrated average value of corresponding free-field motions. Instructure motions are predicted by modifying these average free-field motions based on data collected in conventional weapons tests over the past several years. Computed peak instructure motions are then amplified to estimate the instructure shock spectra.

#### INTRODUCTION

The major concern in the design of a protective structure is to prevent structural failure. However, the operation of sophisticated electronic gear within a facility such as a command and control center may be impaired at shock levels much less than those required to fail the structure, thus preventing the center from completing its mission. In order to economically design shock isolation devices to protect the various components within the structure, the internal shock environment must be well defined. For long motions associated with nuclear events, the procedure for the modification of the free-field ground motion to predict the instructure motion is well documented. However, procedures for predicting the instructure shock environment in the case of short duration ground shock, such as that generated by conventional weapons, are not so well established. The method presented here was developed for the recent revision of TM 5-855-1 (Ref. 1).

#### RECTANGULAR BURIED STRUCTURES

##### Side Burst Load Case

The simplified methods given below will take into account the attenuation of the ground shock as it traverses the structure. The computed value for instructure acceleration, velocity, and displacement will be in the horizontal direction at the center of the structure. Experimental evidence (Ref. 2 and 3) indicates that vertical acceleration, velocity, and displacement will be approximately 20 percent of the horizontal values in the case of a

side burst. Also, the horizontal motions are very uniform over the entire floor of the structure, while the vertical motions at the leading edge are approximately twice the midspan values.

Instructure accelerations, velocities, and displacements may be predicted by modifying the free-field values. The acceleration of a structure, such as the structure shown in Figure 1, may be predicted by using the average value of free-field acceleration over the span of the structure.

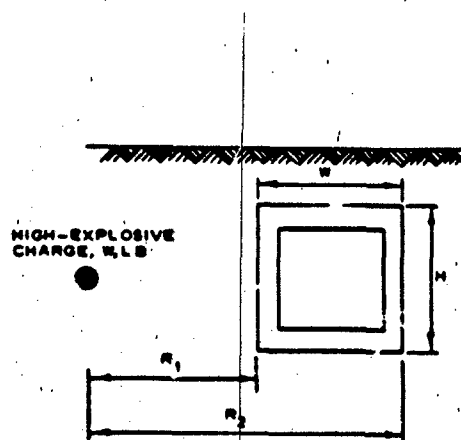


Figure 1. Average acceleration for side burst load case of a buried rectangular structure

The average value of acceleration is found by integrating the acceleration-range function given in Chapter 5 of TM 5-855-1 (or in Ref. 4) over the span of the structure. The average acceleration for the structure is the uniform acceleration which yields the same integral across the structure. The average velocity and displacement are obtained using the same method. Equations 1, 2, and 3 give the average free-field acceleration, velocity, and displacement, respectively across a rectangular buried structure.

$$A_{avg} = \frac{50fcu^{(n+1)/3} [R_1^{-n} - R_2^{-n}]}{n(R_2 - R_1)} \quad g's \quad (1)$$

$$V_{avg} = \frac{160fu^{(n/3)} [R_1^{-(n+1)} - R_2^{-(n+1)}]}{(n-1)(R_2 - R_1)} \quad ft/s \quad (2)$$

$$\frac{d_{avg}}{u^{1/3}} = \frac{500fcu^{(n-1)/3} [R_1^{-(n+2)} - R_2^{-(n+2)}]}{c(n-2)(R_2 - R_1)} \quad ft \quad (3)$$

where

$R_1$  and  $R_2$  = range in feet (Figure 1)

$f$  = coupling factor, from Chapter 5 of TM 5-855-1 (or Ref. 4)

$W$  = weapon yield, pounds

$c$  = seismic velocity, feet per second, from Chapter 5 of TM 5-855-1

$n$  = attenuation coefficient, from Chapter 5 of TM 5-855-1

$A_{avg}$  = average free-field acceleration across structure, gravities

$V_{avg}$  = average free-field velocity across structure, feet per second

$d_{avg}$  = average free-field displacement across structure, feet

The average free-field values of acceleration and velocity overpredict the instructure values. The information shown in Figure 2 may be used to reduce these values.

The reduction factor  $RF$  was determined as the ratio of the pressure ordinate for an

equivalent uniformly distributed load to the maximum pressure ordinate from the actual load distribution. The equivalent uniform load was determined over a wall with dimensions of  $H$  and  $L$ .

Instructure accelerations may be predicted by obtaining the average free-field acceleration from Equation 1 and multiplying this average value by the reduction factor given in Figure 2. Test data (Ref. 2 and 3) have shown this method to be conservative for rectangular buried structures. Velocities are predicted using Equation 2 and Figure 2. Test data (Ref. 2 and 3) have shown that this method yields results close to experimental values.

Equation 3 should be used to predict the instructure displacement with no reduction factor.

#### Overhead Burst

The same equations used for side bursts should be used for an overhead burst.  $R_1$  and  $R_2$  are now defined by Figure 3. These values must be modified by a reduction factor obtained from Figure 2, using the roof dimensions of  $W$  and  $L$ . For large structures, some judgment is required in selecting the dimensions  $W$ ,  $H$  and  $L$  for a burst that is not symmetrically located over the structure roof for an overhead burst and exterior wall for a side burst. Figure 4 shows an example where the dimensions of one bay in a multibay structure were used to calculate instructure shock.

#### Instructure Shock Spectra

Once the peak values for instructure acceleration, velocity and displacement have been determined, they can be used to develop an approximate instructure shock spectra.

Let  $D$  be the maximum relative displacement between a simple spring-mass oscillator and the floor of the structure. The relations between the maximum relative displacement  $D$ , the pseudovelocity  $V$ , and the pseudoacceleration  $A$  are as follows:

$$V = \omega D \quad (4)$$

$$A = \omega V = \omega^2 D \quad (5)$$

where  $\omega$  is the natural circular frequency of the oscillator in radians per second. The pseudovelocity  $V$  is nearly equal to the maximum relative velocity for systems with moderate or high frequencies, but may differ considerably from the maximum relative velocity for very low frequency systems. The pseudoacceleration  $A$  is exactly equal to the maximum acceleration for

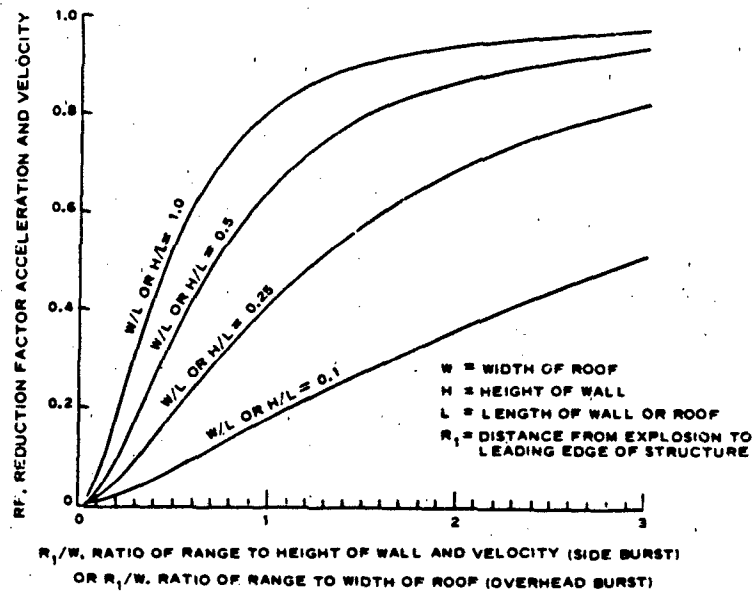


Figure 2. Reduction factor for instructure acceleration and velocity

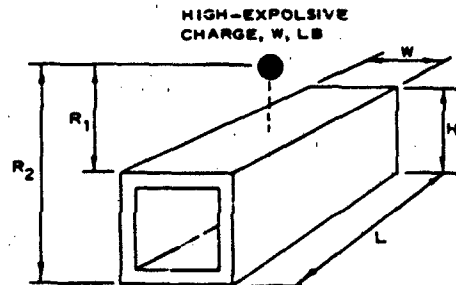


Figure 3. Average acceleration for overhead burst on a rectangular buried structure

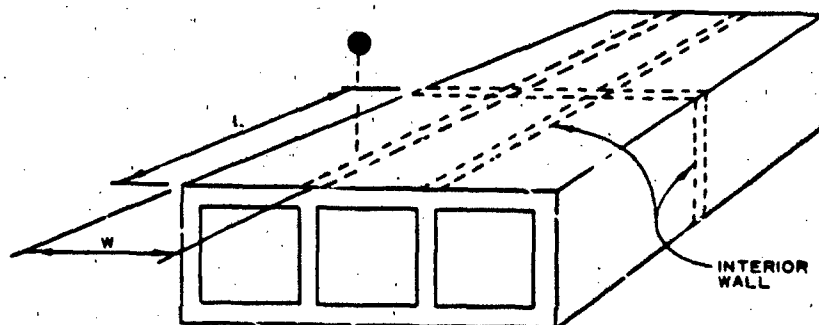


Figure 4. Roof dimensions for overhead burst on a buried multibay structure

systems with no damping and is not greatly different from the maximum acceleration for systems with moderate amounts of damping.

In general, D, V and A will be larger than the peak values of the floor motion. A conservative estimate for D, V and A can be made by multiplying the floor motions by the appropriate amplification factors. A limited amount of data (Ref. 2 and 3) from high explosive tests on model structures indicate average amplification factors for systems damped at 5 percent of critical of approximately 1.2, 1.5, and 1.6 for displacement, velocity and acceleration, respectively. For 5 to 10 percent of critical damping, amplification factors of 1.0, 1.5, and 2.0 for displacement, velocity, and acceleration are recommended in Harris and Crede (Ref. 5). These factors are valid for a wide range of earthquake and ground shock motions. Therefore, for developing an approximate instructure design shock spectra for damping equal to 5 to 10 percent of critical, amplification factors of 1.2, 1.5, and 2.0 for displacement, velocity and acceleration respectively are recommended.

#### ACKNOWLEDGMENTS

The tests described and the resulting data presented herein, unless otherwise noted, were obtained from research conducted under the Revision of TM 5-855-1 of the United States Army

Corps of Engineers by the Waterways Experiment Station. Permission was granted by the Chief of Engineers to publish this information.

#### REFERENCES

- Department of the Army Technical Manual, TM 5-855-1, Fundamentals of Protective Design (Non Nuclear), In preparation by the USAE Waterways Experiment Station, Vicksburg, MS.
- S. A. Kiger, "Instructure Shock Environment of Buried Structures Subjected to Blast Induced Ground Shock," The Shock and Vibration Bulletin, No. 47, September 1977.
- S. A. Kiger and G. E. Albritton, "Response of Buried Hardened Box Structures to the Effects of Localized Explosions," Technical Report SL-80-1, March 1980, USAE Waterways Experiment Station, Vicksburg, MS.
- J. L. Drake and C. D. Little, Jr., "Ground Shock from Penetrating Conventional Weapons," Symposium Proceedings, The Interaction of Non-Nuclear Munitions with Structures, U.S. Air Force Academy, Colorado, May 10-13, 1983.
- Harris, C. M. and Crede, C. E., ed., "Shock and Vibration Handbook," McGraw-Hill Book Company, Second Edition, 1976.

PRELIMINARY DESIGN CRITERIA AND CERTIFICATION TEST SPECIFICATIONS  
FOR BLAST RESISTANT WINDOWS

G. E. Meyers, W. A. Keenan and W. F. Shoemaker  
Naval Civil Engineering Laboratory  
Port Hueneeme, California

Preliminary design criteria for blast resistant windows exposed to blast overpressures up to 25 psi are recommended. Design procedures and design curves for fully tempered glass are presented and parametrized according to glass thickness, glass dimensions, glass aspect ratio, peak blast overpressures and effective blast duration. Curves for annealed glass are also presented for the purpose of analyzing the safety of existing structures. Design criteria for frames and a test certification procedure are also discussed. Additionally, design examples are presented.

## 1. INTRODUCTION

Historical records of explosion effects demonstrate that airborne glass fragments from failed windows are a major cause of injuries from accidental explosions. This risk to life is heightened in modern facilities, which often have large areas of glass for aesthetic reasons.

Guidelines are presented for both the design, evaluation, and certification of windows to safely survive a prescribed blast environment described by a triangular-shaped pressure-time curve. Window designs using tempered glass based on these guidelines can be expected to provide a probability of failure at least equivalent to that provided by current safety standards for safely resisting wind loads.

The guidelines, which apply for peak blast overpressures less than about 25 psi, are presented in the form of load criteria for the design of both the glass panes and framing system for the window. The criteria account for both bending and membrane stresses and their effect on maximum principal stresses and the nonlinear behavior of glass panes. The criteria cover a broad range of design parameters for rectangular-shaped glass panes: a pane aspect ratio  $1.00 < a/b < 2.00$ , pane area  $1.0 < ab < 25 \text{ ft}^2$ , and nominal glass thickness  $1/8 < t < 1/2$  inch. Most of the criteria are for blast resistant windows with fully heat-treated, tempered glass. However, criteria are also presented for annealed glass in order to assess the safety of existing windows that were not designed to resist blast overpressures.

## 2. DESIGN CRITERIA FOR GLAZING

### 2.1 Glazing Materials

The design criteria cover two types of glass: annealed glass and fully tempered glass. Both glazings are required to meet the requirements of Federal Specifications DD-G-1403B and DD-G-451d. Tempered glass is also required to meet the requirements of ANSI Z97.1-1975.

Annealed glass is the most common form of glass available today. Depending upon manufacturing techniques, it is also known as plate, float or sheet glass. During manufacture, it is cooled slowly. The process results in very little, if any, residual compressive surface stress. Consequently, annealed glass is of relatively low strength when compared to tempered glass. Furthermore, it has large variations in strength and fractures into dagger-shaped, razor-sharp fragments. For these reasons, annealed glass is not recommended for use in blast resistant windows. It is included in the design criteria only for safety analysis of existing facilities.

Heat-treated, tempered glass is the most readily available tempered glass on the market. It is manufactured from annealed glass by heating to a high uniform temperature and then applying controlled rapid cooling. As the internal temperature profile relaxes towards uniformity, internal stresses are created. The outer layers, which cool and contract first, are set in compression, while internal layers are set in tension. As it is rare for flaws, which

act as stress magnifiers, to exist in the interior of tempered glass sheets, the internal tensile stress is of relatively minimal consequence. As failure originates from tensile stresses exciting surface flaws in the glass, precompression permits a larger load to be carried before the net tensile strength of the tempered glass pane is exceeded. Tempered glass is typically four to five times stronger than annealed glass.

The fracture characteristics of tempered glass are superior to annealed glass. Due to the high strain energy stored by the prestressing, tempered glass will fracture into small cube-shaped fragments instead of the razor-sharp and dagger-shaped fragments associated with fracture of annealed glass. Breakage patterns of side and rear windows in American automobiles are a good example of the failure mode of heat-treated tempered glass.

Semi-tempered glass is often marketed as safety or heat-treated glass. However, it exhibits neither the dicing characteristic upon breakage nor the higher tensile strength associated with fully tempered glass. Semi-tempered glass is not recommended for blast resistant windows, unless it is laminated or backed by a fragment retention film.

Another common glazing material is wire glass, annealed glass with an embedded layer of wire mesh. Wire glass has the fracture characteristics of annealed glass and although the wire binds fragments, it presents metal fragments as an additional hazard. Wire glass is not recommended for blast resistant windows.

The design of blast resistant windows is restricted to heat-treated fully-tempered glass meeting both Federal Specification DD-G-1403B and ANSI Z97.1-1975. Tempered glass meeting only DD-G-1403B may possess a surface precompression of only 10,000 psi. At this level of precompression, the fracture pattern is similar to annealed and semi-tempered glass. Tempered glass meeting ANSI Z97.1-1975 has a higher surface precompression level and tensile strength which improves the capacity of blast resistant windows. Additionally, failure results in smaller cube-shaped fragments. To assure reliable performance of blast resistant glazing, it is required that heat-treated tempered glass fully conform to ANSI Z97.1-1975.

Although heat-treated tempered glass exhibits the safest failure mode, failure under blast loading still presents a significant health hazard. Results from blast tests reveal that upon fracture, tempered glass fragments may be propelled in large cohesive pieces that only fragment upon impact into smaller rock-salt type fragments. Even if the tempered glass breaks up initially into small fragments, the blast pressure will propel the fragments at a high velocity which constitutes a hazard. Adding fragment retention film (discussed in Section 2.5) to the inside face of heat-treated tempered glass will significantly improve safety.

## 2.2 Design Stresses

The design stress is the maximum principal tensile stress allowed for the glazing. The design stress was derived for a prescribed probability of failure, using a statistical failure prediction model under development by the ASTM. Thus, failure of the glazing is assumed to occur when the maximum principal tensile stress exceeds a design stress associated with a prescribed probability of failure. The model accounts for the area of glazing (as it effects the size, number and distribution of surface flaws), stress intensity duration, thickness and aspect ratio of glazing (as it affects the ratio of maximum to minimum principle stresses in the glazing), degree of glass temper (as it affects the precompression stress in the glazing), strength degradation due to exposure, and the maximum probability of failure required of the glazing. For the full range of design parameters ( $1.0 < ab < 25 \text{ ft}^2$ ,  $1.00 < a/b < 2.00$  and  $1/8 < t < 1/2$  inches), the model predicted a design stress for tempered glass ranging between 16,950 and 20,270 psi based on a probability of failure  $P(F) < 0.001$ . Based on these results, a design stress equal to 17,000 psi was selected for tempered glass. The model predicted a design stress for annealed glass ranging between 3,990 and 6,039 psi, based on  $P(F) < 0.008$ , which is conventional for annealed glass. Based on these results, a design stress of 4,000 psi was selected for annealed glass.

These design stresses for blast resistant glazing are higher than those commonly used in the design for one-minute wind loads. However, these higher design stresses are justified on the basis of the relatively short stress intensity duration (less than one second) produced by blast loads.

## 2.3 Dynamic Response to Blast Load.

An analytical model was used to predict the blast load capacity of annealed and tempered glazings. Characteristic parameters of the model are illustrated in Figure 1.

The glazing is a rectangular glass plate having a long dimension,  $a$ , short dimension,  $b$ , thickness,  $t$ , poisson ratio,  $\nu = 0.22$ , and elastic modulus,  $E = 10,000,000$  psi. The plate is simply supported along all four edges, with no in-plane and rotational restraints at the edges. The relative bending stiffness of the support members is assumed to be infinite relative to the pane. The failure or design stress,  $f_u$ , was assumed to be 17,000 psi for tempered glass and 4,000 psi for annealed glass.

The blast pressure loading is described by a peak triangular-shaped pressure-time curve as shown in Figure 1b. The blast pressure rises instantaneously to a peak blast pressure,  $B$ , and then decays with a blast pressure duration,  $T$ . The pressure is uniformly distributed over the surface of the plate and applied normal to the plate.

The resistance function (static uniform load,  $r$ , versus center deflection,  $X$ ) for the plate accounts for both bending and membrane stresses. The effects of membrane stresses produce nonlinear stiffening of the resistance function as illustrated in Figure 1c. The failure deflection,  $X_u$ , is defined as the center deflection where the maximum principal tensile stress at any point in the glass first reaches the design stress,  $f_u$ .

The model used a single degree of freedom system to simulate the dynamic response of the plate, as shown in Figure 1d. Damping of the window pane is assumed to be 5% of critical damping. The applied load,  $P(t)$ , is shown in Figure 1b. The resistance function,  $r(x)$ , is shown in Figure 1c. Given the design parameters for the glazing, the design or failure stress,  $f_u$ , and the blast load duration,  $T$ , the model calculated the peak blast pressure,  $B$ , required to fail the glazing by exceeding the prescribed probability of failure,  $P(F)$ . The model also assumed failure to occur if the center deflection exceeded ten times the glazing thickness. This restricts solutions to the valid range of the Von Karman plate equations used to develop the resistance function for the glazing.

#### 2.4 Design Charts

Charts are presented in Figures 2 to 16 for both the design and evaluation of glazing to safely survive a prescribed blast loading. The charts were developed using the analytical model described in Section 2.3. The charts relate the peak blast pressure capacity,  $B$ , of both tempered and annealed glazing to all combination of the following design parameters:  $a/b = 1.00, 1.25, 1.50, 1.75$  and  $2.00$ ;  $1.00 < ab < 25 \text{ ft}^2$ ;  $12 < b < 60$  inches;  $2 < T < 1,000$  msec; and  $t = 1/8, 3/16, 1/4, 3/8$  and  $1/2$  inch (nominal) for tempered glass and  $t = 1/8$  and  $1/4$  inch (nominal) for annealed glass.

Each chart has a series of curves. Each curve corresponds to the value of  $b$  (short dimension of pane) shown to the right of the curve. Adjacent to each posted value of  $b$  is the value of  $B$  (peak blast pressure capacity) corresponding to  $T = 1,000$  msec. The posted value of  $B$  is intended to reduce errors when interpolating between curves.

Figures 2 to 11 apply for heat-treated tempered glass meeting Federal Specification DD-G-1403B and ANSI Z97.1-1975. The value of  $B$  is the peak blast capacity of the glazing based on failure defined as  $f_u = 17,000$  psi. This value corresponds to a probability of failure,  $P(F) < 0.001$ .

Figures 12 to 16 apply for annealed (float, plate or sheet) glass. Due to the variation in the mechanical properties and fragment hazard of annealed glass, Figures 12 to 16 are not intended for design, but for safety evaluation of existing glazing. The value of  $B$  is the peak blast pressure capacity of the glazing based on  $f_u = 4,000$  psi. This value corresponds to

$P(F) < 0.008$ , the common architectural standard for annealed glass.

The charts are based on the minimum thickness of fabricated glass allowed by Federal Specification DD-G-451d. However, the nominal thickness should always be used in conjunction with the charts, i.e.,  $t = 1/8$  inch instead of the possible minimum thickness of 0.115 inch.

In a few cases, the charts show a pane to be slightly stronger than the preceding smaller size. This anomaly stems from dynamic effects and the migration of maximum principal stresses from the center to the corner region of the window pane. In such cases, interpolation should be between the two curves that bound the desired value.

#### 2.5 Fragment Retention Film

Most injuries in explosions are caused by glass fragments propelled by the blast wave when a window is shattered. Commercial products have been developed which offer a relatively inexpensive method to improve the shatter resistance of window glass and decrease the energy and destructive capability of glass fragments. The product is a clear plastic (polyester) film which is bonded to the inside surface of window panes. Typical films are about 0.002 to 0.004 inch thick polyester with a self-adhesive face. The film is commercially referred to as shatter resistant film and safety film.

The film increases safety by providing a strong, elastic type backing that will tend to hold the glass even though the glass is shattered. Results from explosives tests demonstrate that the film is highly effective in reducing the number of airborne glass fragments. Even if a complete pane of film reinforced glass is blown away from its frame by a high energy blast wave, it will travel as a single piece while adhering to the film. In this configuration it will travel a shorter distance and the individual fragments will be less hazardous because of the shielding effect of the film covering its sharp edges. If a strong structural member or crossbar is secure across the opening, the window will tend to wrap about the crossbar and not be propelled across an interior room. Additionally, if a projectile strikes the film reinforced glass with sufficient force to pass through it, the glass immediately around the hole will ordinarily adhere to the film. The result is that any fragments broken free by the impact will be few in number and lower in energy content.

There are additional benefits from fragment retention film. The film can be tinted to improve the heat balance of the structure. Also, the film affords benefits in terms of physical security. Additionally, the film protects the inner tensile surface of the glazing from scratches and humidity, thus reducing strength degradation of the glazing with time. Manufacturers of fragment retention film should be consulted for specific applications.

### 3. DESIGN CRITERIA FOR FRAME

#### 3.1 Sealants and Gaskets

The sealant and gasket design should be consistent with industry standards and also account for special requirements for blast resistant windows. The gasket should be continuous around the perimeter of the glass pane and its stiffness should be at least 10,000 psi (pounds/linear inch of frame/inch of gasket deflection). Analysis indicates that the employment of a gasket stiffness below 10,000 psi will increase the failure rate of the window pane. The gasket should provide adequate grip as the glass pane flexes under the applied blast loading.

#### 3.2 Frame Loads

The window frame must develop the static design strength of the glass pane,  $r_u$ , given in Table 1. Otherwise, the design is inconsistent with frame assumptions and the peak blast pressure capacity of the window pane predicted from Figures 2 to 16 will produce a failure rate in excess of the prescribed failure rate. This results because frame deflections induce higher principal tensile stresses in the pane, thus reducing the strain energy capacity available to safely resist the blast loading.

Until criteria are developed to account for the interaction of the frame and panes, the frame, mullions, fasteners, and gaskets should satisfy the following design criteria:

1. **Deflection:** Under the design load,  $r_u$ , no frame member should have a relative displacement exceeding  $1/264$  of its span or  $1/8$  inch, whichever is less.
2. **Stress:** Under the design load,  $r_u$ , the maximum stress in any member should not exceed  $f_y / 1.65$ , where  $f_y$  = yield stress of the members material.
3. **Fasteners:** Under the design load,  $r_u$ , the maximum stress in any fastener should not exceed  $f_y / 2.00$ .
4. **Gaskets:** The stiffness of gaskets should be at least 10,000 psi (pounds/linear inch of frame/inch of gasket deflection).

The design loads for the glazing are based on large deflection theory, but the resulting design loads for the frame are based on small deflection theory for laterally loaded plates. Analysis indicates this approach to be simpler and more conservative than using the frame loading based exclusively on large deflection membrane behavior, characteristic of window panes. According to the assumed plate theory, the design load,  $r_u$ , produces a line shear,  $V_x$ ,

applied by the long side,  $a$ , of the pane equal to:

$$V_x = C_x r_u b \sin (\pi x/a) \quad (1)$$

The design load,  $r_u$ , produces a line shear,  $V_y$ , applied by the short side,  $b$ , of the pane equal to:

$$V_y = C_y r_u b \sin (\pi y/b) \quad (2)$$

The design load,  $r_u$ , produces a corner concentrated load,  $R$ , tending to uplift the corners of the window pane equal to:

$$R = -C_R r_u b^2 \quad (3)$$

Distribution of these forces, as loads acting on the window frame, is shown in Figure 17. Table 2 presents the design coefficients,  $C_x$ ,  $C_y$ , and  $C_R$  for practical aspect ratios of the window pane. Linear interpolation can be used for aspect ratios not presented. The loads given by Equations 1, 2, and 3 should be used to check the frame mullions and fasteners for compliance with the deflection and stress criteria stated above. It is important to note that the design load for mullions is twice the load given by Equations 1 to 3, in order to account for effects of two panes being supported by a common mullion.

#### 3.3 Rebound Stresses

Under a short duration blast load, the window will rebound with a negative (outward) deflection. The stresses produced by the negative deflection must be safely resisted by the window while positive pressures act on the window. Otherwise, the window which safely resists stresses induced by positive (inward) displacements will later fail in rebound while positive pressure still acts. This will propel glass fragments into the interior of the structure. However, if the window fails in rebound during the negative (suction) phase of the blast loading, glass fragments will be drawn away from the structure.

Rebound criteria are currently not available for predicting the equivalent static uniform negative load (resistance),  $r_u$ , that the window must safely resist for various blast load durations. However, analysis indicates that for  $T > 400$  msec, significant rebound does not occur during the positive blast pressure phase for the range of design parameters given in Figures 2 to 16. Therefore, rebound can be neglected as a design consideration for  $T > 400$  msec. For  $T < 400$  msec, it is recommended that the rebound charts in Volume 3 of NAVFAC P-397 be used to estimate  $r_u$ .

The value  $r_u$  is a design load for the frame. Because of symmetry,  $r_u$  need not be considered in the design of the glass panes. Thus, the frame and mullions must safely resist  $r_u$  as the positive design load and  $r_u$  as a negative design load.

#### 4. CERTIFICATION TESTS

Certification tests of the entire window assembly are required unless analysis demonstrates that the window design is consistent with assumptions used to develop the design criteria presented in Figures 2 to 16. The certification tests consist of applying static uniform loads on at least two sample window assemblies until failure occurs in either the tempered glass or frame. Although at least two static uniform load tests until sample failure are required, the acceptance criteria presented below encourage a larger number of test samples. The number of samples, beyond two, is left up to the vendor. Results from all tests shall be recorded in the calculations. All testing shall be performed by an independent and certified testing laboratory.

A probability of failure under testing of less than 0.025 with a confidence level of 90% is considered sufficient proof for acceptance. This should substantiate a design probability of failure,  $P(F)$ , under the design blast load of 0.001.

##### 4.1 Test Procedure - Window Assembly Test

The test windows (glass panes plus support frames) shall be identical in type, size, sealant, and construction to those furnished by the window manufacturer. The frame assembly in the test setup shall be secured by boundary conditions that simulate the adjoining walls. Using either a vacuum or a liquid-filled bladder, an increasing uniform load shall be applied to the entire window assembly (glass and frame) until failure occurs in either the glass or frame. Failure shall be defined as either breaking of glass or loss of frame resistance. The failure load,  $\hat{r}$ , shall be recorded to three significant figures. The load should be applied at a rate of  $0.5 r_u$  per minute which corresponds to approximately one minute of significant tensile stress duration until failure. Table 1 presents the static ultimate resistance for new tempered glass,  $r_u$ , correlated with a probability of failure,  $P(F)$ , = 0.001 and a static load duration of 1 minute.

##### 4.2 Acceptance Criteria

The window assembly (frame and glazing) are considered acceptable when the arithmetic mean of all the samples tested,  $\bar{r}$ , is such that:

$$\bar{r} \geq r_u + s \alpha \quad (4)$$

where:  $r_u$  = ultimate static load capacity of the glass pane

$s$  = sample standard deviation

$\alpha$  = acceptance coefficient

For  $n$  test samples,  $\bar{r}$  is defined as:

$$\bar{r} = \frac{\sum_{i=1}^n \hat{r}_i}{n} \quad (5)$$

where  $\hat{r}_i$  is the recorded failure load of the  $i^{\text{th}}$  test sample. The standard sample deviation,  $s$ , is defined as:

$$s = \sqrt{\frac{\sum_{i=1}^n (\hat{r}_i - \bar{r})^2}{(n-1)}} \quad (6)$$

Convenience in calculation often can be obtained by employing an alternative but equal form of Equation 6:

$$s = \sqrt{\frac{\sum_{i=1}^n \hat{r}_i^2 - \left(\frac{\sum_{i=1}^n \hat{r}_i}{n}\right)^2}{(n-1)}} \quad (7)$$

The minimum value of the sample standard deviation,  $s$ , permitted to be employed in Equation 4 is:

$$s_{\text{min}} = 0.145 r_u \quad (8)$$

This assures a sample standard deviation no better than ideal tempered glass in ideal frames.

The acceptance coefficient,  $\alpha$ , is tabulated in Table 3 for the number of samples,  $n$ , tested.

As an aid to the tester, the following informational equation is presented to aid in determining if additional test samples are justified. If:

$$\bar{r} \leq r_u + s \beta \quad (9)$$

then with 90% confidence, the design will not prove to be adequate with additional testing. The frame should be redesigned or thicker tempered glass used. The rejection coefficient,  $\beta$ , is obtained from Table 3.

If the glass assembly is upgraded with thicker tempered glass than required by the design charts (Figures 2 through 12) to resist a design blast load, it is not required to develop the higher ultimate static load capacity of the thicker glass. Instead, a static load equal to twice the design peak blast overpressure,  $B$ ,

shall be resisted by the window assembly. Thus the window assembly with thicker than required tempered glass shall be acceptable when:

$$\bar{r} \geq 2B + s\alpha \quad (10)$$

If Equation 10 is not satisfied, and:

$$\bar{r} \leq 2B + s\beta \quad (11)$$

then with 90% confidence continued testing will not raise the arithmetic mean of the failure load of the window assembly,  $\bar{r}$ , to the point of acceptance.

#### 4.3 Rebound Tests

The window that passes the window assembly test is an acceptable design if the window assembly design is symmetrical about the plane of the glass or if the design blast load duration,  $T$ , exceeds 400 msec. Otherwise, the window design must pass a rebound load test to prove that the window assembly can develop the necessary strength to resist failure during the rebound phase of response. The rebound tests shall be conducted using a procedure similar to the window assembly tests, except  $r_u$  shall be substituted for  $r$  in Equations 4, 8 and 9 and the uniform load shall be applied on the inside surface of the window assembly. The loading rate shall be 0.5  $r_u$  per minute.

### 5. SAMPLE PROBLEMS

The following examples demonstrate the application of the design criteria in the design and evaluation of windows to safely survive blast overpressures from explosions.

#### 5.1 Problem 1 -- Design of Tempered Glass Panes

**Given:** A nonoperable window having a single pane of glass. Glazing: heat-treated tempered glass meeting Federal Specification DDG-G-1403B and ANSI Z97.1-1975. Dimensions of pane:  $a = 54$  in.,  $b = 36$  in. Blast loading:  $B = 5.0$  psi,  $T = 500$  msec.

**Find:** Minimum thickness of glazing required for  $P(F) \leq 0.001$ .

**Solution:** Step 1: Tabulate the design parameters needed to enter Figure 2 to 16.

Glazing = tempered glass  
 $a/b = 54/36 = 1.50$   
 $b = 36$  in.  
 $B = 5.0$  psi  
 $T = 500$  msec

Step 2: Enter Figures 2 to 16 with the design parameters from Step 1 and find the minimum glazing thickness.

Figures 6 and 7 apply for the given design parameters. Enter Figure 6 and find the minimum glazing thickness required for  $B = 5.0$  psi and  $T = 500$  msec is:

$t = 3/8$  in. ANS

The asterisk adjacent to  $b = 36$  inches indicates that the strength of the glazing is limited by principle stresses in corner regions of the pane.

#### 5.2 Problem 2 -- Safety Evaluation of Existing Windows

**Given:** Multi-pane windows in an existing building. Dimensions of each pane:  $a = 36$  in.,  $b = 36$  in. Glazing: float glass. Glazing thickness:  $t = 1/4$  in. nominal. Blast loading:  $B = 0.60$  psi,  $T = 100$  msec.

**Find:** Safety of windows, based on  $P(F) \leq 0.008$

**Solution:** Step 1: Tabulate the design parameters needed to enter Figures 2 to 16.

Glazing = annealed glass  
 $a/b = 36/36 = 1.00$   
 $B = 0.60$  psi  
 $T = 100$  msec  
 $t = 1/4$  in.

Step 2: Enter Figures 12 to 16 with the design parameters from Step 1 and find the peak blast pressure capacity.

From Figure 12, the peak blast pressure capacity of the glazing is:

$B = 0.53$  psi

Step 3: Determine the safety of the glazing.

The applied peak blast pressure,  $B = 0.60$  psi, exceeds the capacity,  $B = 0.53$  psi. Therefore, the glazing will fail at an average rate exceeding eight per thousand panes. A particular pane may survive  $B = 0.60$  psi but the chance of failure exceeds 8/1,000, the prescribed safety limit. ANS

#### 5.3 Problem 3 -- Design Loads for Window Frame

**Given:** A nonoperable window has a single pane of glass. Glazing: heat-treated tempered glass meeting Federal Specification DDG-G-1403B and ANSI Z97.1-1975. Dimensions of the pane:  $a = 50$  in.,

b = 40 in. Blast loading: B = 1.3 psi, T = 1,000 msec.

**Find:** Thickness of glazing required for  $P(F) < 0.001$  and design loading for window frame.

**Solution:** Step 1: Tabulate the design parameters needed to enter Figures 2 to 16.

Glazing = tempered glass  
a/b = 50/40 = 1.25  
b = 40 in.  
B = 1.3 psi  
T = 1,000 msec

Step 2: Select the minimum glazing thickness.

**Note:** Figures 4 and 5 which apply for the given design parameters. From Figure 5 find the minimum glazing thickness required is:

t = 3/16 in. nominal **ANS**

Step 3: Calculate the static ultimate uniform load that produces the same maximum frame load as the blast load.

Enter Table 1 for tempered glass with b = 40 in., a/b = 1.25 and t = 3/16 in., and find the static ultimate uniform load capacity of the glazing is:

$r_u = 2.31$  psi

Thus, the window frame must be designed to safely support, without undue deflection, a static uniform load equal to 2.31 psi applied normal to the glazing.

Step 4: Calculate the design loading for the window frame.

Enter Table 2 with a/b = 1.25, and find by interpolation the design coefficients for the frame loading are:

$C_R = 0.071$

$C_x = 0.462$

$C_y = 0.459$

From Equation 3, the concentrated load in each corner of the pane is:

R (corners) =  $-0.071 (2.31)(40)^2$   
= -285 lb **ANS**

From Equation 1, the design loading for the frame in the long direction (a) is:

$V_x = 0.462 (2.31)(40) \sin(\pi x/50)$   
= 42.7  $\sin(\pi x/50)$  lb/in. **ANS**

From Equation 2, the design loading for the frame in the short direction (b) is:

$V_y = 0.459 (2.31)(40) \sin(\pi y/40)$   
= 42.4  $\sin(\pi y/40)$  lb/in. **ANS**

Distribution of the design load on the frame is shown in Figure 17.

#### 5.4 Problem 4 -- Design Loads for Multi-pane Frame

**Given:** A nonoperable window consists of four equal size panes of glass. Glazing: heat-treated tempered glass meeting Federal Specification DD-G-1403B and ANSI Z97.1-1975. Dimensions of the panes: a = 22.5 in., b = 18 in. Blast loading: B = 5.0 psi, T = 500 msec.

**Find:** Minimum thickness of glazing required for  $P(F) < 0.001$  and the design loads for the framing system.

**Solution:** Step 1: Tabulate the design parameters needed to enter Figures 2 to 11.

Glazing = tempered glass  
a/b = 22.5/18 = 1.25  
b = 18 in.  
B = 5.0 psi  
T = 500 msec

Step 2: Select the minimum glazing thickness.

Enter Figures 4 and 5 which apply for the given design parameters. From Figure 5, find the minimum glazing thickness required is:

t = 3/16 in. nominal **ANS**

Step 3: Calculate the static ultimate uniform load that produces the same maximum reactions on the window frame as the blast load.

Enter Table 1 with b = 18 in., a/b = 1.25 and t = 3/16 in., and find the static ultimate uniform load capacity of the glazing is:

$r_u = 9.18$  psi

The window frame must be designed to safely support, without undue deflections, a static uniform load equal to 9.18 psi applied normal to the glazing.

**Step 4:** Calculate the design loading for the window frame.

Enter Table 2 with  $a/b = 1.25$ . With interpolation, the design coefficients for the frame loading are:

$$C_R = 0.077$$

$$C_x = 0.462$$

$$C_y = 0.459$$

From Equation 3, the concentrated loads in the corners of each pane are:

$$R (\text{corners}) = -0.077 (9.18)(18)^2 = -229 \text{ lb} \quad \text{ANS}$$

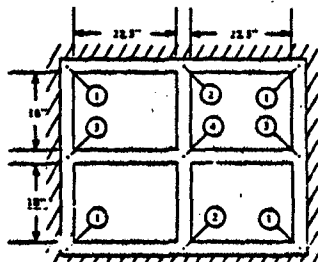
From Equation 1, the design loading for the long spans of the frame and mullions are:

$$V_x = 0.462 (9.18)(18) \sin(\pi x/22.5) = 76.3 \sin(\pi x/22.5) \text{ lb/in.} \quad \text{ANS}$$

From Equation 2, the design loading for the short spans of the frame and mullions are:

$$V_y = 0.459 (9.18)(18) \sin(\pi y/18) = 75.8 \sin(\pi y/18) \text{ lb/in.} \quad \text{ANS}$$

The design loads for the window frame are shown in the following figure and table and are illustrated below.



Location	Design Load
①	R
②-②	2R
③	4R
①-②	$V_x$
①-③	$V_y$
②-③	$2V_y$
①-④	$2V_x$

### 5.5 Problem 5 -- Design Acceptance Based Upon Certification Test Results

**Given:** A window 30 x 30 x 1/4-inch with a single pane of tempered glass is designed to safely resist a blast load, B, of 4.0 psi with an effective blast duration, T, of 200 msec. Certification testing involved testing three window assemblies ( $n = 3$ ) to failure. Failure loads,  $\hat{F}_i$ , were recorded at 8.84, 9.51, and 10.8 psi.

**Find:** Determine if the window design is acceptable based on results from the certification tests.

**Solution:** **Step 1:** Tabulate the design parameters needed to enter Table 1:

$$b = 30 \text{ in.}$$

$$a/b = 30/30 = 1.00$$

$$t = 1/4 \text{ in. nominal}$$

**Step 2:** Employing Table 1, select the static ultimate load,  $r_u$ , corresponding to the pane geometry.

$$r_u = 6.59 \text{ psi}$$

**Step 3:** Calculate the arithmetic mean,  $\bar{r}$ , of all the samples tested.

Using Equation 5:

$$\bar{r} = \frac{\sum_{i=1}^n \hat{F}_i}{n} = \frac{(8.84 + 9.51 + 10.8)}{3} = 9.72 \text{ psi}$$

**Step 4:** Using either Equation 6 or 7, calculate the sample standard deviation,  $s$ .

The sample standard deviation,  $s$ , is calculated using Equation 6 as:

$$s = \sqrt{\frac{\sum_{i=1}^n (\hat{F}_i - \bar{r})^2}{(n - 1)}} = \sqrt{\frac{(8.84 - 9.72)^2 + (9.51 - 9.72)^2 + (10.8 - 9.72)^2}{(3 - 1)}} = 1.01 \text{ psi}$$

Step 5: Verify that the sample standard deviation,  $s$ , is larger than the minimum value,  $s_{\min}$ , prescribed in Equation 8.

$$s = 1.01 \text{ psi} > s_{\min} = 0.145 r_u \\ = 0.145 (6.59) = 0.956 \text{ psi}$$

Thus,  $s = 1.01 \text{ psi}$  is the appropriate value to use in subsequent calculations.

Step 6: Using Table 3, select the acceptance coefficient,  $\alpha$ , that correlates with the three samples tested.

Entering Table 3, with  $n = 3$ , find:

$$\alpha = 3.05$$

Step 7: Verify that the window and frame passed the certification tests by meeting the conditions of Equation 4:

$$\bar{r} = 9.72 \text{ psi} > r_u + s \alpha \\ = 6.59 + 1.01 (3.04) = 9.67 \text{ psi}$$

Therefore, the window assembly design is considered safe for the prescribed blast loading.

#### 6. LIST OF SYMBOLS

a	Long dimension of glass pane, in.
B	Peak blast overpressure, psi
b	Short dimension of glass pane, in.
C	Shear coefficient for load passed from glass pane to its support frame
D	Modulus of rigidity of glass pane, in-lb
E	Modulus of elasticity, psi
$f_u$	Design stress and allowable principal tensile stress in glass pane for prescribed $P(F)$ , psi
$f_y$	Yield stress of frame members and fasteners, psi
I	Moment of inertia of window frame, in. <sup>4</sup>
n	Number of window assemblies tested
$M_e$	Effective total mass (lb-msec <sup>2</sup> /in.)
P	Blast overpressure at any time, psi

$P(F)$	Probability of failure of glass pane
R	Uplifting nodal force applied by glass pane to corners of frame, lb
r	Resistance, psi
$\bar{r}$	Test load at failure of frame or glass during certification tests, psi
$\bar{r}$	Mean failure load of n samples, psi
$r_u$	Uniform static load capacity of the glass pane, psi
$r_u^-$	Uniform static negative load capacity of the window assembly, psi
s	Sample standard deviation, psi
T	Effective duration of blast load, msec
t	Nominal thickness of glass pane, in.; elapsed time, msec
$V_x$	Static load applied by glass pane to long edge of frame, lb/in.
$V_y$	Static load applied by glass pane to short edge of frame, lb/in.
x	Distance from corner measured along long edge of glass pane, in.
X	Center deflection of pane, in.
$X_u$	Center deflection of pane at $r_u$ , in.
$\alpha$	Acceptance coefficient
$\beta$	Rejection coefficient
$\nu$	Poisson's ratio

#### 7. BIBLIOGRAPHY

- G.E. Meyers. Preliminary design procedure for blast-hardened window panes, Naval Civil Engineering Laboratory, Technical Memorandum 51-83-03. Port Hueneme, Calif., Jan 1981.
- G.E. Meyers. A review of adaptable methodology for development of a design procedure for blast hardened windows, Naval Civil Engineering Laboratory, Special Report. Port Hueneme, Calif., Aug 1982.
- C.V.G. Vallabhan and B.Y. Wang. Nonlinear analysis of rectangular glass plates by finite difference method, Texas Technical University, Institute for Disaster Research. Lubbock, Texas, Jun 1981.
- D.M. Moore. Proposed method for determining the thickness of glass in solar collector panels, Jet Propulsion Laboratory, Publication 80-34. Pasadena, Calif., Mar 1980.
- D.M. Moore. Thickness sizing of glass plates subjected to pressure loads, FSA Task

Report No. 5101-291. Pasadena, Calif., Aug 1982.

6. PPG glass thickness recommendations to meet architect's specified 1-minute wind load, PPG Industries. Pittsburg, Pa, Mar 1981.

7. S. Weissman, W. Dobbs, W. Stea, and P. Price. Blast capacity evaluation of glass windows and aluminum window frames, U.S. Army Armament Research and Development Command, ARLCO-CR-78016. Dover, N.J., Jun 1978.

8. W.L. Beason and J.R. Morgan. "A glass failure prediction model," submitted for publication in the Journal of the Structural Division, American Society of Civil Engineers.

9. W.L. Beason. TAMU glass failure prediction model, preliminary report, Texas A&M University. College Station, Tex., Mar 1982.

10. W.L. Beason. A failure prediction model for window glass, Texas Technical University, NSF/RA 800231. Lubbock, Tex., May 1980.

11. S. Levy. Bending of rectangular plates with large deflections, NACA TechNote 845, 1942.

12. D. Amiaz. Experimental study of edge displacements of laterally loaded window glass plates, Institute for Disaster Research, Texas Technical University. Lubbock, Tex., Jun 1980.

13. S. Timoshenko and S. Woinowsky-Krieger. Theory of plates and shells. New York, N.Y., McGraw-Hill Book Company. 1959.

14. Safety performance specifications and methods of test for safety glazing material used in buildings, American National Standards Institute, ANSI Z97.1-1975. New York, N.Y., 1975.

15. A method for improving the shatter resistance of window glass, U.S. Army Picatinny Arsenal, National Bomb Data Center, General Information Bulletin 73-9. Dover, N.J., Nov 1973.

16. Glass, plate (float), sheet, figured, and spandrel (heat strengthened and fully tempered), General Service Administration, Federal Specification DD-G-1403B. Washington, D.C., 1972.

17. Structural performance of glass in exterior windows, curtain walls, and doors under the influence of uniform static loads by destructive method, American Society for Testing Materials, ASTM Standard (draft), Draft of proposed standard by ASTM Committee E06.51. Philadelphia, Pa., Oct 1982.

18. Federal specification glass, plate, sheet, figured (float, flat, for glazing, corrugated, mirrors and other uses), General Service Administration, Federal Specification DD-G-451d. Washington, D.C., 1977.

Table 1. Static Ultimate Loads,  $r_u$ , (psi) for Testing Certification of Tempered Glass

b (in.)	a/b = 1.00*				a/b = 1.25				a/b = 1.50			
	t=1/2 in.	t=3/8 in.	t=1/4 in.	t=3/16 in.	t=1/2 in.	t=3/8 in.	t=1/4 in.	t=3/16 in.	t=1/2 in.	t=3/8 in.	t=1/4 in.	t=3/16 in.
12	106.0	60.7	22.6	16.9	80.8	66.7	19.3	13.0	66.5	30.5	13.7	11.3
14	76.7	39.0	17.5	16.2	56.0	33.7	13.5	17.1	66.9	27.5	13.4	10.1
16	58.1	30.5	15.6	13.7	46.7	25.0	11.0	18.2	36.0	20.6	9.95	9.00
18	45.5	26.8	15.2	10.9	36.0	20.9	11.7	9.10	20.5	16.7	9.60	8.09
20	33.2	20.6	12.4	9.30	26.0	17.5	10.5	7.71	22.7	12.5	9.15	6.76
22	27.8	17.4	10.6	0.12	23.6	13.1	8.93	6.62	18.5	11.0	7.88	5.57
24	23.8	15.3	9.35	7.06	20.6	11.9	7.76	5.55	15.9	10.2	6.79	4.73
26	20.7	14.6	8.33	5.57	17.6	11.0	6.80	4.90	13.9	9.36	5.77	4.18
28	18.2	14.5	7.39	4.96	15.5	10.0	6.02	6.36	11.2	9.07	5.03	3.73
30	16.1	14.0	6.59	4.47	13.5	10.7	5.23	3.82	10.4	8.81	4.62	3.32
32	14.7	12.6	5.32	4.05	11.4	10.1	4.71	3.47	9.83	8.54	4.02	2.96
34	14.2	10.9	4.08	3.69	10.7	9.30	4.27	3.13	9.17	8.20	3.67	2.65
36	13.8	9.97	4.67	3.39	10.4	8.42	3.80	2.86	8.79	7.63	3.33	2.36
38	13.7	9.16	4.12	3.12	10.4	7.70	3.46	2.59	8.71	6.78	3.04	2.12
40	13.5	8.55	3.81	2.80	10.3	7.07	3.25	2.31	8.36	6.20	2.77	1.96
42	12.5	7.99	3.56	2.67	10.2	6.53	2.99	2.12	8.23	5.68	2.53	1.79
44	11.0	7.41	3.29	2.65	9.62	6.05	2.76	1.97	8.10	5.11	2.27	1.57
46	10.3	6.75	3.08	2.28	8.72	5.61	2.56	1.83	7.70	4.70	2.10	1.31
48	9.58	6.43	2.88	2.14	8.10	5.06	2.32	1.65	7.10	4.36	1.99	1.13
50	8.97	5.99	2.71	2.07	7.57	4.76	2.16	1.60				
52	8.50	5.58	2.56	1.89	7.09	4.40	2.02	1.20				
54	8.07	4.82	2.37	1.67								
56	7.68	4.55	2.24	1.63								
58	7.25	4.31	2.12	1.76								
60	6.87	4.09	2.02	1.10								

b (in.)	a/b = 1.75				a/b = 2.00			
	t=1/2 in.	t=3/8 in.	t=1/4 in.	t=3/16 in.	t=1/2 in.	t=3/8 in.	t=1/4 in.	t=3/16 in.
12	57.9	32.7	11.0	9.90	31.1	20.6	11.0	8.57
14	42.7	23.0	10.3	6.85	27.1	21.3	8.86	5.82
16	31.3	17.0	8.30	6.79	20.1	16.2	7.26	5.76
18	26.4	15.9	7.62	6.69	22.0	17.9	5.37	5.15
20	19.5	11.8	7.01	5.86	17.7	10.5	5.07	1.00
22	15.9	10.1	6.73	4.95	16.6	8.86	4.99	4.48
24	13.3	9.03	5.83	4.28	12.3	7.77	4.87	3.85
26	11.8	8.10	5.12	3.76	10.5	6.87	4.66	3.38
28	10.6	7.36	4.50	3.37	9.11	5.36	4.07	2.99
30	9.39	7.08	4.01	3.00	8.00	5.08	3.62	2.66
32	8.66	6.82	3.62	2.83	7.66	4.97	3.26	2.35
34	7.99	6.56	3.31	2.36	6.78	4.86	2.86	2.10
36	7.37	6.30	3.01	2.13	6.21	4.76	2.66	1.88
38	6.93	6.02	2.73	1.96	5.95	4.68	2.72	1.61
40	6.60	5.32	2.60	1.73	4.78	4.53	2.20	1.31
42	6.26	4.96	2.35	1.62	6.00	4.49	2.00	1.00
44	5.93	4.55	2.00	1.18				

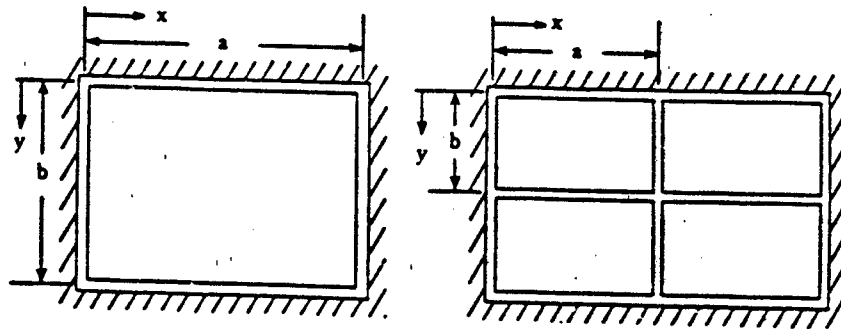
\*a = longest side of window; b = shortest side of window; t = nominal thickness of window.

Table 2. Coefficients for Frame Loading

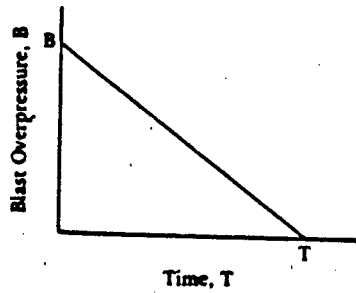
a/b	$C_R$	$C_x$	$C_y$
1.00	0.065	0.420	0.420
1.10	0.070	0.440	0.440
1.20	0.074	0.455	0.453
1.30	0.079	0.468	0.464
1.40	0.083	0.478	0.471
1.50	0.085	0.486	0.480
1.60	0.086	0.491	0.485
1.70	0.088	0.496	0.488
1.80	0.090	0.499	0.491
1.90	0.091	0.502	0.494
2.00	0.092	0.503	0.496

Table 3. Statistical Acceptance and Rejection Coefficients

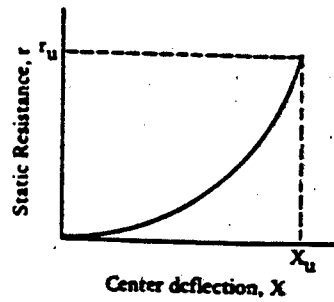
Number of Window Assemblies	Acceptance Coefficient	Rejection Coefficient
$n$	$\alpha$	$\beta$
2	4.14	.546
3	3.05	.871
4	2.78	1.14
5	2.65	1.27
6	2.56	1.36
7	2.50	1.42
8	2.46	1.48
9	2.42	1.49
10	2.39	1.52
11	2.37	1.54
12	2.35	1.57
13	2.33	1.58
14	2.32	1.60
15	2.31	1.61
16	2.30	1.62
17	2.28	1.64
18	2.27	1.65
19	2.27	1.65
20	2.26	1.66
21	2.25	1.67
22	2.24	1.68
23	2.24	1.68
24	2.23	1.69
25	2.22	1.70
30	2.19	1.72
40	2.17	1.75
50	2.14	1.77



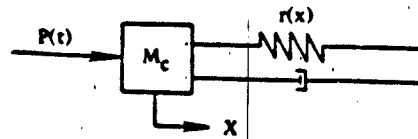
(a) Window pane geometry



(b) Blast loading



(d) Dynamic response model



(c) Resistance of glass pane

Figure 1. Characteristic parameters for glass pane, blast loading, resistance function and response model.

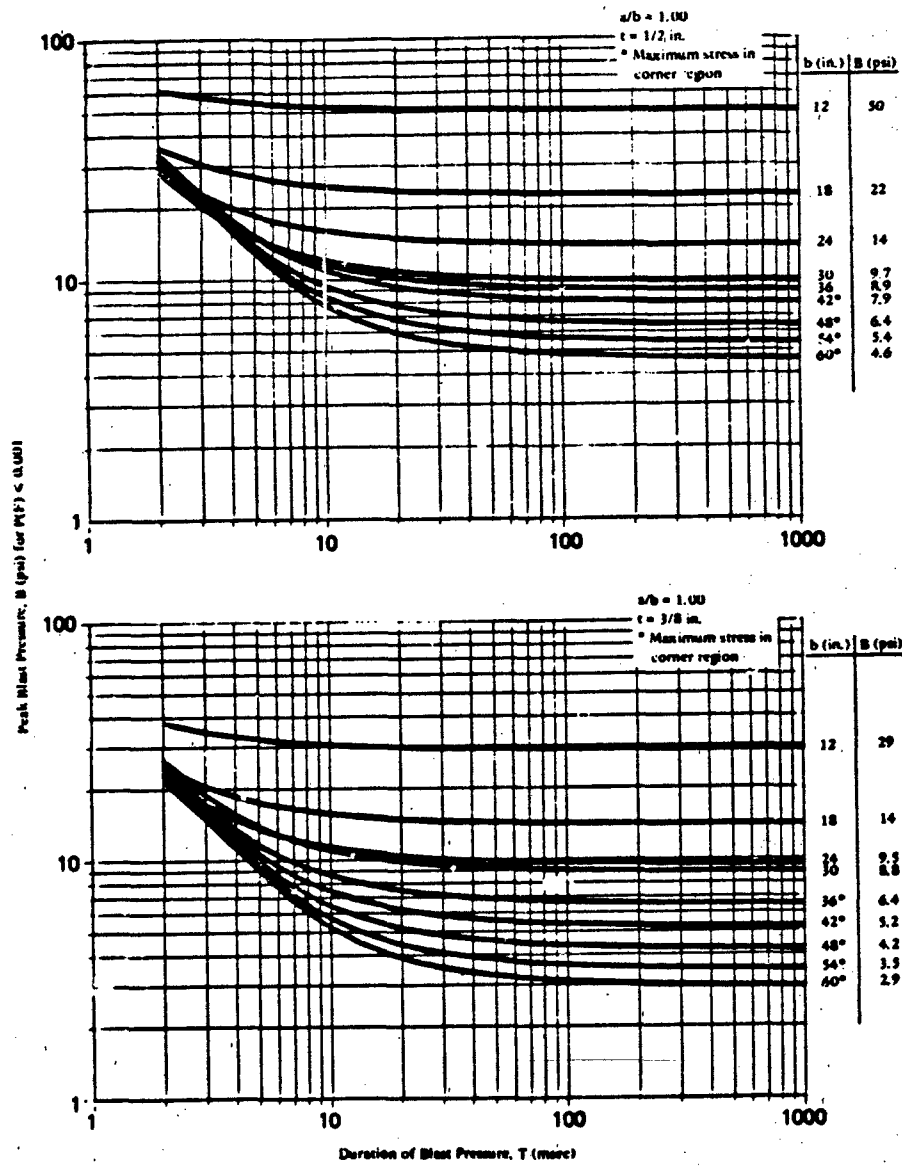


Figure 2. Peak blast pressure capacity for tempered glass panes:  $a/b = 1.00$ ,  $t = 1/2$  and  $3/8$  in.

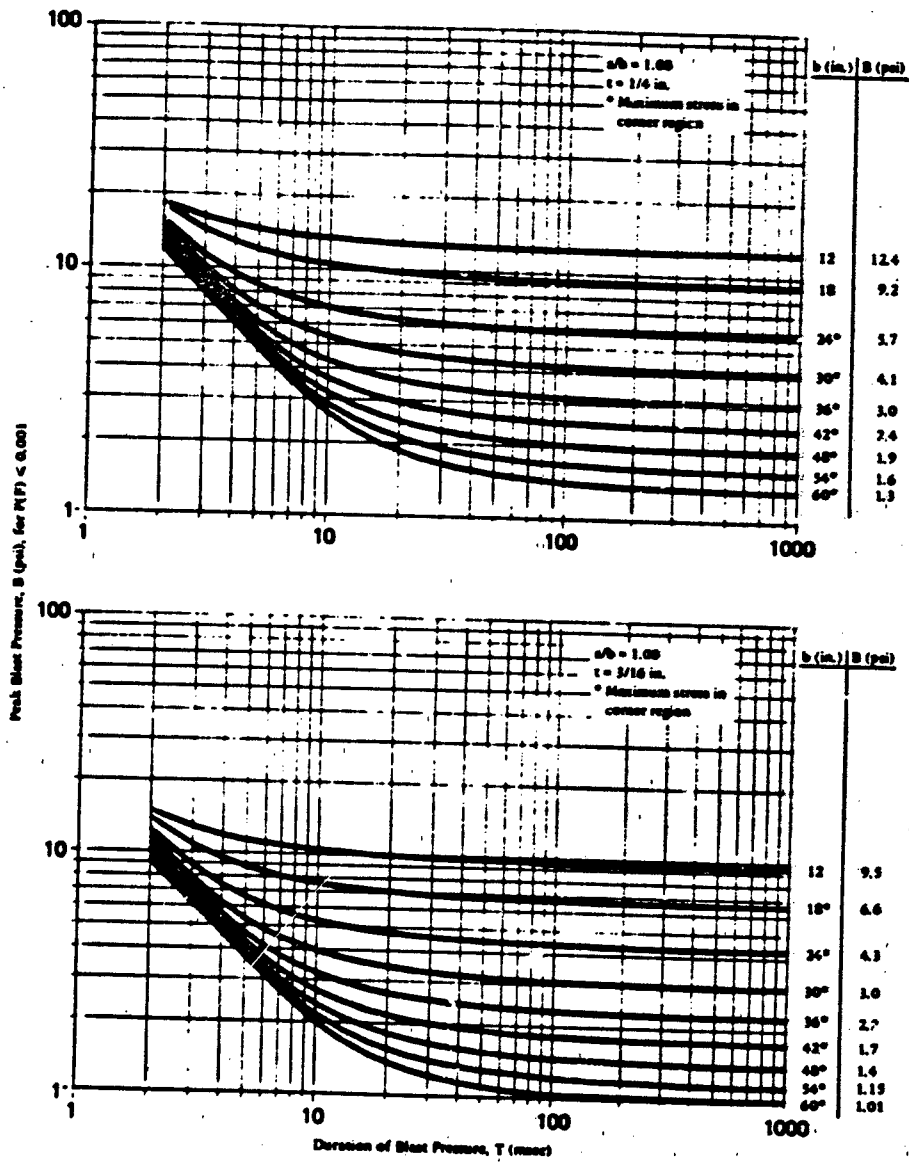


Figure 3. Peak blast pressure capacity for tempered glass panes:  $a/b = 1.00$ ,  $t = 1/4$  and  $3/16$  in.

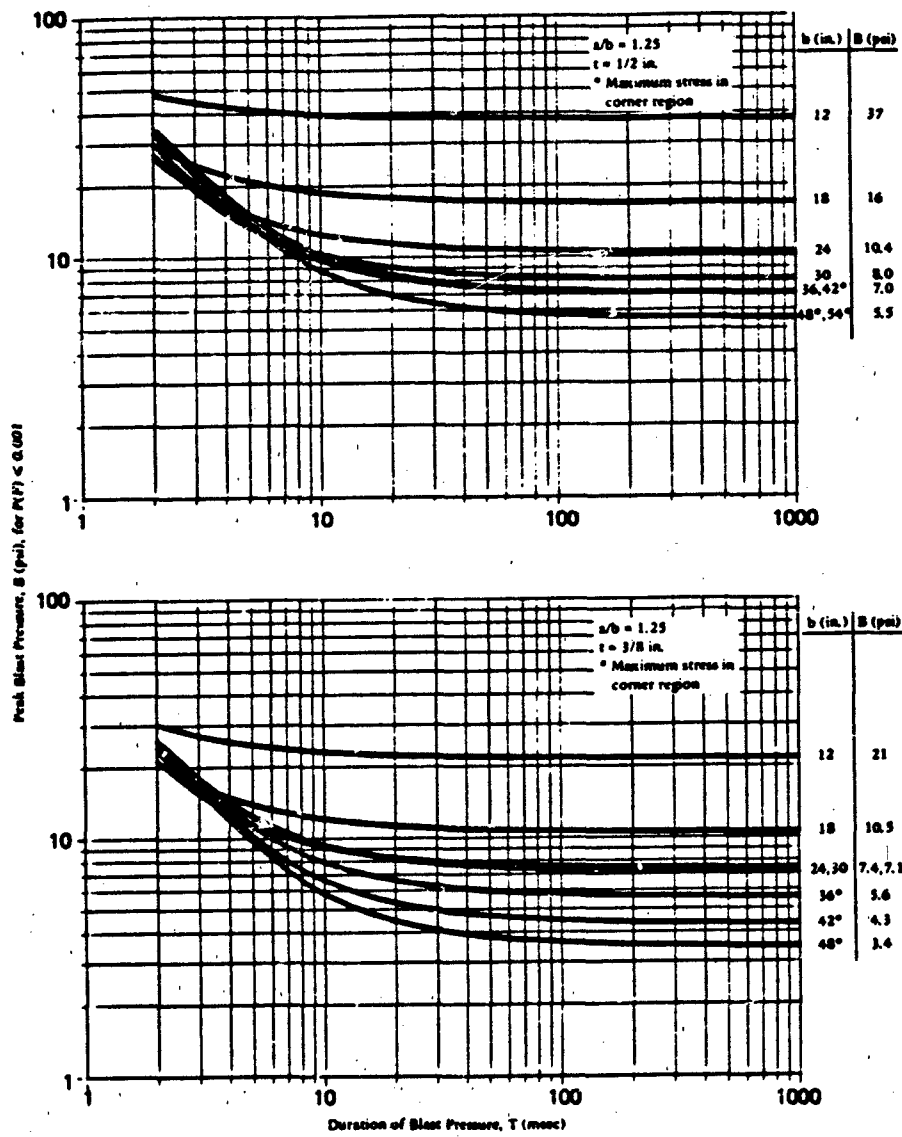


Figure 4. Peak blast pressure capacity for tempered glass panes:  $a/b = 1.25$ ,  $t = 1/2$  and  $3/8$  in.

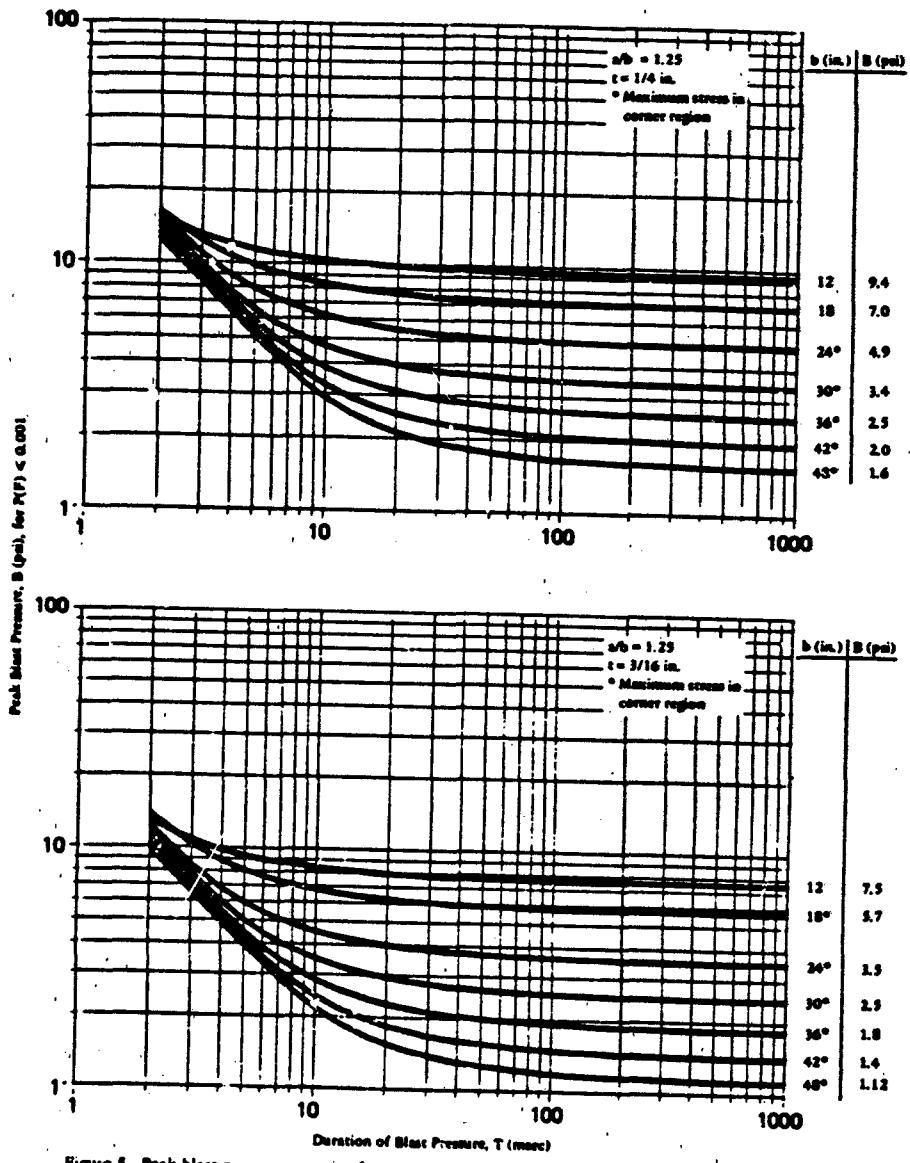


Figure 5. Peak blast pressure capacity for tempered glass panes:  $a/b = 1.25$ ,  $\tau = 1/4$  and  $3/16$  in.

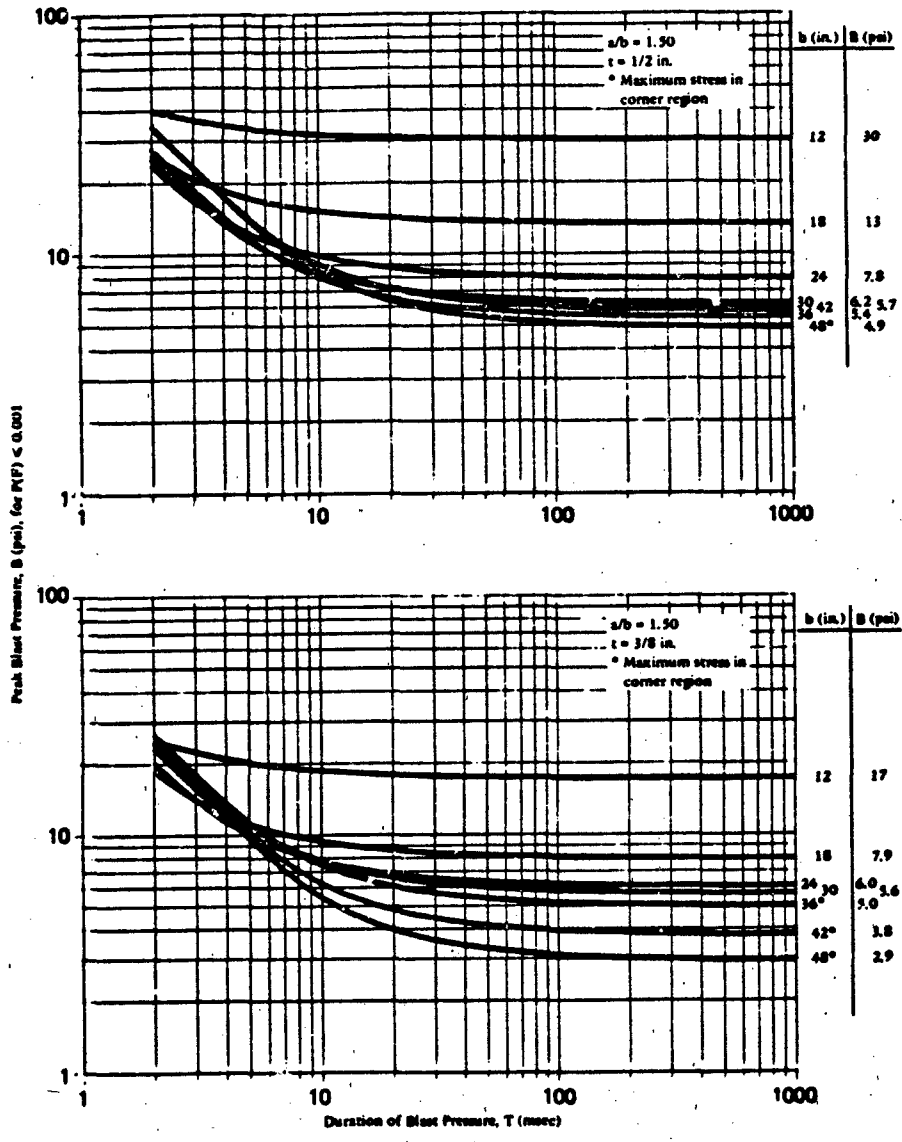


Figure 6. Peak blast pressure capacity for tempered glass panes:  $a/b = 1.50$ ,  $\tau = 1/2$  and  $3/8$  in.

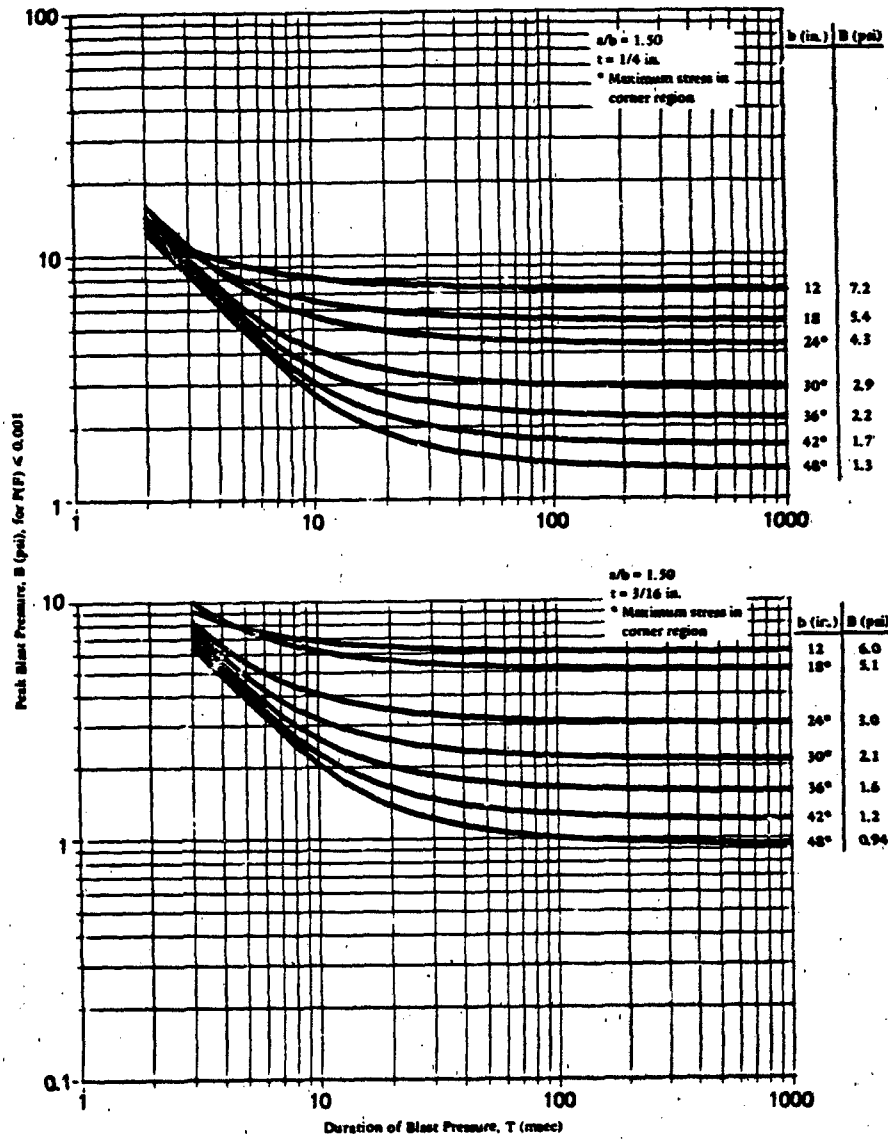


Figure 7. Peak blast pressure capacity for tempered glass panes:  $a/b = 1.50$ ,  $t = 1/4$  and  $3/16$  in.

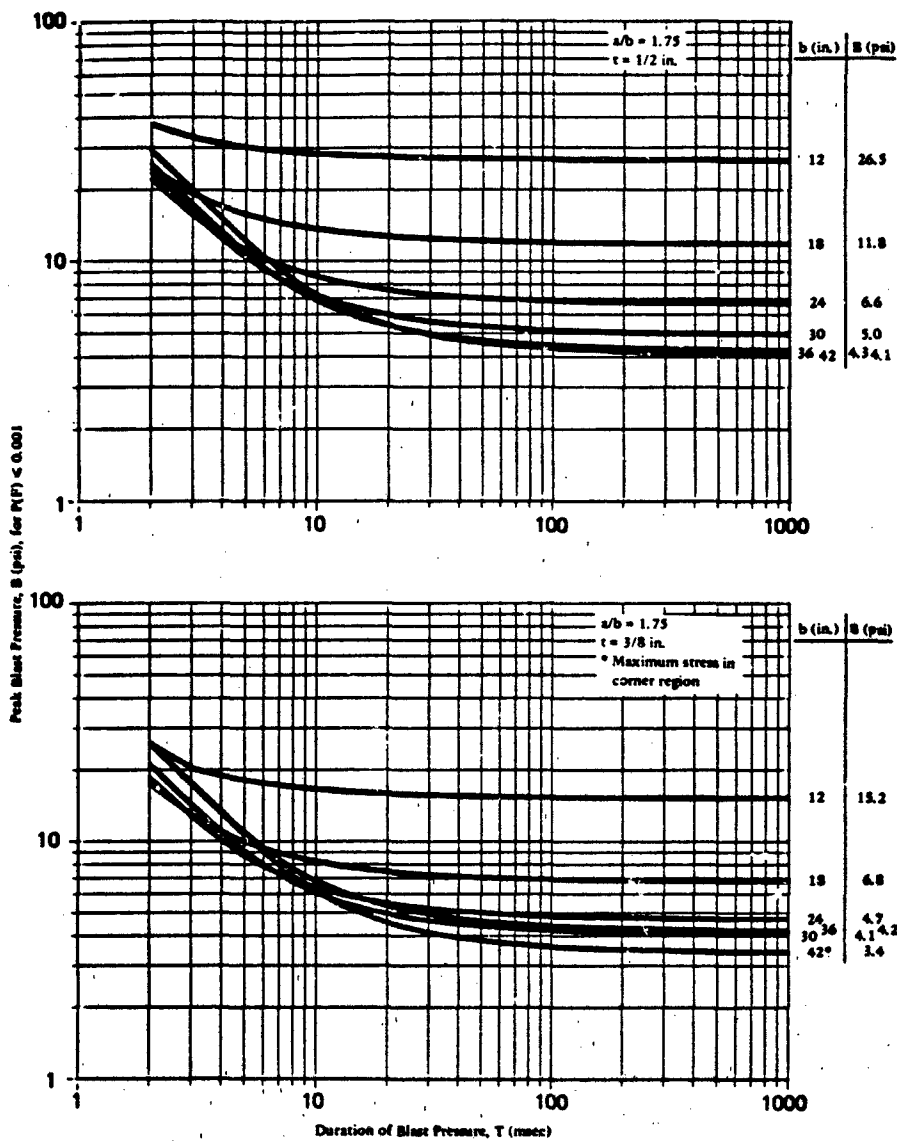


Figure 8. Peak blast pressure capacity for tempered glass panes:  $a/b = 1.75$ ,  $t = 1/2$  and  $3/8$  in.

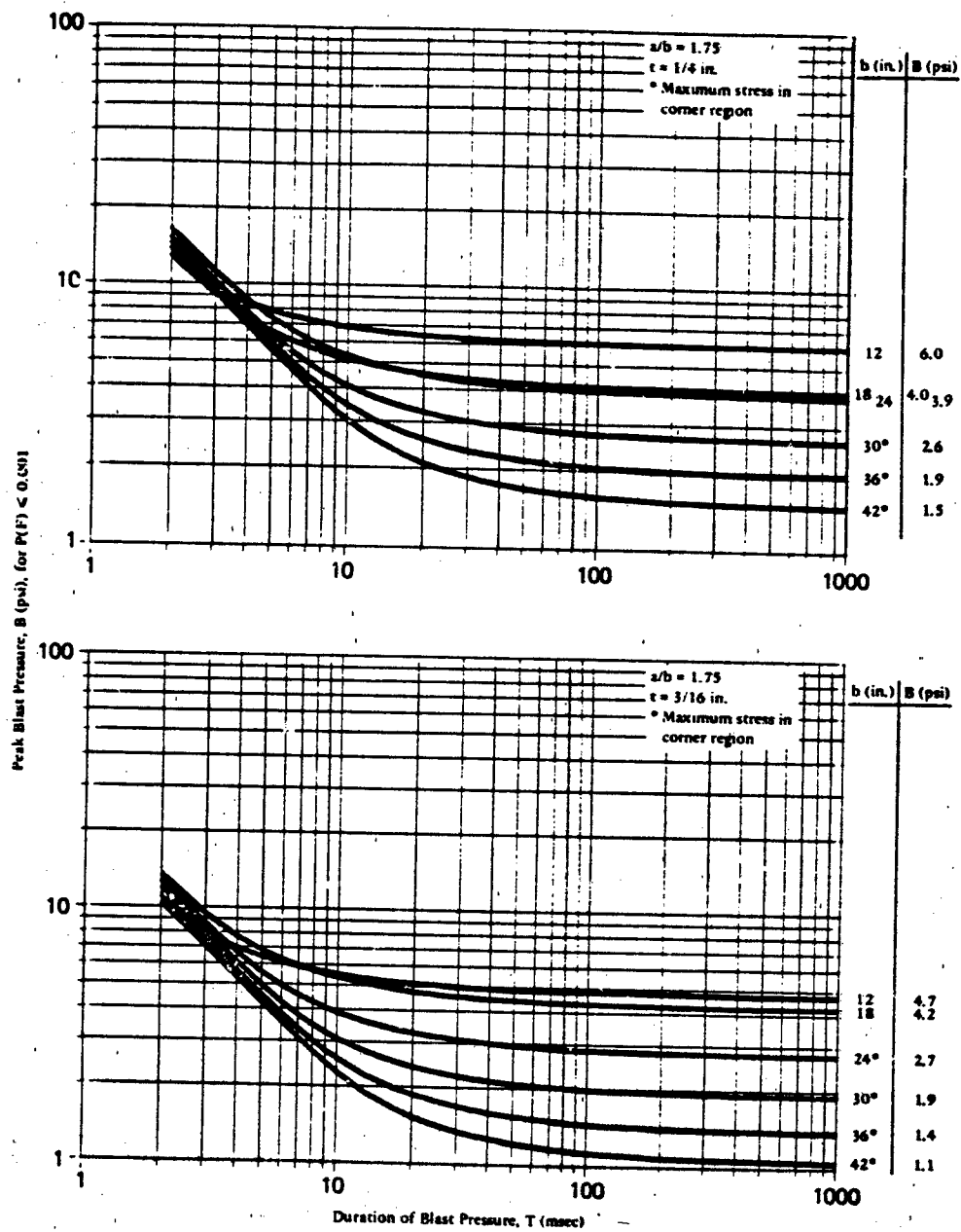


Figure 9. Peak blast pressure capacity for tempered glass panes:  $a/b = 1.75$ ,  $t = 1/4$  and  $3/16$  in.

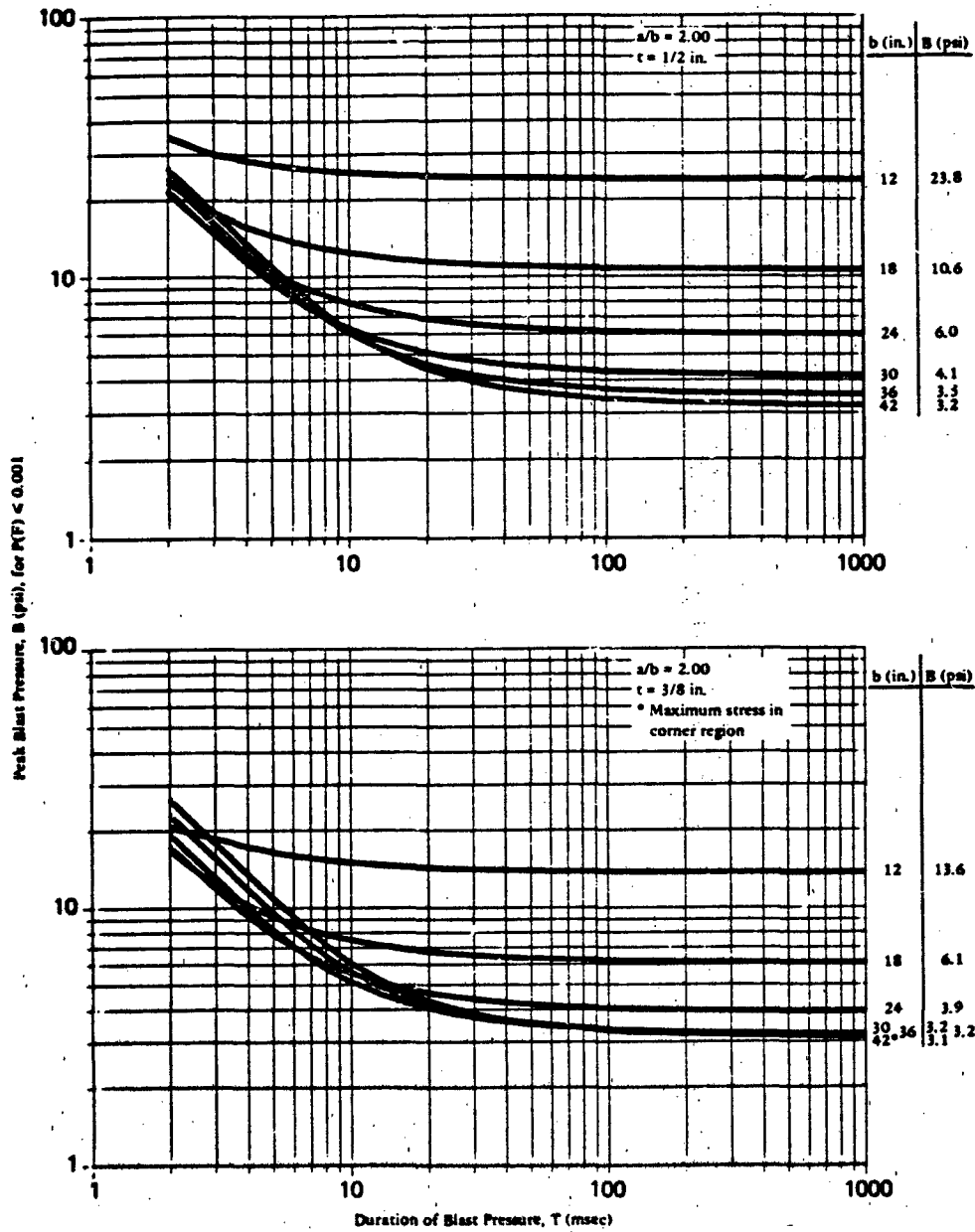


Figure 10. Peak blast pressure capacity for tempered glass panes:  $a/b = 2.00$ ,  $t = 1/2$  and  $3/8$  in.

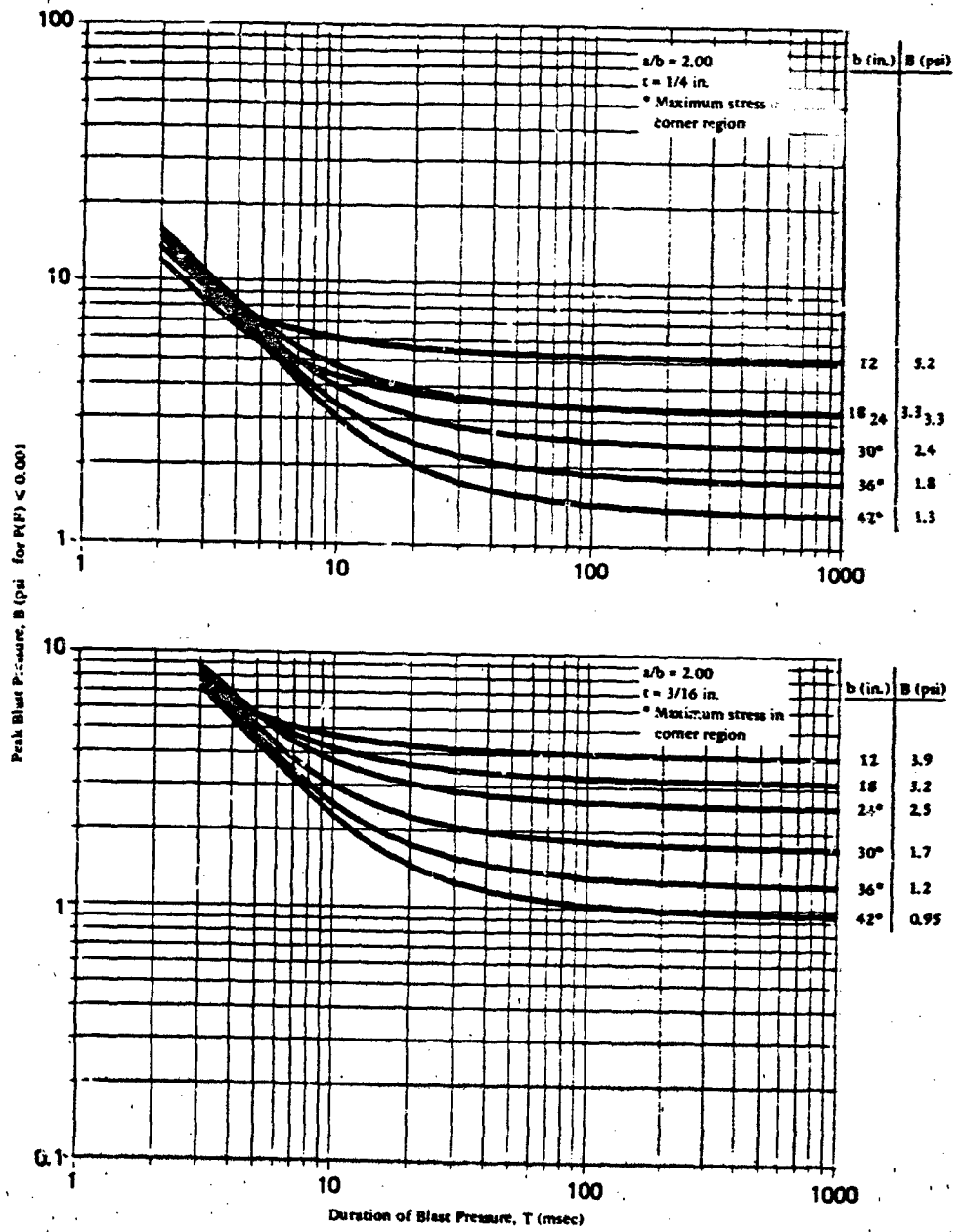


Figure 11. Peak blast pressure capacity for tempered glass panes:  $a/b = 2.00$ ,  $t = 1/4$  and  $3/16$  in.

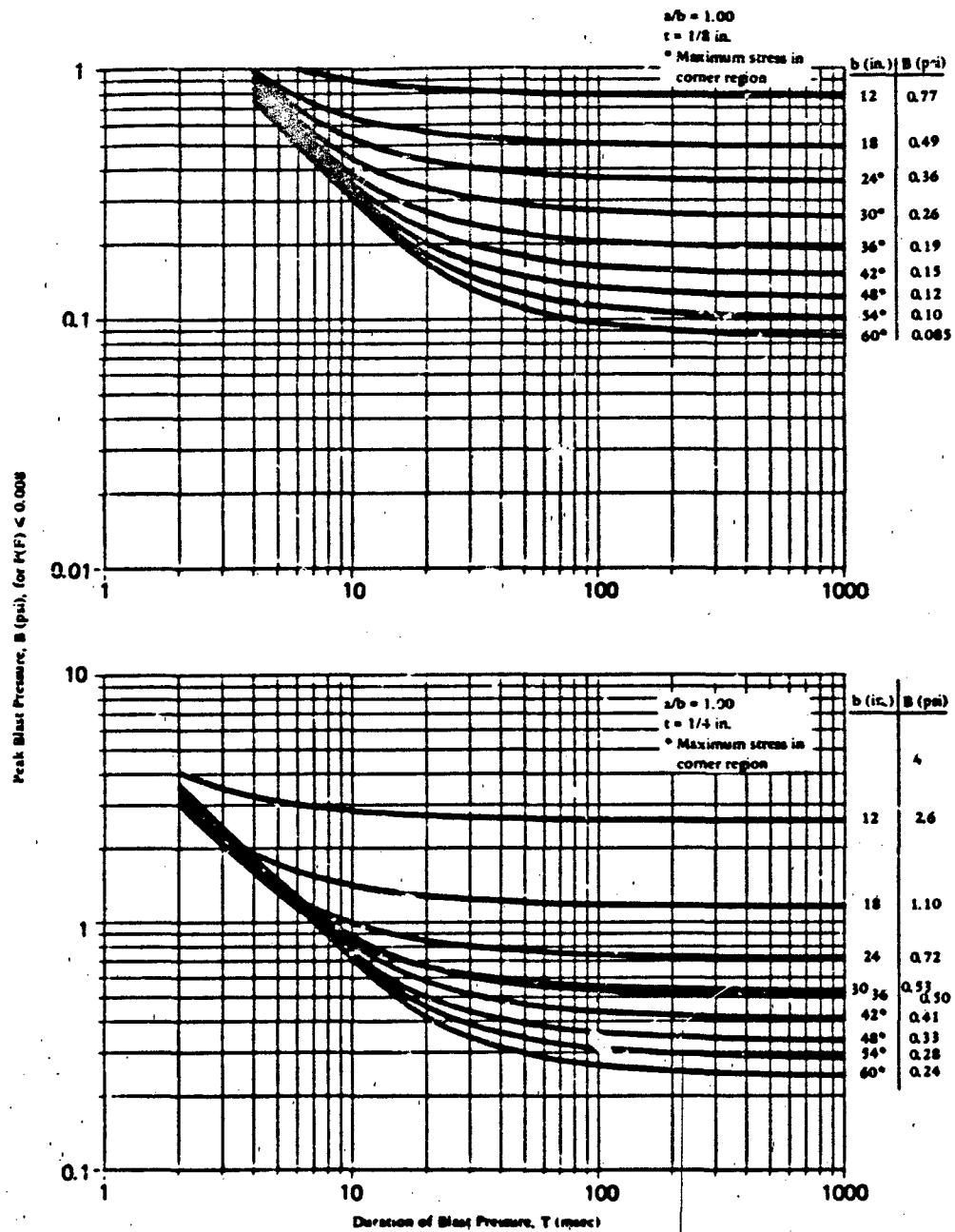


Figure 12. Peak blast pressure capacity for annealed glass panes:  $a/b = 1.00$ ,  $t = 1/8$  and  $1/4$  in.

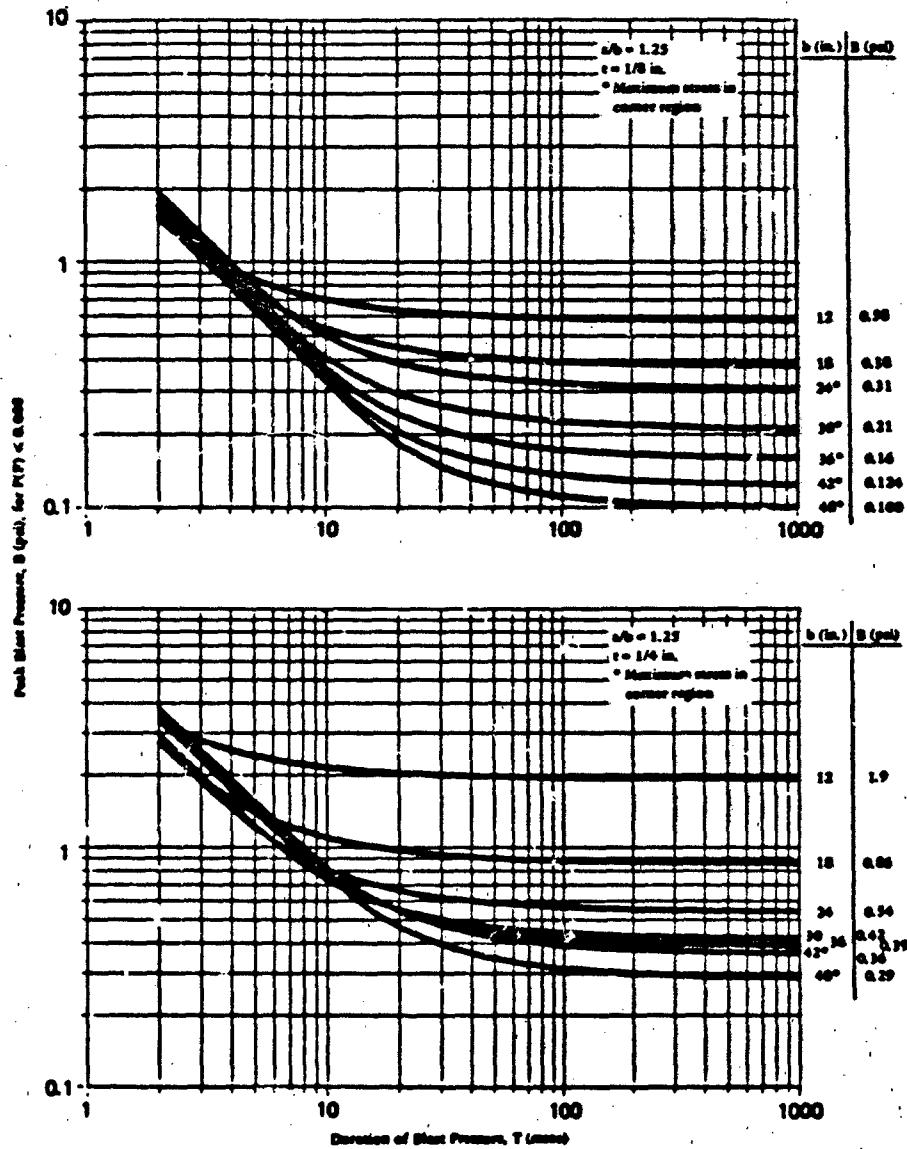


Figure 13. Peak blast pressure capacity for annular glass panes:  $a/b = 1.25$ ,  $t = 1/8$  and  $1/4$  in.

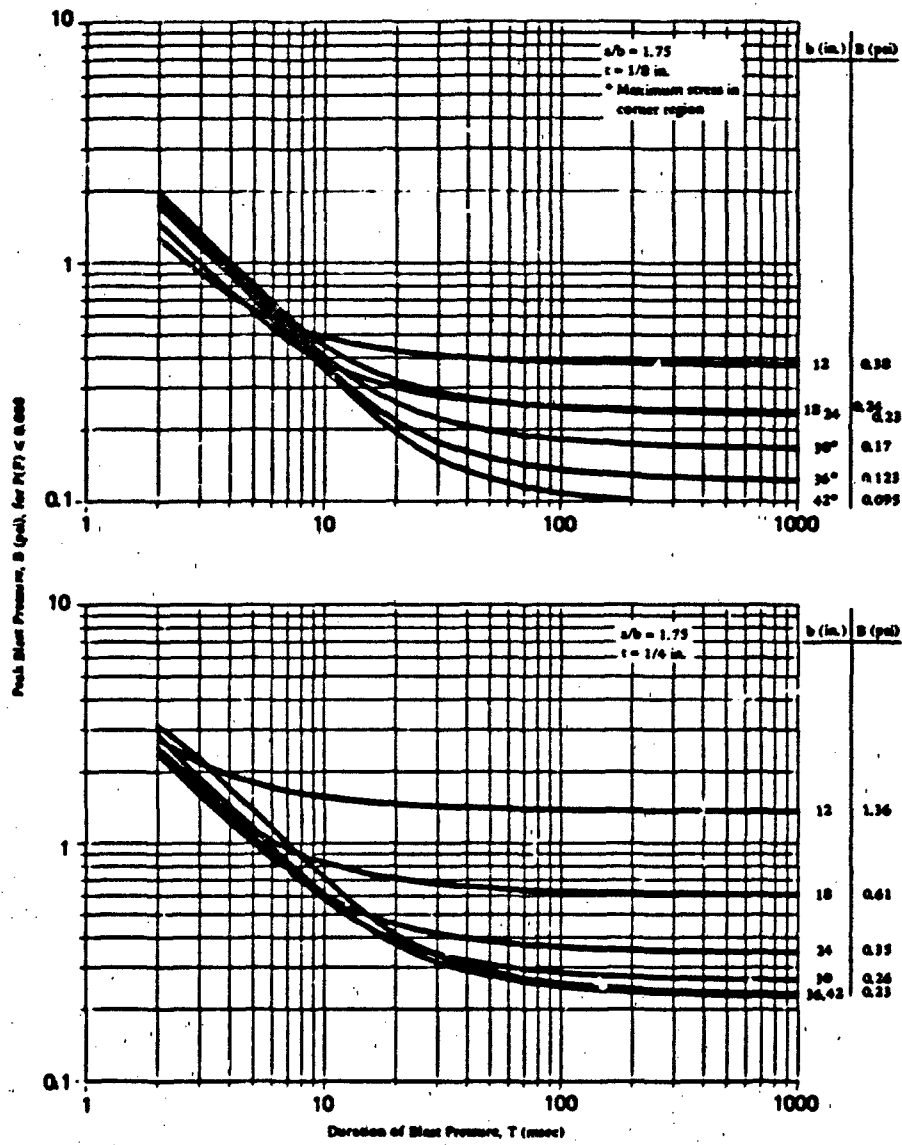


Figure 15. Peak blast pressure capacity for annealed glass panes:  $a/b = 1.75$ ,  $t = 1/8$  and  $1/4$  in.

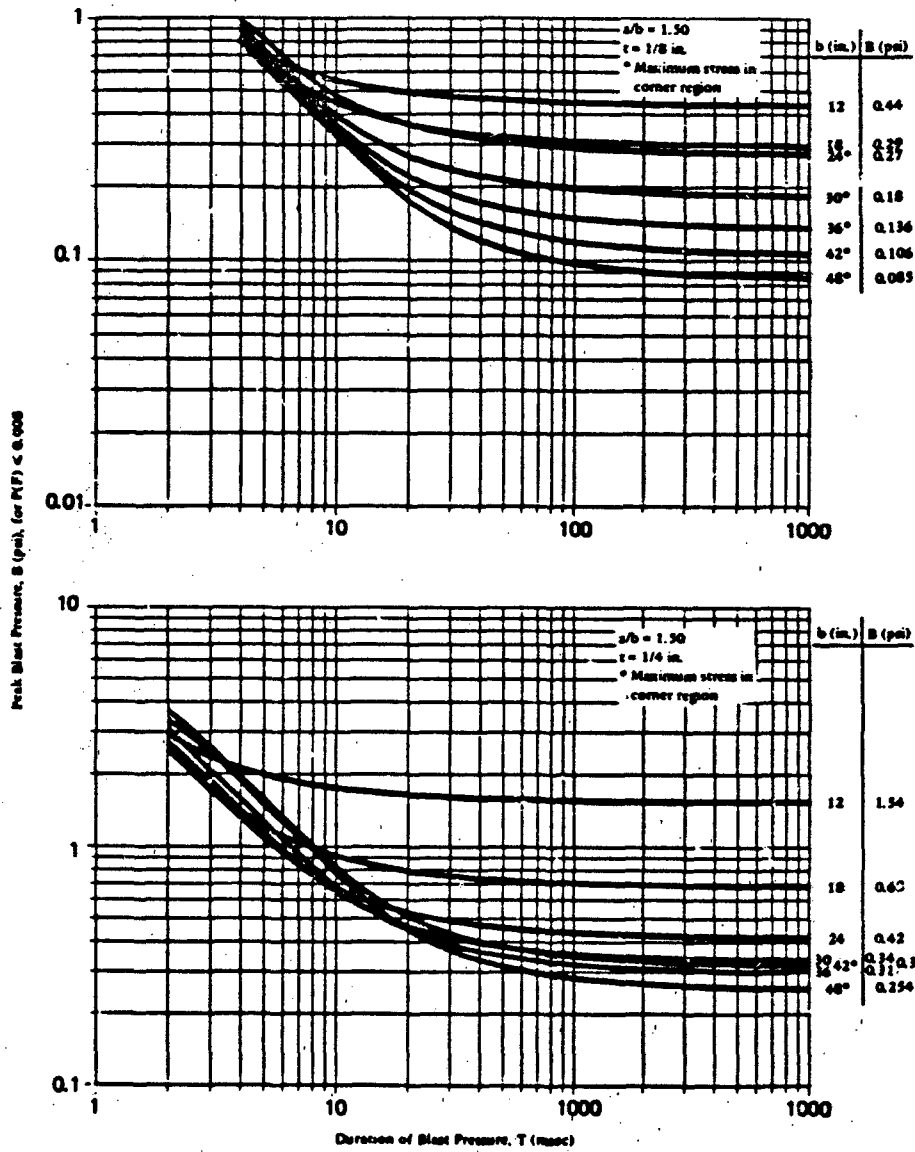


Figure 14. Peak blast pressure capacity for annealed glass panes:  $a/b = 1.50$ ,  $t = 1/8$  and  $1/4$  in.

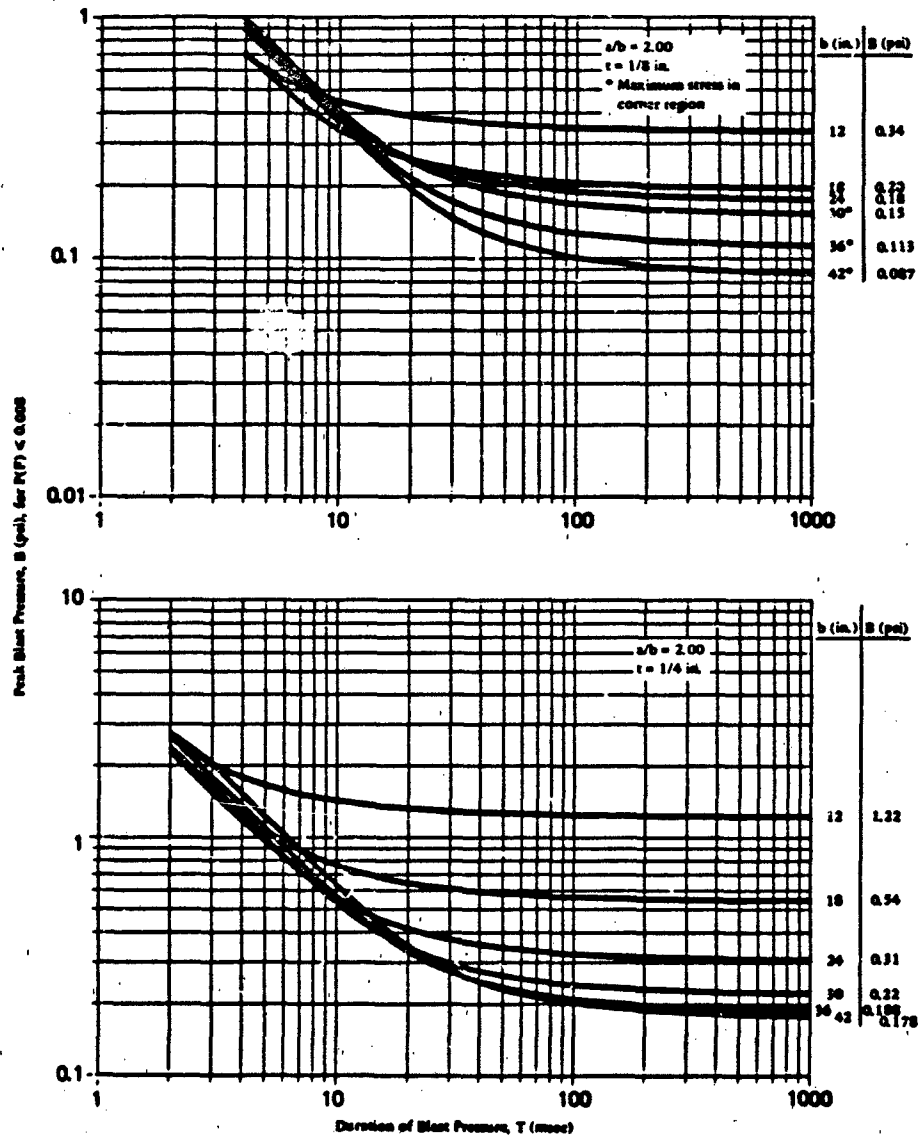


Figure 16. Peak blast pressure capacity for annealed glass panes:  $a/b = 2.00$ ,  $t = 1/8$  and  $1/4$  in.

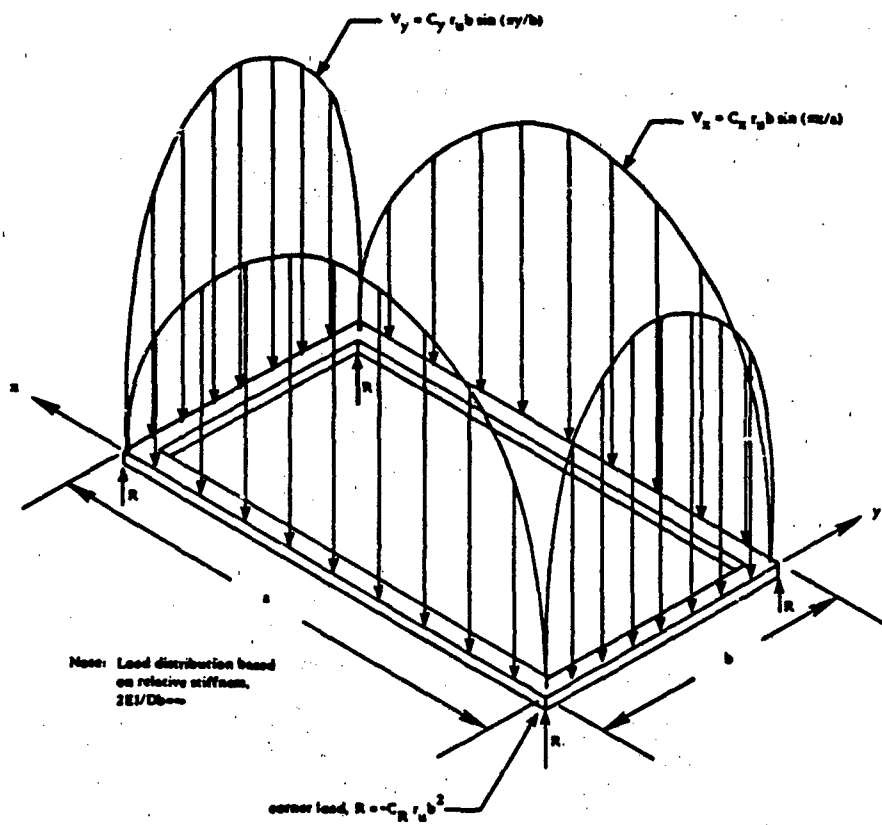


Figure 17. Distribution of lateral load transmitted by glass pane to the window frame.

## DISCUSSION

Mr. Bahn (Martin Marietta): We deal with a lot of electro-optical systems with silicon windows and the like. Do you intend to include criteria for the use of opaque type glass?

Mr. Meyers: Are you designing aircraft windows?

Mr. Bahn: No. These are electro-optical systems, operating on different wave lengths, and I wondered what you had included in your inventory of glass?

Mr. Meyers: We have dealt solely with monolithic tempered glass. We are tending to go to a laminated glass. It is a more difficult type of glass to design because the interlaminar material is viscoelastic. It behaves differently at different temperatures, and we are not quite sure how it will transfer shear between the interlaminar panes of glass. We don't think it will act as a monolithic plate.

Mr. Bahn: How about the details of the different types of glass? I am thinking specifically of a couple of proposals to the Navy concerning electro-optical systems. That is kind of a primary concern to operate at sea under a close range missile blast.

Mr. Meyers: These windows are primarily for large buildings that are being built closer and closer to sources of conventional explosions. So, we basically address this particular criteria to what would be the most economical glass.

Mr. Bahn: Are you concerned with commercial type glass?

Mr. Meyers: Yes.

Mr. Bahn: I would like to suggest that you expand your criteria to cover glass for electro-optical systems.

Mr. Coulter (U.S. Army Ballistic Research Lab): Yes. That sounds like a very good area. Perhaps you could expand your criteria into it. There is obviously a need for it.